A Data Driven Approach to Process & Product Simulations of Coffee Roasting

A thesis by

Mark Al-Shemmeri

A thesis submitted to the
University of Birmingham
for the degree of
DOCTOR OF ENGINEERING

Formulation Engineering
School of Chemical Engineering
College of Engineering and Physical Sciences
University of Birmingham
July 2024

Abstract

Coffee roasting is an intersection of engineering, physics, chemistry, sensory, discipline and creativity. To truly master the artistry, the fundamentals must be learned. This thesis provides an engineer's perspective of the art of roasting, whereby the architecture of a data-driven approach to simulations of heat and mass transfer is presented, with the intention of developing a coffee roaster's digital twin.

Process equipment and applied roasting conditions were appropriately characterised to convert arbitrary set-points to values that enable cross-comparison of roasters and their viable process conditions. The effect of thermocouple diameter on temperature measurement was defined both from a first-principles approach and a convenient, rapid analysis of the thermocouple's response time, demonstrating that the thermocouple response coefficient can be coupled with the later described heat transfer simulations to predict the bean's actual temperature and further support cross-comparison of process conditions across roaster design and scale.

Measurement techniques that characterise coffee's relevant physicochemical properties were developed in the context of heat and mass transfer. These measurements facilitate quantification of coffee's transformation during roasting, thus revealing the effect of process conditions on coffee's physicochemical development. The effect of different constant inlet air temperatures, as well as different batch sizes and airflows on a Kenyan Arabica coffee was captured, with a focus on the novel use of x-ray Micro-Computed Tomography (MicroCT) to enumerate coffee's porous development during roasting. The effect of thermocouple diameter on in-situ measurement of coffee's temperature response was analysed experimentally and aligned with the first-principles approach.

Studies of particle motion in different roasters was mapped using Positron Emission Particle Tracking (PEPT) and revealed the impact of process parameters and product properties on the system's particle dynamics. In both the spouted bed and rotating drum roasters, the emergence of two distinct regions of occupancy and velocity was found. These regional dif-

ferences in particle motion have a profound effect on the heat transfer rates and so extracted velocities and residence times were used to instruct dynamic boundary conditions in the later described heat and mass transfer simulations.

The physicochemical development of coffee during roasting was modelled using a chemical reaction analogy. In this way, the complex confluence of physics and chemistry was lumped into simplified Arrhenius-type kinetics. The evolution of mass, moisture, density, volume and porosity were effectively modelled using n^{th} order reaction kinetics, with the models of mass and moisture used as subroutines in the later described simulations of heat and mass transfer.

A batch-scale, zero-dimensional simulation of heat and mass transfer in a spouted bed roaster was formulated via energy balance. The simulation was rigorously calibrated using empirically derived process and product data, kinetic models of mass and moisture and a global heat transfer coefficient. A bean-scale, three-dimensional simulation of heat and mass transfer in a spouted bed roaster was also formulated via energy balance. In addition to being calibrated with empirically derived process and product data, the coffee's real particle motion (velocity and residence time) was used to estimate the regional heat transfer coefficients and instructed the time-step of the simulation. Both the batch-scale and bean-scale simulations of coffee roasting time-temperature profiles and corresponding physicochemical were effective and enable the development of a digital model of a coffee roaster with real-system accuracy.

Acknowledgements

Every line of code, every turn of phrase, every second guess, every other day. A little tired, a little too intense, too many variables, too few constants. Worked more than I slept, drank more coffee than I should. It *will* eventually make sense. The studies went well, the patterns I found, too many ideas, too many to list. The lunch meal-deals, the EngD workbench, the coffee routines, those are memories of friends. It *eventually* all makes sense. The patience, the learning, the strive for completion. The rewording and rewriting, and then realising, I actually preferred the first iteration. The love, the support, the friendships and thought, the time I eventually got it to work. The posters, the papers, the conferences and talks. The need to run before I could walk. There's beauty at least, between pretend and profound, yet in the end, my thesis is bound. There's always more, to do and be done, but here it is, at least it's been fun.

There were numerous role models, endless support, words of wisdom and lessons learned. This is for everyone who helped to make, 5 years full of memories and keepsakes.

To my ever patient and loving partner Dulce and the next chapter of our life with little Daniela.

Contents

List of Figures

List of Tables

Nomenclature

Symbols corresponding to bean properties

Property	Symbol	Units
bean volume	V_b	mm^3
bean porosity	γ	%
bean moisture	X_b	kg kg^{-1}
bean density	ρ_b	kg m^{-3}
bean intrinsic density	ρ_b	kg m^{-3}
bean packing density	N_b	kg^{-1}
bean thermal conductivity	k_b	W m^{-1} K^{-1}
bean specific heat capacity	$C_{p,b}$	J kg^{-1} K^{-1}
bean thermal diffusivity	D_b	mm^2 s^{-1}
bean surface area	$A_{s,b}$	mm^2
bean principal dimensions	a, b, c	mm
bean sphericity	ψ_b	

Symbols corresponding to air

Property	Symbol	Units
air thermal conductivity	k_a	W m^{-1} K^{-1}
air specific heat capacity	$C_{p,a}$	J kg^{-1} K^{-1}
air viscosity	μ_a	Pa s
air temperature	T_a	K
air density	ρ_a	kg m^{-3}
air mass flow rate	G_a	kg s^{-1}
air velocity	u_a	m s^{-1}
air flow setting	f	Hz, %
air volumetric flow rate	V_a	m^3 s^{-1}
air pressure	P_a	Pa
air gas constant	R_a	J kg^{-1} K^{-1}

Symbols corresponding to coffee properties

Property	**Symbol**	**Units**
coffee water activity	a_w	
coffee mass loss	M_{loss}	%
coffee batch size (mass basis)	m_{bs}	g
coffee batch mass	M	kg
green coffee batch mass	M_0	kg
coffee dry matter batch size (mass basis)	m_{db}	kg
coffee colour (whole bean)	c_w	
coffee colour (ground)	c_g	
coffee density via calipers	$\rho_{w,c}$	kg m^{-3}
coffee free-flow bulk density	ρ_{bulk}	kg m^{-3}
coffee density via pycnometry	$\rho_{w,p}$	kg m^{-3}
coffee density (whole bean)	ρ_w	kg m^{-3})
coffee density (ground)	ρ_g	kg m^{-3}
coffee porosity via microCT	γ_{CT}	%)
coffee porosity via pycnometry	γ_p	%
coffee median particle size	x_{50}	μm
coffee percentage Gas Type Void Volume	$\%GTVV$	%
coffee's thermal diffusivity	κ_b	m^2 s^{-1}
coffee emissivity	ε	

Symbols relevant to non-coffee materials

Property	**Symbol**	**Units**
water specific heat capacity	$C_{p,w}$	J kg^{-1} K^{-1}
solid matter specific heat capacity	$C_{p,s}$	J kg^{-1} K^{-1}

Symbols corresponding to dimensionless numbers

Property	**Symbol**	**Units**
Nusselt number	Nu	
Reynolds Number	Re	
Reynolds number in the bean-bed	Re_{BB}	
Reynolds number in the freeboard	Re_{FB}	
Froude number	Fr	
Biot number	Bi	
Prandtl number	Pr	
dimensionless intrinsic property	Y	

Symbols corresponding to temperature measurements

Property	**Symbol**	**Units**
temperature	T	K
temperature set-point	T_{set}	°C
inlet air temperature	$T_{a,i}$	°C
steady-state product temperature	$T_{s,s}$	°C
bean temperature	T_b	K
outlet air temperature	$T_{a,o}$	K
roaster's metal temperature	T_m	K
initial thermocouple temperature	$T_{T,0}$	K
initial bean temperature	$T_{b,0}$	K
surrounding temperature	T_s	K

Symbols corresponding to the roaster

Property	**Symbol**	**Units**
pipe diameter	d_p	m
pipe cross-sectional area	A_p	m^2
roasting chamber radius	R	m
roasting chamber diameter	R_d	m
total energy consumption	ε	kWh

Symbols corresponding to time

Property	**Symbol**	**Units**
time	t	s
roasting end time	t_{end}	s
time at first crack	t_{FC}	s
time-step	Δt	
simulation end time	t_∞	s

Symbols relevant to coffee bean motion

Property	**Symbol**	**Units**
occupied area	A_o	cm^2
number of non-zero elements	n_{nze}	
elemental area	A_e	cm^2
bean bed area	$A_b b$	cm^2
Bean Bed Mass Fraction	$BBMF$	kg kg^{-1}
angular velocity	ω	s^{-1}
gravitational acceleration	g	m s^{-2}
particle radius	r	m

Symbols relevant to kinetic modelling

Property	**Symbol**	**Units**
reaction rate	k_Y	s^{-1}
activation energy	E	J mol^{-1}
universal gas constant	R	J mol^{-1} K^{-1}
reaction order index	n_Y	
modified activation energy	$E_{a,Y}$	K
mass rate constant (first order)	$k_{m_{bs}}$	s^{-1}
mass activation energy	$E_{a,m_{bs}}$	K
moisture rate constant	k_{X_b}	s^{-1}
moisture activation energy	E_{a,X_b}	K
density rate constant	k_{ρ_b}	kg^{-1} m^3 s^{-1}
density activation energy	E_{ρ_b}	K
volume rate constant	k_{V_b}	s^{-1}
volume activation energy	E_{a,V_b}	K
porosity rate constant	k_{γ_b}	s^{-1}
porosity activation energy	E_{a,γ_b}	K

Symbols relevant to discretisation

Property	**Symbol**	**Units**
number of elements	N_e	
mesh's maximum element size	h	mm
spatial scaling factor	ε_s	
temporal scaling factor	ε_t	
simulation error	ϵ	°C

Symbols corresponding to heat transfer & thermal energy

Property	**Symbol**	**Units**
total heat flux	q_{total}	W
convective heat flux	q_{conv}	W
conductive heat flux	q_{cond}	W
transient energy flux into unit volume of the bean	q_b	W m^{-3}
conductive heat flux into unit volume of the bean	q_{cd}	W m^{-3}
endothermic heat flux into unit volume of the bean	q_e	W m^{-3}
exothermic heat flux out of unit volume of the bean	q_r	W m^{-3}
endothermic cooling occurring at the bean surface	$q_{e,s}$	W m^{-3}
radiant power of exothermic reactions	q_{exo}	W
convective heat flux	j_{cv}	W m^{-2}
heat transfer into the bean	Q_b	W
air-to-bean heat transfer	Q_{ab}	W
air-to-metal heat transfer	Q_{am}	W
metal-to-bean heat transfer	Q_{mb}	W
exothermic heat generation	Q_r	W
evaporative cooling	Q_e	W
air-to-bean heat transfer coefficient	h_{ab}	W m^{-2} K^{-1}
air-to-metal heat transfer coefficient	h_{am}	W m^{-2} K^{-1}
metal-to-bean heat transfer coefficient	h_{mb}	W m^{-2} K^{-1}
air-to-thermocouple heat transfer coefficient	h_{at}	W m^{-2} K^{-1}
overall air-to-thermocouple heat transfer coefficient	U_t	W m^{-2} K^{-1}
modified heat transfer coefficient	α_{ab}	W m^{-2} K^{-1}
specific enthalpy of reaction	ΔH_r	J kg^{-1}
specific enthalpy of vaporisation of water	ΔH_v	J kg^{-1}
heat transfer effectiveness factor	η_A	
Stefan Boltzmann constant	σ	W m^{-2} K^{-4}
air-to-bean heat transfer area	A_{ab}	m^2
air-to-metal heat transfer area	A_{am}	m^2
metal-to-bean heat transfer area	A_{mb}	m^2

Symbols corresponding to thermocouples

Property	**Symbol**	**Units**
thermocouple radius	r_t	m
thermocouple diameter	d_T	m
thermocouple characteristic length	L_t	m
thermocouple exposed length	$L_{t,e}$	m
thermocouple cross-sectional area	$A_{c,t}$	m^2
thermocouple surface area	$A_{s,t}$	mm^2
thermocouple total heat transfer area	A_t	mm^2
thermocouple temperature	T_T	K
thermocouple surface temperature	$T_{t,s}$	K
thermocouple core temperature	$T_{t,c}$	K
thermocouple mass	m_t	kg
thermocouple specific heat capacity	$C_{p,t}$	J kg^{-1} K^{-1}
thermocouple effective thermal conductivity	$k_{t,e}$	W m^{-1} K^{-1}
thermocouple thermal resistance	R_t	m^2 K W^{-1}
thermocouple sheath radius	$r_{t,s}$	m
thermocouple sheath thermal conductivity	$k_{t,s}$	W m^{-1} K^{-1}
thermocouple insulation radius	$r_{t,i}$	m
thermocouple insulation thermal conductivity	$k_{t,i}$	W m^{-1} K^{-1}
thermocouple junction radius	$r_{t,j}$	m
thermocouple junction thermal conductivity	$k_{t,j}$	W m^{-1} K^{-1}
thermocouple time constant	τ	s^{-1}
thermocouple time constant from first principles	τ_{fp}	s^{-1}
thermocouple response coefficient	K	s^{-1}
thermocouple response coefficient via model system	K_e	s^{-1}
thermocouple response coefficient via first principles	K_{fp}	s^{-1}

Aims & Objectives

Coffee roasting is a heat treatment process wherein green coffee is transformed via application of specific time-temperature roasting profiles. The physicochemical transformations that occur during coffee roasting are numerous and inter-related. Whilst many attempts to observe, detail and predict process kinetics have been made, it is difficult to validate findings due to the diversity of process technology, process conditions and variability of green coffee.

As technology advances, so must our comprehension of the process. With product and process sensors it is possible to quantify relevant physicochemical properties and process parameters. Although analytical, off-line measurements are common place, interpretation of data and subsequent implementation of knowledge to industrial practices is the limiting factor. Therefore, there is a need to connect raw material variability and process variance with appropriate measurement techniques that both feed-back and feed-forward product and process data to inform real-time, ad-hoc adjustments of process conditions. Inevitably, these well-connected systems will rely on big-data approaches that are guided by calibrated physics-driven models of process behaviour and are implemented within the existing logic controllers and thus be fully autonomous.

To accurately predict coffee's physicochemical transformation during roasting, the typical approach is a composite of (i) a series of assumptions about the product and process, (ii) knowledge and data harvested from existing literature or, (iii) comprehensive, empirically derived, analytical data generated from extensive roasting trials. Whilst each approach has merit, it is the latter that will enable accurate simulations to be developed. The level of detail that is required from models dictates the approach needed for their design and creation. Furthermore, the various approaches seen in existing studies are often compartmentalised, constrained by limited resources. Whilst the rigorous calibration of a physics-driven model is costly in terms of both time and money, well-calibrated digital models can provide product and process developers with a reference tool (i.e., a starting point) that could be further developed to construct digital shadows and twins.

The studies herein detail a methodical, data-driven approach to develop a series of calibrated simulations that can collectively be assembled to form a digital twin of a coffee roaster. Investigations begin with the characterisation of the coffee roasting process and its relevant process parameters. Time-forgotten optimisation studies tend to manifest as process strategies with arbitrary set points. Through systematic evaluation of process parameters and their effect on time-temperature profiles and coffee's transient properties, coffee's kinetic behaviour during roasting can be established. These kinetics can then be modelled using chemical reaction analogies to simplify the physical and chemical behaviour and nested within more complex heat and mass transfer simulations.

Heat transfer phenomena in roasters are governed by the particle dynamics, which in turn are influenced by the applied process parameters. As the product transforms during roasting, particle motion evolves. Using advanced process analytics, the particle motion in coffee roasters can be mapped and leveraged to instruct heat transfer rates during roasting. A thermal balance can be formulated to determine these heat and mass transfer rates during roasting. Through conjugation of models describing coffee's physicochemical transformation, particle motion data and multi-scale heat transfer simulations, prediction of coffee's time-temperature profile and corresponding physicochemical development can be achieved with real-system accuracy.

Coffee roasting is often considered a black box, a combination of art and science. Whilst many of the approaches to coffee roasting can be shaped by the developer, coffee's physicochemical transformation during roasting is a product of the green coffee's agronomy, the roaster's engineering and the physics of heat transfer. Therefore, by using a data-driven approach to formulate, calibrate and validate a digital model of a coffee roaster, the engineering understanding of coffee roasting can be improved.

Relevance to Industry

JDE Peet's is a coffee company with a long history and global presence, marketing brands such as Kenco, Jacobs, Douwe Egberts, L'OR, Tassimo and Senseo across multiple formats (whole beans, roast and ground, pads, capsules and soluble). In 2022, JDE Peet's generated €8.2 billion in total sales, corresponding to 132 billion cups of coffee. Every gram of coffee in those cups is roasted at one of the 43 facilities across 24 countries.

For JDE Peet's, the roasting process is key to flavour development but is also a focus area for reduction of green house gas emissions and mitigation of acrylamide in the final product. JDE Peet's look to develop digital models that virtualise the roasting process and enable process and product development *in-silico*. Through digitalisation, the roasting conditions can be optimised for flavour, energy, acrylamide and roast yield; through automation, digital twins can be implemented into existing logic controllers to minimise process variance and consistently maximise yield.

A coffee roasting digital twin can provide JDE Peet's with fundamental process and product insights that can be leveraged to inform the importance of green coffee sourcing and screening of coffee's phyiscochemical and sensorial properties, as well as the impact of green coffee variability, equipment design and process parameters on coffee's physicochemical and sensorial development during roasting. Once the connection between thermal, physical, chemical and sensorial properties is forged, the digital twin could be used to (i) get the best from each and every bean, obtaining the coffee's full flavour potential, whilst (ii) mitigating acrylamide and being compliant with EU regulations and, (iii) minimising roast losses and energy requirements to conform with the company's sustainability efforts.

Publications & Outreach

List of Publications

Al-Shemmeri, M., Windows-Yule, K., Lopez-Quiroga, E. & Fryer, P. (2021) Coffee bean particle motion in a spouted bed measured using Positron Emission Particle Tracking (PEPT). Journal of Food Engineering 311, 110709. DOI:10.1016/j.jfoodeng.2021.110709.

Al-Shemmeri, M., Lopez-Quiroga, E. & Fryer, P. (2022) Simulation of coffee roasting time-temperature profiles. In Proceedings of 12th International Conference on Simulation and Modelling in the Food and Bio-Industry (FOODSIM). Ghent (Belgium). EUROSIS-ETI.

Che, H., Al-Shemmeri, M., Fryer, P., Lopez-Quiroga, E., Kokalova Wheldon, T. & Windows-Yule, K. (2023) PEPT validated CFD-DEM model of aspherical particle motion in a spouted bed. Chemical Engineering Journal, 453(1). DOI:10.1016/j.cej.2022.139689.

Al-Shemmeri, M., Windows-Yule, K., Lopez-Quiroga, E. & Fryer, P. (2023) Coffee bean particle motion in a rotating drum measured using Positron Emission Particle Tracking (PEPT). Food Research International (163). DOI:10.1016/j.foodres.2022.112253.

Al-Shemmeri, M., Lopez-Quiroga, E. Farr, R. & Fryer, P. (2024) Development of coffee bean porosity and thermophysical properties during roasting. Journal of Food Engineering 378, 112096. DOI:10.1016/j.jfoodeng.2024.112096.

List of Conferences

28th ASIC Conference on Coffee Science (2021) Coffee bean particle motion: implications for heat transfer during roasting. Talk - Online.

Institute of Food Technologists (IFT) first: Annual Event and Expo (2021) Using Positron Emission Particle Tracking (PEPT) to study the particle dynamics of a spouted bed coffee roaster. Poster - Online.

35th European Federation of Food Science and Technology (EFFoST) International Confer-

ence (2021) Positron Emission Particle Tracking (PEPT) as a tool to study particle dynamics of a spouted bed coffee roaster. Poster.

Institute of Physics (IoP) Food Physics (2022) Positron Emission Particle Tracking (PEPT) as a Tool to Study Particle Dynamics in a Rotating Drum Coffee Roaster. Poster - Online. Won Best Poster Prize.

12th International Conference on Simulation and Modelling in the Food and Bio-Industry: FoodSim (Eurosis) (2022) Simulation of Coffee Roasting Time-Temperature Profiles. Talk & Extended paper - Ghent, BE.

Institute of Food Technologists (IFT) first: Annual Event and Expo (2022) Particle Dynamics of Coffee Beans in a Drum Roaster Measured Using Positron Emission Particle Tracking (PEPT). Poster & Talk - Chicago, USA. Won Food Engineering Division Student Oral Competition.

15th World Congress on Computational Mechanics (WCCM) (2022) Regional Heat Transfer in Coffee Roasters Determined via PEPT Validated DEM & CFD-DEM Simulations of Coffee Bean Particle Motion. Talk - Online.

15th Conference of Food Engineering (CoFE) (2022) A heat and mass transfer model of coffee roasting in spouted beds. Talk - Raleigh, USA.

36th European Federation of Food Science and Technology (EFFoST) International Conference (2022) A multidimensional heat and mass transfer study of coffee roasting in spouted bed roasters. Talk - Dublin, UK.

Thesis Layout

List of Chapters

- Preface
- Chapter 1 Introduction to coffee & coffee roasting
- Chapter 2 Characterisation of a Coffee Roaster
- Chapter 3 Coffee's Physicochemical Transformation during Roasting
- Chapter 4 Coffee bean particle motion in pilot-scale roasters measured using Positron Emission Particle Tracking (PEPT)
- Chapter 5 Modelling Coffee's Physicochemical Transformation during Roasting
- Chapter 6 Batch-Scale Simulations of Heat and Mass Transfer during Roasting
- Chapter 7 Bean-Scale Simulations of Heat and Mass Transfer during Roasting
- Chapter 8 Conclusions & Future Work

An Overview of Each Chapter

The Preface provides an overview of the commercial relevance, objectives and layout of thesis, as well as the publications that have been generated from material herein.

Chapter 1 establishes context for the thesis, briefly detailing coffee's production from farm to cup, with emphasis on the coffee roasting process. Methods to characterise roasting machines, including those to monitor and control the relevant process parameters, are then introduced to guide readers toward the compilation of experimental and modelling studies of coffee's physicochemical transformation during roasting. Recent approaches to simulations of heat and mass transfer during roasting are then presented, outlining how these relate to process measurements of time-temperature roasting profiles.

Chapter 2 presents the characteristics of different lab-scale and pilot-scale roasters. Their feasible operating range is mapped out to guide product and process developers and to provide readers with the methods used to monitor, control and specify the roasting process as it relates to the experimental studies detailed in Chapters 3 and 4. An experimental and modelling study is also given to demonstrate the difficulty of process characterisation due to temperature measurements and their reliance on thermocouples and their thermophysical properties.

Chapter 3 investigates the effect of process parameters on coffee's physicochemical transformation during roasting in a spouted bed roaster. In this chapter, methods to characterise green, part-roasted and roasted coffee are presented alongside four cases studies that implement these characterisation methods. In these studies, the effects of inlet air temperature, batch size and airflow on roasting performance are studied using a Kenyan Arabica coffee, whilst the effect of thermocouple diameter on temperature measurement is explained. To indicate the viability of x-ray tomography and its application to coffee, porosity development during roasting is studied in detail, such that correlations of physicochemical properties are generated for integration with subsequent models and simulations. These studies therefore outline the:

I variation of constant inlet air temperature and its effect on roasting performance

II variation of batch size and airflow and its effect on roasting performance

III evolution of coffee porosity and its influence on coffee's thermophysical properties

IV effect of thermocouple diameter on temperature measurement

Chapter 4 examines the particle motion of coffee beans within pilot-scale roasters. The effects of process parameters and coffee properties on granular flow fields were mapped with Positron Emission Particle Tracking (PEPT) for a spouted bed and a rotating drum roaster. Changes in the regional particle dynamics observed in this chapter imply significant, regional variation of the heat transfer coefficient within the roasting chamber, such that these data

can inform developers of best strategies for process control, and also be coupled with heat and mass transfer simulations that are set out in Chapters 6 and 7.

Chapter 5 outlines the modelling approach used to describe coffee's physicochemical transformation during roasting. Using the chemical reaction analogy, kinetic models are developed based on data presented in Chapter 3, wherein changes in coffee's mass, moisture, volume, density and porosity during roasting were demonstrated. The generation of exothermic reactions in the final moments of roasting are examined empirically, with the aim of providing developers insight regarding the control of coffee's roasting development. These kinetic models drive the physics of the heat and mass transfer simulations formulated in Chapters 6 and 7.

Chapter 6 develops a simulation of heat and mass transfer at the batch-scale using experimental time-temperature roasting profiles generated in Chapter 3 for calibration, in conjunction with the roaster's characteristics determined in Chapter 2 and the kinetic models outlined in Chapter 5. The case studies of Chapter 3 provide data that not only calibrate the simulation, but also illustrate that the prescribed simulation methods can successfully match the temperature response of coffee roasted under a wide-range of process conditions.

Chapter 7 reports a single-bean simulation of heat and mass transfer at the bean-scale using experimental particle motion data captured in Chapter 4. These particle motion data inform the boundary conditions of the simulation, whereby the convective heat transfer coefficient is dependent on the bean's location in the roaster. Experimental data from Chapter 3 provide the initial conditions for the simulation, whilst the kinetic models of coffee's physicochemical transformation of Chapter 5 and batch-scale time-temperature profile simulations of Chapter 6 are integrated here for a cohesive calibration.

Chapter 8 closes the thesis with a summary of the work to date, an outlook on coffee roasting fundamentals and an insight regarding future studies of coffee roasting technologies.

Chapter One

Introduction to coffee & coffee roasting

During coffee roasting, a complex series of physical and chemical changes generate the coffee's signature flavour and aroma. As technology advances, the need for quantitative comprehension of product and process becomes more integral to product quality, operating costs and consumer acceptance. Predictive tools are at the forefront of developing the roaster's knowledge, yet factors of roaster design, process conditions, green coffee variability and analytical measurements must be addressed. This Chapter reviews coffee as a raw material, the roasting process, empirical roasting studies, investigations of particle and fluid motion and modelling approaches that enable prediction of the thermal and physicochemical development of coffee during roasting. This review offers a succinct outlook of coffee and the roasting process, how to measure and define the product and process and, most importantly, provides the tools and background knowledge to (successfully) simulate coffee roasting *in-silico*.

1.1 Coffee as a raw material

Coffee is an agricultural commodity produced in tropical and sub-tropical countries across the Americas, Africa and Asia. Producing countries with the most predominant yields include Brazil, Vietnam, Colombia, Indonesia and Ethiopia; Figure 1.1 shows the predominant coffee growing regions (ICO, 2023).

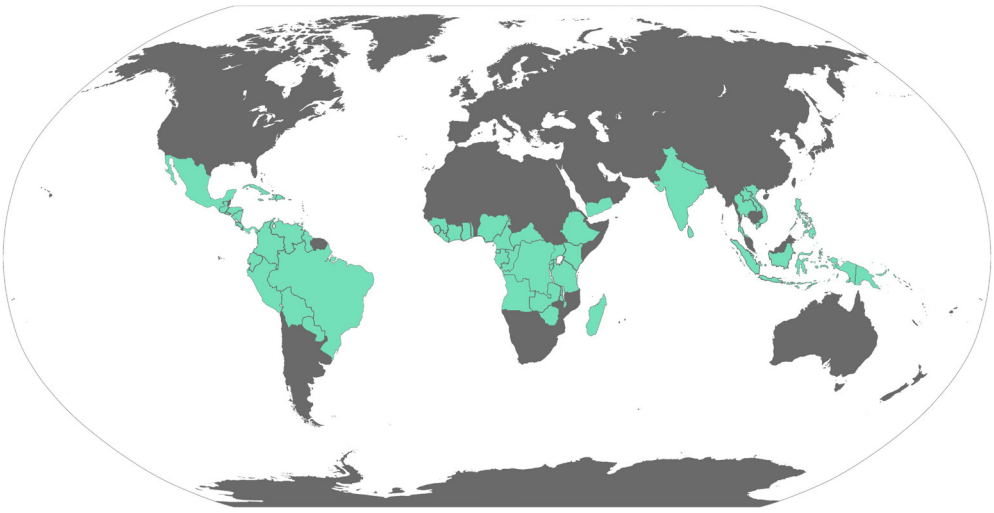

Figure 1.1: Illustration of coffee producing countries - highlight in green - adapted from Wikipedia with data from ICO (2023)

1.1.1 Green coffee anatomy

Green (unroasted) coffee beans are the dried seeds of fruit (or cherries) harvested from *Coffea* trees. The anatomy of coffee fruits comprises the pericarp (outer skin), mesocarp (mucilage, fruit, pulp, pectin layer), endocarp (parchment) and a thin, inner membrane (silverskin, chaff) surrounding hemi-ellipsoidal seeds – as shown in Figure 1.2 (Melo Pereira et al., 2019). In some instances, only one seed develops; these seeds, termed peaberries, are more ellipsoidal (with higher sphericities, hence the name) (Ram, Sreenivasan, and Ramaiah, 1990).

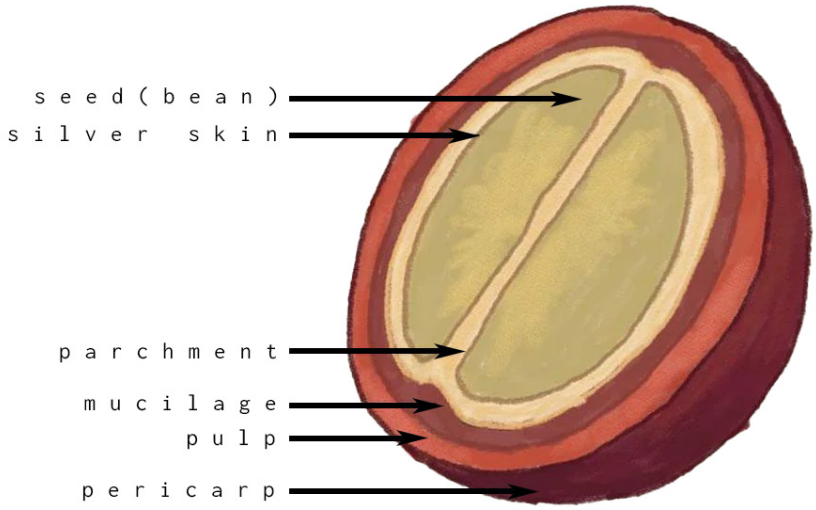

Figure 1.2: Illustration of a coffee cherry's anatomy (adapted from Green Coffee Collective (2023)).

1.1.2 Green coffee technology

Production of green coffee beans requires (i) pre-harvest processing (cultivation of seedlings, growing trees to yield fruit, harvesting fruit) and (ii) post-harvest processing (sorting of fruit, demucilagination, drying and hulling of parchment, further sorting and storage) (Farah, 2019; Pereira et al., 2021; Haile et al., 2019). Each unit operation influences in-cup flavour and aroma (Melo Pereira et al., 2019), so understanding the fundamentals is critical for optimisation of the roasting process and final product. Studies of post-harvest processing are more comprehensively and comparatively documented than those concerning pre-harvest processing due to the long time-scales (5-7 years) of coffee tree growth and shortage of labour and resources to execute research studies. For studies of post-harvest technology and their influence on in-cup flavour and aroma, readers are directed toward the academic field works of Lucas Louzada Pereira (Louzada Pereira and Rizzo Moreira, 2021), laboratory studies of Liang Wei Lee (Lee et al., 2015), as well as podcasts from Lucia Solis (Solis, 2023). Comprehensive reviews of post-harvest processing factors on coffee flavour can be found in (Melo Pereira et al., 2019; Cortés-Macías et al., 2022; Cao et al., 2023; Rotta et al., 2021). Figure 1.3 details various post-harvest processing practices that are common across both commodity and specialty producers (Olam Speciality, 2023).

1.1.3 Green coffee characteristics

Green coffee exhibits variability between species, producing region and crop year. Growing and post-harvest treatments are predominantly carried out in countries with limited access to process technology, which leads to variability between batches (Herrera and Lambot, 2017). Significant differences in size and chemical composition of Arabica and Robusta species imply that roasting these beans under identical conditions will yield a product with appreciable differences (Farah, 2019). Characterisation of the green bean's physicochemical properties aims to identify the most predominant physical transformations, alongside the most influential precursors for flavour and aroma development. Characteristics important in the context of heat and mass transfer are outlined in Tables 1.1-1.2 - relevant studies are cited. These studies are further detailed in Section 1.3.

The commercial need regarding green coffee is to understand the influence of pre- and post-harvest processing on coffee's roasting performance and eventual in-cup flavour and aroma profile. Through management of these processes in producing countries, alongside physicochemical analyses of the green coffee delivered to the roastery, developers can acquire a comprehensive overview of green coffee characteristics and thereafter enable quantification of the transformations of coffee from green to roasted.

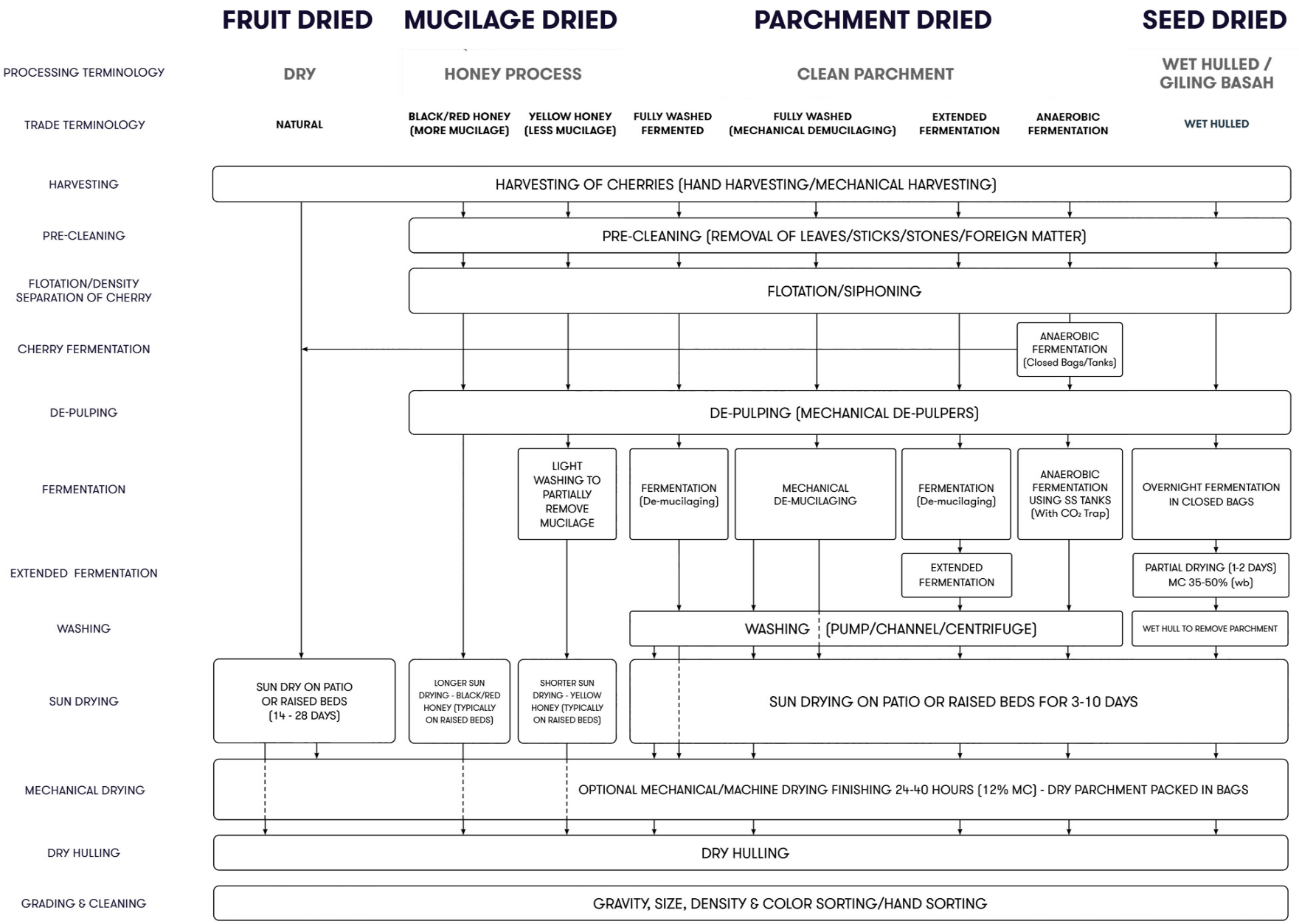

Figure 1.3: Process flow diagram detailing various post-harvest processing practices (recoloured from Olam Speciality (2023)).

Table 1.1: Green coffee characteristics that are important in the context of heat and mass transfer.

Property	**Relevance**	**Relevant Studies**
Mass & Batch Size	Affects mass loss, the required roasting process parameters (airflow, drum speed, etc.) and heat transfer rate.	(Dutra et al., 2001; Schenker, 2000; Alessandrini et al., 2008; Geiger, 2004; Vargas-Elias et al., 2016; Perrone et al., 2010; Poisson, Schmalzried, et al., 2009; X. Wang and L.-T. Lim, 2014a; N. Wang, 2012; Bustos-Vanegas et al., 2018; Baggenstoss, Poisson, et al., 2008b; Pramudita et al., 2017; Schenker and Rothgeb, 2017; Schwartzberg, 2013).
Moisture Content	This affects mass and moisture loss, the required heat transfer rate and energy requirement.	(Schwartzberg, 2002; Baggenstoss, Poisson, et al., 2008b; Bustos-Vanegas et al., 2018; X. Wang and L.-T. Lim, 2014b; G. H. H. d. Oliveira et al., 2017; Rodrigues et al., 2019; Schenker, Heinemann, et al., 2002; Chu et al., 2018; Geiger, Perren, Kuenzli, et al., 2005; Adnan et al., 2017; Tugnolo et al., 2019; Santos, Lopo, et al., 2016; Alessandrini et al., 2008; Caporaso et al., 2018; Chindapan, Soydok, and Devahastin, 2019; Geiger, 2004; N. Wang, 2012; Pramudita et al., 2017)
Principal Dimensions	Affect surface area & volume, expansion rate and heat transfer rate.	(Hernández, Heyd, and Trystram, 2008; Bustos-Vanegas et al., 2018; Fischer et al., 2001; Schenker, Handschin, et al., 2000; Geiger, 2004).
Colour	Affected by post-harvest processing practices and can indicate thermal history.	(Hernández, Heyd, and Trystram, 2008; Mendes et al., 2001; N. Wang, 2012; X. Wang and L.-T. Lim, 2014a; Pramudita et al., 2017; Bicho et al., 2014; Santos, Viegas, et al., 2016; Chu et al., 2018; Esteban-Díez, González-Sáiz, and Pizarro, 2004; Consuelo Pizarro et al., 2007; Dong et al., 2015; De Vleeschouwer et al., 2010; Fischer et al., 2001; Pittia, Dalla Rosa, and Lerici, 2001; Kim et al., 2018).

Table 1.2: Green coffee characteristics that are important in the context of heat and mass transfer.

Property	**Relevance**	**Relevant Studies**
Density	Affects batch volume, as well as the required heat transfer rate and energy requirement.	(Alessandrini et al., 2008; Romani et al., 2012; Eggers, 2001; Bustos-Vanegas et al., 2018; Geiger, 2004; Cardoso et al., 2018).
Electrical Conductivity	This reflects cellular integrity and is influenced by post-harvest processing practices.	(Ribeiro et al., 2011; Silva Araújo et al., 2020; P. D. d. Oliveira et al., 2018).
Thermal Properties	These influence the heat transfer rate and energy requirements.	(Small and Horrell, 1993; Singh et al., 1997; Pittia, Dalla Rosa, and Lerici, 2001; Eggers, Von Blittersdorf, et al., 2004; M. Rao, Rizvi, and Datta, 1994; Hammerschmidt and Abid, 2016; Fabbri, Cevoli, Alessandrini, et al., 2011; Berbert et al., 1995; Cardoso et al., 2018; Burmester and Rudolf Eggers, 2010).
Chemical Composition	Green coffee chemistry is complex, varies significantly and is affected by both pre- and post-harvest processing. Chemical composition affects development of colour, flavour and aroma during roasting.	(Ky et al., 2001; Casal et al., 2003; Alonso-Salces et al., 2009; Garrett et al., 2012; Poisson, Blank, et al., 2017).

1.2 Coffee roasting process

Coffee roasting is a heat treatment process, wherein application of specific time-temperature profiles transform the coffee's physicochemical properties and develop its characteristic flavour and aroma (Schenker, 2000; Schwartzberg, 2002; Oliveros et al., 2017).

1.2.1 Coffee's physicochemical transformation

Figure 1.4(a) presents a time-temperature profile obtained using a spouted bed roaster and Figure 1.4(b), coffee's subsequent physicochemical transformation.

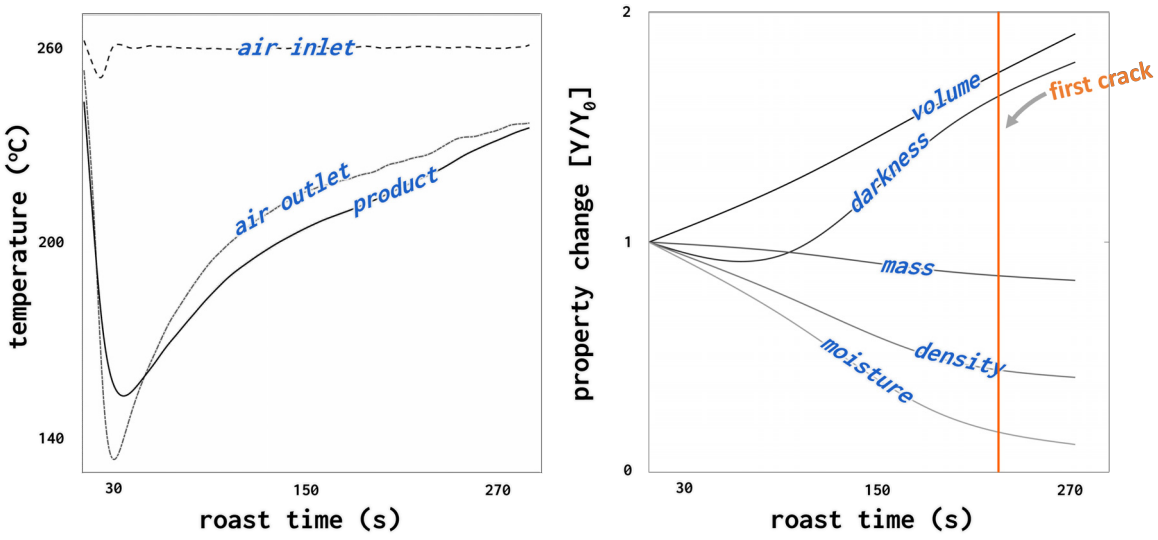

(a) Time-Temp. Profile

(b) Coffee Transformation

Figure 1.4: Example of (a) a time-temperature profile obtained by roasting under constant thermal load in a spouted bed roaster and (b) coffee's subsequent physicochemical transformation during roasting.

Coffee's physicochemical transformation begins with rapid dehydration in an endothermic drying process, with coffee gradually changing colour from pale green to yellow, see for example Schenker (2000), Geiger, Perren, Kuenzli, et al. (2005), N. Wang (2012), S. Rao (2014), and Hoos (2015). Bean temperatures exceeding 170-190°C initiate Maillard reactions, wherein coffee colour further shifts from yellow to brown (Schenker, 2000). Once the glass transition temperature is exceeded, cellular polysaccharides (cellulose, mannan and

arabinogalactan) begin to soften and become elastic (i.e., transition from glassy to rubbery states) (Geiger, 2004). Water vapour and CO_2 (a Maillard reaction by-product (X. Wang and L.-T. Lim, 2017)) in the bean's core are both attributed to increasing internal pressure (Geiger, 2004). Whilst cellular material is rubbery, this leads to rapid porosity development and subsequent volumetric expansion. Volumetric expansion culminates in a structural failure that coincides with an audible 'crack' – a process indicator termed 'first crack' (Schenker, 2000; Geiger, 2004; S. Rao, 2014; Wilson, 2014). After first crack, cellular pressure decreases and constituent polysaccharides are in semi-crystalline, glassy states, in which further porosity development and volumetric expansion are inhibited (Geiger, 2004). However, coffee's transformation in mass, colour, flavour and aroma is rapid after first crack and so, roaster control in the late stages of roasting is critical for coffee quality (Alessandrini et al., 2008; Bustos-Vanegas et al., 2018; Garcia et al., 2018).

Roasting beyond first crack leads to the increase and rapid dissipation of acetic acid, alongside the caramelisation of simple sugars (X. Wang and L.-T. Lim, 2017; Perrone et al., 2010; Hoos, 2015; Chu et al., 2018) until a second crack occurs (Wilson, 2014; Yergenson, 2019; Vargas-Elias et al., 2016). The second crack is more often observed when roasting commodity grade coffees, or when roasting darker for large milk-based drinks (lattes & cappuccinos), but is not as common in most speciality roasteries (as it occurs beyond the specified end-point for most specialty roasts). In academic studies, where extreme cases are investigated, or for very dark roasts, there are many cases where second crack is observed, including Nagaraju et al. (1997), N. Wang (2012), N. Wang and L.-T. Lim (2012), S. Rao (2014), Wilson (2014), Vargas-Elias et al. (2016), and Yergenson (2019).

At the roasting end-point, coffee is rapidly cooled either by quench water or high flow rate ambient temperature air to minimise post-roast development (Schenker, 2000; Baggenstoss, Poisson, et al., 2008b). Although the cooling of the beans holds significance in the context of heat and mass transfer, this phase of the process will not be considered here in detail. For a more in depth discussion of the quenching and cooling of roasted coffee readers are referred to the thesis of Baggenstoss (2008).

1.2.2 Evolution of temperature during roasting

Temperatures in the roasting chamber depend on roaster design and capacity, but typically range 200-300°C. Spouted bed and tangential roasters operate at the higher end of this range, drum roasters at the lower. In spouted bed roasters, heated air propels a spout of beans into the air that then falls back into a slow-moving bed; heat transfer in the spouting region will be most rapid both because of the high air-to-bean heat transfer coefficient and the high temperature of the air (Brown and Lattimer, 2013). In contrast, for drum roasters (where the drum wall is heated via gas burners, or electric induction heaters), beans are lofted via drum wall lifting and experience high convective heat transfer for short periods of time, whilst beans near the drum wall will be subject to higher conductive heat transfer rates for greater periods of time.

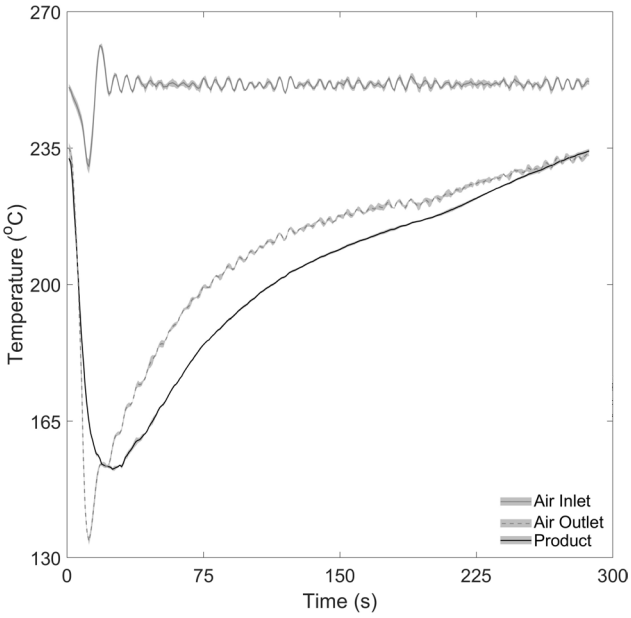

Figure 1.5: A time-temperature roasting profile corresponding to a roast of 350 g of Kenyan Arabica coffee with a constant inlet air temperature of 250 °C and an air velocity of 7.2 m s^{-1} for 278 s in a spouted bed roaster.

The evolution of temperature is described here for roasting in a spouted bed roaster with a constant inlet air temperature. Figure 1.5 displays a time-temperature roasting profile obtained from a roast of 350 g of Kenyan Arabica coffee with a constant inlet air temperature of 250 °C and an air velocity of 7.2 m s^{-1} for 278 s in a spouted bed roaster.

As coffee drops into a batch roaster (at $t = 0\ s$), the thermocouple temperature will decrease rapidly from the charge temperature (the steady-state temperature of the roaster prior to loading) due to the intake of beans at ambient temperature (*c.* 20°C). As the roasting chamber's temperature equilibrates, the temperature decreases. Thermocouples are surrounded by a sheath of considerable thickness to protect them from damage, therefore the thermocouple's response time and the measured rate of change of temperature are dependent on the diameter, as well as their location in the roaster and the temperature and relative humidity of the beans and ambient air. As the system equilibrates, the rate of change of temperature tends to zero, whilst the measured thermocouple temperature tends to a minimum. This inflection point (where the rate of change of thermocouple temperature goes from negative to positive) is a consequence of the thermocouple response and is often termed the turning-point or turn-around. Beyond this point, the measured temperature will increase, with a positive rate of change. Although the global minimum of the time-temperature profile has no physical correspondence to the coffee, it informs process consistency, indicating the roaster's residual thermal energy between batches, charge temperature, coffee fill volume (i.e., packing density) and coffee's initial temperature were controlled.

In the early stages of roasting (where coffee temperature approaches 170°C), convective heat transfer to the bean surface and subsequent conduction through the bean dominates, so thermocouple temperature increases rapidly (Schenker, 2000; Alessandrini et al., 2008; Pittia, Sacchetti, et al., 2011; Romani et al., 2012). Endothermic processes associated with water vapourisation and corresponding latent heat opposes the beans temperature increase but this does not greatly influence heat flux and only slightly decreases measured temperatures (c. 0.5-1.0°C when estimated via simulation). Nonetheless, as the coffee's cellular matrix enters the rubbery state, coffee's porosity increases (Schenker, 2000; Geiger, 2004), whilst the effective thermal conductivity decreases and heat capacity increases (Cardoso et al., 2018). Under a constant inlet air temperature, the rate of change of thermocouple temperature decreases as roasting progresses and will decay to zero at long times (i.e., $T_T \to 0$ as $t \to \infty$) for low temperature inlet air temperatures.

Coinciding with first crack, a rapid increase in temperature is observed under certain process conditions in some washed coffees. Low temperature roasting (environmental temperatures c. 180-200°C) suppresses/counteracts exothermic reactions – indicative of a thermal activation energy. For environmental temperatures greater than 200°C, exothermic reactions become dominant and the rate of change of temperature increases rapidly. Due to these exothermic reactions, constant inlet temperature roasting profiles might not produce optimal in-cup flavour profiles for dark-roasted coffees. For light-roasted coffees, these exothermic reactions might not have a significant impact on the in-cup flavour but the roasting strategy is often varied as the roast progresses to counteract exothermic reactions and optimise in-cup flavour (Münchow et al., 2020).

1.2.3 Process technology & roaster design

Heat is transferred from the roaster to the coffee beans in a combination of high temperature air and further mechanical agitation - a roaster's specific design determines the heat transfer phenomena (Clarke and Vitzthum, 2001; Fernandes, 2019). Roasting is carried out within equipment with a variety of designs. The type used depends on the desired process flexibility and product specifications - common designs include: rotating drum roasters, tangential (paddle) roasters, centrifugal (rotating bowl) and spouted (or fluid) bed roasters - these are displayed in Figure 1.6 (Schenker and Rothgeb, 2017).

Drum roasters feature a horizontal, cylindrical roasting chamber, partially filled with beans. Hot air flows along the drum, whilst baffles are used to promote air and bean mixing as the drum revolves (Schenker and Rothgeb, 2017; Probat, 2019b). The rotation of the drum induces homogenisation of the batch and improves bulk heat transfer, which enables operation with a reduced air-to-bean ratio (mass of drying air input during roasting divided by the total mass of coffee in the batch), although at the expense of a high inlet air temperature (relative to other roaster designs). With regards to the heat transfer phenomena (i.e., convective and conductive heat transfer), the high surface temperature of the drum plays a crucial role in rapid, localised heating of the beans in rotating drums (Schenker and Rothgeb, 2017).

Tangential roasters consist of a static roasting chamber, at the centre of which an impeller provides mechanical agitation (Probat, 2019a). Drying air is input tangentially to the roasting chamber from the bottom upwards (Schenker and Rothgeb, 2017), such that coffee beans are almost entirely in constant suspension around the impeller and conductive heat transfer from the walls of the roaster is mitigated - although this depends on the air-to-bean ratio and corresponding particle dynamics. Tangential roasters are recommended for roasting batches of coffee that are heterogeneous or contain a high fraction of small, or broken beans (Borém and Andrade, 2019; Probat, 2019a).

In centrifugal (rotating bowl) roasters, the roasting chamber rotates to ensure that the beans are well distributed and in constant motion whilst an air flow is applied downwards through the centre of the bowl (Borém and Andrade, 2019). The beans follow a downward spiralling motion towards the centre of the bowl, at which point the centrifugal forces cause the beans to be returned to the periphery of the bowl and the motion is repeated (Borém and Andrade, 2019; Probat, 2019c). The range of applicable air-to-bean ratios is limited due to the inherent design of the roaster (Schenker and Rothgeb, 2017; Probat, 2019c).

Spouted (or fluid) bed roasters rely on high mass flow rates of air to agitate the beans (Borém and Andrade, 2019). The fluidisation (and rotation) of the bed ensures the beans are in constant motion, promoting uniform roasting – further mechanical agitation is not required (Borém and Andrade, 2019; Putra, Hanifah, and Karim, 2019). Due to the decrease in bean density during roasting, the air flow must be reduced to keep process conditions constant (Eggers and Pietsch, 2008). Heat transfer via convection is dominant in spouted beds, however, depending on the batch size, particle dynamics and roaster design, there may also be conductive heat transfer from the walls of the roaster (Schenker and Rothgeb, 2017; Borém and Andrade, 2019).

As roaster selection is influenced by capital expenditure, productivity and product specification, a roastery may concurrently operate roasters of different designs. For all roaster designs, manipulation of process parameters such as air temperature (or burner gas flow), airflow, drum rotation speed, batch size and roast time will enable optimisation of the heat

transfer rates during roasting and allow roasters to control batch homogeneity and mitigate roast defects (Hoos, 2015; Schenker and Rothgeb, 2017; Giacalone et al., 2019; Münchow et al., 2020; S. Rao, 2020; Rusinek et al., 2022).

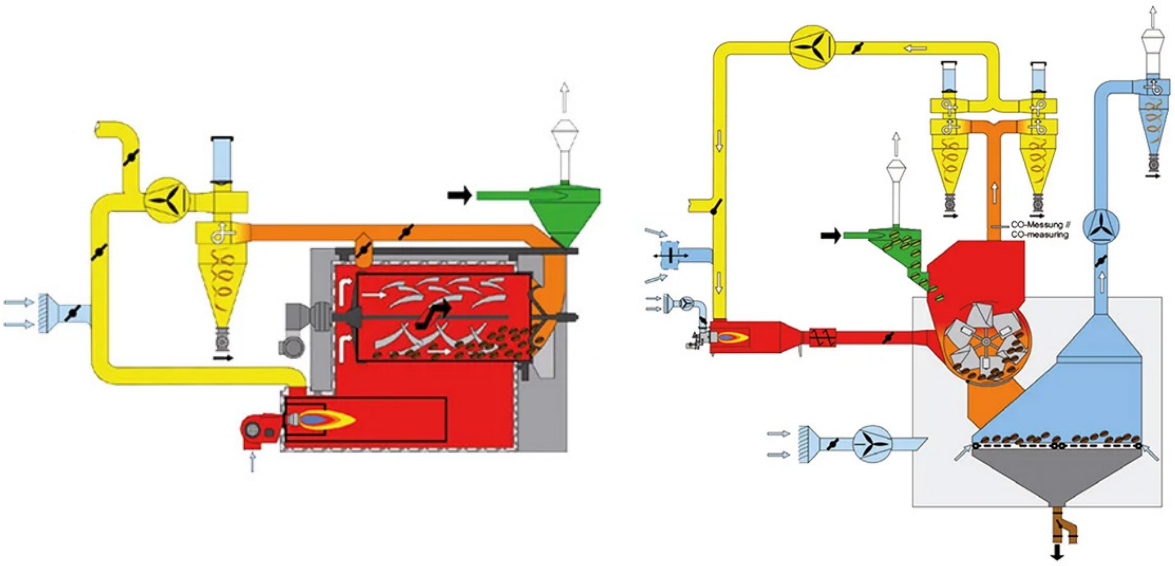

(a) Probat drum roaster

(b) Probat tangential roaster

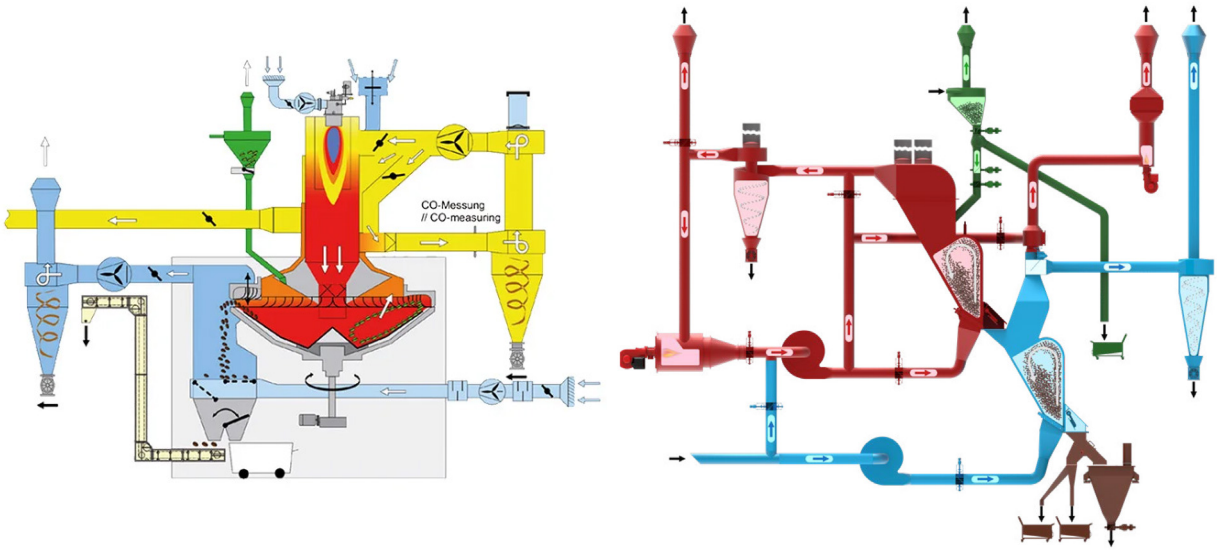

(c) Probat centrifugal roaster

(d) Neuhaus Neotec spouted bed roaster

Figure 1.6: Process diagrams of different roaster designs: (a) Probat rotating drum, (b) Probat tangential (paddle), (c) Probat centrifugal (bowl), (d) Neuhaus Neotec spouted (fluid) bed. (a)-(c) Probat (2023); (d) Neuhaus Neotec (2023).

Commercially, understanding the interactions between roasting conditions and coffee properties support development of both process and product quality (Garcia et al., 2018). Translation of products from one roaster to another (i.e., making identical products on different roasters) is critical for product quality, process flexibility and the supply chain. Process design factors such as raw material properties, process specification and control strategy influence coffee's physicochemical changes during roasting, so monitoring process parameters and the product's physicochemical transformation will equip developers with a methodology for product translation products.

1.2.4 Thermal strategies during roasting

Roasting philosophies vary greatly across the industry; typical roasting strategies are depicted in Figure 1.7.

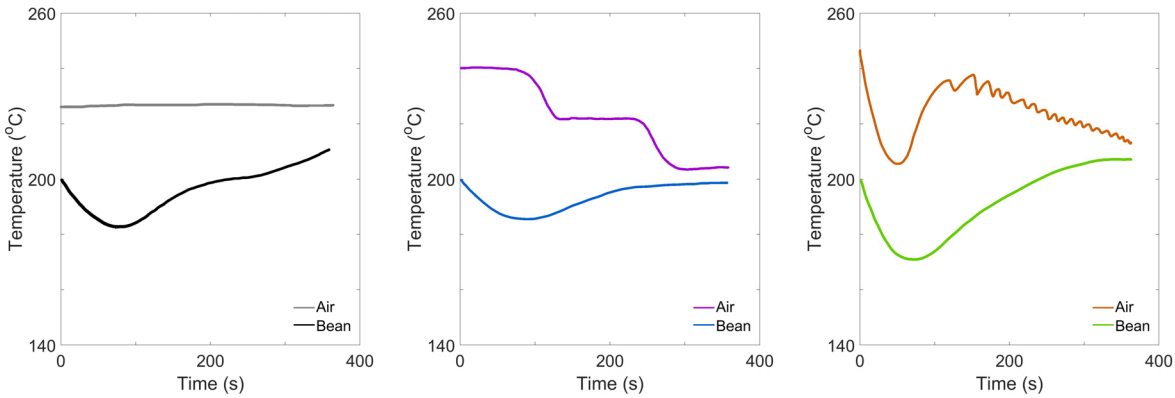

(a) Constant (b) Three-step (c) Replication

Figure 1.7: Illustrated examples of time-temperature profiles that depict typical inlet air temperature control strategies in commercial roasting processes: (a) constant thermal load, (b) three-step decreasing thermal load, (c) varied thermal load that replicates previous product time-temperature profile.

For academic research, constant inlet air temperature (and thermal load) (as seen in Figure 1.7(a)) is applied to minimise the number of factors and simplify cross-comparison of roasting conditions. In commercial settings, the thermal load (inlet air temperature) is often decreased during roasting to slow the endothermic and exothermic effects that commonly occur in

washed processed coffees, as well as to decrease development in the late stages of roasting - this allows for greater control of coffee's physicochemical properties, and is outlined in Figure 1.7(b). Once a product and its process are developed, automation facilitates production consistency. Figure 1.7(c) gives an example of the inlet air temperature profile often seen for roasters that are equipped with control software that enables a specified product time-temperature profile to be replicated through modulation of relevant process parameters (inlet air temperature, airflow, etc.). The input parameters (i.e., thermal load) can vary from batch to batch but the thermocouple's time-temperature history is retained - variation is incurred by coffee variability.

1.2.5 Thermal strategies during preheating

Prior to roasting, roasters are preheated until a thermal steady-state is reached, whereby the product, environmental or outlet (exhaust) thermocouples are approximately constant with time (i.e., the rate of change of temperature approaches zero) - Figure 1.8 gives examples of preheating profiles in spouted bed and rotating drum roasters.

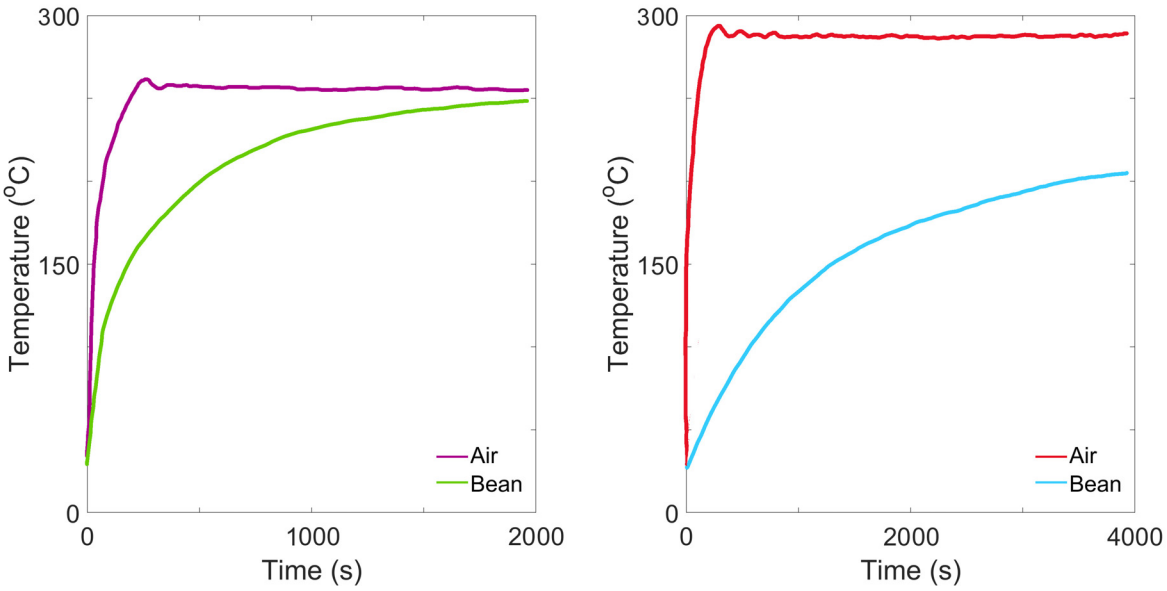

(a) Spouted bed roaster

(b) Rotating drum roaster

Figure 1.8: Illustrated example of pre-heating time-temperature profiles for (a) spouted bed and (b) rotating drum roasters. Although no beans are present during preheating, the plots are denoted by air and beans for consistency with roasting time-temperature profiles.

At steady-state, temperature variations across the roaster will exist due to heat loss from the system and thermocouple location. When the roaster is at steady-state (with no product), the inlet air will be higher, with outlet (exhaust) and product thermocouples showing lower temperatures. Although dependent on the system, outlet air temperature is typically higher than the product at early times. During coffee's development after first crack, exothermic reactions generate higher bean-bed temperatures that can result in the thermocouple temperature exceeding outlet temperature.

1.2.6 Temperature measurement in roasters

Temperatures in coffee roasters are most commonly measured using mineral insulated (often type-J or type-K) thermocouples. Product thermocouples inherently measure some combination of the roasting chamber's environmental air and the coffee beans tumbling around the thermocouple. In spouted bed roasters that depend on high airflows to agitate and heat the coffee, the product thermocouple is in a position that minimises the impact of airflow; in drum roasters, thermocouples are placed to ensure they are at the centre of the bean-bed. Thermocouple response rates are typically discussed in terms of time constants, defined as the time taken for the thermocouple to achieve a 20.0 or 63.2% of an instantaneous step change (Carbon, Kutsch, and Hawkins, 1950; Carroll and Shepard, 1977). A thermocouple's time constant is affected by the applied flow conditions, namely fluid velocity and temperature (Carroll and Shepard, 1977; Majdak and Jaremkiewicz, 2016). Thermocouple response will thus vary based on location within the roaster, with applied process parameters and lag behind the real bean temperature.

Use of infrared technology has enabled manufacturers to measure the bean surface temperature, negating the dependence on air temperature (Aillio, 2023), yet due to moving parts in some roaster types, complex algorithms are required to reduce noise and counter variation of coffee emissivity across coffee types and during roasting.

1.3 Empirical studies of coffee roasting kinetics

Coffee's physicochemical transformation during roasting depends on roaster design, process conditions and raw materials. Coffee characterisation techniques and process measurements also impact observations. In this way, studies of coffee roasting are often unique and cross-comparison can be difficult. This section provides an overview of existing coffee roasting studies and outlines the variability in the observations.

1.3.1 Mass & batch size

The mass of the bean (and total batch size) is relevant for definition of roasting yield (i.e., mass loss) and provides insight into other physicochemical properties, such as moisture, dry matter and colour (Schenker, 2000; Dutra et al., 2001; N. Wang, 2012; X. Wang and L.-T. Lim, 2014a). Mass loss includes the evaporation of water, formation and release of organic volatiles, as well as other organic matter (chaff, dust and bean fragments) (Geiger, 2004). Evaporated water is the greatest contributor to roast loss on a wet basis, so roast losses are often described in terms of organic matter (i.e., Dry Matter Roast Loss (DMRL)) to decouple mass and moisture loss. Typically, roast losses (wet basis) comprise initial moisture content (8-12%), carbon dioxide 0.25-1.20%, chaff 1.0-1.5% with the remainder attributed to aromatics and organic matter degraded during pyrolysis (Geiger, 2004; Smrke et al., 2018; Bustos-Vanegas et al., 2018; Schwartzberg, 2013). Typically, the rate of mass loss increases with both inlet air temperature and initial moisture content (Baggenstoss, 2008; Perrone et al., 2010; X. Wang and L.-T. Lim, 2014a; Vargas-Elias et al., 2016; Pramudita et al., 2017).

DMRL correlates with colour (lightness), although correlation depends on the green bean chemistry (Schenker, 2000; Schenker and Rothgeb, 2017). Baggenstoss, Poisson, et al. (2008b) suggested a lower DMRL for coffees with a higher initial moisture content, which suggests slower kinetics due to removal of a greater water volume. Interestingly, Pramudita et al. (2017) found that removal of organic matter begins prior to the total loss of free moisture, due to the consumption of organic matter during the onset of Maillard reactions.

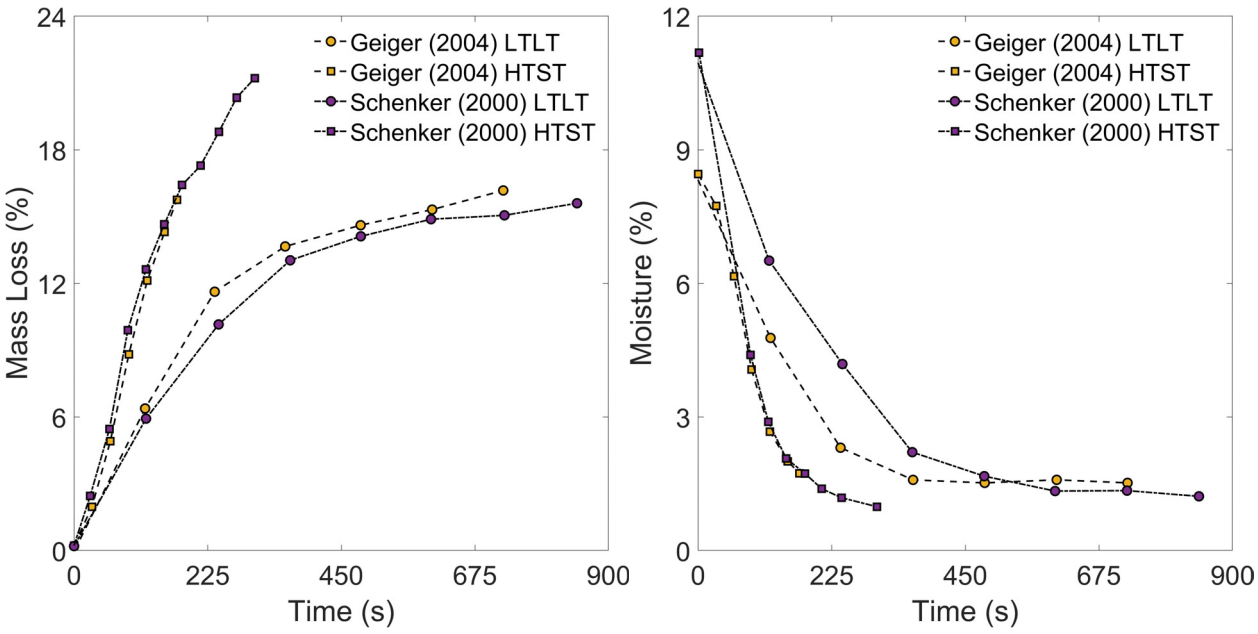

(a) Mass

(b) Moisture

Figure 1.9: Experimental data detailing (a) mass and (b) moisture loss during roasting - data reproduced from Schenker (2000) & Geiger (2004).

1.3.2 Moisture

Green coffee typically has a moisture content in the range of 8-12%. Coffee's moisture content influences the kinetics of both chemical reactions and physical transformations during roasting (G. H. H. d. Oliveira et al., 2017; Rodrigues et al., 2019). Moisture diffusivity in turn depends on the bean's porosity, density and size (Huamaní-Meléndez and Darros-Barbosa, 2018; Ramírez-Martínez et al., 2013; Fadai et al., 2017), as well as the applied thermal load, as a greater heat transfer rate increases the rate of moisture loss (Schenker, Heinemann, et al., 2002; Geiger, Perren, Kuenzli, et al., 2005; Baggenstoss, Poisson, et al., 2008b; Chindapan, Soydok, and Devahastin, 2019). Schwartzberg (2002), Geiger (2004), and Baggenstoss, Poisson, et al. (2008b) studied the effects of varying the initial moisture content on the roasting profile and demonstrated that the energy required to obtain an equivalent colour increased with initial moisture content. Geiger (2004) also found that the rate of moisture loss increased with heat transfer rate, although the residual moisture did not change with process conditions. Geiger (2004) monitored water evolution during roasting

of pre-dried Arabica coffee and found that water is released towards the end of the process; attributed to water formed by chemical reactions during roasting - later confirmed by N. Wang (2012).

As the roast is terminated by quenching the beans with water, particularly in large scale roasters, the moisture content is altered, making it difficult to validate roasting kinetics (Schenker and Rothgeb, 2017; Baggenstoss, Poisson, et al., 2008b).

1.3.3 Size, volume & surface Area

Air-to-bean heat transfer rates are determined by the bean's available surface area (Bergman et al., 2011) and so estimation of the bean's surface area is critical for model accuracy. A coffee bean can be approximated by three geometries: (i) spherical, (ii) ellipsoidal and (iii) hemi-ellipsoidal. For most coffees where the sphericity, $\psi_b \leq 0.8$, hemi-ellipsoidal geometry is recommended; for high sphericity (peaberry) coffees, where $0.8 \leq \psi_b \leq 0.9$, ellipsoidal geometry is more appropriate; for very high sphericity coffees where $\psi_b \geq 0.9$, a spherical geometry is appropriate (Dutra et al., 2001; Pramudita et al., 2017; Bustos-Vanegas et al., 2018). By measuring the beans in three dimensions (i.e., width, depth and length), volume, and surface area can be estimated (Dutra et al., 2001; Pramudita et al., 2017; Bustos-Vanegas et al., 2018). Projected surface area can also be determined via dynamic image analysis and used to monitor bean expansion rate during roasting (Hernández, Heyd, and Trystram, 2008).

The volume of a coffee bean increases during roasting; expansion rate increasing with applied thermal load (Schenker, 2000; Geiger, 2004; Baggenstoss, Poisson, et al., 2008a; Bustos-Vanegas et al., 2018). Small and Horrell (1993) proposed that CO_2 formed via degradation of chlorogenic acids is the main driver of volumetric expansion. Whilst Dutra et al. (2001) and Bustos-Vanegas et al. (2018) agreed with this, both recognised the role of water vaporisation, which Geiger (2004) indicated was more likely the main driving force for volume expansion.

1.3.4 Density

Bean density depends on the porosity and informs coffee's thermal properties (Cardoso et al., 2018). Coffee's density is determined by its mass and volume and is measured via several methods. Intrinsic bean density can be determined based on the individual bean's mass and volume, measured using a precision balance and digital calipers (Dutra et al., 2001; Pramudita et al., 2017; Bustos-Vanegas et al., 2018). Bulk density (a volumetric based method for a batch of beans in a small beaker) and packing density (specific number of beans per unit mass - determined by measuring the mass of a known number of beans) are also relevant for heat and mass transfer properties.

Bean density decreases during roasting, with the rate of change depending on process conditions (Dutra et al., 2001; Alessandrini et al., 2008; Romani et al., 2012), although it is not clear from literature if heat transfer rates affect the final density at the same roasting degree Baggenstoss, Poisson, et al. (2008a) and Eggers (2001). Geiger, Perren, Schenker, et al. (2001) found that the initial moisture content has no effect on the final bean density, yet Bustos-Vanegas et al. (2018) correlated density's evolution during roasting with moisture content.

1.3.5 Porosity

Evolution of porosity during roasting plays a key role in the changes in properties such as the density, specific heat capacity, thermal conductivity, both thermal and mass diffusivities, as well as the bean's textural properties which influence roasting and grinding processes (Telis-Romero et al., 2009; Pittia, Sacchetti, et al., 2011; Oliveros et al., 2017; G. H. H. d. Oliveira et al., 2017). Porosity can be determined using a pycnometer (Schenker, 2000; Geiger, 2004), Scanning Electron Microscopy (SEM) (N. Wang, 2012), or X-ray Micro-Computed Tomograpghy (Micro-CT) (Frisullo et al., 2012).

Porosity increases during roasting and the internal pressure is the dominant driving force for volume expansion (Geiger, 2004; Frisullo et al., 2012; Oliveros et al., 2017). Green coffee beans are initially in a glassy state, and as a function of moisture and temperature transition

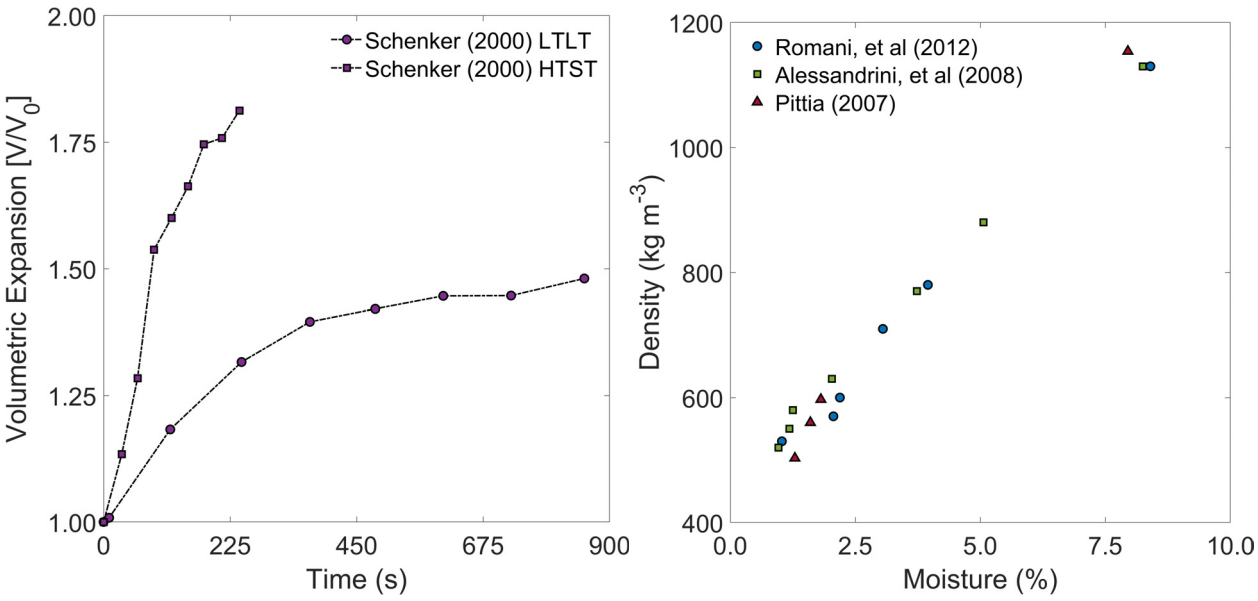

(a) Volume

(b) Density vs Moisture

Figure 1.10: Experimental data detailing changes in (a) volume and (b) density during roasting - data reproduced from Schenker (2000), Pittia, Nicoli, and Sacchetti (2007), Alessandrini et al. (2008), and Romani et al. (2012).

into a rubbery state, wherein volumetric expansion occurs, before returning to a glassy state at the end of roasting (Schenker, 2000; Geiger, 2004). Higher heat transfer rates increase the rate of change of porosity (Schenker, 2000; Geiger, 2004; Schenker and Rothgeb, 2017).

1.3.6 Colour & lightness

Bean colour, described as a lightness and hue, is a measurement often associated with coffee flavour (or 'strength') and is therefore used to indicate the roast degree (Schenker and Rothgeb, 2017). Colour measurement is often by techniques using visible light or Near-Infrared Spectroscopy (NIRS) and can be based on the surface of whole or ground beans, although the latter is most common (Hernández, Heyd, and Trystram, 2008; Romani et al., 2012; Yergenson, 2019).

Coffee colour darkens during roasting (Geiger, 2004; N. Wang, 2012; X. Wang and L.-T. Lim, 2014a; Mendes et al., 2001; Alessandrini et al., 2008). Colour formation is due to browning compounds (Melanoidins) generated during Maillard reactions (De Vleeschouwer

et al., 2010). Alessandrini et al. (2008) and Mendes et al. (2001) found that hue angle decreases with time, i.e., the colour became browner as roasting progressed. The kinetics of changes in lightness, as well as hue, are typically similar, varying only in magnitude (Fischer et al., 2001; Pittia, Dalla Rosa, and Lerici, 2001; Kim et al., 2018).

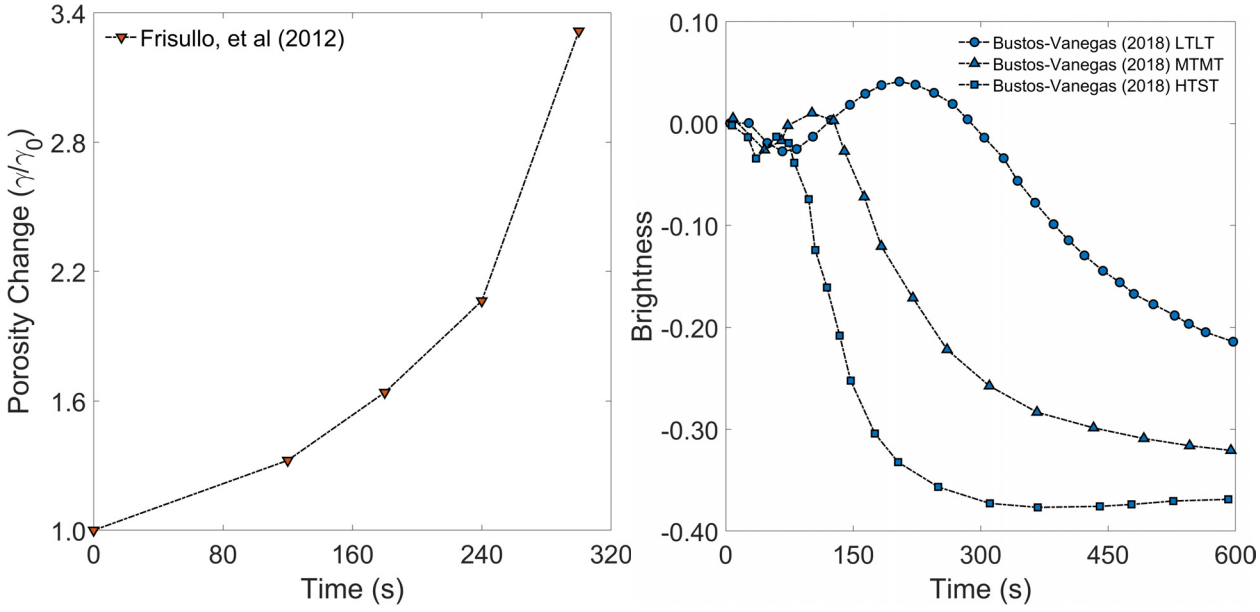

(a) Porosity

(b) Brightness

Figure 1.11: Experimental data detailing changes in (a) porosity and (b) brightness during roasting - data reproduced from Frisullo et al. (2012) & Hernández, Heyd, and Trystram (2008)

1.3.7 Specific heat capacity & thermal conductivity

During roasting, coffee's thermophysical properties evolve due to mass transfer phenomena; dehydration drives porosity development, with coffee density decreasing due to both volumetric expansion and loss of organic matter (i.e., mass). Thermal properties can be determined empirically by measuring the rate of heat transfer to the coffee (Telis-Romero et al., 2009; Hammerschmidt and Abid, 2016).

Thermophysical properties are inherently related to density and moisture (Singh et al., 1997; Schwartzberg, 2002; Burmester and Rudolf Eggers, 2010; Fabbri, Cevoli, Alessandrini, et al., 2011; Cardoso et al., 2018). Fabbri, Cevoli, Alessandrini, et al. (2011) and Cardoso et al.

(2018) found that specific heat capacity increases during roasting, yet Eggers (2001) showed specific heat capacity decreased linearly with time. The findings of these studies likely differ due to the measurement technique and sample variability. As porosity increases during roasting, thermal conductivity decreases due to the low thermal conductivity of air, relative that of the solid and liquid fractions of the bean (M. Rao, Rizvi, and Datta, 1994; Eggers, 2001; Fabbri, Cevoli, Alessandrini, et al., 2011; Cardoso et al., 2018).

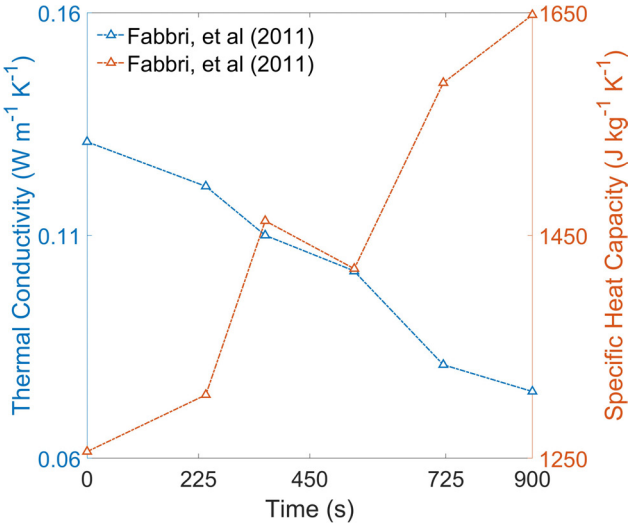

(a) Thermal Properties

Figure 1.12: Experimental data detailing changes in specific heat capacity and thermal conductivity during roasting - data reproduced from Fabbri, Cevoli, Alessandrini, et al. (2011).

1.4 Particle motion in coffee roasters

1.4.1 Particle-fluid interactions

Different roaster designs (as outlined in Section 1.2) demonstrate distinct particle and fluid dynamics. Particle and fluid interactions during roasting govern heat and mass transfer (Bergman et al., 2011), yet little work has been done to understand the effect of air flow and batch size on coffee's development during roasting (Kwak, Ji, and Jeong, 2017). Empirical studies are limited to imaging of transparent model systems, where accuracy is low and restricted to two-dimensional analysis Cristo et al. (2006) and Resende et al. (2017). Computational Fluid Dynamics (CFD) can be used to model flow behaviour in dilute granular systems (Abdul Ghani et al., 2019; Alonso-Torres et al., 2013; Chiang, Wu, and Kang, 2017; Oliveros et al., 2017).

Coupled CFD and Discrete Element Method (DEM) models can simulate lumped and distributed temperature distributions within spouted bed roasters (Azmir, Hou, and Yu, 2018; Bruchmüller et al., 2010) but are often difficult to validate. Bruchmüller et al. (2010) established a DEM model to describe the temperature and moisture distribution within a fluidised bed of spherical particles during roasting. Azmir, Hou, and Yu (2018) studied a similar system at lower temperatures (50-200°C) incorporating particle shrinkage – effects of initial moisture content, density and particle size were highlighted. Ma et al. (2022) recently reviewed CFD-DEM simulations of non-spherical particles. Although difficult to validate, CFD-DEM simulations can determine both lumped and distributed temperature distributions within spouted bed roasters (Bruchmüller et al., 2010; Machado et al., 2018; Azmir, Hou, and Yu, 2018). Che et al. (2023) presented a CFD-DEM model calibrated using data generated here in Chapter 4, with model parameters and drag coefficients optimised to accurately capture particle recirculation times, occupancy and velocity profiles, and regional mass fractions.

Granular flow in rotating drums with simplified geometries (i.e., no baffles or vanes) (Henein, Brimacombe, and Watkinson, 1983; Mellmann, 2001; González et al., 2015), and/or with

simple (often monodispersed) particle shapes (Ding et al., 2002; S. Y. Lim et al., 2003; Pathmathas, 2015; Govender, 2016; Morrison et al., 2016; C. R. Windows-Yule, Scheper, et al., 2016; C. R. Windows-Yule, Van Der Horn, et al., 2017) has been well documented. Granular systems of polydisperse, aspherical particles in rotating drums with internally mounted vanes are less understood.

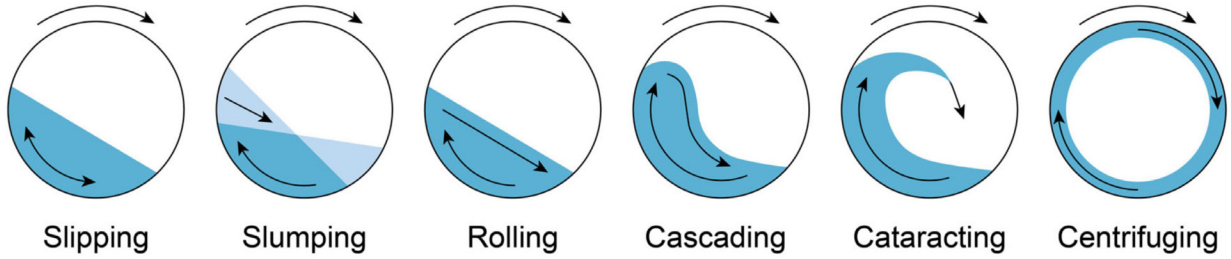

Figure 1.13: Granular flow regimes observed in rotating drums (Jones et al., 2021).

For granular materials in rotating drums, particle motion can be characterised into several regimes: of relevance here are rolling, cascading and cataracting motions - these are illustrated in Figure 1.13 (Henein, Brimacombe, and Watkinson, 1983; Mellmann, 2001; Arntz et al., 2008; Jones et al., 2021). The Froude number, a dimensionless number describing the ratio of inertial (i.e., centripetal) and gravitational forces, is often used to define particle dynamics and characterise the flow regime in granular systems (Henein, Brimacombe, and Watkinson, 1983; Mellmann, 2001; Arntz et al., 2008). Jones et al. (2021) studied the motion of fabrics in tumble dryers using PEPT and found that both the axial and radial displacement of particles was determined by the load size and used an effective Froude number to characterise particle behaviour relative to the drum wall. This approach is suitable for aspherical particles (i.e., coffee beans).

1.4.2 Positron Emission Particle Tracking (PEPT)

PEPT is a non-invasive technique that can characterise flow behaviour within granular systems. For systems within the detector's field of view, the trajectories of particles labelled with positron-emitting radioisotopes can be tracked in three-dimensions with high temporal and spatial resolution (Windows-Yule et al., 2020). The principles of PEPT, namely tracer labelling, detection and algorithms required to identify tracer location, are described in de-

tail by D J Parker et al. (1993) and D J Parker (2017), while PEPT's best practices and applications were recently reviewed by (Windows-Yule et al., 2020).

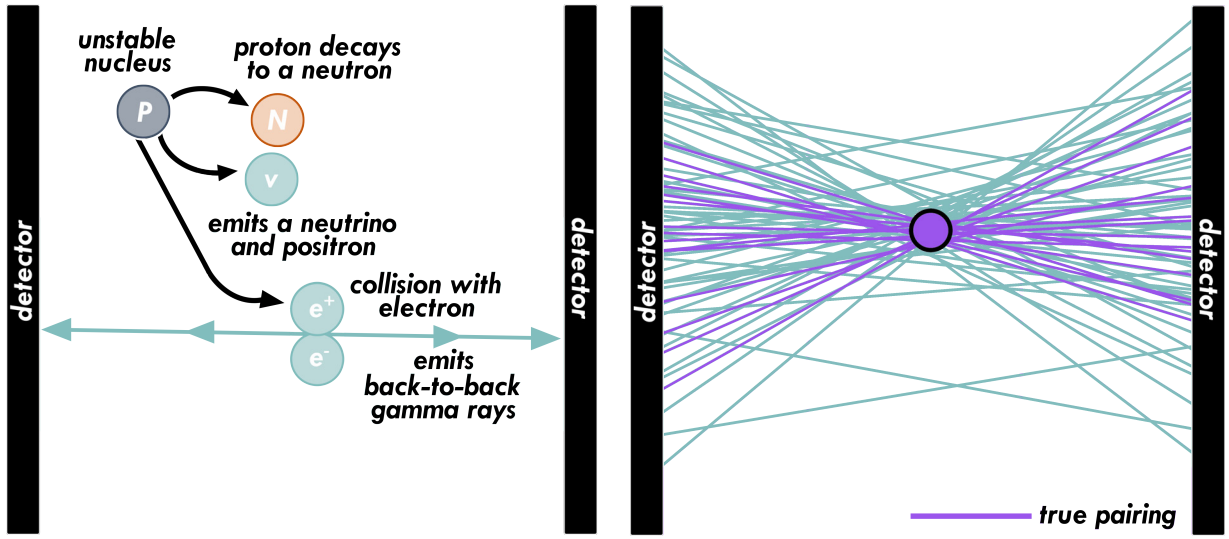

(a) Annihilation events

(b) Lines of Response (LoRs)

Figure 1.14: Visualisation of (a) annihilation events and (b) compilation of Lines of Response (LoRs) resultant from particles labelled with positron-emitting radioisotopes within the detector heads of the positron camera.

Tracer particles decay to a neutron, neutrino and positron. When the positron collides with an electron (known as an annihilation event), a pair of back-to-back γ-photons are emitted. These γ-photon pairs follow a collinear trajectory (Windows-Yule et al., 2020) and when detected on adjacent detector heads within a specified time (c. 15 ns) (D J Parker et al., 1993), the photon pairs are considered to have originated from the same annihilation event (Windows-Yule et al., 2020). Figure 1.14(a) depicts the annihilation events and subsequent detection of back-to-back γ-photon pairs. Compiling the Lines of Response (LoRs) attributed to collinear trajectories of detected γ-photon pairs enables triangulation of the tracer's location - as shown in Figure 1.14(b). Note that purple LoRs refer to true pairings from 'true coincidences', whilst other pairings reconstructed from false coincidences are considered non-true (i.e., noise) (K. Windows-Yule et al., 2022).

PEPT measurements rely on the ergodic assumption (Wildman et al., 2000): for steady-state systems, time-averaged behaviour exhibited by a single particle in a homogenous system is assumed representative of the ensemble-averaged behaviour of all particles in the system. In this way, measurements are typically performed on steady-state systems in real process equipment for extended periods of time (c. 20-60 mins) to allow labelled particles to explore the system (Windows-Yule et al., 2020). Resultant data comprises Cartesian coordinates that describe the tracer's location within the system at a given time.

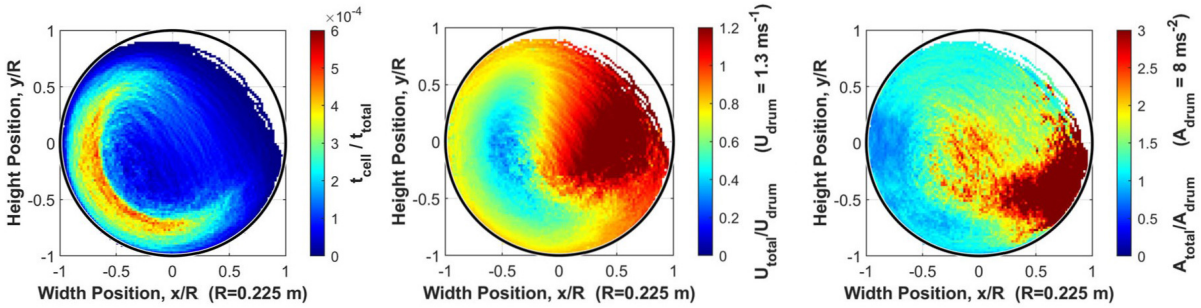

(a) Occupancy (b) Velocity (c) Acceleration

Figure 1.15: Particle motion data corresponding to a wool dryer ball in a tumble dryer measured using PEPT (Jones et al., 2021).

From the LoRs obtained using a positron camera, positional data can be determined via machine-learning algorithms based on cluster analysis (Nicuşan and Windows-Yule, 2020), where resultant data comprises time-stamped Cartesian coordinates that describe the tracer's location within the system (i.e., the tracer's position in x,y,z) at a time (t). From the PEPT-captured Lagrangian trajectories, particle velocities and recirculation times can be identified and converted to time-averaged Eulerian data that detail occupancy and velocity fields. Figure 1.15 presents an example of Eulerian data generated via PEPT.

1.5 Modelling & simulation

Virtualisation of manufacturing processes can be understood through the concepts of digital models, digital shadows & digital twins. These terms differ in their level of integration with the process (Sjarov et al., 2020). Digital models can be considered as mathematical representations of real technologies or processes typically calibrated with offline product measurements or historical process data. Calibrated digital models provide accurate representations of processes, yet in the context of food systems, these calibrations might rapidly drift in time and thus only momentarily represent a process. Digital shadows are digital models that are autonomously connected to the process via sensors and appropriate data flow systems. This integration ensure that the calibration of the models is continually updated, reflecting real-time changes in the process and product. Digital twins are fully-integrated digital shadows that directly control the process via actuators. The control systems of digital twins are driven by simulated process and product data, enabling them to make real-time adjustments and optimisation of the process. Sjarov et al. (2020) reviewed the origin of these concepts, with subsequent discussion in Lechler et al. (2020) that begins to define the progressive integration of digital models toward development of digital twins.

Both digital models and digital shadows are useful tools for product developers, provided they are graphically interfaced to enable users to query them with a combination of input, process, or output data. Digital twins are invaluable for operational excellence, autonomising the process to assure product quality. In the context of coffee, the complexity of mathematical models that represent the bean's temperature response and corresponding physicochemical transformation during roasting depend on their intended application. Batch-scale, zero-dimensional models are rapidly solved and can easily be integrated within existing Programmable Logic Controllers (PLCs) - ideal for development of digital twins - but won't necessarily provide accurate particle temperatures, or spatial resolution of thermal gradients within the bean. Conversely, bean-scale, three-dimensional models of a particle's mean temperature and distribution of temperature across the particle can provide critical information regarding bean homogeneity yet require great computational expense, are diffi-

cult to empirically validate (Heyd et al., 2007; Fabbri, Cevoli, Alessandrini, et al., 2011) and are most suitable for digital models, or shadows.

1.5.1 Modelling of coffee's physicochemical transformation

Numerous experimental studies of mass and moisture loss during roasting are available. Many of these studies captured the kinetic (time-series) data corresponding to coffee as it evolves during roasting (Tsiafitsa et al., 2022; Dutra et al., 2001; X. Wang and L.-T. Lim, 2014a; Schenker, 2000; Bustos-Vanegas et al., 2018; Alessandrini et al., 2008; Vargas-Elias et al., 2016; Pramudita et al., 2017; Baggenstoss, Poisson, et al., 2008b; G. H. H. d. Oliveira et al., 2017; Rodrigues et al., 2019; Geiger, 2004; N. Wang, 2012; Chu et al., 2018; Chindapan, Soydok, and Devahastin, 2019). Although many of these studies are based on laboratory model roasters with roasting times longer than those used commercially, these data can be used to develop kinetic models that describe coffee's transformation (Mendes et al., 2001; Hernández, Heyd, Irles, et al., 2007; Pittia, Nicoli, and Sacchetti, 2007; Perrone et al., 2010; Vargas-Elias et al., 2016; Oliveros et al., 2017; Pramudita et al., 2017; Bustos-Vanegas et al., 2018; Cardoso et al., 2018).

Kinetic models using n^{th}-order Arrhenius-type reaction rates are often used to predict the temperature dependent physicochemical behaviour of many food systems (Corradini and Peleg, 2006b; Corradini and Peleg, 2006a) and have also been used to characterise coffee's physicochemical development in different roasting systems, such as those by Perrone et al. (2010), Bustos-Vanegas et al. (2018), Vargas-Elias et al. (2016), and X. Wang and L.-T. Lim (2014a). This modelling approach simplifies the complex reactions that take place during roasting (for example, colour formation via Maillard reactions) by lumping the chemistry into an n^{th}-order reaction rate (L. Oliveira et al., 2016). The ordinary differential equation corresponding to n^{th}order chemical reaction kinetics is:

$$\frac{dC(t)}{dt} = -k(T)C(t)^n \tag{1.1}$$

where the rate of change of dimensionless property C, with respect to time, t (s), depends on the temperature-dependent rate constant, k ($\text{s}^{-1}[\text{C}]^{1-n}$) and the reaction order n.

Kinetics of mass and moisture loss during roasting have been determined using different modelling approaches (Perrone et al., 2010; X. Wang and L.-T. Lim, 2014a; Vargas-Elias et al., 2016; Pramudita et al., 2017; Schwartzberg, 2002). Schwartzberg (2002) empirically derived the rate of change of moisture, X_b (kg kg^{-1}) as a function of bean diameter, d_b (mm) and bean temperature, T_b (K), using second-order kinetics:

$$\frac{dX_b}{dt} = -\frac{4.32 \times 10^9}{d_b^2} \exp\left(\frac{-9889}{T_b}\right) X_b^2 \tag{1.2}$$

Mass and moisture loss are often used as the basis for correlation of different physicochemical properties and are therefore most studied (Eggers, 2001; Bustos-Vanegas et al., 2018). For mass loss, Vargas-Elias et al. (2016) used zero-order kinetics (i.e., $n = 0$ in Eq. 1.1), yet X. Wang and L.-T. Lim (2014a) found that a two-stage zero-order model better described their data - the latter being confirmed by Pramudita et al. (2017). Chindapan, Soydok, and Devahastin (2019) used a reaction order of 0.1 (i.e., $n = 0.1$ in Eq. 1.1) to describe moisture loss, whilst Zhu et al. (2022) used first-order kinetics to describe both moisture and mass loss during roasting. Each study achieved reasonable accuracy but yield rate coefficients with high specificity and sensitivity.

Colour development during roasting is typically described via lightness (X. Wang and L.-T. Lim, 2014a) or brightness (Hernández, Heyd, and Trystram, 2008) as colour descriptors – lightness understood as perceived reflectance and brightness as perceived luminance (Gilchrist, 2007). X. Wang and L.-T. Lim (2014a) described lightness with a two-stage, first-order model, where the rate coefficients take the Arrhenius form, and revealed a more significant effect of temperature on bean colour (i.e. decrease of lightness, darkening) during the second stage of roasting. Prediction of the transition between the two observed stages limits the application of this model. Hernández, Heyd, and Trystram (2008) used a neural network model to describe changes in brightness during roasting - although these types of model might not be robust to different roasting conditions.

1.5.2 Modelling heat and mass transfer at the batch-scale

Heat and mass transfer during roasting is described via energy balance. The legacy of Schwartzberg (2002), Schwartzberg (2006a), Schwartzberg (2006b), and Schwartzberg (2013) provides the foundation for simulation of time-temperature roasting profiles. An energy balance over a spouted bed roaster describes the coffee's temperature evolution during roasting:

$$\frac{dT_b}{dt} = \frac{G_a C_{p,a}(T_{a,i} - T_{a,o}) + m_{bs,db}(Q_r + \Delta H_v \frac{dX_b}{dt}) - Q_{am} + Q_{mb}}{m_{bs,db}(1+X)C_{p,b}} \tag{1.3}$$

where G_a is the inlet air mass flow rate (kg s^{-1}), $C_{p,b}$ and $C_{p,a}$ are the specific heat capacity of the coffee bean and inlet air (J kg^{-1} K^{-1}). The specific energy associated with the air-to-metal, metal-to-bean and reaction are Q_{am}, Q_{mb} and Q_r respectively (J kg^{-1}). ΔH_v is the latent heat of vaporisation of water (J kg^{-1}), X_b is the bean's moisture content ($d.b$) (kg kg^{-1}) and $m_{bs,db}$ is the mass of beans ($d.b$) (kg). The difference between the inlet and outlet air temperature ($T_{a,i}$ and $T_{a,o}$ (K)) - as depicted in Figure 1.4 - is estimated via:

$$(T_{a,i} - T_{a,o}) = (T_{a,i} - T_b)\left(1 - \exp\left(\frac{-\alpha_{ab} A_{ab}}{G_a C_{p,a}}\right)\right) \tag{1.4}$$

where α_{ab} is the air-to-bean heat transfer coefficient (W m^{-2} K^{-1}) and A_{ab} is the area available for air-to-bean heat transfer (m^2). As an approximation, heat transfer is modelled as a constant wall-temperature heat exchanger, with the beans as a tube surrounding the air. In practice, this is not correct and correction factors must be used.

Schwartzberg (2002) also considered the measured product temperature, $T_{b,m}$ (K) and how it relates to the actual product temperature, $T_{b,a}$ (K). Using a first-order differential equation governed by heat transfer between the thermocouple and the bean bed:

$$m_t C_{p,t} = \frac{dT_{b,m}}{dt} = h_{bt} A_{s,bt}(T_{b,a} - T_{b,m}) \tag{1.5}$$

where m_t and $C_{p,t}$ are the mass (kg) and specific heat capacity (J kg^{-1} K^{-1}) of the thermocouple, h_{bt} is the convective heat transfer coefficient between the coffee and thermocouple (W m^{-2} K^{-1}) and $A_{s,bt}$ is the corresponding heat transfer area (m^2); $T_{b,a}$ and $T_{b,m}$ are the actual

and measured bean temperatures. Thus, the thermocouple's response can be described using a thermometric lag coefficient (K):

$$K = \frac{h_{bt} A_{s,bt}}{m_t C_{p,t}} \tag{1.6}$$

The model was further developed by Schwartzberg (2006a) to account for the thermocouple's response, whereby the thermometric lag coefficient was estimated - ranging from 0.0147 s^{-1} for a sample roaster, down to 0.0042 s^{-1} for a 400 kg centrifugal roaster (Schwartzberg, 2006a); the operational significance of these phenomena were later discussed by (Schwartzberg, 2013). Since then, the Schwartzberg model has been validated (Bopape et al., 2016; Hernández Pérez, 2002; Bottazzi et al., 2012; Palma et al., 2021; Vosloo, 2017; Uren et al., 2023) and further developed in conjunction with CFD models (Alonso-Torres et al., 2013) and coffee's porosity development (Oliveros et al., 2017).

Zero-dimensional, batch-scale simulations of heat and mass transfer are of most relevance to process control systems due to their rapid solver times and hence their ability to predict the effect of disturbances on the time-temperature profile in real-time. Figure 1.16 shows the expected difference between the thermocouple and bean temperature during roasting - time-temperature profiles were resolved from a zero-dimensional heat and mass transfer model (Schwartzberg, 2002).

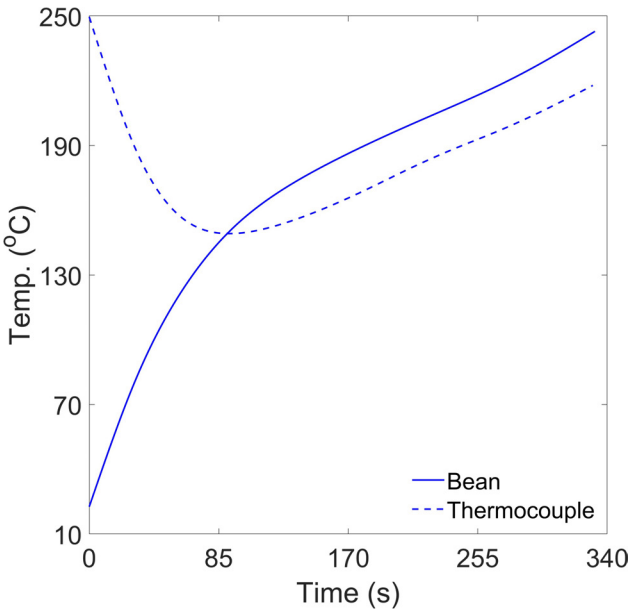

Figure 1.16: Simulated time-temperature profile corresponding to the bean and thermocouple measurements - resolved from a zero-dimensional heat and mass transfer model (Schwartzberg, 2002).

1.5.3 Modelling heat and mass transfer at the bean-scale

Modelling coffee at the bean-scale enables the spatial variation of coffee's properties to be resolved - providing insight that is difficult to ascertain experimentally. The spatial variation of temperature and moisture in coffee can be simulated with three-dimensional models (Heyd et al., 2007; Hernández-Díaz et al., 2008; Fabbri, Cevoli, Alessandrini, et al., 2011; Fadai et al., 2017; Abdul Ghani et al., 2019).

The spatial variation of moisture within a coffee bean can be predicted via mass transfer phenomena (Heyd et al., 2007; Hernández-Díaz et al., 2008; Fabbri, Cevoli, Alessandrini, et al., 2011; Fadai et al., 2017; Abdul Ghani et al., 2019), such that for spherical geometry with radius, r (mm) :

$$\frac{\partial X_b}{\partial t} = D\left(\frac{\partial^2 X_b}{\partial r^2} + \frac{2}{r}\frac{\partial X_b}{\partial r}\right) \tag{1.7}$$

where D is mass diffusivity ($\text{mm}^2\ \text{s}^{-1}$) dependent on the mass transfer coefficient and concentration gradient across the bean.

The spatial variation of temperature can be simulated via heat transfer phenomena (Fadai et al., 2017; Kikic and Basile, 2009; Heyd et al., 2007), such that for spherical geometry with radius, r (mm):

$$\rho_b C_{p,b} \frac{\partial T_b}{\partial t} = \lambda_b \left(\frac{\partial^2 T_b}{\partial r^2} + \frac{2}{r} \frac{\partial T_b}{\partial r} \right) \tag{1.8}$$

where ρ_b is the coffee's density (kg m^{-3}) and λ_b is the effective thermal conductivity of the bean (W m^{-1} K^{-1}).

In a Cartesian coordinate system (i.e., for three-dimensional space along axes x, y, z), Eq. 1.7 becomes:

$$\frac{\partial X_b}{\partial t} = D \left(\frac{\partial^2 X_b}{\partial x^2} + \frac{\partial^2 X_b}{\partial y^2} + \frac{\partial^2 X_b}{\partial z^2} \right) \tag{1.9}$$

and Eq. 1.8 becomes (Kikic and Basile, 2009; Hobbie and Eggers, 2001; Fabbri, Cevoli, Alessandrini, et al., 2011; Fadai et al., 2017):

$$\rho_b C_{p,b} \frac{\partial T_b}{\partial t} = \lambda_b \left(\frac{\partial^2 T_b}{\partial x^2} + \frac{\partial^2 T_b}{\partial y^2} + \frac{\partial^2 T_b}{\partial z^2} \right) \tag{1.10}$$

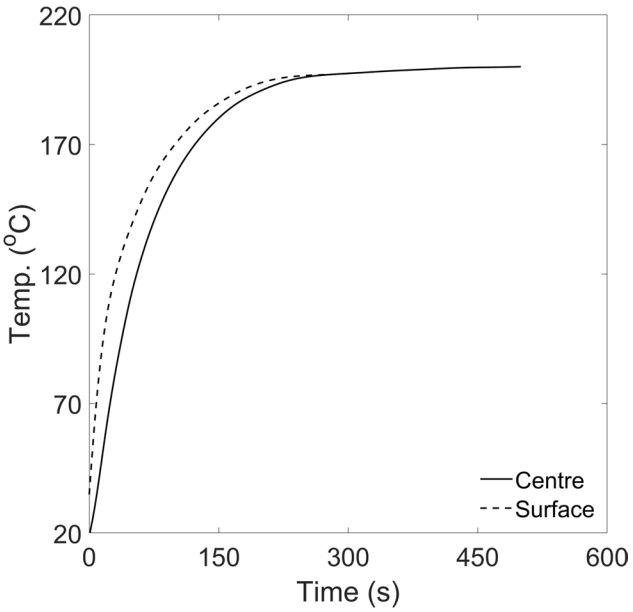

Figure 1.17: Simulated time-temperature profiles corresponding to the surface and centre of the bean - resolved using a three-dimensional heat and mass transfer model (Fabbri, Cevoli, Alessandrini, et al., 2011).

Three-dimensional, bean-scale simulations of heat and mass transfer are invaluable for process and product developers, although their commercial implementation for real-time control can not yet be realised due to computational requirements and validation is often difficult for commercial roasters. Figure 1.17 illustrates the difference between the bean's surface and centre temperature during roasting - time-temperature profiles were resolved from a three-dimensional heat and mass transfer model (Fabbri, Cevoli, Alessandrini, et al., 2011).

1.6 Outlook

1.6.1 Considerations for the product and process developer

Definitions of roast degree differ across the industry. Whilst most relate to the measured colour (Schenker and Rothgeb, 2017), mass loss, density or moisture could also be used as effective process indicators. Measured colour is dependent on the instrument, colour scale, time after roasting and particle size. This imposes difficulties in standardising quality criteria, as well as translating products and processes from one roaster to another (Schenker and Rothgeb, 2017). Extensive research into correlating roast degree with other physicochemical properties has been performed in recent years but definition is not yet standardised (Dutra et al., 2001; Fiore et al., 2006; Alessandrini et al., 2008; Franca et al., 2009; Romani et al., 2012; Kim et al., 2018).

Focusing on commercial roasting, if specifications only state the target colour, there is freedom within the range of operational time-temperature profiles that can achieve the same colour. As a result, the roasting strategy, i.e. how thermal energy is applied during roasting must be carefully considered to achieve consistency.

1.6.2 Relevance of the thesis

Heat and mass transfer simulations of coffee roasting are often based on numerous assumptions and comprehensive data relating to commercially relevant roasters are rare. Many studies that detail kinetic models of coffee's physicochemical transformation during roasting exist, however the estimated parameters are highly specific and sensitive to diverse conditions not within the experimental range. Therefore, this thesis aims to use a data-driven approach

to calibration, whereby the calibration data is (i) comprehensive, (ii) experimentally determined using relevant, accessible measurement techniques and (iii) robust to diverse roasting conditions and green beans.

It's important to acknowledge that although only coffee literature were reviewed so far, these studies provide a framework for developing and calibrating process models applicable beyond coffee roasting. These models can be reformulated and recalibrated using data from various other sectors and applications.

Chapter Two

Process characterisation

For modelling and simulation of coffee roasting systems to be applicable and useful for developers, fundamental knowledge of the roaster, its operation and quantification of process parameters is necessary. Successful and consistent operation of roasters also requires comprehension of thermal equilibrium during preheating and between batches, as well as capturing how rapidly the system responds to changes in thermal load during roasting. All of these should influence the applied control philosophy during roasting. Considerations of airflow, batch size, drum rotation speed, temperature and time support a developer's quest to optimise, explore and innovate both processes and products. By mapping the feasible operating range, nominal process conditions can be applied, and experimental process and product data can subsequently be collected robustly. These data can then be used by modellers to develop digital models and shadows of the roasting process, so developers can virtually query process parameters and their impact on roasting conditions.

This chapter presents the characteristics of five roasters of different designs and scales, their feasible operating range as it relates to realistic production (i.e., that create products whose physical, chemical and sensory attributes are of relevance and value to consumers), outlines the process measurements and specification used in experimental roasting studies and provides a means to characterise and subsequently capture the impact of thermocouple properties on temperature measurement in model systems and a pilot-scale roaster.

2.1 Methodology: Roasters

Five roasters of different designs and scales have been studied and are depicted in Figure 2.1. These roasters represent three distinct designs (fluid bed, spouted bed and rotating drum) and three different scales (sample, lab-scale and pilot-scale): (i) 0.5 kg spouted bed (RFB-S, Neuhaus Neotec), (ii) 5 kg spouted bed (RFB-Jr, Neuhaus Neotec), (iii) 50 g sample roaster (Pro V3, Ikawa), (iv) 1 kg rotating drum (Bullet R1 V2, Aillio) and (v) 5 kg rotating drum (TT8-10, Petroncini).

(a) Neuhaus Neotec RFB-S (b) Neuhaus Neotec RFB-Jr (c) Ikawa V3 Pro

(d) Aillio Bullet R1 V2 (e) Petroncini TT8-10

Figure 2.1: Roasters used for studies: (a) 0.50 kg RFB-S, (b) 5.00 kg RFB-Jr, (c) 0.05 kg Ikawa Pro V3, (d) 1.00 kg Aillio Bullet R1 V2 and (e) 5.00 kg Petroncini TT8-10.

In this chapter, the critical process parameters and feasible operating range of each of the five roasters were identified. In later chapters that detail coffee's physical transformation and modelling of coffee's thermal and physical response, two of the pilot-scale roasters (the 0.5 kg spouted bed roaster (RFB-S, Neuhaus Neotec) and 1.0 kg rotating drum roaster (Bullet R1 V2, Aillio)) were comprehensively investigated to identify the roasting behaviour in two distinct roaster designs of similar scales. Many of the roasting studies in Chapter 3 Coffee's Physicochemical Transformation During Roasting were performed on the pilot-scale spouted bed roaster (RFB-S) as under some process conditions, primarily convective heat transfer phenomena can be assumed and thermal considerations for heat and mass transfer simulations are thus simplified. To compare different roasting systems, the rotating drum (Bullet) roaster was used as fill volumes are comparable to the RFB-S.

Simplified schematics of the roasting chambers are presented in Figures 2.2 & 2.4 for the RFB-S (spouted bed) and Bullet (rotating drum) roasters.

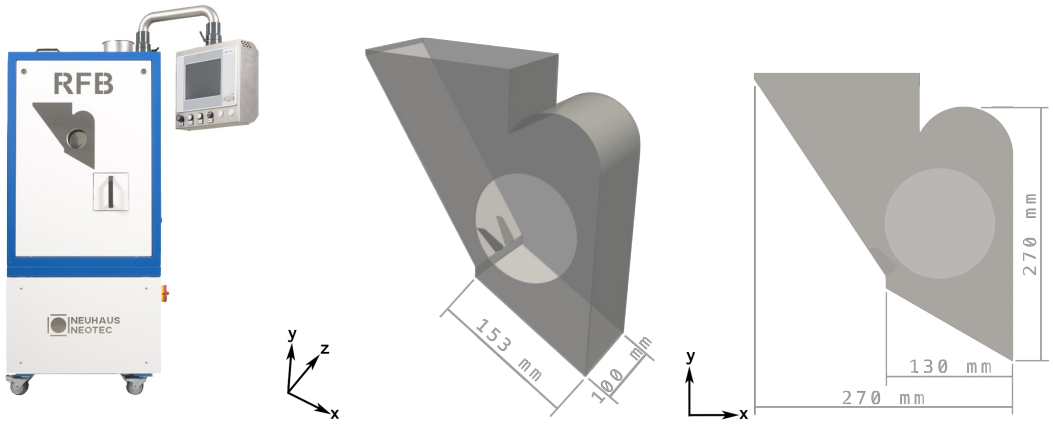

(a) (b) (c)

Figure 2.2: The Neuhaus Neotec RFB-S spouted bed roaster, illustrating the system's external and internal geometries - [geometry provided by Neotec].

The roasting chamber of the spouted bed (Figure 2.2) has a width (in x) of approximately 200 mm, height (in y) of 270 mm and a depth (in z) of 98 mm. The spouted bed uses air distributed via a distributor plate to agitate and mix coffee in the roasting chamber. The distributor is detailed in Figure 2.3(a), wherein airflow is directed into the roasting chamber

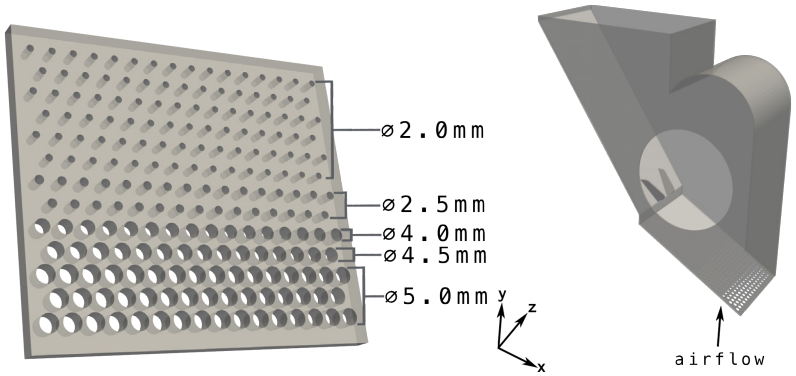

(a) (b)

Figure 2.3: Reconstructed design of the spouted bed roaster's air distributor.

from the lower right of the system (in xy) as indicated in Figure 2.3(b). The distributor design consists of approximately 200 holes with diameters that range from 2-5 mm as presented in Figure 2.3(a).

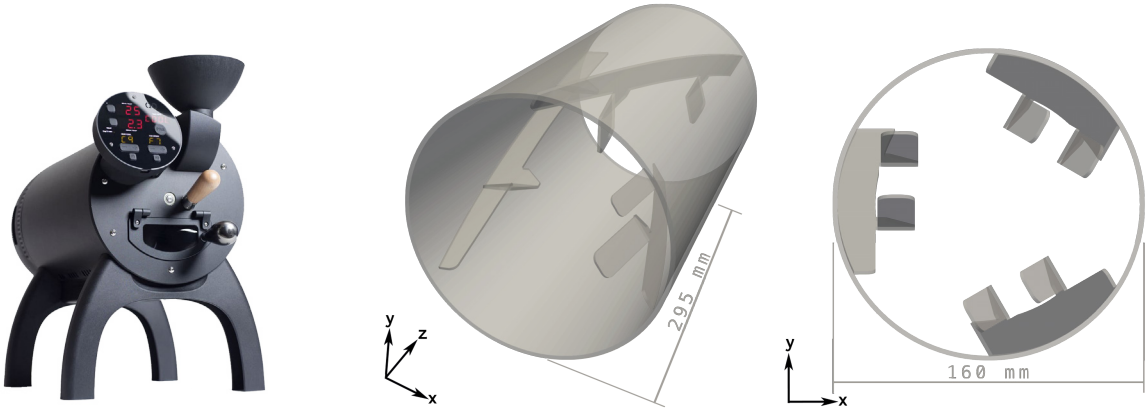

(a) (b) (c)

Figure 2.4: The Aillio Bullet R1 V2 rotating drum roaster, illustrating the system's external and internal geometries - [geometry provided by Aillio].

The roasting chamber of the rotating drum (Figure 2.4) has a diameter (in the x,y plane) of 160 mm, with a depth (in z) of 295 mm. The drum roaster, rotating clockwise in xy, employs three internal vanes (shown in Figure 2.4) to: (i) promote bean lift in the bottom left region of the roaster (in the x,y plane), (ii) improve axial mixing (in z) and (iii) positively displace the beans toward the front face (in xy) (necessary to remove coffee after roasting).

2.2 Definition of process parameters and the feasible operating conditions

Establishing the feasible operating range for a roaster is critical to ensure the experimental design explores a realistic range of process parameters employed in commercial settings. The process parameters considered here are: (i) batch size (fill volume), (ii) airflow, (iii) drum rotation speed and (iv) time-temperature profile. As the particle motion of coffee beans in the roasting chamber defines the heat transfer mechanisms and resulting physicochemical transformation rates, roaster operators must understand the influence of process parameters on coffee transformation but must also consider that process parameters should be adjusted according to the transient properties and thermal response of both product and equipment. Concerns about roast defects and batch homogeneity arise when roasters are not properly managed and so developers must quantify the boundaries (limitations) of their roaster, to provide a sensible range to start exploration. In this section, tools to characterise roasting processes and the factors that influence roasting conditions are described, and the established operating ranges of roasters of different type and scale presented.

2.2.1 Coffee bean particle motion

Process parameters such as batch size, airflow (in spouted bed roasters) and drum rotation speed (in drum roasters), influence coffee bean particle motion and have profound effects on heat transfer rates during roasting. Specification of these parameters are therefore critical for process characterisation, as well as process and product development. For each roaster, process parameters were varied within the ranges specified in Table 2.1 and used to inform the minimum, maximum and nominal operating conditions as a function of the relevant process parameters. In Chapter 4, the effect of coffee properties on coffee bean particle motion indicates that these optimal ranges evolve during roasting.

Table 2.1: Details of manufacturer recommended process parameters (batch size, airflow setting and rotation speed) for roasters used in these studies - units au refer to arbitrary units, Hz to fan frequency and % to normalised power.

Roaster Type	**Roaster Model**	**Airflow Setting**	**Drum Rotation Speed Setting**	**Batch Size (kg)**
Spouted Bed	Neotec RFB-S	30-65 Hz		0.2-0.5
Spouted Bed	Neotec RFB-Jr	30-50 Hz		2.0-5.0
Fluid bed	Ikawa Pro V3	60-100%		0.05
Rotating Drum	Bullet R1 V2	1-9 au	1-9 au	0.3-1.0
Rotating Drum	Petroncini TT8-10	50-100%	0-100%	3.0-8.0

2.2.2 Time-temperature profiles

Temperature measurement

For roasting equipment, temperature measurements are often performed using mineral-insulated thermocouples. The roasting studies in Chapter 3 are carried out on a spouted bed roaster, where inlet air, product and outlet air temperatures were measured using 1 mm diameter stainless steel (310) sheathed, mineral insulated, Type-K thermocouples (RS Components) and logged with an 8-channel type-K temperature logger (TC-08, PicoTechnology).

Preheating the roaster

Roaster preheating is as a process that enables repeatability and reproducibility and should be considered when formulating an energy balance over the roaster. For pilot-scale spouted bed & rotating drum roasters, steady-state is typically achieved within 15-30 mins, although for larger and less thermally efficient systems, time to obtain steady-state temperature is greater (S. Rao, 2014; S. Rao, 2020). Figure 2.5 depicts preheating profiles for roasters of different design and scale - outlining the importance of prescribed preheating profiles prior to roasting. These procedures ensure that roasting experiments and acquired roasted coffee samples are repeatable and reproducible.

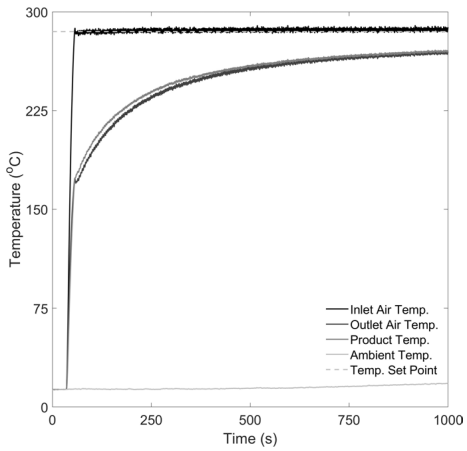

(a) Neotec RFB-S

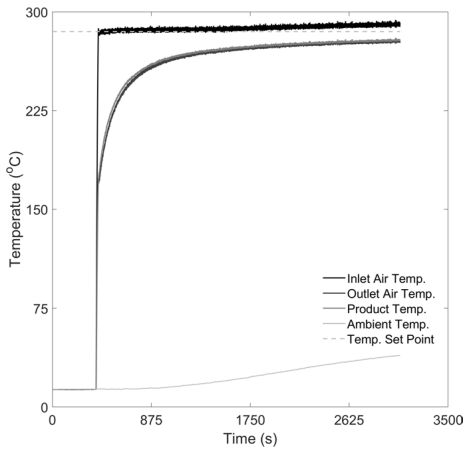

(b) Neotec RFB-Jr

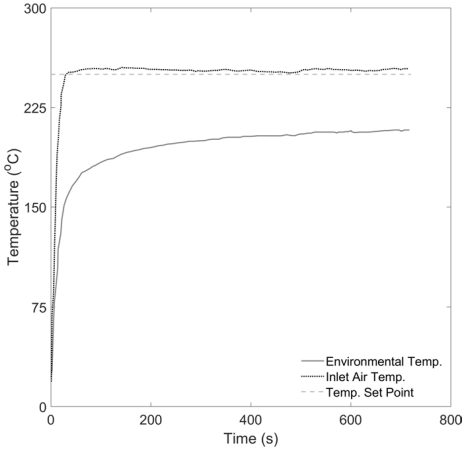

(c) Ikawa Pro V3

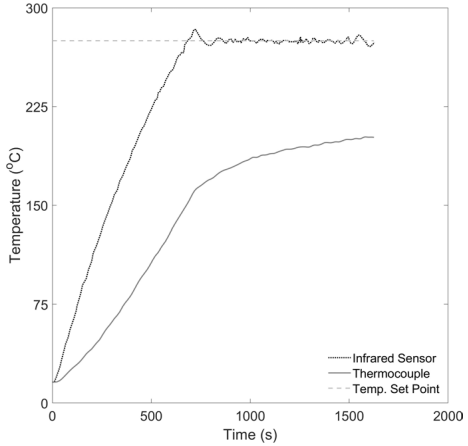

(d) Aillio Bullet R1 V2

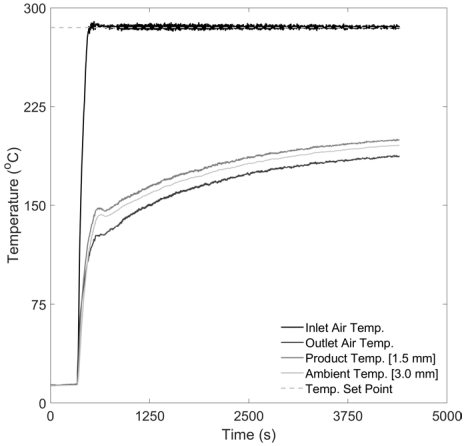

(e) Petroncini TT8-10

Figure 2.5: Time-temperature preheating profiles for the (a) RFB-S, (b) RFB-Jr, (c) Ikawa, (d) Bullet and (e) Petroncini roaster, corresponding to (a)-(c) constant inlet air temperature set-points, depicting the time-temperature responses of the inlet air, outlet air and product thermocouples, as well as the time-temperature responses of (d) the drum (via an IR sensor) and product thermocouple and (e) the inlet air, outlet air and product thermocouples.

Figures 2.5(a)-(b) show the 0.5 kg and 5.0 kg spouted bed roasters (RFB-S and RFB-Jr) required 20 minutes and 45 minutes to reach steady-state. Differences in the system's thermal capacity and heat loss explain variation across scale. In Figure 2.5(c), the Ikawa sample roaster reached steady-state in 10-12 minutes. Due to the roaster's large glass top and low thermal mass, preheating was the most rapid out of all the roasters studied here. Preheating the 1 kg Bullet roaster (Figure 2.5(d)) revealed a controlled temperature rise with steady-state achieved in 25-30 mins, although the 8 kg Petroncini roaster is shown in Figure 2.5(e) to eventually reach thermal equilibrium after 75 mins.

Although the roasting chambers are insulated, temperature variations across the roaster indicated that significant heat loss occurred. Whilst increasing thermal insulation would improve preheating times, thermal agility (i.e., the system's rapid temperature response to changes in process parameters) during roasting might be lost, such that higher airflows would be required to modulate the environmental temperature within the roasting chamber.

Effect of process parameters on steady-state charge temperature

In this subsection, the impact of process parameters on the steady-state charge temperature obtained during system pre-heating is presented for each roaster. Considerations of roasting defects are critical for charge temperatures, as preheating protocols directly determine the roasting chamber's surface temperature prior to roasting, with higher charge temperatures increasing the likelihood of product defects caused by rapid localised heating - such as facing, tipping and scorching (Hoos, 2015; Giacalone et al., 2019).

For the 0.5 and 5.0 kg spouted bed roasters (RFB-S and RFB-Jr), the steady-state product temperature was determined at different airflow and inlet air temperature set points - Figure 2.6(a)-(b) present these responses. Utility functions were produced to describe steady-state product temperature, $T_{s,s}$ (°C), as a function of both the inlet air temperature, $T_{a,i}$ (°C), and air mass flow rate, G_a (kg s^{-1}) for both the RFB-S and RFB-Jr roasters. For the RFB-S (R^2=0.9975),

$$T_{s,s} = 0.88T_{a,i} + 221G_a + 9.5 \tag{2.1}$$

For the RFB-Jr (R^2=0.9958),

$$T_{s,s} = 0.94T_{a,i} + 345G_a - 14.4 \tag{2.2}$$

For the 5 kg drum roaster (Petroncini), the impact of airflow on the steady-state temperature was non-linear (Figure 2.6(c)) and was often difficult to replicate due to long response times and significant thermal losses.

For the sample roaster (Ikawa), the steady-state temperature was determined at different inlet air temperature and airflow set-points. Product temperatures (measured via thermocouple) at steady-state, $T_{s,s}$ (°C), are displayed as a function of temperature set-point, T_{set} (°C), in Figure 2.7(a). Airflow did not have a statistically significant impact on the steady-state temperature. For the Ikawa (R^2=0.9998),

$$T_{s,s} = 0.79T_{set} + 7.9 \tag{2.3}$$

For the 1 kg drum roaster (Bullet), the steady-state temperature was determined at different temperature set-points (according to the on-board IR temperature sensor). Product temperatures (measured via the in-drum thermocouple) at steady-state, $T_{s,s}$ (°C) are displayed as a function of temperature set-point, T_{set} (°C) in Figure 2.7(b). For the Bullet (R^2=0.9956),

$$T_{s,s} = 0.8T_{set} - 32.3 \tag{2.4}$$

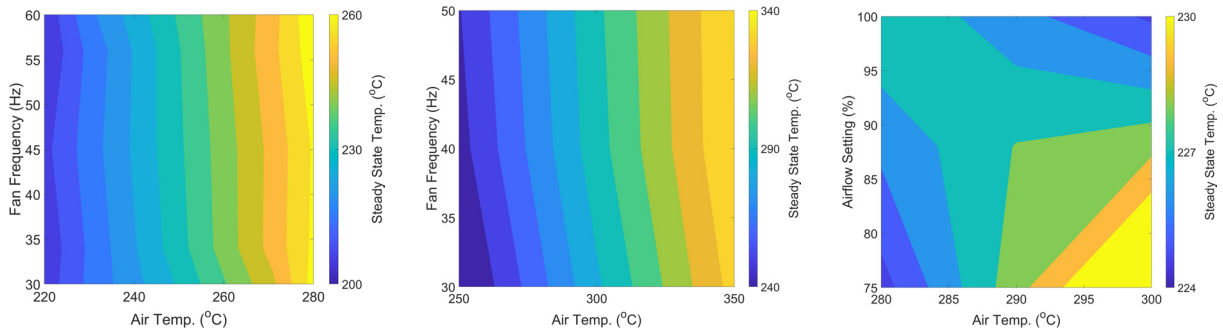

(a) (b) (c)

Figure 2.6: The effect of process parameters on steady-state temperature in the (a) RFB-S, (b) RFB-Jr and (c) Petroncini roasters.

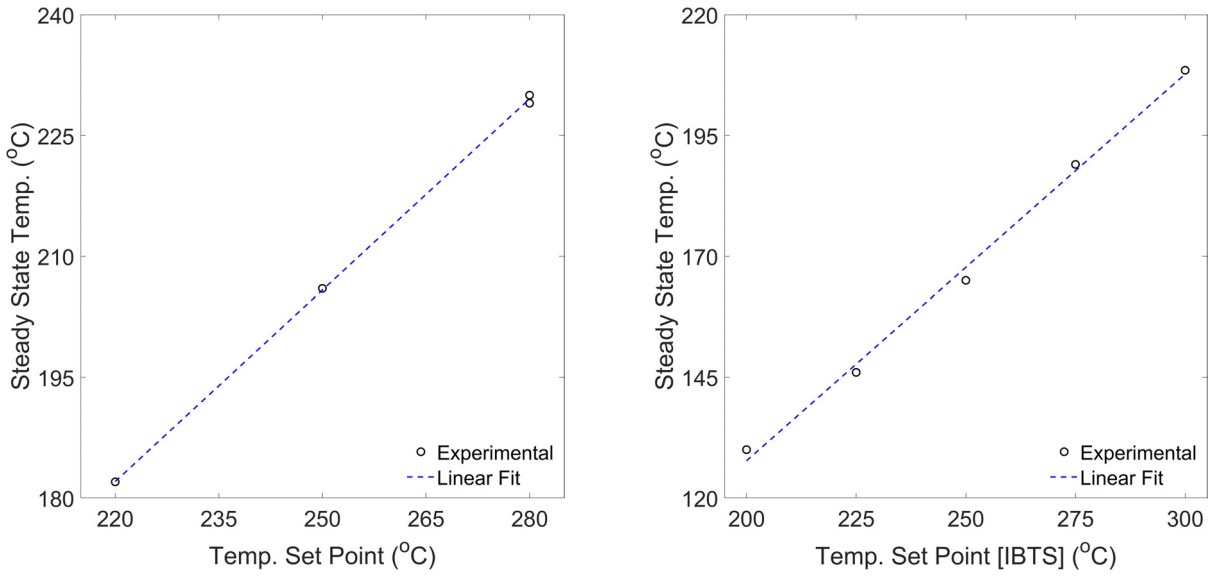

(a) (b)

Figure 2.7: Calibration of measured steady-state temperature (according to the product thermocouple) in the (a) Ikawa and (b) Bullet roasters.

Specification of roasting time-temperature profiles

In this subsection, the feasible time-temperature range was determined for each roaster to inform the appropriate experimental design space. This ensured that the full flavour space was explored, and realistic commercial products were studied. In these studies, a constant inlet air temperature (or constant power setting) was employed during roasting. During preliminary experiments, the appropriate roasting (i.e., time and temperature) space was explored for each roaster using a washed-processed Kenyan Arabica coffee until the following criteria were satisfied:

(i) "fully-roasted" coffees reflect realistic commercial products (i.e., are valued by consumers)

(ii) "fully-roasted" coffees roasted are not under-developed and can be ground to a median particle size of 500 µm using both at-home and commercial grinders

(iii) "fully-roasted" coffees are not over-developed (i.e., carbonised flavour defective), and end of roast temperatures were not expected to risk operator safety (i.e., start fires)

Table 2.2: Feasible roasting conditions that satisfy prescribed criteria for each roaster determined in preliminary experiments using a washed processed Kenyan Arabica coffee.

Roaster		**Minimum feasible Conditions**				**Maximum feasible Conditions**			
Type	**Model**	Batch Size	Inlet Air Temp.	Airflow Setting	Roasting Time	Batch Size	Inlet Air Temp.	Airflow Setting	Roasting Time
Spouted Bed	RFB-S	500 g	220°C	30 Hz	800 s	200 g	280°C	65 Hz	180 s
Spouted Bed	RFB-Jr	5 kg	250°C	30 Hz	800 s	2 kg	320°C	50 Hz	180 s
Sample	Ikawa	50 g	240°C	70%	420 s	50 g	260°C	90%	300 s

Roaster		**Minimum feasible Conditions**				**Maximum feasible Conditions**			
Type	**Model**	Batch Size	Power Setting	Drum Setting	Roasting Time	Batch Size	Power Setting	Drum Setting	Roasting Time
Drum	Bullet	1 kg	7	5	800 s	0.3 kg	9	9	360 s

Roaster		**Minimum feasible Conditions**				**Maximum feasible Conditions**			
Type	**Model**	Batch Size	Inlet Air Temp.	Drum Speed	Roasting Time	Batch Size	Inlet Air Temp.	Drum Speed	Roasting Time
Drum	Petroncini	8 kg	500°C	50 rpm	900 s	3 kg	550°C	78 rpm	360 s

The term "fully-roasted" refers to a coffee roasted to a roasting time that satisfies the above criteria and does not imply flavour preferences. The term development refers to the coffee's physicochemical transformation required to satisfy criteria (ii)-(iii). The feasible operating range of each roaster is presented in Table 2.2, which details the appropriate process parameters established in preliminary experiments. Minimum feasible conditions correspond to large batch sizes, low thermal loads and long residence times; maximum feasible conditions correspond to small batch sizes, high thermal loads and short residence times. The extremes of these operating ranges are not expected to yield preferred in-cup flavour and aroma, but the parameter space informs roasters of the boundaries of the roaster's capability. Process parameters are specified here as they would be set by developers during operation.

2.2.3 Airflow calibration

Experimental determination of airflow properties

For comparison across systems and with previous studies, it is essential to discuss process parameters in SI units, rather than arbitrary values. As many roasters use fan frequency or normalised power for airflow set-points, conversion of these settings to velocity and mass flow rate will enable cross-comparison. In this subsection, a framework for airflow calibrations is outlined, wherein utility functions that estimate air velocity and mass flow rate in the roaster are established. These functions can be integrated within heat and mass transfer models to provide a user-friendly interface for developers to interact with digital models and shadows.

For the airflow calibration, both the velocity and mass flow rate of air inputs to the roasters were determined as a function of airflow setting using a hot-wire anemometer (405i, Testo). For RFB-S and RFB-Jr roasters the anemometer was installed on the air inlet, between the blower and heating element; for the Ikawa, Bullet and Petroncini roasters the anemometer was installed on the roaster's exhaust (for visualisation of installation, see Figure 2.8). The roasters were operated at ambient temperature (ca. 20-25°C) with airflow settings varied between the minimum and maximum values stated in Table 2.1. Once steady-state conditions (i.e., constant airflows) were established, air velocity was measured for 5 mins. Measurements were duplicated, with the mean and standard deviation of velocities for each airflow setting

calculated and subsequently used to determine inlet air mass flow rates.

During measurements in the spouted bed roasters (RFB-S and RFB-Jr), as the fan frequency increased, measured temperature increased (ca. +19 and +16°C, respectively) - likely due to dissipated heat from the fan's motor, surface friction between air and the fan's blades or pipe walls, as well as intermolecular friction between air molecules (the latter only becomes significant under turbulent flow). As the air density is corrected according to the ideal gas law, roasters are typically operated above 200°C and are often controlled to specified inlet air temperature, fan induced heating is assumed negligible during roasting and not expected to impact experimental or model responses.

Both air velocity, u_a (m s^{-1}) and mass flow rate, G_a (kg s^{-1}) were determined as a function of airflow setting, f (units as in Table 2.1), for each roaster and are shown in Figures 2.9-2.10. Data are also presented as utility functions in Table 2.3. These utility functions were generated based on the following framework.

Table 2.3: Airflow calibrations that estimate velocity (u_a) and mass flow rate (G_a) of air as a function of the fan setting (f) in different roaster types and scales - experimental data is also shown in Figures 2.9-2.10.

Property	**Roaster**	**Utility Function**	**R²**
Air Velocity (m s^{-1})	Neotec RFB-S	$u_a = 0.165f - 0.716$	0.999
	Neotec RFB-Jr	$u_a = 0.554f + 0.126$	0.993
	Ikawa Pro V3	$u_a = 0.047f - 0.815$	0.986
	Bullet R1 V2	$u_a = 0.133f + 0.421$	0.998
	Petroncini TT8-10	$u_a = 0.080f + 3.800$	0.999
Air Mass Flow Rate (kg s^{-1})	Neotec RFB-S	$G_a = 4.84 \times 10^{-4}f - 4.12 \times 10^{-4}$	0.998
	Neotec RFB-Jr	$G_a = 1.56 \times 10^{-3}f + 7.25 \times 10^{-3}$	0.987
	Ikawa Pro V3	$G_a = 3.90 \times 10^{-5}f - 6.70 \times 10^{-4}$	0.987
	Bullet R1 V2	$G_a = 3.17 \times 10^{-4}f + 1.01 \times 10^{-4}$	0.998
	Petroncini TT8-10	$G_a = 1.93 \times 10^{-3}f + 9.19 \times 10^{-2}$	1.000

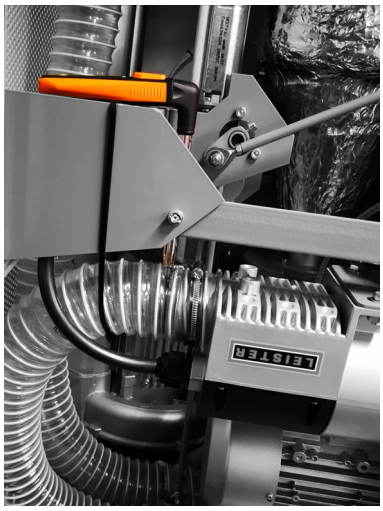

(a) Neotec RFB-S

(b) Neotec RFB-Jr

(c) Ikawa Pro V3

(d) Aillio Bullet R1 V2

(e) Petroncini TT8-10

Figure 2.8: Installation of the hot wire anemometer (highlighted in colour) on (a) RFB-S, (b) RFB-Jr, (c) Ikawa, (d) Bullet and (e) Petroncini roasters (desaturated for clarity) for airflow measurements.

The volumetric flow rate of air is a function of its velocity, u_a (m s^{-1}) and the cross-sectional area of the pipe, A_p (m^2) (Bergman et al., 2011):

$$V_a = u_a A_p \tag{2.5}$$

Assuming turbulent flow (where Re»1) and that the mean air speed does not vary across the pipe, the air mass flow rate, G_a (kg s^{-1}), is a function of its density, ρ_a (kg m^{-3}) and volumetric flow rate, V_a (m^3 s^{-1}) (Bergman et al., 2011):

$$G_a = V_a \rho_a \tag{2.6}$$

The cross-sectional area of the pipe being a function of the pipe diameter, d_p (m) (Bergman et al., 2011):

$$A_p = \frac{\pi d_p^2}{4} \tag{2.7}$$

where measured equivalent pipe diameters for the RFB-S, RFB-Jr, Ikawa, Bullet and Petroncini roasters were 60, 60, 30, 50 and 160 mm, respectively.

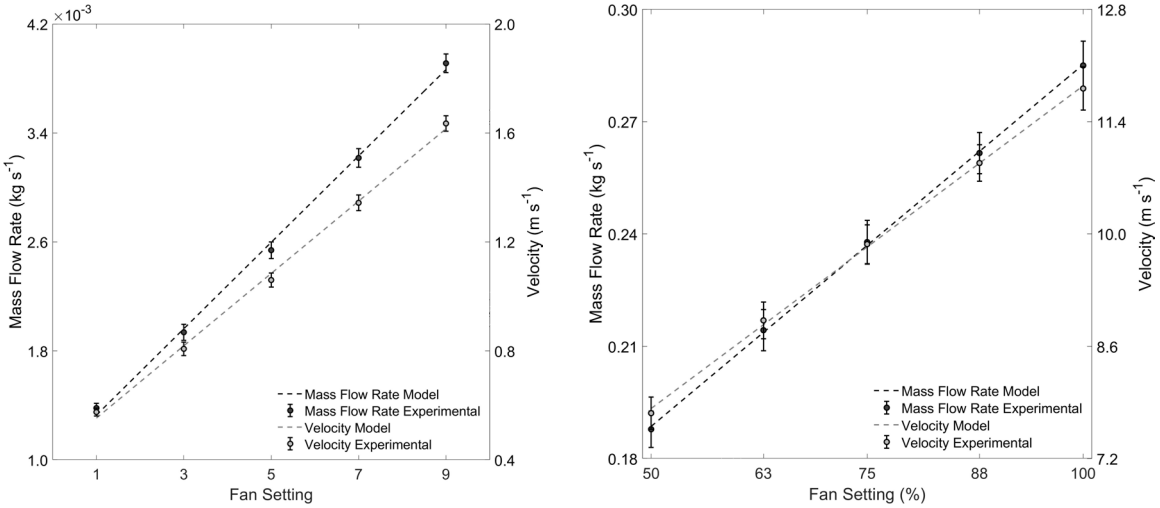

(a) Aillio Bullet R1 V2 (b) Petroncini TT8-10

Figure 2.9: Correlation of velocity and air mass flow rate as a function of airflow setting for the (a) Bullet and (b) Petroncini roaster - mass flow rate data correspond to the primary (left-hand) axis, velocity to the secondary (right-hand) axis.

Using the ideal gas law, the air density can be determined as a function of pressure, P_a (Pa) and temperature, T_a (K) (Bergman et al., 2011):

$$\rho_a = \frac{P_a}{R_a T_a} \tag{2.8}$$

where air pressure is assumed atmospheric and the gas constant for air, R_a, is equal to 287 J kg^{-1} K^{-1}; the air temperature is that recorded by the anemometer.

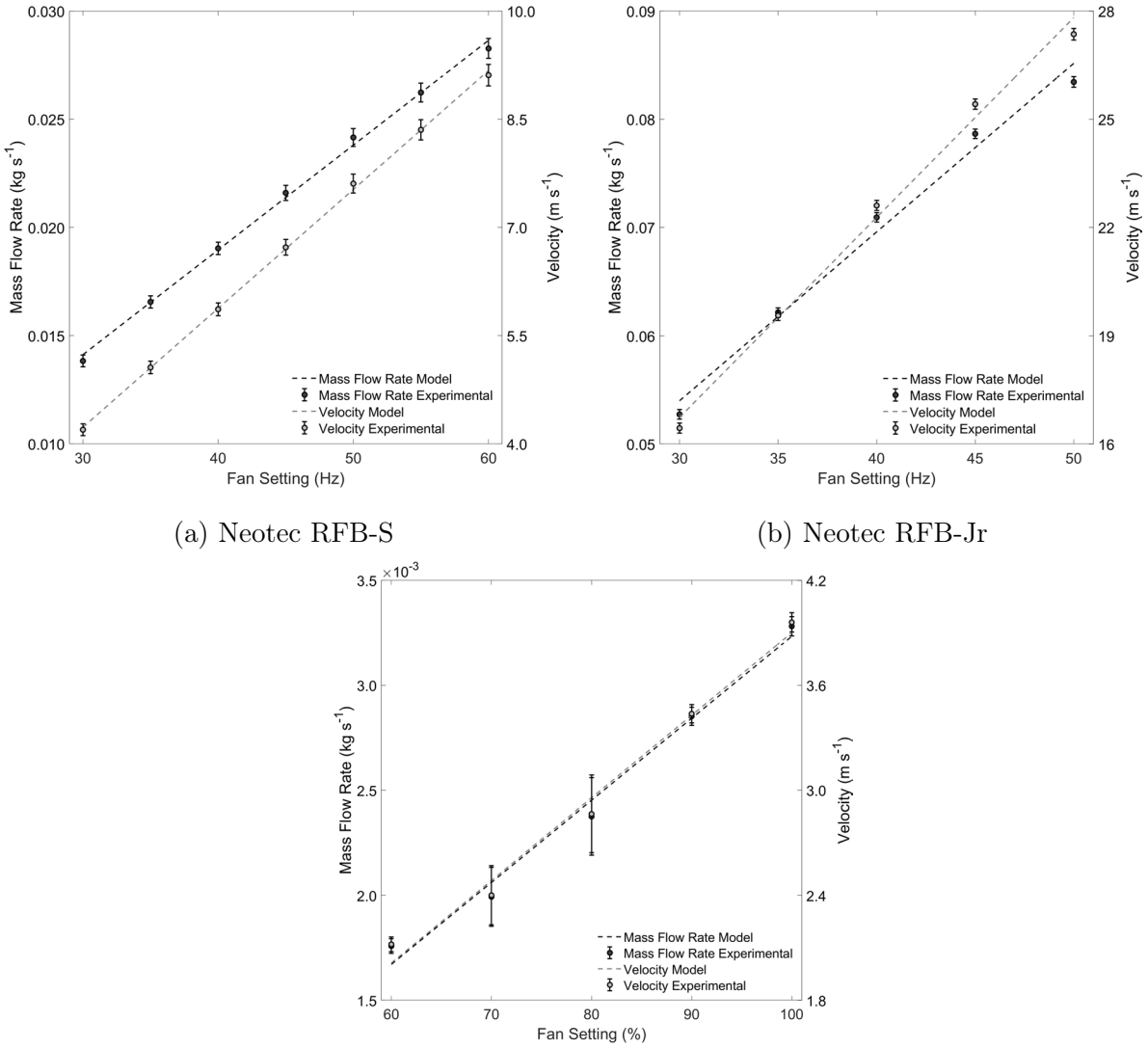

(a) Neotec RFB-S

(b) Neotec RFB-Jr

(c) Ikawa Pro V3

Figure 2.10: Correlation of velocity and air mass flow rate as a function of airflow setting for the (a) RFB-S, (b) RFB-Jr and (c) Ikawa roaster - mass flow rate data correspond to the primary (left-hand) axis, velocity to the secondary (right-hand) axis.

The effect of the air distributor

For the RFB-S roaster, fan frequencies of 30-65 Hz, correspond to air velocities of 4.2-10.0 m s^{-1} and inlet air mass flow rates of 0.0141-0.0311 kg s^{-1} at the inlet of the roaster. The effect of the roaster's air distributor (Figure 7.3) on air velocity in the roasting chamber (i.e., the superficial air velocity) was considered to increase model accuracy (Che et al., 2023).

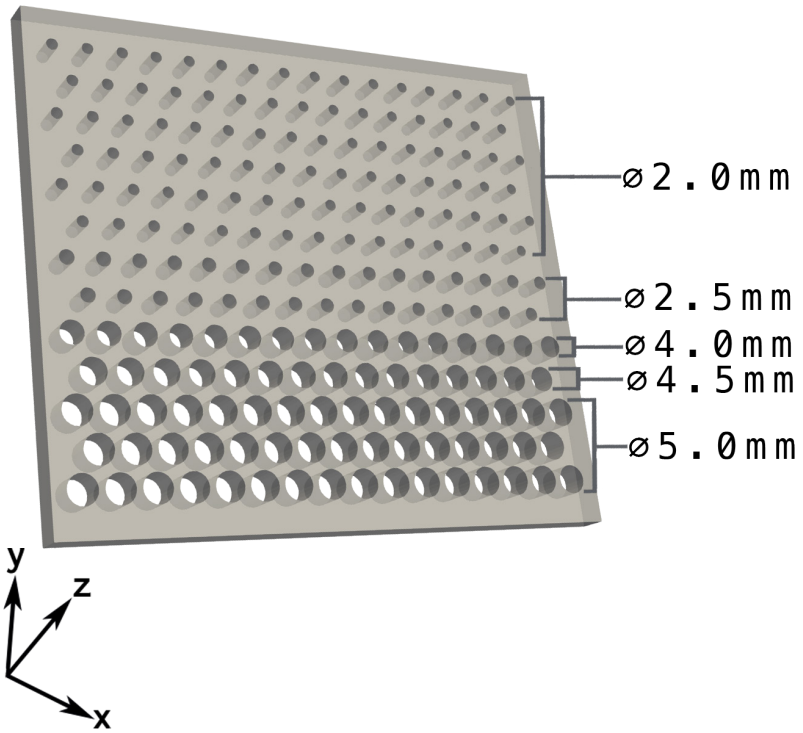

Figure 2.11: Geometry of the air distributor of the spouted bed roaster used to determine the air velocity at the roaster's spout.

The air velocity at the roaster's spout was estimated via the distributor's open area across the largest 5 rows of the plate design, according to the continuity equation (Bergman et al., 2011). Orifice diameters < 2.5 mm (rows 6-13) are expected to have little impact on the spout's air velocity. For an open area of 1.36 cm^3, assuming no change in density, the superficial air velocity through the orifice and into the roasting chamber for fan frequencies of 30, 39, 48 and 65 Hz are 8.79, 11.87, 14.95 and 20.77 m s^{-1}, respectively, at ambient temperature (ca. 20°C).

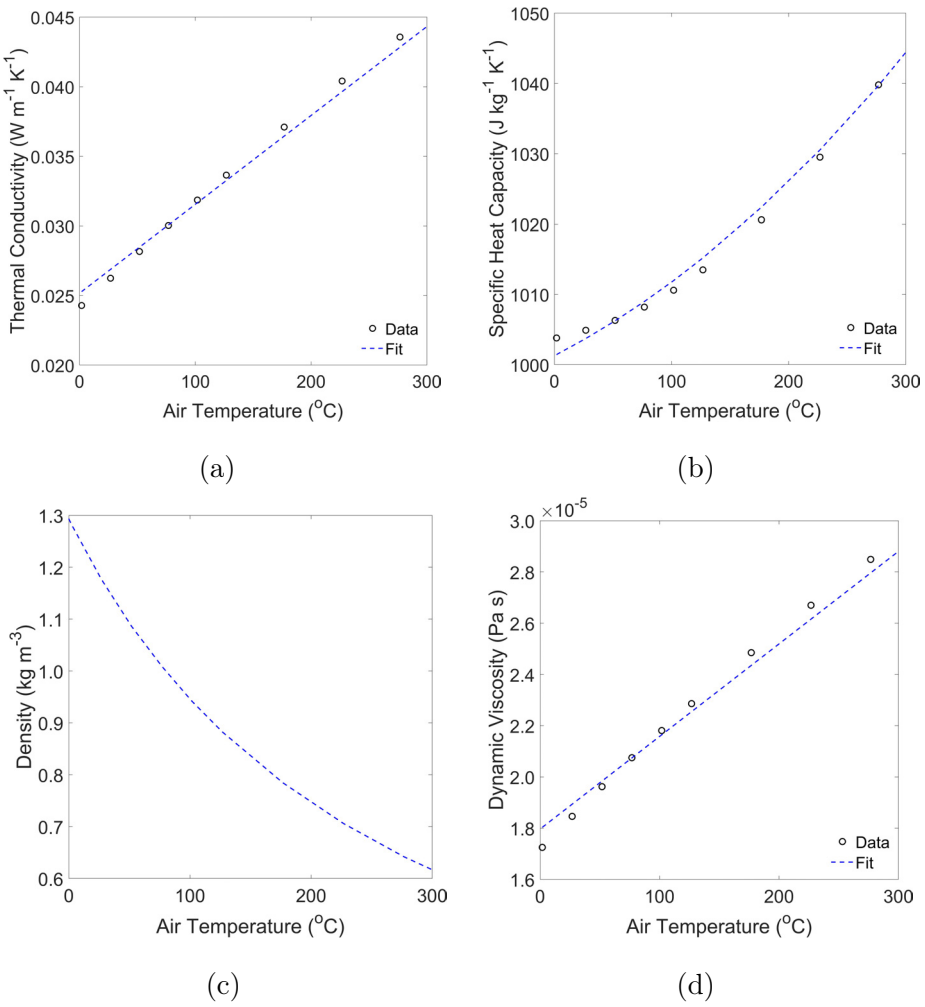

Figure 2.12: Correlation of air's thermal properties (a) thermal conductivity, (b) specific heat capacity, (c) density and (d) dynamic viscosity with air temperature.

Thermophysical properties of air

The thermophysical properties of air are dependent on air temperature. Utility functions were generated via regression of thermophysical data from Engineering-ToolBox to describe the air's thermal conductivity, k_a (W m^{-1} K^{-1}), specific heat capacity, $C_{p,a}$ (J kg^{-1} K^{-1}) and viscosity, μ_a (Pa s) as a function of air temperature, T_a (K). Air density, ρ_a (kg m^{-3}) was determined according to the ideal gas law, using the gas constant for air (287.05 $J\ kg^{-1}\ K^{-1}$ (Engineering-ToolBox, 2020)) with roaster pressure assumed to be atmospheric (101325 Pa).

$$k_a = 6.38 \times 10^{-5} T_a + 7.72 \times 10^{-3} \tag{2.9}$$

$$C_{p,a} = 6.16 \times 10^{-5} T_a^{2.15} + 990 \tag{2.10}$$

$$\mu_a = 3.61 \times 10^{-8} T_a + 8.1 \times 10^{-6} \tag{2.11}$$

The RMSE of models for thermal conductivity, specific heat capacity and viscosity were $6.0\times\ 10^{-4}$ W m^{-1} K^{-1}, 1.5 J kg^{-1} K^{-1} and $4.4\times\ 10^{-7}$ Pa s, respectively. Correlation of these data are displayed in Figure 2.12). Eqs. 2.9-2.11 can then be integrated within heat and mass transfer simulations to improve model accuracy.

2.2.4 Thermocouple characterisation

A thermocouple's temperature response depends largely on the thermocouple's diameter. In this subsection, the effect of thermocouple diameter on its temperature response was predicted using first principle approximations, experimentally validated using a lab-scale model system and, later in Chapter 3, verified *in-situ* in a pilot-scale spouted bed roaster.

First principles prediction of thermocouple time constants

Thermocouples with diameters in the range of 0.5-3.0 mm were considered as they can sensibly be installed in lab- and pilot-scale roasters. For thin thermocouples ($d_T \leq 3.0$ mm), radial heat transfer through the sheath is rapid (Yilmaz, 2011), radial heat transfer across the insulated cross-section is slow (Yilmaz, 2011) and radiative heat transfer is small in comparison, so is assumed negligible (Papaioannou, Leach, and Davy, 2018).

To predict the heat transfer properties of a thermocouples with a diameter d_t, it's assumed that: (i) the sheath thickness is $0.32d_t$ and is formed from stainless steel 310 (25% Nickel, 20% Chromium) (Yilmaz, 2011), (iii) the exposed length is equal to the diameter and (iv) the thermocouple tip is hemi-spherical, (v) the insulation thickness is $0.68d_t$ and is formed from Magnesium Oxide (MgO) (Yilmaz, 2011), (vi) the junction (thermoelement) is formed from Alumel with a thickness of $0.29d_t$ (Yilmaz, 2011) and (vii) the effective thermophysical properties are determined as a composite of the individual components evaluated at the process temperature. These properties are displayed in Table 2.4.

Table 2.4: Thermophysical properties of air and thermocouple components at 200°C, where C_p denotes specific heat capacity (J kg^{-1} K^{-1}), ρ density (kg m^{-3}) and k thermal conductivity (W m^{-1} K^{-1}).

Component	ρ **(kg m^{-3})**	$\mathbf{C_p}$ **(J kg^{-1} K^{-1})**	**k (W m^{-1} K^{-1})**	**Data Source**
Sheath	7762.3	518.2	15.7	(Blumm et al., 2007)
Insulation	3480	1114.5	5.26	(Yilmaz, 2011)
Thermoelement	8100	32.5	536.3	(Yilmaz, 2011)
Air	0.729	1025.1	0.0385	(Engineering-ToolBox, 2020)

For transient heat transfer in cylindrical geometry, the total heat flux, q_{total} (W) is considered to be convective, q_{conv} (W) and conductive, q_{cond} (W) heat (Bergman et al., 2011):

$$q_{total} = q_{conv} + q_{cond} = h_{at}A_{s,t}(T_a - T_{t,s}) + \frac{k_{t,e}A_{c,t}}{L_t}(T_{t,s} - T_{t,c}) \tag{2.12}$$

where $k_{t,e}$ is the effective thermal conductivity, the characteristic length, L_t (m) is related to the thermocouple radius, r_t (m) and corresponding cross-sectional area, $A_{c,t}$ (m^2), whilst subscripts $_{t,s}$ and $_{t,c}$ refer to the surface of the thermocouple (i.e., of the sheath) and core (i.e., the centre of the junction), respectively.

The thermal balance to describe the transient conduction is thus (Bergman et al., 2011):

$$m_t C_{p,t}\frac{dT_t}{dt} = U_t A_t(T_a - T_{t,c}) \tag{2.13}$$

where $C_{p,t}$ is the thermocouple's specific heat capacity (J kg^{-1} K^{-1}), A_t is the thermocouple's total heat transfer area (mm^2), the thermocouple's mass, m_t (kg), was estimated using the density and volume of its components and the overall heat transfer coefficient, U_t (W m^{-2} K^{-1}) is defined in terms of the thermocouple's thermal resistance, R_t (m^2 K W^{-1}) (Bergman et al., 2011):

$$U_t = \frac{1}{R_t} = \frac{1}{\frac{1}{h_{at}} + \frac{r_{t,s}}{k_{t,s}}\ln\left(\frac{r_{t,s}}{r_{t,i}}\right) + \frac{r_{t,i}}{k_{t,i}}\ln\left(\frac{r_{t,i}}{r_{t,j}}\right)} \tag{2.14}$$

subscripts $_s$, $_i$ & $_j$ refer to the sheath, insulation, and junction of the thermocouple, respectively.

The convective heat transfer coefficient, h_{at} (W m^{-2} K^{-1}) is found from the Nusselt number, Nu, thermal conductivity of drying air, k_a (W m^{-1} K^{-1}) over a characteristic length (Whitaker, 1972):

$$h_{at} = \frac{Nuk_a}{L_t} \tag{2.15}$$

where $L_t = d_t$ (i.e., assumed to be the thermocouple's diameter) and the Nusselt number, for rods in a crossflow, is approximated via the Reynolds number, Re (Whitaker, 1972):

$$Nu \approx 0.35(Re)^{1/2} + 0.052(Re)^{2/3} \tag{2.16}$$

and the Reynolds number is a function of the density, ρ_a (kg m^{-3}), velocity, u_a (m s^{-1}) and viscosity, μ_a (Pa s) of air and the thermocouple's exposed length, $L_{t,e}$ (m) (Whitaker, 1972):

$$Re = \frac{\rho_a u_a L_{t,e}}{\mu_a} \tag{2.17}$$

where $L_{t,e} = d_t$ (i.e., the thermocouple's diameter). Air velocity reflects that of the model system described below (2.12, 2.87 and 3.96 m s^{-1}) and viscosity (2.56x10^{-5} Pa s at the (later specified) model system's air temperature of 200°C); the thermophysical properties of air are outlined in Table 2.4 (Engineering-ToolBox, 2020).

The time constant, τ (s^{-1}) is the ratio of the thermocouple's thermal energy to the applied convective thermal energy (Papaioannou, Leach, and Davy, 2018):

$$\tau = \frac{m_t C_{p,t}}{h_{at} A_{s,t}} \tag{2.18}$$

Over the length of the exposed thermocouples, the Reynolds number varied from 181.0-338.1, with corresponding Nusselt numbers of 6.37-8.96. Heat transfer coefficients for each thermocouple diameter at the measured air velocities are displayed in Figure 2.13(a). Eq. 2.18 was used to estimate the time constants based on the thermocouple's thermophysical properties, shown in Figure 2.13(b).

For all thermocouples, the convective heat transfer coefficient increases with air velocity according to the Reynolds number (Bergman et al., 2011) and is lower for larger thermocouples due to a reduced heat transfer area per unit mass. The response time of thin thermocouples is only slightly impacted by air velocity (visible in Figure 2.13(b)) and are largely governed by

their diameter and the corresponding convective heat transfer to their surface. For simplification, the time constant predicted from first principles (τ_{fp}) can be reduced to a single-term power law as a function of the thermocouple's diameter (RMSE = 0.61 s):

$$\tau_{fp} = 1.85 d_t^{1.47} \tag{2.19}$$

The predicted time constants are inversely proportional to both the convective heat transfer coefficient and associated heat transfer area, thus over-estimation of these two parameters will significantly decrease the predicted time constants. Assumptions of the thermocouple's effective thermophysical properties also impact the predicted time constants. Nevertheless, based on these values extracted from literature, Eq. 2.19 can inform the relative effect of diameter on response time for the specified geometry.

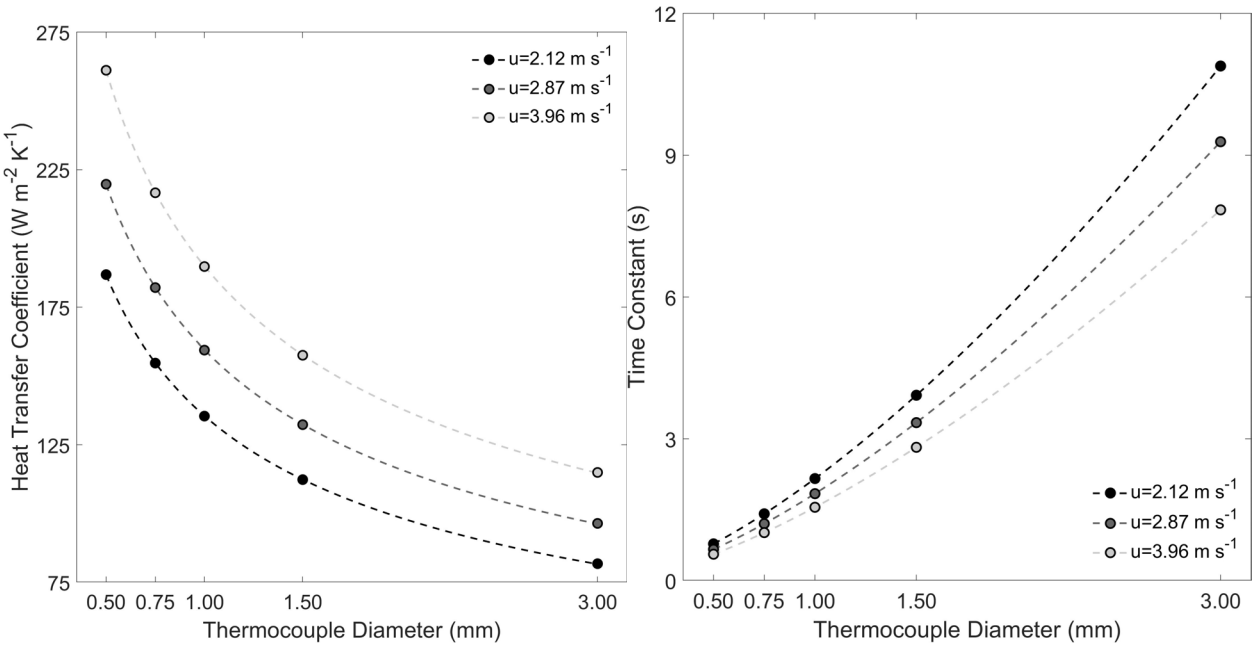

(a) (b)

Figure 2.13: Predicted a) convective heat transfer coefficients and b) corresponding time constants for thermocouples of varying diameters in airflows with different velocities.

Lab-Scale validation of thermocouple time constants

Here, the first principles approach was validated using a lab-scale model system. For both experimental validation and verification, temperature measurements were performed using five thermocouples of different diameters (0.50, 0.75, 1.00, 1.50 and 3.00 mm), each with a length of 150 mm (TC Direct), logged with an 8-channel type-K temperature logger (TC-08, Pico Technology). Data were analysed in MATLAB (2020a, MathWorks).

Thermocouple time constants were determined experimentally using a model system comprising the Ikawa Pro V3 roaster, a retort stand and a make-shift support for the thermocouples, as depicted in Figure 2.14. Using a constant exhaust temperature (200°C) and different airflow settings (60, 80 and 100% fan power which correspond to velocities of 2.12, 2.87 and 3.96 m s^{-1}, respectively), thermocouples were 'plunged' into the air stream of the roaster's exhaust from ambient air (ca. 20°C), held for 2 minutes, removed from the air stream, held in ambient conditions (ca. 20°C) for 5 minutes to cool, and repeated in triplicate.

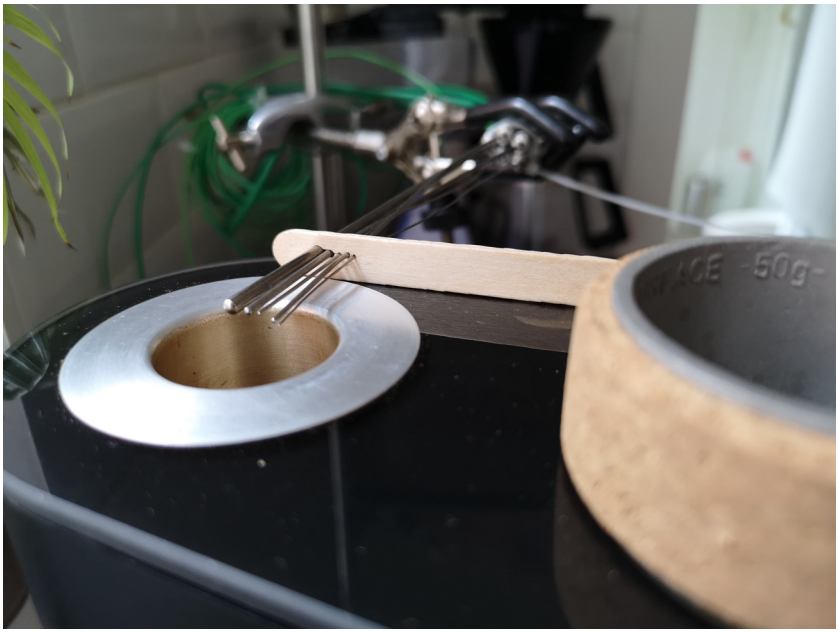

Figure 2.14: Model system used to determine thermocouple time constants comprising the Ikawa Pro V3 roaster, a retort stand and a make-shift support for the thermocouples.

Figure 2.15 illustrates the steady-state temperatures achieved during heating (to measurement temperature) and cooling (to ambient temperatures) in the model system.

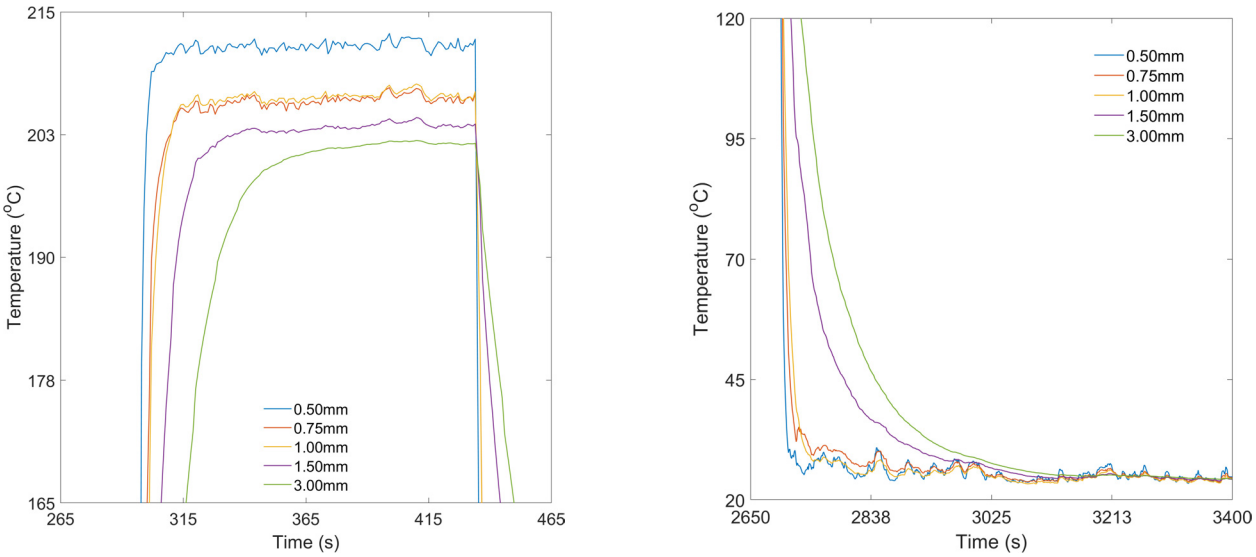

(a) Air (200°C; 3.96 m s^{-1} airflow) (b) Air (20°C; no airflow)

Figure 2.15: Steady-state temperatures of thermocouples of different diameters in (a) high temperature, high velocity (200°C, 3.96 m s^{-1}) airflow and (b) ambient air (20°C, no airflow).

For the model system, the steady-state temperature decreases with thermocouple diameter (visible in Figure 2.15). A difference of approx. 10°C was observed between 3.00 mm and 0.50 mm thermocouples due to differences in the radial pathlengths over which thermal conduction occurs, as well as heat transfer areas over which convection occurs (Yilmaz, 2011). Despite differences in diameter, responses for 0.75 mm and 1.00 mm thermocouples appear insignificant, perhaps due to variation in physical properties due to manufacturing (Carroll and Shepard, 1977).

Thermocouple time constants were determined as the time taken to achieve 20.0 and 63.2% of the step-change (Carroll and Shepard, 1977). The dependency of thermocouple time constants on thermocouple diameter for the model system is shown in Figure 2.16. For the model system, the time constants at both 20.0% (Figure 2.16(a)) and 63.2% (Figure 2.16(b)) increase with thermocouple diameter. For the system's dead-time (time constants at 20.0%), air velocity has no apparent effect; for those at 63.2%, the dependence of air velocity is only apparent for larger diameters (≥1.50 mm), likely due to the rapid response

of smaller diameter thermocouples. Figure 2.16 shows that the model system can determine thermocouple time constants with little variability, although dependence on flow conditions is not definitive likely due to the roaster's limited range of airflow. Therefore, the systemic time constants were devised to simplify the model using values corresponding to 63.2% of the steady-state temperature.

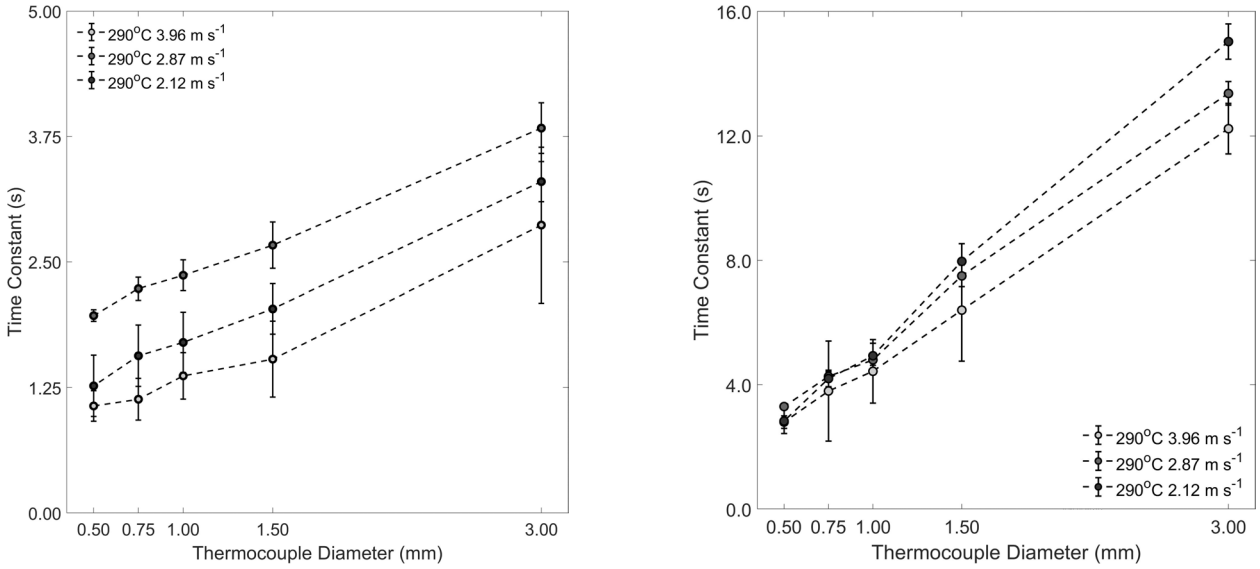

(a) 20.0% (b) 63.2%

Figure 2.16: Impact of flow conditions on determined time constants at (a) 20.0% and (b) 63.2% for the model system at different velocities.

Figure 2.17 presents the systemic time constants for the model system as they relate to thermocouple diameter. Note that the standard deviation of data indicated in Figure 2.17 is a function of both experimental variation and applied conditions. The systemic time constants (at 63.2% of the steady-state temperature), τ (s^{-1}) as a function of thermocouple diameter, d_t (mm) is thus (RMSEτ=0.68 s):

$$\tau = 4.25d_t + 0.78 \tag{2.20}$$

Based on the data presented in Figure 2.17, the model system can be used to characterise thermocouple time constants and develop a utility function to describe the thermocouple time constants as a function of thermocouple diameter (Eq. 2.20).

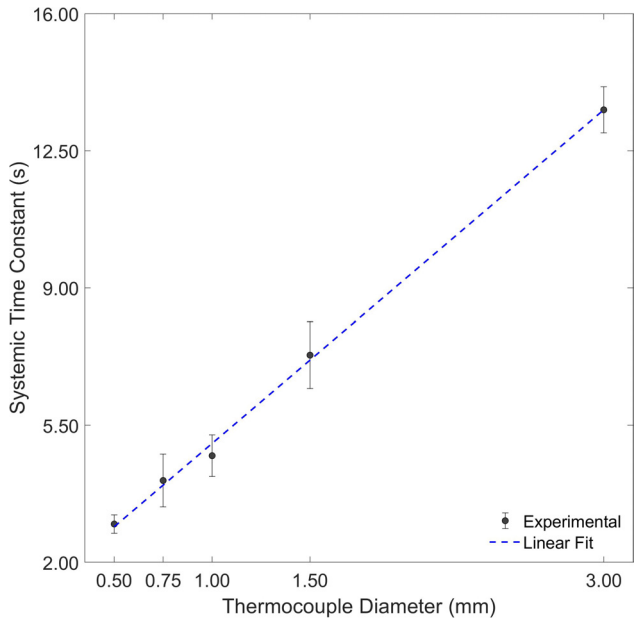

Figure 2.17: Correlation of systemic time constants for the model system.

Comparison of first principles and experimental approaches

To quantify discrepancies between the experimental and first principles approach, the systemic time constants (i.e., those estimated via experiment and first principles modelling) were correlated and are presented in Figure 2.18.

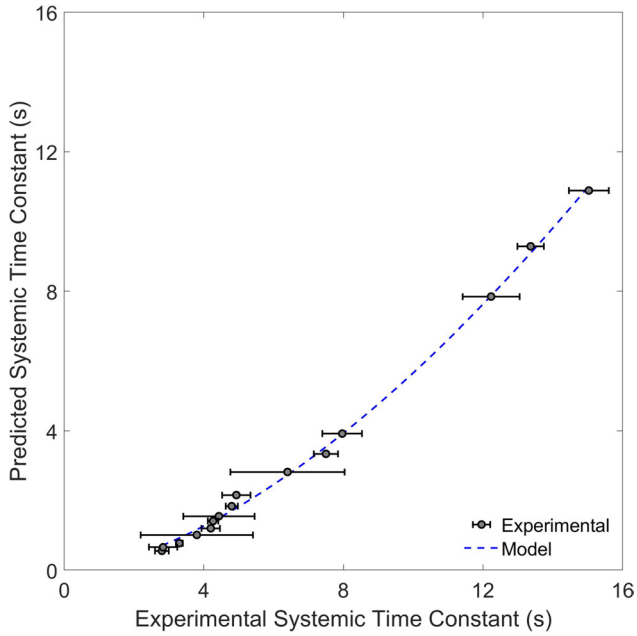

Figure 2.18: Comparison of predicted and experimental systemic time constants of thermocouples in a hot air stream - dependent only on thermocouple diameter.

A single-term power law was used to correlate the systemic time constants from the first principle and experimental approaches (RMSE = 0.18 s):

$$\tau_{fp} = 0.13\tau_e^{1.63} \tag{2.21}$$

With Eq. 2.21, the true thermal response coefficient of the experimental system is estimated. Thus, combining Eq. 2.20 & 2.21, a thermocouple's response to changes in the temperature of a roaster ($\Delta_T \approx 200°C$) can be predicted and the turning-point of a time-temperature roast profile be approximated. These utility functions can be integrated within heat and mass transfer studies used for time-temperature profile simulations and help approximate the translation of time-temperature profiles from one roaster to another.

2.3 Conclusions & outlook

This chapter described the roasters used for roasting studies and established techniques to characterise process conditions in roasters of different designs and scales. Determination of the viable operating range included the impact of preheating on the steady-state temperature, the influence of agitation on particle motion and the appropriate time-temperature range that collectively can be used to guide developers during process and product development.

To convert arbitrary setpoint values, a calibration was developed to determine the airflow in the roaster as a function of the fan frequency. This calibration can be nested within heat and mass transfer simulations to convert arbitrary setpoints to SI units.

To appreciate the impact of thermocouple properties on temperature measurement, an energy balance was used to predict the heat transfer in thermocouples of different diameters. This first-principles approach was validated by a rapid experimental method designed to characterise the thermal response coefficient of thermocouples of different diameters. A calibration was then developed to predict the thermal response coefficient as a function of the thermocouple's diameter. These techniques enable appropriate characterisation and specification of roasting conditions and facilitate cross-comparison of roasters and use of real process data to calibrate heat and mass transfer simulations.

2.4 Appendix: Determination of the viable operating range

For each roaster, the feasible operating range with regards to particle motion were determined qualitatively. Under ambient temperature conditions (such that coffee properties can be assumed constant with time), coffees of different density (green, part-roasted and roasted), selected to emulate physical changes during roasting, were loaded into the roaster, and batch size (mass basis), (m_{bs}), drum rotation speed (where appropriate), S_r (rpm, or arbitrary setpoint), and airflow (Hz, %, or arbitrary setpoint) were varied according to manufacturer recommendations (see Table 2.1). Different density coffees were obtained by roasting 8 kg of natural-processed Brazilian Arabica coffee in a drum roaster (TT8-10, Petroncini) to different roast degrees using a constant inlet air temperature (525°C) for 0, 5 and 10 mins to obtain green, part-roasted and roasted coffee samples whose bulk densities, ρ_{bulk} (kg m^{-3}), were 666, 456 and 319 kg m^{-3}, respectively.

For spouted (and fluid) bed roasters (RFB-S, RFB-Jr and Ikawa), airflow was increased from the minimum setpoint until particles spouted and motion in the bean-bed was established. Airflow required for minimum spouting was thus dependent on batch size, with larger batches requiring higher airflow for spouting. The maximum airflow setting was specified to ensure no beans were propelled beyond the roasting chamber (i.e., into the outlet, or chaff bin). Based on preliminary experiments, the recommended operating range for spouted (and fluid) bed roasters (RFB-S, RFB-Jr and Ikawa) are detailed in Table 9.1. For RFB-S and RFB-Jr roasters, the maximum airflow set point (allowed by the control system) was appropriate for all tested batch sizes and coffee densities. For the Ikawa, the maximum airflow set point was dependent on coffee density only (i.e., batch size had no statistical impact).

For rotating drum roasters (Bullet and Petroncini), the drum's rotation speed was increased from the minimum setpoint until bean-bed motion was established and the flow regime resembled cascading motion. The minimum drum rotation speed was that at the transition from rolling to cascading motion (Henein, Brimacombe, and Watkinson, 1983). For all roasters, these tests were repeated for batch sizes in the range given in Table 2.1 and for coffees of different densities (green, part-roasted and roasted). Recommended operating

Table 2.5: Utility functions that predict the recommended range of airflow setting (f) for RFB-S, RFB-Jr and Ikawa roasters according to coffee's batch size (m_{bs}) and bulk density (kg m^{-3}) (i.e., fill volume).

Roaster	**Set Point Type**	**Utility Function**	**R²**
Neotec RFB-S	Minimum (Hz)	$f = 4.41 \times 10^{-3}\rho_{bulk} + 0.0389m_{bs} + 23.72$	0.930
	Recommended (Hz)	$f = 2.20 \times 10^{-3}\rho_{bulk} + 0.0194m_{bs} + 44.36$	0.930
	Maximum (Hz)	$f = 65$	
Neotec RFB-Jr	Minimum (Hz)	$f = -0.0199\rho_{bulk} + 4.71m_{bs} + 30.67$	0.797
	Recommended (Hz)	$f = 9.95 \times 10^{-3}\rho_{bulk} + 2.35m_{bs} + 40.33$	0.797
	Maximum (Hz)	$f = 50$	
Ikawa Pro V3	Minimum (%)	$f = 0.0284\rho_{bulk} + 0.50m_{bs} + 37.20$	0.921
	Recommended (%)	$f = 0.0416\rho_{bulk} + 0.25m_{bs} + 51.26$	0.892
	Maximum (%)	$f = 0.0548\rho_{bulk} + 65.33$	0.822

Table 2.6: Utility functions that predict recommended range of rotational speeds, (S_r) for the Petroncini drum roaster - units *au* refer to arbitrary units.

Roaster	**Set Point TYpe**	**Utility Function**	**R²**
Bullet R1 V2	Minimum (au)	$S_r = 1$	
	Recommended (au)	$S_r = 5$	
	Maximum (au)	$S_r = 9$	
Petroncini TT8-10	Minimum (rpm)	$S_r = -0.0416\rho_{bulk} + 2.67m_{bs} + 53.32$	0.888
	Recommended (rpm)	$S_r = -0.0350\rho_{bulk} + 2.33m_{bs} + 63.48$	0.951
	Maximum (rpm)	$S_r = -0.0284\rho_{bulk} + 2.00m_{bs} + 73.64$	0.993

ranges for Petroncini and Bullet roasters are detailed in Table 9.2 – the R-squared of the function is also displayed to indicate goodness of fit. For the Bullet roaster, all applicable rotation speeds were appropriate for roasting and thus utility functions are invariant.

Chapter Three

Coffee's physicochemical transformation during roasting

By establishing standardised protocols for coffee characterisation, specification of coffee's intrinsic properties before, during and after roasting can be defined. Through tracking coffee's physicochemical transformation during roasting and subsequently mapping the impact of process parameters on coffee's development, a network of roasting pathways and their products can be documented. These tools can then be used by process and product developers to (i) enhance our fundamental understanding of roasting, (ii) navigate various roasting pathways for exploration and innovation of in-cup flavour, and (iii) improve the accuracy and robustness of physics-driven models used for process virtualisation.

Subsequently, monitoring the kinetic behaviour of coffee during roasting provides a fundamental understanding of both the process and product. Characterisation of the final product's colour and moisture is standard practice, however these properties, and several others, can be useful tools to understand the transformation of coffee during roasting - from green to part-roasted and fully-roasted. Novel tools were established here to characterise coffee before, during and after roasting - providing developers with valuable information for a data-driven approach to product and process optimisation.

In the following sections, several case studies are documented to highlight how developers can leverage process parameters to manipulate coffee's physicochemical transformation during

roasting. These studies were performed using a pilot-scale spouted bed roaster and include:

Case Study I - Variation of constant inlet air temperature and its effect on roasting performance

In this study, the development of coffee's physicochemical properties during roasting via different time-temperature profiles was captured, wherein Kenyan Arabica coffee was roasted in a spouted bed roaster under different constant inlet air temperatures to an equivalent surface (whole bean) colour. To obtain time-series (i.e., kinetic) data, roasting with each process condition was performed at four equally distributed intervals in time. The colour (whole and ground), mass, moisture, geometry (principal dimensions, volume, surface area), porosity, water activity and density were evaluated for all coffee samples.

Case Study II - Variation of batch size and airflow and its effect on roasting performance

This study is an extension of case study I, however roasting conditions aimed to replicate the study of coffee bean particle motion detailed later in Chapter 4, whereby different batch sizes (i.e., fill volumes) were roasted under different airflows using the same constant inlet air temperature. To obtain time-series (i.e., kinetic) data, roasting at each process condition was performed at three equally distributed times. The colour (whole and ground), mass, moisture, geometry (principal dimensions, volume, surface area), porosity, water activity, density and thermal properties (thermal conductivity and diffusivity, heat capacity) were evaluated for all coffee samples.

Case Study III - Evolution of coffee porosity and its influence on coffee's thermophysical properties

A novel method has been developed to characterise coffee's porosity using X-ray Micro Computed Tomography (MicroCT). With this tool, coffee's porous development during roasting was captured for a Kenyan Arabica coffee roasted under different roasting conditions (corresponding to case studies I-II). The influence of coffee's porosity on its thermophysical properties (density, thermal conductivity, effective heat capacity) and common process indicators (colour, moisture, water activity) were also evaluated.

Case Study IV - Effect of thermocouple diameter on temperature measurement

In this case study, the effect of thermocouple diameter on temperature measurement was examined *in-situ* and aims to: (i) develop a simple and rapid method to determine the time constant of a thermocouple in a model system, (ii) estimate the time constant of a thermocouple using a first principle approximation based on its thermophysical properties and (iii) establish the impact of process conditions and thermocouple diameter on the measured temperature response in a pilot-scale spouted bed coffee roaster.

These comprehensive data comprise fundamental roasting knowledge and can be used by developers to inform process and product development, with new insight on porosity development and indicates how to translate time-temperature profiles across roaster design and scale. Together, these case studies also provide readers with a comprehensive understanding of coffee's transformation during roasting, which establishes context for the following chapters. In Chapters 5-6, these data are utilised to build physics-driven models that predict coffee's thermal and physical transformation during roasting.

3.1 Methodology: Coffee characterisation

3.1.1 Batch size & mass loss

The batch size (specified on a mass basis) of green and roasted whole beans was determined directly before and after roasting (once cooled to ambient temperatures) using a 0.01 g precision balance (Lunar, Acaia). Mass loss, M_{loss} (%), was the difference in the roasted batch's mass, m_{bs} (kg), relative to the initial green bean batch mass, M_0 (kg):

$$M_{loss} = 100\% \times \frac{(M_0 - m_{bs})}{M_0} \tag{3.1}$$

3.1.2 Dry matter mass

Coffee's dry matter batch size (mass basis), m_{db} (kg), was calculated using the batch size (wet basis) and moisture content (wet basis), X_b (kg kg^{-1}):

$$m_{db} = M(1 - X_b) \tag{3.2}$$

3.1.3 Moisture content

Coffee's moisture content was determined gravimetrically. 5.0 ± 0.1 g whole bean samples were dried in a circulating oven (Model 100-800, Memmert - Figure 3.1(a); WF200, Lenton - Figure 3.1(b)) at 105°C for 24 h. After drying, samples were cooled in a desiccator for 15 mins. Sample mass was measured before and after drying with a 0.1 mg precision balance (XSR204, Mettler-Toledo). Samples were duplicated; measured values are expressed in kg kg^{-1} (wet basis). Data corresponding to the enthalpy of vaporisation of water at different temperatures (Engineering-ToolBox, 2020) were fitted with a two-term exponential model (RMSE$_{\Delta H_v, T_b}$ = 44.88 kJ kg^{-1}). Water temperature is assumed equal to the mean bean temperature, T_b (K).

$$\Delta H_v = -0.251 \exp(2.318 \times 10^{-2} T_b) + 2530 \exp(-1.268 \times 10^{-3} T_b) \tag{3.3}$$

(a) (b)

Figure 3.1: Circulating ovens used for moisture content measurements, showing (a) Memmert Model 100-800 and (b) Lenton WF200.

3.1.4 Geometry, size & intrinsic density

Principal dimensions - a (width), b (depth) & c (length) (mm) - of whole bean coffees were measured using 0.01 mm precision digital calipers (RS PRO, RS Components) according to Figure 3.2. For each sample, 25 beans were measured. From principal dimensions, volume, V_b (mm^3), surface area, $A_{s,b}$ (mm^2), and sphericity, ψ_b, were calculated, as detailed in Table 3.1. Coffee geometry can be approximated to three geometries: (i) spherical, (ii) ellipsoidal and (iii) hemi-ellipsoidal. Modelled geometry is dependent on application. For most coffees, where $\psi_b \leq 0.8$, hemi-ellipsoidal geometry is recommended; for high sphericity (peaberry) coffees, where $0.8 \leq \psi_b \leq 0.9$, ellipsoidal geometry is more appropriate; for very high sphericity coffees where $\psi_b \geq 0.9$, spherical geometry is appropriate.

For each of the 25 beans from the sample set, the individual particle mass, m_b (kg), was measured using a 0.1 mg precision balance (XSR204, Mettler-Toledo). A coffee bean's intrinsic density, ρ_b (kg m^{-3}), is thus:

$$\rho_b = \frac{m_b}{V_b} \tag{3.4}$$

Table 3.1: Geometry dependent calculation of volume, surface area and sphericity from principal dimensions.

Geometry	**Property**		
	Volume, $\mathbf{V_b}(\mathbf{mm^3})$	**Surface Area, $\mathbf{A_{s,b}}(\mathbf{mm^2})$**	**Sphericity, $\psi_\mathbf{b}$**
Spherical	$V_b = \frac{4\pi d^3}{3}$(3.5)	$A_{s,b} = \pi d^2$(3.6)	$\psi_b = 1$(3.7)
Ellipsoidal	$V_b = \frac{4\pi(abc)^3}{3}$(3.8)	$A_{s,b} \approx 4\pi \left(\frac{(0.5ab)^{1.6}+(0.25ac)^{1.6}+(0.5bc)^{1.6}}{3}\right)^{\frac{1}{1.6}}$ (3.9)	$\psi_b = \frac{(abc)^{(1/3)}}{a}$(3.10)
Hemi-Ellipsoidal	$V_b = \frac{4\pi(abc)^3}{6}$(3.11)	$A_{s,b} \approx 2\pi \left(\frac{(0.5ab)^{1.6}+(0.25ac)^{1.6}+(0.5bc)^{1.6}}{3}\right)^{\frac{1}{1.6}} + \frac{\pi ac}{4}$(3.12)	$\psi_b = \frac{(abc)^{(1/3)}}{a}$(3.13)

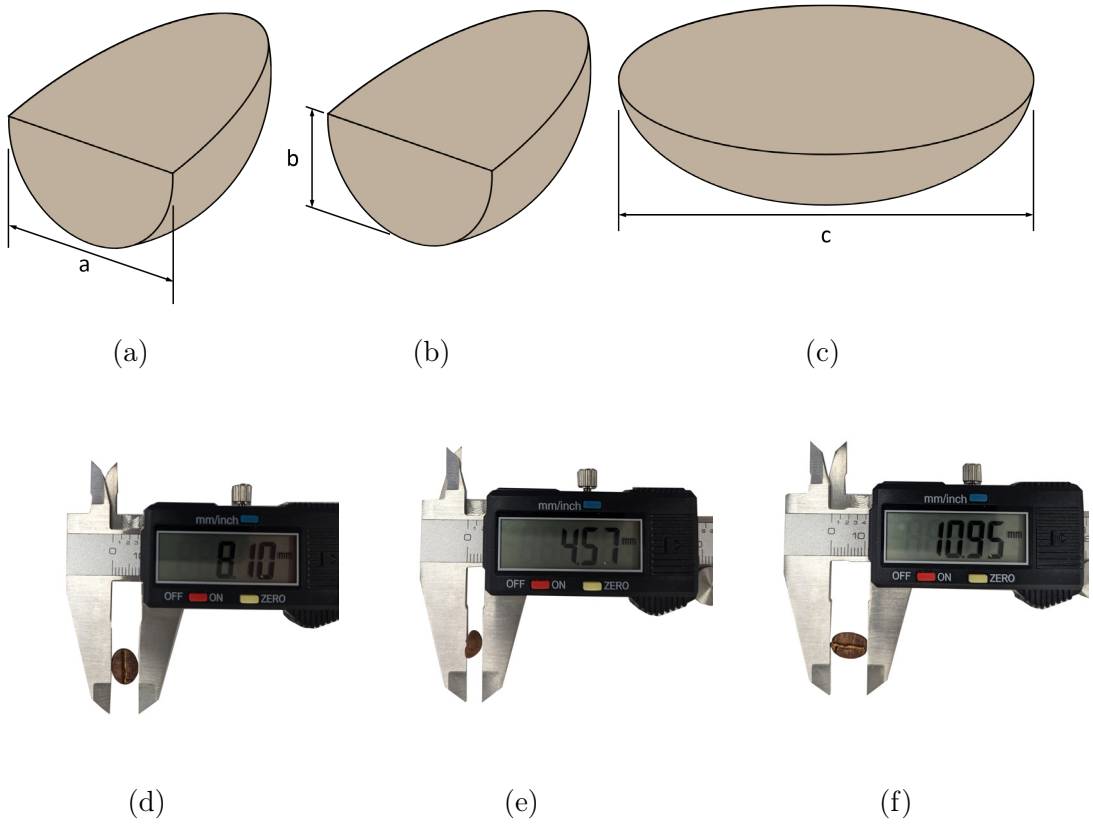

(a) (b) (c)

(d) (e) (f)

Figure 3.2: Definition and visualisation of a coffee bean's principal dimensions as measured using digital calipers.

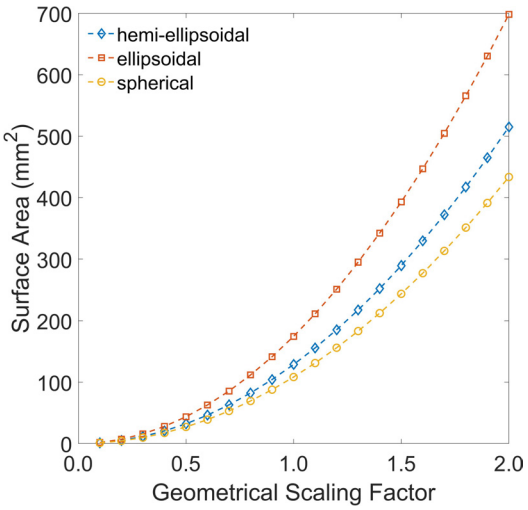

Figure 3.3: The effect of geometry selection and scale on the approximated surface area of a coffee bean.

Using Table 3.1, the assumed geometry of the bean will determine the appropriate method to approximate the bean's surface area. For the Kenyan Arabica coffee used in these studies, the impact of the selected geometry on the approximated surface area was determined. The effect of scale was also assessed by considering beans using geometrical scaling factors of 0.5-2.0. Figure 3.3 displays the effect. This effect is particularly relevant for the simulations in Chapters 6 and 7.

3.1.5 Density (bulk, packing, pycnometric)

The bulk density of whole bean (Figure 3.4(a)) and ground (Figure 3.4(b)) coffee was calculated from the measured mass of coffee, M_b (kg), that occupies a beaker with a volume, V_{beaker} (m^3) where beans settled freely. The top of the beaker was smoothed to ensure a level fill; sampling and measurement was triplicated using aliquots of each sample set. Beakers with the same diameter and volume were used to ensure repeatability across samples. The bulk density, ρ_{bulk} (kg m^{-3}), was thus:

$$\rho_{bulk} = \frac{M_b}{V_{beaker}} \tag{3.14}$$

(a) (b)

Figure 3.4: Measurement of (a) whole bean and (b) ground coffee bulk density using a free-settling method.

Packing density (i.e., number of beans per unit mass, N_b (kg^{-1})), was calculated from the cumulative mass of 50 coffee beans, performed in duplicate, expressed as beans per kg (kg^{-1}). Pycnometric (intrinsic) density and volume measurements of 2.0 ± 0.1 g samples (whole bean and ground) were performed in duplicate using helium pycnometry (AccuPyc II 1330, Micromeritics). Reported values of density and volume are expressed in kg m^{-3} and m^3, respectively.

3.1.6 Colour (whole & ground)

Whole bean and ground coffee colour was measured via reflectance (ColorTrack Benchtop, Fresh Roast Systems shown in Figure 3.5). A sample volume of 250 ml and sampling time of 60 seconds was used for both whole and ground coffees. Whole bean coffee was allowed to equilibrate its temperature and moisture, and degas, for 24 hours prior to grinding and measurement. Coffees were ground to a target ground coffee median particle size, $x_{50} \approx 500$ μm, to reduce scattering effects. Sampling and measurements were duplicated using aliquots of the sample. Measurements via the ColorTrack Benchtop device are expressed in arbitrary colour units.

Figure 3.5: Fresh Roast Systems ColorTrack Benchtop - used for colour measurement of whole and ground coffee samples.

3.1.7 Porosity (microCT, pycnometry)

Porosity was measured using X-ray Micro-Computed Tomography (MicroCT) (SkyScan 1172, Bruker). X-ray images of samples were obtained using an 80 kV & 100 μA x-ray beam with no filter, and system settings of 795 ms exposure time, 3.65 μm pixel size, no frame averaging and an up-to-date bright and dark flat-field correction. During scanning, samples were rotated through 180°, with a step of 0.6°, to produce 300 x-ray images - an exemplar x-ray image is shown in Figure 3.6(a).

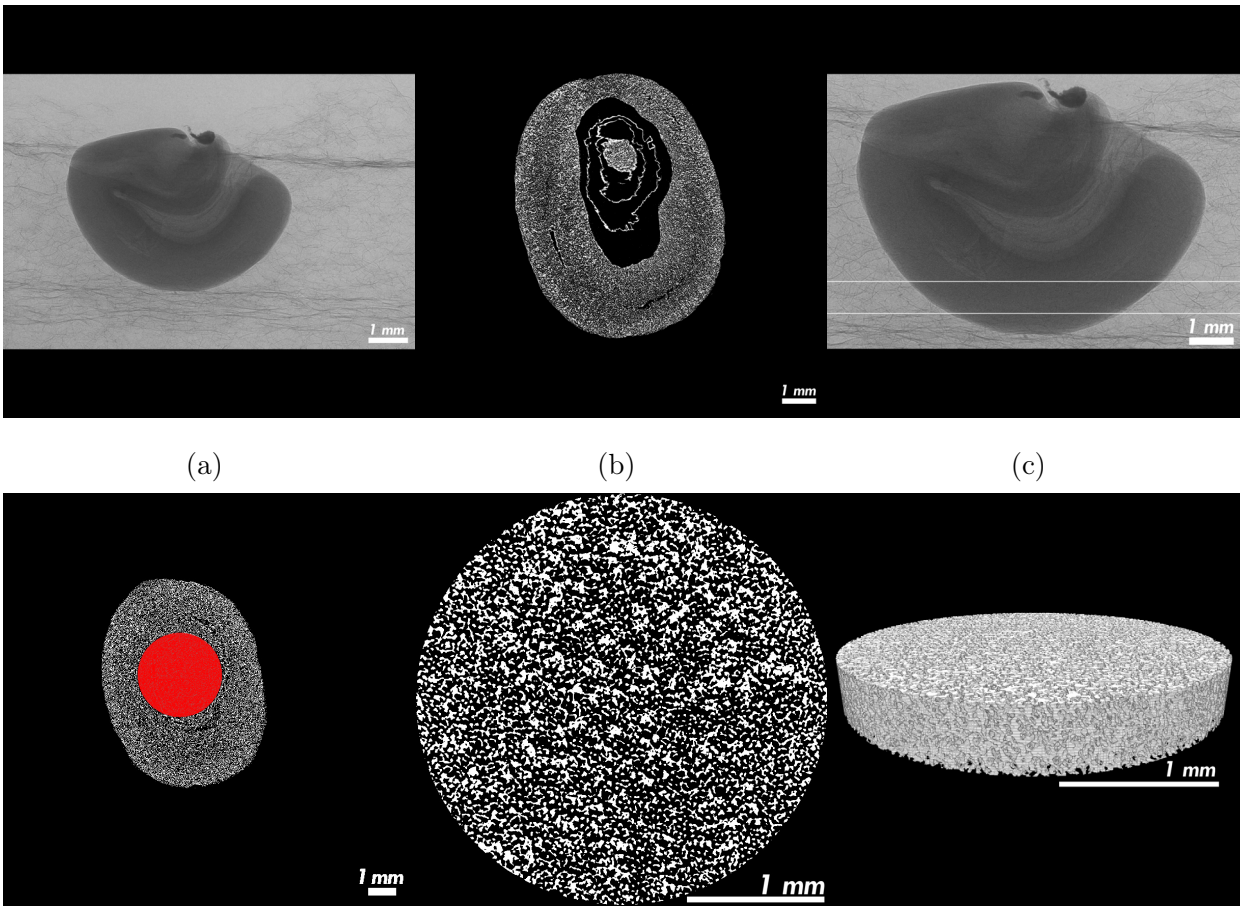

(a) (b) (c)

(d) (e) (f)

Figure 3.6: Data captured via X-ray MicroCT, detailing (a) x-ray images, (b) 2D reconstruction, (c) selected Region of Interest (ROI) height, (d) selected ROI diameter, (e) binarized ROI and (f) 3D Volume of Interest (VOI) reconstruction of a roasted coffee bean.

2D reconstructions were performed using NRecon software (SkyScan, Bruker) with beam hardening at 75%, ring artefact correction at 50, automatically calculated post-alignment, no smoothing and a dynamic range of 0.00-0.25 for the attenuation coefficient. Approximately 1600 cross-sectional images were obtained during reconstruction, dependent on specified layer height. Binary cross-sectional images were produced by applying a threshold (with a lower and upper level of 25 and 125, respectively) to each layer - an exemplar 2D cross-section is presented in Figure 3.6(b). Porosity was analysed using CTAn software (SkyScan, Bruker).

To reduce computational power and analysis time, 100 cross-sectional layers, with a height of 0.36 mm, were selected from an area beneath the bean's furrow (see Figure 3.6(c)) that was common in all scanned samples. To further reduce computational power and to reduce surface effects, a circular Region of Interest (ROI) with an area of 7.14 mm^2 was applied to each layer (see Figure 3.6(d)); each sample's Volume of Interest (VOI) equalled 2.58 mm^3. To ensure that no defects were present in the specified VOI, every stack of ROIs (as in Figure 3.6(e)) was visually inspected in CTVox (as shown in Figure 3.6(f)). Samples with large voids (much larger than typical pore diameter (i.e., $\varnothing \leq$ 250 μm) that might significantly impact porosity values) were resampled.

Porosity analysis included determination of total VOI volume, object volume, number and volume of closed pores, open and closed porosity, total volume of pore space and total porosity. Open pore volume is the volume of space connected to the surface of the VOI, whilst closed pore volume is the volume of space completely enclosed by solid material.

Coffee porosity (or Percentage Gas Type Void Volume (%GTVV)) was also estimated from the pycnometric density of whole bean, ρ_w (kg m^{-3}), and finely ground, ρ_g (kg m^{-3}), samples (median particle size, $x_{50} \leq 200$ μm):

$$\%GTTV = 100\% \times \rho_w \left(\frac{1}{\rho_w} - \frac{1}{\rho_g} \right) \tag{3.15}$$

3.1.8 Water activity

The water activity, a_w, of whole bean (green) and ground (part-roasted and roasted) samples was measured using a dew-point sensor (AQUALAB 3TE & 4TE, METER Group - Figure 3.7). Samples of 2.0 ± 0.1 g (Lunar, Acaia) were analysed in duplicate.

Figure 3.7: Dew-point sensor (Aqualab 4TE, METER Group) used for measurement of water activity in whole (green) and ground (part-roasted and roasted) coffee samples.

3.1.9 Thermal properties (thermal conductivity, specific heat capacity, thermal diffusivity)

The thermal properties (thermal conductivity, thermal diffusivity and volumetric heat capacity) of ground (green, part-roasted and roasted) samples were determined using a thermal properties analyser (TEMPOS, METER Group) using the SH-3 dual needle sensor. Samples were ground to a target median particle size, $x_{50} \approx 500$ μm. 30 g samples were poured freely into a 250 ml beaker. The SH-3 sensor was inserted into the sample through the beaker's wall (via pre-drilled holes), before the coffee bed was consolidated around the sensor using a 3D-printed tamper. Thermal properties were determined in duplicate over a 2 min sampling time using the experimental setup detailed in Figure 3.8.

Figure 3.8: Measurement of the thermal properties of ground coffee samples using a thermal properties analyser (TEMPOS, METER Group).

The specific heat capacity, $C_{p,b}$ (J kg^{-1} K^{-1}) was calculated from the measured thermal diffusivity D_b (mm^2 s^{-1}), thermal conductivity k_b (W m^{-1} K^{-1}) and bulk density (ρ_{bulk}):

$$C_{p,b} = \frac{k_b}{\rho_{bulk} D_b} \tag{3.16}$$

where the specific heat capacity of the coffee (wet-basis) can be considered as the weighted fraction of the three-phase components, the moisture content, X_b (kg kg^{-1}), porosity, γ_b (%) and specific heat capacities of water, $C_{p,w}$, dry, solid matter, $C_{p,s}$, and air in porous voids $C_{p,a}$ (J kg^{-1} K^{-1}):

$$C_{p,b} = X_b C_{p,w} + (1 - X_b - \gamma_b) C_{p,s} + \gamma_b C_{p,a} \tag{3.17}$$

3.1.10 Particle size distribution & grinder characterisation

Particle size analysis of 10.0 ± 0.1 g ground coffee samples were performed in duplicate using laser diffraction (HELOS/KF + RODOS/M + VIBRI/R, Sympatec). For some analyses (colour, thermal properties, bulk density, etc.), the particle size distribution must be consistent across samples – here, a median particle size of 500 μm was specified.

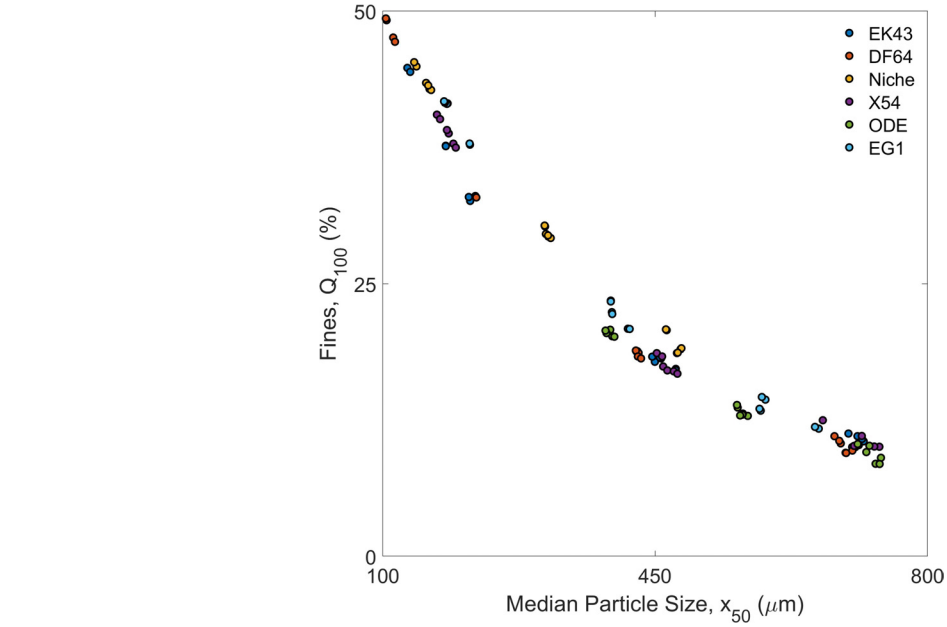

(a)

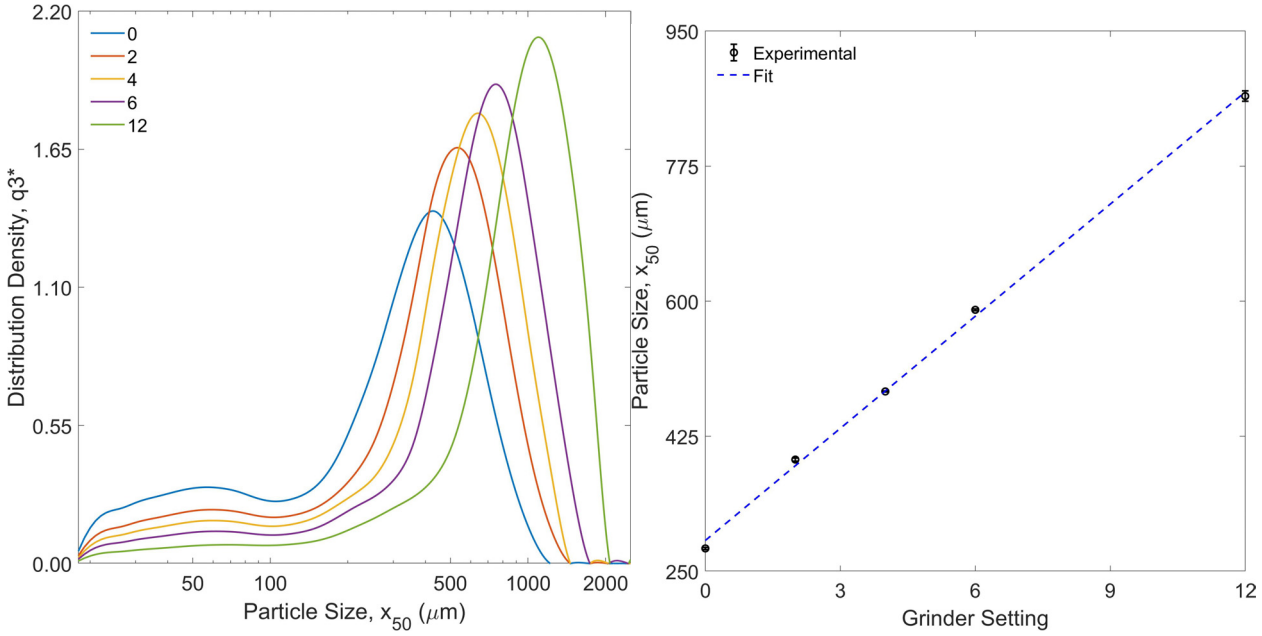

(b) (c)

Figure 3.9: Grinder characterisation methodology generates plots of (a) fines percentage (%fines) vs median particle size (x_{50}), (b) Particle Size Distributions (PSDs) and (c) median particle size (x_{50}) vs grinder setting (i.e., burr gap), for coffees ground at different grinder settings

To obtain the target median particle size, the grinders used herein were characterised accordingly: (i) coffee was ground at different grinder settings (i.e., burr gaps), (ii) each sample's Particle Size Distribution (PSD) was measured via laser diffraction, (iii) median particle size, x_{50} (μm), and percentage (%) fines ($\leq$100 μm) was correlated (Figure 3.9(a)), (iv) the PSDs of all coffees were overlayed for visualisation (Figure 3.9(b)) and (v) median particle size was correlated with grinder setting (i.e., burr gap) (Figure 3.9(c)). This characterisation methodology was performed for coffees roasted to different densities (i.e., roast degrees), with statistical models generated to provide a reference to inform grinder parameters and subsequent grinding performance.

3.2 Case study I: Variation of constant inlet air temperature and its effect on roasting performance

3.2.1 Methodology

Coffee & roasting conditions

Kenyan Arabica coffee was roasted in a pilot-scale spouted bed roaster (RFB-S, Neuhaus Neotec) under constant process conditions to a surface colour of 70±1 (ColorTrack), confirmed in triplicate via colourimetry (ColorTrack Benchtop Device R-100B, FreshRoastSystems, Inc.). The roaster's fan frequency was set to 48 Hz, with batch sizes of 350.0±0.1g (Acculab Atilon, Sartorius). Constant inlet air temperature (220, 235, 250, 265 and 280°C) and time (distributed equally between time $t = 0$, corresponding to the moment the coffee beans were loaded into the roasting chamber, and the final time required to achieve a colour of 70±1, $t = t_{70}$ - i.e., $t = t_{70}$, $t = 3t_{70}/4$, $t = t_{70}/2$, $t = t_{70}/4$ & $t = 0$ - rounded to the nearest integer) were varied according to Table 3.2 to obtain samples roasted under five different process conditions, each at four equally distributed intervals in time. At the specified roasting end-time, ambient air (ca. 230 °C) was used to cool the beans for 60 s. Roasted coffee was then packaged in valved, aluminium foil laminated bags (Maxilla Packaging) and stored in a temperature controlled room prior to characterisation.

Table 3.2: Process parameters corresponding to coffees roasted under different constant inlet air temperatures in a spouted bed roaster to a colour of 70±1 (ColorTrack.

Inlet Air	**Time (s)**				
Temp. (°C)	$\mathbf{t = 0}$	$\mathbf{t = t_{70}/4}$	$\mathbf{t = t_{70}/2}$	$\mathbf{t = 3t_{70}/4}$	$\mathbf{t = t_{70}}$
220	0	175	350	525	700
235	0	104	208	312	415
250	0	69	138	209	278
265	0	54	108	164	218
280	0	42	84	126	168

Coffee characterisation

Green and roasted coffee analyses included mass, intrinsic density, moisture content (and calculation of dry matter mass), colour (whole), size (principal dimensions, volume and surface area) and porosity (via MicroCT). For roast & ground coffee analyses, coffees were ground using a flat burr grinder (EK43, Mahlkönig); analyses included colour, thermal properties (thermal conductivity, specific heat capacity & thermal diffusivity) and median particle size (via laser diffraction).

3.2.2 Results

Time-temperature profiles

Measured inlet air, product and outlet air temperatures for all process conditions (220, 235, 250, 265 and 280°C) are shown in Figure 3.10. Product time-temperature profiles (Figure 3.10(b)) show a drop in the measured product temperature at early times ($0 \leq t \leq 35s$), resulting from the thermocouple's response to the influx of beans and air at ambient temperatures (ca. 20°C). As explained in previous chapters (see Chapters 1-2), the product thermocouple's measured temperature depends on heat transfer from both the drying air and beans in the bean-bed and depends on its location inside the roasting chamber. In spouted bed roasters, the product thermocouple is positioned to minimise the impact of airflow on temperature measurement, yet this is inherently unavoidable (Schwartzberg, 2006a). Thereafter, product temperature rises rapidly due to the high temperature differential between the drying air and beans. Provided the coffee's residence time in the roaster is sufficient, inlet air and product temperatures should converge, although due to heat loss and thermocouple positioning, this is not observed.

The rate of change of product temperature (Figure 3.11) tends to zero during low temperature roasting ($T_{a,i} = 220°C$), implicit of a thermal equilibrium, whereas at higher temperatures ($T_{a,i} > 220°C$), the rate of change of product temperature varies due to the apparent initiation of endothermic and exothermic reactions (Hobbie and Eggers, 2001). During low temperature roasting, these reactions have a negligible impact on the measured temperature, indicative of an activation energy that is suppressed at lower temperatures.

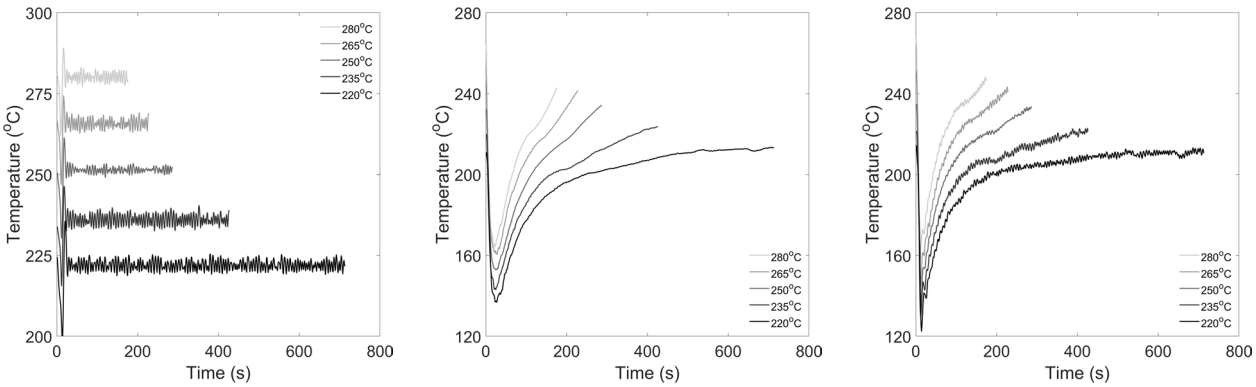

(a) Inlet Air (b) Product (c) Outlet Air

Figure 3.10: Time-temperature profiles corresponding to constant inlet air temperature roasts of Kenyan Arabica coffee in a spouted bed roaster at different inlet air temperatures of 220, 235, 250, 265 and 280°C as detailed in Table 3.2.

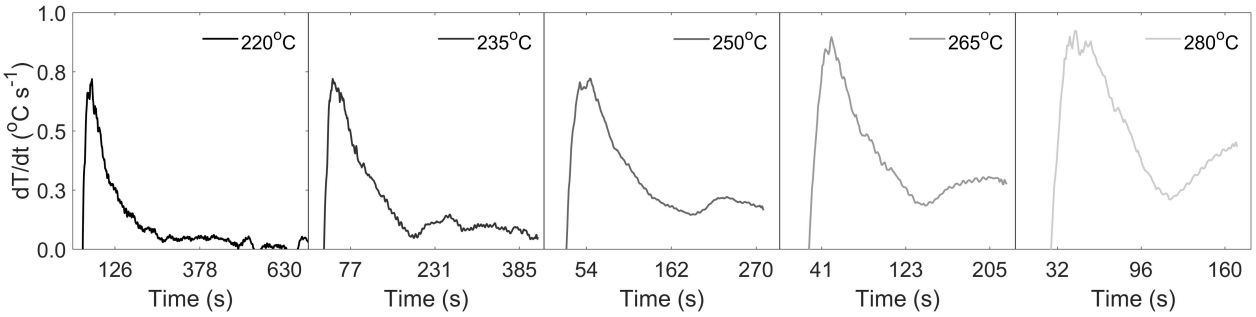

Figure 3.11: Rate of change of product time-temperature profiles, corresponding to constant inlet air temperature roasts of Kenyan Arabica coffee in a spouted bed roaster at different inlet air temperatures of 220, 235, 250, 265 and 280°C as detailed in Table 3.2.

Mass & moisture

Mass loss on a wet basis (wb) during roasting ranged 15.8-17.0% (see Figure 3.12(a)); whilst the dry matter mass loss (i.e., dry basis, db) spanned 7.9-8.7% (Figure 3.12(b)). Mass loss rates (both wb and db) were temperature dependent, with greater rates observed for higher inlet air temperatures. The mass of chaff lost during roasting was approximately 0.4% of the initial batch mass, with the remaining dry matter loss, accounting for the generation of volatiles due to cellular degradation (Schenker, 2000), spanned 6.9-7.6%.

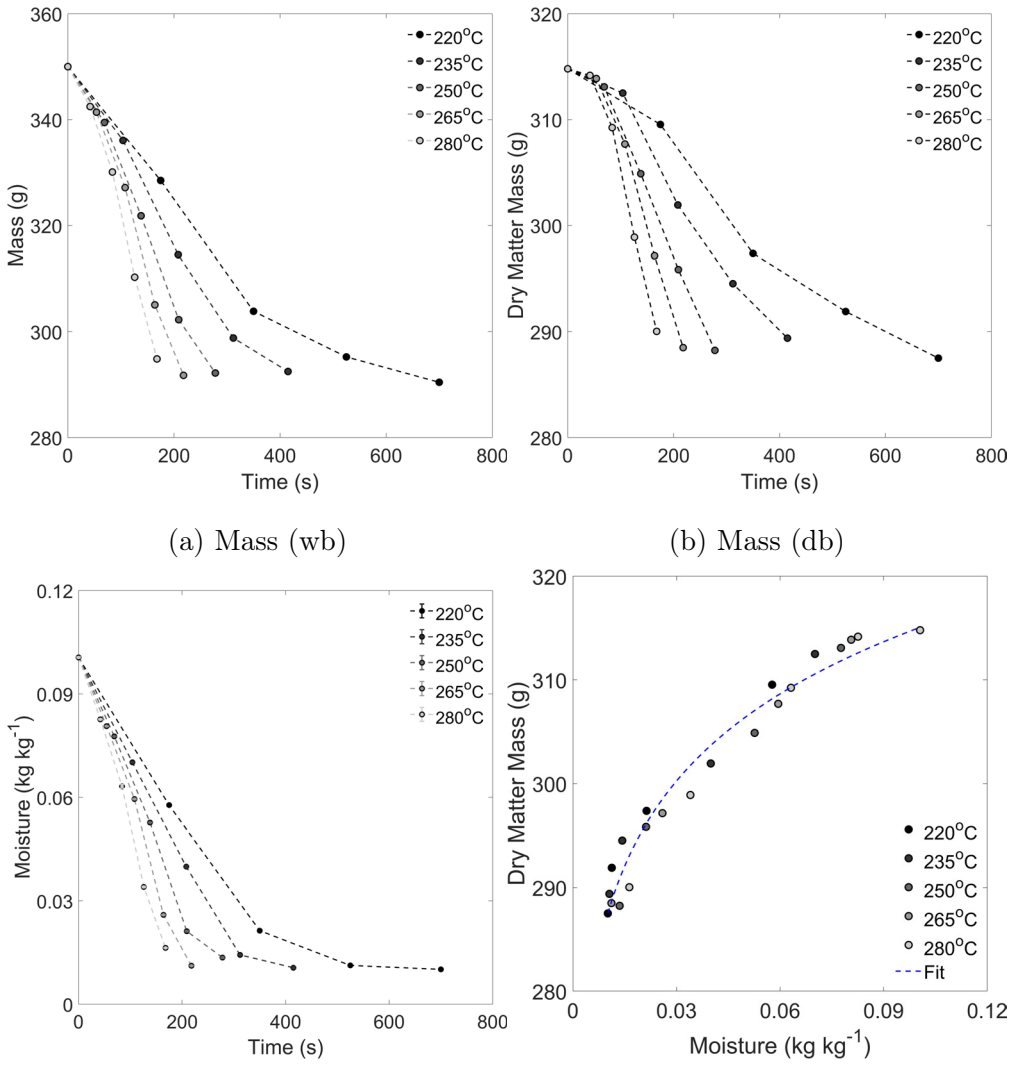

(a) Mass (wb)

(b) Mass (db)

(c) Moisture

(d) Mass (db) vs Moisture

Figure 3.12: Changes in (a) mass (wb), (b) mass (db) and (c) moisture during roasting and (d) correlation of mass (db) and moisture - data corresponds to roasts of Kenyan Arabica coffee in a spouted bed roaster at different constant inlet air temperatures of 220, 235, 250, 265 and 280°C as in Figure 3.10.

The rate of moisture loss, displayed in Figure 3.12(c), was also temperature dependent, with a greater rate of loss observed for higher inlet air temperatures. Moisture content decreased from 0.1006 kg kg^{-1} (10.06%) to 0.0101-0.0163 kg kg^{-1} (1.01-1.63%) during roasting. Moisture content plateaued at lower inlet air temperatures ($T_{a,i} \leq 235$ °C), yet this was not observed for higher inlet air temperatures ($T_{a,i} > 235$ °C). Both final mass (db) and moisture increased with inlet air temperature, demonstrating that higher temperature roasting

gives higher residual mass and moisture. These data show that high temperature roasting to an equivalent surface colour increases the batch yield and reduces process time.

Figure 3.12(d) shows that batch mass (db), $m_{bs,db}$ (g) and moisture, X_b (kg kg^{-1}) are linearly correlated ($R^2 = 0.9732$):

$$m_{bs,db} = 345 X_b^{0.4} \tag{3.18}$$

Colour

The rate of colour change is temperature dependent, with a greater rate of change observed during higher temperature roasting. An initial decrease in colour is observed for whole (Figure 3.13(a)) and ground (Figure 3.13(b)) coffee samples for all roasting conditions. This might be associated with the removal of chaff in the early stages of the roast, diffusion of moisture to the surface (Hernández, Heyd, and Trystram, 2008) or changes in hue (not appreciable in mono-chromatic colourimeters).

Due to rapid heat transfer rates, a difference between the surface (whole bean) colour and core (ground) colour is expected (Hobbie and Eggers, 2001) and is highlighted in Figure 3.13(c), where whole bean and ground coffee colours are correlated. Due to high bean density and the limited capabilities of the grinder, it was difficult to obtain a consistent particle size (median particle size, $x_{50} \approx 500$ μm) for all roasted samples. Part-roasted samples that did not fit this criterion were therefore discounted from this analysis. Figure 3.13(c) reveals that coffee's surface colour, c_w, is greater (darker) than ground coffee colour, c_g, for all samples and could be correlated (RMSE$_{c_w,c_g}$=2.08): $c_g = 1.4c_w - 32$.

Although application of greater air temperatures increases the temperature differential between the bean's core and the drying air, and increases heat flux, the time for mass transfer and colour development via Maillard reactions was reduced. A greater colour differential was seen at early times when roasting at higher temperatures, but for darker colours ($c \geq 60$), the difference between the sample's whole and ground colours is significant but not dependent on the constant inlet air temperature. Current data therefore suggests that the whole bean-ground colour difference is generated later in the roast.

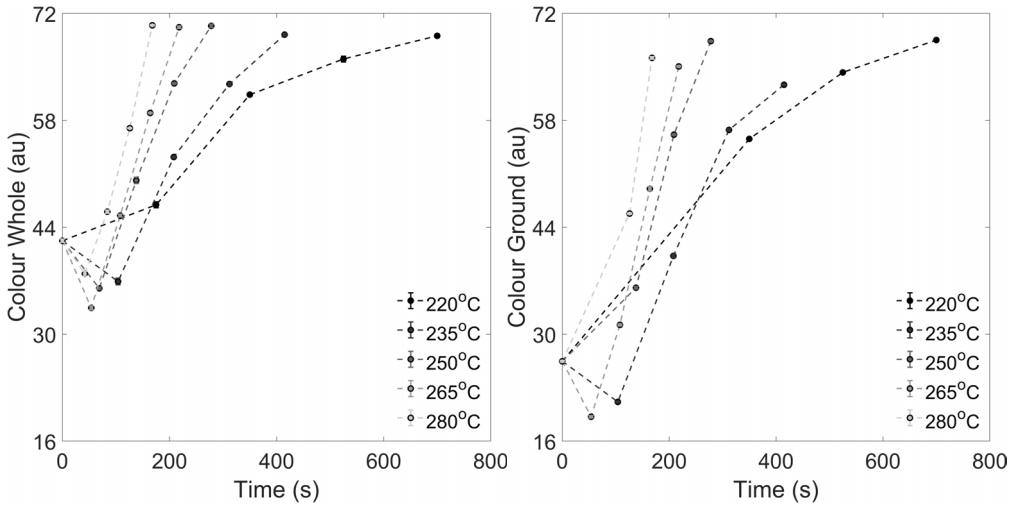

(a) Whole bean (b) Ground

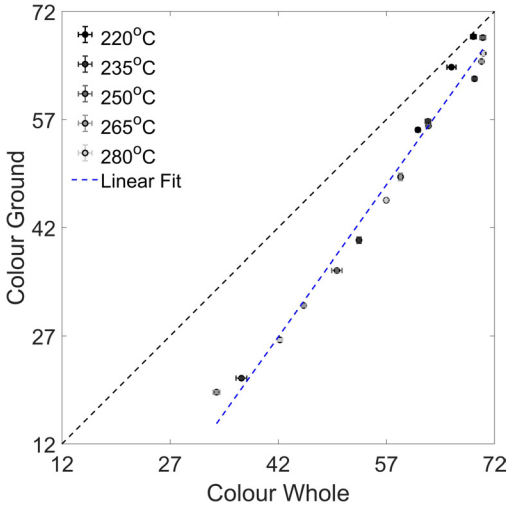

(c) Whole vs Ground

Figure 3.13: Changes in colour for (a) whole bean and (b) ground coffee samples, outlining (c) the correlation between whole and ground coffee colour. Data corresponding to roasts of Kenyan Arabica coffee in a spouted bed roaster at different constant inlet air temperatures of 220, 235, 250, 265 and 280°C as in Figure 3.10.

Bean geometry

Figure 3.14 presents changes in coffee's principal dimensions (a, b and c) during roasting at 250°C. An increase in size was observed in all dimensions during roasting for all roasting conditions, with dimensional expansion ranging 18-30%.

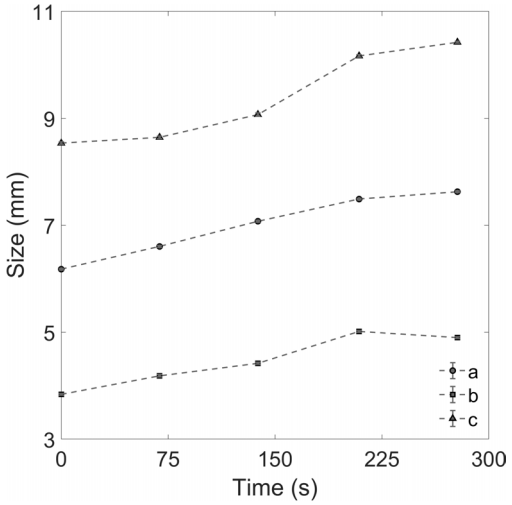

Figure 3.14: Changes in coffee's principal dimensions (a, b and c, according to Figure 3.2) during roasting of Kenyan Arabica coffee in a spouted bed roaster at a constant inlet air temperature of 250°C.

Changes in each principal dimension (a, b and c, according to Figure 3.2) of the coffee bean for all process conditions are presented in Figure 3.15. The rate of expansion in each dimension was temperature dependent, with greater expansion for higher temperature roasting. During low temperature roasting ($T_{a,i} = 220°C$), a decrease in size was observed in some dimensions towards the end of the roast. This decrease was not observed for all roasting conditions, either due to low sampling frequency or bean variability, but coincides with the start of first crack. After first crack, a decrease was seen. This implies a structural collapse prior to further expansion in the final stages of the roast (Schenker, Handschin, et al., 2000).

As volume and surface area are a function of principal dimensions, changes in these two properties, displayed in Figure 3.16(a) and Figure 3.16(b), respectively, follow similar trends to those shown in Figure 3.15. Increases in volume and surface area were temperature dependent, caused by the development of porosity through generation of carbon dioxide, vaporization of water and softening of cellular material (Geiger, Perren, Schenker, et al.,

2001). Coffee's expansion rate varies during roasting, with significant expansion occurring in the moments prior to first crack, wherein the glass transition conditions are surpassed and the cellular matrix becomes rubbery and the internal pressure facilities expansion of closed pores. First-crack, occurred at approx. 286, 200, 186, 142 and 120 s for 220, 235, 250, 265 and 280°C roasts, respectively. As the coffee's moisture and temperature further develop, the cellular material returns to the glassy state, wherein volume expansion is inhibited and there is no clear influence of process temperature on volume expansion (Geiger, 2004).

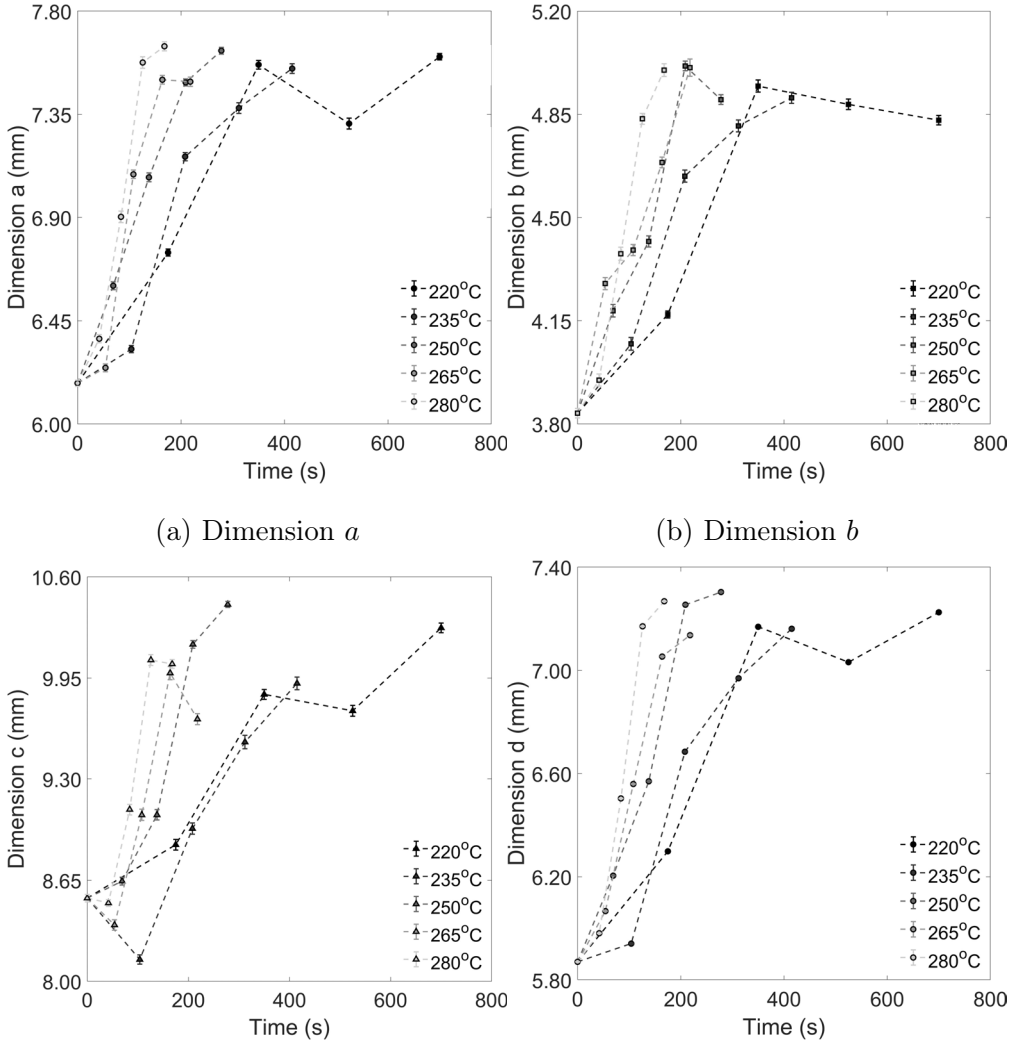

(a) Dimension a (b) Dimension b

(c) Dimension c (d) Equivalent Diameter d

Figure 3.15: Changes in coffee's principal dimensions (a) a, (b) b, (c) c, according to Figure 3.2, and (d) equivalent diameter, d, (where $d = (abc)^{(1/3)}$) corresponding to roasts of Kenyan Arabica coffee in a spouted bed roaster at different constant inlet air temperatures of 220, 235, 250, 265 and 280°C as in Figure 3.10.

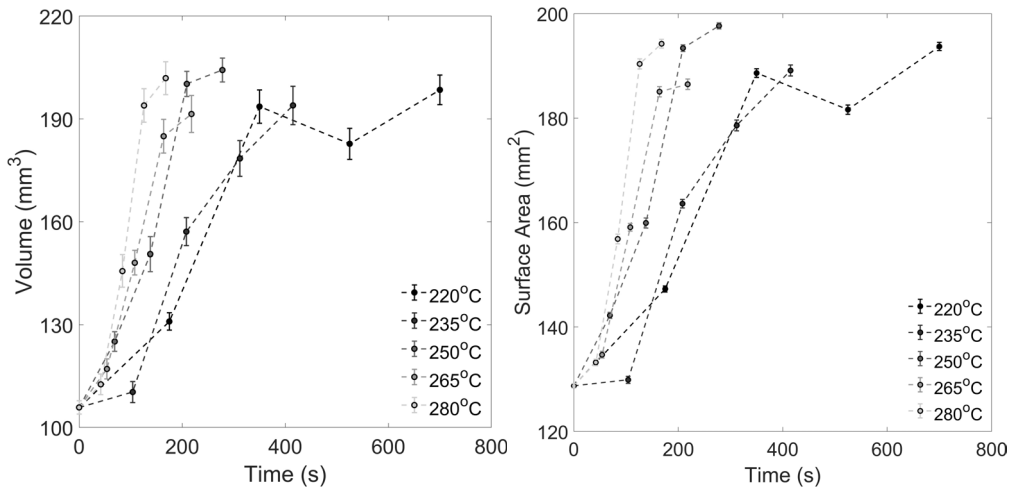

(a) Volume (b) Surface Area

Figure 3.16: Changes in (a) volume and (b) surface area of coffee corresponding to roasts of Kenyan Arabica coffee in a spouted bed roaster at different inlet air temperatures of 220, 235, 250, 265 and 280°C as in Figure 3.10.

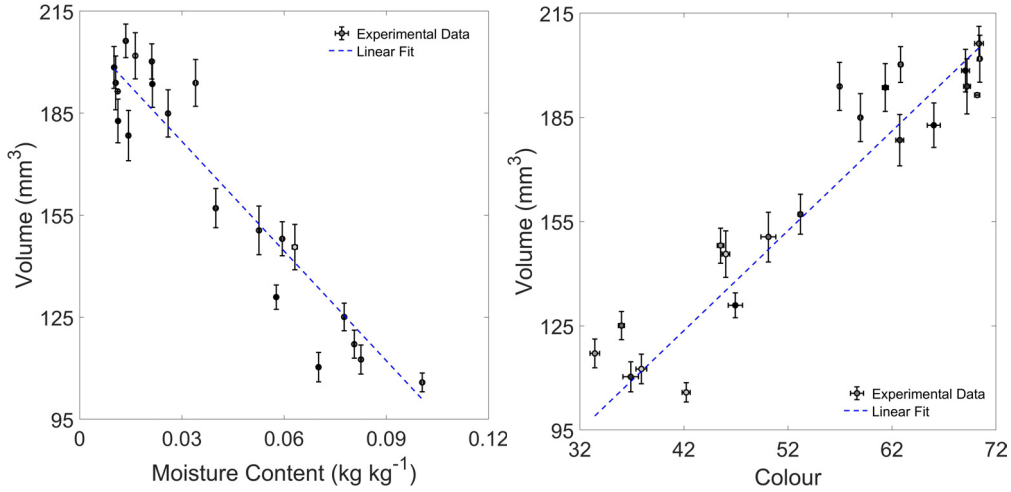

(a) Volume & Moisture (b) Volume & Colour

Figure 3.17: Correlation of coffee bean volume with (a) moisture content and (b) whole bean (surface) colour corresponding to roasts of Kenyan Arabica coffee in a spouted bed roaster at different constant inlet air temperatures of 220, 235, 250, 265 and 280°C as in Figure 3.10.

Dehydration and subsequent porosity development of coffee are known drivers of volume expansion during roasting. Figure 3.17(a) shows that for all roasting conditions in this study, bean volume, V_b (mm^3) exhibits a linear dependence on moisture content, X_b (kg kg^{-1}) (Eq. 3.19: RMSE$_{V_b,X_b}$=10 mm^3) where dehydrated/roasted beans have greater volume. Influence

of air temperature is not evident. Coffee colour, although an invaluable indicator of process consistency and product quality, is found by optical techniques that are prone to errors arising from differences in particle size, temperature, moisture, and degassing times. Figure 3.17(b) presents a correlation of volume with whole bean colour, c_w (Eq. 3.20: RMSE_{V_b,c_w}=13 mm^3) that suggests that volume (measured via particle size analysers) could be used as a product quality indicator that minimises measurement error.

$$V_b = -1074X_b + 209 \tag{3.19}$$

$$V_b = 2.87c_w + 3.04 \tag{3.20}$$

Density & porosity

The evolution of coffee's density (Figure 3.18(a)) was temperature dependent, with higher temperature roasting increasing the rate of change of density. After first crack, development of bean density is reduced, with a decrease in the apparent rate of density change. Structural collapse (during first crack) and reduced volume expansion towards the end of roasting (due to the cellular material's return to the glassy state) explain this observation (Geiger, 2004; Schenker, Handschin, et al., 2000). Greater bean density was achieved when roasting at lower temperatures, although large bean size distributions might reduce the significance of this observation.

Porosity changes during roasting are displayed in Figure 3.18(b). The rate of porosity development increases with applied air temperature. The driving forces for porosity development are discussed in more detail in case study III (Section 3.4).

Figure 3.19 presents correlations between density and moisture (Figure 3.19(a) & Eq. 3.21: RMSE_{ρ_b,X_b} = 61 kg m^{-3}) and density and whole bean colour (Figure 3.19(b) & Eq. 3.22: RMSE_{ρ_b,c_w} = 130 kg m^{-3}). Similarly, Figure 3.20 presents correlations of porosity and moisture (Figure 3.20(a) & Eq. 3.23: $\text{RMSE}_{\gamma_b,X_b}$ = 2.9%) and porosity and whole bean colour (Figure 3.20(b) & Eq. 3.24: $\text{RMSE}_{\gamma_b,c_w}$ = 4.0%).

$$\rho_b = 8286X_b + 463 \tag{3.21}$$

$$\rho_b = -20.7c_w + 1977 \tag{3.22}$$

$$\gamma_b = -204X_b + 62.2 \tag{3.23}$$

$$\gamma_b = 0.51c_w + 24.7 \tag{3.24}$$

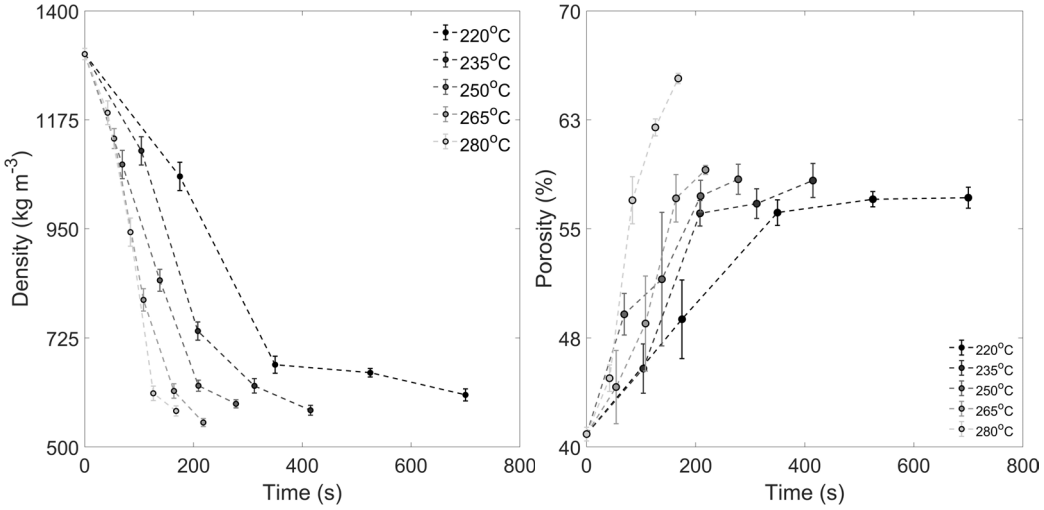

(a) Density (b) Porosity

Figure 3.18: Changes in coffee bean (a) density and (b) porosity corresponding to roasts of Kenyan Arabica coffee in a spouted bed roaster at different constant inlet air temperatures of 220, 235, 250, 265 and 280°C as in Figure 3.10.

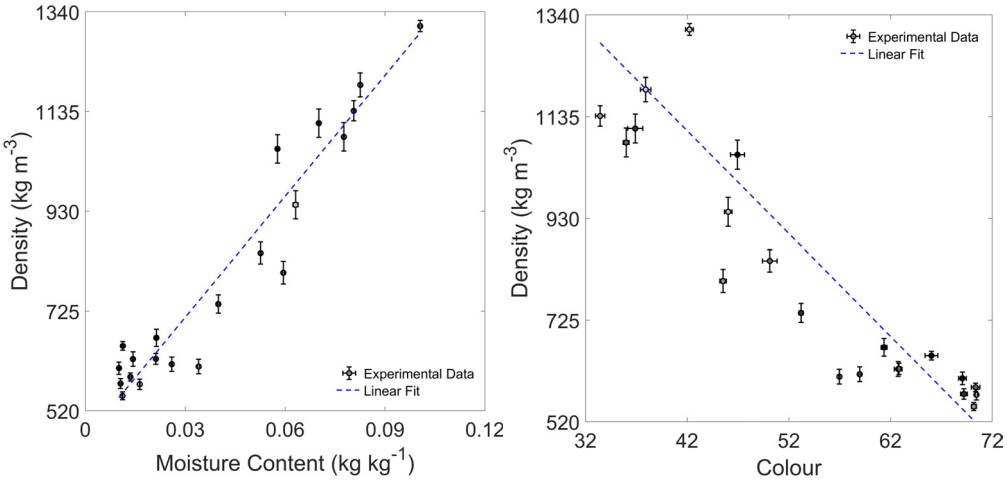

(a) Density & Moisture (b) Density & Colour

Figure 3.19: Correlation of coffee's intrinsic density with (a) moisture content and (b) whole bean (surface) colour corresponding to roasts of Kenyan Arabica coffee in a spouted bed roaster at different constant inlet air temperatures of 220, 235, 250, 265 and 280°C as in Figure 3.10.

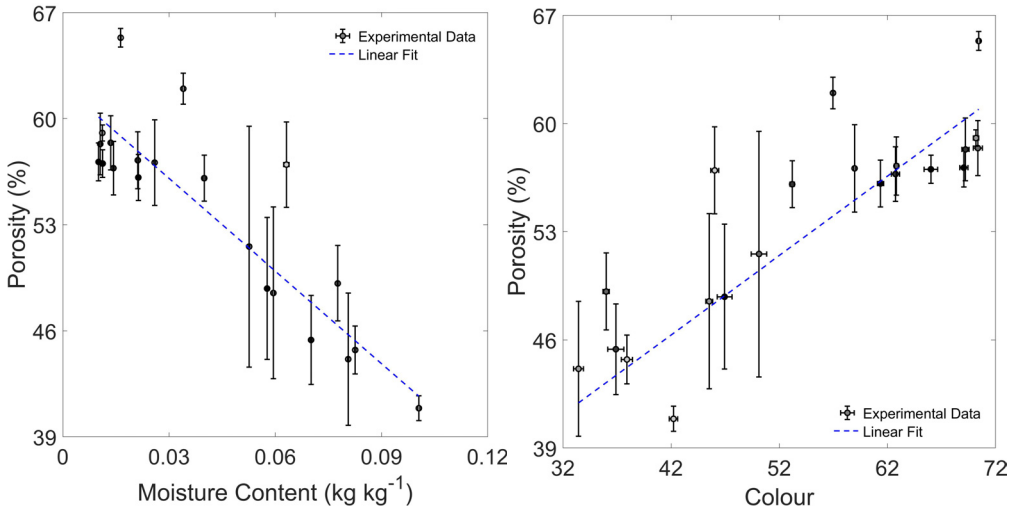

(a) Porosity & Moisture (b) Porosity & Colour

Figure 3.20: Correlation of coffee's porosity with (a) moisture content and (b) whole bean (surface) colour corresponding to roasts of Kenyan Arabica coffee in a spouted bed roaster at different constant inlet air temperatures of 220, 235, 250, 265 and 280°C as in Figure 3.10.

Developers rely on colour to inform process variance and to adjust subsequent batches, yet Figures 3.17 3.19 suggest that intrinsic coffee properties such as porosity, volume, density and moisture might provide more accurate and reliable data to inform process and product development. With that said, utilisation of water-quenching technology render moisture measurements redundant for indication of roasting performance.

Thermal properties

As coffee's moisture content decreases and porosity increases during roasting, the greater air and lower moisture volumes within the bean increases the thermal resistance. Correlations between the coffee's thermal properties (volumetric heat capacity, thermal conductivty) and moisture are presented in Figure 3.21, whilst Figure 3.22 shows correlations between the coffee's thermal properties and whole bean colour.

These data show that the effective thermal conductivity decreases, whilst specific heat capacity increases, as previously seen in Fabbri, Cevoli, Alessandrini, et al. (2011) and Cardoso et al. (2018). As similar kinetic behaviour was observed for all roasting conditions, the impact of process temperature on the development of coffee's thermophysical properties during

roasting is unclear, however both thermal conductivity and heat capacity show a dependency on moisture content (Figure 3.21(a) & Eq. 3.25: $R^2_{k_b,X_b}$=0.752; Figure 3.21(b) & Eq. 3.27: $R^2_{C_{v,b},X_b}$=0.862) and colour (Figure 3.22(a) & Eq. 3.26: $R^2_{k_b,c_w}$=0.813; Figure 3.22(b) & Eq. 3.28: $R^2_{C_{v,b},c_w}$=0.902).

$$k_b = 0.322X_b + 0.088 \tag{3.25}$$

$$k_b = -6.64 \times 10^{-4} c_w + 0.14 \tag{3.26}$$

$$C_{v,b} = 4.61 \times 10^6 X_b + 8.34 \times 10^5 \tag{3.27}$$

$$C_{v,b} = -9353 c_w + 1.52 \times 10^6 \tag{3.28}$$

These correlations (Eqs. 3.25-3.28) enable sub-routines to be implemented within kinetic models and heat and mass transfer simulations to estimate thermal properties (density, porosity, thermal conductivity and heat capacity) based on quality indicators (moisture and colour) for a given product and process. This approach is detailed in Chapters 5-6.

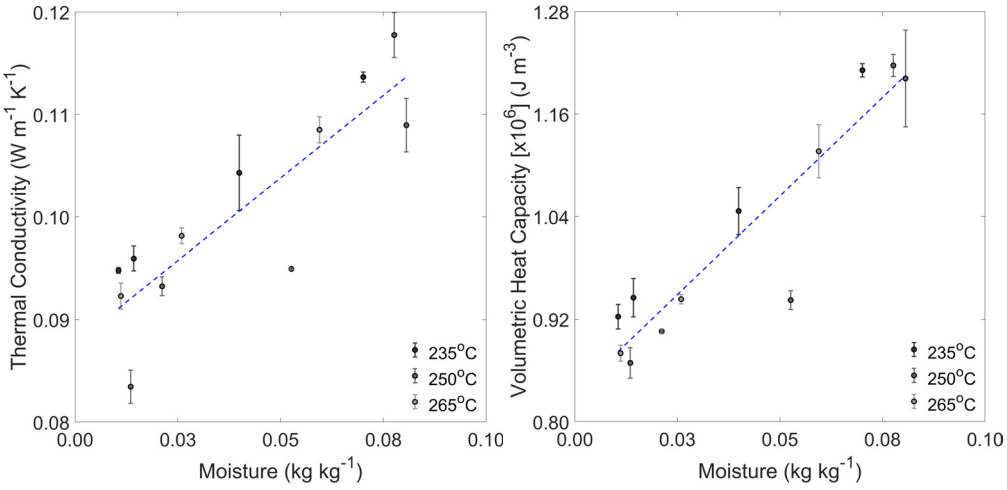

(a) Thermal Conductivity & Moisture (b) Heat Capacity & Moisture

Figure 3.21: Correlation of coffee's (a) thermal conductivity and (b) volumetric heat capacity with its moisture content corresponding to roasts of Kenyan Arabica coffee in a spouted bed roaster at different constant inlet air temperatures of 235, 250 and 265°C as in Figure 3.10.

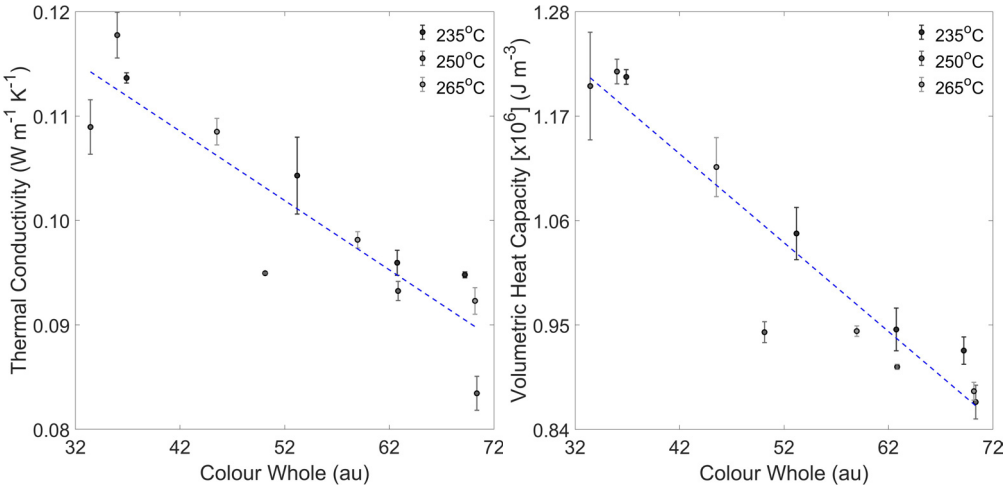

(a) Thermal Conductivity & Colour (b) Heat Capacity & Colour

Figure 3.22: Correlation of coffee's (a) thermal conductivity and (b) volumetric heat capacity with its whole bean (surface) colour corresponding to roasts of Kenyan Arabica coffee in a spouted bed roaster at different constant inlet air temperatures of 235, 250 and 265°C as in Figure 3.10.

3.3 Case study II: Variation of batch size and airflow and its effect on roasting performance

3.3.1 Methodology

Roasting conditions

Kenyan Arabica coffee was roasted in a pilot-scale spouted bed roaster (RFB-S, Neuhaus Neotec) with a constant inlet air temperature of 250°C to a final surface (whole bean) colour of 70±1 – determined via colourimetry (ColorTrack Benchtop R-100B, FreshRoastSystems). Batch size and airflow were varied; the roaster's fan frequency ranged from 30-65 Hz for batch sizes between 200-500 g. To obtain time-series (i.e., kinetic) data, roasts were repeated at equally distributed times between the start time, $t = 0$, corresponding to the moment the coffee beans were loaded into the roasting chamber, and the final time required to achieve a colour of 70±1, $t = t_{70}$ - i.e., at $t = t_{70}$, $t = 2t_{70}/3$, $t = t_{70}/3$ & $t = 0$ (rounded to the nearest integer). Process parameters for each of the roasting conditions are displayed in Table 3.3. Airflow properties corresponding to the specified fan frequencies are displayed in Table 3.4. Energy consumption was monitored during roasting using a 3-phase energy monitor (Intuition-LC, OWL). Once the specified roasting end-point was achieved, ambient air was used to cool the beans for 60 s. Roasted coffee was then packaged in valved, aluminium foil laminated bags (Maxilla Packaging) and stored in a temperature controlled room prior to characterisation.

Coffee characterisation

Green and roasted coffee analyses included mass, density (bulk & intrinsic), moisture content (and calculation of dry matter mass), colour (whole), size (principal dimensions, volume and surface area) and porosity (via MicroCT). For roast & ground coffee analyses, coffees were ground using a flat burr grinder (EG1, Weber Workshops); analyses included colour (ground), thermal properties (thermal conductivity, specific heat capacity & thermal diffusivity), water activity and median particle size (via laser diffraction).

Table 3.3: Process parameters corresponding to coffees roasted under different batch size - airflow combinations to a colour of 70±1.

Batch	**Fan**	**Roast Time (s)**			
Size (g)	**Freq. (Hz)**	$\mathbf{t = 0}$	$\mathbf{t = t_{70}/3}$	$\mathbf{t = 2t_{70}/3}$	$\mathbf{t = t_{70}}$
200	30	0	75	150	225
200	48	0	52	143	215
200	65	0	58	117	175
350	39	0	109	219	328
350	48	0	93	185	278
350	65	0	85	170	255
500	48	0	115	230	345
500	65	0	107	213	320

Table 3.4: Airflow properties corresponding to fan frequency set points described in Table 3.3, calculated according to process characterisation methods outlined in Chapter 2.

Fan	**Air Mass Flow**	**Superficial Air**
Freq. (Hz)	**Rate (kg s^{-1})**	**Velocity (m s^{-1})**
30	0.0141	8.79
39	0.0185	11.87
48	0.0228	14.95
65	0.0310	20.77

3.3.2 Results

Time-temperature roasting profiles

Measured product time-temperature profiles – corresponding to the roasting conditions specified in Table 3.5 – are presented in Figure 3.23.

For all batch sizes (200, 350 and 500 g), Figure 3.23 shows that an increase in airflow decreases the measured product temperature at the turning-point (i.e., the profile's minimum measured temperature) but has no effect on the time this occurs. This observation is

likely caused by: (i) greater airflow induces more rapid heat transfer, so the thermocouple's measured temperature more rapidly converges with the real system's temperature, (ii) the system is more disperse at higher airflows - with reduced bean-thermocouple interactions the thermocouple measures more of the drying air than the beans.

Figure 3.23 shows that greater batch sizes yield a lower measured temperature at the turning-point. Greater batches correspond to a greater mass in the bean bed (see Chapter 4), wherein measured temperatures are less influenced by airflow due to particle packing at the bean-thermocouple interface. Beyond the turning-point, the rate of change of temperature is greater for higher airflows due to the associated increase in the convective thermal load. This effect leads to significant variation in the end of roast temperature (*c.* 2-9°C as outlined in Table 3.5).

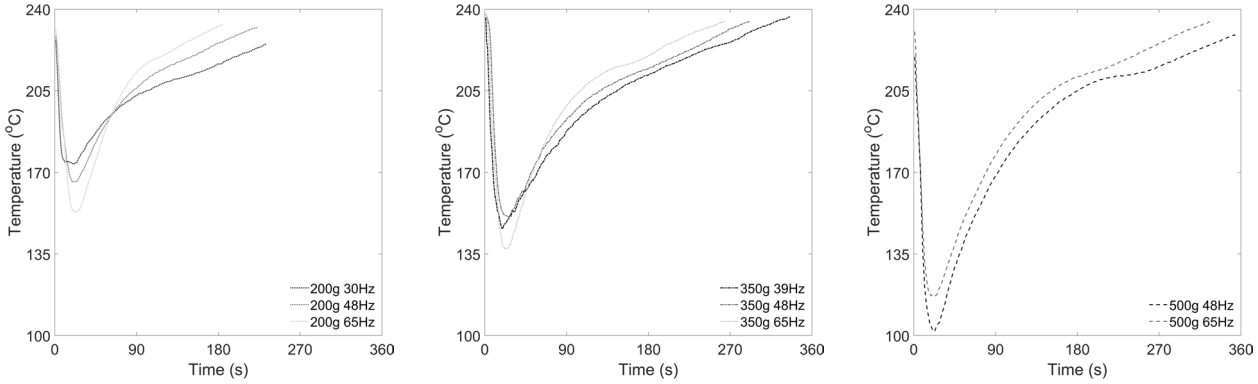

(a) 200 g (b) 350 g (c) 500 g

Figure 3.23: Time-temperature profiles obtained from constant inlet air temperature roasting of (a) 200 g, (b) 350 g and (c) 500 g of Kenyan Arabica coffee at different airflow settings.

Although the occurrence of first crack is not a discrete time event (Wilson, 2014; Yergenson, 2019), time to first crack decreased as airflow increased (and as batch size decreased) due to the higher rates of convective heat transfer associated with a larger fraction of beans in the dilute, in-flight region of the roaster and the effect of thermocouple response. Approximate times and temperatures at first crack and likely onset of exothermic reactions are stated in Table 3.5.

Table 3.5: Experimental roasting process data, detailing the thermal response and energy consumption during roasting under different batch size - airflow combinations to a surface (whole bean) colour of 70±1 (ColorTrack).

Batch Size (g)	**Fan Freq. (Hz)**	**Roast Time (s)**	**End of Roast Temp. (°C)**	**First Crack Time (s)**	**First Crack Temp. (°C)**	**Energy Used (kWh)**
200	30	225	225	180	217	0.40
200	48	215	232	150	220	0.49
200	65	175	234	110	219	0.57
350	39	328	237	185	213	0.67
350	48	278	235	175	214	0.70
350	65	255	235	155	216	0.83
500	48	345	229	220	211	0.79
500	65	320	235	190	212	0.92

Mass & moisture

The rate of change of both mass (Figure 3.24(a)-(c)) and moisture (Figure 3.24(d)-(f)) were dependent on airflow and batch size. For a given batch size, increasing airflow increases the rate of change of mass and moisture due to greater heat transfer rates, whilst increasing batch size at a specified fan frequency decreased the rate of change of mass and moisture due to the increased batch mass and reduced heat transfer rates. Although rates of mass and moisture loss are dependent on process conditions, when roasting to similar whole bean surface colours, the final mass and moisture are invariant.

Size, colour & density

Once coffee's cell walls transition to the rubbery state, the equivalent diameter (i.e., size) increases (Figure 3.25(a)-(c)). Although greater batch sizes expanded at lower rates, the effect of airflow on expansion prior to first crack was not as significant - the natural variability of bean size was of the same order of magnitude as the experimental error, thus a greater sample size would be required to confirm this hypothesis. As the cellular matrix returns to

the glassy state after first crack, bean size tended toward an equilibrium value invariant to process conditions (Geiger, 2004).

Due to the coupled effects of volumetric expansion (Figure 3.25(a)-(c)) and mass loss (Figure 3.24(a)-(c)), coffee's density decreased during roasting (Figure 3.25(d)-(f)). Prior to first crack, density evolution rate was dependent on batch size and airflow, wherein greater airflows increased the rate of change of density and greater batch sizes decreased the density evolution rate.

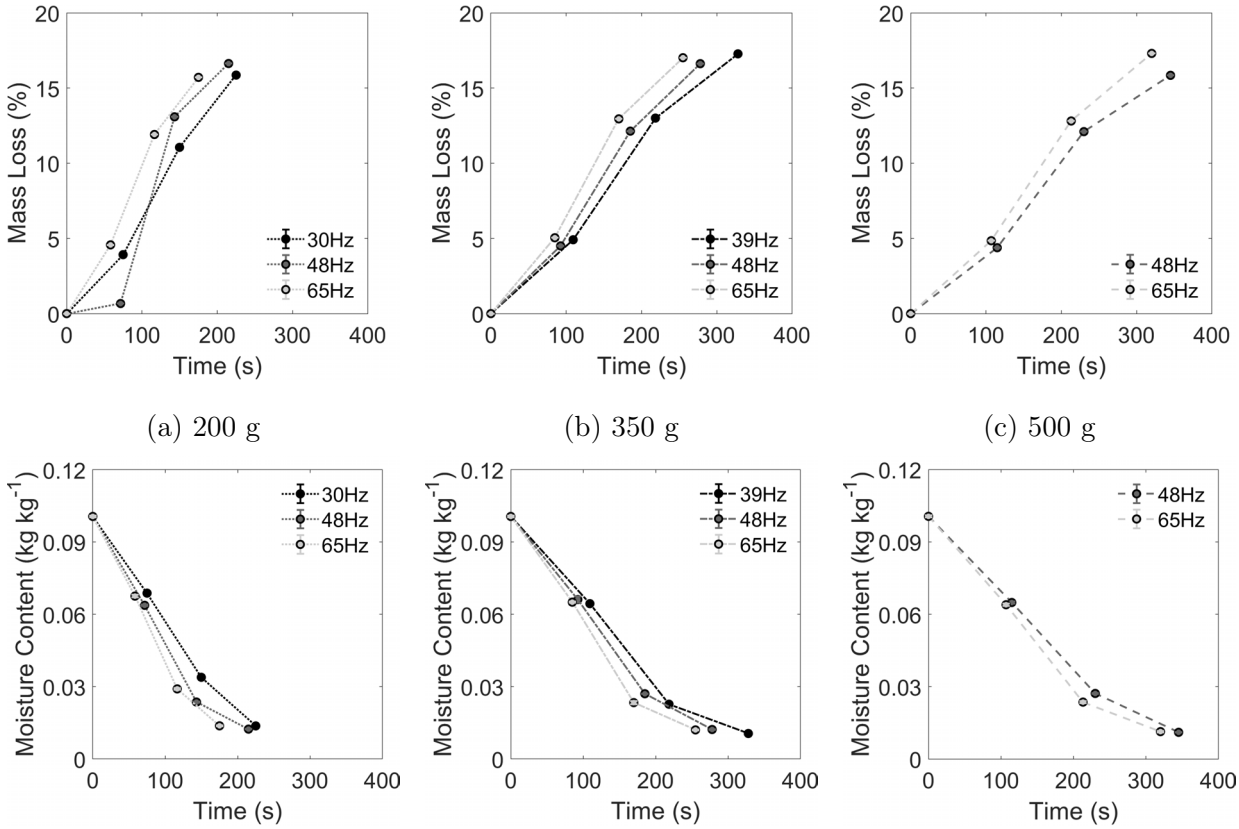

(a) 200 g (b) 350 g (c) 500 g

(d) 200 g (e) 350 g (f) 500 g

Figure 3.24: Transformation of (a)-(c) mass and (d)-(f) moisture during constant inlet air temperature roasting of (a)&(d) 200 g, (b)&(e) 350 g and (c)&(f) 500 g of Kenyan Arabica coffee at different airflow settings. Corresponding mass flow rates and superficial air velocities are displayed in Table 3.4 for reference.

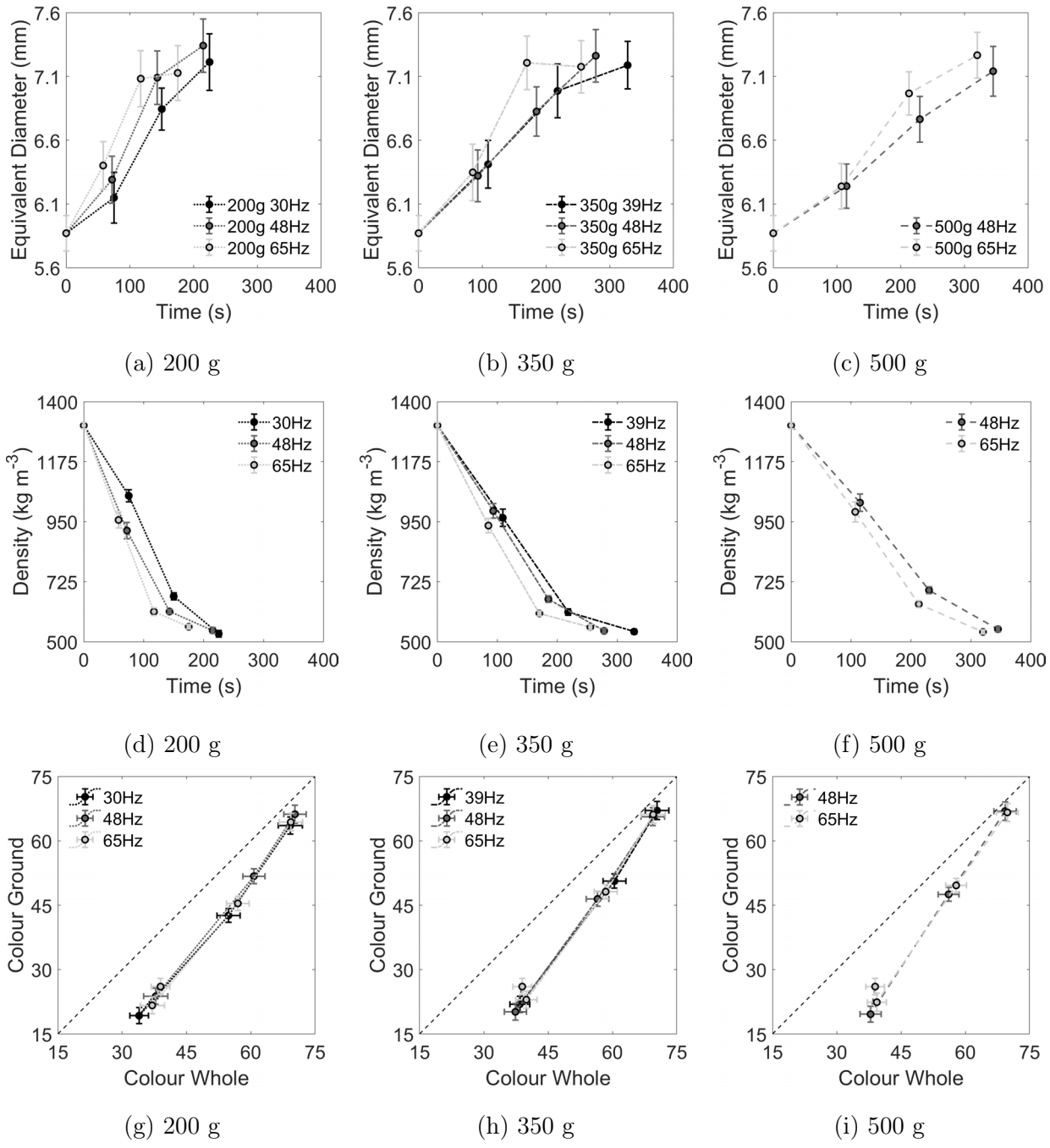

(a) 200 g (b) 350 g (c) 500 g

(d) 200 g (e) 350 g (f) 500 g

(g) 200 g (h) 350 g (i) 500 g

Figure 3.25: Transformation of (a)-(c) equivalent diameter, (d)-(f) density and (g)-(i) colour during constant inlet air temperature roasting of (a),(d)&(g) 200 g, (b),(e)&(h) 350 g and (c),(f)&(i) 500 g of Kenyan Arabica coffee at different airflow settings.

Figure 3.25(g)-(i) shows that although coffee's whole bean (i.e., surface) colour was greater than the ground colour for all process conditions and roast times, the difference between them decreased as the roast progressed. The colour difference at the end of the roast was not significantly influenced by process conditions, indicating uniform colour development.

Thermophysical properties

Many of coffee's physicochemical properties correlated with moisture content as demonstrated in Figure 3.26 and Table 3.6.

Figure 3.26 shows coffee's dependence on moisture content: lower moisture (more roasted) coffees were less dense (Figure 3.26(a)), have greater volumes (Figure 3.26(b)), lower water activities (Figure 3.26(c)) and greater porosities (Figure 3.26(d)). Vapourisation of moisture is a key driver for coffee's porosity development (Geiger, 2004); as coffee's porosity and volume increased, and mass decreased, a corresponding decrease in density was observed.

Table 3.6: Correlation of physicochemical properties with moisture content for coffee roasted under different airflow and batch size combinations in a spouted bed roaster - corresponding data is presented in Figure 3.26.

Property	**Function**	**RMSE**	**Figure**
Density	$\rho_b = 8721X_b + 422$ (3.29)	28 kg m^{-3}	3.26(a)
Volume	$V_b = -1045X_b + 207$ (3.30)	7.3 mm^3	3.26(b)
Water activity	$a_w = 6.70X_b + 0.02$ (3.31)	0.015	3.26(c)
Porosity	$\gamma_b = -214.5X_b + 62.1$ (3.32)	2.0%	3.26(d)

Coffee's effective thermal properties are a function of its solid, liquid and gaseous phases present in the bean and thus, coffee's thermal properties depend on its density. Correlations between density and (i) thermal conductivity, k_b (W m^{-1} K^{-1}) and (ii) specific heat capacity, $C_{p,b}$ (J kg^{-1} K^{-1}), displayed in Figure 3.27 and Table 3.7, clearly illustrate this. Figure 3.27(a) shows that thermal conductivity increased with density whilst Figure 3.27(b) shows that specific heat capacity increased as density decreased. These data confirm that thermal resistance is governed by coffee's moisture loss and subsequent porosity development, wherein a greater gaseous fraction inhibits thermal diffusion through the bean.

Established relationships between coffee's physicochemical and thermophysical properties (i.e., Eqs. 3.29-3.34) can be implemented as subroutines within the batch-scale simulations to account for coffee's transient properties - an approach developed in Chapter 6.

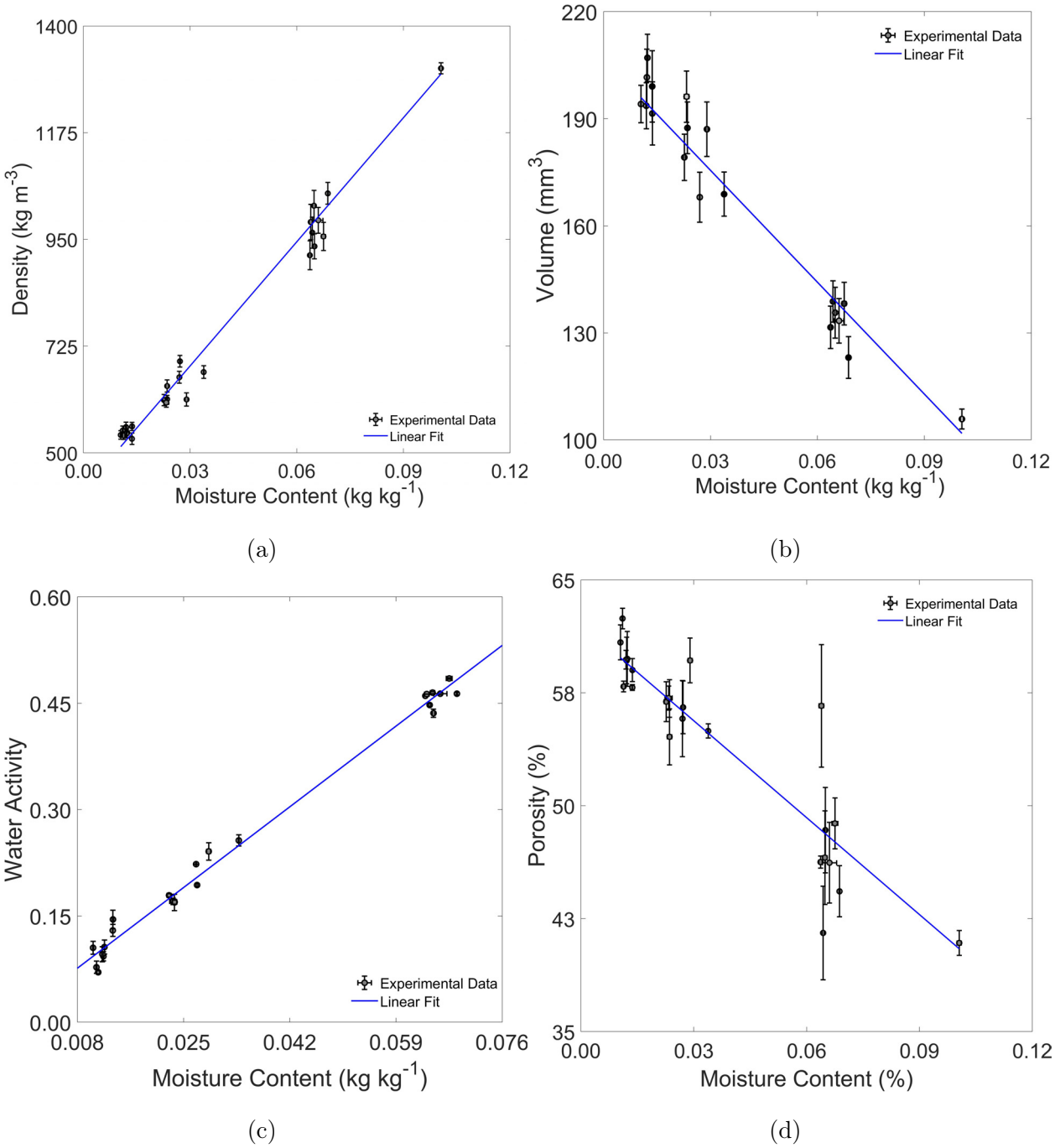

Figure 3.26: Linear regression used to correlate (a) density, (b) volume, (c) water activity and (d) porosity and moisture content for coffee roasted under different airflow and batch size combinations in a spouted bed roaster.

Table 3.7: Correlation of thermophysical properties with density for coffee roasted under different airflow and batch size combinations in a spouted bed roaster - corresponding data is presented in Figure 3.27.

Property	Function	RMSE	Figure
Thermal conductivity	$k_b = 7.31 \times 10^{-5}\rho_b + 0.045$ (3.33)	0.002 W m^{-1} K^{-1}	3.27(a)
Specific heat capacity	$C_{p,b} = 2.59 \times 10^{4}\rho_b^{-0.45}$ (3.34)	24 J kg^{-1} K^{-1}	3.27(b)

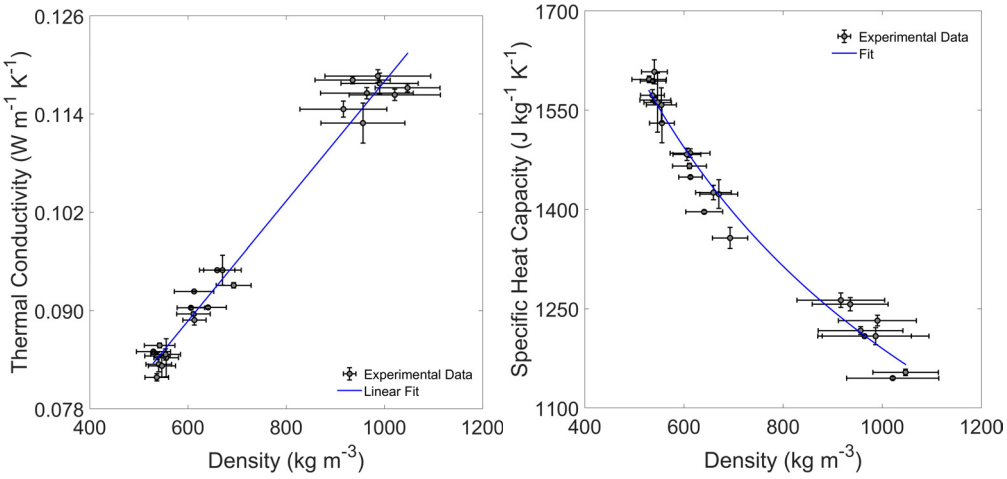

(a) (b)

Figure 3.27: Correlation of (a) thermal conductivity and (b) specific heat capacity with density for coffee roasted under different airflow and batch size combinations in a spouted bed roaster.

Batch homogeneity

Coffee colour is a valuable indicator of process consistency for commercial roasters and batch homogeneity is critical for consumer perception of quality. Distributions of colour (both whole and ground) and size (i.e., dimensions a, b, c) provide valuable insights for batch homogeneity and the difference between the whole bean (i.e., surface) and ground colour is indicative of the heat and mass transfer efficacy. Colour distributions for whole (Figure 3.28) and ground (Figure 3.29) coffee reveal that there was an initial increase in lightness (Hernández, Heyd, Irles, et al., 2007). As roasting progressed, the coffee's darkness increases and batch homogeneity generally increased (for moderate to high batch sizes (350-500 g).

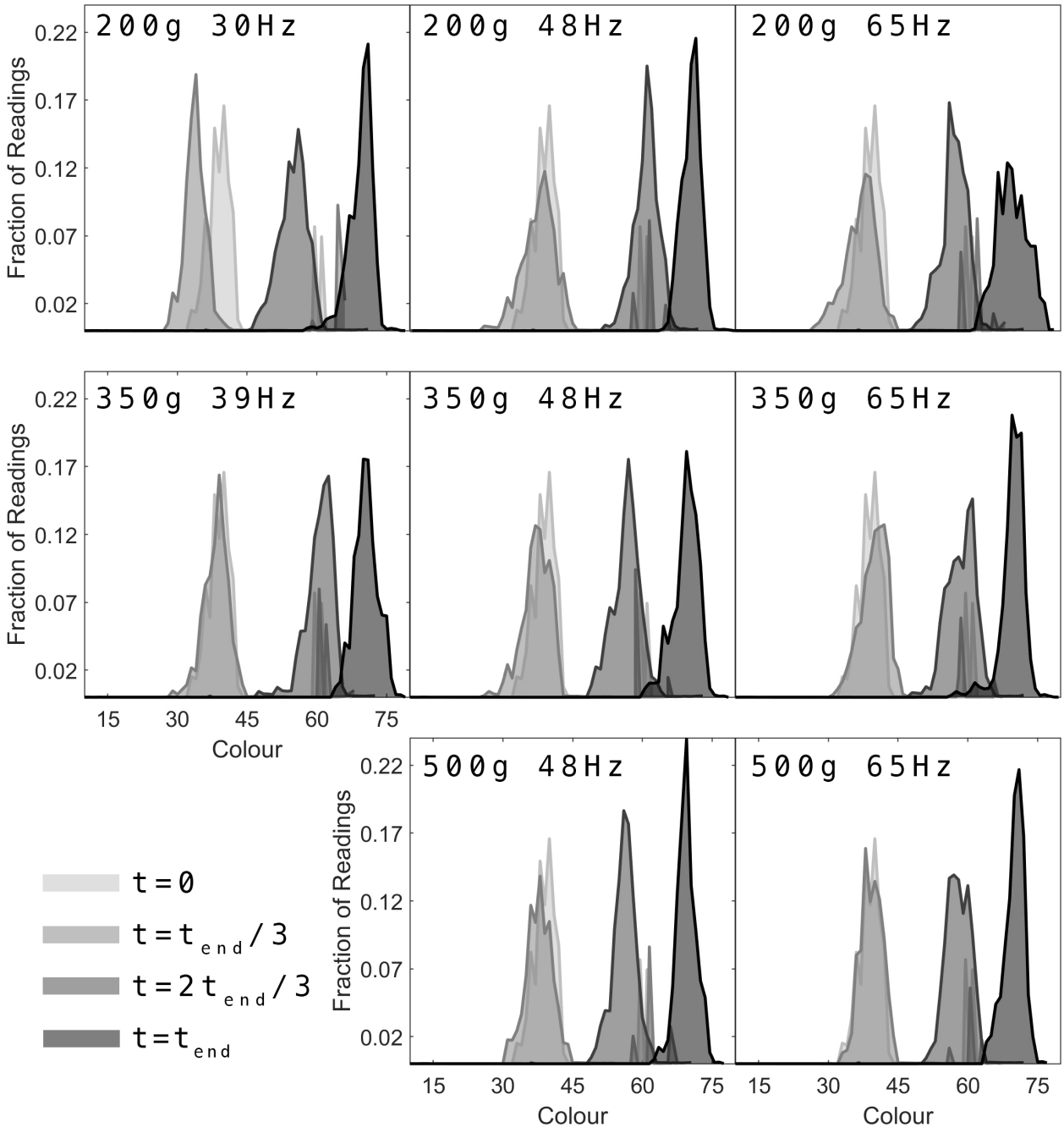

Figure 3.28: Colour distributions for whole bean coffee roasted under different process conditions and roasting times. Corresponding mass flow rates and superficial air velocities are displayed in Table 3.4 for reference.

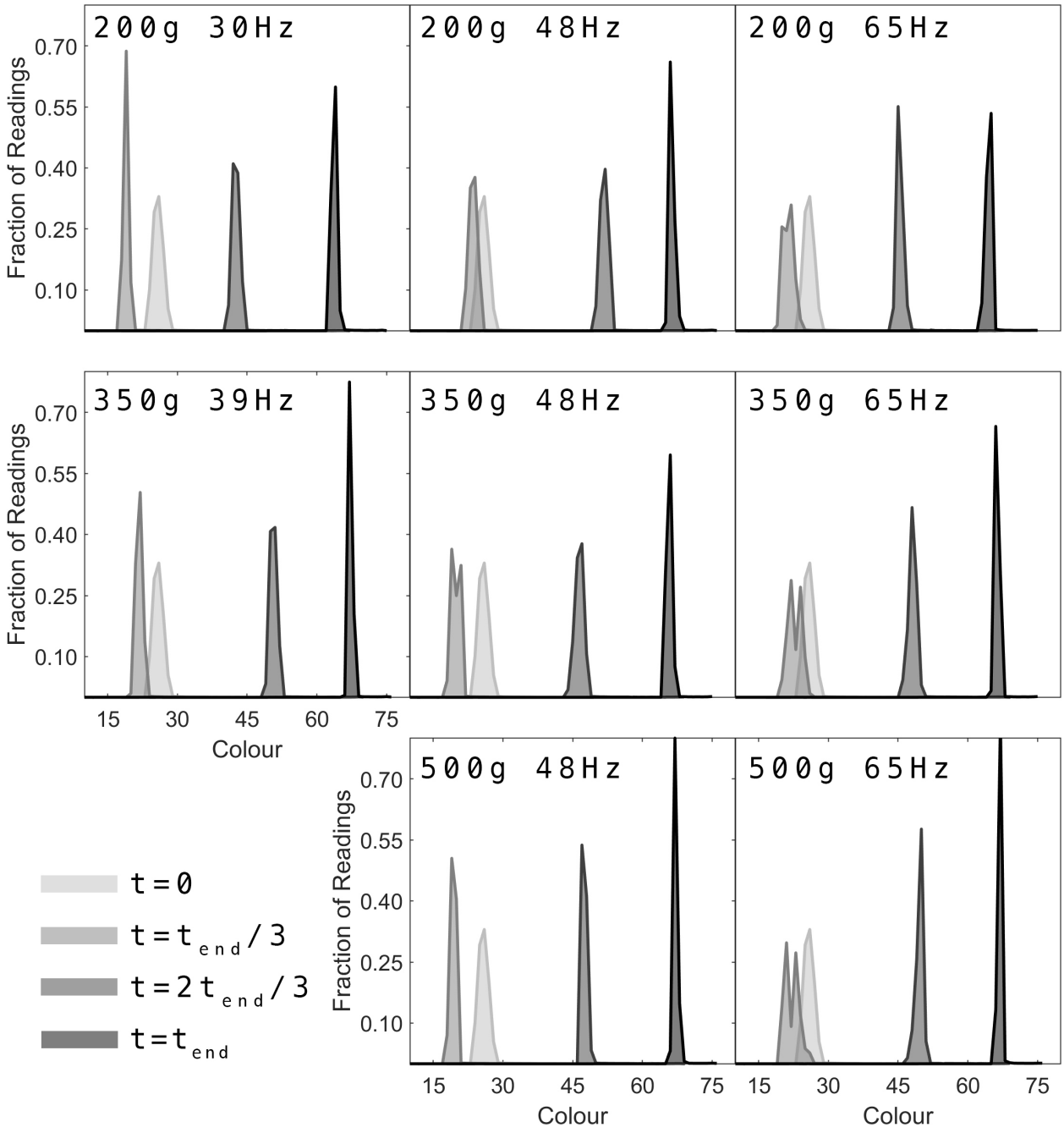

Figure 3.29: Colour distributions for ground coffee corresponding to coffees roasted under different process conditions and roasting times. Corresponding mass flow rates and superficial air velocities are displayed in Table 3.4 for reference.

The spread of colour for lower batch size roasts was greater than that of larger batches, attributed to increased convective heating that rapidly increases localised surface heating. For small batch sizes (200 g) the spread of colour decreased during roasting for low to moderate airflows (30-48 Hz fan frequencies), yet for high airflow (65 Hz), homogeneity decreased during roasting - particle motion and granular flow regime greatly influence bean bed dynamics and heat transfer rates. For combinations of low batch sizes and high airflows, batch homogeneity was low, whereas roasting larger batch sizes (350-500 g) at moderate to high airflows (48-65 Hz), batch homogeneity was greater and thus product quality is expected to be improved. Developers must consider that greater batch homogeneity might yield a visually uniform whole bean product, but a mono-dimensional flavour in-cup could result. Conversely, a lower batch homogeneity will yield low visual uniformity in whole bean products but possibly result in a more complex in-cup flavour.

Energy consumption

The spouted bed roaster is electrically powered, with a 13 kW total draw. The energy consumption of the roaster was monitored during roasting, expressed here cumulatively. Figure 3.30 presents the impact of batch size and airflow on energy consumption - data corresponds to electrical energy consumed at final roast times.

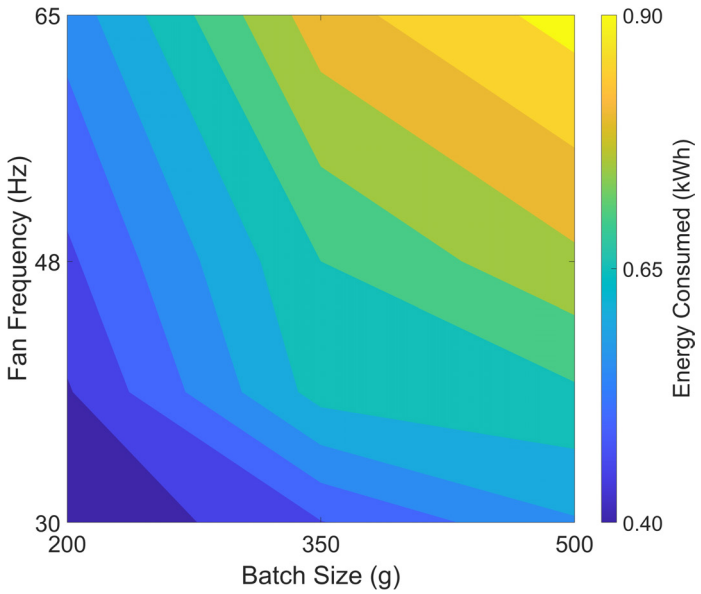

Figure 3.30: Energy consumption and its dependence on batch size and airflow - data corresponds to electrical energy consumed at final roast times.

Data in Tables 3.4 & 3.5 show that roasting larger batches or using lower airflow settings increased the time to achieve a specified colour due to lower convective heat transfer rates, yet Figure 3.30 shows greater fan frequencies (i.e., higher airflows) and larger batch sizes increase energy requirements. Data therefore implies total energy requirements are largely attributed to minimum requirements for operation of the blower and heating element (the latter being constant for the studied conditions). The total energy consumption, ε (kWh) required to roast coffee in the spouted bed roaster to a surface colour of 70±1 (ColorTrack) is therefore a function of the fan frequency, f (Hz) and batch size, m_{bs} (g):

$$\varepsilon = 1.12 \times 10^{-3} m_{bs} + 5.87 \times 10^{-3} f \tag{3.35}$$

When considering the specific energy consumption (i.e., energy per unit coffee mass), large (500 g) batch sizes roasted under low (48 Hz fan frequency) airflow required less energy per unit coffee mass (1.6 kWh/kg) than small (200 g) batch sizes at high (65 Hz fan frequency) airflow (2.8 kWh/kg). Whilst changes in fan frequency influence heat transfer rates and roast time, roasting larger batch sizes at lower airflow settings is preferable to improve batch homogeneity and minimise energy consumption.

3.4 Case study III: Evolution of coffee porosity and its influence on coffee's thermophysical properties

3.4.1 Methodology

The porosity of coffees generated in the first two case studies were measured using X-ray Micro-Computed Tomography (MicroCT) (SkyScan 1172, Bruker).

3.4.2 Results

Structural observations of roasted coffee beans

Data reveal that the bean can be considered as a 3D shell-like structure (Figure 3.6(a)); in 2D, a ring-like structure is apparent at the midpoint of the bean's height (Figure 3.6(b)). Inhomogeneity within the coffee ring is highlighted in Figure 3.31, a magnified view of the cross-section presented in Figure 3.6(b), which reveals a porous gradient. Some symmetry is present within the sample shown in Figure 3.31. This suggests that pores at the centre of the coffee ring are predominantly closed and independent in the early stages of roasting, whilst pore connectivity (open porosity) increases toward the outer surface. These density differences between the centre and surface of the bean are likely a result of surface shrinkage and the development of the drying front (Geiger, 2004; Fadai et al., 2017). Frisullo et al. (2012) presented tomographs that further support this.

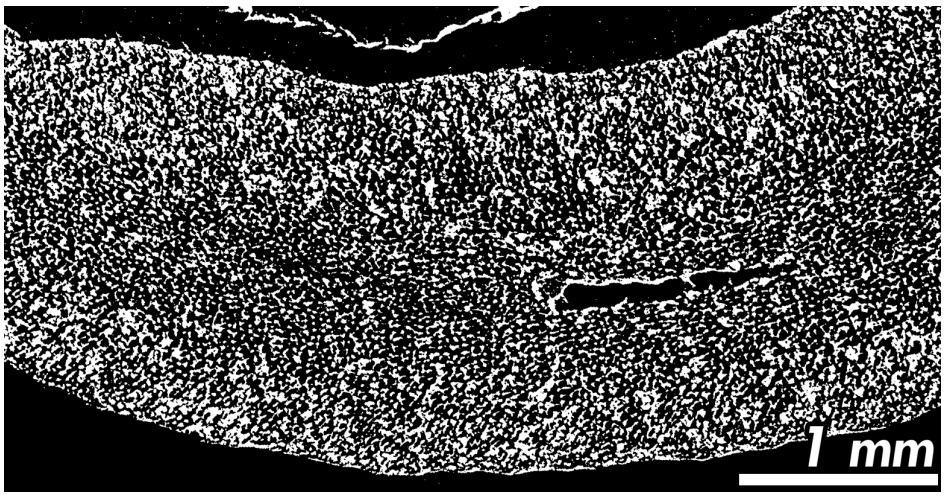

Figure 3.31: A porous gradient within the bean's ring-like structure.

Porosity development during roasting

The time-dependent porosity development can be assessed visually from the reconstructed cross-sections shown in Figure 3.32. These reconstructions highlight the increase in total pore area (black) against the total area of cellular material (white). Total pore area is visibly higher in roasted coffee (Figure 3.32(e)) than in green coffee (Figure 3.32(a)).

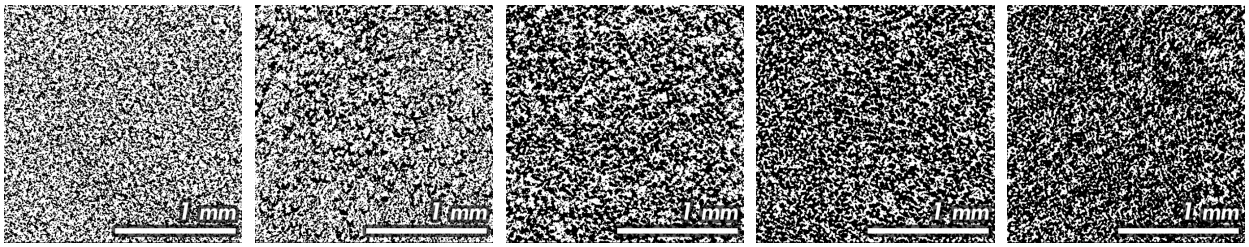

(a) $t = 0\ s$ (b) $t = 42\ s$ (c) $t = 84\ s$ (d) $t = 126\ s$ (e) $t = 168\ s$

Figure 3.32: 2 mm cross-sections of coffee roasted with a constant inlet air temperature of 280°C (as shown in Figure 3.10) for (a) 0 s (green, unroasted coffee), (b) 42 s, (c) 84 s, (c) 126 s and (d) 168 s (roasted coffee).

The kinetic behaviour of coffee during roasting is presented in Figure 3.33(a); for visual clarity, only data for constant inlet air temperature roasts at 220, 265 and 280°C are displayed. Total porosity increased with time for all roasting conditions - in agreement with Schenker (2000) and Frisullo et al. (2012). There is an initial phase of slow porous development due to the rapid diffusion of moisture and the corresponding drying front. Schenker (2000) and Frisullo et al. (2012) explained that transitions from glassy to rubbery states promote development of porosity and therefore bean volume. At lower roasting temperatures (220°C) the rate of change of porosity decreases with time and porosity plateaus shortly after first crack, shown in Figure 3.33(a). The return of the bean's cellular material to a glassy state towards the end of lower temperature roasting inhibited further porosity development. Figure 3.33(a) shows that the rate of porosity change increases with air temperature. Increased air temperatures provide a greater temperature difference between the bean core and drying air that increases heat flux (Fadai et al., 2017).

Large standard errors associated with measured porosity (*c.* 4.6%) were observed for some part-roasted samples as indicated in Figure 3.33(a). Whilst steps were taken to ensure no major defects were present in the tomographs, coffee is a natural product and variability is unavoidable. It is assumed that bean variability is the source of uncertainty among part-roasted samples.

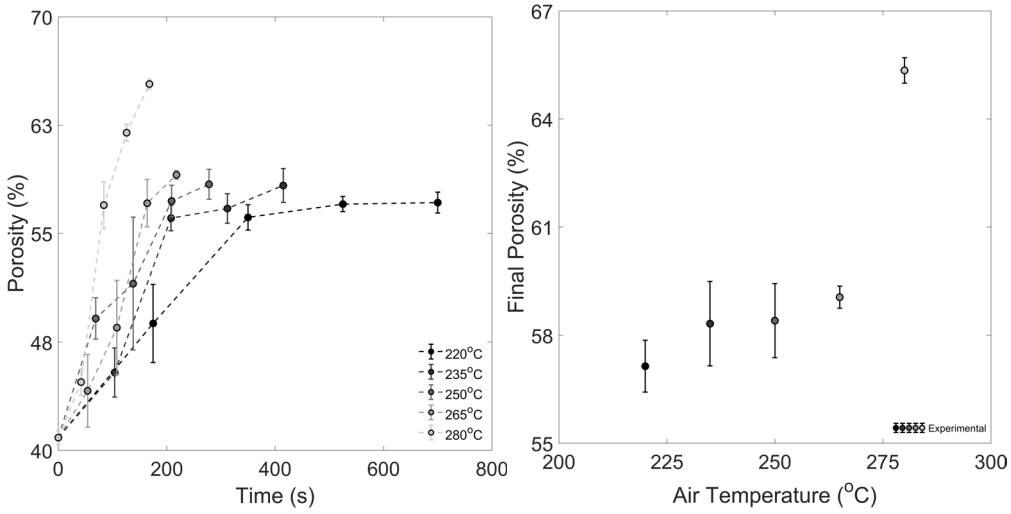

(a) (b)

Figure 3.33: Experimental data that detail (a) coffee's porosity development during roasting and (b) final porosity as a function of constant inlet air temperature when roasted to an equivalent surface colour.

When roasted to an equivalent surface colour, Figure 3.33(b) suggests that the coffee's final porosity is temperature dependant. For coffees roasted under constant inlet air temperatures in the range of 220-265°C, final porosity increases slightly with applied temperature, yet for a constant inlet air temperature of 280°C, there is a significant difference in the rate of porosity development and final porosity. This indicates a high activation energy is required to significantly increase coffee's porosity through variation of the applied time-temperature profile. Heat transfer coefficients associated with these high porosity development rates are only feasible in high airflow roasters such as spouted bed, or tangential roasters, unless low batch sizes (i.e., fill volumes) are used.

Correlation of coffee's physical properties

Case studies I & II show that the inter-relation of coffee's physical properties is complex. To begin to disentangle these relations, correlations were developed to use easily measured properties (moisture, density, colour and water activity) to predict more specialised, analytical methods (porosity and pycnometry).

Table 3.8 and Figure 3.34 present correlations of coffee's (a) moisture content, X_b (kg kg^{-1}) (b) density, ρ_b (kg m^{-3}) (c) whole bean colour, c_w (ColorTrack) and (d) water activity, a_w, with its porosity, γ_b (%). Table 3.9 and Figure 3.35 present correlations of coffee's whole bean colour, moisture content and water activity.

Table 3.8: Correlation of physicochemical properties with porosity for coffee roasted under different constant inlet air temperatures, batch sizes and airflows in a spouted bed roaster - corresponding data is presented in Figure 3.34.

Property	**Function**	**RMSE**	**Figure**
Moisture & Porosity	$X_b = -3.66 \times 10^{-3}\gamma_b + 0.24$ (3.36)	0.01 kg kg^{-1}	3.34(a)
Density & Porosity	$\rho_b = -30\gamma_b + 2365$ (3.37)	90 kg m^{-3}	3.34(b)
Colour (Whole) & Porosity	$c_w = 2.0\gamma_b - 52.0$ (3.38)	6.0	3.34(c)
Water Activity & Porosity	$a_w = -0.02\gamma_b + 1.45$ (3.39)	0.10	3.34(d)

Table 3.9: Correlation of physicochemical properties for coffee roasted under different constant inlet air temperatures, batch sizes and airflows in a spouted bed roaster - corresponding data is presented in Figure 3.35.

Property	**Function**	**RMSE**	**Figure**
Colour (Whole) & Moisture	$c_w = -537.3X_b + 74.4$ (3.40)	2.2	3.35(a)
Colour (Whole) & Water Activity	$c_w = -71.2a_w + 76.3$ (3.41)	6.9	3.35(b)
Moisture & Water Activity	$X_b = 5.68a_w + 0.09$ (3.42)	0.08 kg kg^{-1}	3.35(c)

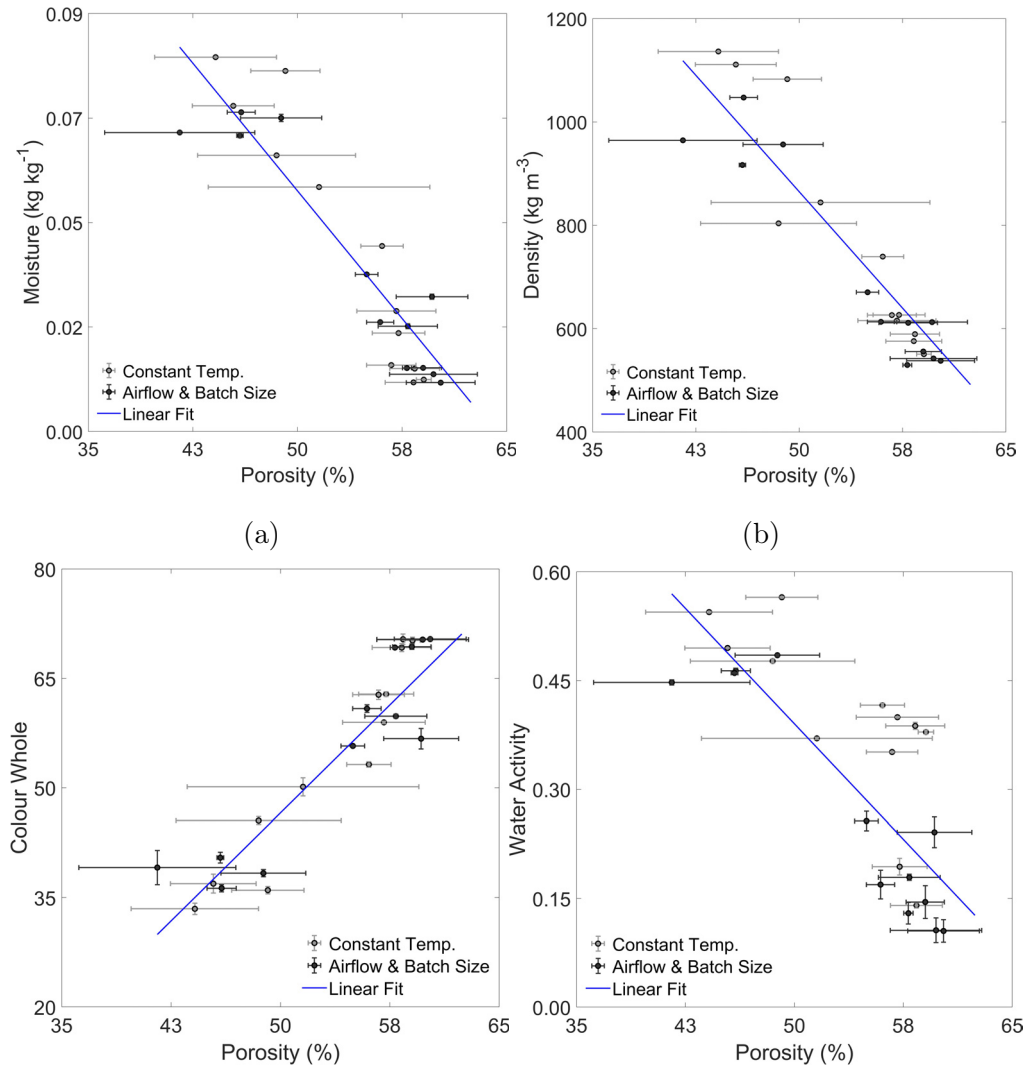

Figure 3.34: Correlation of coffee porosity with physical properties (a) moisture, (b) density, (c) whole bean colour and (d) water activity - data corresponding to kinetic transformation studies in spouted bed roasters: (i) constant inlet temperature roasting and (ii) variation of airflow and batch size.

As colour and moisture correlate with porosity, these analyses can be used interchangeably to monitor process performance and product quality. Optical methods such as those used for colour measurements are sensitive to ambient temperature and time after roasting - the latter explained by changes in coffee temperature and degassing - both impact coffee's emissivity and reflectivity. Through using intrinsic coffee properties such as moisture, or mass, process performance and product quality can rapidly and more consistently be maintained.

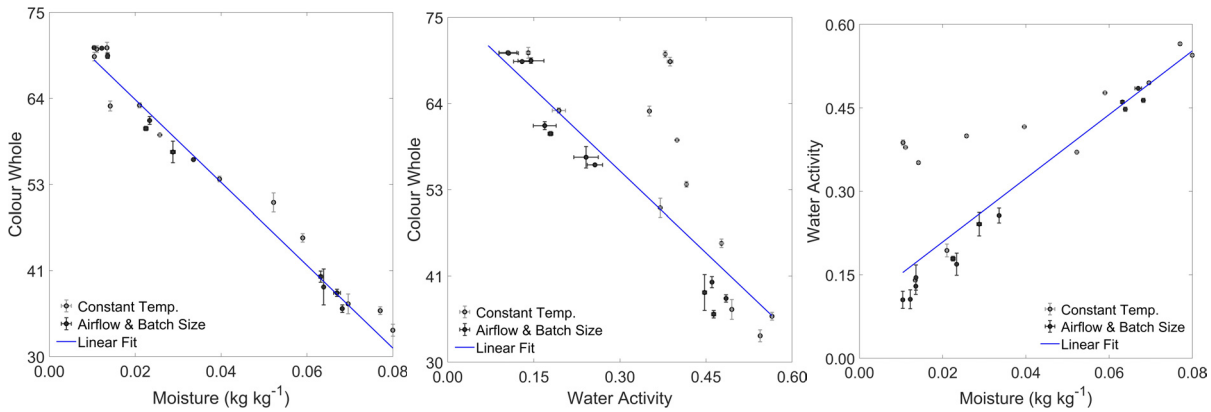

(a) (b) (c)

Figure 3.35: Correlation of coffee's physical properties: (a) colour and moisture, (b) colour and water activity, and (c) moisture and water activity - data corresponding to kinetic transformation studies in spouted bed roasters: (i) constant inlet temperature roasting and (ii) variation of airflow and batch size.

Correlation of coffee's thermophysical properties

Coffee's specific heat capacity (calculated based on bulk density) and thermal conductivity are governed by physical composition (i.e., solid, liquid and gaseous fractions) and their respective thermal properties. Therein, with knowledge of coffee's moisture loss and porous development during roasting, thermal properties of each phase can be determined and implemented within prescribed physics-driven models.

Table 3.10 and Figure 3.36 present correlations of coffee's thermal properties (thermal conductivity, k_b (W m^{-1} K^{-1}) and specific heat capacity, $C_{p,b}$ (J kg^{-1} K^{-1})) with (a)-(b) moisture and (c)-(d) porosity. Table 3.11 and Figure 3.37 present correlations of coffee's thermal properties (thermal conductivity and specific heat capacity) with (a)-(b) water activity and (c)-(d) whole bean colour.

As moisture decreases and porosity increases during roasting, coffee's effective thermal conductivity decreases whilst its effective specific heat capacity increases. Due to the greater volume fraction of gaseous voids within the bean's matrix, the higher thermal resistance in roasted coffee paints an interesting perspective on heat transfer rates after first crack. Darker

(i.e., more roasted) coffees are more porous, have lower moisture contents, and lower water activities than lighter (less roasted) coffees. Coffee's thermal conductivity is therefore lower for lighter coffees with higher water activities. Conversely, coffee's specific heat capacity is greater for the same lighter coffees with higher water activities.

Table 3.10: Correlation of coffee's thermophysical properties with moisture and porosity - data corresponding to Figure 3.36.

Property	**Function**	**RMSE**	**Figure**
Thermal Conductivity & Moisture	$k_b = 0.50X_b + 0.08$ (3.43)	0.005 W m^{-1} K^{-1}	3.36(a)
Specific Heat Capacity & Moisture	$C_{p,b} = -6687X_b + 1634$ (3.44)	59 J kg^{-1} K^{-1}	3.36(b)
Thermal Conductivity & Porosity	$k_b = -1.86 \times 10^{-3}\gamma_b + 0.20$ (3.45)	0.007 W m^{-1} K^{-1}	3.36(c)
Specific Heat Capacity & Porosity	$C_{p,b} = 24.3\gamma_b + 75.2$ (3.46)	94 J kg^{-1} K^{-1}	3.36(d)

Table 3.11: Correlation of thermophysical properties with water activity and colour - data corresponding to Figure 3.37.

Property	**Function**	**RMSE**	**Figure**
Thermal Conductivity & Water Activity	$k_b = 0.075a_w + 0.076$ (3.47)	0.005 W m^{-1} K^{-1}	3.37(a)
Specific Heat Capacity & Water Activity	$C_{p,b} = -831a_w + 1641$ (3.48)	112 J kg^{-1} K^{-1}	3.37(b)
Thermal Conductivity & Colour (Whole)	$k_b = -9.25 \times 10^{-4}c_w + 0.15$ (3.49)	0.004 W m^{-1} K^{-1}	3.37(c)
Specific Heat Capacity & Colour (Whole)	$C_{p,b} = 12.2c_w + 720.4$ (3.50)	61 J kg^{-1} K^{-1}	3.37(d)

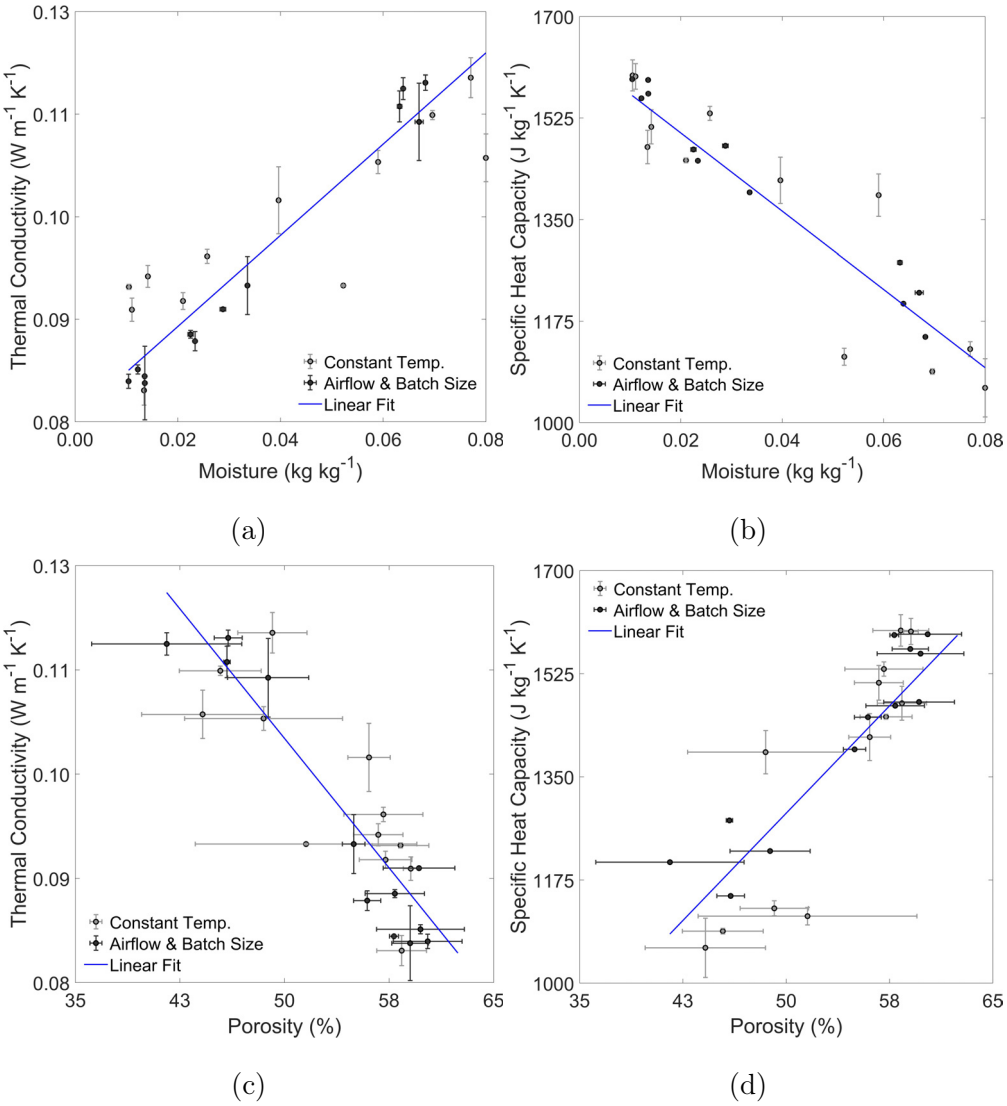

Figure 3.36: Correlation of coffee's physicochemical properties: (a) thermal conductivity and moisture, (b) specific heat capacity and moisture, (c) thermal conductivity and porosity, and (d) specific heat capacity and porosity - data corresponding to kinetic transformation studies in spouted bed roasters: (i) constant inlet temperature roasting and (ii) variation of airflow and batch size.

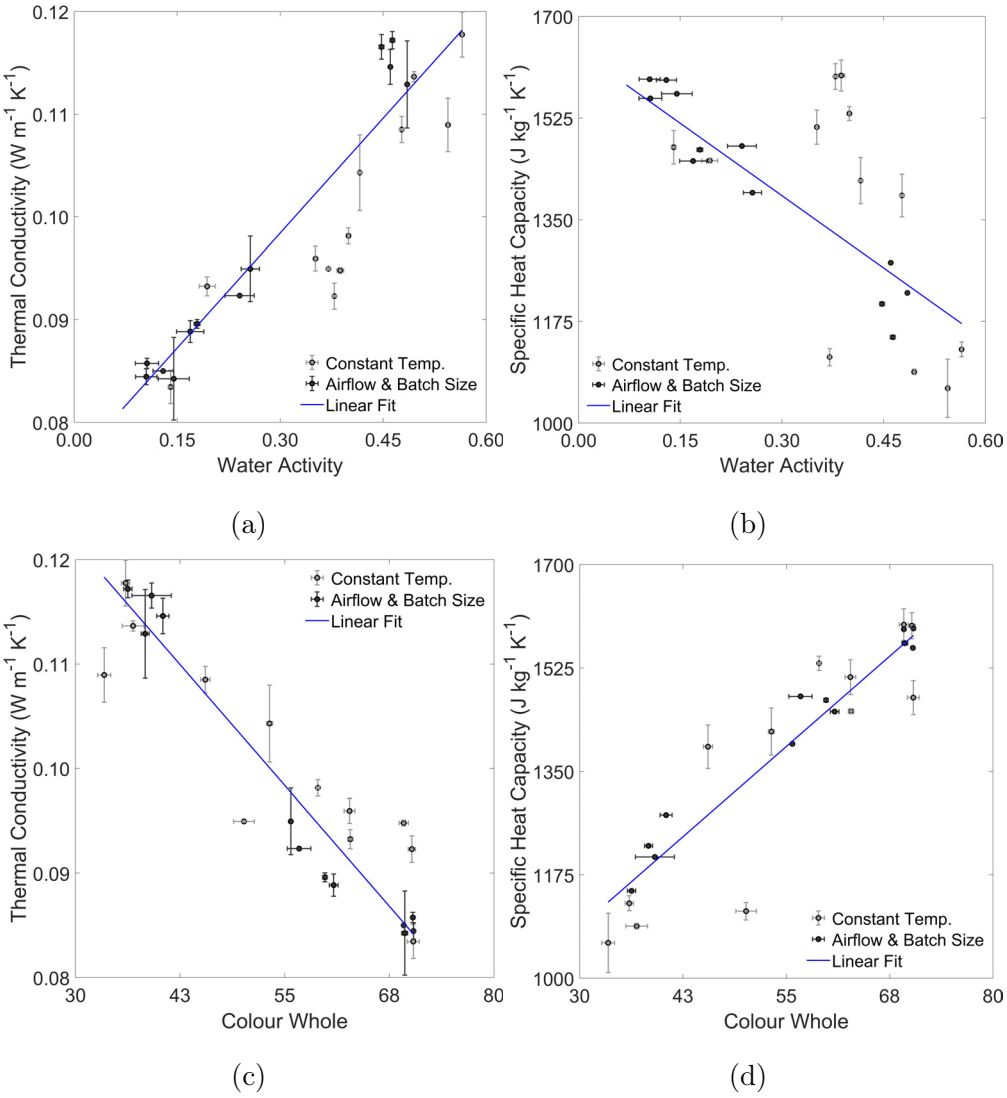

Figure 3.37: Correlation of coffee's physical properties: (a) thermal conductivity and water activity, (b) specific heat capacity and water activity, (c) thermal conductivity and whole bean colour, and (d) specific heat capacity and whole bean colour - data corresponding to kinetic transformation studies in spouted bed roasters: (i) constant inlet temperature roasting and (ii) variation of airflow and batch size.

Comparison of density & porosity methods

Techniques employed to determine density and porosity depend on the desired accuracy, precision and representivity but also on the cost (monetary and temporal) of the analyses. Here, density measurements determined via (i) digital calipers, $\rho_{w,c}$ (kg m^{-3}), (ii) free-flow bulk density, ρ_{bulk} (kg m^{-3}) and (iii) pycnometry, $\rho_{w,p}$ (kg m^{-3}) were compared. Porosity measurements determined via (i) microCT, γ_{CT} (%) and (ii) pycnometry, γ_p (%) were also compared. Table 3.38 and Figure 3.38 present correlations of density and porosity measurements for data corresponding to case study II and demonstrate a high goodness of fit for all prescribed methods.

Table 3.12: Correlation of physicochemical properties with porosity for coffee roasted under different constant inlet air temperatures in a spouted bed roaster - corresponding data is presented in Figure 3.38.

Measurement Technique	Function		RMSE	Figure
Density: Calipers & Pycnometer (Whole)	$\rho_{w,c} = 0.898\rho_{w,p} + 0.003$	(3.51)	0.023 g cm^{-3}	3.38(a)
Density: Free-flow & Pycnometer (Whole)	$\rho_{bulk} = 0.533\rho_{w,p} - 0.016$	(3.52)	0.021 g cm^{-3}	3.38(b)
Density: Pycnometer (Ground) & Pycnometer (Whole)	$\rho_g = 0.596\rho_w + 0.600$	(3.53)	0.0120 g cm^{-3}	3.38(c)
Porosity: MicroCT & Pycnometer (Whole)	$\gamma_{CT} = 0.49\gamma_p + 41.41$	(3.54)	2.9 %	3.38(d)

Figure 3.38(a) shows that whole bean density measured via calipers and pycnometry agree (Eq. 3.51) and are almost at unity. Although the standard deviation of densities via calipers is large for higher density (i.e., green and part-roasted) coffees. Figure 3.38(b) reveals that although bulk density and density via pycnometry measurements are not at unity there is good correlation (Eq. 3.52). Figure 3.38(c) shows that ground and whole bean pycnometric densities correlate well (Eq. 3.53) but are not equal. For higher density (i.e., green and part-roasted) coffees, ground coffee values were closer to whole bean values than for lower

density (i.e., roasted) coffees. This phenomenon suggests that coffee's porosity influences pycnometry measurements, wherein the gas is unable to fully explore the internal matrix of the bean. Figure 3.38(d) shows that porosity determined via MicroCT and pycnometry are not equal in value but correlate.

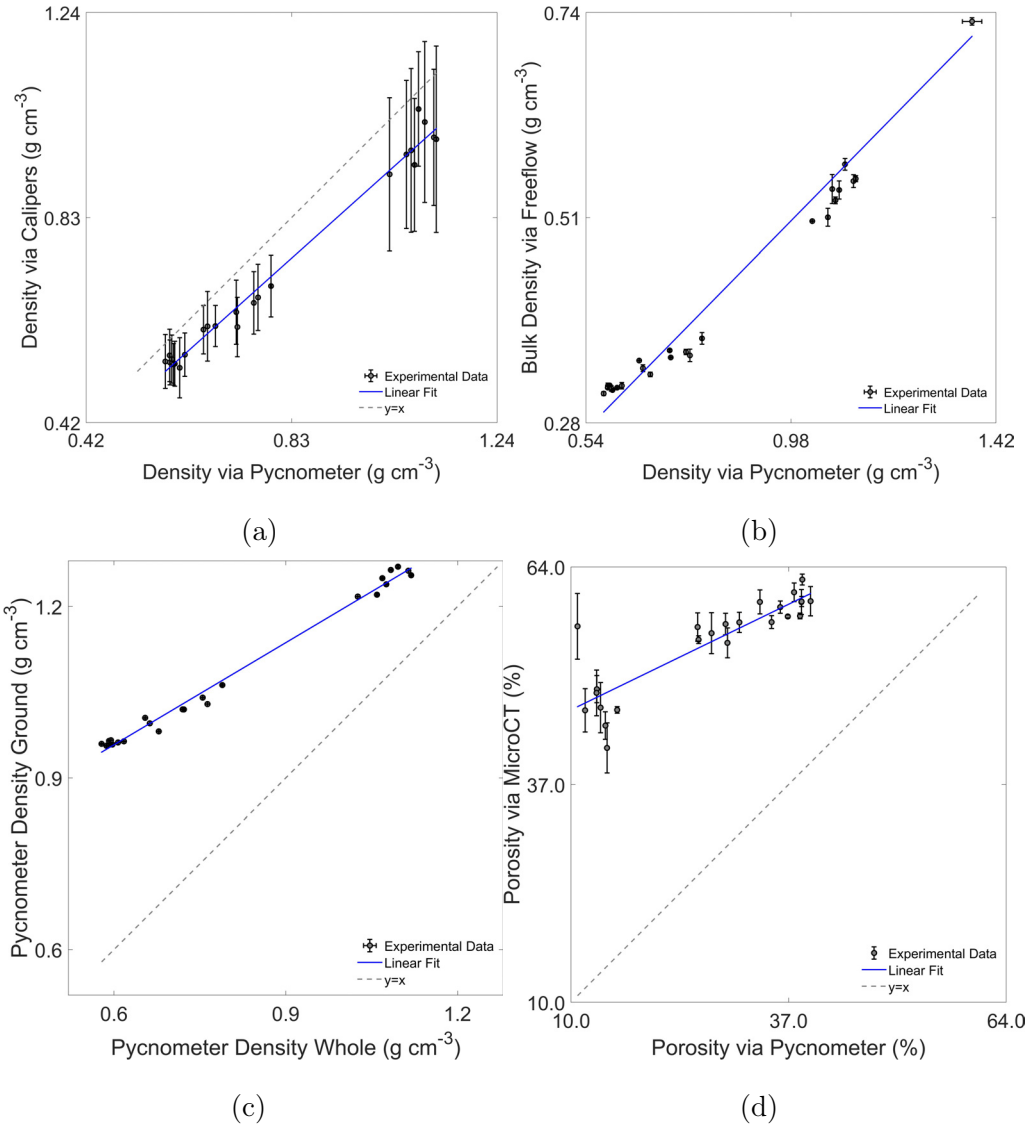

Figure 3.38: Comparison of density and porosity measurement techniques showing correlations of (a) density via calipers and pycnometry, (b) free-flow bulk density and density via pycnometry, (c) ground and whole bean density via pycnometry and (d) porosity via microCT and pycnometry.

Whilst pycnometry is accurate, the sample size is small (2 g) and likely not representative of the batch. As the sample size for caliper measurements (3-4 g) and bulk density (60-200 g) are greater, their representivity is greater. As all density measurements correlate (Figure 3.38(a)-(b); Eqs. 3.51-3.52), proposed density measurements should align with the needs of the developer, although as bulk density measurements are more rapid, and more representative, they are well suited for most applications.

3.5 Case study IV: Effect of thermocouple diameter on temperature measurement

3.5.1 Methodology

Kenyan Arabica coffee was roasted in a pilot-scale spouted bed roaster (RFB-S, Neuhaus Neotec) with an constant inlet air temperature of 250°C to a final surface (whole bean) colour of 70±1 - determined via colourimetry (ColorTrack Benchtop R-100B, FreshRoast-Systems). The roaster's fan frequency was set to 48 Hz, with batch sizes of 350.0±0.1g (Acculab Atilon, Sartorius). Both inlet air and product temperature were measured using a Type-K thermocouple with a length of 100 mm and diameter of 1 mm (RS Components Ltd.). Product temperature was measured using four stainless steel (310) sheathed, mineral insulated Type-K thermocouples of different diameters (0.50, 0.75, 1.00 and 1.50 mm), each with a length of 150 mm (TC Ltd.). Once the specified roasting end-point was achieved, ambient air was used to cool the beans for 60 s. Roasts were performed in triplicate using one thermocouple at a time, with 12 roasts in total.

3.5.2 Results

Experimental time-temperature profiles

The time-temperature profiles in Figure 3.39 display the mean recorded profile from triplicate constant inlet air temperature roasts at 250°C using thermocouples with diameters of 0.50, 0.75, 1.00 and 1.50 mm.

The time and temperature of the turning-points (the minima of the time-temperature profiles) increased with thermocouple diameter (detailed in Table 3.13). Differences in response rate are due to variations in the pathlength for transient thermal conduction (Kar et al., 2004; Majdak and Jaremkiewicz, 2016; Papaioannou, Leach, and Davy, 2018) and reflect expectation; the thinner the thermocouple, the quicker the response. Both the recorded temperature of first crack and the end of roast temperature were greater for thinner thermocouples (also detailed in Table 3.13) - the difference between the end of roast temperature

for thinnest (0.5 mm) and thickest (3.0 mm) thermocouples was significant (7.2°C).

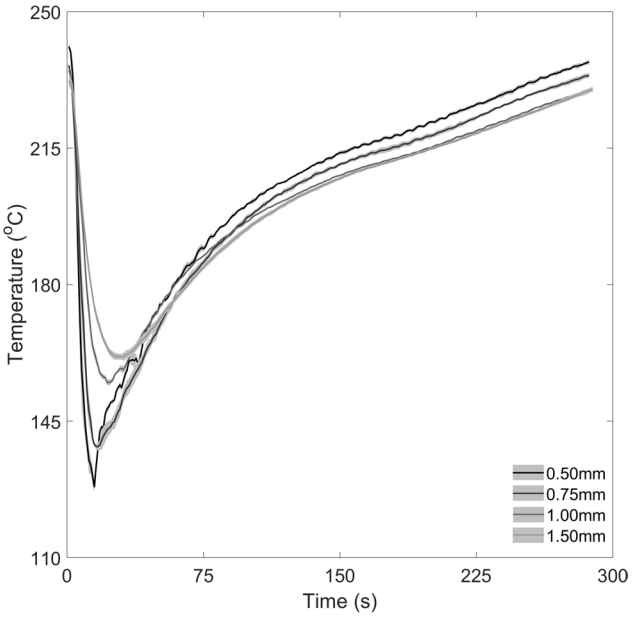

Figure 3.39: Time-temperature profiles obtained from constant inlet air temperature roasts at 250°C using 0.50, 0.75, 1.00 and 1.50 mm thermocouples - shaded area indicates the standard error of triplicate roast profiles.

Table 3.13: Roasting progress indicators as inferred from time-temperature roasting profiles recorded with thermocouples of various diameter mineral insulated type-K thermocouples

Thermocouple	**Turning-Point**		**Exothermic Onset**		**End of Roast**
Diameter (mm)	**Time (s)**	**Temp. (°C)**	**Time (s)**	**Temp. (°C)**	**Temp. (°C)**
0.50	15	128	170	216.8	237.0
0.75	16	138	172	214.4	233.6
1.00	24	160	176	211.9	229.5
1.50	30	162	181	212.3	229.8

The rate of change of temperature highlights changes in time-temperature profiles that might not be observed when monitoring the time-temperature profile alone due to the observed scale. The rate of change of temperature profiles (Figure 3.40) were used to identify the onset of endothermic and exothermic reactions – defined here as the time corresponding to the minimum rate of change of temperature prior to the observed rate of change of temperature increase. The impact of thermocouple diameter on the determination of first

crack and subsequent onset of endothermic and exothermic reactions is apparent from data presented in both Table 3.13 and Figure 3.40. The rate of change of temperature profiles (Figure 3.40) suggest that use of roasting profiles recorded by larger diameter thermocouples would underestimate the effects of endothermic and exothermic reactions.

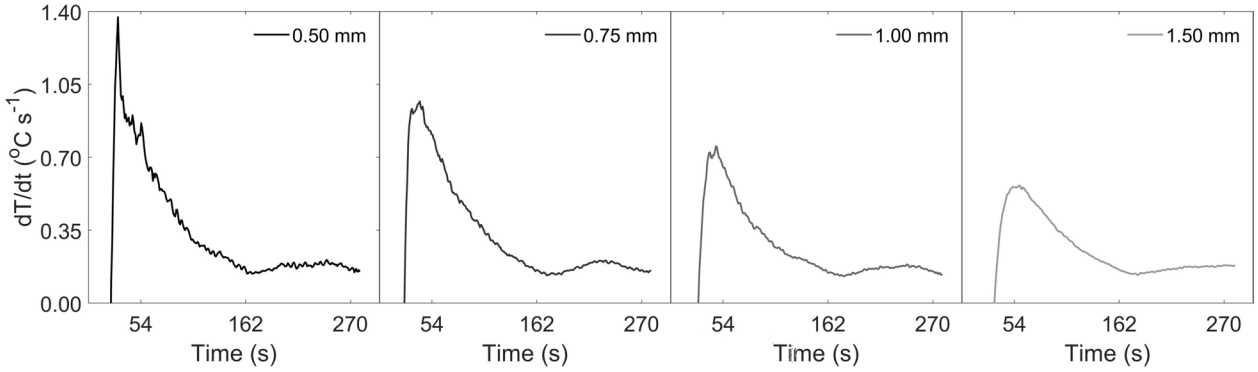

Figure 3.40: Rate of change of temperature profiles recorded with thermocouples of various diameter mineral insulated type-K thermocouples.

The observed effects on the roasting progress indicators (Table 3.13) show that thin thermocouples provide more rapid responses to temperature changes. As there are significant differences in the recorded temperature of the progress indicators due to thermocouple diameter, and the recorded product temperature is lower than the actual temperature of the roaster, the response of the thinnest thermocouple might cautiously be considered as the most accurate.

Although thermocouple-coffee interactions are difficult to quantitatively assess, they must be considered. The product thermocouple describes the temperature of both the air and coffee in the roaster. For thin thermocouples, the contact surface between itself and a coffee bean ($d_b \approx$5 mm) will be far smaller than that of thicker thermocouples, but the packing density of a bean bed would be greater around a thinner thermocouple. Another consideration is the measurement noise; a thin thermocouple will inherently be more sensitive to temperature changes than a thicker thermocouple. A thin thermocouple will thus be more susceptible to reveal rapid oscillations in both inlet and outlet air temperatures typically seen due to the action of a temperature controller, as well as 'flicks' and 'crashes' visible in the rate of change of product temperature often seen due to thermocouple-bean interactions (S. Rao,

2014).

3.6 Conclusions & outlook

In this chapter, techniques to characterise coffee's physicochemical properties have been established for whole and ground coffee. For developers, these characterisation techniques enable: (i) discrimination of green coffee components, (ii) monitoring of coffee's transformation during roasting and (iii) determination of the roasted coffee's properties. If measurements of green, part-roasted and roasted coffees are embedded within production practices, then these data can be used to both feed-forward and feed-back raw material and product variance to modulate process conditions and minimise further product variance.

These characterisation techniques were then used to monitor changes in coffee's physicochemical properties as they transform during roasting in a spouted bed roaster. The effect of diverse roasting conditions on an Arabica coffee was established in a series of case studies that considered different constant inlet air temperatures, airflows and batch sizes. These empirical data outline the evolution of temperature and several physicochemical properties under different roasting conditions. As each of these process parameters significantly affected heat transfer rates and coffee's subsequent physicochemical transformation, developers have several degrees of freedom that can be explored during process and product development.

Developers are required to innovate and optimise processes with minimal impact on product quality. Two drivers for process optimisation are productivity and energy consumption. Whilst data showed that different airflow and batch size combinations can reduce energy consumption and increase productivity (by reducing roasting time), there are clear implications for batch homogeneity. Colour distributions are a tool that provide developers with metrics to monitor batch homogeneity during process improvements. Whilst colour is a common indicator of roasting performance, due to its correlation with sensory properties, data show that moisture is an intrinsic property that can be used to correlate well with thermophysical properties (including porosity, specific heat capacity, thermal conductivity and density). This enables modellers to couple fundamental thermophysical properties with heat and mass transfer studies to include system-accurate physics. This approach is developed in Chapters 5-6.

A method to determine coffee bean porosity was developed using x-ray Micro-Computed Tomography (MicroCT), wherein a Volume of Interest (VOI) within the lower portion of a bean facilitated comparative analysis. Here, the technique was used for whole coffee beans with different densities and has established the impact of different time-temperature profiles on porosity development, highlighting the phases of the roast that have the greatest impact on porosity. The technique is appropriate for many coffee products, from seed maturation and ripeness in growing regions, through post-harvest processing from cherry to green coffee, through roasting from part-roasted to full-roasted whole beans, coarse ground roasted coffee, as well as soluble coffee granules.

Whilst many coffee roasters rely on the manipulation of time-temperature roasting profiles to highlight a coffee's natural flavour and aroma, many also depend on them for operational consistency. Consideration of thermocouple diameter helped probe the accuracy of process temperature measurements. The roasting study validated the experimental and first principles approaches that determined the response time of thermocouples with different diameters. Measurement of a roast's time-temperature profile, and its accuracy, thus becomes integral to operational and product excellence. This work provides a framework that enable developers to translate time-temperature roasting profiles between machines – reducing the time, cost and coffee required during product and process development.

3.7 Appendix: Experimental data

Table 3.14: Experimental Data - Case Study I (Table 1 of 3)

Air Temp. (°C)	Initial Mass (g)	Final Mass (g)	Dimension (mm) a (mm)	b (mm)	c (mm)	Surface Area (mm^2)	Volume (mm^3)	Density (kg m^{-3})
220	349.98	328.50	6.75±0.08	4.17±0.06	8.88±0.17	147.29±2.90	130.93±3.58	1058.13±29.23
220	350.01	303.85	7.57±0.09	4.95±0.10	9.84±0.16	188.62±4.13	193.58±6.88	669.93±17.65
220	350.03	295.23	7.31±0.12	4.88±0.09	9.74±0.17	181.61±4.44	182.72±6.41	653.35±8.77
220	349.97	290.44	7.60±0.07	4.83±0.08	10.27±0.15	193.70±3.95	198.47±6.15	607.57±12.64
235	350.05	336.07	6.33±0.08	4.07±0.11	8.14±0.15	129.89±3.29	110.34±4.34	1110.98±29.12
235	349.95	314.50	7.17±0.09	4.64±0.10	8.98±0.18	163.61±4.01	157.07±5.76	739.46±18.96
235	350.02	298.80	7.38±0.12	4.81±0.10	9.54±0.22	178.60±5.12	178.44±7.40	626.25±14.86
235	350.02	292.48	7.55±0.11	4.91±0.09	9.92±0.20	189.11±5.29	193.93±7.92	575.92±10.28
250	350.00	339.45	6.60±0.08	4.18±0.11	8.64±0.13	142.22±2.92	125.09±4.04	1082.75±29.23
250	350.01	321.83	7.08±0.10	4.42±0.09	9.07±0.16	159.92±4.81	150.55±7.14	844.23±22.57
250	350.00	302.26	7.49±0.08	5.01±0.08	10.17±0.13	193.39±3.19	200.21±5.18	626.59±11.33
250	350.02	292.19	7.63±0.07	4.90±0.08	10.42±0.10	197.65±2.92	204.26±4.90	589.18±8.27
265	349.99	341.40	6.24±0.09	4.28±0.10	8.36±0.17	134.69±3.27	117.08±4.13	1136.31±20.65
265	349.99	327.15	7.09±0.09	4.39±0.09	9.07±0.18	159.10±3.59	148.07±5.00	803.79±23.15
265	350.00	305.06	7.50±0.09	4.69±0.09	9.98±0.21	185.06±4.90	184.92±6.93	615.65±14.85
265	349.96	291.75	7.49±0.10	5.01±0.15	9.69±0.18	186.47±4.95	191.42±7.63	550.58±8.06
280	350.01	342.46	6.37±0.09	3.95±0.10	8.50±0.11	133.22±3.11	112.58±4.25	1189.61±24.56
280	349.98	330.09	6.90±0.12	4.38±0.11	9.10±0.16	156.86±4.69	145.64±6.66	942.99±29.04
280	349.98	310.28	7.58±0.13	4.83±0.09	10.07±0.18	190.37±4.79	193.91±6.90	610.84±14.91
280	350.02	294.85	7.65±0.10	5.00±0.11	10.04±0.14	194.23±4.21	201.88±6.78	574.41±10.57
Green	350.00	350.00	6.18±0.07	3.84±0.08	8.54±0.12	128.73±2.15	105.84±2.78	1310.8±11.75

Table 3.15: Experimental Data - Case Study I (Table 2 of 3)

Air Temp. (°C)	Time (s)	Moisture (kg kg^{-1})	Dry Mass (g)	Colour Whole	Colour Ground	Median Particle Size (µm)	Porosity (%)
220	175	0.0577±0.0003	309.54±0.12	46.94±0.68			48.79±4.68
220	350	0.0213±0.0002	297.37±0.09	61.36±0.29	55.57±0.04	461.70±2.86	56.11±1.52
220	525	0.0113±0.0001	291.90±0.06	66.02±0.63	64.27±0.05	454.65±2.42	57.03±0.91
220	700	0.0101±0.0002	287.50±0.07	69.06±0.38	68.51±0.20	462.06±3.06	57.14±1.25
235	104	0.0701±0.0002	312.50±0.09	36.89±0.75	21.13±0.09	476.57±1.83	45.4±2.94
235	208	0.0399±0.0005	301.94±0.23	53.19±0.21	40.25±0.43	463.44±4.73	56.07±1.52
235	312	0.0143±0.0001	294.53±0.03	62.75±0.37	56.74±0.26	433.12±0.88	56.73±1.77
235	415	0.0106±0.0004	289.39±0.16	69.22±0.32	62.65±0.07	428.87±0.05	58.32±2.03
250	69	0.0777±0.0001	313.09±0.04	36.00±0.29			49.13±2.48
250	138	0.0526±0.0001	304.89±0.04	50.13±0.72	36.08±0.27	473.06±2.51	51.55±7.95
250	209	0.0212±0.0003	295.85±0.11	62.83±0.19	56.12±0.13	444.81±1.05	57.25±1.88
250	278	0.0135±0.0003	288.23±0.13	70.36±0.41	68.37±0.14	471.44±1.23	58.41±1.79
265	054	0.0806±0.0001	313.88±0.07	33.44±0.45			44.13±4.37
265	108	0.0595±0.0003	307.69±0.13	45.52±0.32	31.22±0.20	470.27±0.58	48.5±5.66
265	164	0.0259±0.0002	297.15±0.09	58.96±0.10	49.04±0.52	441.46±0.04	57.1±2.83
265	218	0.0112±0.0000	288.49±0.02	70.19±0.25	65.05±0.14	459.51±1.58	59.06±0.53
280	42	0.0826±0.0002	314.17±0.10	37.92±0.51			44.73±1.58
280	84	0.0632±0.0007	309.24±0.34	46.03±0.36			56.96±2.82
280	126	0.0340±0.0003	298.90±0.14	56.97±0.07	45.79±0.14	451.65±1.77	61.98±1.03
280	168	0.0163±0.0001	290.03±0.04	70.44±0.11	66.18±0.30	453.86±1.31	65.35±0.61
Green	0	0.1006±0.0003	314.80±0.14	42.22±0.39			40.89±0.82

Table 3.16: Experimental Data - Case Study I (Table 3 of 3)

Air Temp. (°C)	Time (s)	Thermal Diffusivity ($mm^2\ s^{-1}$)	Volumetric Heat Capacity ($J\ m^{-3}$)	Thermal Conductivity ($W\ m^{-1}\ K^{-1}$)	Specific Heat Capacity ($J\ kg^{-1}\ K^{-1}$)
235	104	0.094±0.000	1.21±0.01	0.114±0.000	1088.3±4.7
235	208	0.100±0.001	1.05±0.03	0.104±0.004	1417.4±39.9
235	312	0.102±0.001	0.95±0.02	0.096±0.001	1509.6±29.4
235	415	0.103±0.001	0.92±0.01	0.095±0.000	1598.3±26.7
250	69	0.097±0.001	1.22±0.01	0.118±0.002	1126.9±12.7
250	138	0.101±0.001	0.94±0.01	0.095±0.000	1113.7±14.8
250	209	0.103±0.001	0.91±0.00	0.093±0.001	1451.9±4.3
250	278	0.096±0.000	0.87±0.02	0.083±0.002	1474.9±28.7
265	054	0.091±0.002	1.20±0.06	0.109±0.003	1060.0±50.3
265	108	0.097±0.001	1.12±0.03	0.109±0.001	1391.9±36.6
265	164	0.104±0.000	0.94±0.01	0.098±0.001	1532.9±12.1
265	218	0.105±0.000	0.88±0.01	0.092±0.001	1596.6±22.0

Table 3.17: Experimental Data - Case Study II (Table 1 of 2)

Batch	Fan	Roast	Mass	Bulk	Water	Moisture	Porosity	Dimension			
Size	Freq.	Time	Loss	Density	Activity	Content		a	b	c	d
(kg)	(Hz)	(s)	(%)	(kg m^{-3})		(%)	(%)	(mm)	(mm)	(mm)	(mm)
200	30	0	0	730.0±4.1	0.529±0.002	10.06±0.06	40.9±0.8	6.2±0.3	3.8±0.4	8.5±0.6	5.9±0.7
200	30	75	3.920588	541.0±10.1	0.464±0.004	6.88±0.01	44.3±1.7	6.7±0.7	4.2±0.5	8.4±0.9	6.1±1.0
200	30	150	11.05611	355.8±7.0	0.257±0.013	3.38±0.01	55.0±0.5	7.3±0.4	4.7±0.5	9.2±0.8	6.8±0.8
200	30	225	15.86238	319.6±0.7	0.130±0.015	1.37±0.00	57.9±0.2	7.6±0.7	5.0±0.6	9.9±1.0	7.2±1.1
200	48	0	0	730.0±4.1	0.529±0.002	10.06±0.06	40.9±0.8	6.2±0.3	3.8±0.4	8.5±0.6	5.9±0.7
200	48	72	0.669967	506.1±0.2	0.461±0.001	6.37±0.04	46.3±0.4	6.7±0.7	4.3±0.4	8.7±1.0	6.3±0.9
200	48	143	13.08631	334.5±2.6	0.169±0.020	2.36±0.02	57.1±1.2	7.3±0.5	5.1±0.6	9.6±0.9	7.1±1.0
200	48	215	16.63167	313.0±2.2	0.106±0.017	1.23±0.01	59.8±1.8	7.7±0.4	5.1±0.6	10.1±0.9	7.3±1.0
200	65	0	0	730.0±4.1	0.529±0.002	10.06±0.06	40.9±0.8	6.2±0.3	3.8±0.4	8.5±0.6	5.9±0.7
200	65	58	4.570457	510.4±10.1	0.485±0.001	6.75±0.08	48.8±1.7	6.7±0.5	4.5±0.5	8.8±0.8	6.4±0.9
200	65	117	11.91262	341.5±3.9	0.241±0.021	2.90±0.06	59.6±1.5	7.5±0.5	5.0±0.7	9.5±1.0	7.1±1.1
200	65	175	15.71107	321.8±3.7	0.145±0.023	1.37±0.02	59.0±0.8	7.5±0.5	4.8±0.6	9.9±1.0	7.1±1.1
350	39	0	0	730.0±4.1	0.529±0.002	10.06±0.06	40.9±0.8	6.2±0.3	3.8±0.4	8.5±0.6	5.9±0.7
350	39	109	4.91213	542.1±16.2	0.448±0.004	6.44±0.03	41.6±3.1	6.6±0.5	4.5±0.5	8.9±1.0	6.4±0.9
350	39	218	13.00323	353.5±0.7	0.179±0.004	2.27±0.05	56.9±1.3	7.4±0.4	4.9±0.7	9.4±0.8	7.0±1.1
350	39	328	17.27468	317.0±0.5	0.105±0.016	1.05±0.01	60.8±1.2	7.6±0.4	4.9±0.6	10.0±0.8	7.2±0.9
350	48	0	0	730.0±4.1	0.529±0.002	10.06±0.06	40.9±0.8	6.2±0.3	3.8±0.4	8.5±0.6	5.9±0.7
350	48	93	4.503243	551.0±7.2	0.464±0.002	6.61±0.19	46.2±2.7	6.7±0.5	4.3±0.6	8.9±0.9	6.3±1.0
350	48	185	12.13533	359.7±3.0	0.223±0.000	2.70±0.01	55.8±2.5	7.4±0.5	4.7±0.5	9.2±1.0	6.8±1.0
350	48	278	16.62094	321.5±3.1	0.093±0.011	1.22±0.01	59.6±1.5	7.5±0.5	5.0±0.6	10.2±0.8	7.3±1.0
350	65	0	0	730.0±4.1	0.529±0.002	10.06±0.06	40.9±0.8	6.2±0.3	3.8±0.4	8.5±0.6	5.9±0.7
350	65	85	5.044849	529.4±3.8	0.436±0.010	6.50±0.04	48.4±2.8	6.8±0.8	4.4±0.5	8.6±1.0	6.3±1.1
350	65	170	12.95032	350.0±0.1	0.171±0.008	2.33±0.09	57.2±0.8	7.6±0.6	5.0±0.6	9.9±0.9	7.2±1.0
350	65	255	17.01611	319.7±1.2	0.096±0.018	1.20±0.02	59.7±0.6	7.4±0.4	5.1±0.6	9.8±0.9	7.2±1.0
500	48	0	0	730.0±4.1	0.529±0.002	10.06±0.06	40.9±0.8	6.2±0.3	3.8±0.4	8.5±0.6	5.9±0.7
500	48	115	4.383649	569.8±6.5	0.465±0.003	6.49±0.06	46.6±3.1	6.8±0.6	4.1±0.4	8.6±0.8	6.2±0.9
500	48	230	12.10248	374.9±6.6	0.194±0.004	2.72±0.03	56.5±1.8	7.2±0.4	4.7±0.5	9.2±0.9	6.8±0.9
500	48	345	15.846	322.1±0.8	0.078±0.015	1.11±0.01	62.4±0.7	7.5±0.6	4.9±0.5	9.9±0.9	7.1±1.0
500	65	0	0	730.0±4.1	0.529±0.002	10.06±0.06	40.9±0.8	6.2±0.3	3.8±0.4	8.5±0.6	5.9±0.7
500	65	107	4.847709	553.6±3.4	0.463±0.000	6.39±0.06	56.6±4.1	6.7±0.5	4.3±0.5	8.6±0.8	6.2±0.9
500	65	213	12.80902	361.4±0.9	0.170±0.005	2.36±0.06	54.6±1.9	7.4±0.3	4.9±0.5	9.4±0.9	7.0±0.9
500	65	320	17.30331	318.7±3.1	0.071±0.004	1.13±0.04	57.9±0.4	7.6±0.4	5.0±0.5	10.1±0.9	7.3±0.9

Table 3.18: Experimental Data - Case Study II (Table 2 of 2)

Batch Size (kg)	**Fan Freq. (Hz)**	**Roast Time (s)**	Surface Area (mm^2)	Volume (mm^3)	Intrinsic Density ($kg\ m^{-3}$)	Colour Whole Bean	Colour Ground	Thermal Diffusivity ($mm^2\ s^{-1}$)	Heat Capacity ($kJ\ m^{-3}$)	Thermal Conductivity ($W\ m^{-1}\ K^{-1}$)	Specific Heat Capacity ($kJ\ kg^{-1}$)
200	30	0	161.6±15.2	105.8±13.9	1310.8±58.7	38.9±3.1	26.04±2.69	0.086±0.001	1698±20	0.145±0.003	1297.3±17.0
200	30	75	173.4±28.0	123.1±29.2	1047.1±114.5	33.9±3.1	19.25±2.65	0.097±0.000	1206±5	0.117±0.001	1153.9±8.4
200	30	150	213.5±27.5	168.9±30.9	670.4±66.1	54.8±3.8	42.62±2.30	0.100±0.001	952±27	0.095±0.003	1423.2±37.6
200	30	225	239.3±38.7	199.1±50.0	529.7±60.1	69.2±4.0	63.60±2.82	0.101±0.001	849±3	0.085±0.000	1596.6±8.6
200	48	0	161.6±15.2	105.8±13.9	1310.8±58.7	38.9±3.1	26.04±2.69	0.086±0.001	1698±20	0.145±0.003	1297.3±17.0
200	48	72	181.8±28.3	131.5±29.8	916.6±153.1	37.8±4.0	23.78±2.64	0.099±0.000	1156±17	0.115±0.002	1262.8±18.7
200	48	143	230.6±32.0	187.4±36.2	613.2±41.0	60.7±3.6	51.76±2.42	0.100±0.001	889±2	0.089±0.001	1449.0±3.2
200	48	215	248.0±28.5	207.1±33.1	542.4±54.0	70.3±3.7	66.22±2.98	0.101±0.000	850±5	0.086±0.000	1565.4±9.0
200	65	0	161.6±15.2	105.8±13.9	1310.8±58.7	38.9±3.1	26.04±2.69	0.086±0.001	1698±20	0.145±0.003	1297.3±17.0
200	65	58	188.8±27.7	138.2±29.8	956.4±148.2	37.0±4.0	21.65±2.81	0.097±0.003	1160±8	0.113±0.004	1216.9±10.3
200	65	117	228.7±32.8	187.1±38.1	612.7±69.6	57.0±3.7	45.43±2.31	0.102±0.001	912±7	0.092±0.000	1485.1±11.5
200	65	175	234.9±38.0	191.5±44.3	555.9±43.4	69.3±3.9	64.38±2.89	0.099±0.001	825±3	0.084±0.004	1530.6±51.4
350	39	0	161.6±15.2	105.8±13.9	1310.8±58.7	38.9±3.1	26.04±2.69	0.086±0.001	1698±20	0.145±0.003	1297.3±17.0
350	39	109	190.4±28.9	138.8±28.9	964.4±163.6	38.4±3.3	21.93±2.67	0.100±0.001	1171±5	0.117±0.001	1208.5±4.6
350	39	218	222.7±28.6	179.2±32.4	611.3±59.4	60.5±3.8	50.64±2.38	0.100±0.000	896±6	0.090±0.000	1465.7±6.9
350	39	328	238.3±22.3	194.1±26.1	537.8±44.8	70.4±3.9	67.08±3.00	0.099±0.001	856±2	0.084±0.001	1594.2±3.2
350	48	0	161.6±15.2	105.8±13.9	1310.8±58.7	38.9±3.1	26.04±2.69	0.086±0.001	1698±20	0.145±0.003	1297.3±17.0
350	48	93	185.3±29.5	133.4±31.3	990.4±136.1	37.3±3.6	20.15±2.74	0.097±0.001	1217±13	0.118±0.002	1232.0±13.9
350	48	185	212.5±32.5	168.0±35.1	659.6±62.4	56.5±3.7	46.47±2.44	0.101±0.001	942±11	0.095±0.000	1425.5±18.9
350	48	278	244.5±31.5	201.6±39.4	540.6±44.9	69.4±3.9	65.65±2.96	0.096±0.000	869±18	0.083±0.002	1608.1±31.3
350	65	0	161.6±15.2	105.8±13.9	1310.8±58.7	38.9±3.1	26.04±2.69	0.086±0.001	1698±20	0.145±0.003	1297.3±17.0
350	65	85	184.1±32.9	135.6±35.6	935.4±132.6	39.9±3.5	22.98±2.85	0.101±0.001	1176±10	0.118±0.001	1256.8±17.1
350	65	170	239.0±29.2	196.2±35.9	606.1±48.5	58.4±3.8	48.16±2.41	0.101±0.001	898±12	0.090±0.000	1483.3±16.2
350	65	255	236.6±27.7	193.6±32.3	554.5±52.4	69.5±4.0	66.16±2.94	0.098±0.001	865±23	0.085±0.001	1558.0±44.6
500	48	0	161.6±15.2	105.8±13.9	1310.8±58.7	38.9±3.1	26.04±2.69	0.086±0.001	1698±20	0.145±0.003	1297.3±17.0
500	48	115	179.0±26.6	128.5±28.1	1021.2±160.9	37.9±3.5	19.60±2.64	0.100±0.001	1170±4	0.116±0.001	1145.1±3.7
500	48	230	208.9±30.9	163.4±35.0	693.2±61.7	56.1±3.4	47.54±2.29	0.099±0.001	942±15	0.093±0.001	1356.9±27.6
500	48	345	234.9±32.6	191.8±39.9	547.1±48.1	69.3±3.7	66.94±2.99	0.098±0.002	854±46	0.083±0.002	1561.6±77.7
500	65	0	161.6±15.2	105.8±13.9	1310.8±58.7	38.9±3.1	26.04±2.69	0.086±0.001	1698±20	0.145±0.003	1297.3±17.0
500	65	107	178.4±23.4	127.6±24.3	986.8±186.4	39.3±3.1	22.39±2.96	0.100±0.001	1189±19	0.119±0.001	1208.5±22.3
500	65	213	221.5±25.3	177.3±26.9	641.0±64.1	57.8±3.4	49.62±2.35	0.101±0.000	898±4	0.090±0.000	1396.4±4.4
500	65	320	244.1±31.3	202.1±36.0	536.6±41.5	69.8±3.6	66.64±2.97	0.097±0.000	840±7	0.082±0.001	1572.4±14.9

Chapter Four

Coffee bean particle motion in pilot-scale roasters measured using Positron Emission Particle Tracking (PEPT)

Particle motion studies were conducted to establish the impact of process parameters and product properties on coffee bean particle motion in roasters. Positron Emission Particle Tracking (PEPT), a non-invasive imaging technique, was used to characterise the granular flow of coffee in two pilot-scale roasters: (i) a 0.5 kg spouted bed and (ii) a 1.0 kg rotating drum. From the PEPT-captured Lagrangian trajectories, particle velocities and recirculation times were identified. Conversion of single-particle Lagrangian data to time-averaged Eulerian data enabled occupancy and velocity fields to be generated. These flow fields revealed distinct regions of occupancy from which the dense bean bed could be delineated using an Otsu method threshold. Regional residence times and particle velocities were thus established.

PEPT data have provided fundamental knowledge of particle dynamics and helped to understand heat transfer phenomena in two different roasting designs. This chapter also presents comprehensive data that enable:

(i) informed best practices for the roasting process and product developers in both aca-

demic and commercial settings,

(ii) combination of particle dynamics with predictive heat and mass transfer models to specify temperature distributions within the roasting chamber and track temperature variations both on the bean surface and within the bean core during roasting,

(iii) calibration of DEM and CFD-DEM simulations to complement digital twins of pilot-scale coffee roasters that provide new process and product development opportunities.

This chapter comprises two flow studies that have been published in peer-reviewed journals. The spouted bed roaster study was published in the Journal of Food Engineering (2021), and the rotating drum roaster study was published in Food Research International (2023). These data were also presented at several conferences (2021-2022) and used to calibrate a CFD-DEM simulation of the spouted bed roaster published in the Chemical Engineering Journal (2023).

- Mark Al-Shemmeri, Kit Windows-Yule, Estefania Lopez-Quiroga, Peter J. Fryer (2021) Coffee bean particle motion in a spouted bed measured using Positron Emission Particle Tracking (PEPT). Journal of Food Engineering (311). DOI:10.1016/j.jfoodeng.2021.110709.

- Mark Al-Shemmeri, Kit Windows-Yule, Estefania Lopez-Quiroga, Peter J. Fryer (2023) Coffee bean particle motion in a rotating drum measured using Positron Emission Particle Tracking (PEPT). Food Research International (163). DOI:10.1016/j.foodres.2022.112253.

- Hanqiao Che, Mark Al-Shemmeri, Peter Fryer, Estefania Lopez-Quiroga, Tzany Kokalova Wheldon, & Kit Windows-Yule (2023) PEPT validated CFD-DEM model of aspherical particle motion in a spouted bed. Chemical Engineering Journal, 453(1). DOI:10.1016/j.cej.2022.139689.

4.1 Methodology: Positron Emission Particle Tracking (PEPT)

4.1.1 Coffee roasters

For flow studies, two different pilot-scale roasters were used: (i) a 0.5 kg spouted bed roaster (RFB-S, Neuhaus Neotec) and (ii) a 1.0 kg rotating drum roaster (Bullet R1 V2, Aillio). These roasters, their schematics and internal geometries are detailed in Chapter 2.

4.1.2 Coffee beans

Before PEPT measurements, 350 g batches of Kenyan Arabica coffee were roasted in a spouted bed roaster (RFB-S, Neuhaus Neotec) at a constant inlet air temperature of 250°C and a fan frequency of 48 Hz (i.e., inlet air velocity of 7.2 m s^{-1}). Roast time was varied to obtain green (unroasted, i.e., roast time, t = 0 s), part-roasted (t = 138 s) and roasted (t = 278 s) coffee samples, corresponding to whole bean (surface) colours of 42, 50 and 70 for green, part-roasted and fully-roasted coffees (ColorTrack Benchtop Device R-100B, FreshRoastSystems, Inc.), respectively. The density of these samples is representative of coffee and independent of the roaster used in preparation of the samples. Coffee samples from triplicate roasts were combined and well mixed prior to PEPT studies.

Coffee characterisation included mass, density (bulk, packing & intrinsic), colour (whole), size (principal dimensions, volume and surface area) - measured properties are detailed in Table 4.1.

4.1.3 Process conditions

Coffee roasting occurs over much shorter timescales (5-10 mins) than those required for PEPT measurements (30-60 mins). Particle dynamics corresponding to different stages of real roasting were inferred by studying coffee with different roast degrees and densities (i.e., green, part-roasted and roasted) to emulate physicochemical changes that occur during roasting. The experimental design for the flow studies (depicted in Figure 4.1) reflects realistic variations of process parameters that a roaster might employ.

Table 4.1: Properties of Kenyan Arabica coffee beans of different roast degrees used for flow studies.

Coffee Sample	**Roast Time**	**Roast Loss**	**Dimension**			**Volume**	**Intrinsic Density**	**Bulk Density**	**Packing Density**
	(s)	**(%)**	**a (mm)**	**b (mm)**	**c (mm)**	**(mm^3)**	**(kg m^{-3})**	**(kg m^{-3})**	**(kg^{-1})**
Green	0	0.0	6.11±0.39	3.95±0.48	8.36±0.93	106.0±20.2	1279.4±86.5	705±11	7420±280
Part-Roasted	138	8.1	7.05±0.52	4.61±0.56	8.82±0.86	151.0±30.7	805.8±110.7	460±9	8370±500
Roasted	278	16.6	7.49±0.54	4.91±0.53	9.97±1.07	192.9±37.8	563.4±51.4	301±6	9250±330

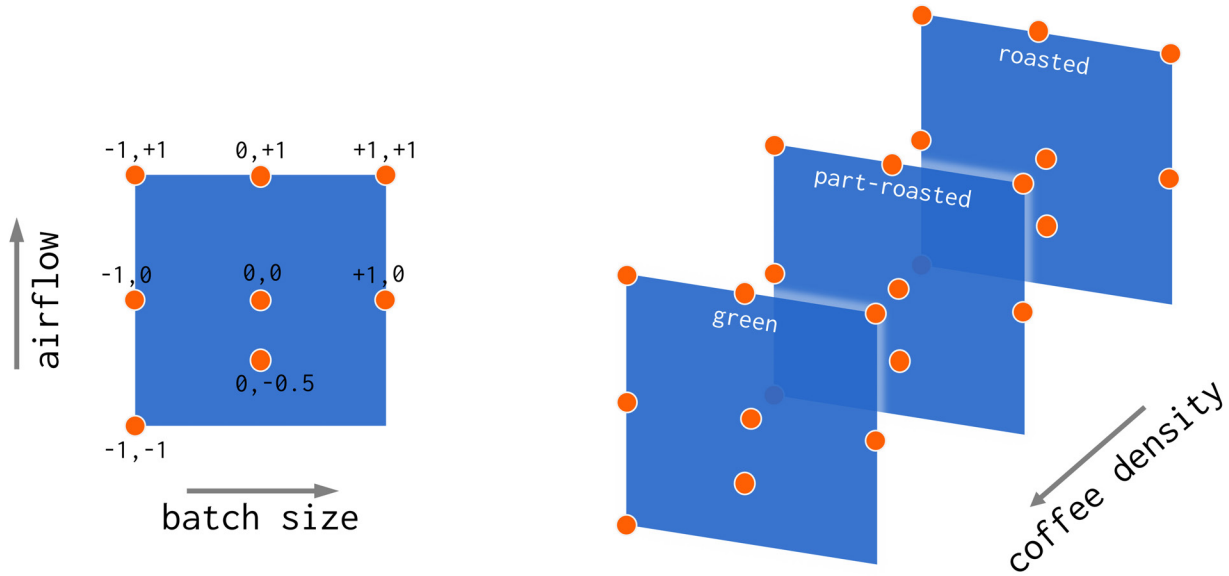

(a)

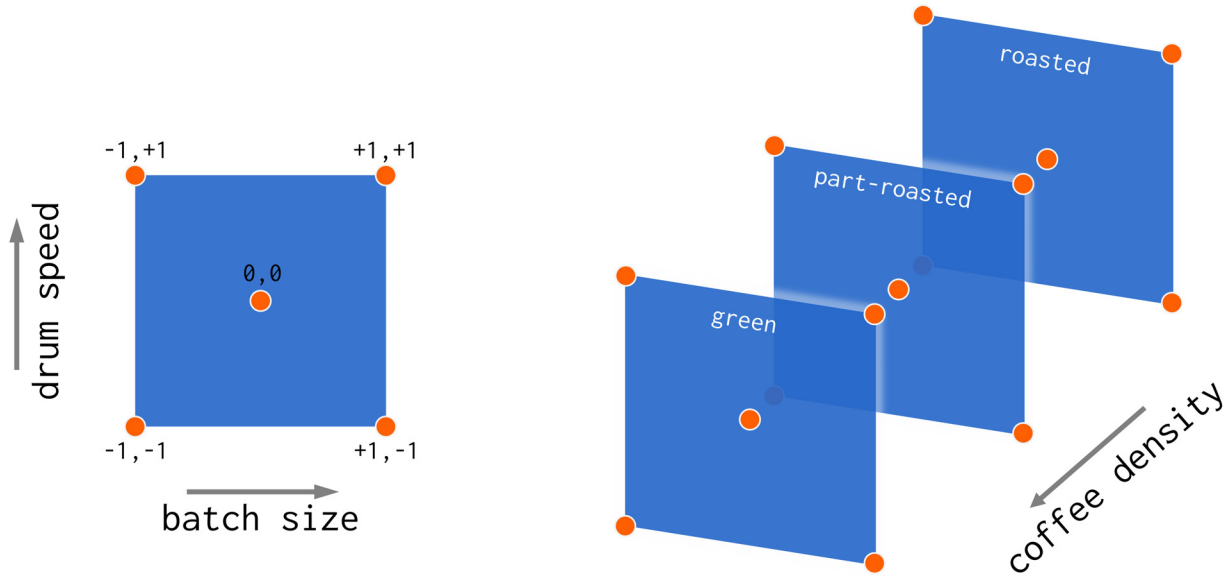

(b)

Figure 4.1: Visualisation of flow study experimental designs for (a) spouted bed and (b) rotating drum roasters. Markers refer to experimental conditions of each test case, where marker labels refer to the coded level of factors with three levels: high (+1), moderate (0) and low (-1). Each set of process conditions was explored for coffees of different density, i.e., green, part-roasted and roasted coffee samples.

Table 4.2: Static bean bed area of coffee beans in the spouted bed and rotating drum roasters as a function of batch size and bean density in plane *xy*.

Roaster Design	**Coffee Sample**	**Batch Size (g)**	**Fill Vol. (cm^3)**	**Fill (%)**	**Bed Area in *xy* (cm^2)**
Rotating Drum	Green	300	426	7.2	14.4±0.2
Rotating Drum	Green	600	851	14.3	28.8±0.4
Rotating Drum	Green	900	1277	21.5	43.3±0.7
Rotating Drum	Part-Roasted	300	652	11.0	22.1±0.5
Rotating Drum	Part-Roasted	600	1304	22.0	44.2±0.9
Rotating Drum	Part-Roasted	900	1957	33.0	66.3±1.4
Rotating Drum	Roasted	300	997	16.8	33.7±0.7
Rotating Drum	Roasted	600	1993	33.6	67.5±1.3
Rotating Drum	Roasted	900	2990	50.4	101.2±2.0
Spouted Bed	Green	200	284	6.2	28.8±0.4
Spouted Bed	Green	350	496	10.9	50.5±0.8
Spouted Bed	Green	500	709	15.5	92.7±2.2
Spouted Bed	Part-Roasted	200	435	9.5	44.2±0.9
Spouted Bed	Part-Roasted	350	761	16.7	103.3±3.0
Spouted Bed	Part-Roasted	500	1087	23.8	169.6±4.3
Spouted Bed	Roasted	200	664	14.6	83.4±2.5
Spouted Bed	Roasted	350	1163	25.5	184.7±4.6
Spouted Bed	Roasted	500	1661	36.4	286.0±6.4

Batch size & airflow in the spouted bed

In the spouted bed roaster, both airflow and batch size influence particle dynamics. In this study, process conditions covered a range of batch sizes (200g, 350g, 500g) and fan frequencies (30, 39, 48 65 Hz), which determined air flows. The specified fan frequency ranges correspond to the viable operating range, which depends on both bean density and batch size. For each coffee sample (green, part-roasted and roasted), 8 process conditions were employed, as detailed in Table 4.2 & Figure 4.1(a). The roaster was operated at ambient temperatures

(ca. 20°C) with an inlet air temperature set point of 20°C, i.e., no applied heating.

Batch size & rotation speed in the drum

In drum roasters, both drum rotation speed and batch size influence particle dynamics. Here, three different batch sizes (300g, 600g, 900g) as well as three different drum rotation speeds (42 rpm, 56 rpm, 78 rpm) were chosen, such that the experimental design consisted of five process conditions for each coffee sample, as depicted in Table 4.2 & Figure 4.1(b). The Bullet roaster utilises arbitrary values for drum rotation speed, airflow and power (ranging over integers 1-9). For PEPT measurements, the roaster was operated with an airflow setting of 7 (corresponding to an air velocity of 1.35 m s^{-1}) and a power setting of 0, i.e., no heating.

Airflow

The airflow calibration in Chapter 2 was used here to convert fan frequency to air velocity and mass flow rate. For reference, Table 4.3 restates the utility functions to estimate air velocity (u_a) and mass flow rate (G_a) for several airflow set points (f) in both the spouted bed and rotating drum roasters.

Table 4.3: Airflow utility functions describing air velocity (u_a) and mass flow rate (G_a) for the spouted bed and rotating drum roasters determined via anemometer measurements at ambient temperature (ca. 20°C).

Roaster	**Airflow Range**	**Utility Function**	$\mathbf{R^2}$
Spouted Bed	30-65 Hz	$u_a = 0.165f - 0.716$	0.999
Spouted Bed	30-65 Hz	$G_a = 4.84 \times 10^{-4} - 4.12 \times 10^{-4}$	0.998
Rotating Drum	1-9	$u_a = 0.133f + 0.421$	0.998
Rotating Drum	1-9	$G_a = 3.17 \times 10^{-4} f + 1.01 \times 10^{-3}$	0.998

Fill volume

To inform the batch size on a volume basis (i.e., the volume occupied by a static bean bed, where coffee beans within the roasting chamber with agitation) was determined using the coffee's bulk density, specified batch size and roaster geometry. The bean bed was assumed uniform along the z axis with a depth of 9.8 cm for the spouted bed and 29.5 cm for the

rotating drum. The equivalent area occupied by a static bed of beans in the plane xy of the roasters is listed in Table 4.2 for different batch sizes and roast degrees (densities) in both spouted bed and rotating drum roasters. For reference, the spouted bed roaster has a volume of 4562 cm^3 and a maximum area in the xy plane of 456.2 cm^2; the rotating drum roaster has a volume of 5931 cm^3 and a maximum area in the xy plane of 201.1 cm^2.

4.1.4 Positron Emission Particle Tracking (PEPT)

Experimental setup

The roasters were placed between two gamma-ray detector heads of a modified ADAC Forte positron camera (shown in Figure 4.2). The entire system was positioned within the camera's most sensitive field of view to ensure maximal acquisition rate and precision (Herald, Wheldon, and Christopher Windows-Yule, 2021). Further details of the positron camera are given in D. J. Parker et al. (2002), Herald, Wheldon, and Christopher Windows-Yule (2021), and Windows-Yule et al. (2020).

(a) (b)

Figure 4.2: Photographs of the (a) spouted bed and (b) rotating drum roasters, used for flow studies, positioned in the ADAC Forte positron camera.

Tracer labelling

A single coffee bean whose principal dimensions were within one standard deviation of the mean was selected from each sample set. Selected particles were indirectly labelled with 2

ml of water – containing ions of Fluorine-18, a β^+-emitting radioisotope - onto the particle's surface (D J Parker, 2017). After allowing time for absorption of irradiated water, excess water, determined gravimetrically, was removed by drying the particle under a heat lamp. The labelled coffee bean was returned to the sample set and placed in the roaster.

All experiments were conducted in accordance with the Positron Imaging Centre's local rules, under the supervision of a trained radiation protection supervisor.

Data capture & post-processing

To ensure ergodicity, once particle motion was established at ambient temperatures (ca. 20°C, with no heating), data were captured for 60 mins - a period sufficient for the tracer particle to explore the roasting chamber. On this time-scale, with the ergodic assumption, the fractional residence time of the tracer in any given region is directly proportional to the fraction of total particles in that region at any given point in time (Windows-Yule et al., 2020).

Recent PEPT studies (Nicuşan and Windows-Yule, 2020; Jones et al., 2021) established a framework for post-processing and analysis of PEPT data that was employed here. Lines of Response (LoRs) were obtained using the positron camera, with positional data determined through implementation of location and trajectory machine-learning algorithms (Nicuşan and Windows-Yule, 2020). The algorithms used to locate the tracer were implemented using PEPT-ML – an open-source Python framework (https://github.com/uob-positron-imaging-centre/pept). All computational work - corresponding to PEPT-ML generated time-stamped Cartesian coordinate data for each experimental run - was performed using the BlueBEAR HPC service of the University of Birmingham.

The post-processing pipeline enables the location of tracer particles, identification of Lagrangian trajectories and conversion to Eulerian data, with subsequent visualisation tools. Experimental datasets – containing Cartesian coordinates at time intervals of 0.01-0.1 milliseconds (dependent on tracer activity) – were segmented to account for systemic variability such that each 60 min experiment generated two 30 mins datasets. These time-segmented

datasets were subsequently analysed in MATLAB (2020a, MathWorks). In both studies, the centre of the roasting chamber was used as the origin for the data.

Lagrangian trajectories

Lagrangian trajectories can be visualised by plotting the time-stamped Cartesian co-ordinates. Particle displacement was considered here by studying the horizontal (maximum difference in x position) and vertical (maximum difference in y position) distances travelled by the particle during each rotation (Windows-Yule et al., 2020). Single-cycle trajectories were segmented based on the timestamped Cartesian coordinates, with each cycle initialising when the tracer crosses a specified boundary. For both roasting systems, a boundary of $y = 0$, when $x < 0$ in the plane xy was used - corresponding to when the particle is (i) returned to the bean bed after being in-flight in the spouted bed roaster and (ii) lifted along the drum wall in the rotating drum roaster.

Eulerian flow fields

Lagrangian trajectories (i.e., timestamped Cartesian coordinates) were transformed to time-averaged Eulerian flow fields through division of the system volume into uniform elements (pixels in 2D). A 2D mesh of 100x100 elements was defined for the spouted bed roaster (as depicted in Figure 4.3); for the rotating drum roaster, a 2D mesh of 85x85 elements was defined. In both systems, element dimensions were equivalent to the approximate intrinsic spatial resolution of the camera - approximately 3.5x3.5 mm (Herald, Wheldon, and Christopher Windows-Yule, 2021; K. Windows-Yule et al., 2022). For analysis of ergodic systems, allowing sufficient time for data capture and appropriate sizing of mesh element dimensions, the decay of tracer activity (half-life of 109 mins), is assumed to have no significant impact on the measurements.

Occupancy profiles are determined from the residence time of the tracer in each element (Windows-Yule et al., 2020). The velocity magnitude of the tracer in each element is expressed as $\sqrt{(v_x^2 + v_y^2)}$ in the plane xy and $\sqrt{(v_x^2 + v_y^2 + v_z^2)}$ in xyz. Particle velocities are later discussed as the median of velocities calculated at each time step corresponding to the obtained Cartesian data, whilst presented velocity profiles are determined from the velocity

magnitude of the tracer in each element (Jones et al., 2021).

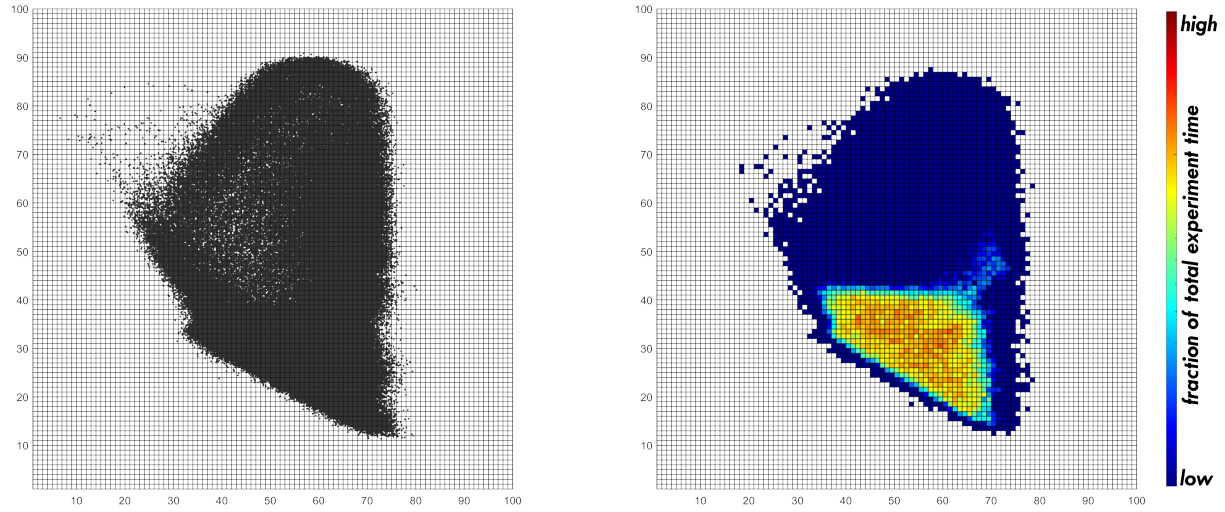

(a) (b)

Figure 4.3: Subdivided system volume of 100x100 elements of 3.5x3.5 mm - in plane xy - overlaid with (a) all Cartesian data and (b) the occupancy profile of an individual run. Data displayed relate to a 200g batch of part-roasted coffee beans with a fan frequency of 48 Hz.

Types of data obtained

Figure 4.4 shows the type of data obtained from PEPT. Typical individual particle trajectories are illustrated in Figure 4.4(a), while occupancy and velocity fields are represented in Figure 4.4(b)&(c), respectively. Particle trajectories - illustrated by coloured lines in Figure 4.4(a) - show the characteristic behaviour of both systems, with a bed of beans of high density and a region of beans in-flight. From these trajectories, both velocity and time spent by a particle in each region (i.e., residence time) were determined. Eulerian flow fields are first presented as occupancy profiles (Figure 4.4(b)) – where high occupancy regions are red and low occupancy regions are dark blue. Empty regions are absent of data (i.e., particles did not pass through these elements). All are expressed as a fraction of total experimental time. These data can be turned into velocity fields overlaid with particle velocity vectors (Figure 4.4(c)) – where high velocity regions are red, low velocity regions are dark blue and arrow size indicates the magnitude of the velocity vector – expressed as the velocity magnitude of the tracer in each element. Again, the slow-moving bed and rapid in-flight region can be

seen in Figure 4.4(c); the bed contains a region of near-zero flow around which beans rotate.

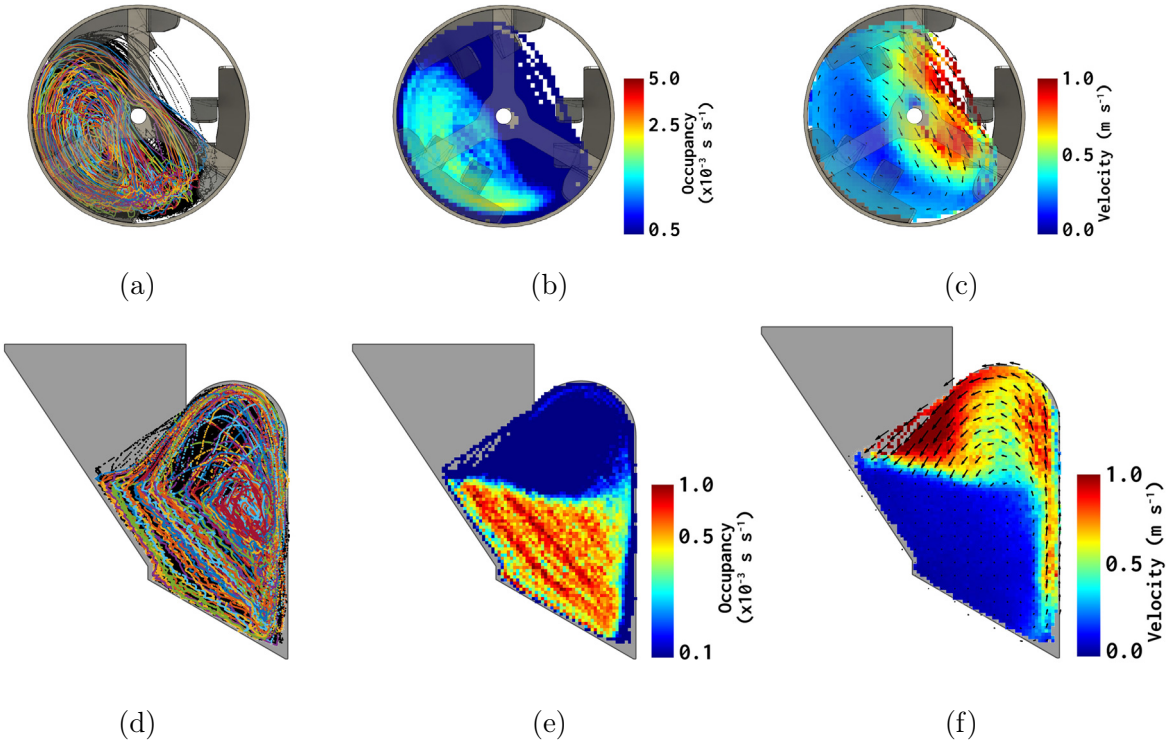

Figure 4.4: Visualisation of PEPT data: (a)&(d) Cartesian coordinates, overlayed with individual Lagrangian particle trajectories, (b)&(e) Eulerian occupancy profiles and (c)&(f) Eulerian velocity profiles. Figures (b)-(c) & (e)-(f) clearly show the dense bean bed and low occupancy in-flight regions. Spouted bed data correspond to 30 mins of data for 500 g of roasted coffee with a fan frequency of 48 Hz; rotating drum data correspond to 30 mins of data for 900 g of roasted coffee with a drum rotation speed of 42 rpm (clockwise).

Delineation of the bean bed

Through quantitation of the bean bed's size and shape, changes in regional particle behaviour that result from physicochemical transformations and changes in process parameters during roasting can be inferred. Occupancy profiles corresponding to particle motion in both spouted bed and rotating drum roasters revealed the existence of two different regions: a dilute (i.e., low occupancy) in-flight region, and a dense (i.e., high occupancy) bean bed. The total area of the roaster occupied by particles in a given two-dimensional plane (A_o) is determined from the number of non-zero elements in a given two-dimensional plane (n_{nze})

and the elemental area (A_e) of occupancy profiles as follows:

$$A_o = \Sigma(n_{nze} A_e) \tag{4.1}$$

The bean bed area is determined via application of an Otsu method (Otsu, 1979) to normalised probability distributions of one-dimensional (in y) occupancy profiles – implemented in MATLAB (2020a, MathWorks) and visualised in Figure 4.5.

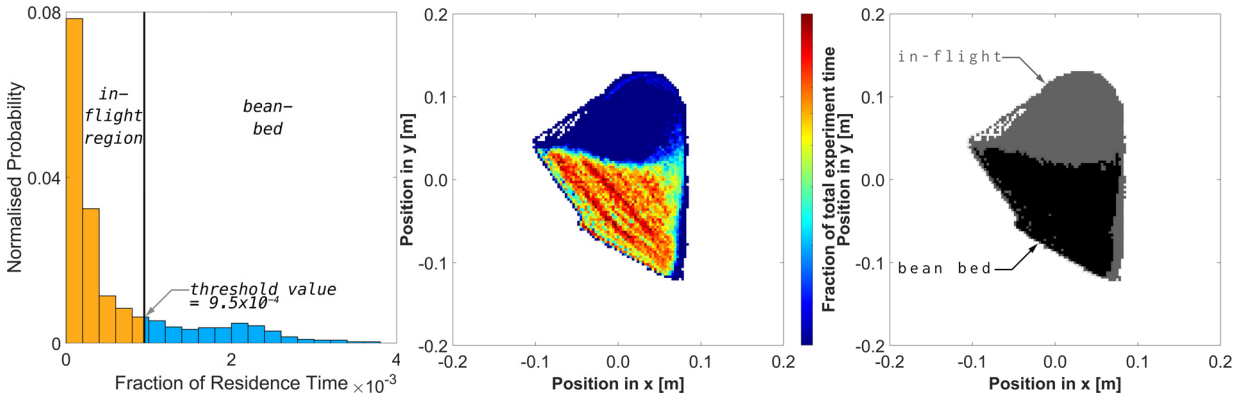

(a) (b) (c)

Figure 4.5: Visualisation of Otsu method thresholding process, showing (a) segmentation of normalised probability distributions of one-dimensional occupancy (in y), (b) an occupancy profile before segmentation and (c) a segmented occupancy profile, showing distinct regions attributed to the in-flight and bean bed regions.

Threshold values were determined for each occupancy profile - as illustrated in Figure 4.5 - as the value is dependent on the distribution of fractional residence times observed for each occupancy profile. It is assumed that occupancies below the threshold value are associated with the dilute in-flight region, while occupancies over the threshold value relate to the dense bean bed - see Figure 4.5(c). The area occupied by the bean bed ($A_b b$) is calculated using a similar approach to that used to calculate the overall occupied area (i.e., Equation 4.1).

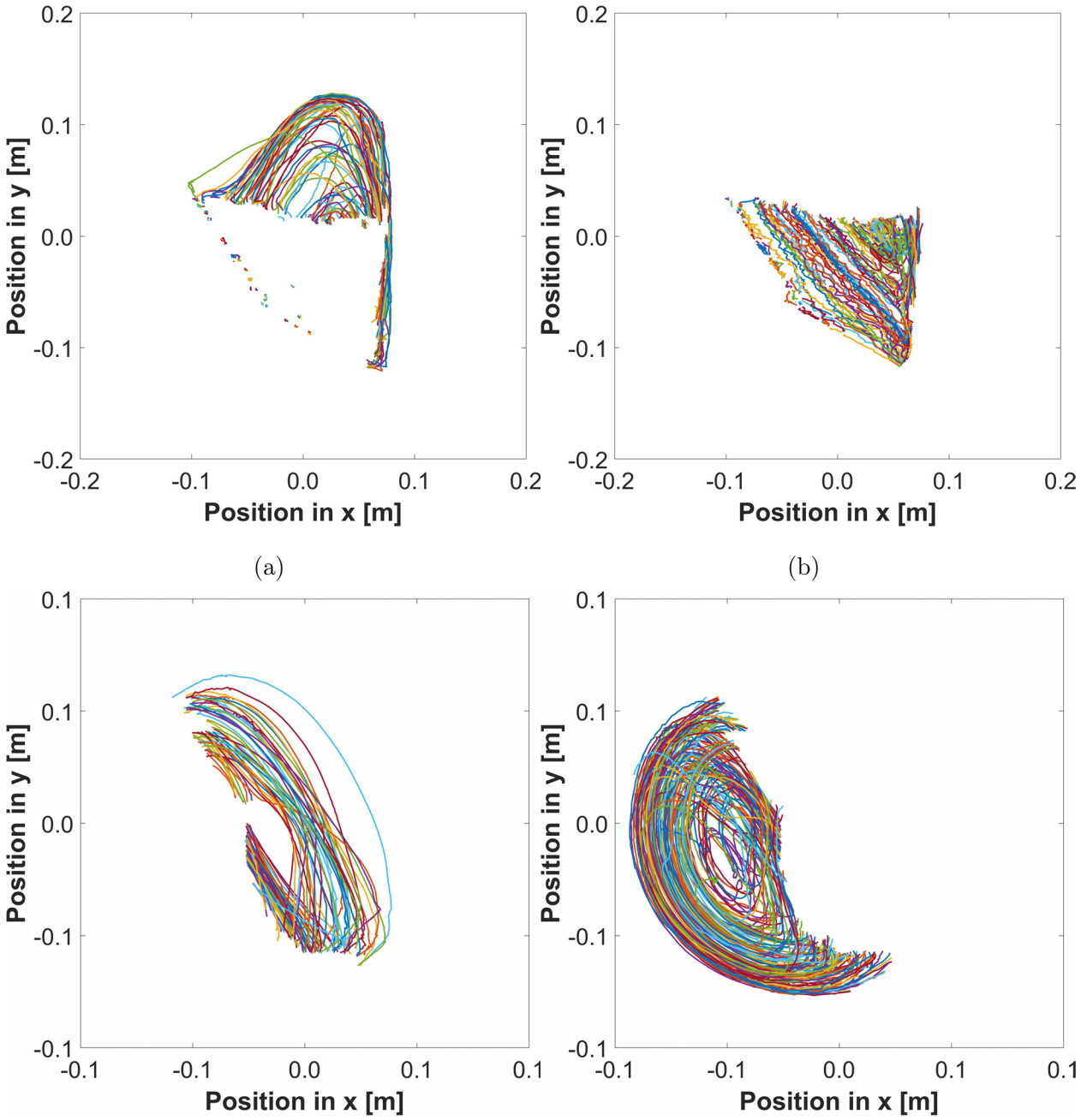

Figure 4.6: Segmented Lagrangian data showing particle trajectories corresponding to (a)&(c) in-flight and (b)&(d) bean bed regions in the (a)&(b) spouted bed and (c)&(d) rotating drum roasters.

Regional mass fractions were determined based on the coffee sample bulk density, roaster geometry and the delineated area estimated from occupancy profiles, such that the Bean Bed Mass Fraction ($BBMF$) is determined via the bean bed area (A_{bb}), batch size (m_{bs}) and coffee bulk density (ρ_b), assuming that the bed is uniform in the axial (z) direction of the roasting chamber (which is of length R_d):

$$BBMF = (R_d A_{bb} \rho_b)/m_{bs} \tag{4.2}$$

Both the velocity of and residence time a particle in each region was determined from these data - Figure 4.6 shows consecutive particle trajectories defined using the bed's location. Velocity distributions are used here to identify granular flow patterns, where particle velocities were determined as described by Jones et al. (2021).

Drum characterisation via the Froude number

The drum's rotation speed was determined via PEPT measurements where a labelled tracer was affixed to the drum in a known location, with the drum operated at arbitrary set points 1, 5 and 9. LoRs analysis was performed using PEPT-ML. Trajectory analysis performed in MATLAB (2020a, MathWorks), wherein the trajectories were segmented each time the particle crossed the boundary of $y = 0$, when $x < 0$ in the plane xy. The rotation speed of the drum was determined as the inverse of the mean cycle time. Drum rotation speeds corresponding to the test drum speed set points are outlined in Table 4.4.

Table 4.4: Drum rotation speeds determined at set points used for PEPT measurements.

Drum Speed Set Point	**Drum Rotation Speed (rpm)**	**Drum Wall Froude Number, Fr**
1	42.2±0.3	0.16
5	56.2±0.5	0.28
9	77.7±1.0	0.54

Froude number (Fr) is calculated as a function of the angular velocity (ω), drum radius (R) and gravitational acceleration (g) (Henein, Brimacombe, and Watkinson, 1983):

$$Fr = (\omega^2 R)/g \tag{4.3}$$

Froude numbers corresponding to rolling and cascading motion are typically expected to fall

in the range $10^{-4} < Fr < 10^{-1}$, with the transition from cascading to cataracting motion occurring at $Fr \approx 10^{-1}$ (Mellmann, 2001). Fr at the drum wall (i.e., where $R = r_{drum} = 0.08m$) was calculated according to Eq. 4.3 for each drum rotation speed – values are stated in Table 4.4. To account for particle size – where particle radius (r) is significant relative to the drum radius – Fr becomes (Arntz et al., 2008; Juarez, Chen, and Lueptow, 2011):

$$Fr = (\omega^2(R - r))/g \tag{4.4}$$

Here, particle Froude numbers were determined via Eq. 4.3 for those with positive velocities (i.e., for upward trajectories in the lifting region only) at the boundary of $y = 0$, when $x < 0$ in xy (i.e., the initial point of individual particle trajectories). The internal vanes in the roasting chamber increase drum wall lift and push particles toward the drum front face. Particle angular velocity will be influenced by both the forces induced by the drum, and the lifting force of the vanes. For dense particles and low rotation speeds, particles at the drum wall will show greater Froude numbers than those in the bean bed bulk, where Fr is approximately equal to that of the drum wall itself (see Table 4.4 for reference values).

4.2 Coffee bean particle motion in a spouted bed measured using PEPT

PEPT-captured particle motion data for the spouted bed roaster is presented here. These data depict the impact of process parameters (batch size and airflow) and product properties (roast degree/density) on system particle dynamics.

4.2.1 Effect of process parameters on particle behaviour

Both occupancy and velocity profiles were obtained from PEPT data for different bean densities (i.e., green, part-roasted and roasted), air flow frequencies (i.e., velocities) and batch sizes (mass basis). Overall, these results define two different occupancy regions (i) a bed of high solids fractions - the bean bed - in the lower left region of the roaster, through which beans move slowly (< 0.5 m s^{-1}), together with (ii) a spout of beans – the disperse freeboard – beginning in the lower right region of the roaster, moving rapidly (0.5-1.5 m s^{-1}) upwards at the air inlet which then fall to the surface of the bed.

Effect of roast degree on particle dynamics

Figure 4.7 shows PEPT data for 350 g batches of green, part-roasted and roasted coffee at a constant fan frequency of 48 Hz, thus indicating how particle (i.e., bean) motion in the roaster changes as a function of bean density. During a real roast, the density of the beans would change, reflecting that of the studied green, part-roasted and roasted beans. Occupancy plots, i.e., Figure 4.7(d)-(f), show low occupancy values for the upper part of the roaster (the freeboard), while area of occupancy at the bottom of the chamber decreases with increasing bean density. For example, green beans, with higher bean density, tend to occupy the bottom region of the roaster, forming a small bed of high occupancy (red region in Figure 4.7(d)). Fully roasted beans with lower bean density form larger beds, but are less densely occupied (green region in Figure 4.7(f)) – lower density makes beans easier to fluidise and spout. Velocity profiles presented in Figure 4.7(g)-(i) reveal that there is a general rotation of beans around a point within the bed near the spout region (most evident in Figure 4.7(c)), with the highest bean velocities corresponding to the rise and fall of beans

in the spouted bed freeboard.

Effect of batch size on particle dynamics

Figure 4.8 shows PEPT data for 200, 350 and 500 g batches of roasted coffee at a fan frequency of 48 Hz, thus showing how bean motion changes with batch size. For these conditions, the region with the higher occupancy levels – red area at the bottom of the roaster in Figure 4.8(d) - becomes larger and less dense as batch size increases - see Figure 4.8(e)-(f). Bean velocities associated to these bed regions are the slowest within each of the systems, as shown in Figure 4.8(g)-(i). For larger batches of roasted coffee (see Figure 4.8(f)), two occupancy bands are visible in the bean bed. The larger band in the centre of the bean bed (see Figure 4.8(f)), corresponds to beans that follow the modal freeboard trajectory, from the spout into the bed - shown by the densely populated particle trajectories in the top part of the roasting chamber (visible in Figure 4.8(c)) - and fall downward to the spout, parallel to the wall. The smaller band is formed at the top of the bean bed, near the spout, and is caused by beans that are propelled with less force, leading to scattered motion in this region, as shown in Figure 4.8(c).

Effect of air flow on particle dynamics

Figure 4.9 shows PEPT data for 200 g batches of green coffee at different fan frequencies, thus showing how bean motion changes with airflow. As air flow increases, the total area occupied by coffee in the roaster significantly increases (see Figure 4.9(d)-(f)), as higher air flows ease fluidisation. The corresponding velocity profiles (see Figure 4.9(g)-(i)) also show an increase of bean velocity in the freeboard with increasing airflow; the high occupancy region (i.e., the bed) is again slow moving. Figure 4.9(i) shows the rotational nature of the flow most clearly. At this highest airflow, a new, circulating flow regime with no true bean bed was established (Figure 4.9(f)). This shows in the reduced red region of high occupancy (see Figure 4.9(f)) and the corresponding velocity profile (see Figure 4.9(i)), which shows the rotation of beans around a point closer to the spout. This phenomenon is unique to these conditions due to the combination of a high coffee density and high air-to-bean ratio - smallest batch and highest fan frequency.

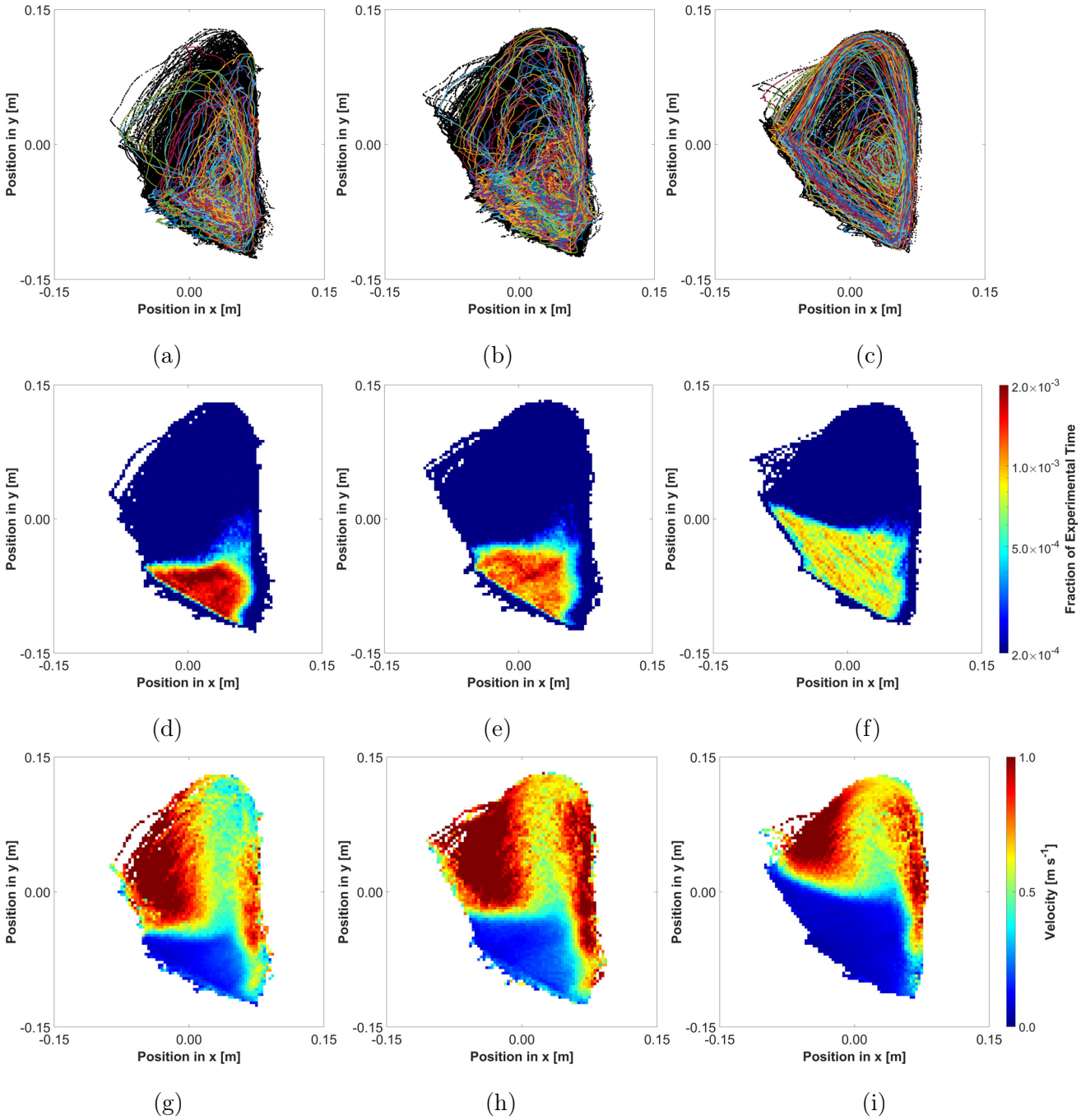

Figure 4.7: Experimental PEPT data detailing (a)-(c) Cartesian data overlayed with individual particle trajectories, (d)-(f) occupancy profiles and (g)-(i) velocity profiles for 350 g of coffee of different density studied at a fan frequency of 48 Hz. Coffee bean densities correspond to: (a),(d),(g) green; (b),(e),(h) part-roasted; (c),(f),(i) roasted coffee.

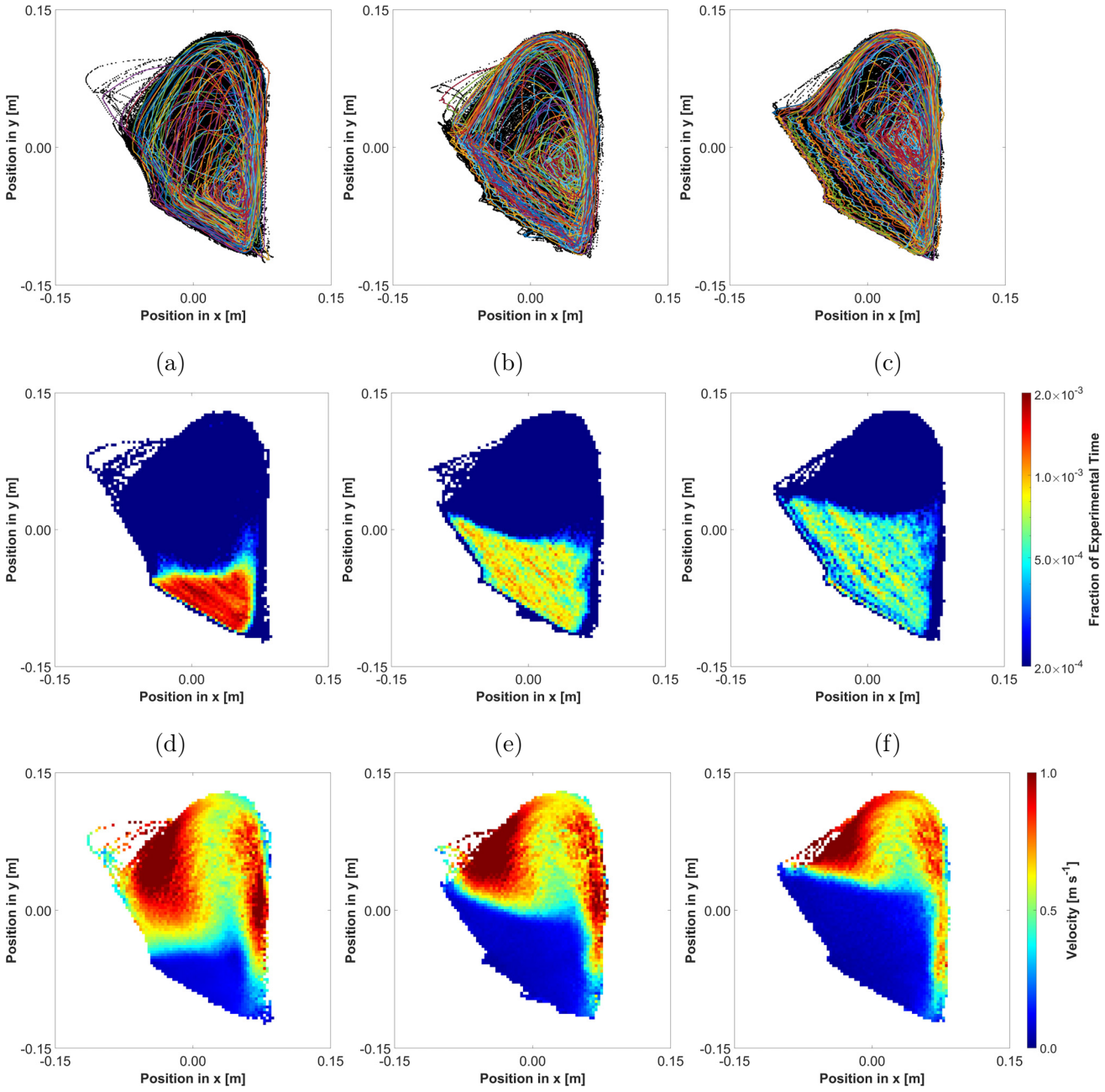

Figure 4.8: Experimental PEPT data detailing (a)-(c) Cartesian data overlayed with individual particle trajectories, (d)-(f) occupancy profiles and (g)-(i) velocity profiles for roasted coffee of different batch sizes subject to air at a fan frequency of 48 Hz. Batch sizes correspond to: (a),(d),(g) 200 g; (b),(e),(h) 350 g; (c),(f),(i) 500 g.

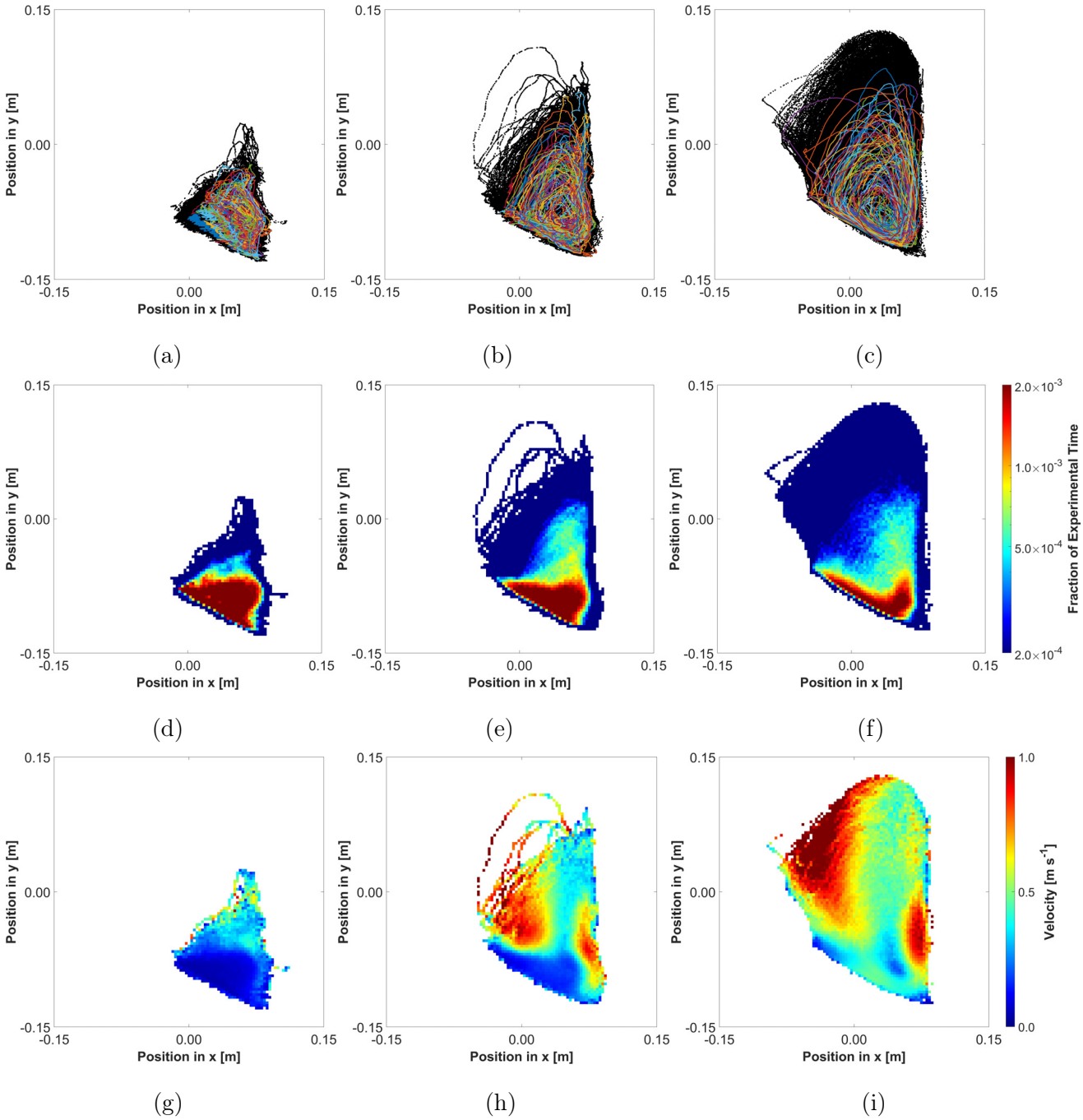

Figure 4.9: Experimental PEPT data detailing (a)-(c) Cartesian data overlayed with individual particle trajectories, (d)-(f) occupancy profiles and (g)-(i) velocity profiles for 200 g of green coffee subject to different airflows. Airflows correspond to: (a),(d),(g) 30 Hz; (b),(e),(h) 48 Hz; (c),(f),(i) 65 Hz.

4.2.2 Analysis across process conditions - combined effect of coffee roast degree, batch size and air flow

Flow fields

Figure 4.10 (a)-(c) plots the variation of total occupied area of the roasting chamber for all experimental conditions obtained from PEPT data - note that bulk density decreases with a higher roasting degree (see Table 4.1).

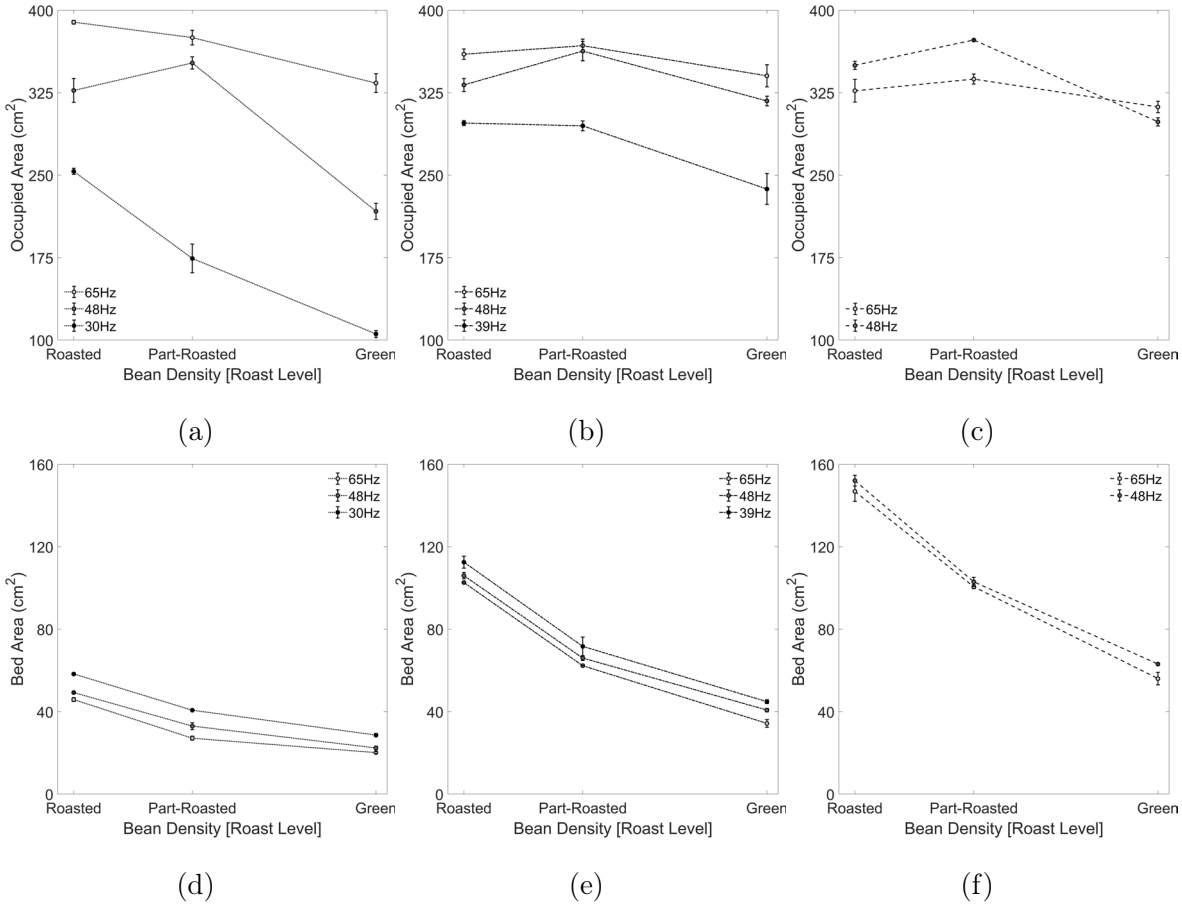

Figure 4.10: Changes in (a)-(c) total occupied area and (d)-(f) bean bed area as a function of coffee density and airflow for batch sizes of: (a),(d) 200 g; (b),(e) 350 g; (e),(f) 500 g

The occupied area of all batch sizes tends toward the capacity of the roasting chamber as airflow increases. For low air-to-bean ratios (i.e., large batch size and low airflow), the maximum area is achieved at lower airflow (Figure 4.10 (a)-(c)) due to the greater fill volumes (i.e., larger occupied areas in plane xy) for larger batch sizes. Occupied area at high airflow (65 Hz) decreases with batch size and increases as coffee density decreases. For moderate

airflow (48 Hz), occupied area increases as coffee density decreases, yet occupied areas of part-roasted and roasted coffee systems are not significantly different, thus the impact of batch size is not significant for part-roasted and roasted coffee. Figure 4.10 (d)-(f) plots the variation in bed area for all experimental conditions. Lower density coffees (i.e., roasted beans that have lost mass, but increased in size) are more easily spouted than the higher density (green) coffee, and thus bean bed mass decreases with density, however bed area increases with decreasing density due to volumetric expansion (see 4.1). For all conditions, bed area increases with batch size; for a given batch size, while increasing airflow decreases the bed area, the effect is less significant than the change in density.

Residence time

Figure 4.11 presents cumulative distributions of residence time that result from changes in coffee density, airflow and batch size. The data is presented as the residence times in the bean bed, the freeboard, and recirculation times (from spout-to-spout). Figure 4.11(a) shows that as coffee density decreases, residence times in the bed increase, while freeboard residence times decrease slightly. As coffee bean density decreases, beans are more easily fluidised, and have faster freeboard velocities leading to smaller residence times (Figure 4.11(b); also seen in Figures 4.7-4.8). Figure 4.11(d)-(f) shows bean bed residence times increase at lower airflows; they also indicate that, for roasted coffee, the variation in residence time (as seen in Figure 4.8(c)) decreases with airflow. Spout-to-spout recirculation times presented in Figure 4.11(b) are mostly affected by bean bed travel as particle velocities in the freeboard are much greater than in the bed for all bean densities.

Under moderate airflow (48 Hz), Figure 4.11(g) reveals that the larger the batch size, the greater the bean bed residence time: greater fill volumes (i.e., larger bed areas in plane xy, as shown in Figure 4.8) result in longer bean bed travel distances from the surface to the spout. For moderate airflows (48 Hz), batch sizes of 500 and 200 g roasted coffee correspond to bed heights of 17.5 and 11.9 cm, respectively. As bed height increases with fill volume, the downward freeboard travel distance decreases, thus in the freeboard, larger batch sizes are associated with shorter residence times.

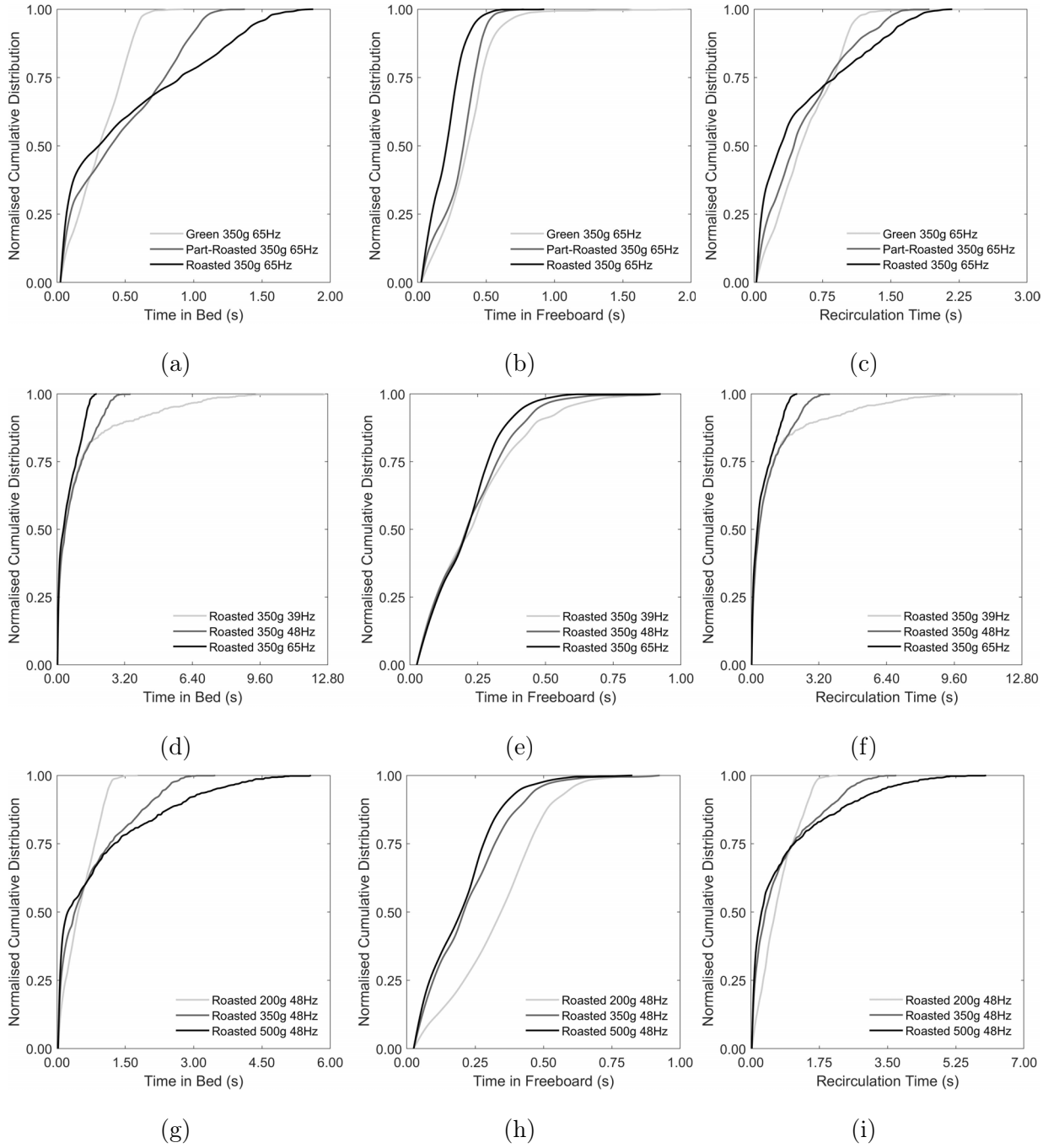

Figure 4.11: Cumulative distributions of residence time (a), (d),(g) in the bed, (b),(e),(h) in the freeboard and (c),(f),(i) from spout-to-spout (i.e., recirculation times, where spout-to-spout residence times are the sum of the freeboard and bed residence times). The effect of coffee density is shown in (a)-(c) for 350 g of coffee with different densities subject to high (65 Hz) airflow; the effect of air flow is shown in (d)-(f) for 350 g of roasted coffee subject to different air flows; the effect of batch size is shown in (g)-(i) for different batch sizes of roasted coffee at moderate (48 Hz) airflow.

Bean dispersion

The occupied area of coffee in the roasting chamber is defined by the dispersion of the beans propelled from the spout, i.e., the variation between individual freeboard trajectories, such as those shown in Figure 4.8(c) (Windows-Yule et al., 2020). The distribution of the vertical component for coffees of different densities in a 200 g batch at moderate airflow (48 Hz), is presented in Figure 4.12(a), and that for the horizontal component is shown in Figure 4.12(b). It can be seen that (i) for green coffee, there is very little vertical distance travelled, reflecting the low fluidisation of high-density particles, whilst there is much greater vertical displacement of the roasted, and thus lighter, coffees, (ii) the horizontal distance travelled by beans increases as the coffee density decreases.

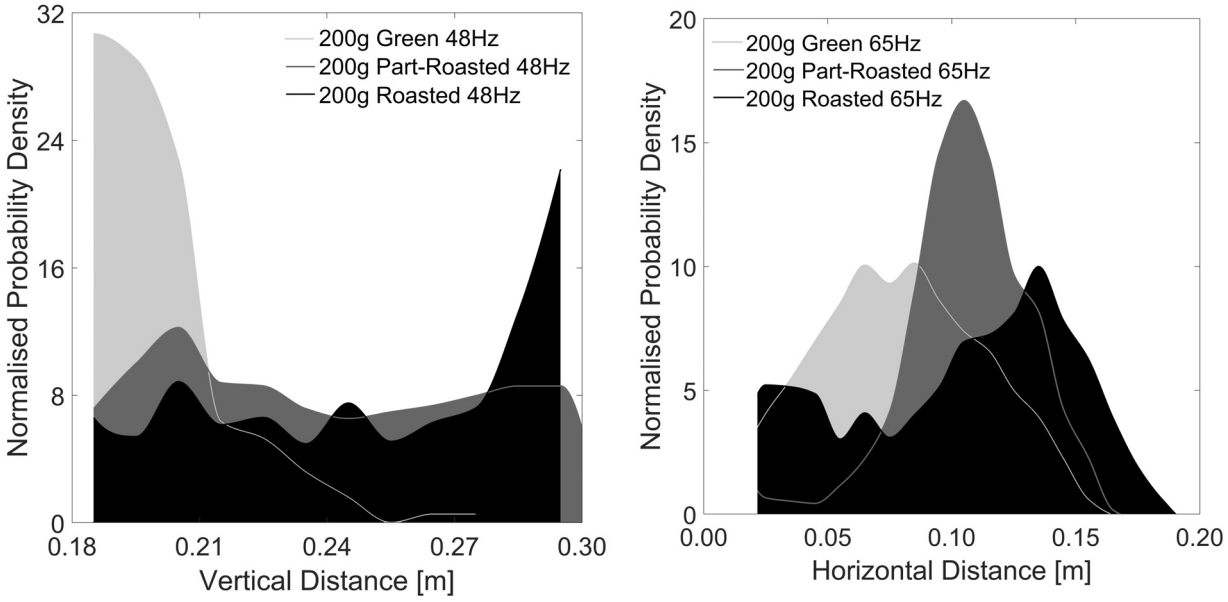

(a) (b)

Figure 4.12: Changes in (a) vertical and (b) horizontal travel distances traversed by coffees beans of different densities in a 200 g batch at (a) moderate (48 Hz) and (b) high (65 Hz) air flow that show coffee's travel distance depends on bean density. Shaded areas correspond to: (i) green coffee in light grey, (ii) part-roasted coffee dark grey and (iii) roasted coffee in black.

4.3 Coffee bean particle motion in a rotating drum measured using PEPT

PEPT-captured particle motion data for the rotating drum roaster is presented next. These data depict the impact of process parameters (batch size and rotation speed) and product properties (roast degree/density) on system particle dynamics.

4.3.1 Effect of process parameters on particle behaviour

PEPT-generated flow fields for different bean densities (i.e., green, part-roasted and roasted), drum rotation speeds (i.e., agitation) and batch sizes (mass basis), detail variation of occupancy and velocity within the roaster. These data depict two distinct regions of occupancy: (i) a bed of high solids fraction through which beans move slowly ($<$0.2 m s^{-1}) as they are lifted upwards along the drum wall from the lower left region, together with (ii) an in-flight region of beans where, after detaching from the drum wall in the upper left region of the drum, fall rapidly (0.3-0.9 m s^{-1}) towards the lower right region of the drum.

Effect of roasting degree on particle dynamics

Figure 4.13(a)-(c) presents PEPT-obtained Cartesian data, overlayed with individual particle trajectories (in different colours). These plots illustrate particle-level motion of different density coffees in the roasting chamber under the same process conditions (batch size of 900 g and drum rotation speed of 42 rpm). Roasted bean trajectories are significantly more uniform and show rotation about a stationary point, as comparison of trajectories presented in Figure 4.13(a) and Figure 4.13(b) reveal. Lagrangian trajectories and Eulerian flow fields show two distinct particle behaviours: (i) particles in the bean bed rotate around the bed centre of mass, and (ii) particles near the drum wall are subject to lifting (either by the drum centrifugal force, or by the vanes), detach in the upper left quadrant of the drum (in $x<0$ $y>0$) and then free fall through the disperse region (i.e., are in-flight).

Increasing roast degree and bean volume significantly change the behaviour of the system. During roasting, beans lose mass – this affects drum wall lifting. Increasing roast degree

increases vertical travel distances due to their lower mass and thus improved attachment in the upper left region of the drum, similar to phenomena seen by Jones et al. (2021). Changes in roast degree (from green to roasted) decrease the size of the bean bed - see the change in the green/yellow region in Figures 4.16 – and thus increase the occupancy in other regions – i.e., see how the light blue region in Figure 4.13(d)-(f) changes. Readers are referred to Ingram et al. (2005) for studies of particle dispersion, and to Ding et al. (2002) for studies of segregation in rotating drums.

Effect of batch size on particle dynamics

The effect of batch size for roasted coffee operated with a drum rotation speed of 42 rpm (shown in Figure 4.14) reveals that as batch size increases, the bean bed area (in xy) increases but is less densely occupied (Figure 4.14(c)-(d)), not dissimilar to observations of increasing bean volume. The corresponding velocity profiles (Figure 4.14(e)-(f)) show that in-flight velocities are greater for lower batch sizes (300 g). Again, the highest batch size shows more uniform rotational behaviour (Figure 4.14(a)-(b)), with the point about which the beans rotate – the centre of the deep blue low velocity region in Figure 4.14(e)-(f) – being closer to the centre of the drum.

Effect of drum rotation speed on particle dynamics

Figure 4.15 demonstrates the effect of drum rotation speed on particle dynamics for 900 g of part-roasted coffee. Whilst bean bed occupancy was marginally lower at lower rotation speeds (Figure 4.15(c)-(d)), the bean bed area (in xy) decreases significantly as drum rotation speed increases due to increasing homogeneity of particle trajectories (Figure 4.15(a)-(b) and centrifugal effects of rotation. Figure 4.15(e)-(f) shows that in-flight velocities are comparable, although there is a greater fraction of the batch travelling at higher velocities for higher drum rotation speeds. Bean bed velocities also increase as drum rotation speed increases, due to transfer of momentum from the drum to the beans and an effective no-slip boundary at the wall.

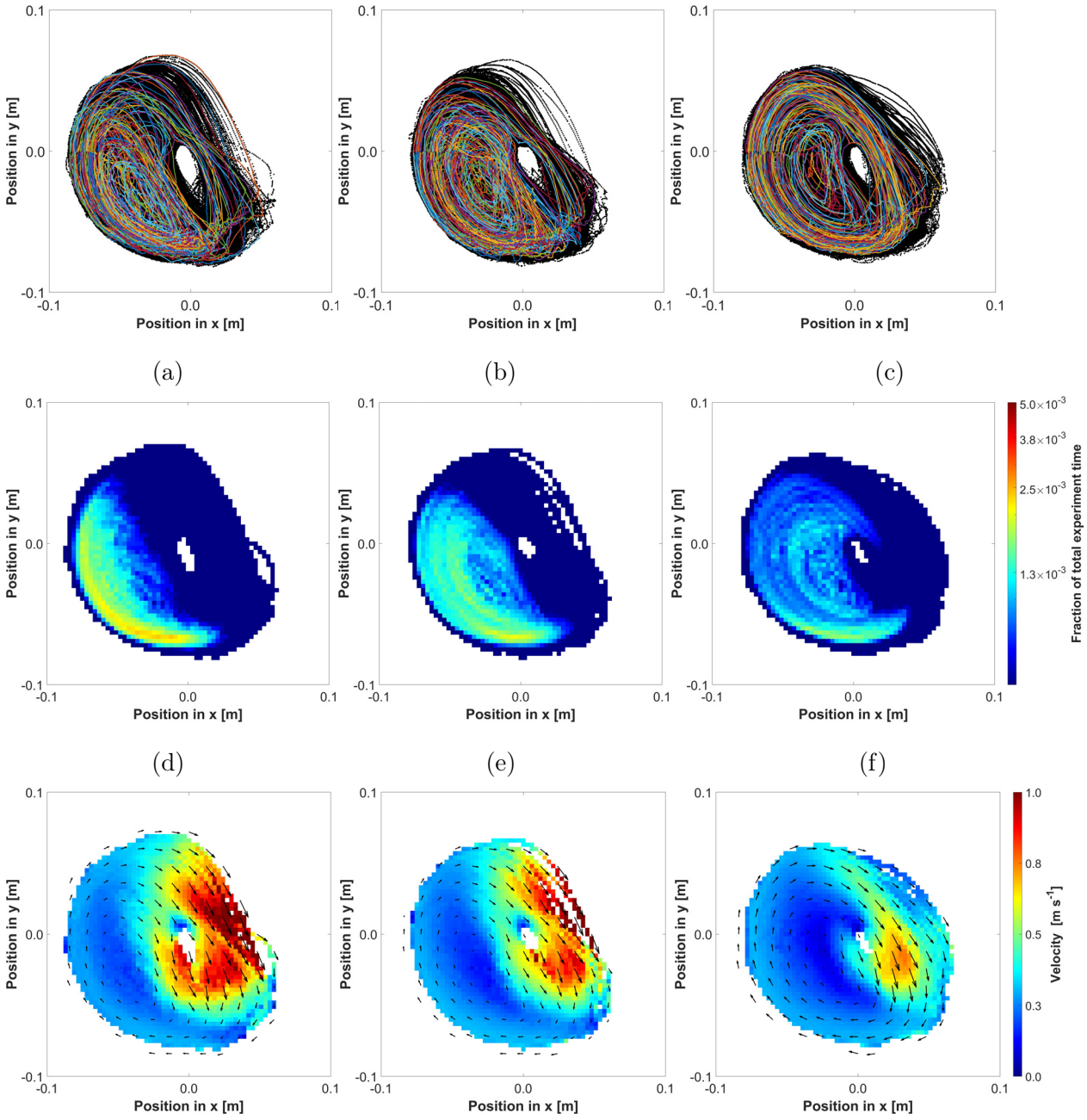

Figure 4.13: Experimental PEPT data detailing (a)-(c) Cartesian data overlayed with individual particle trajectories, (d)-(f) occupancy profiles and (g)-(i) velocity profiles for 900 g of (a),(d),(g) green, (b),(e),(h) part-roasted and (c),(f),(i) roasted coffee operated at 42 rpm, depicting the impact of roast degree.

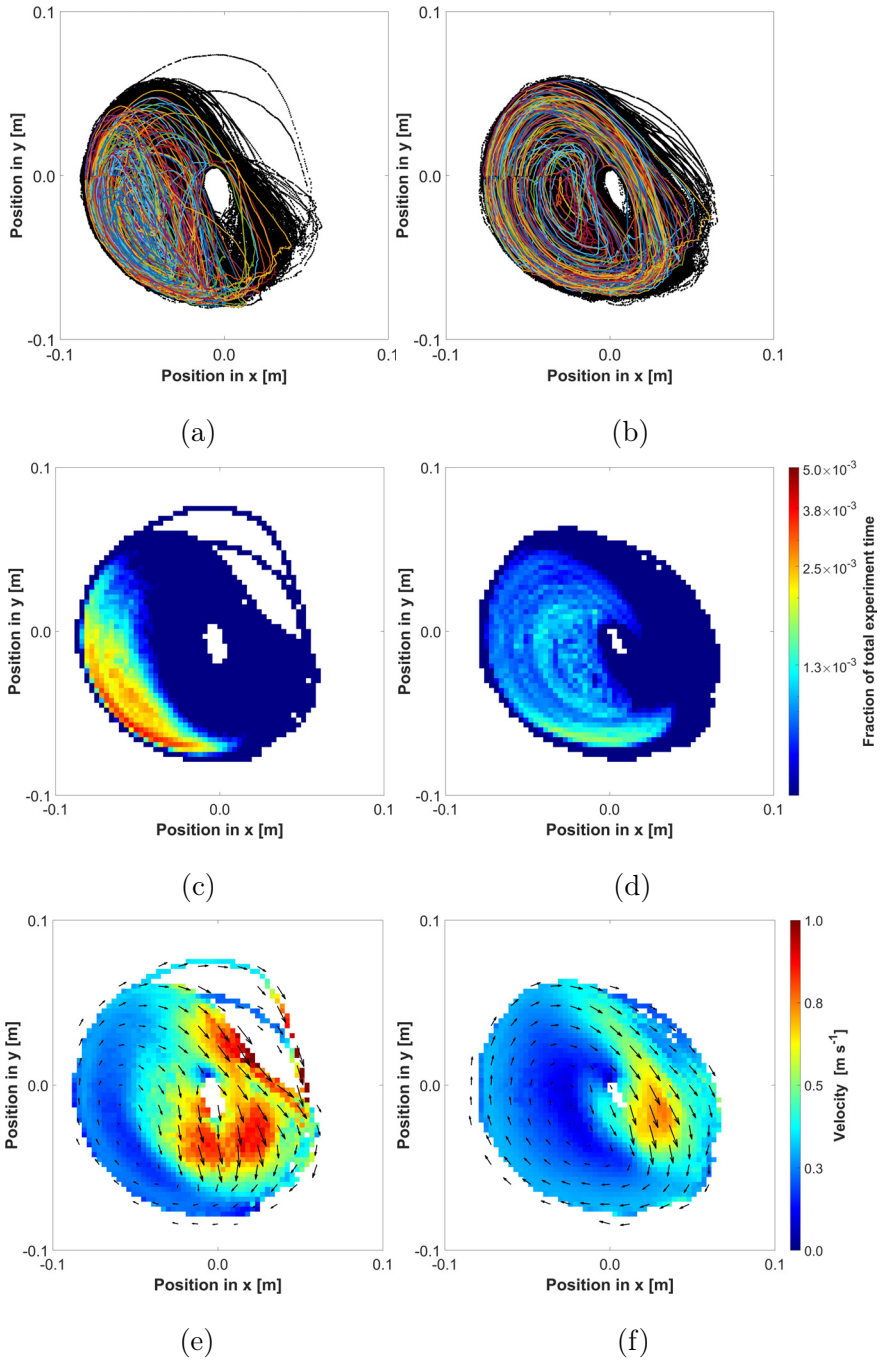

Figure 4.14: Experimental PEPT data detailing (a)-(b) Cartesian data overlayed with individual particle trajectories, (c)-(d) occupancy profiles and (e)-(f) velocity profiles for (a),(c),(e) 300 g and (b),(d),(f) 900 g of roasted coffee operated at 42 rpm, depicting the impact of batch size.

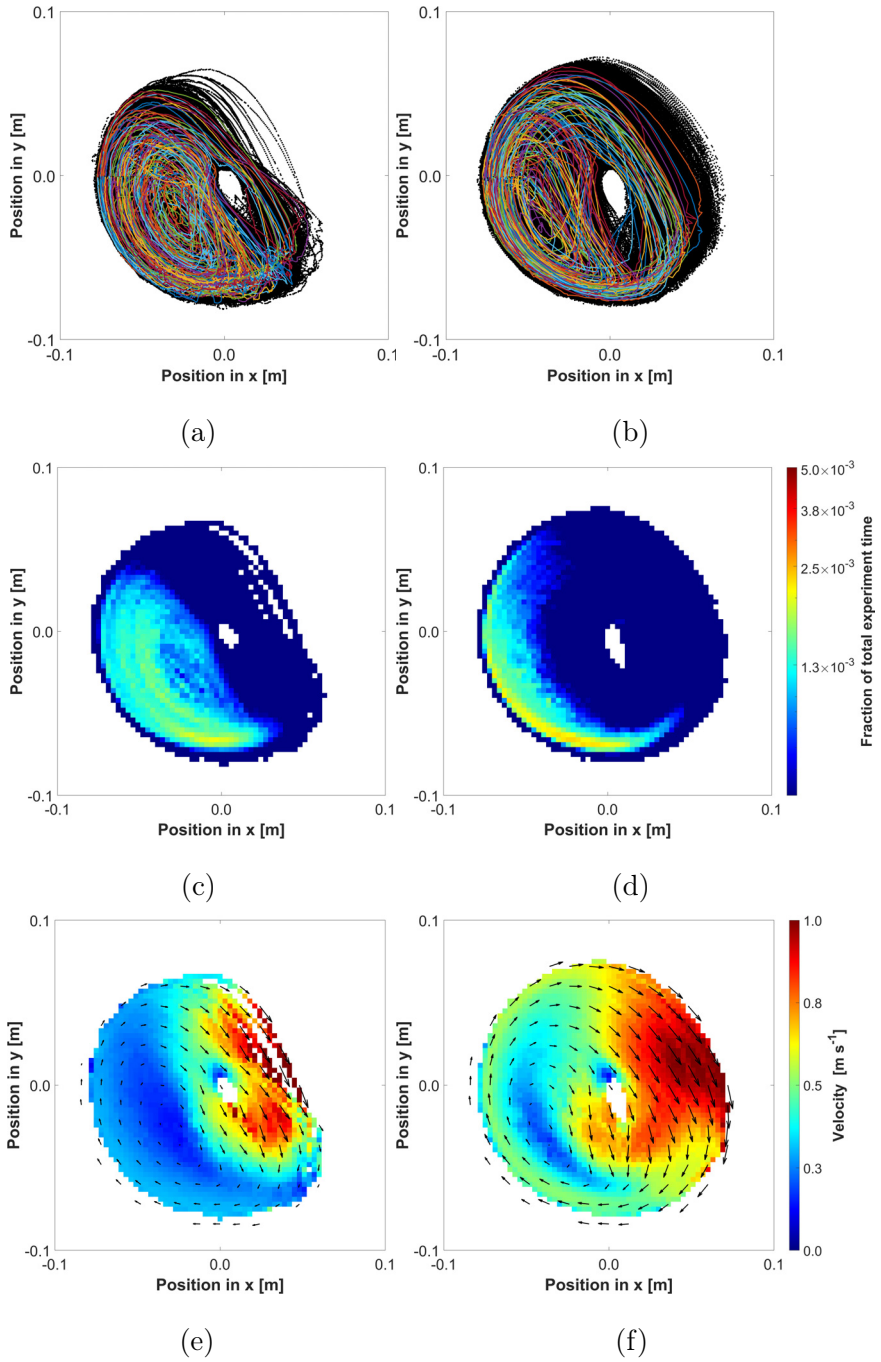

Figure 4.15: Experimental PEPT data detailing (a)-(b) Cartesian data overlayed with individual particle trajectories, (c)-(d) occupancy profiles and (e)-(f) velocity profiles for 900 g of part-roasted coffee operated at (a),(c),(e) 42 rpm and (b),(d),(f) 78 rpm, depicting the impact of drum rotation speed.

4.3.2 Analysis across processing conditions – combined effect of roast degree, batch size and drum speed

Flow fields

Both process parameters and product properties have a significant impact on occupancy and velocity. Figures 4.13(d)-(i), Figure 4.14(c)-(f) and Figure 4.15(c)-(f) show two distinct regions of occupancy and velocity: (i) a dense bean bed of high solids fraction, where beans move slowly (0.0-0.5 m s^{-1}) and (ii) a disperse in-flight region, where beans travel at higher velocities (0.5-2.0 m s^{-1}). In Figure 4.17, the impact of batch size, drum speed and roast degree on occupied area, bean bed area and magnitude of particle velocity are presented. These data (particularly those in Figures 4.16-4.17) highlight the potential to modulate particle dynamics via simple roasting control strategies – changing the speed of rotation has a clear effect on the bed and in-flight volumes (see Figure 4.15), so changing drum rotation speed during processing could be used to account for changes in bean density.

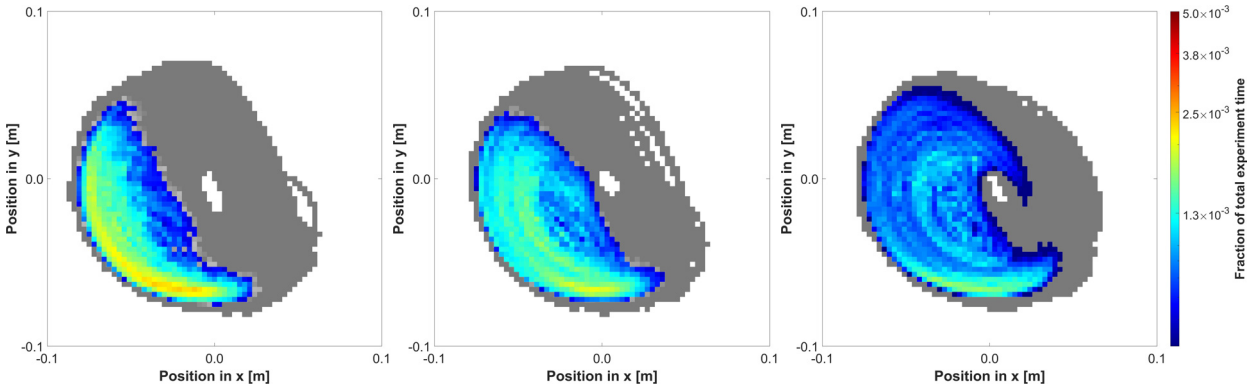

(a) (b) (c)

Figure 4.16: Bean bed delineation – indicating bed area (in xy) – for 900g of (a) green, (b) part-roasted and (c) roasted coffee operated at 42 rpm; effect of drum speed and batch size on Bean Bed Mass Fraction (BBMF) for (d) green, (e) part-roasted and (f) roasted coffee.

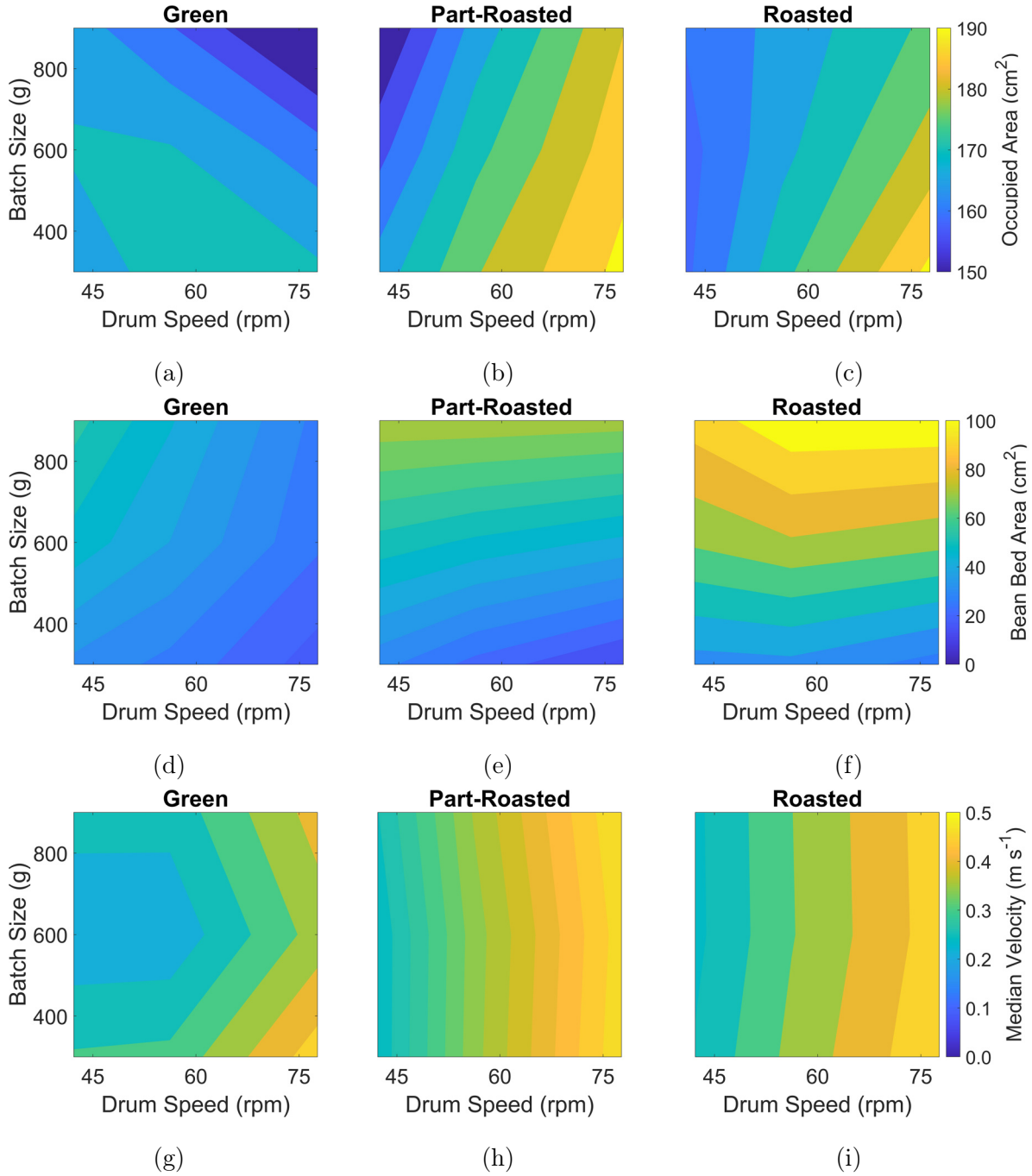

Figure 4.17: Contours of (a)-(c) occupied area, (d)-(f) bean bed area and (g)-(i) magnitude of particle velocity (v_p) for (a),(d),(g) green, (b),(e),(h) part-roasted and (c),(f),(i) roasted coffee.

Bean dispersion

Distributions of occupancy in x and in y are outlined in Figure 4.18 & 4.19, whilst Figures 4.20 and 4.21 show the variation of particle travel distance (for a single cycle) in vertical and horizontal directions, respectively.

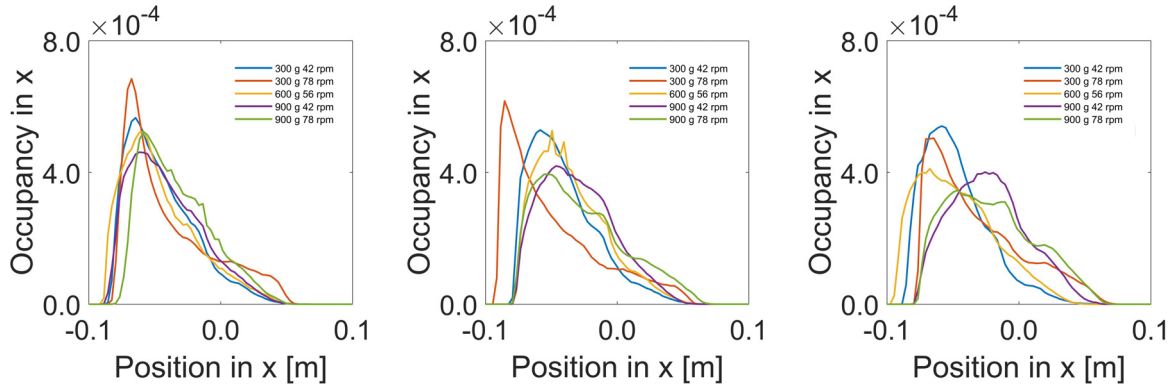

(a) (b) (c)

Figure 4.18: Distributions of occupancy in x for (a) green, (b) part-roasted and (c) roasted coffee studied at different process conditions.

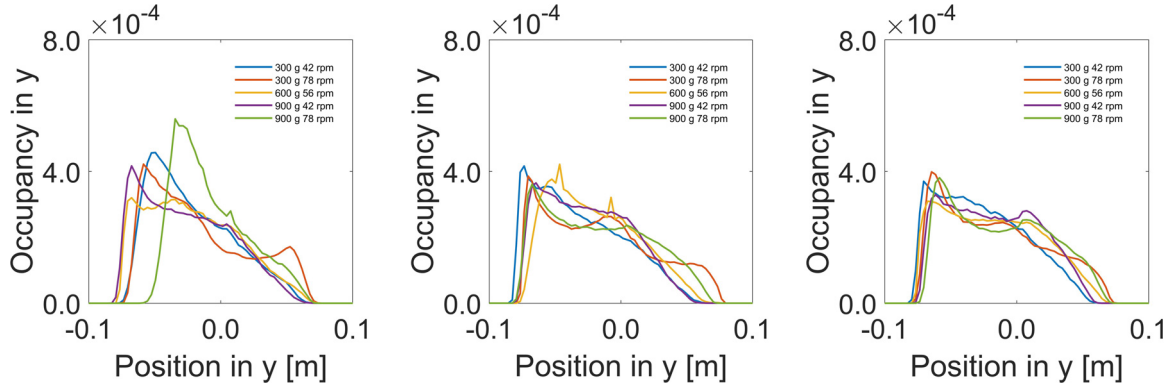

(a) (b) (c)

Figure 4.19: Distributions of occupancy in y for (a) green, (b) part-roasted and (c) roasted coffee studied at different process conditions.

The vertical distances travelled are ca. 0.16 m, i.e., close to the diameter of the roaster, showing the efficiency of the drum vanes. Movement is greater for higher drum rotational velocities. For horizontal travel, the behaviour is bimodal, with peaks ca. 0.05-0.08 and 0.12-0.16 m; this probably corresponds to beans in the dense bed and dilute in-flight regions, demonstrated by the flow fields in Figure 4.13(d)-(e), but not in Figure 4.13(f). For vertical

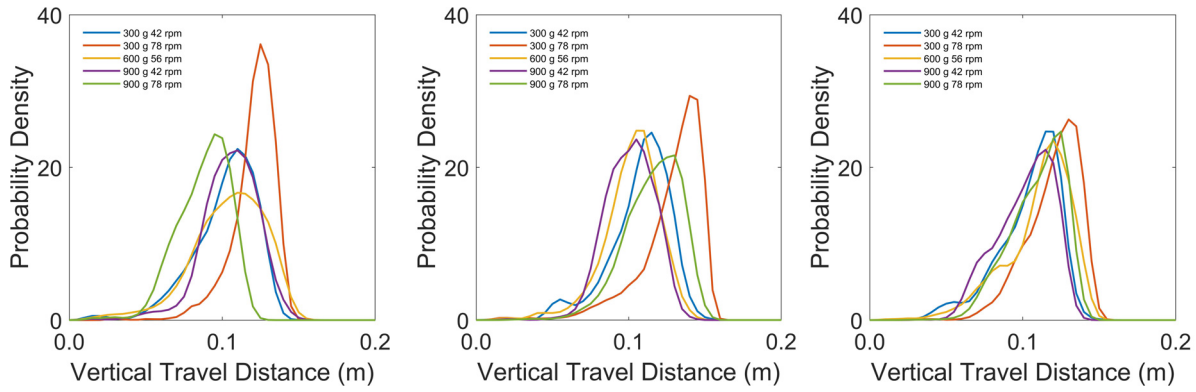

(a) (b) (c)

Figure 4.20: Distributions of vertical travel distance for (a) green, (b) part-roasted and (c) roasted coffee studied at different process conditions.

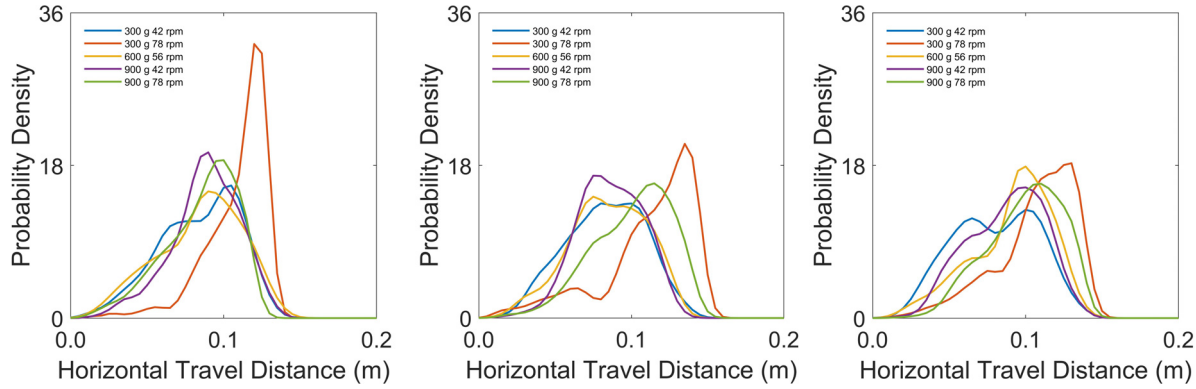

(a) (b) (c)

Figure 4.21: Distributions of horizontal travel distance for (a) green, (b) part-roasted and (c) roasted coffee studied at different process conditions.

travel distances, the impact of roast degree is most apparent for high drum rotation speeds (78 rpm). Under these conditions, increasing roast degree increases the vertical travel distances due to the improved attachment in the upper left region of the drum.

At low to moderate drum speeds (42-56 rpm), batch size has no significant impact on vertical travel distance (Figure 4.20). When green and part-roasted coffees are subject to high drum speeds (78 rpm), smaller batches - with fewer beans in the bed and more in-flight particles - cause beans to travel over greater vertical distances than for larger batches. This phenomenon is not observed for roasted coffee and can be attributed to drum wall lifting – i.e., beans of higher density are more easily lifted along the wall.

For smaller batches of green and part-roasted coffee, motion tends toward cataracting, and particle behaviour becomes more homogenous (i.e., a greater number of particles follow similar trajectories). For roasted coffee at high drum speeds (78 rpm), there is little impact of batch size on both vertical and horizontal travel distances, which might be a result of particle collisions with the drum central axis - this generates a bi-modal distribution of horizontal travel distances (seen in Figure 4.21 with a local minimum at approximately 0.08 m (the drum radius).

Figure 4.21(b) shows that at low drum speeds (42 rpm) all coffees tend to travel horizontal distances less than the drum radius (falling through the in-flight region at $r < R$) during a single rotation. Increasing drum speed increased the vertical travel distance (Figure 4.20), where particles are subject to drum wall lifting. The impact of drum speed on vertical travel distance decreased as particle density decreased. For large batches (900 g), drum rotation speed has little impact on the median horizontal travel distance, but greater drum speeds lead to more particles travelling distances greater than the drum radius (as illustrated by Figure 4.20 and Figure 4.21). There is no real impact of drum speed on horizontal travel distances for large batches (900 g) of roasted coffee due to the large fill volume, which increases bed volume and causes more beans to follow similar trajectories (i.e., bean behaviour becomes more homogenous).

Particle velocity

Velocity (magnitude of velocity vector in xyz) distributions for all conditions are displayed in Figure 4.22. Particle velocity is governed by drum rotation speed. The slow-moving core within the bean bed has no real impact on velocity distributions due to the low fraction of the batch that fall into such trajectories. For a specified drum rotation speed, increasing batch size has little influence on the magnitude of particle velocity, although it increases the homogeneity of particle behaviour (i.e., decreases the range of particle velocities). Batch homogeneity is critical to most definitions of quality, particularly for products sold as whole beans, where large distributions in size and colour (a result of roast defects such as tipping and scorching) are likely to be perceived negatively by consumers (Giacalone et al., 2019).

Whilst bean breakage in large roasting systems is a concern (particularly when whole beans are conveyed at high speed to packing lines), in the pilot-scale roaster there was no evidence of bean breakage that would suggest process conditions influence coffee's susceptibility to breakage.

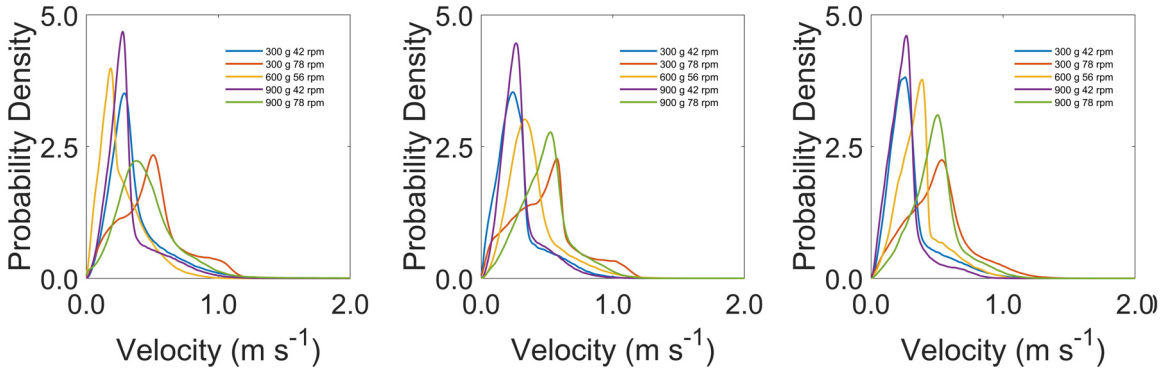

(a) (b) (c)

Figure 4.22: Distributions of velocity for (a) green, (b) part-roasted and (c) roasted coffee studied at different process conditions.

4.3.3 System characterisation using Froude number

Froude numbers were calculated for particles lifted by the drum wall via Eq. 4.3. Figure 4.23 presents the probability density of apparent Froude number for all conditions - there are clear differences.

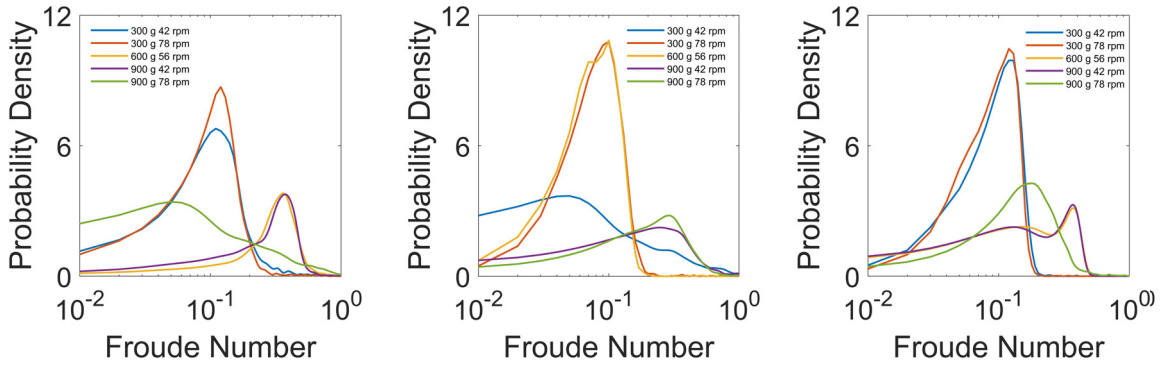

(a) (b) (c)

Figure 4.23: Distributions of Froude number for (a) green, (b) part-roasted and (c) roasted coffee studied at different process conditions.

For small batch sizes, a peak at $Fr \approx 0.1$ corresponds to particles near the drum wall whose motion is driven by drum wall lifting - beans exhibit cascading motion in the transitional region ($10^{-2} < Fr < 10^{-1}$). For moderate-to-large batch sizes, the distribution changes, and a peak in the range $0.2 < Fr < 0.5$ is observed; for these conditions, there is a skewed distribution of Fr, indicative of slow-moving particles further from the drum wall. For part-roasted coffee, Figure 4.23 implies that low to moderate batch sizes (300-600 g), with low to moderate drum speeds (42-56 rpm) fall in the transitional regime between cascading and cataracting motion. Conditions corresponding to cataracting motion ($Fr < 10^{-1}$) are seen for the large batch sizes, and the transitional regimes seen here agree with previous studies of cascading to cataracting motion (Resende et al., 2017; Beaulieu et al., 2022).

In Figure 4.13, the effect of roast degree (i.e., bean volume and density) on flow regimes is shown. High density (green) coffee exhibits cascading motion (Figures 4.13(d)&(g)), with the dense particles falling down over the surface of the bed. As density decreases, part-roasted coffee (Figure 4.13(e)&(h)) shows motion in the transitional regime between cascading and cataracting motion. For low density (roasted) coffee, cataracting motion is established (Figure 4.13(f)&(i)), with roasted beans propelled much further and the bean bed being much smaller than for green coffee.

Volume expansion occurring between part-roasted and fully roasted stages would result in a transition in flow regime, from cascading to cataracting, during roasting. In cascading regimes, particle velocity is related to drum rotation speeds (i.e., governed by centripetal forces). In cataracting regimes ($Fr > 10^{-1}$), particles in motion at the drum wall will still be lifted, and thus governed by, the rotation speed of the drum, but in the dispersed in-flight region, particles move under gravity. Particles in these regimes are thus expected to exhibit two distinct behaviours corresponding to (i) lifting and (ii) in-flight regions.

4.4 Implications for heat transfer

4.4.1 Heat transfer in spouted bed roasters

Bean bed and freeboard heat transfer behaviour will be different due to the distinct flow patterns in each region. In the freeboard, the convective heat transfer coefficient in the spout is high, so coffee temperature increases rapidly. As the beans are propelled from the spout, the temperature difference between bean and air decreases, so will heat transfer (Brown and Lattimer, 2013). In the bean bed, heat transfer rates are lower than in the freeboard region as here, heat transfer is governed by several mechanisms, including: bean internal conduction, bean-to-bean surface conduction (contact), bean-to-bean surface radiation (non-contact), air-to-bean convection, convection in voids, and the effective thermal conductivity of the bed (Díaz-Heras, Belmonte, and Almendros-Ibáñez, 2020). As a result, the region of the bean bed adjacent to the spout will be at a higher temperature than the centre of the bed and the temperature of the metal will be close to that of the adjacent beans. Cheng et al. (2020) found that heat conduction through bed voids increases with bed porosity and is significant for systems where the air to particle conductivity ratio is less than 5, as it is here. Therefore, as bed fluidisation and porosity increases, conductive heat transfer through the voids can be expected to increase, improving bed heat transfer.

To improve air-to-bean convective heat transfer, as well as convection through bean bed voids, air flow should be maximised to maintain a large fraction of beans in the freeboard. Although increasing heat transfer rates is desirable to improve productivity and yield, shorter roasts often yield underdeveloped coffees with grassy flavour attributes in-cup (Giacalone et al., 2019). To counter this, developers could roast with moderate air flow in the early stages of roasting and reduce airflow as coffee density changes to maintain a consistent occupancy profile. Reduction of air flow during roasting also acts to control endothermic and exothermic reactions that initiate around first crack (Schwartzberg, 2002) and will increase batch homogeneity, and potentially energy consumption - provided the necessary changes to maintain similar time-temperature profiles are minimal. To increase conductive heat transfer (similar to that in drum roasters), process conditions that give a large bean bed area with

little bed fluidisation and a high preheating temperature are needed.

4.4.2 Heat transfer in rotating drum roasters

For rotating drum roasters, PEPT also revealed two distinct regions of occupancy, wherein beans travel (i) slowly and have greater residence times in the bean bed and (ii) rapidly and have shorter residence times in the in-flight region. In the in-flight region, convective heat transfer is dominant, so beans will experience heat transfer governed by the convective heat transfer coefficient. In the bean bed, convective heat transfer between the roasting air and individual beans will be much lower than in the in-flight region so, for beans in the bulk of the bed, conductive heat transfer both within the bean, and bean-to-bean, will dominate.

The drum wall is preheated to 250-300°C, with steady-state charge temperatures in the range of 180-220°C (Garcia et al., 2018). When beans are close to the drum wall, metal-to-bean conductive heat transfer rates will be high, inducing rapid, localised heating of the beans. Similar phenomena have been described for roasting of specialty malts (Robbins, 2003) where most heating occurs to particles in the wall region. Controlling the behaviour of the bed and the drum wall temperature are thus be critical, as changes in bean properties will affect the bed size and the induced heat transfer rates. As mapped changes in the bean bed mass fraction are attributed to the evolution of bulk density, operators can adapt their control strategy accordingly.

4.4.3 Impact on temperature measurement

In both roasters, thermocouples in the bean bed measure a combination of bean and air temperature, so the flow pattern affects the measured temperature. At the start of roasting, the temperature of the air in the roasting chamber will be higher than in the beans but, as the roast progresses, bean temperature will approach that of the air (or the drum). As the packing density around the thermocouple will be affected by the local flow behaviour, heat transfer from the bean bed environment to the thermocouple will be affected. It is expected that as the packing density decreases during roasting (i.e., the bed expands and becomes less densely occupied) there would be increased contact area between the thermocouple and

the air, and a decreased contact area between the thermocouple and beans. The measured 'bean' temperature will thus be overestimated, as the air temperature is greater than the beans. This problem adds complexity to comparing time-temperature profiles for dissimilar roasting conditions and will cost accuracy during simulations.

4.4.4 Limitations

As PEPT measurements are captured at ambient temperatures (c. 20°C) over long times to ensure the system tends toward ergodicity, particle motion in spouted bed roasters might vary at higher temperatures (c. 200°C). Air density decreases as temperature increases, so for a given fan frequency (and air mass flow rate), air velocity increases. The effect of higher air temperatures on particle motion are therefore expected to be directionally similar to the demonstrated effect of higher airflows.

4.5 Conclusions & outlook

4.5.1 A summary of PEPT measurements

Using PEPT, aspherical (coffee bean) particle motion has been characterised in two real, pilot-scale roasters (a spouted bed and a rotating drum). Coffee roasting was emulated through the study of coffees with different roast degrees and densities, while process parameters (batch size and air mass flow rate in the spouted bed; batch size and rotation speed in the rotating drum) were varied to study their impact on particle dynamics.

Translation of PEPT-captured Lagrangian trajectories to time-averaged Eulerian flow fields revealed the impact of process parameters (batch size and agitation) and product properties (roast degree/density) on the system particle dynamics.

Distinct regions of occupancy and velocity were identified, corresponding to (i) a disperse region of in-flight particles, with lower occupancy and higher velocities and (ii) a dense bean bed, with higher occupancy and lower velocities. From the Eulerian flow fields, regional mass fractions and median particle velocities can be obtained as a function of process parameters and product properties. In rotating drums, these can then be used with effective Froude

numbers to characterise granular flow. The effect of process parameters and their variation on coffee bean particle motion has been also demonstrated here, revealing that process and product developers have two critical parameters to leverage in the pursuit of quality: batch size and extent of agitation.

4.5.2 Best practices for roasters

Process parameters - batch size and agitation (rotation speeds in drums; airflow in spouted beds) - have been shown to strongly determine particle dynamics, for example in the different bed shapes seen in Figure 4.13(d)-(f) 4.13(d)-(f). Use of small batch sizes with high agitation (operating in the cataracting regime in rotating drums, where greater drum wall lifting is observed, or in highly disperse conditions under high airflow in spouted beds), may increase the likelihood of roast defects due to greater convective heat transfer in the in-flight region (and localised conductive heat transfer near the wall in drums), due to greater residence times in both regions.

These phenomena will decrease batch homogeneity if the time-temperature profile is not well managed. Best practice to minimise roast defects and preserve quality may involve operating near the roaster load capacity, with moderate agitation (rotation speeds in drums; airflow in spouted beds) that decreases during roasting; this protocol, combined with a well-managed time-temperature profile, would ensure maximum productivity and efficiency. For process and product consistency, current industry practices maintain a constant batch size on a mass basis. Green coffee, the unroasted raw material, is an agricultural product with inherent natural variability, so coffee density varies not only due to post-harvest processing differences, but also within a coffee lot from a single producer. Specification of batch size on a volume basis, calculated from bulk density, would enable constant fill volumes to be achieved from batch to batch. Constant fill volume would ensure that the bean bed on a macro-scale would be of equivalent size across batches, with similar (and more predictable) particle dynamics and heat transfer conditions.

Batch homogeneity is critical for downstream processes at both factory and consumer level. Uniform coffee development can be achieved by modulating process parameters (i.e., decreas-

ing agitation and thermal set point) as coffee properties evolve during roasting. Common roasting defects such as tipping, scorching and baking, that occur due to poorly managed roasting profiles, can also be avoided by tuning process conditions such as the preheating protocol, charge temperature and batch-to-batch protocol. PEPT has thus provided fundamental tools to guide roasting developers in their quest for great coffee.

4.5.3 Outlook for process virtualisation

These data can also be used to virtualise the development of processes and products, improving both in-cup quality and engineering efficiency. Both the Lagrangian and Eulerian data can be used to (i) calibrate DEM simulations, (ii) generate physics-driven models to describe the transient properties of the bean bed and in-flight regions, and (iii) inform the convective boundary conditions and time-step in zero- and three-dimensional heat and mass transfer simulations. Che et al. (2023) recently outlined a framework for validation of CFD-DEM simulations using PEPT. This approach could be applied to DEM simulations of rotating drum roasters.

4.6 Appendix: All Lagrangian trajectories & Eulerian flow fields

On the following pages, all captured data relating to the study of particle motion in both the spouted bed and rotating drum roasters are presented. These data depict Cartesian coordinate data overlayed with individual particle (Lagrangian) trajectories, as well as time-averaged (Eulerian) flow fields occupancy and velocity.

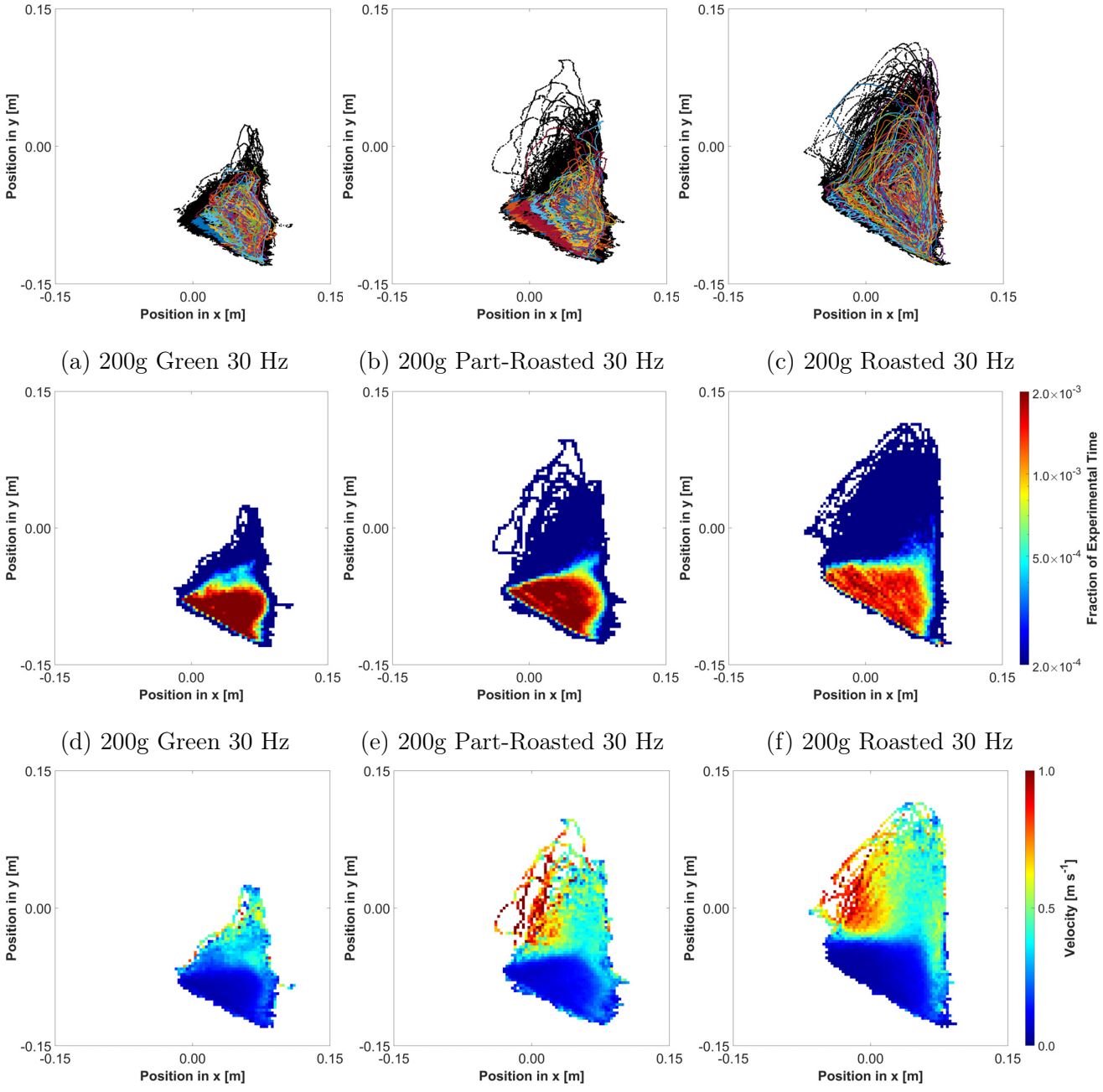

(a) 200g Green 30 Hz (b) 200g Part-Roasted 30 Hz (c) 200g Roasted 30 Hz

(d) 200g Green 30 Hz (e) 200g Part-Roasted 30 Hz (f) 200g Roasted 30 Hz

(g) 200g Green 30 Hz (h) 200g Part-Roasted 30 Hz (i) 200g Roasted 30 Hz

Figure 4.24: Experimental PEPT data detailing (a)-(c) Cartesian data overlayed with individual particle trajectories, (d)-(f) occupancy profiles and (g)-(i) velocity profiles for 200 g of (a),(d),(g) green, (b),(e),(h) part-roasted and (c),(f),(i) roasted coffee operated at a fan frequency of 30 Hz, depicting the impact of roast degree.

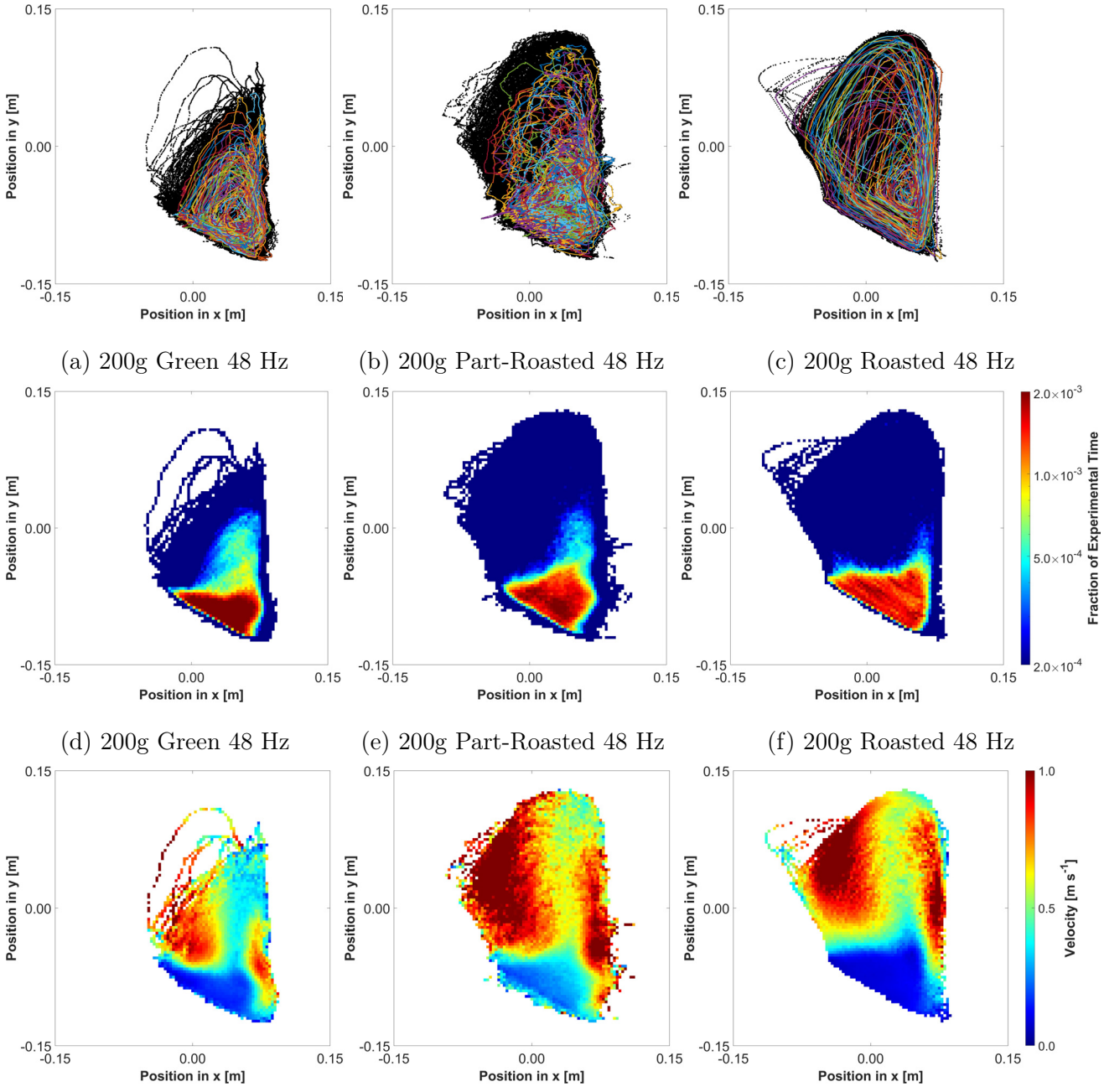

(a) 200g Green 48 Hz (b) 200g Part-Roasted 48 Hz (c) 200g Roasted 48 Hz

(d) 200g Green 48 Hz (e) 200g Part-Roasted 48 Hz (f) 200g Roasted 48 Hz

(g) 200g Green 48 Hz (h) 200g Part-Roasted 48 Hz (i) 200g Roasted 48 Hz

Figure 4.25: Experimental PEPT data detailing (a)-(c) Cartesian data overlayed with individual particle trajectories, (d)-(f) occupancy profiles and (g)-(i) velocity profiles for 200 g of (a),(d),(g) green, (b),(e),(h) part-roasted and (c),(f),(i) roasted coffee operated at a fan frequency of 48 Hz, depicting the impact of roast degree.

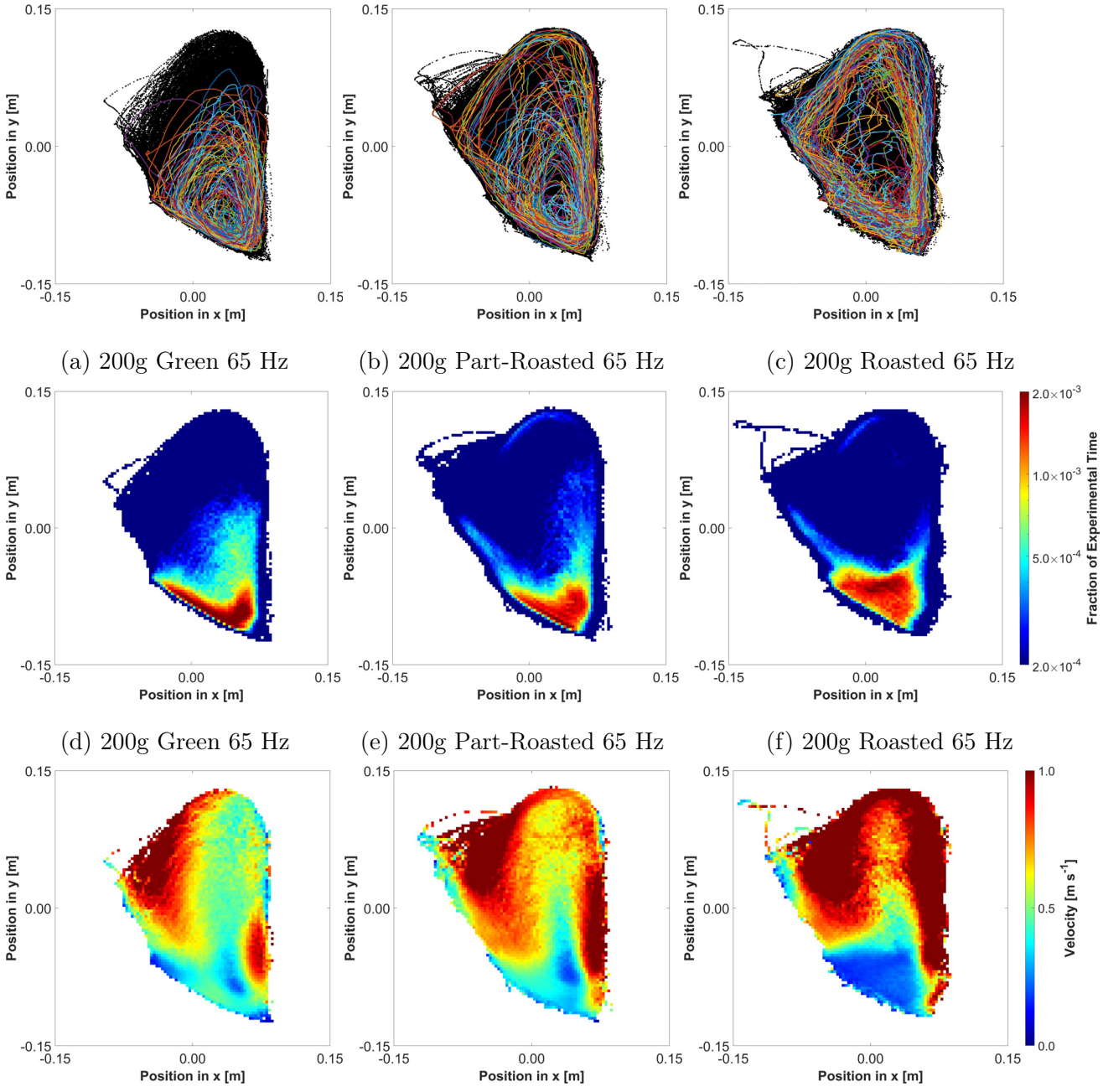

(a) 200g Green 65 Hz (b) 200g Part-Roasted 65 Hz (c) 200g Roasted 65 Hz

(d) 200g Green 65 Hz (e) 200g Part-Roasted 65 Hz (f) 200g Roasted 65 Hz

(g) 200g Green 65 Hz (h) 200g Part-Roasted 65 Hz (i) 200g Roasted 65 Hz

Figure 4.26: Experimental PEPT data detailing (a)-(c) Cartesian data overlayed with individual particle trajectories, (d)-(f) occupancy profiles and (g)-(i) velocity profiles for 200 g of (a),(d),(g) green, (b),(e),(h) part-roasted and (c),(f),(i) roasted coffee operated at a fan frequency of 65 Hz, depicting the impact of roast degree.

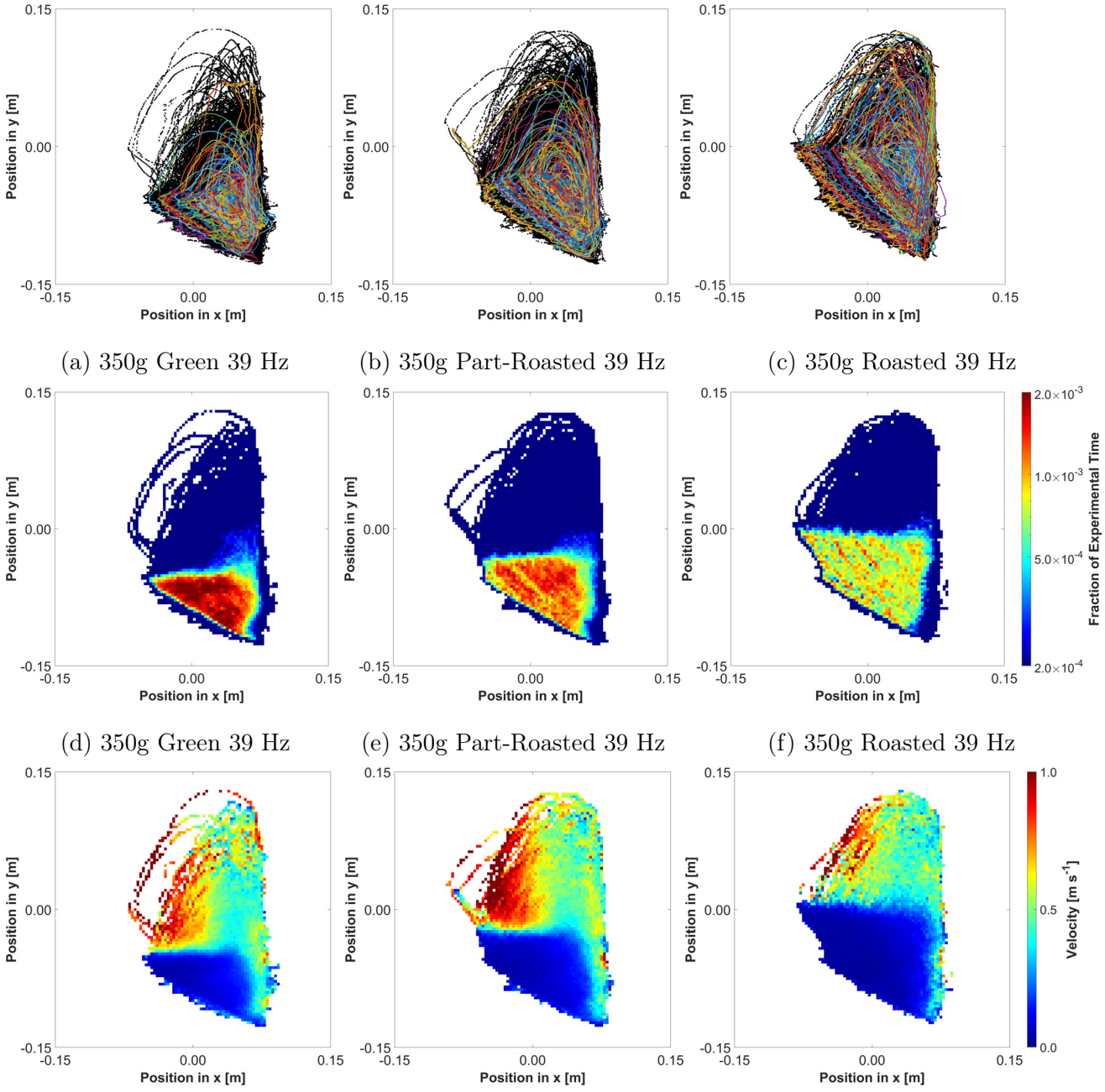

(a) 350g Green 39 Hz (b) 350g Part-Roasted 39 Hz (c) 350g Roasted 39 Hz

(d) 350g Green 39 Hz (e) 350g Part-Roasted 39 Hz (f) 350g Roasted 39 Hz

(g) 350g Green 39 Hz (h) 350g Part-Roasted 39 Hz (i) 350g Roasted 39 Hz

Figure 4.27: Experimental PEPT data detailing (a)-(c) Cartesian data overlayed with individual particle trajectories, (d)-(f) occupancy profiles and (g)-(i) velocity profiles for 350 g of (a),(d),(g) green, (b),(e),(h) part-roasted and (c),(f),(i) roasted coffee operated at a fan frequency of 39 Hz, depicting the impact of roast degree.

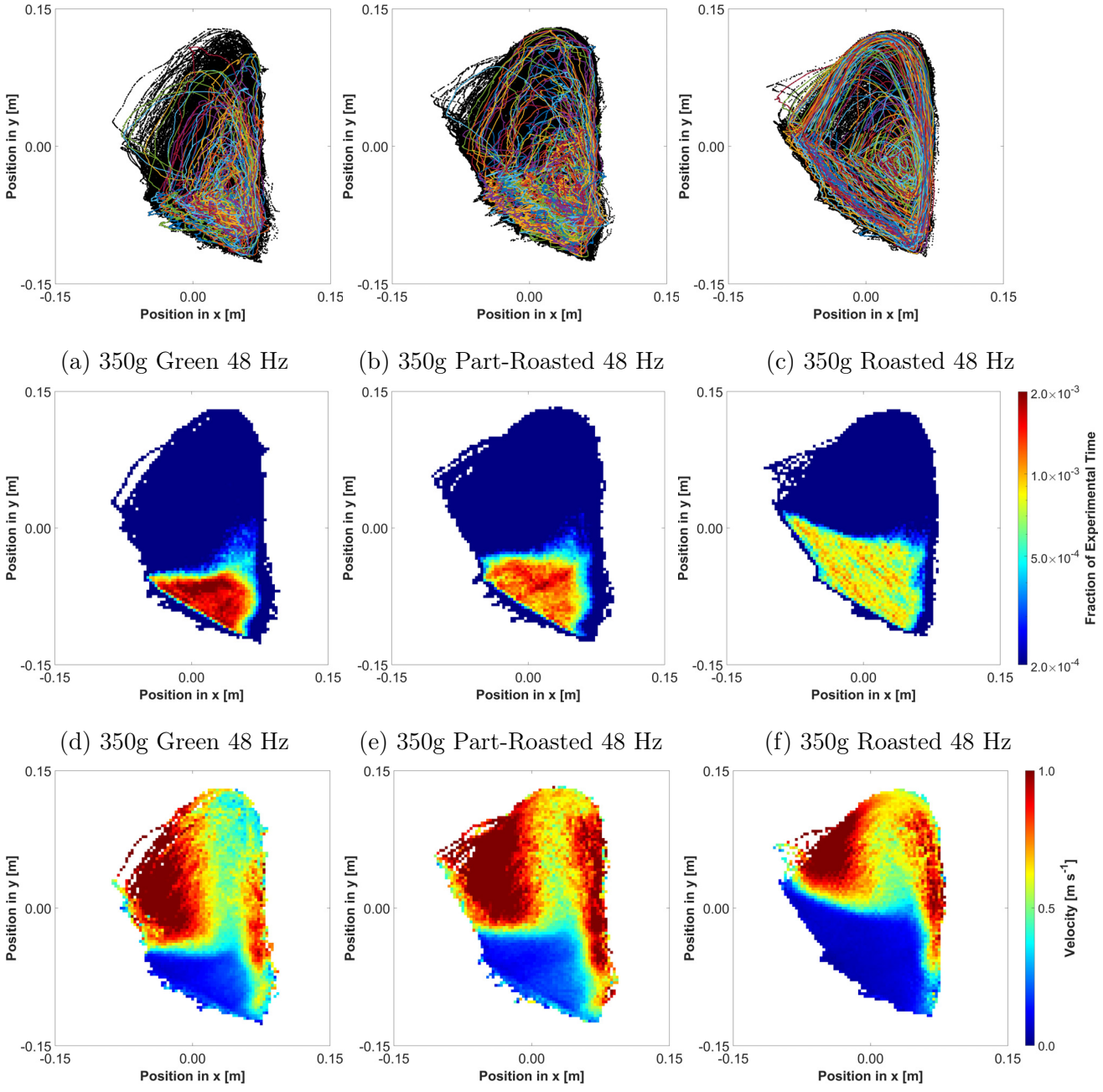

(a) 350g Green 48 Hz (b) 350g Part-Roasted 48 Hz (c) 350g Roasted 48 Hz

(d) 350g Green 48 Hz (e) 350g Part-Roasted 48 Hz (f) 350g Roasted 48 Hz

(g) 350g Green 48 Hz (h) 350g Part-Roasted 48 Hz (i) 350g Roasted 48 Hz

Figure 4.28: Experimental PEPT data detailing (a)-(c) Cartesian data overlayed with individual particle trajectories, (d)-(f) occupancy profiles and (g)-(i) velocity profiles for 350 g of (a),(d),(g) green, (b),(e),(h) part-roasted and (c),(f),(i) roasted coffee operated at a fan frequency of 48 Hz, depicting the impact of roast degree.

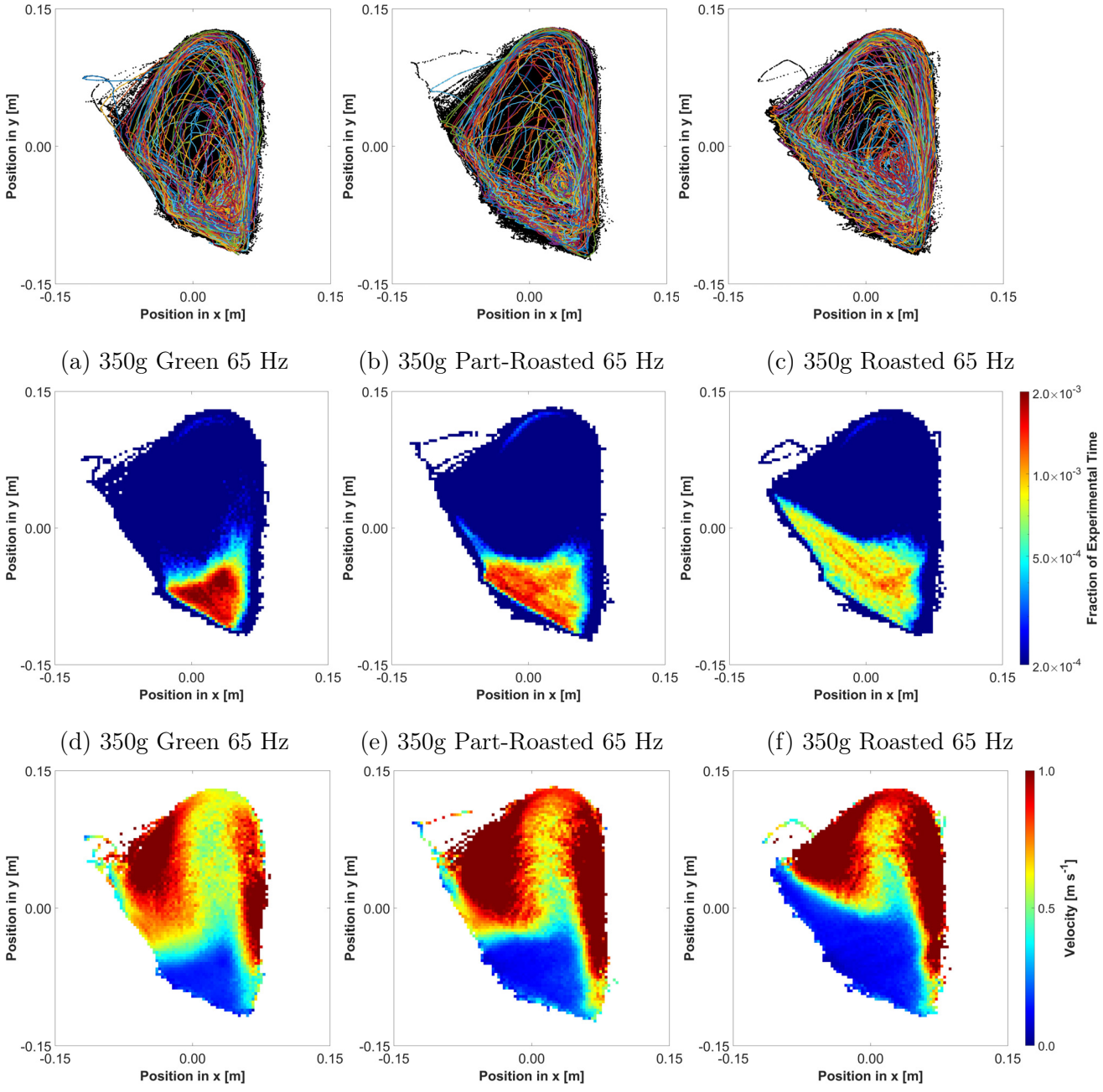

(a) 350g Green 65 Hz (b) 350g Part-Roasted 65 Hz (c) 350g Roasted 65 Hz

(d) 350g Green 65 Hz (e) 350g Part-Roasted 65 Hz (f) 350g Roasted 65 Hz

(g) 350g Green 65 Hz (h) 350g Part-Roasted 65 Hz (i) 350g Roasted 65 Hz

Figure 4.29: Experimental PEPT data detailing (a)-(c) Cartesian data overlayed with individual particle trajectories, (d)-(f) occupancy profiles and (g)-(i) velocity profiles for 350 g of (a),(d),(g) green, (b),(e),(h) part-roasted and (c),(f),(i) roasted coffee operated at a fan frequency of 65 Hz, depicting the impact of roast degree.

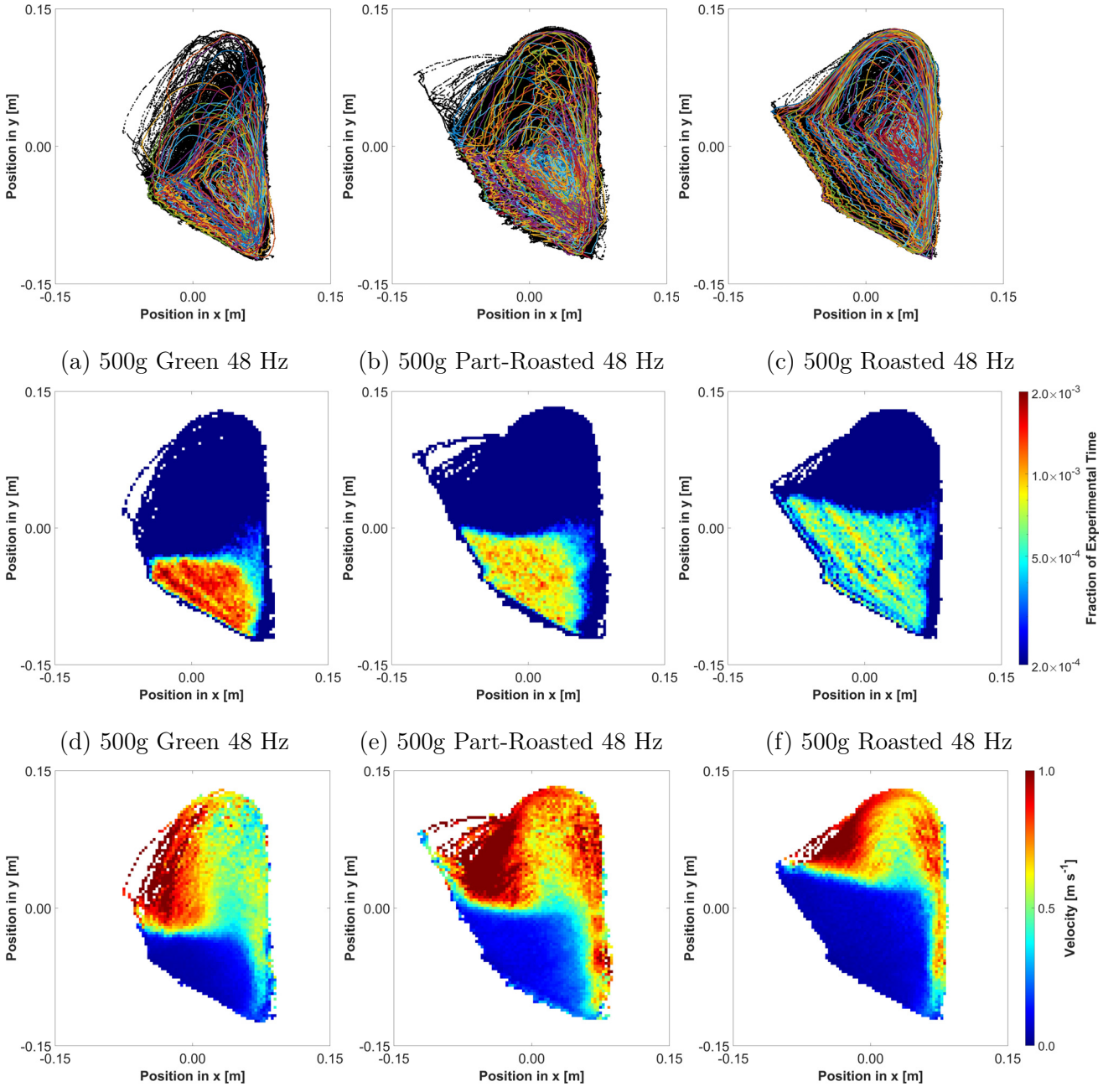

(a) 500g Green 48 Hz (b) 500g Part-Roasted 48 Hz (c) 500g Roasted 48 Hz

(d) 500g Green 48 Hz (e) 500g Part-Roasted 48 Hz (f) 500g Roasted 48 Hz

(g) 500g Green 48 Hz (h) 500g Part-Roasted 48 Hz (i) 500g Roasted 48 Hz

Figure 4.30: Experimental PEPT data detailing (a)-(c) Cartesian data overlayed with individual particle trajectories, (d)-(f) occupancy profiles and (g)-(i) velocity profiles for 500 g of (a),(d),(g) green, (b),(e),(h) part-roasted and (c),(f),(i) roasted coffee operated at a fan frequency of 48 Hz, depicting the impact of roast degree.

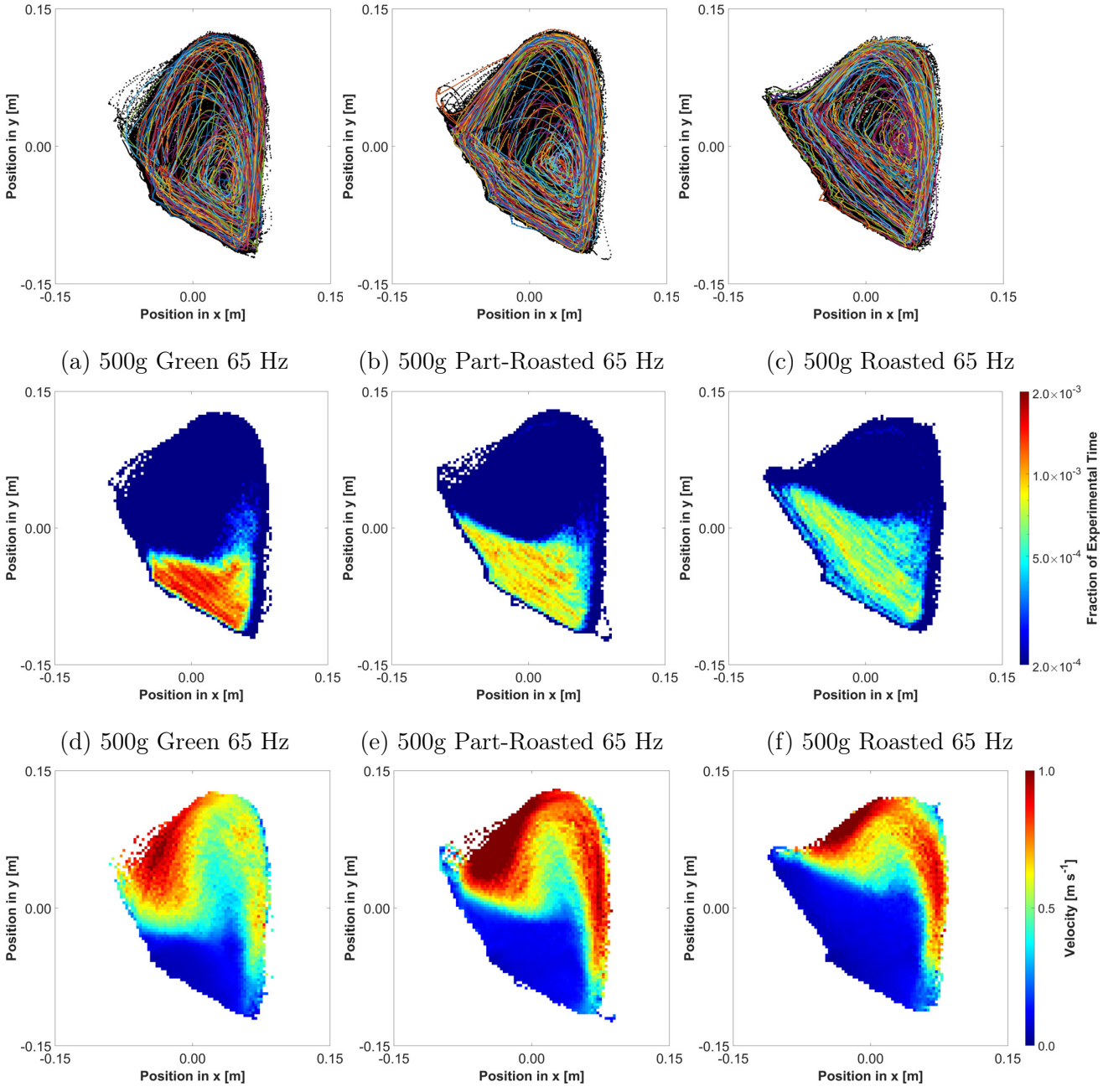

(a) 500g Green 65 Hz (b) 500g Part-Roasted 65 Hz (c) 500g Roasted 65 Hz

(d) 500g Green 65 Hz (e) 500g Part-Roasted 65 Hz (f) 500g Roasted 65 Hz

(g) 500g Green 65 Hz (h) 500g Part-Roasted 65 Hz (i) 500g Roasted 65 Hz

Figure 4.31: Experimental PEPT data detailing (a)-(c) Cartesian data overlayed with individual particle trajectories, (d)-(f) occupancy profiles and (g)-(i) velocity profiles for 500 g of (a),(d),(g) green, (b),(e),(h) part-roasted and (c),(f),(i) roasted coffee operated at a fan frequency of 65 Hz, depicting the impact of roast degree.

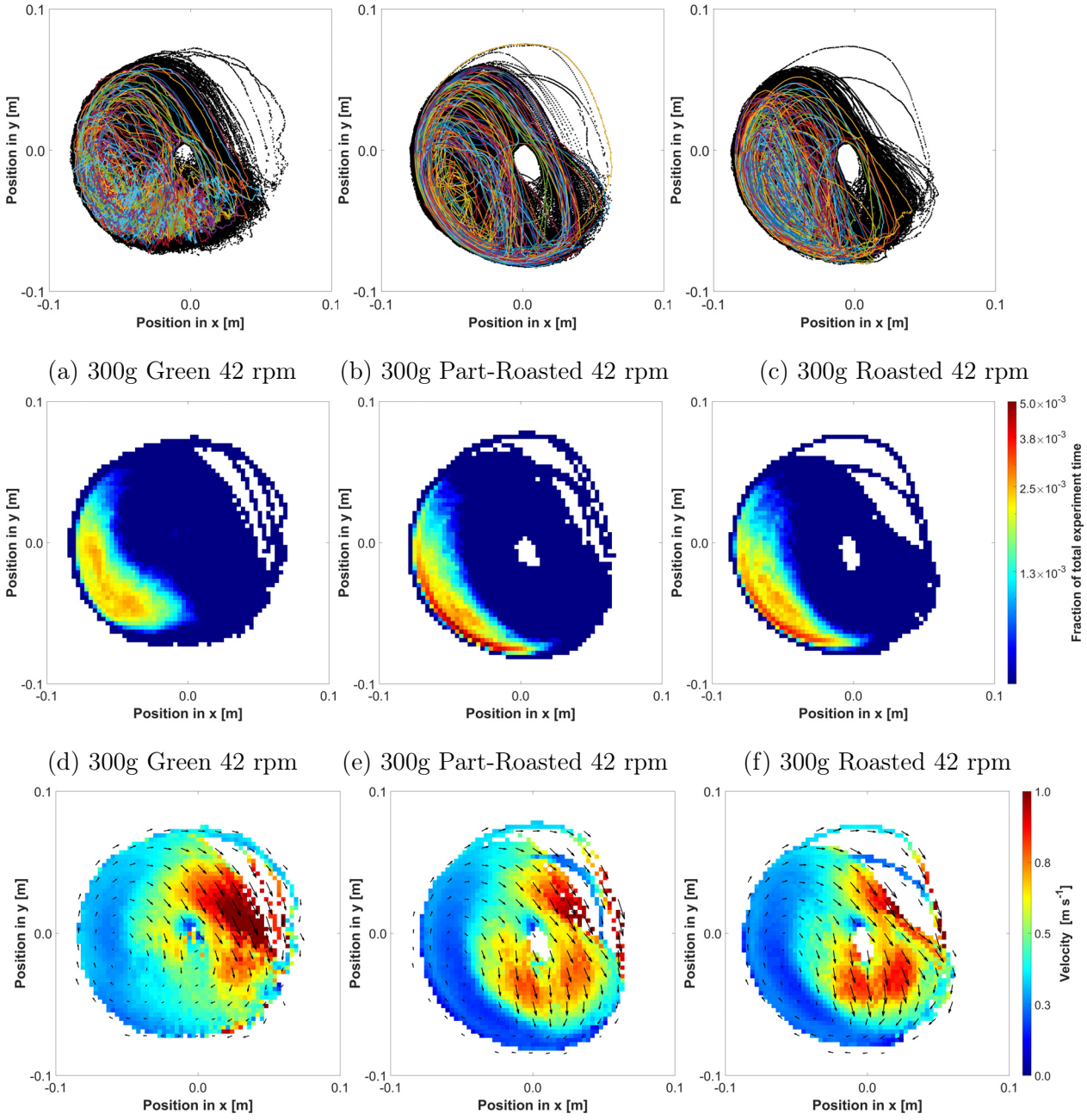

(a) 300g Green 42 rpm (b) 300g Part-Roasted 42 rpm (c) 300g Roasted 42 rpm

(d) 300g Green 42 rpm (e) 300g Part-Roasted 42 rpm (f) 300g Roasted 42 rpm

(g) 300g Green 42 rpm (h) 300g Part-Roasted 42 rpm (i) 300g Roasted 42 rpm

Figure 4.32: Experimental PEPT data detailing (a)-(c) Cartesian data overlayed with individual particle trajectories, (d)-(f) occupancy profiles and (g)-(i) velocity profiles for 300 g of (a),(d),(g) green, (b),(e),(h) part-roasted and (c),(f),(i) roasted coffee operated at 42 rpm, depicting the impact of roast degree.

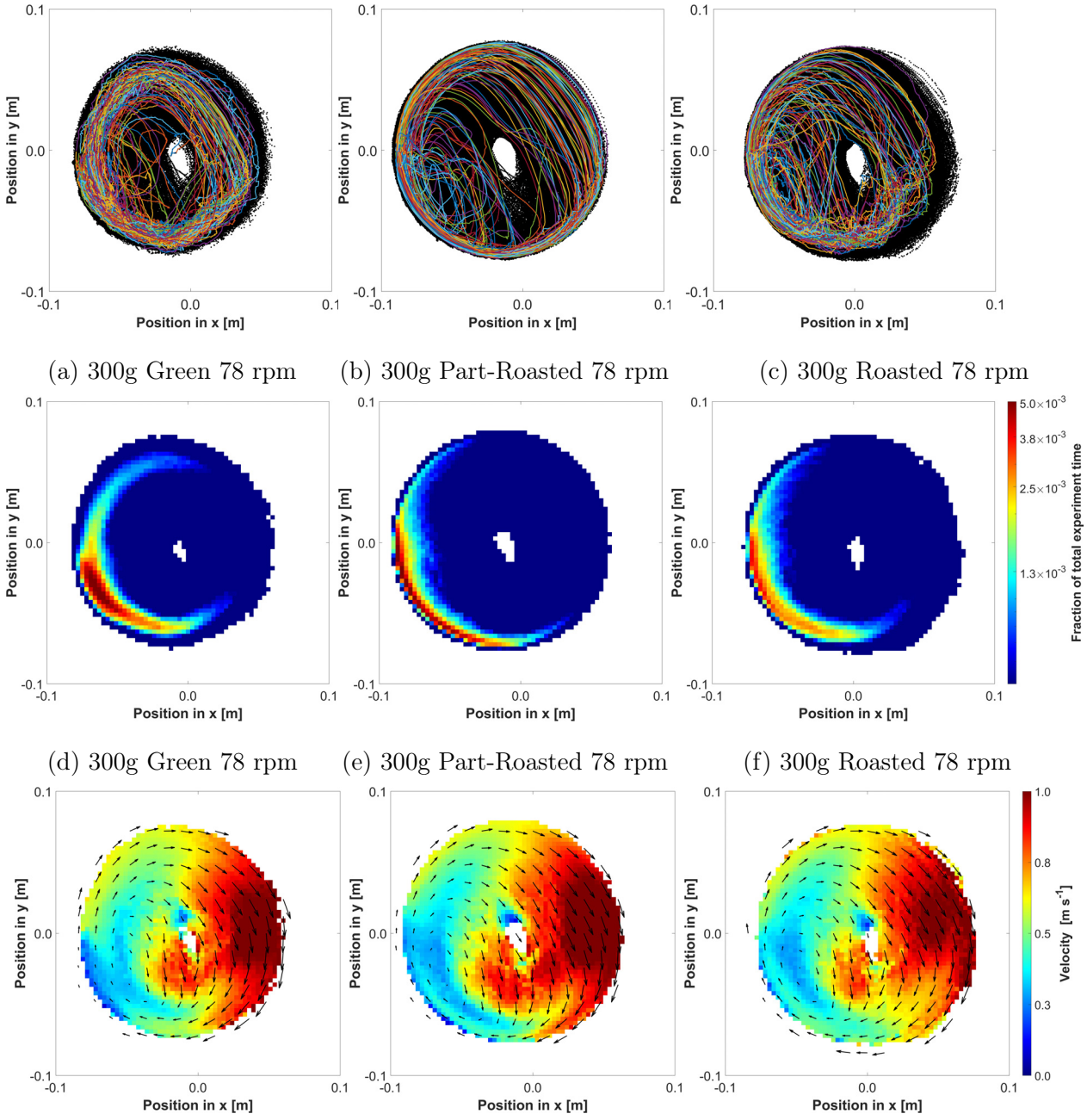

(a) 300g Green 78 rpm (b) 300g Part-Roasted 78 rpm (c) 300g Roasted 78 rpm

(d) 300g Green 78 rpm (e) 300g Part-Roasted 78 rpm (f) 300g Roasted 78 rpm

(g) 300g Green 78 rpm (h) 300g Part-Roasted 78 rpm (i) 300g Roasted 78 rpm

Figure 4.33: Experimental PEPT data detailing (a)-(c) Cartesian data overlayed with individual particle trajectories, (d)-(f) occupancy profiles and (g)-(i) velocity profiles for 300 g of (a),(d),(g) green, (b),(e),(h) part-roasted and (c),(f),(i) roasted coffee operated at 78 rpm, depicting the impact of roast degree.

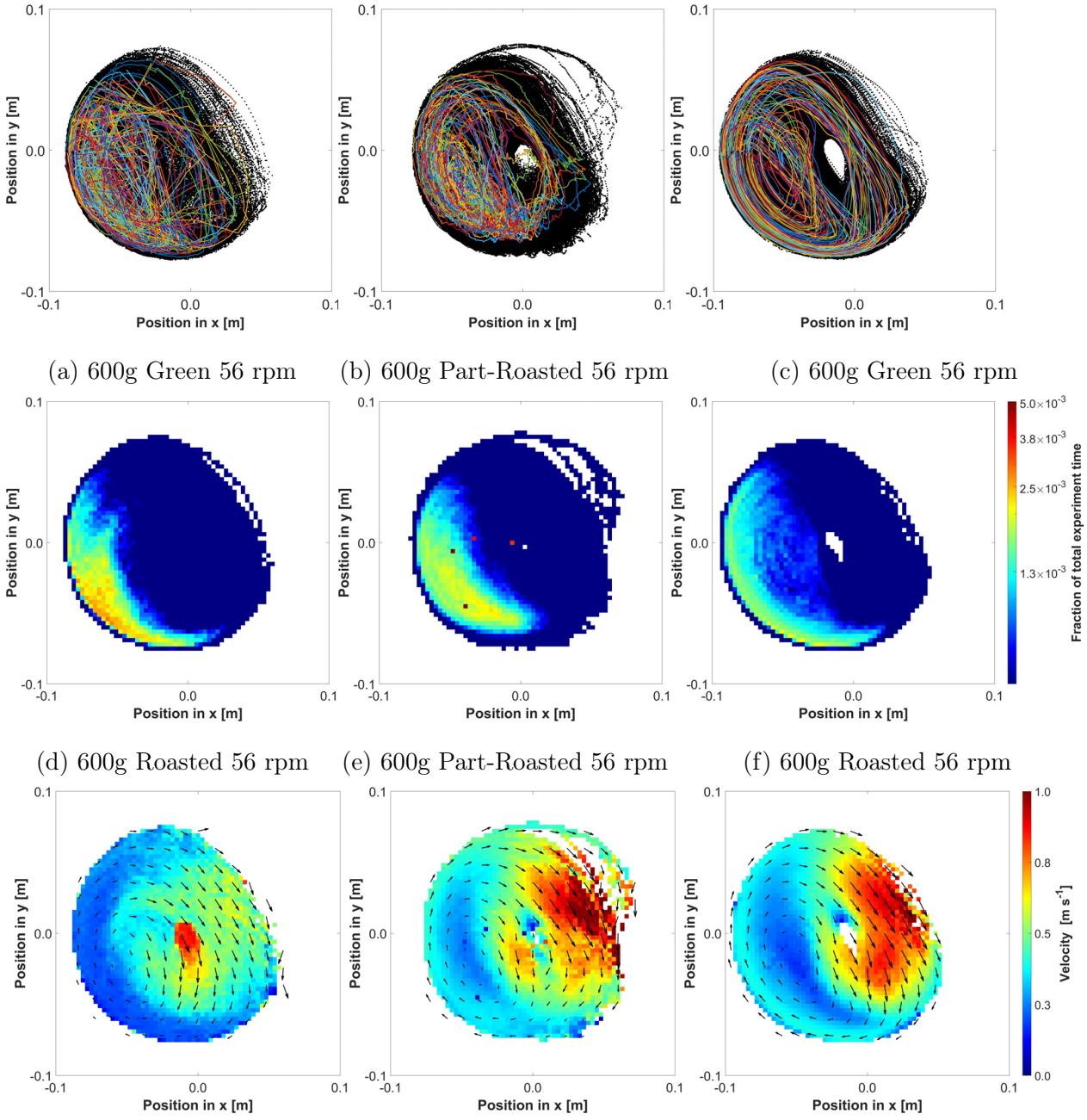

(a) 600g Green 56 rpm (b) 600g Part-Roasted 56 rpm (c) 600g Green 56 rpm

(d) 600g Roasted 56 rpm (e) 600g Part-Roasted 56 rpm (f) 600g Roasted 56 rpm

(g) 600g Green 56 rpm (h) 600g Part-Roasted 56 rpm (i) 600g Roasted 56 rpm

Figure 4.34: Experimental PEPT data detailing (a)-(c) Cartesian data overlayed with individual particle trajectories, (d)-(f) occupancy profiles and (g)-(i) velocity profiles for 600 g of (a),(d),(g) green, (b),(e),(h) part-roasted and (c),(f),(i) roasted coffee operated at 56 rpm, depicting the impact of roast degree.

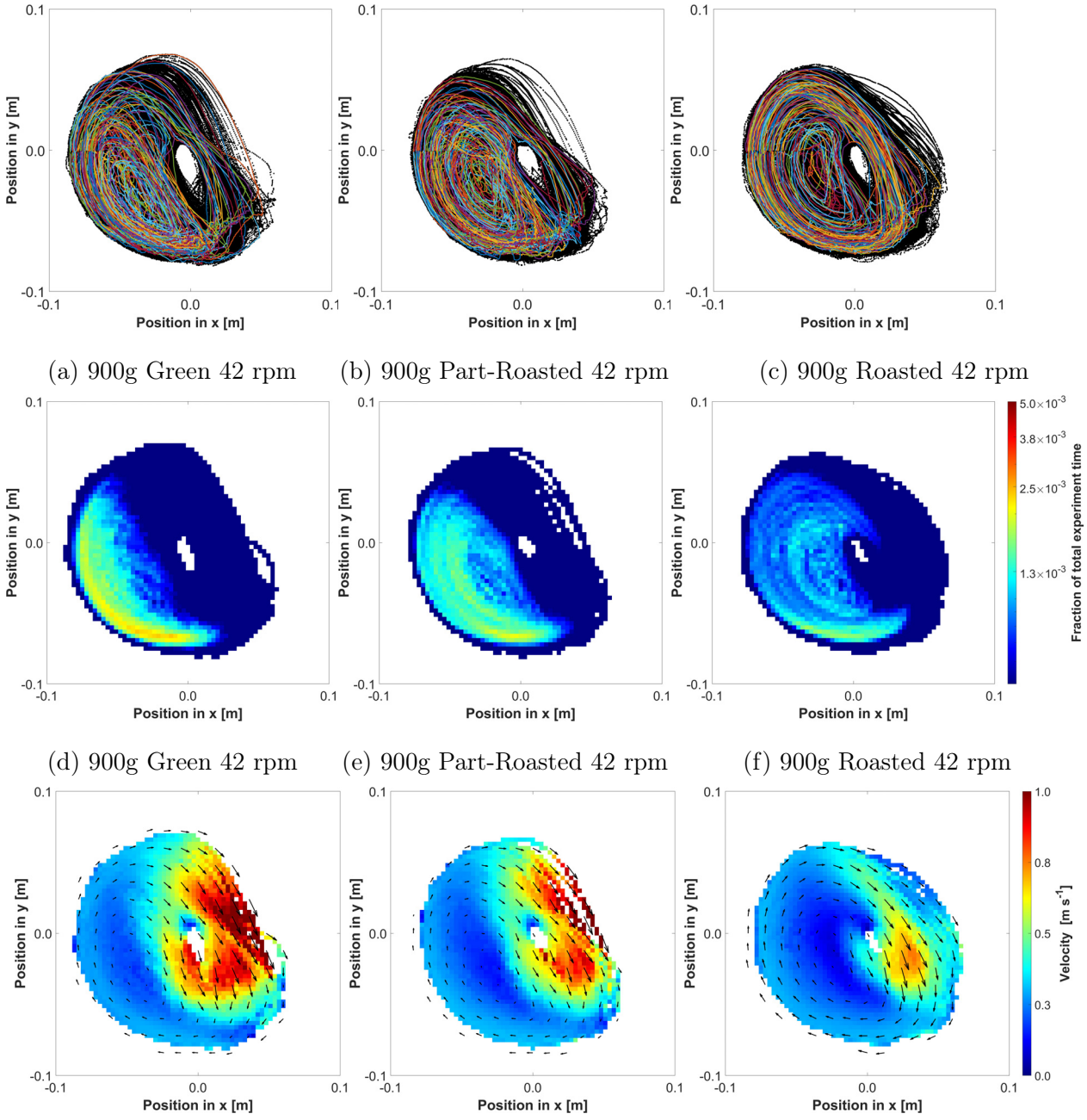

(a) 900g Green 42 rpm (b) 900g Part-Roasted 42 rpm (c) 900g Roasted 42 rpm

(d) 900g Green 42 rpm (e) 900g Part-Roasted 42 rpm (f) 900g Roasted 42 rpm

(g) 900g Green 42 rpm (h) 900g Part-Roasted 42 rpm (i) 900g Roasted 42 rpm

Figure 4.35: Experimental PEPT data detailing (a)-(c) Cartesian data overlayed with individual particle trajectories, (d)-(f) occupancy profiles and (g)-(i) velocity profiles for 900 g of (a),(d),(g) green, (b),(e),(h) part-roasted and (c),(f),(i) roasted coffee operated at 42 rpm, depicting the impact of roast degree.

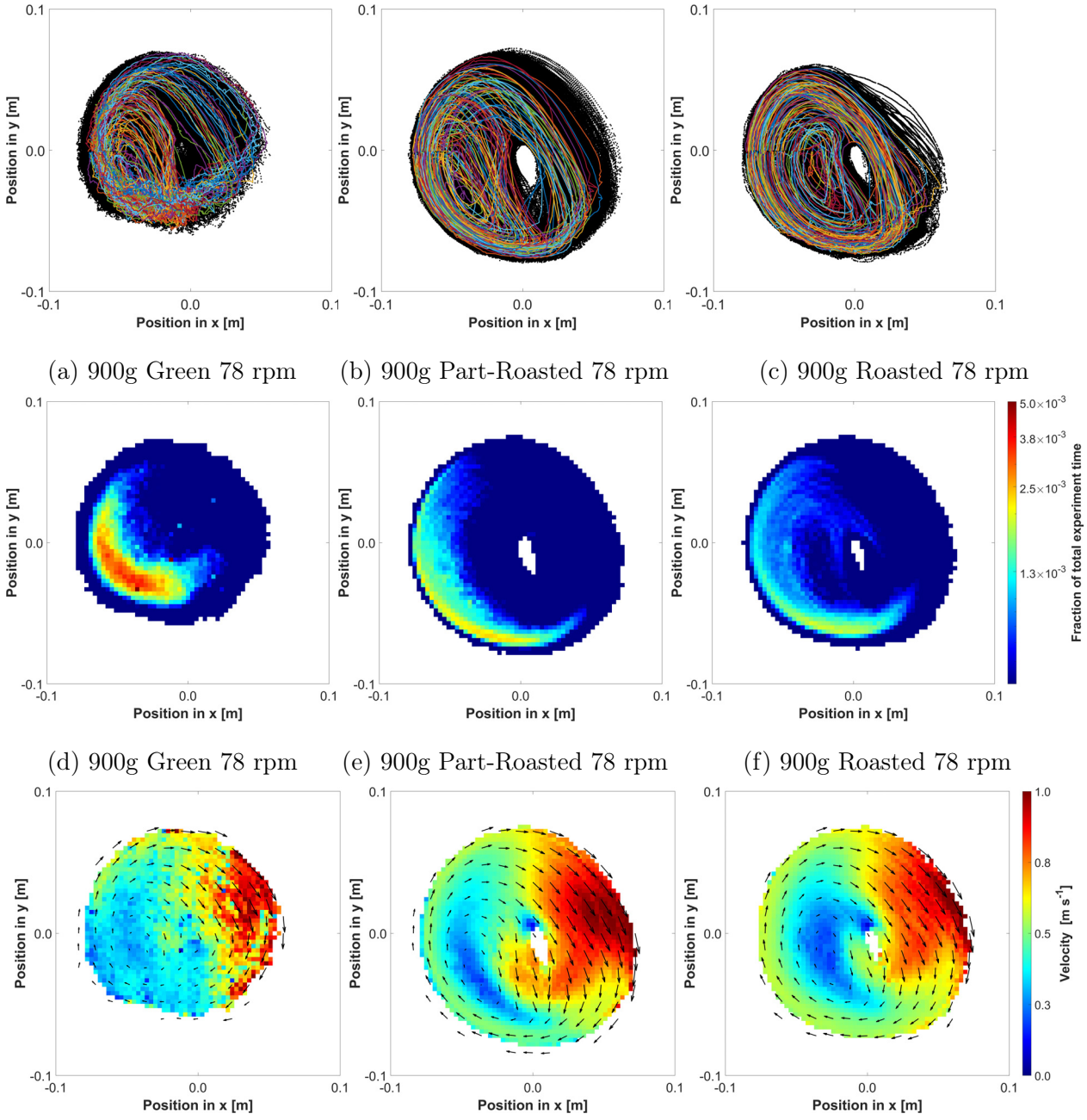

(a) 900g Green 78 rpm (b) 900g Part-Roasted 78 rpm (c) 900g Roasted 78 rpm

(d) 900g Green 78 rpm (e) 900g Part-Roasted 78 rpm (f) 900g Roasted 78 rpm

(g) 900g Green 78 rpm (h) 900g Part-Roasted 78 rpm (i) 900g Roasted 78 rpm

Figure 4.36: Experimental PEPT data detailing (a)-(c) Cartesian data overlayed with individual particle trajectories, (d)-(f) occupancy profiles and (g)-(i) velocity profiles for 900 g of (a),(d),(g) green, (b),(e),(h) part-roasted and (c),(f),(i) roasted coffee operated at 78 rpm, depicting the impact of roast degree.

Chapter Five

Modelling coffee's physicochemical transformation during roasting

In food systems, transient physicochemical phenomena are oftentimes complex and require simplification to enable quantification. During roasting, the numerous changes in coffee's physicochemical properties (described in Chapter 3) can be mapped using kinetic models to describe their change in time according to different process conditions. Analysis of the estimated parameters in these models across roaster design and scale, process conditions, and green coffee components will help to develop a comprehensive tool built on a network of kinetic models that developers can use to predict (i) product properties resulting from specified process conditions and known green coffee properties, (ii) prescribed process conditions (i.e., time-temperature profile) required to transform a green coffee with known properties to specified product properties, or (iii) green coffee properties required to produce a specified product with a prescribed time-temperature profile. Whilst there is difficulty in fully capturing the complexity of a real food system (Van Boekel, 1996; Peleg, Normand, and Corradini, 2012), if the transformation of a food's physicochemical properties are considered analogous to chemical reaction kinetics, simplified models of can be generated (Corradini and Peleg, 2006a).

In this section, kinetic models are developed based on data generated in case studies I-II of Chapter 3. Coffee's transformation during roasting is mapped across process conditions by

modelling the mass and moisture loss, porous development, volumetric expansion and density evolution. The exothermic reactions that occur at the end of roasting are also considered. These empirical models can be used to directly inform product and process development, but can also be nested within heat and mass transfer simulations to accurately predict roasting time-temperature profiles - as shown later in Chapter 6.

5.1 Methodology

5.1.1 Chemical reaction analogies

Due to the complex reaction network that drives the physicochemical transformation of coffee during roasting, development of a mechanistic model to describe coffee's transformation is not a simple task. Using the chemical reaction analogy, whereby n^{th} order reaction kinetics are combined with Arrhenius-type rate constants, coffee's physicochemical properties can be likened to a chemical concentration. The complex physicochemical mechanisms can therefore be emulated using process-dependent parameters that will allow developers to predict roasting behaviour within the experimental range.

For a given dimensionless intrinsic property (Y), the rate of change of Y (i.e., $\frac{dY}{dt}$) is a function of temperature, T (K), the reaction rate, k_Y (s^{-1}), activation energy, E (J mol^{-1}), universal gas constant, R (J mol^{-1} K^{-1}) and reaction order index, n_Y. The ordinary differential equation that governs the rate of change of Y is then (Levenspiel, 1999):

$$\frac{dY}{dt} = -k_Y \exp\left(-\frac{E}{RT}\right) Y^{n_Y} \tag{5.1}$$

For application to coffee's physicochemical transformation during roasting, two terms in Eq. 5.2 are reconsidered. Firstly, temperature, T, is assumed equal to the bean temperature, T_b, measured by the roaster's product thermocouple, which relates to the measurement of coffee beans and air in the roasting chamber as discussed in Chapters 1-2. Whilst this will inherently reduce the accuracy and robustness of the estimated parameters, relative to the use of the actual bean temperature (which is more difficult to measure and validate in real roasting systems - but can be predicted using heat and mass transfer simulations as demonstrated in Chapters 6-7), this will enable developers to implement the generated models with no adaptation. Secondly, the units of the activation energy, E and universal gas constant R can be confusing. How can the number of moles of coffee be quantified? To avoid this existential issue, the activation energy, $E_{a,Y}$ (K) will replace the ratio of E/R (Levenspiel, 1999; Peleg, Normand, and Corradini, 2012).

In this way, Eq. 5.2 applied here to the transformation of a coffee's intrinsic property (dimensionless in this example) during roasting becomes:

$$\frac{dY}{dt} = -k_Y \exp\left(-\frac{E_{a,Y}}{T_b}\right) Y^{n_Y} \tag{5.2}$$

For Eq. 5.2, an initial value problem was implemented in MATLAB (2022a, Mathworks), with a non-linear least squares fitting procedure to estimate parameters (k_Y, $E_{a,Y}$, n_Y) using the Levenberg-Marquardt algorithm. The procedure (i) minimises the sum of squares according to the cost function, Δ_Y (i.e., the sum-of-squared differences between experimental and simulated values) to a specified first-order optimality, where the function tolerance (i.e., the gradient of cost function) is small ($<$ 1e-8), (ii) constrains parameters to specified bounds, (iii) generates initial guesses (i.e., starting points) of parameters as random points within the specified bounds and (iv) is iterated three times to ensure a global minimum is located. The estimated parameters that yield the lowest relative error are used for validation and data visualisation.

In the solver: (i) an ODE is established based on Eq. 5.2, (ii) experimental data are interpolated across the experimental time span (with a fixed time-step of 0.1 s) using a smoothing spline (smoothing parameter, p = 1), (iii) a stiff-solver (ode23s) is used to solve the specified ODEs, (iv) initial values are experimental data at t=0 (i.e., green coffee data).

For each test case, the Root Mean Squared Error (RMSE) is calculated as the difference of the solutions using the estimated parameters and the experimental values. For validation, data are presented as time-series, and parity plots are used to compare experimental and predicted data.

Data from case studies I & II in Chapter 3 were used for model development. In these experimental studies, the effect of batch size and airflow (case study II) on coffee's physicochemical transformation was greater than the influence of constant inlet air temperature (case study I), therefore data from case study II were first used to estimate model parameters, with data from case study I used to validate and assess the robustness of the generated models. During parameter estimation, first and second order kinetics (i.e., $n = 1$ or $n = 1$ in Eq. 5.2) were

explored. To represent these physical transformations using the chemical reaction analogy, it is difficult to assess the relevance of reaction order. In this way, first order kinetics were preferred, with second order kinetics only specified if the increased reaction order significantly reduced the RMSE of model. In some cases, second order kinetics improved predictions at early and late times, fully capturing the response's delay corresponding to the activation energy and the properties decreased rate of change as roasting progressed.

5.2 Modelling coffee's mass loss

5.2.1 Variation of batch size and airflow

First order kinetics (i.e., $n = 1$ in Eq. 5.2) were used to model and predict mass loss (i.e., reduction in batch size (mass basis), m_{bs} (g)) during roasting, such that:

$$\frac{dm_{bs}}{dt} = -k_{m_{bs}} \exp\left(-\frac{E_{a,m_{bs}}}{T_b}\right) m_{bs} \tag{5.3}$$

During parameter estimation, model parameters (rate constant, $k_{m_{bs}}$ (s^{-1}) and activation energy, $E_{a,m_{bs}}$ (K)) were estimated with imposed constraints of $0.001 \leq k_{m_{bs}} \leq 0.010$ s^{-1} & $100 \leq E_{a,m_{bs}} \leq 2000$ K but revealed no correlation between activation energy and process conditions. A second pass parameter estimation was then performed with activation energy specified as the mean value from the first pass (i.e., $E_{a,m_{bs}} = 656.8$ K) and the rate constant constrained as before ($0.001 \leq k_{m_{bs}} \leq 0.010$ s^{-1}).

For first order kinetics based on bean temperature, with an activation energy insensitive to process conditions, Eq. 5.4 predicts coffee's mass loss during roasting with good accuracy at all roasting times (RMSE = 2.11 g) and is robust to different batch sizes and airflows.

$$\frac{dm_{bs}}{dt} = -k_{m_{bs}} \exp\left(-\frac{656.8}{T_b}\right) m_{bs} \tag{5.4}$$

A comparison of predicted (via Eq. 5.4) and experimental mass loss for first order kinetics are presented as time-series data in Figure 5.1 and a parity plot in Figure 5.2; to compare across batch sizes, data are presented as normalised mass loss (i.e., as a fraction of initial batch mass).

The impact of process conditions (i.e., batch size and airflow) on the mass loss rate constant is presented in Figure 5.3 and shows that high air flows and lower batch sizes correspond to greater mass loss rates. From these data, a statistical model to predict the mass loss rate constant was defined as a function of initial batch size, $m_{bs,0}$ (kg) and air mass flow rate, G_a (kg s^{-1}), where R^2=0.9732:

$$k_{m_{bs}} = 3.59 \times 10^{-3} - 5.63 \times 10^{-3} m_{bs,0} + 6.30 \times 10^{-2} G_a \tag{5.5}$$

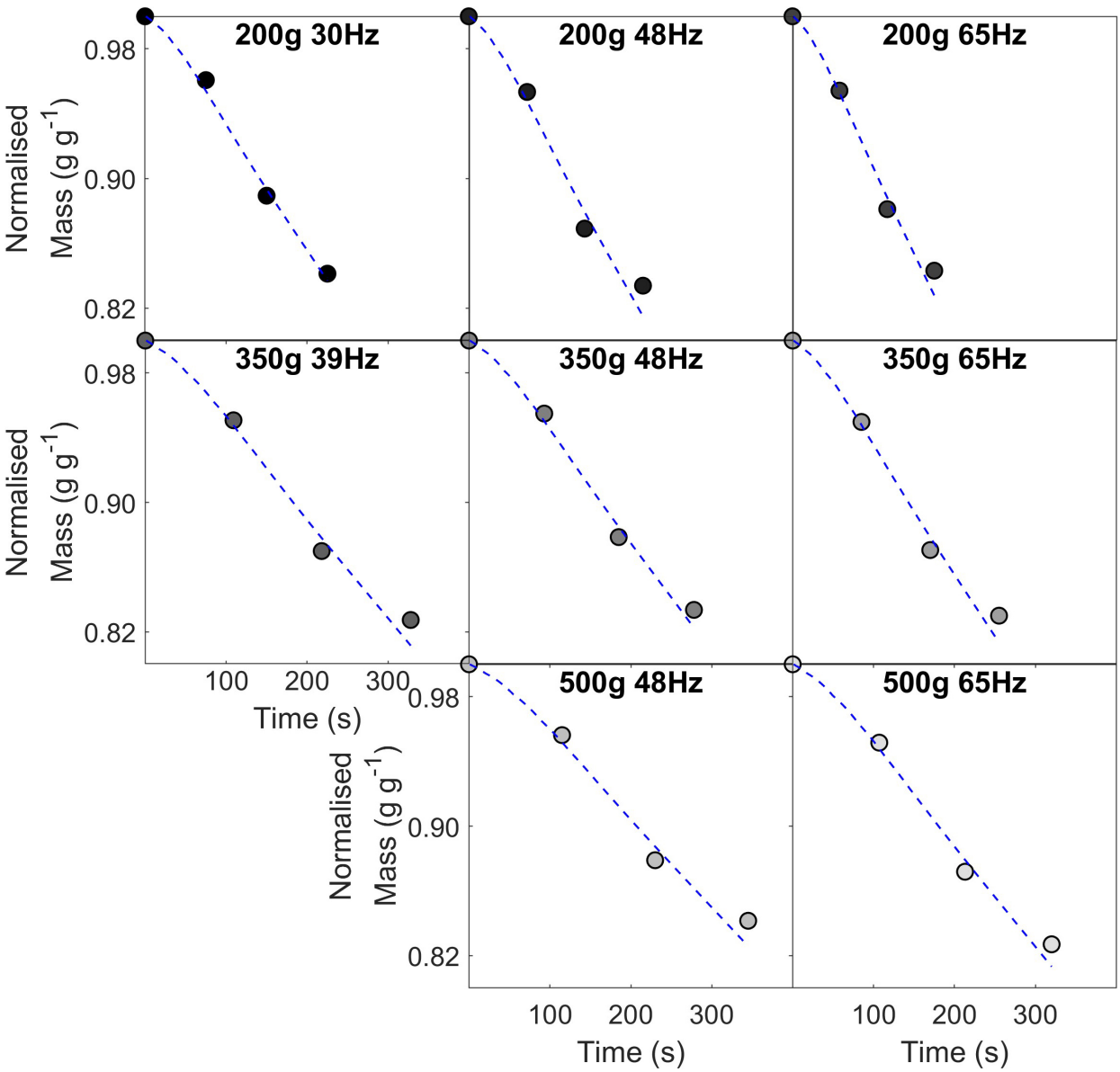

Figure 5.1: Comparison of predicted (dashed blue lines) and experimental (greyscale markers) data normalised mass loss profiles modelled using 1st order kinetics (via Eq. 5.4) for the variation of batch size and airflow study (experimental data shown in Chapter 3) - data presented as kinetic time-series.

Within the bounds of the experimental study, coupling Eqs. 5.4 & 5.5 enabled prediction of mass loss with good accuracy at all roasting times. However, if the model were extrapolated in time, beyond what was experimentally captured, even if exothermic reactions do not dominate, the model is expected to overestimate mass loss. These deviations are likely incurred by endo- and exo-thermic phenomena that were observed as product temperature disturbances in the time-temperature profiles in Chapter 3.

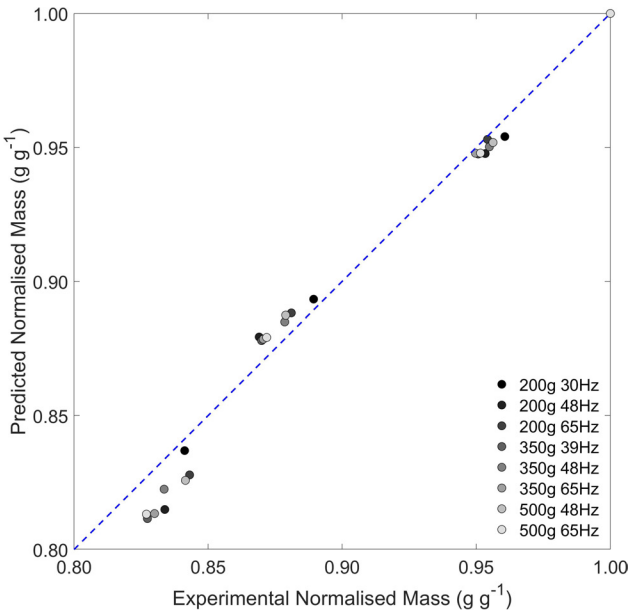

Figure 5.2: Comparison of predicted (dashed blue lines) and experimental (greyscale markers) data normalised mass loss profiles modelled using 1st order kinetics (via Eq. 5.4) for the variation of batch size and airflow study (experimental data shown in Chapter 3) - data presented as parity plot.

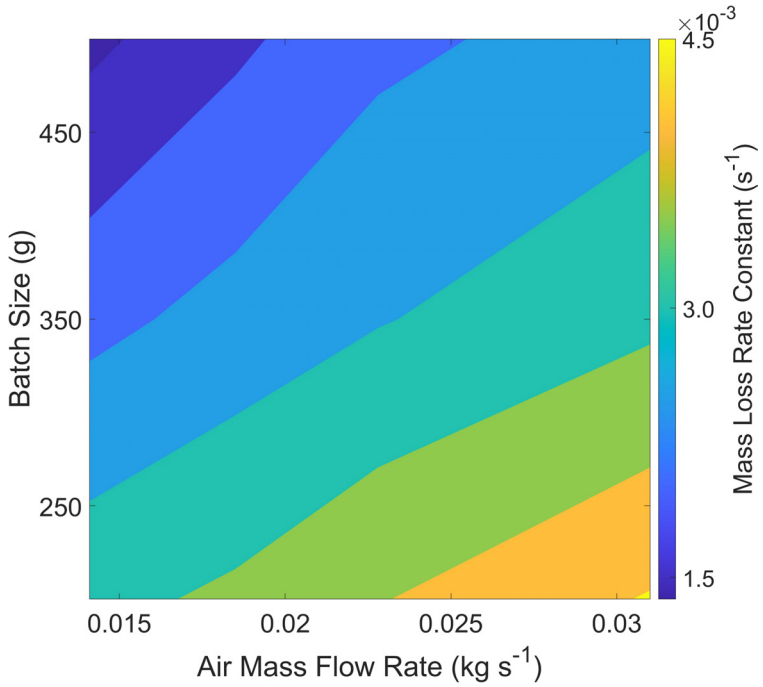

Figure 5.3: Impact of process conditions (i.e., batch size and airflow) on the rate constant (Eq. 5.5) for 1st order kinetic models of mass loss (from Eq. 5.4).

5.2.2 Variation of constant inlet air temperature

For the data presented in Chapter 3, coffee's mass loss was again modelled using first order kinetics, with the activation energy specified as in Eq. 5.4. The rate coefficient was estimated with imposed constraints of $0 \leq k_{m_{bs}} \leq 1$ s^{-1}.

First order kinetics captured in Eq. 5.4 also predict coffee's mass loss during roasting with different constant inlet air temperatures with good accuracy at all roasting times (RMSE = 5.1 g).

Figure 5.4 presents a comparison of predicted and experimental data, with a parity plot presented in Figure 5.5. To compare across batch sizes, data are presented as normalised mass loss (i.e., as a fraction of initial batch mass).

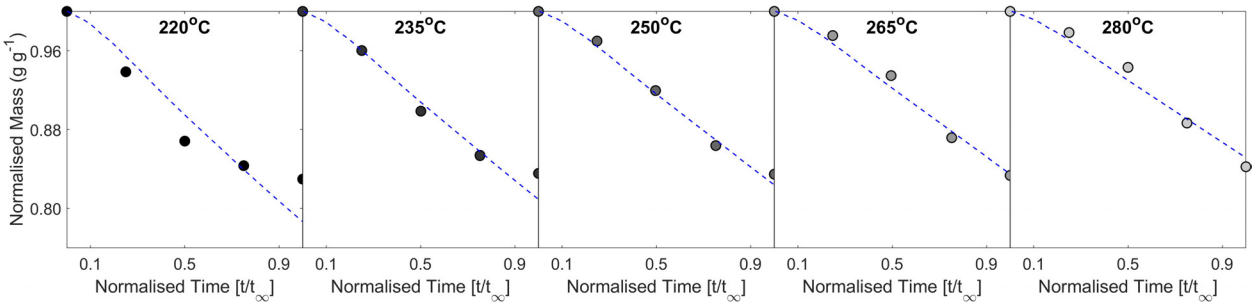

Figure 5.4: Comparison of predicted (dashed blue lines) and experimental (greyscale markers) data for 1st order kinetic models of mass loss (via Eq. 5.4) for the constant inlet air temperature study (experimental data shown in Chapter 3) - data presented as kinetic time-series.

The rate coefficient, $k_{m_{bs}}$ (s^{-1}) depended on the constant inlet air temperature, $T_{a,i}$ (K), where R^2=0.994.

$$k_{m_{bs}} = 4.21 \times 10^{-5} T_{a,i} - 0.0192 \tag{5.6}$$

As shown in Figure 5.6, higher constant inlet air temperatures increased the rate coefficient, with a similar effect (and in a similar range) as was observed for different combinations of batch size and airflow.

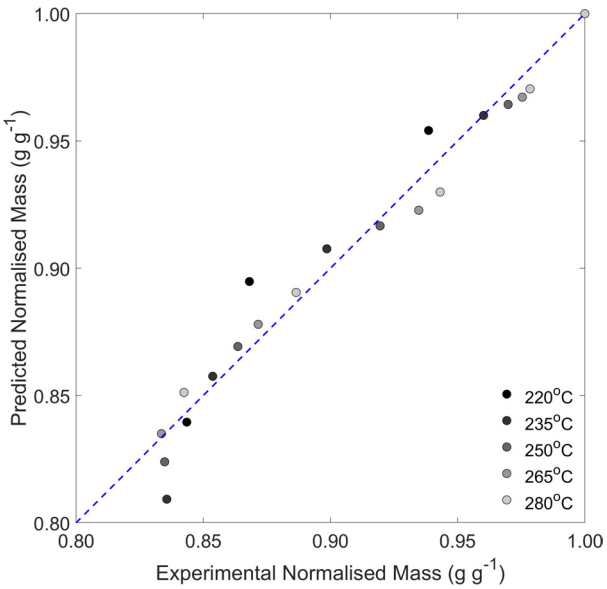

Figure 5.5: Comparison of predicted (dashed blue lines) and experimental (greyscale markers) data for 1st order kinetic models of mass loss (via Eq. 5.4) for the constant inlet air temperature study (experimental data shown in Chapter 3) - data presented as parity plot.

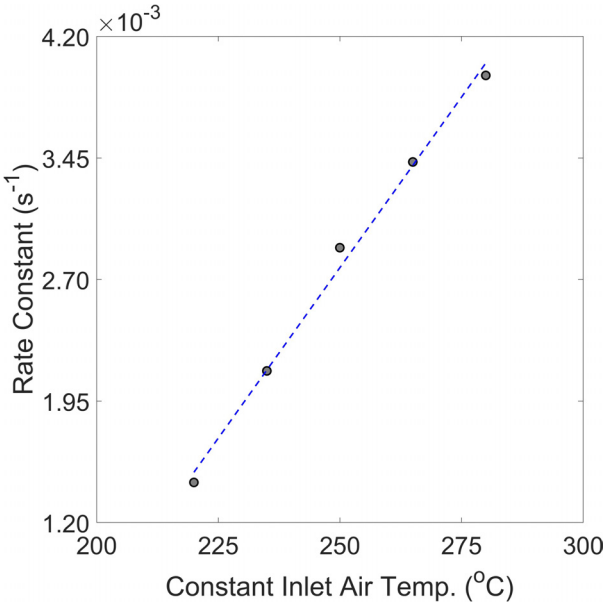

Figure 5.6: Correlation of rate coefficient and constant inlet air temperature (Eq. 5.6) for 1st order kinetic models of mass loss (via Eq. 5.4) for the constant inlet air temperature study.

5.3 Modelling coffee's moisture loss

5.3.1 Variation of batch size and airflow

Second order kinetics (i.e., $n = 2$ in Eq. 5.2) were used to model and predict the change in coffee's moisture content, X_b (kg kg^{-1}) during roasting (in a similar approach to Schwartzberg (2002)), such that:

$$\frac{dX_b}{dt} = -k_{X_b} \exp\left(-\frac{E_{a,X_b}}{T_b}\right) X_b^2 \tag{5.7}$$

For parameter estimation, the model's rate constant, k_{X_b} (s^{-1}) and activation energy, E_{a,X_b} (K) were estimated with imposed constraints of $1 \times 10^6 \leq k_{X_b} \leq 1 \times 10^7$ s^{-1} and $7500 \leq E_{a,X_b} \leq 8500$ K. Predicted moisture kinetics agreed well with experimental data (RMSE = 0.005 kg kg^{-1}) but activation energy and rate constant had no clear impact on the predicted moisture kinetics within the specified constraints. Mean estimated parameters ($k_{X_b} = 4.13 \times 10^6$ s^{-1}; E_{a,X_b}=7908 K) from the first-pass estimation were used to correlate moisture loss for all roasting conditions with no significant impact on the model's accuracy ($\Delta_{RMSE} \approx$ 0.000 kg kg^{-1}).

For second order kinetics based on bean temperature, with an activation energy insensitive to process conditions, Eq. 5.8 predicts moisture loss with good accuracy at all roasting times (RMSE = 0.005 kg kg^{-1}).

$$\frac{dX_b}{dt} = -4.13 \times 10^6 \exp\left(-\frac{7908}{T_b}\right) X_b^2 \tag{5.8}$$

A comparison of predicted and experimental moisture loss for second order kinetics are presented as time-series data in Figure 5.7 and a parity plot in Figure 5.8.

For different batch sizes and airflows, and at all roasting times, Eq. 5.8 can be used to predict moisture loss with good accuracy, although a greater sampling frequency would be beneficial to more accurately capture the early- and long-time behaviour during roasting.

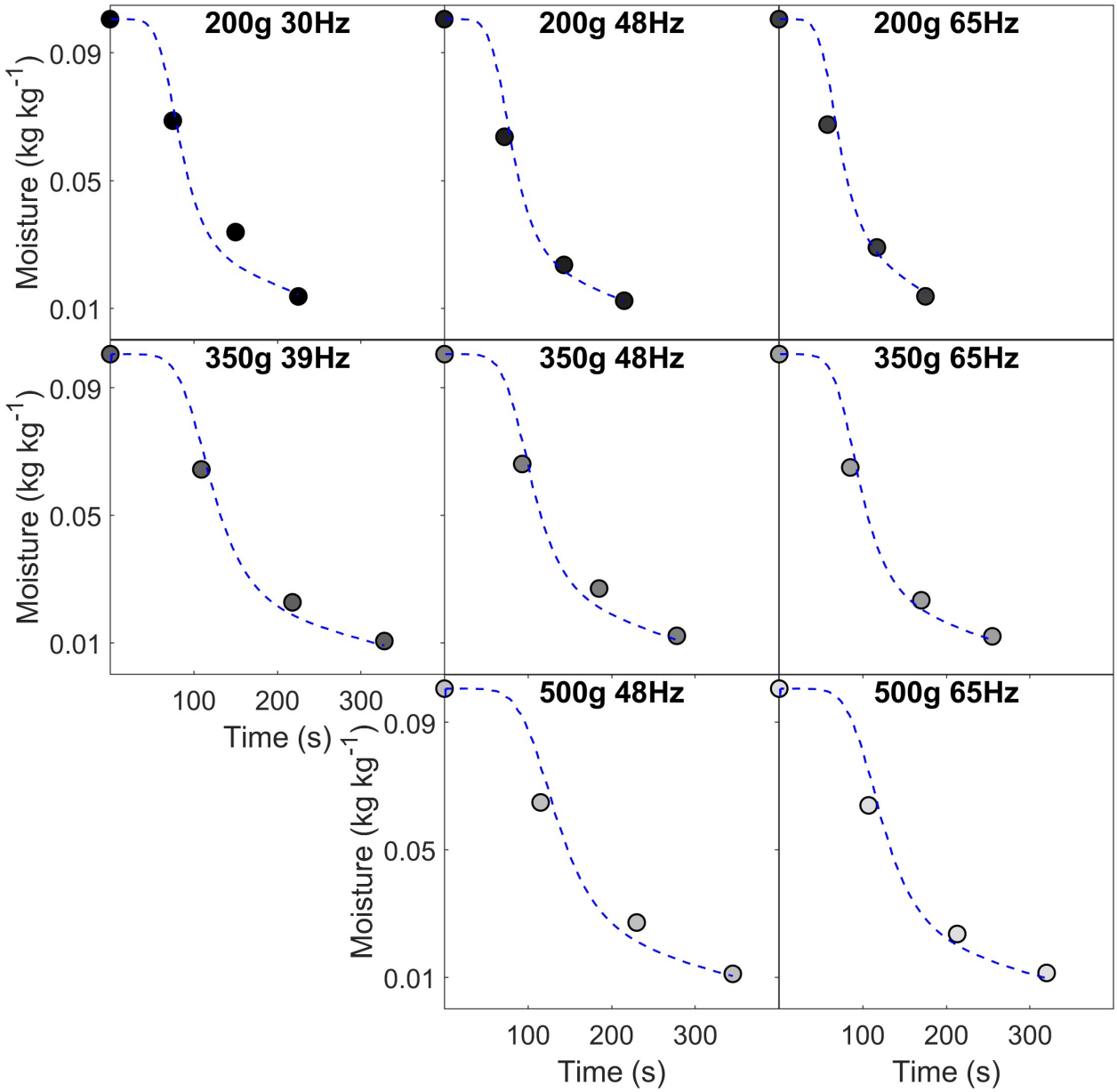

Figure 5.7: Comparison of predicted (dashed blue lines) and experimental (greyscale markers) moisture loss profiles modelled using 2nd order kinetics (Eq. 5.8) for the variation of batch size and airflow study (experimental data shown in Chapter 3) - data presented as kinetic time-series.

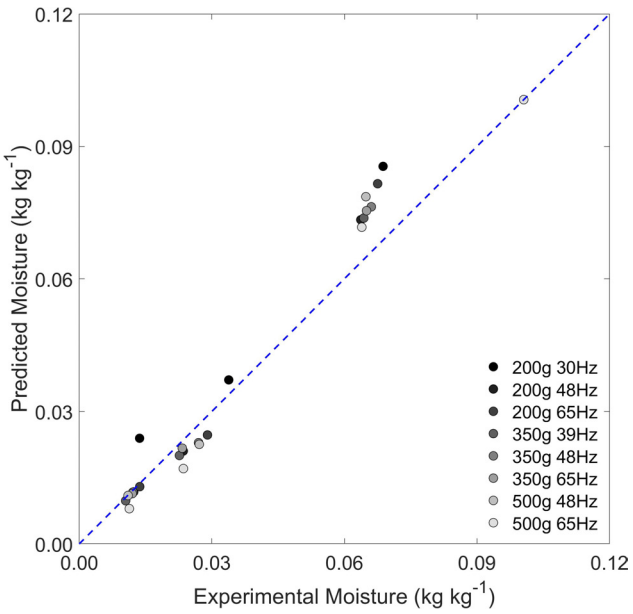

Figure 5.8: Comparison of predicted (dashed blue lines) and experimental (greyscale markers) moisture loss profiles modelled using 2nd order kinetics (Eq. 5.8) for the variation of batch size and airflow study (experimental data shown in Chapter 3) - data presented as parity plot.

5.3.2 Variation of constant inlet air temperature

Coffee's dehydration during roasting was again modelled using second order kinetics as in Eq. 5.7. Variation of the rate coefficient ($2\times10^6 \leq k_{X_b} \leq 6\times10^6 s^{-1}$) at constant activation energy (E_a = 7908 K) had little impact on predicted second order moisture kinetics (RMSE = 0.009 kg kg^{-1}), thus the estimated parameter from the variation of batch size and airflow study is used here (i.e., $k_{X_b} = 4.13 \times 10^6 s^{-1}$). Variation of activation energy ($7000 \leq E_a \leq 9000$ K) for a constant rate coefficient ($k_{X_b} = 4.13 \times 10^6 s^{-1}$) slightly improved the accuracy of the model (Δ_{RMSE} = -0.002 kg kg^{-1}) but had little impact on predicted moisture kinetics. Using both the rate coefficient and activation energy that were determined for the variation of airflow and batch size study (i.e., Eq. 5.8), the moisture kinetics were accurately predicted for roasts at different constant inlet air temperatures.

The second order model presented in Eq. 5.8 also correlates coffee's moisture during roasting with different constant inlet air temperatures with good accuracy at all roasting times (RMSE = 0.007 kg kg^{-1}).

Figures 5.9 & 5.10 present a comparison of predicted and experimental moisture kinetics.

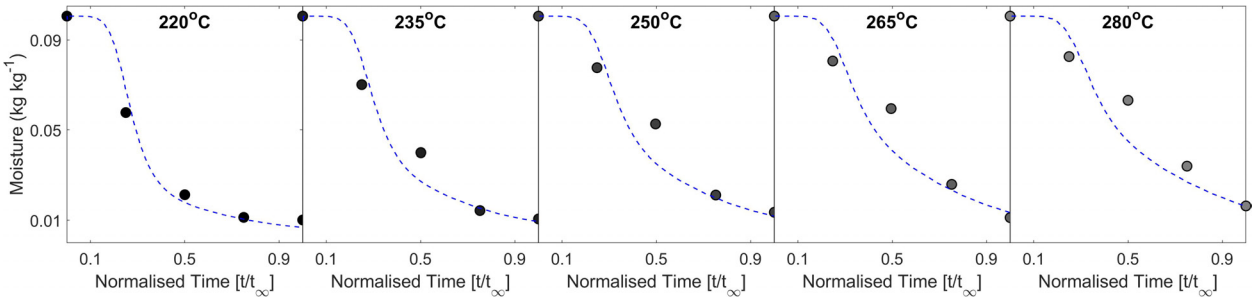

Figure 5.9: Comparison of predicted (dashed blue lines) and experimental (greyscale markers) data for 2nd order kinetic models of moisture loss (Eq. 5.8) for the constant inlet air temperature study (experimental data shown in Chapter 3) - data presented as kinetic time-series.

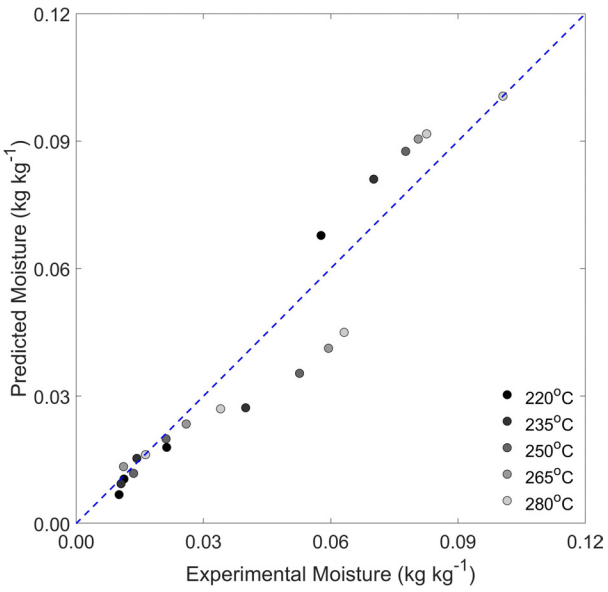

Figure 5.10: Comparison of predicted (dashed blue lines) and experimental (greyscale markers) data for 2nd order kinetic models of moisture loss (Eq. 5.8) for the constant inlet air temperature study (experimental data shown in Chapter 3) - data presented as parity plot.

For higher constant inlet air temperatures in Figure 5.9, the goodness of fit for coffees roasted to $t = 0.5t_{end}$ was lower than roasts using lower constant inlet air temperatures. This lower goodness of fit suggests that although the overall RMSE of the model is low (i.e., predictions are accurate), the activation energy is temperature dependent and likely collinear with the rate constant. This collinearity is thus disguising the real physics of the system, which is not fully captured via the chemical reaction analogy. That said, Eq. 5.8 is robust to all

conditions (i.e., to variations of constant inlet air temperature, airflow and batch size) in the spouted bed roaster for the Kenyan Arabica coffee.

5.4 Modelling coffee's density evolution

5.4.1 Variation of batch size and airflow

Second order kinetics (i.e., $n = 2$ in Eq. 5.2) were used to describe the evolution of coffee's intrinsic bean density, ρb m^{-3}, during roasting, such that:

$$\frac{d\rho_b}{dt} = -k_{\rho_b} \exp\left(-\frac{E_{a,\rho_b}}{T_b}\right) \rho_b^2 \tag{5.9}$$

For parameter estimation, the model's rate constant, k_{ρ_b} (kg^{-1} m^3 s^{-1}) and activation energy, E_{ρ_b} (K) were estimated with imposed constraints of $0.001 \leq k_{\rho_b} \leq 0.010$ kg^{-1} m^3 s^{-1} and $1000 \leq E_{\rho_b} \leq 3000$ K). Neither the rate constant nor activation energy correlated with process conditions. The rate constant's high sensitivity lead to a second pass parameter estimation with a specified value ($k_{\rho_b} = 0.001$ kg^{-1} m^3 s^{-1}) whilst the activation energy was constrained as before ($1000 \leq E_{\rho_b} \leq 3000$ K).

For second order kinetics based on bean temperature, with a specified rate constant, Eq. 5.10 predicts coffee's density evolution during roasting with good accuracy at all roasting times (RMSE = 67 kg m^{-3}) and is robust to different batch sizes and airflows.

$$\frac{d\rho_b}{dt} = -0.001 \exp\left(-\frac{E_{a,\rho_b}}{T_b}\right) \rho_b^2 \tag{5.10}$$

A comparison of predicted (via Eq. 5.10) and experimental density evolution for second order kinetics are presented as time-series data in Figure 5.11 and a parity plot in Figure 5.12.

The impact of process conditions (i.e., batch size and airflow) on the density evolution rate constant is presented in Figure 5.13 and shows that high air flows and lower batch sizes correspond to greater evolution rates. From these data, a statistical model to predict the activation energy associated with density evolution was defined as a function of initial batch

size, $m_{bs,0}$ (g) and air mass flow rate, G_a (kg s^{-1}), where R^2=0.979:

$$E_{a,\rho_b} = 2398 + 0.923 m_{bs,0} - 11405 G_a \tag{5.11}$$

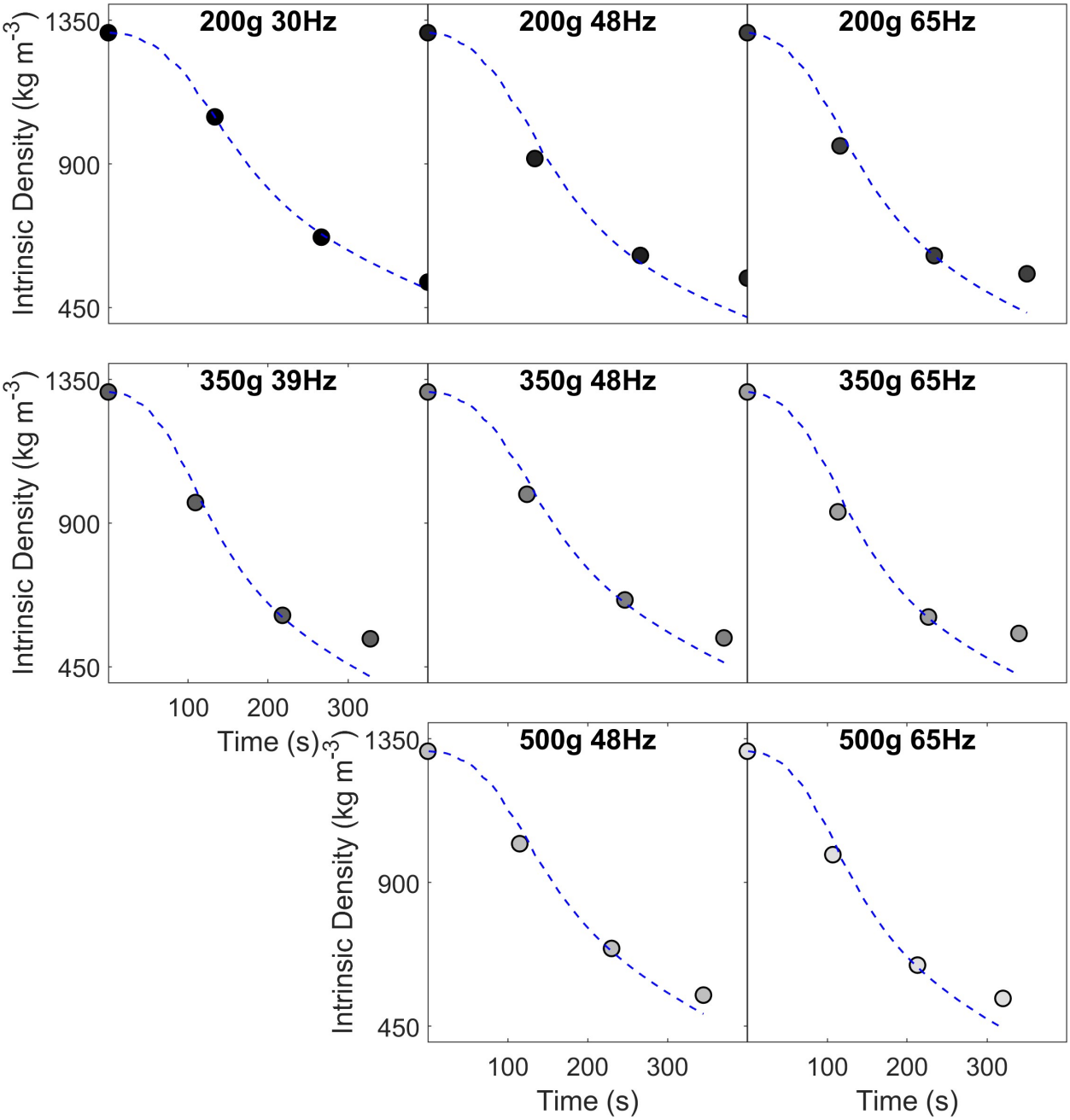

Figure 5.11: Comparison of predicted (dashed blue lines) and experimental (greyscale markers) density evolution profiles modelled using 2nd order kinetics (Eq. 5.10) for the variation of batch size and airflow study (experimental data shown in Chapter 3) - data presented as kinetic time-series.

At early-to-moderate times (t $\leq$ 100 s), coupling Eqs. 5.10 & 5.11 enabled prediction of the onset (activation energy) of coffee's density evolution (as shown in Figure 5.11) - at the same constant inlet air temperature with different airflows and batch sizes - with good accuracy. At longer times, the model underestimates the experimental results. Although the error is small at the captured roasting times, the rapid deceleration in the change of density (in the range of $150 \leq t \leq 250$) implies there is a physical phenomenon that the chemical reaction rate analogy was unable to capture. To better understand density changes during roasting, experimental data of moisture, mass, porosity and volume data would be required with an increased sampling frequency; these data might correlate with the coffee's glass transition temperature (Geiger, 2004).

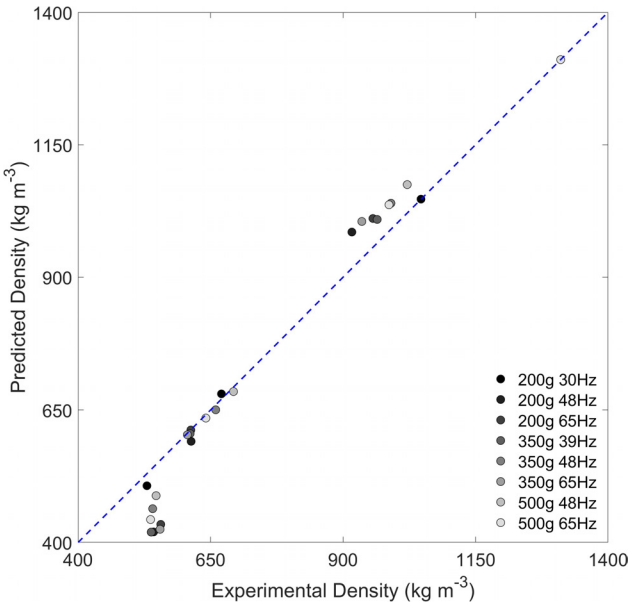

Figure 5.12: Comparison of predicted (dashed blue lines) and experimental (greyscale markers) density evolution profiles modelled using 2nd order kinetics (Eq. 5.10) for the variation of batch size and airflow study (experimental data shown in Chapter 3) - data presented as parity plot.

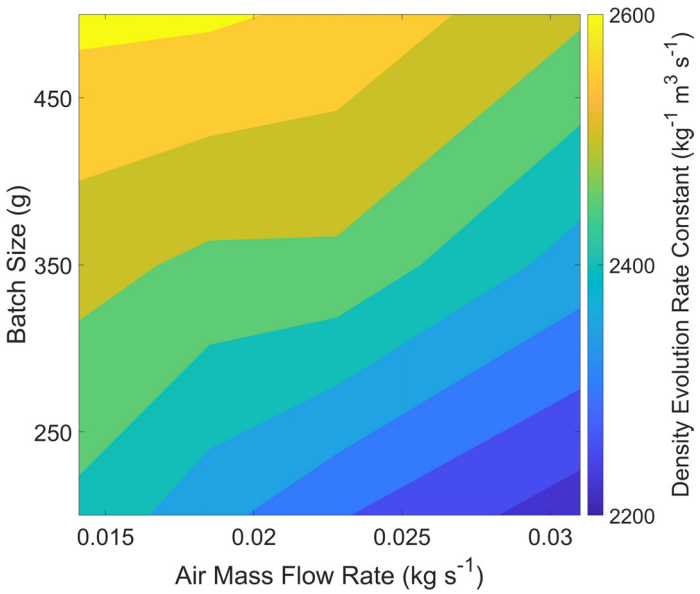

Figure 5.13: Impact of process conditions (i.e., batch size and airflow) on the rate constant (Eq. 5.11) for 2nd order kinetic models of density evolution (Eq. 5.10).

5.4.2 Variation of constant inlet air temperature

The evolution of coffee's intrinsic bean density was again modelled using second order kinetics as in Eq. 5.9. During parameter estimation, the rate constant, k_{ρ_b} (kg^{-1} m^3 s^{-1}) was highly sensitive, so was specified as in the variation of batch size and airflow study (i.e., $k_{\rho_b} = 0.001$ kg^{-1} m^3 s^{-1}). To evaluate Eq. 5.10's application to different constant inlet temperatures, the activation energy was estimated in the range $1000 \leq E_{a,\rho_b} \leq 3000$ (K). For second order kinetics based on bean temperature, with a specified rate constant, Eq. 5.10 also predicts coffee's density evolution during roasting with different constant inlet air temperatures with good accuracy at all roasting times (RMSE = 56 kg m^{-3}).

A comparison of predicted (via Eq. 5.10) and experimental density evolution for second order kinetics are presented as time-series data in Figure 5.14 and a parity plot in Figure 5.15.

The activation energy corresponding to density evolution, E_{a,ρ_b} (K), was correlated with constant inlet air temperature, $T_{a,i}$ (K). Using a two-term power law function, the activation

energy can be estimated via the constant inlet air temperature, where R^2=0.952:

$$E_{a,\rho_b} = 2.22 \times 10^6 \left(\frac{1}{T_{a,i}}\right) - 1663 \tag{5.12}$$

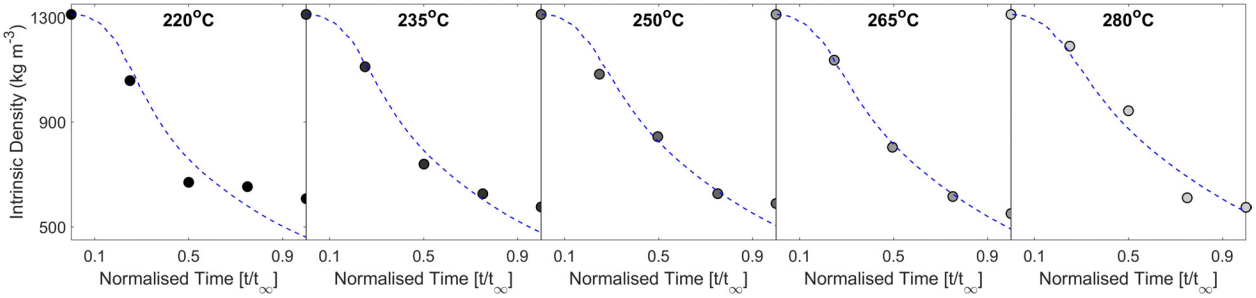

Figure 5.14: Comparison of predicted (dashed blue lines) and experimental (greyscale markers) density evolution profiles modelled using 2nd order kinetics (Eq. 5.10) for the constant inlet air temperature study (experimental data shown in Chapter 3) - data presented as kinetic time-series.

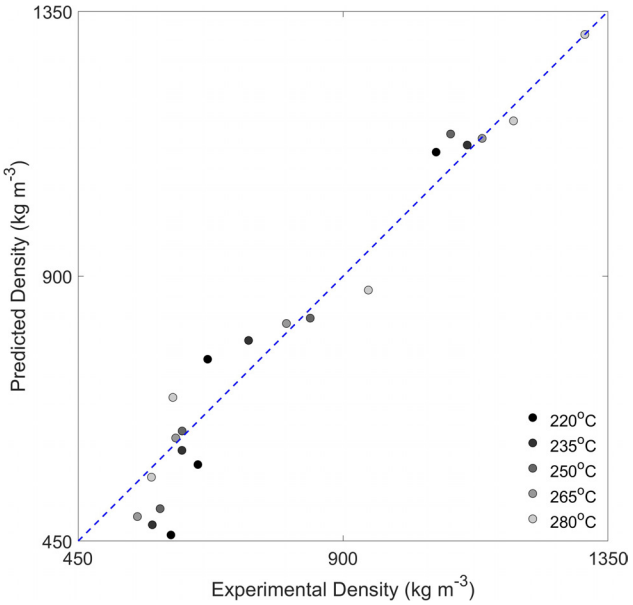

Figure 5.15: Comparison of predicted (dashed blue lines) and experimental (greyscale markers) density evolution profiles modelled using 2nd order kinetics (Eq. 5.10) for the constant inlet air temperature study (experimental data shown in Chapter 3) - data presented as parity plot.

As seen in Figure 5.16, higher constant inlet air temperatures correspond to lower activation energies. According to Figures 5.14-5.15, predicted density profiles are more accurate for higher constant inlet air temperatures, as those roasted at lower constant inlet air temperatures had much lower rates of evolution after first crack that were not well simulated by

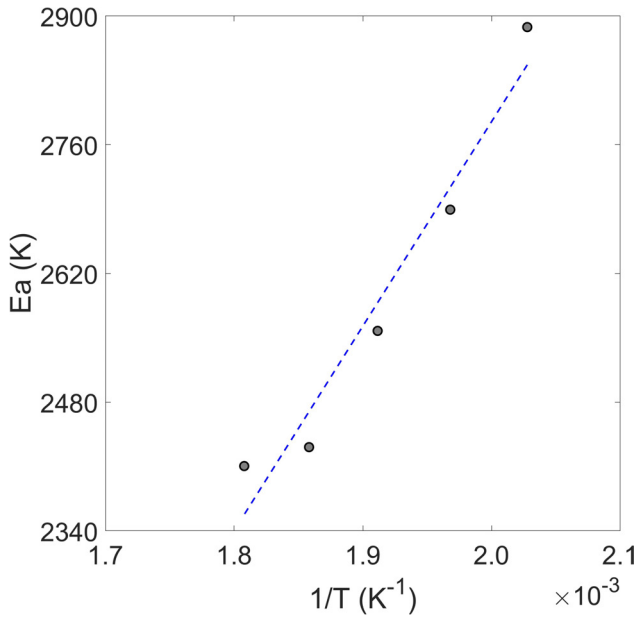

Figure 5.16: Correlation of density evolution activation energy with process temperature (Eq. 5.12) for 2nd order kinetic models of density evolution (Eq. 5.10) for the constant inlet air temperature study.

the model. Although the model provides reasonable accuracy during higher temperature roasts and at early times, where the most significant density changes occur, the falling rate phenomenon is not well captured in this model. To improve the kinetic model, phenomena resulting from events around first crack (i.e., state transitions between rubbery and glassy states) may need to be used to trigger changes in the model's rate constant and activation energy.

The 'bean' temperature used in this modelling approach is assumed equal to the product temperature – measured by a thermocouple in a cascading pile of beans. Measurement therefore depends on heat transfer from both the drying air and beans and so, corresponds to the bulk temperature (i.e., some combination of air and bean). The dependence of the activation energy on process temperature (shown in Figure 5.16) reinforces this fact. The robustness of the proposed kinetic models might be improved if a more accurate bean temperature is used. This could be obtained via (i) actual measurement of bean core temperature using a fine thermocouple (with thermocouple diameter, d_T (mm), in the range of $0.25 \leq d_T \leq 0.50$ mm) or (ii) simulation of time-temperature profiles.

5.5 Modelling coffee's volumetric expansion

5.5.1 Variation of batch size and airflow

The coffee bean's volumetric expansion (i.e., change in bean volume, V_b (mm^3)) was modelled using a modified 2nd order kinetic model that included a second term to conjugate moisture loss, defined here as the difference between initial moisture content, X_0, and moisture content at time, t, X_b, (i.e., $X_0 - X_b$ (kg kg^{-1})), which is a key driver of porosity development and subsequent volumetric expansion:

$$\frac{d(1/V_b)}{dt} = -k_{V_b} \exp\left(-\frac{E_{a,V_b}}{T_b}\right)\left(\frac{1}{V_b}\right)^2 + k'_{X_b} \exp\left(-\frac{E'_{a,X_b}}{T_b}\right)(X_0 - X_b) \tag{5.13}$$

For the volumetric expansion rate coefficient, k_{V_b} (mm^3 s^{-1}), with imposed constraints of $1 \leq k_{V_b} \leq 50$ (mm^3 s^{-1}), variation of activation energy in the range $500 \leq E_{a,V_b} \leq 1500$ (K) had no clear impact on predicted volumetric expansion, and the system's behaviour was subsequently lumped into k_{V_b}. A value of $E_{a,V_b} = 1500$ K was therefore specified, with k_{V_b} estimated with imposed constraints of $1 \leq k_{V_b} \leq 50$ (mm^3 s^{-1}). The moisture coupled rate coefficient, k'_{X_b} (s^{-1}) and activation energy, E'_{a,X_b} (K) were insensitive to applied process temperatures and specified as 0.04 s^{-1} and 3000 K.

The modified second order model (Eq. 5.14) predicts bean volume with good accuracy at all roasting times (RMSE = 5.8 mm^3) and is robust to different batch sizes and airflows.

$$\frac{d(1/V_b)}{dt} = -k_{V_b} \exp\left(-\frac{1500}{T_b}\right)\left(\frac{1}{V_b}\right)^2 + 0.04 \exp\left(-\frac{3000}{T_b}\right)(X_0 - X_b) \tag{5.14}$$

Figure 5.17 presents a time-series comparison of predicted and experimental volumetric expansion, whilst Figure 5.18 displays a parity plot of these data.

The impact of process conditions (i.e., batch size and airflow) on the volumetric expansion rate constant is presented in Figure 5.19 and shows that high air flows and lower batch sizes give to greater volumetric expansion rates. From these data, a statistical model to predict the volumetric expansion rate constant was defined as a function of initial batch size, $m_{bs,0}$

(g) and air mass flow rate, G_a (kg s^{-1}), where R^2=0.964:

$$k_{V_b} = 13.26 + 0.0277 m_{bs,0} + 402 G_a \tag{5.15}$$

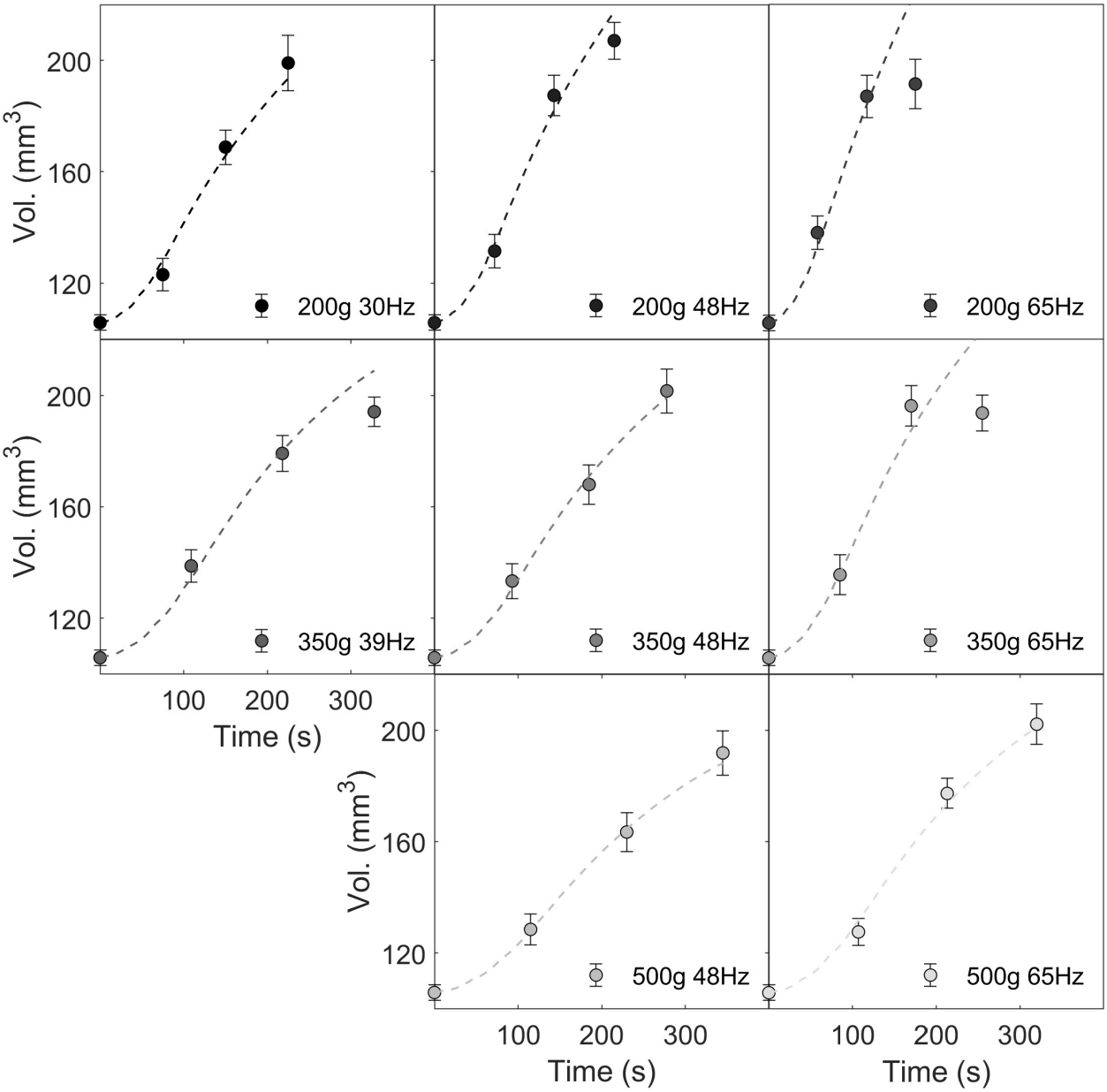

Figure 5.17: Comparison of predicted (dashed blue lines) and experimental (greyscale markers) volumetric expansion profiles modelled using modified 2nd order kinetics (Eq. 5.13) for the variation of batch size and airflow study (experimental data shown in Chapter 3) - data presented as kinetic time-series.

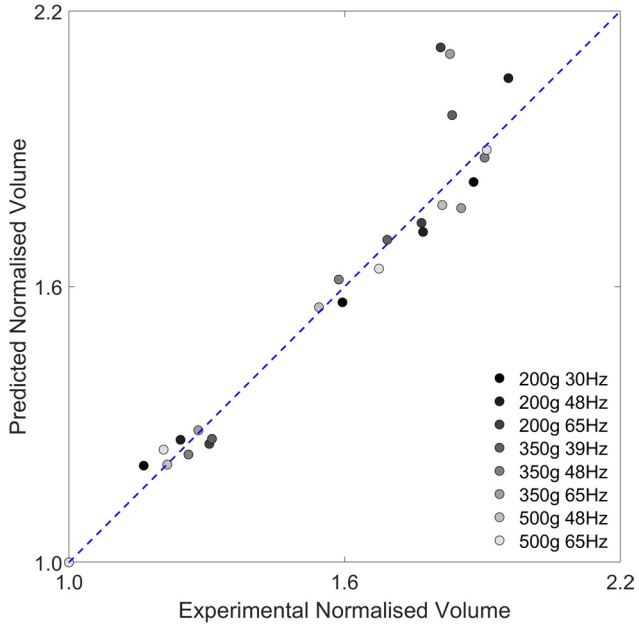

Figure 5.18: Comparison of predicted (dashed blue lines) and experimental (greyscale markers) volumetric expansion profiles modelled using modified 2nd order kinetics (Eq. 5.13) for the variation of batch size and airflow study (experimental data shown in Chapter 3) - data presented as parity plot.

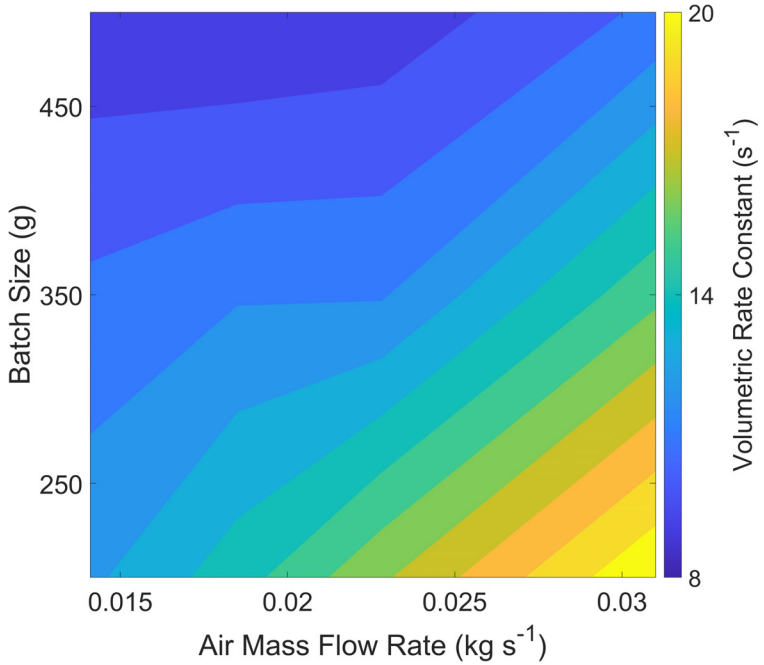

Figure 5.19: Impact of process conditions (i.e., batch size and airflow) on the rate constant (Eq. 5.15) for modified 2nd order kinetic models of volumetric expansion (Eq. 5.13).

Coupling Eqs. 5.14 & 5.15 enabled prediction of the coffee bean's volumetric expansion at early-to-moderate times (t $\leq$ 100 s) during roasting - at the same constant inlet air temperature with different airflows and batch sizes - with good accuracy. At longer times, coffee's cellular material transitions from the rubbery-state back to the glassy-state around the time of first crack, whereby volumetric expansion is inhibited (Geiger, 2004). This physical phenomenon is not well captured within the model, so coffee's volume is overestimated for high airflow and low batch size process conditions. To increase the real-system accuracy of the model would require reconsideration of the (i) low sampling frequency, (ii) experimental uncertainty of coffee's intrinsic volume post-first crack and (iii) thermal properties, particularly glass transition data to trigger changes in the rate constant.

5.5.2 Variation of constant inlet air temperature

Volumetric expansion was again modelled using a modified second order kinetic model that included a second term to conjugate coffee's moisture loss as in Eq. 5.13.

As in the variation of batch size and airflow study, for a volumetric expansion rate coefficient (k_{V_b}) with imposed constraints of $1 \leq k_{V_b} \leq 50$ (s^{-1}), variation of activation energy in the range $500 \leq E_{a,V_b} \leq 1500$ (K) had no clear impact on predicted volumetric expansion, and estimated values were subsequently lumped into k_{V_b}. A value of $E_{a,V_b} = 1500$ K was therefore specified, with k_{V_b} estimated for imposed constraints of $1 \leq k_{V_b} \leq 50$ (s^{-1}). The moisture coupled rate coefficient, k'_{X_b} (s^{-1}) and activation energy, E'_{a,X_b} (K) were similarly invariant to applied process temperatures and specified as 0.04 s^{-1} and 3000 K.

The modified second order model (Eq. 5.14) also predicts bean volume for different constant inlet air temperatures with good accuracy at all roasting times (RMSE = 8.5 mm^3).

Figure 5.20 presents a time-series comparison of predicted and experimental volumetric expansion, whilst Figure 5.21 displays these data as a parity plot.

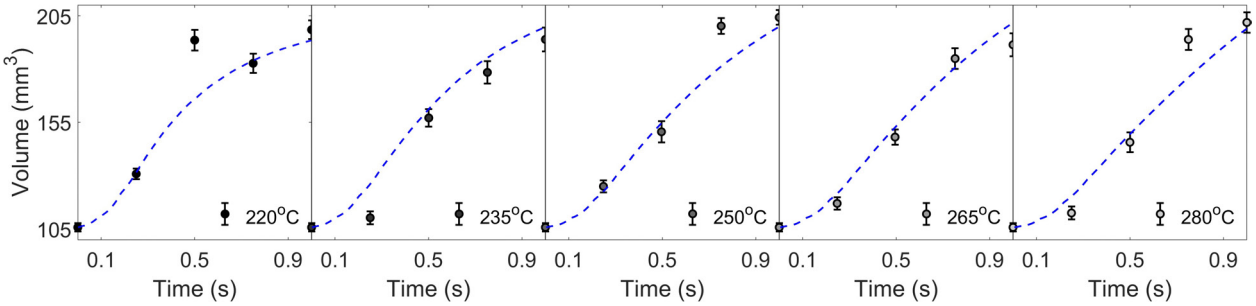

Figure 5.20: Comparison of predicted (dashed blue lines) and experimental (greyscale markers) volumetric expansion profiles modelled using modified 2nd order kinetics (Eq. 5.13) for the constant inlet air temperature study (experimental data shown in Chapter 3) - data presented as kinetic time-series.

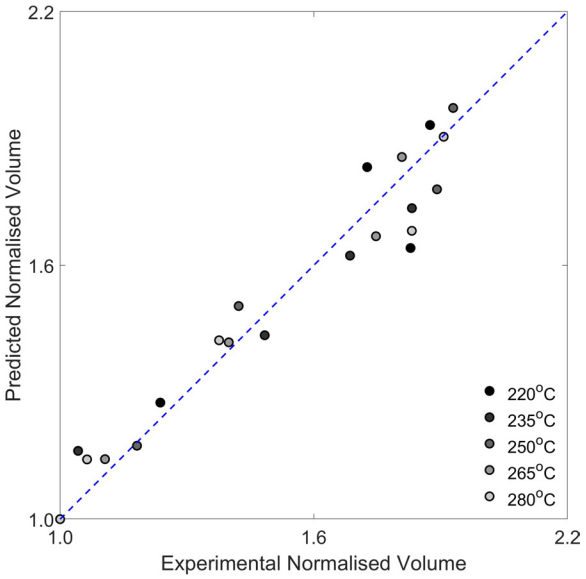

Figure 5.21: Comparison of predicted (dashed blue lines) and experimental (greyscale markers) volumetric expansion profiles modelled using modified 2nd order kinetics (Eq. 5.13) for the constant inlet air temperature study (experimental data shown in Chapter 3) - data presented as parity plot.

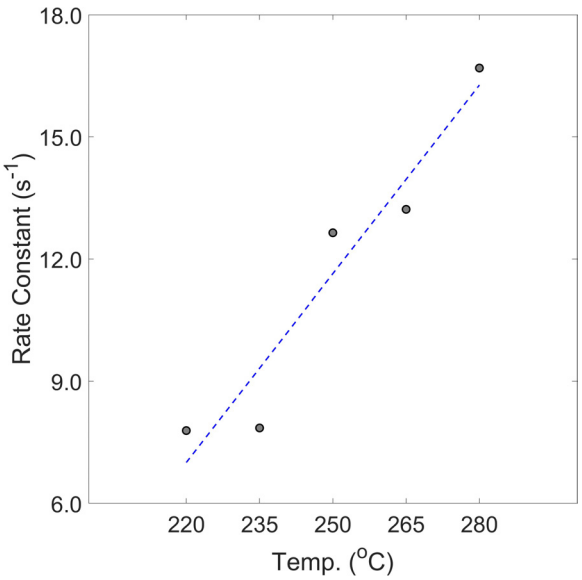

Figure 5.22: Correlation of moisture coupled rate coefficient with process temperature (Eq. 5.16) for modified 2nd order kinetic models of volumetric expansion for the constant inlet air temperature study.

The volumetric expansion rate constant, k_{V_b} (s^{-1}) was correlated with constant inlet air temperature, $T_{a,i}$ (K), as seen in Figure 5.22 (R^2=0.923), such that:

$$k_{V_b} = 0.15T_{a,i} - 69 \tag{5.16}$$

The proposed kinetic model (Eqs. 5.14-5.16) predicts volumetric expansion during roasting with good accuracy at all times. Predictions are also sensible for longer roasting times than tested ($t \leq 1.5t_{end}$) - beyond this time, model validity might fail due to the dependency on moisture kinetics that decay to zero at long times.

5.6 Modelling coffee's porosity development

5.6.1 Variation of batch size and airflow

Coffee's porosity development was modelled using a modified 2nd order kinetic model that included a second term to conjugate coffee's moisture loss, which is a key driver for porosity development and subsequent volume expansion.

$$\frac{d(1/\gamma_b)}{dt} = -k_{\gamma_b} \exp\left(-\frac{E_{a,\gamma_b}}{T_b}\right)\left(\frac{1}{\gamma_b}\right)^2 + k'_{X_b} \exp\left(-\frac{E'_{a,X_b}}{T_b}\right)(X_0 - X_b)^2 \tag{5.17}$$

For the porosity development rate coefficient, k_{γ_b} (% s^{-1}), with imposed constraints of $0.1 \leq k_{\gamma_b} \leq 10$ (% s^{-1}), variation of activation energy in the range $100 \leq E_{a,\gamma_b} \leq 1000$ (K) had no clear impact on predicted porosity development, and the system's behaviour was subsequently lumped into k_{γ_b}. A value of $E_{a,\gamma_b} = 1000$ K was therefore specified, with k_{γ_b} estimated with imposed constraints of $0.1 \leq k_{V_b} \leq 10$ (% s^{-1}). The moisture coupled rate coefficient, k'_{X_b} (s^{-1}) and activation energy, E'_{a,X_b} (K) were not sensitive to applied process temperatures in the ranges of $0.01 \leq k'_{X_b} \leq 0.05$ (s^{-1}) and $500 \leq E'_{a,X_b} \leq 1500$ (K) and were therefore specified as the midpoint in those ranges (i.e., 0.025 s^{-1} and 1000 K).

The modified second order model (Eq. 5.18) predicts the volumetric expansion of coffee during roasting with different batch sizes and airflows with good accuracy at all roasting times (RMSE = 1.1 %).

$$\frac{d(1/\gamma_b)}{dt} = -k_{\gamma_b} \exp\left(-\frac{E_{a,\gamma_b}}{T_b}\right)\left(\frac{1}{\gamma_b}\right)^2 + 0.025 \exp\left(-\frac{1000}{T_b}\right)(X_0 - X_b)^2 \tag{5.18}$$

Figure 5.23 presents a time-series comparison of predicted and experimental porosity development, whilst Figure 5.24 displays a parity plot of these data.

The impact of process conditions (i.e., batch size and airflow) on the porosity development rate constant is presented in Figure 5.25 and shows that high air flows and lower batch sizes correspond to greater porosity development rates. From these data, a statistical model to predict the porosity development rate constant was defined as a function of initial batch size, $m_{bs,0}$ (g) and air mass flow rate, G_a (kg s^{-1}), where R^2=0.876:

$$k_{\gamma_b} = 0.792 + 1.58 \times 10^{-3} m_{bs,0} + 30.7 G_a \tag{5.19}$$

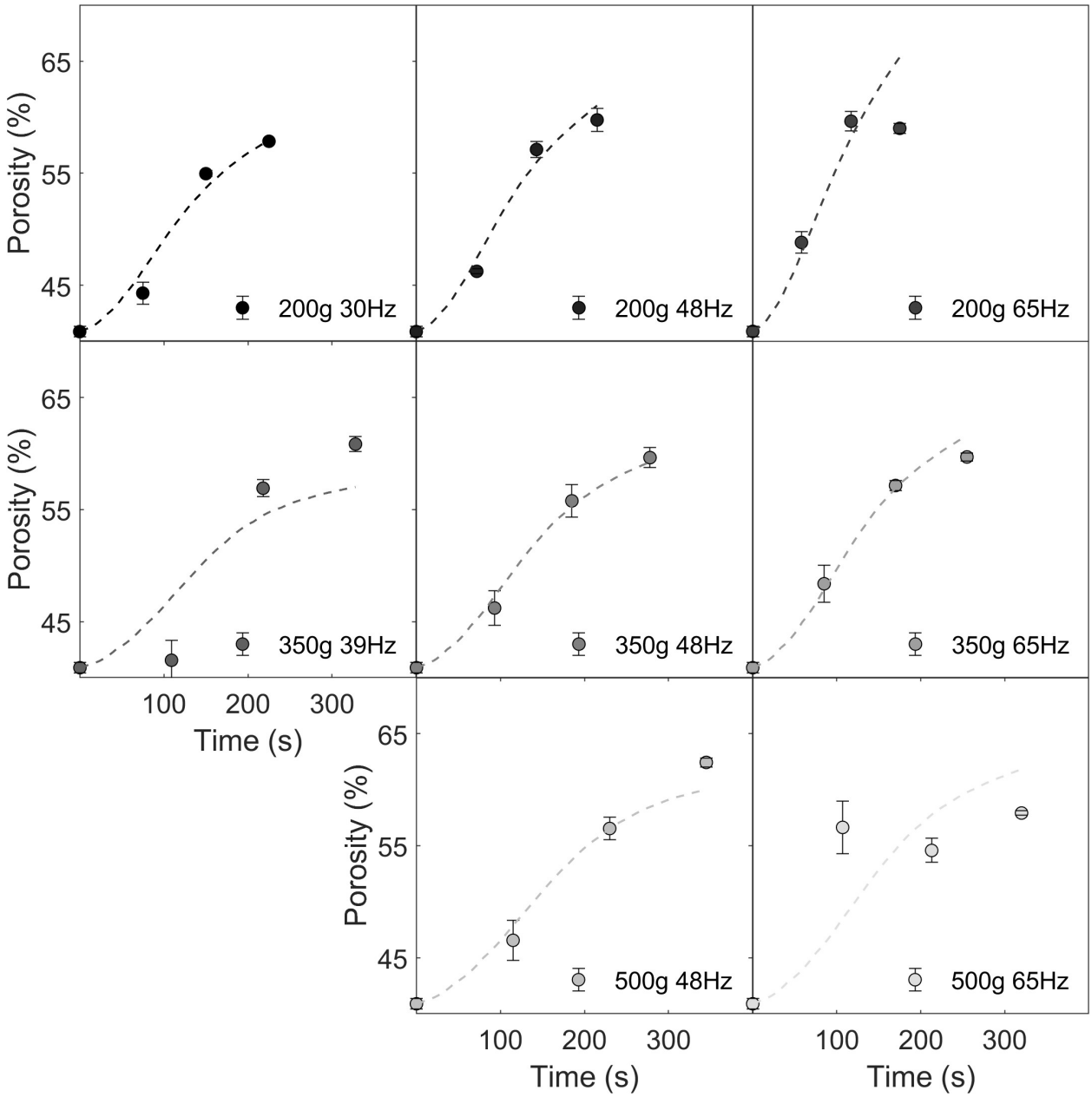

Figure 5.23: Comparison of predicted (dashed blue lines) and experimental (greyscale markers) porosity development profiles modelled using modified 2nd order kinetics (Eq. 5.17) for the variation of batch size and airflow study (experimental data shown in Chapter 3) - data presented as kinetic time-series.

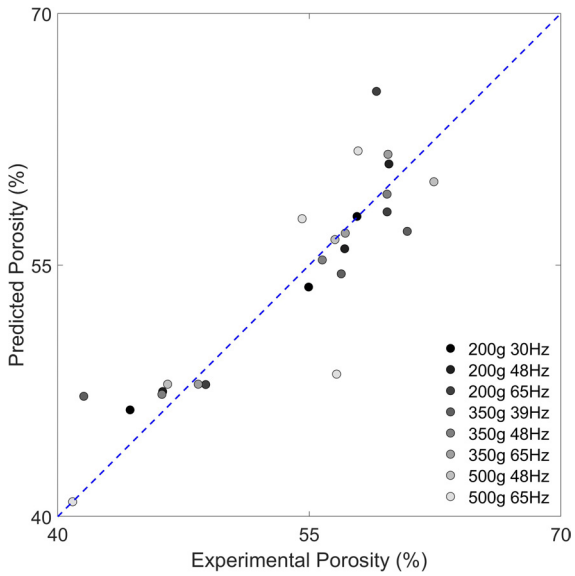

Figure 5.24: Comparison of predicted (dashed blue lines) and experimental (greyscale markers) porosity development profiles modelled using modified 2nd order kinetics (Eq. 5.17) for the variation of batch size and airflow study (experimental data shown in Chapter 3) - data presented as parity plot.

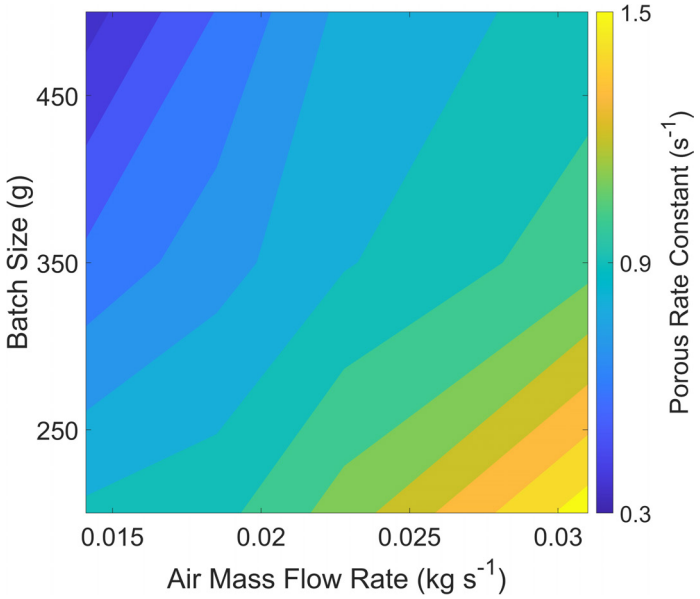

Figure 5.25: Impact of process conditions (i.e., batch size and airflow) on the rate constant (Eq. 5.19) for modified 2nd order kinetic models of porosity development (Eq. 5.17).

Coupling Eqs. 5.18 & 5.19 enabled prediction of coffee's porosity development at early-to-moderate times ($t \leq 100$ s) during roasting - at the same constant inlet air temperature with different airflows and batch sizes - with good accuracy. At longer times, coffee's cellular material transitions from the rubbery-state back to the glassy-state around the time of first

crack, whereby the porosity development and volumetric expansion is inhibited. This physical phenomenon is not well captured within the model, so coffee's porosity is overestimated for high airflow and low batch size process conditions. To increase the real-system accuracy of the model would require reconsideration of the (i) low sampling frequency, (ii) experimental uncertainty of coffee's intrinsic porosity post-first crack and (iii) thermal properties, particularly glass transition data to trigger changes in development rates.

5.6.2 Variation of constant inlet air temperature

Porosity development was modelled using a modified second order kinetic model that included a second term dependent on the coffee's moisture loss:

$$\frac{d(1/\gamma_b)}{dt} = -k_{\gamma_b} \exp\left(-\frac{E_{a,\gamma_b}}{T_b}\right)\left(\frac{1}{\gamma_b}\right)^{n_{\gamma_b}} + k'_{X_b} \exp\left(-\frac{E'_{a,X_b}}{T_b}\right)(X_0 - X_b)^2 \tag{5.20}$$

As in the variation of batch size and airflow study, for a porosity development rate coefficient (k_{γ_b}) with imposed constraints of $0.1 \leq k_{\gamma_b} \leq 10$ (s^{-1}), variation of activation energy in the range $100 \leq E_{a,\gamma_b} \leq 1000$ (K) had no clear impact on predicted porosity development, and estimated values were subsequently lumped into k_{γ_b}. A value of $E_{a,\gamma_b} = 1000$ K was therefore specified, with k_{γ_b} estimated for imposed constraints of $0.1 \leq k_{\gamma_b} \leq 10$ (s^{-1}). The moisture coupled rate coefficient, k'_{X_b} (s^{-1}) and activation energy, E'_{a,X_b} (K) were similarly invariant to applied process temperatures and specified as 0.025 s^{-1} and 1000 K.

The modified second order model (Eq. 5.18) also predicts the volumetric expansion of coffee during roasting under different constant inlet air temperatures with good accuracy at all roasting times (RMSE = 1.0 %).

Figure 5.26 presents a time-series comparison of predicted and experimental Porosity development, whilst Figure 5.27 displays these data as a parity plot.

The porosity development rate constant, k_{γ_b} (s^{-1}) was correlated with constant inlet air temperature $T_{a,i}$ (K), as seen in Figure 5.28 (R^2=0.880), such that:

$$k_{\gamma_b} = 1.93 \times 10^{-15}(T_{a,i} - 273.15)^6 + 0.278 \tag{5.21}$$

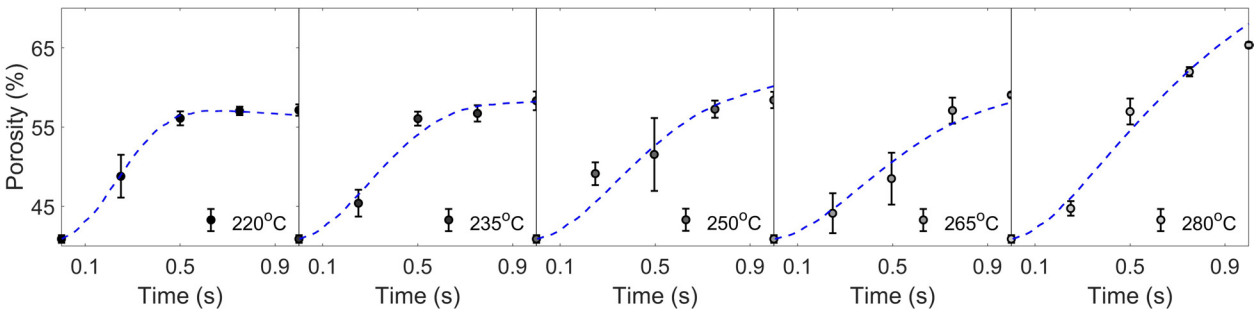

Figure 5.26: Comparison of predicted (dashed blue lines) and experimental (greyscale markers) porosity development profiles modelled using modified 2nd order kinetics (Eq. 5.17) for the constant inlet air temperature study (experimental data shown in Chapter 3) - data presented as kinetic time-series.

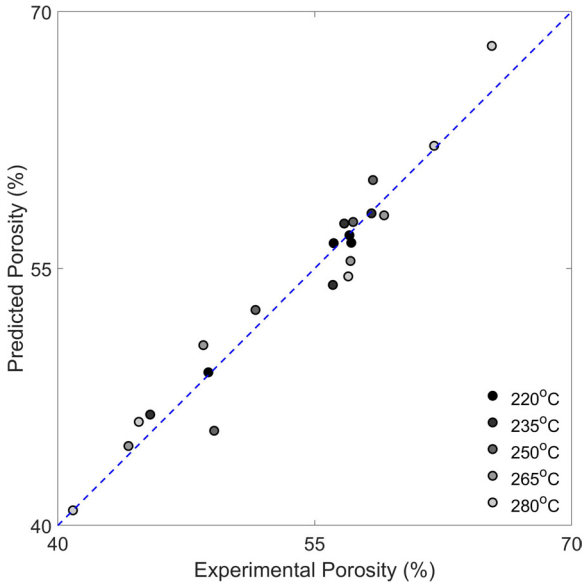

Figure 5.27: Comparison of predicted (dashed blue lines) and experimental (greyscale markers) porosity development profiles modelled using modified 2nd order kinetics (Eq. 5.17) for the constant inlet air temperature study (experimental data shown in Chapter 3) - data presented as parity plot.

The proposed model (Eqs. 5.20-5.21) predicts coffee's porosity development accurately within the experimentally range. At long times, the inhibition of porosity development is well captured for lower constant inlet air temperatures ($T_{a,i} \leq 265°C$) but at high constant inlet air temperatures ($T_{a,i} > 265°C$), the falling development rate after first crack is not fully captured, likely due to the rapid development rate at early-to-moderate times (t $\leq$ 100 s) - this is reflected in the high estimated development rate constant in Figure 5.28.

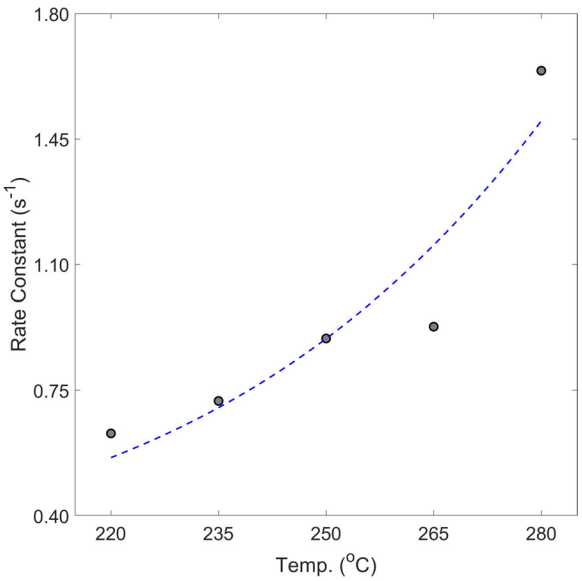

Figure 5.28: Correlation of moisture coupled rate coefficient with process temperature (Eq. 5.21) for modified 2nd order kinetic models of porosity development for the constant inlet air temperature study.

Determination of the onset temperatures for the coffee's cellular transitions between rubbery and glassy states could improve the physics of the prescribed model.

5.7 Conclusions & outlook

Models of coffee's transformation during roasting was based on experimental data presented in Chapter 3 Transformation of Coffee's Physicochemical Properties During Roasting. The empirically-derived kinetic models capture the development of coffee's batch size (i.e., mass), moisture, density, volume and porosity during roasting for two different case studies. These test cases comprised roasts of the same beans at different airflows, batch sizes and temperatures.

Mass loss was modelled using first-order kinetics, wherein (i) for the same constant inlet air temperature, the rate constant depended on both batch size and airflow, and (ii) for the same batch size and airflow, both the rate constant and activation energy were dependent on the constant inlet air temperature. Moisture loss was modelled using second-order kinetics that were invariant to process conditions, and thus dependent only on the bean's intrinsic physical properties and temperature. Coffee's evolution of intrinsic density was modelled using

second-order kinetics, wherein the rate constant was invariant and the activation energy was dependent on process conditions (i.e., on batch size and airflow for the same constant inlet air temperature and constant inlet air temperature for different batch sizes and airflows). Coffee's porous development and subsequent volumetric expansion were both modelled using modified moisture-coupled second-order kinetics, wherein the activation energy was dependent on the system and the rate constant dependent on process conditions (i.e., on batch size and airflow for the same constant inlet air temperature and constant inlet air temperature for different batch sizes and airflows).

Kinetic models developed in this section were constructed using chemical reaction analogies with Arrhenius type rate coefficients. It's worth noting that the Arrhenius framework relies on the accuracy of the bean temperature, and in some cases, estimated activation energies correlated with the applied, constant inlet air temperature. This suggests that thermocouple measurements are dependent on process conditions (which influence packing densities at the thermocouple - particularly for the variation of batch size and airflow study), wherein the temperature response corresponds to the thermodynamics of the drying air - and not only on bean temperature. Although the developed models are robust to the variation of process conditions in this study, and accurately predict coffee's physicochemical transformation during roasting, these models lack physical meaning. For this reason, parameters estimated herein are likely not robust to different roasting machines or bean types.

That said, by nesting these empirically-derived kinetic models within physics-driven heat and mass transfer simulations of coffee roasting time-temperature profiles the roasting process can be virtualised, with process and product development guided by digital models of the coffee roaster. This approach is further developed in Chapter 6.

5.8 Appendix: Experimental data

Table 5.1: Estimated parameters corresponding to kinetic models of coffee's physicochemical transformation during roasting.

Coffee	Inlet Air	Batch	Fan Freq.	Time	Mass Loss		Moisture Loss	
Type	Temp. (oC)	Size (g)	(Hz)	(s)	$k_{m_{bs}}$	$E_{a_{m_{bs}}}$	k_{X_b}	$E_{a_{X_b}}$
Kenyan Arabica	220	350	48	700	3.29×10^{-4}	0	4.13×10^{6}	7908
Kenyan Arabica	235	350	48	415	4.86×10^{-3}	2	4.13×10^{6}	7908
Kenyan Arabica	250	350	48	278	4.97×10^{-3}	902	4.13×10^{6}	7908
Kenyan Arabica	265	350	48	218	3.33×10^{-2}	1704	4.13×10^{6}	7908
Kenyan Arabica	280	350	48	168	7.40×10^{-2}	2015	4.13×10^{6}	7908
Kenyan Arabica	250	200	30	225	3.35×10^{-3}	657	4.13×10^{6}	7908
Kenyan Arabica	250	200	48	215	3.97×10^{-3}	657	4.13×10^{6}	7908
Kenyan Arabica	250	200	65	175	4.56×10^{-3}	657	4.13×10^{6}	7908
Kenyan Arabica	250	350	39	328	2.69×10^{-3}	657	4.13×10^{6}	7908
Kenyan Arabica	250	350	48	278	2.97×10^{-3}	657	4.13×10^{6}	7908
Kenyan Arabica	250	350	65	255	3.40×10^{-3}	657	4.13×10^{6}	7908
Kenyan Arabica	250	500	48	345	2.38×10^{-3}	657	4.13×10^{6}	7908
Kenyan Arabica	250	500	65	320	2.74×10^{-3}	657	4.13×10^{6}	7908

Table 5.2: Estimated parameters corresponding to kinetic models of coffee's physicochemical transformation during roasting.

Coffee	Inlet Air	Batch	Fan Freq.	Time	Volumetric Expansion				Density Evolution	
Type	Temp. (oC)	Size (g)	(Hz)	(s)	k_{V_b}	$E_{a_{V_b}}$	k'_{X_b}	$E'_{a_{X_b}}$	k_{ρ_b}	$E_{a_{\rho_b}}$
Kenyan Arabica	220	350	48	700	7.79	1500	0.04	3000	0.001	2901
Kenyan Arabica	235	350	48	415	7.85	1500	0.04	3000	0.001	2689
Kenyan Arabica	250	350	48	278	12.67	1500	0.04	3000	0.001	2563
Kenyan Arabica	265	350	48	218	13.22	1500	0.04	3000	0.001	2431
Kenyan Arabica	280	350	48	168	16.69	1500	0.04	3000	0.001	2409
Kenyan Arabica	250	200	30	225	12.79	1500	0.04	3000	0.001	2437
Kenyan Arabica	250	200	48	215	16.83	1500	0.04	3000	0.001	2305
Kenyan Arabica	250	200	65	175	20.96	1500	0.04	3000	0.001	2222
Kenyan Arabica	250	350	39	328	11.90	1500	0.04	3000	0.001	2488
Kenyan Arabica	250	350	48	278	11.89	1500	0.04	3000	0.001	2489
Kenyan Arabica	250	350	65	255	15.74	1500	0.04	3000	0.001	2377
Kenyan Arabica	250	500	48	345	9.35	1500	0.04	3000	0.001	2588
Kenyan Arabica	250	500	65	320	11.22	1500	0.04	3000	0.001	2508

Table 5.3: Estimated parameters corresponding to kinetic models of coffee's physicochemical transformation during roasting.

Coffee Type	Inlet Air Temp. (oC)	Batch Size (g)	Fan Freq. (Hz)	Time (s)	Porosity Development			
					k_{γ_b}	$E_{a_{\gamma_b}}$	k'_{X_b}	$E'_{a_{X_b}}$
Kenyan Arabica	220	350	48	700	0.63	1000	0.025	1000
Kenyan Arabica	235	350	48	415	0.72	1000	0.025	1000
Kenyan Arabica	250	350	48	278	0.89	1000	0.025	1000
Kenyan Arabica	265	350	48	218	0.93	1000	0.025	1000
Kenyan Arabica	280	350	48	168	1.64	1000	0.025	1000
Kenyan Arabica	250	200	30	225	0.92	1000	0.025	1000
Kenyan Arabica	250	200	48	215	1.15	1000	0.025	1000
Kenyan Arabica	250	200	65	175	1.56	1000	0.025	1000
Kenyan Arabica	250	350	39	328	0.76	1000	0.025	1000
Kenyan Arabica	250	350	48	278	0.89	1000	0.025	1000
Kenyan Arabica	250	350	65	255	1.06	1000	0.025	1000
Kenyan Arabica	250	500	48	345	0.83	1000	0.025	1000
Kenyan Arabica	250	500	65	320	0.94	1000	0.025	1000

Chapter Six

Batch-scale simulation of heat and mass transfer of coffee roasting in spouted bed roasters

Understanding heat and mass transfer phenomena is fundamental to a successful roasting practices. These phenomena can be quantified via an energy balance over the roaster, whereby heat and mass transfer equations can be formulated. Through rigorous calibration of the simulation with experimentally derived data, obtained using a spouted bed roaster (in Chapters 2-3), a zero-dimensional model of coffee roasting was developed to predict time-temperature roasting profiles. Calibration involved implementation of: (i) an airflow calibration to determine the air mass flow rate and velocity of air input to the roaster, (ii) kinetic models and empirical correlations to describe coffee's physichochemical development during roasting, and (iii) a non-linear least squares fitting procedure to estimate system-dependent parameters that are otherwise difficult to determine. The simulation was analysed for sensitivity to input factors varied in the calibration data, as well as for variation of the estimated parameters. In this way, the sensitivity analysis informed the appropriate parameter space and assessed the collinearity of model coefficients as they relate to process parameters. System-dependent parameters were ascertained through correlation with input factors that relate to roasting conditions.

In this chapter, development of the zero-dimensional, batch-scale simulations is described, alongside rigorous calibration with experimental case studies from Chapters 2 and 3, and kinetic modelling from Chapter 5. These simulations can be used by product and process developers to roast coffee *in-silico*, providing not just an informative tool, but one that can be instructive and predict requirements for raw material (green coffee) properties, roasting process conditions, or roasted coffee properties.

6.1 Methodology

The works of Schwartzberg (2002), Schwartzberg (2006b), and Schwartzberg (2006a) and Schwartzberg (2013) have been studied, adapted and developed by many (Hernández Pérez, 2002; Fabbri, Cevoli, Alessandrini, et al., 2011; Bottazzi et al., 2012; Alonso-Torres et al., 2013; Bustos-Vanegas et al., 2018; Bopape et al., 2016) to model and predict time-temperature profiles for several roasters of different scales and designs. Following the promise of these models, this chapter postulates use of the batch-scale energy balance proposed by Schwartzberg (2002) to simulate time-temperature roasting profiles in a pilot-scale spouted bed roaster. The simulation will be calibrated with experimental data and models developed in previous chapters to increase its accuracy, robustness and applicability.

6.1.1 Experimental approach: Process & product characterisation

Time-temperature profile simulations in this Chapter are developed based on case studies I, II and IV, detailed in Chapters 3.2, 3.3 and 3.5, respectively, wherein coffee's temperature response and subsequent physicochemical transformation were mapped out. Across the three case studies, the same Kenyan Arabica coffee was used. Roasting conditions in case study I considered the variation of constant inlet air temperature, whilst those in case study II aimed to replicate the coffee bean particle motion study of the spouted bed roaster (documented in Chapter 4.2), wherein the variation of batch size and airflow was considered. Case study IV considered the impact of thermocouple diameter on the temperature response at moderate roasting conditions. Together, these experimental data are used here to calibrate a zero-dimensional heat and mass transfer model at the batch-scale.

Readers are directed to Chapter 2 to recall the roaster's airflow calibration, which determined: (i) the air mass flow rate and velocity of air through the roaster as a function of the applied fan frequency and (ii) the effect of temperature on air's thermophysical properties.

Also in Chapter 2, the response times of different diameter thermocouples were determined from first principles and validated experimentally using a model system. Readers are reminded that (i) for thin thermocouples (d_T<1.5mm), airflow had a small effect on response

time, which is not expected to significantly affect the thermocouple response during roasting, (ii) the thermocouple's response time could be reduced to a single-term power law model as a function of diameter, wherein the estimated parameters are lumped to account for the dimensionless Reynolds and Nusselt numbers, the heat transfer coefficient, geometry and effective thermal properties, (iii) response times from the first principle approach were then experimentally validated in the exhaust of a sample roaster, and (iv) the effect of airflow on response times in the model-system were not significant, although model-system response times were greater than those predicted from first principles.

Readers are further referred to Chapter 3, where (i) Section 3.1 provides methods used here to characterise coffee's physicochemical development during roasting, (ii) Section 3.3.1 outlines the roasting conditions used for case study I (variation of constant inlet air temperature) and (iii) Section 3.4.1 outlines the roasting conditions used for case study II (variation of batch size and airflow). Data in these Sections are also used to develop correlations of physicochemical properties such that several physicochemical properties are predicted from coffee's moisture content and density.

Later in Chapter 3, the impact of thermocouple diameter on the measured temperature during roasting was established in a pilot-scale roaster. Readers should recall that (i) thinner thermocouples responded more rapidly to changes in temperature induced at early times during roasting due to the influx of beans and air at ambient temperature, (ii) due to shorter response times, higher temperatures were logged with thinner thermocouples at all times and therefore, reasonably suggesting that (iii) thinner thermocouples provide a more accurate measurement of the system's real temperature.

6.1.2 Modelling approach: Coffee's physicochemical development

In Chapter 5, kinetic models were developed to describe changes in mass and moisture during roasting using the chemical reaction analogy. Whilst the model of moisture loss can be used for both case studies I & II, the mass loss rate coefficient in the model of mass loss was developed separately for each case study and thus are implemented as such.

6.1.3 Modelling approach: Thermal balance at the batch-Scale

An energy balance over the roaster can be used to determine the batch mean (i.e., zero-dimensional) temperature evolution during roasting:

$$Q_b = (Q_{ab} + Q_{am}) - Q_{am} + Q_{mb} + Q_r - Q_e \tag{6.1}$$

where the heat of the bean is Q_b (W); air-to-bean heat transfer is Q_{ab} (W); heat loss from drying air to the roaster's internal metal surfaces is Q_{am} (W); heat transfer between the roaster's internal metal surfaces and beans is Q_{mb} (W); exothermic heat generated due to reactions is Q_r (W) and evaporative cooling is Q_e (W):

$$Q_b = m_{bs,db}(1 + X_b)C_{p,b}\frac{dT_b}{dt} \tag{6.2}$$

$$Q_{ab} + Q_{am} = G_a C_{p,a}(T_{a,i} - T_{a,o}) \tag{6.3}$$

$$Q_{am} = h_{am}A_{am}(T_{a,i} - T_m) \tag{6.4}$$

$$Q_{mb} = h_{mb}A_{mb}(T_m - T_b) \tag{6.5}$$

$$Q_r = \Delta H_r \frac{dm_{bs,db}}{dt} \tag{6.6}$$

$$Q_e = m_{bs,db}\Delta H_v \frac{dX_b}{dt} \tag{6.7}$$

Definition of terms and their units in Eqs. 6.2-6.7 are outlined in Table 6.1.

To reduce the model complexity, the following assumptions were made:

- Inlet air temperature data was used to approximate the applied thermal load, assuming no temperature differential before and after the air is distributed by the orifice plate.
- Heat transfer between the roaster's internal metal surfaces and the beans (i.e., conductive heat transfer) is negligible, as metal-bean contact areas and times are low in spouted bed roasters - thus $Q_{mb} = 0$.
- Exothermic reactions are negligible prior to first crack (FC) - thus for $t \leq t_{FC}$, $Q_r = 0$.
- Roasting conditions induce particle dynamics that create a thermally homogenous bean bed and thus bean-to-bean conductive and radiative heat transfer are negligible.

- Measured coffee bean moisture content, density, specific heat capacity and thermal conductivity correspond to the batch mean and they are representative of the total batch and are uniform within the bean.
- An equivalent coffee bean diameter represents the characteristic length for Nusselt number approximations, which were evaluated for spherical particles.
- Water enthalpy of vaporisation is assumed to occur at saturation pressure, dependent on water temperature; water temperature is assumed equal to that of the simulated bean (i.e., particle) temperature.

An adaptation of the energy balance proposed by Schwartzberg (2002), based on the stated assumptions, was used to predict the batch mean (i.e., zero-dimensional) temperature change during roasting:

$$\frac{dT_b}{dt} = \frac{G_a C_{p,a}(T_{a,i} - T_{a,o}) + m_{bs,db}(\Delta H_v \frac{dX_b}{dt}) - Q_{am}}{m_{bs,db}(1 + X_b)C_{p,b}} \tag{6.8}$$

where G_a is the inlet air mass flow rate (kg s^{-1}), $C_{p,b}$ and $C_{p,a}$ are the specific heat capacity of the coffee bean and inlet air (J kg^{-1} K^{-1}), Q_{am} is the air-to-metal heat loss (W), ΔH_v is the latent heat of vaporisation of water (J kg^{-1}), X_b is the bean's moisture content (kg kg^{-1}) and $m_{bs,db}$ is the dry-basis mass of beans (kg).

The air temperature differential across the roaster, $(T_{a,i} - T_{a,o})$ (K), is given by (Schwartzberg, 2002):

$$(T_{a,i} - T_{a,o}) = (T_{a,i} - T_b)\left(1 - \exp\left(\frac{-\alpha_{ab} A_{ab}}{G_a C_{p,a}}\right)\right) \tag{6.9}$$

where A_{ab} is the area available for heat transfer (m^2) and α_{ab}, the overall heat transfer coefficient (W m^{-2} K^{-1}) is determined via the air-to-bean heat transfer coefficient h_{ab} (W m^{-2} K^{-1}), Biot number, $(Bi = (h_{ab} d_b)/k_b)$ and effectiveness factor, η_A, to correct for inhibited convective heat transfer within the bean bed (Schwartzberg, 2002):

$$\alpha_{ab} \approx \frac{h_{ab}}{1 + \eta_A Bi} \tag{6.10}$$

The Ranz-Marshall equation proposed by (Froessling, 1968) describes the flow of drying air around spherical particles:

$$Nu \approx 2 + 0.6 Re^{1/2} Pr^{1/3} \tag{6.11}$$

Table 6.1: Thermal balance nomenclature for Eqs. 6.2-6.7.

Definition	**Term**	**Units**
Batch size (db)	$m_{bs,db}$	kg
Specific moisture content of coffee	X_b	kg kg^{-1}
Specific heat capacity of coffee	$C_{p,b}$	J kg^{-1} K^{-1}
Bean temperature	T_b	K
Roasting time	t	s
Air mass flow rate	G_a	kg s^{-1}
Specific heat capacity of air	$C_{p,a}$	J kg^{-1} K^{-1}
Air inlet temperature	$T_{a,i}$	K
Air outlet temperature	$T_{a,o}$	K
Heat transfer coefficient between the air and roaster's internal metal surfaces	h_{am}	W m^{-2} K^{-1}
Heat transfer area between the air and roaster's internal metal surfaces	A_{am}	m^2
Roaster's internal metal surface temperature	T_m	K
Heat transfer coefficient between the roaster's internal metal surfaces and bean	h_{mb}	W m^{-2} K^{-1}
Heat transfer area between the roaster's internal metal surfaces and bean	A_{mb}	m^2
Specific enthalpy of reaction	ΔH_r	J kg^{-1}
Specific enthalpy of vaporisation of water	ΔH_v	J kg^{-1}

where Nu, Re and Pr are dimensionless Nusselt ($Nu = \frac{h_{ab}d_b}{k_a}$), Reynolds ($Re = \frac{d_b \rho_a u_a}{\mu_a}$) and Prandtl ($Pr = \frac{C_{p,a}\mu_a}{k_a}$) numbers, respectively. The air-to-bean heat transfer coefficient, h_{ab} (W m^{-2} K^{-1}), can therefore be approximated as:

$$h_{ab} = \frac{Nuk_a}{d_b} \tag{6.12}$$

Here, the surface area of the coffee bean was approximated assuming spherical geometry

with an equivalent diameter, d_b (mm). Principal dimensions, a, b & c, defined in Chapter 3, were used to estimate the equivalent-volume diameter, such that $d_b = (abc)^{1/3}$. In this way, spherical geometry was selected to simplify the implementation of bean expansion (which is back-calculated from the correlation of volume and moisture). Data in Chapter 3.1 outlined the potential error of this simplification. The difference between the area approximated using spherical and hemi-ellipsoidal geometries is similar to the standard deviation of the measurement. The surface area of a coffee bean, $A_{s,b}$ (m^2), is thus:

$$A_{s,b} \approx \pi d_b^2 \tag{6.13}$$

whereas the total area of the batch available for air-to-bean heat transfer is:

$$A_{ab} \approx n_b A_{s,b} \tag{6.14}$$

where n_b is the number of coffee beans in the batch.

The thermocouple response coefficient, K (s^{-1}), is introduced to correct for the response time of the thermocouple in the roasting chamber. The thermocouple's measured temperature, T_T (K), is thus:

$$\frac{dT_T}{dt} = K(T_b - T_T) \tag{6.15}$$

6.1.4 Implementation of zero-dimensional model

A zero-dimensional simulation was developed to predict the batch mean temperature during roasting with a constant thermal load (i.e., a constant inlet air temperature and airflow). The data-driven approach - using measured process parameters (inlet air temperature, product temperature and airflow) and product properties (batch size (mass basis), moisture content, size and thermophysical properties) - reduced the number of unknown parameters to be estimated. In this simulation, the process temperature - measured by a thermocouple in the bean bed - was predicted via an energy balance coupled with two kinetic models (with Arrhenius-type rate coefficients) to describe changes in mass and moisture during roasting. Here, three unknown parameters relating to characteristics of the roasting system (thermocouple response coefficient, K) and applied process conditions (heat transfer effectiveness factor, η_A, and heat loss across the roaster, Q_{am}) were estimated.

An initial value problem for a system of four Ordinary Differential Equations (ODEs) describing changes in mass, moisture, bean temperature and thermocouple temperature was solved in MATLAB (R2021b, MathWorks) using a stiff solver (ODE23S).

Inlet air and product temperatures were first extracted from experimental data. Thermophysical properties of air (specific heat capacity, thermal conductivity, dynamic viscosity and density) and calculated as a function of inlet air temperature. Airflow (velocity and mass flow rate) was determined based on constant fan frequency set-points using the prescribed calibration and corrected due to temperature dependent changes in air density. Both temperature and airflow data (with a sample interval of 1 s) were interpolated using a smoothing spline (smoothing parameter 0.99) according to the solver's time span and step size.

Initial conditions for batch mass and moisture content were specified as the measured green coffee properties (as in Table 6.2). Initial product (thermocouple) temperature was the measured value at product loading during roasting trials, whilst the initial 'actual' bean temperature was assumed equal to the ambient temperature (c. 20 °C). The number of beans in the batch was estimated from the initial batch mass, $m_{bs,0}$ (kg) and packing density - i.e., number of beans per unit mass (kg^{-1}) - as noted in Table 6.2.

The coffee's transient thermophysical properties were estimated via empirical correlations established in Chapter 3.3-3.4 Bean diameter was determined based on equivalent spherical volume, with the total surface area of the beans in the batch, assumed available for air-to-bean heat transfer, determined using the equivalent diameter.

Table 6.2: Initial condition values used in simulation of time-temp profiles.

Property	**Units**	**Value**
Moisture, X_b	kg kg^{-1}	0.1006
Dimension a	mm	6.18
Dimension b	mm	3.84
Dimension c	mm	8.54
Equivalent Diameter, d_b	mm	5.87
Packing Density	kg^{-1}	10224
Bean Temperature, T_b	°C	20

Dimensionless numbers Re, Pr, Nu and Bi were used to describe the flow regime and thermal effectiveness associated with the air-to-bean heat transfer. The Biot number, Bi, was employed initially to approximate the thermal inertia of the bean bed, wherein convective heat transfer rates are lower relative to those expected in the spouting region shown in Chapter 4 and also postulated by Schwartzberg (2002) and Brown and Lattimer (2013). These similarity parameters were designed to be dynamic, responding to the temperature dependent properties of the drying air and transient physical properties of the coffee beans that evolve during roasting.

Endothermic cooling was determined based on the latent heat of vaporisation, where the water temperature was assumed equal to the simulated bean temperature.

Kinetic models outlined in Chapter 5 were used to predict changes in mass and moisture, respectively, whilst the drying air's temperature differential across the roaster was approximated as in Eq. 6.9. The actual bean temperature was translation into the product (thermocouple) temperature via Eq. 6.15 to account for the thermocouple response time and thus can be compared with experimentally measured time-temperature profiles.

A non-linear least squares fitting procedure was implemented using a trust-region-reflective algorithm to estimate parameters η_A, K and Q_{am}, within specified constraints - the estimation procedure is discussed in the next section. Initial guesses for estimated parameters were

random values between the specified bounds. The ODE solver's time span was specified as the time to first crack for each test case, with a step size of 0.1 s for all cases.

The aim was to minimise the Root Mean Square Error (RMSE) between the time-temperature profiles predicted via Eq. 6.15 and those obtained experimentally - this temperature difference, Δ_T, was thus the objective for the fitting procedure. The fitting procedure was based on a gradient descent algorithm. The stop condition corresponded to a local minimum where the gradient of the cost function was $<$ 1e-7 (after dividing by S.I. units). The fitting procedure was performed three times and checked for parameter convergence.

Time-temperature roasting profiles according to process conditions described in Chapter 3 were simulated using the zero-dimensional, batch-scale model - RMSE was evaluated up to the onset of endo/exothermic reactions around first crack. An example of experimental and predicted time-temperature profiles are displayed in Figure 6.1.

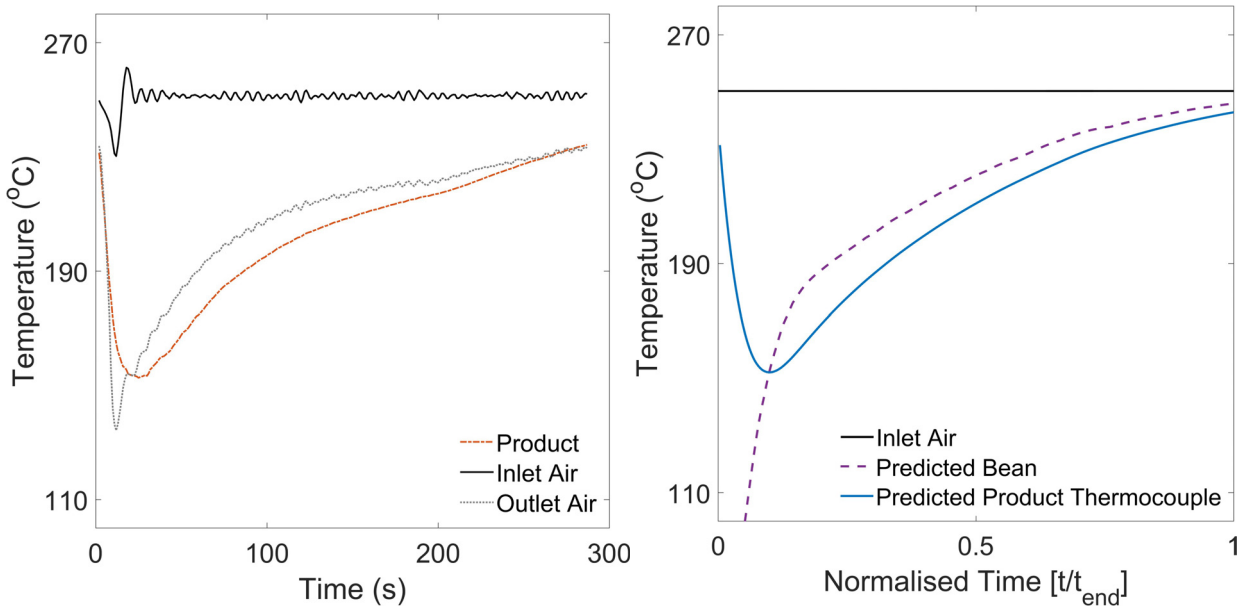

(a) Experimental

(b) Predicted

Figure 6.1: Exemplar time-temperature roasting profiles illustrating (a) inlet air, outlet air and product thermocouple data collected experimentally and (b) inlet air, product thermocouple and bean temperatures predicted from the batch-scale simulation. Data corresponding to 350g batches roasted at 250°C with a fan frequency of 48 Hz for 278 s.

For case study IV, data in Chapter 3.5 were used to estimate the thermocouple response coefficient, K. As the kinetic models of mass and moisture were developed using roasting data corresponding to a 1.00 mm diameter thermocouple, the experimental time-temperature profile corresponding to the 1.00 diameter thermocouple was used to estimate the mass and moisture loss for consistency.

6.1.5 Validation of the numerical scheme

The zero-dimensional model was calibrated with process and product data from Schwartzberg (2002) and validated using experimental data presented therein. A comparison of experimental and predicted data is shown in Figure 6.2.

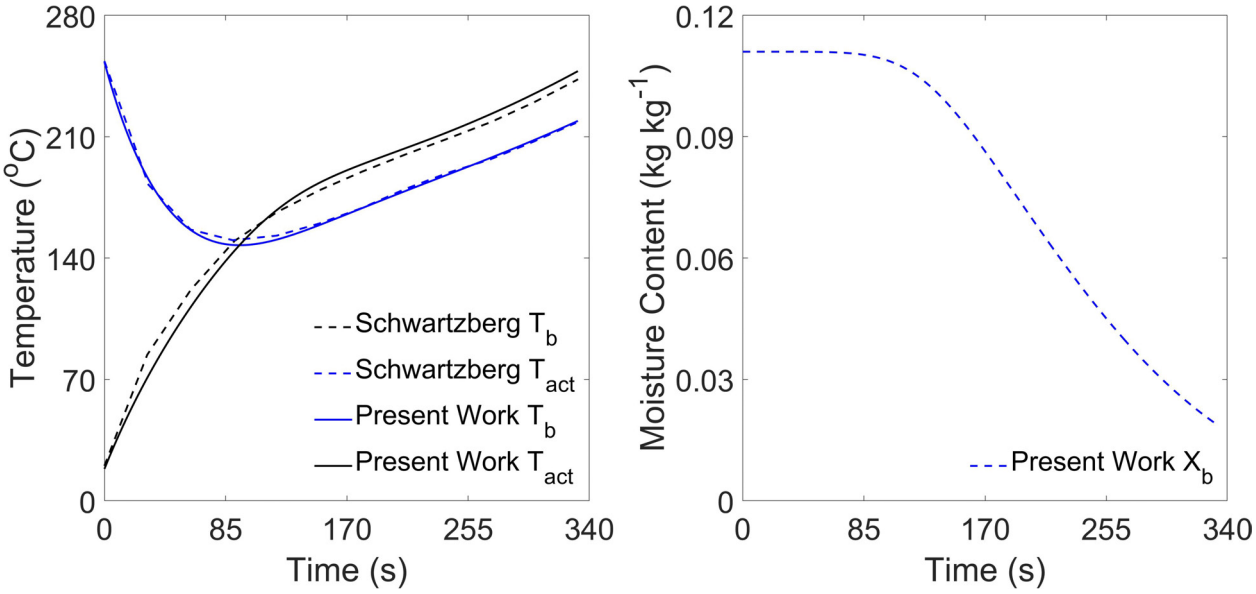

Figure 6.2: Validation of model against data published by Schwartzberg (2002).

For implementation of the model, roast time was specified as 332 s and constant inlet air temperature as 482°C. Air mass flow rate varies with thermocouple temperature, T_T, such that for $T_T \leq 182$°C, G_0=43 kg s^{-1}, when $182 \leq T_T \leq 199$°C, $G = 0.89G_0$ and when $T_T \geq 199$°C, $G = 0.78G_0$. The heat transfer effectiveness factor was specified as 0.3. Air-to-bean heat transfer area was specified as 48 m^2. Although air mass flow rate varies with time, there was insufficient data to define a correlation between air velocity and air mass flow rate, so air velocity was set constant as 4 m s^{-1} (Hernández Pérez, 2002).

Air thermal conductivity, specific heat capacity, air density and dynamic viscosity were constant, with values extracted from Engineering-ToolBox (2020): 4.04×10^{-2} W m^{-1} K^{-1}, 1029.5 J kg^{-1} K^{-1}, 0.4567 kg m^{-3}, 2.67×10^{-5} kg m^{-1} s^{-1}. Bean diameter was 6 mm and initial moisture content 0.111 kg kg^{-1}. The bean's thermal conductivity, k_b and specific heat capacity, $C_{p,b}$ were a function of moisture content, X_b ($k_b = 0.356 + 0.139X_b$; $C_{p,b} = (1099 + 7T_b + 5000X_b)/(1 + X_b)$) (Hernández Pérez, 2002). Initial bean temperature was 18.3°C, batch size 400 kg and dry matter mass assumed constant. Heat generation from exothermic reactions was a function of an apparent activation energy ($dQ_r/dt = Aexp(-E_a/RT_b)((H_{et} - H_e)/H_{et})$) - where A=116200 kJ kg^{-1}, $-E_a/R$=5500 K, H_{et}=232 kJ kg^{-1} and initial heat generation is zero, i.e., H_e=0 kJ kg^{-1}. Latent heat of vaporisaiton was ΔH_v=2790 kJ kg^{-1} and the moisture loss was a kinetic model ($dX/dt = (4.3210^9X^2)/d^2exp((-9889)/(T_b + 273.15))$). Bean temperature was a function of the thermocouple temperature ($(dT_T)/dt = K(T_b - T_T)$), where K=0.013 s^{-1}. Initial thermocouple temperature was 253°C.

Reasonable agreement between the predicted and experimental time-temperature profile is shown in Figure 6.2. Therefore, the numerical scheme and implemented model is sensible.

6.2 Results

6.2.1 Sensitivity to unknown parameters

This Subsection aims to identify the sensitivity of the model outputs (i.e., the predicted time-temperature response) to variation of each of the estimated parameters - the thermocouple response coefficient (K in Eq. 6.15), the air-to-metal heat transfer (Q_{am} in Eq. 6.8) and the heat transfer effectiveness factor (η_A in Eq. 6.10). From these analyses, a feasible range of parameter values can be used to define the constraints of the parameters during estimation.

Thermocouple response coefficient, K

The thermocouple response coefficient was varied in the range of 0.01-1 s^{-1}, whilst air-to-metal heat transfer was assumed negligible (i.e., $Q_{am} = 0$) and the heat transfer effectiveness factor was specified as 0.5. Figure 6.3 illustrates the effect of different thermocouple response coefficients on the predicted time-temperature response.

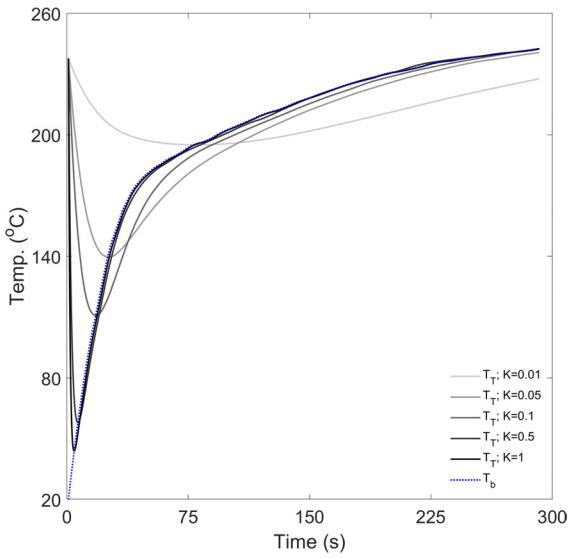

Figure 6.3: The effect of thermocouple response coefficient, K, on the predicted time-temperature profile.

As the thermocouple response coefficient, K, increases, the thermocouple response time decreases, thus reducing the time and temperature of the 'turning point' (the time-temperature profile's global minimum). The difference between the predicted temperatures of the thermocouple and the bean (T_T and T_b in Figure 6.3, respectively), which can be considered as the RMSE if T_b is the reference, decreases as K increases. Therefore, for thermocouples with higher values of K (i.e., with smaller diameters, as shown in Chapters 2-3), the response is more rapid and accurate, relative to the predicted bean temperature - so as $1/K \rightarrow 0, T_T \rightarrow T_b$. The effect of airflow, bean bed dynamics and the temperature within the roasting chamber on the thermocouple response coefficient is sensible, as all of these will influence heat transfer rates from the system (i.e., the beans and the air) to the thermocouple. Conversely, this shows that for large diameter thermocouples with low values of K, the temperature measured by the thermocouple is expected to be delayed relative to the 'thermal reality' of the system.

Air-to-metal heat transfer, Q_{am}

The air-to-metal heat transfer rate was varied in the range of 0-1500 W, whilst the thermocouple response coefficient was specified as 0.1 s^{-1} and the heat transfer effectiveness factor was specified as 0.5. Figure 6.4 illustrates the effect of different air-to-metal heat transfer rates on the predicted time-temperature response.

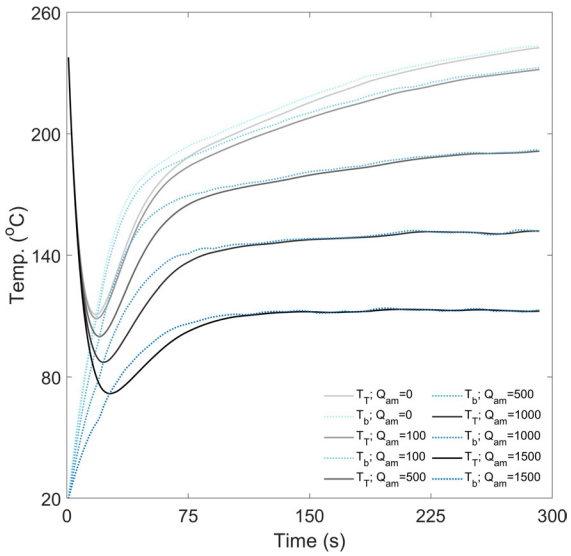

Figure 6.4: The effect of air-to-metal heat transfer rate, Q_{am}, on the predicted time-temperature profile.

The air-to-metal heat transfer rate, Q_{am}, was introduced to account for heat loss across the system, which was observed as a difference between the measured inlet, product and outlet thermocouple temperatures (ca. 30°C) at pseudo steady-state during preheating (shown in Chapter 2). Figure 6.4 shows that when Q_{am} is high, a pseudo steady-state is achieved during roasting, whereby the rate of change of temperature approaches zero. As Q_{am} decreases, the time and temperature to achieve the pseudo steady-state increases. These effects can be likened to a decrease in the applied thermal load, (i.e., a lower constant inlet air temperature) or reduced heat transfer efficacy. Therefore, Q_{am} is expected to be a function of the constant inlet air temperature and heat transfer effectiveness factor, which implies collinearity can be expected of the estimated parameters. For this reason, the air-to-metal heat transfer rate will be assumed negligible (i.e., $Q_{am} = 0$) for the time-temperature profile simulations, so that these effects are lumped into the heat transfer effectiveness factor to prevent collinear parameters, which could reduce their accuracy and robustness.

Heat transfer effectiveness, η_A

The heat transfer effectiveness factor was varied in the range of 0.001-10, whilst the thermocouple response coefficient was specified as 0.1 s^{-1} and the air-to-metal heat transfer was assumed negligible (i.e., $Q_{am} = 0$). Figure 6.5 illustrates the effect of different heat transfer effectiveness factors on both the heat transfer coefficient and predicted time-temperature response.

The dimensionless heat transfer effectiveness factor, η_A, aims to account for heat loss across the system (such as air-to-metal heat transfer), as well as the availability of the coffee's surface area (both on the bean- and batch-scale). When roasting under flow regimes that produce large bean beds (i.e., those with a large batch size and low airflow, as shown in Chapter 4), the Bean Bed Mass Fraction (BBMF) is high and η_A is expected to be high due to the reduced airflow and lower convective heat transfer in the bean bed. When roasting under flow regimes that minimise the bean bed (i.e., those with a small batch size and high airflow), beans are in a constant recirculating motion and the convective heat transfer is greater - in this scenario, η_A is expected to be low. These effects are clearly depicted in

Figure 6.5, whereby low values of η_A correspond to large heat transfer coefficients (Figure 6.5(a)) and rapid time-temperature responses (Figure 6.5(b)).

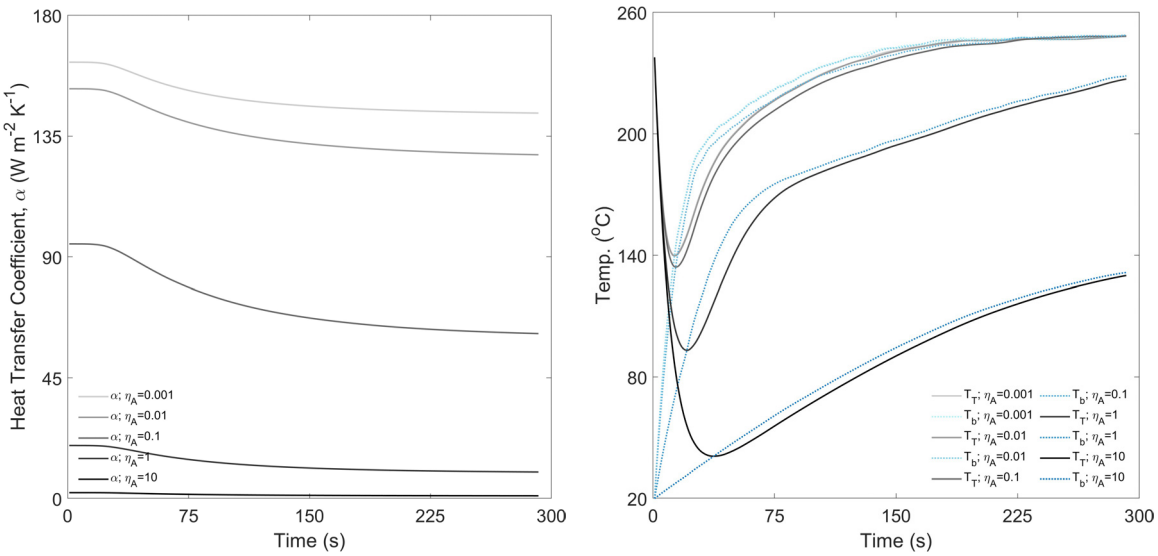

(a) Heat Transfer Coefficient

(b) Temperature

Figure 6.5: The effect of air-to-metal heat transfer rate, Q_{am}, on the predicted time-temperature profile.

6.2.2 Sensitivity to input variables

This Subsection aims to establish the sensitivity of the simulation (and the predicted time-temperature response) to the relevant input variables that were studied in Chapter 3: (i) the constant inlet air temperature, $T_{a,i}$ in Eq. 6.8, (ii) the fan frequency, which relates to the air mass flow rate, G_a, in Eq. 6.8 and air velocity, u_a, in the Reynolds number used in Eq. 6.11, and (iii) the batch size, $m_{bs,db}$ in Eq. 6.8.

For these analyses, the steady-state (i.e., charge) temperature prior to loading the roaster with coffee was specified as 200°C, therefore this was the initial condition for the product thermocouple temperature, $T_{T,0}$, whilst the initial bean temperature, $T_{b,0}$, was assumed to be 20°C and initial moisture, $X_{b,0}$, was 0.1006 kg kg^{-1} as in Table 6.2. The thermocouple response coefficient (K) was specified as 0.1 s^{-1}, the heat transfer effectiveness (η_A) 0.5 and the air-to-metal heat transfer rate (Q_{am}), assumed negligible.

Constant inlet air temperature

The constant inlet air temperature modulates the heat transfer rate and therefore influences the: (i) Reynolds and Prandtl numbers (Eq. 6.11) and thus the heat transfer coefficient (Eq. 6.12), (ii) thermocouple response coefficient due to differences in the air flow over the thermocouple (described later in Section 6.2.3), as well as (iii) mass and moisture kinetics in Chapters 5.2 & 5.3, respectively. Figure 6.6 demonstrates the effect of constant inlet air temperature in the range of 220-280°C on coffee's predicted temperature and subsequent physicochemical development - for the simulations here, a fan frequency of 48 Hz and a batch size of 0.35 kg was specified.

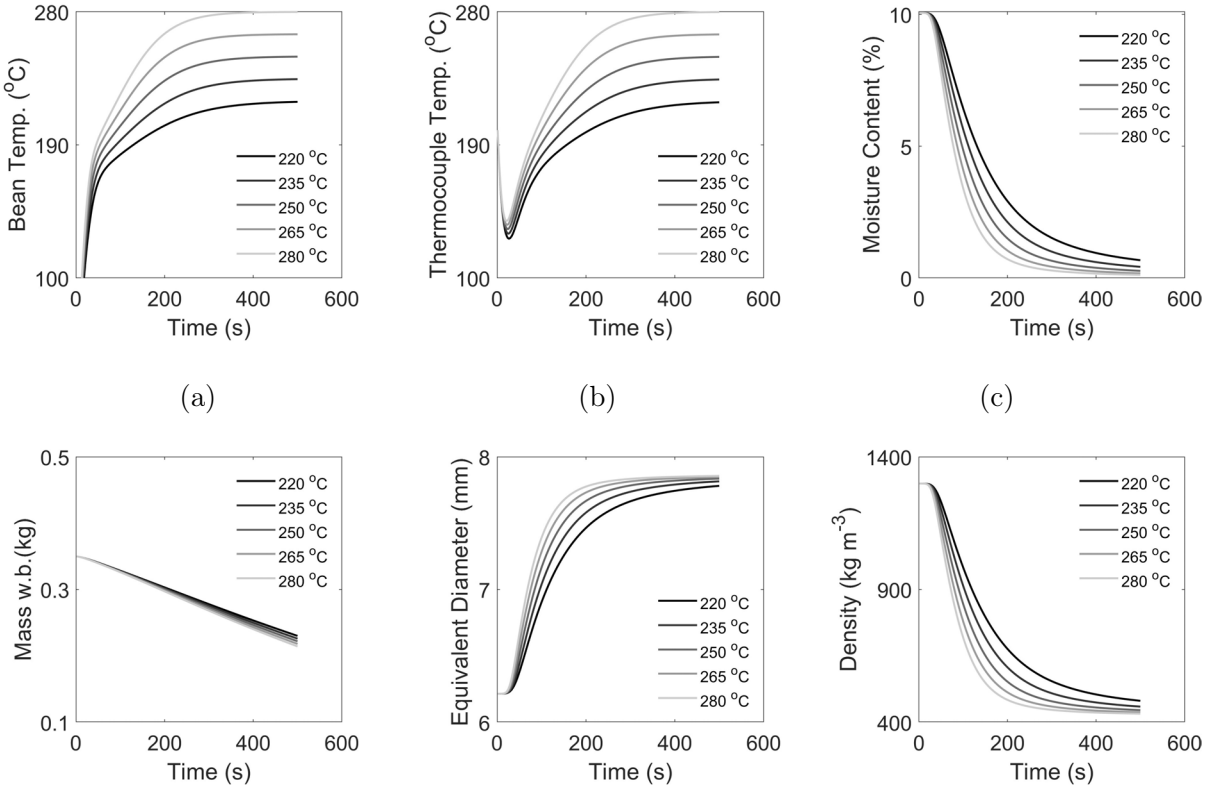

Figure 6.6: The effect of constant inlet air temperature in the range of 220-280°C on predicted (a) bean temperature, (b) thermocouple temperature, (c) moisture, (d) batch size (mass), (e) bean size (equivalent diameter) and (f) density.

Greater constant inlet air temperatures correspond to higher thermal loads and, therefore, to a greater rate of change of bean and thermocouple temperature, greater mass and moisture loss, as well as a more rapid volumetric expansion and density reduction. Regarding predicted thermocouple temperatures, there is only a slight effect of constant inlet air temperature on the thermocouple response (observed as the 'turning point'), yet for times $>$ 60 s, the temperature profiles deviate significantly with pseudo steady-state (and convergence with bean temperature) achieved around 500 s for all conditions. The difference in pseudo steady-state temperatures correspond exactly to the difference in the applied constant inlet air temperature. These predicted phenomena agree with existing literature (Heyd et al., 2007; Uren et al., 2023), yet temperature differentials observed across the roaster during preheating (i.e., heat loss) suggest that the predicted thermocouple temperature should not converge with the inlet air temperature and is higher than expected during real roasting - also shown in Figure 6.1(a).

Airflow

Similarly to the constant inlet air temperature, airflow modulates the heat transfer rate and affects the heat transfer coefficient, thermocouple response coefficient and physicochemical development rates. Figure 6.7 demonstrates the effect of airflow in the range of 4.2-10.0 m s^{-1} (corresponding to fan frequencies of 30-65 Hz) on coffee's predicted temperature and subsequent physicochemical development - for the simulations here, a constant inlet air temperature of 250°C and a batch size of 0.35 kg was used.

Greater fan frequencies correspond to higher air mass flow rates and velocities, as well as higher heat transfer coefficients, which results in a higher rate of change of temperature for both the bean and the thermocouple. Although the effect of airflow on moisture, bean size and density was less than was seen for different constant inlet air temperatures, mass loss was more sensitive. This indicates that airflow could be a powerful tool to modulate mass loss, whilst not greatly affecting bean size, moisture or density - at the pilot-scale, this might also be attributed to bean/batch homogeneity.

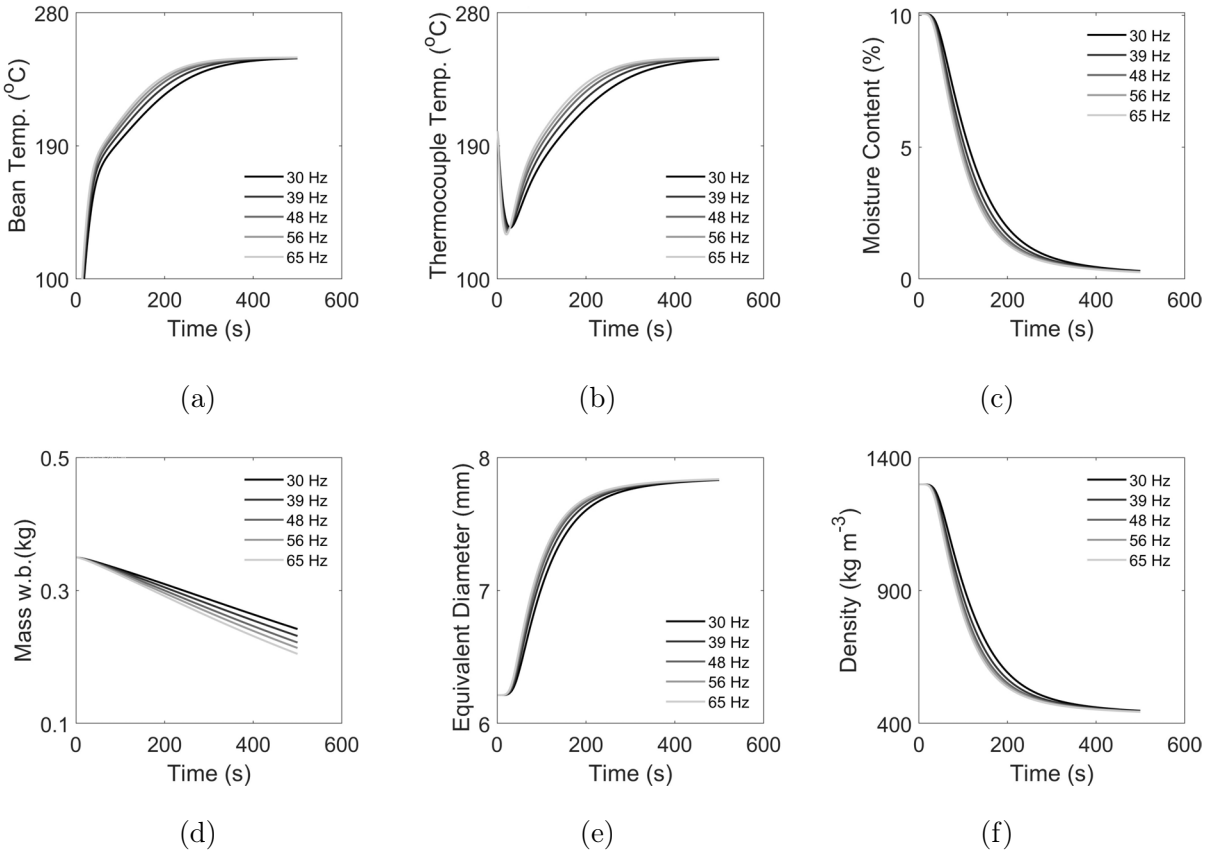

Figure 6.7: The effect of airflow in the range of 4.2-10.0 m s^{-1} (corresponding to fan frequencies of 30-65 Hz) on predicted (a) bean temperature, (b) thermocouple temperature, (c) moisture, (d) batch size (mass), (e) bean size (equivalent diameter) and (f) density.

Batch size

The batch size determines the number of beans and the total surface area of the batch available for heat transfer. In the simulation, the number of beans scales based on the specified batch size and subsequently, the heat transfer area, A_{ab}, scales with it. The batch size also determines the BBMF (as shown in Chapter 4), which affects the resulting thermocouple response coefficient and effectiveness factor. Figure 6.8 demonstrates the effect of batch size in the range of 200-500 g on coffee's predicted temperature and subsequent physicochemical development - for the simulations here, a constant inlet air temperature of 250°C and a fan frequency of 48 Hz was used.

Batch size has a significant effect on all predicted properties. Greater batch sizes correspond to lower rates of bean and thermocouple temperature evolution, which in turn reduces the rate of change of moisture, mass, bean size and density. The predicted profiles show that at a given time, smaller batch sizes will have lower moisture and density, yet experimental data (in Chapter 3) established that at the same colour, larger batch sizes, whose physicochemical transformation rates are lower, correspond to greater moisture and mass loss and thus have lower roast yields.

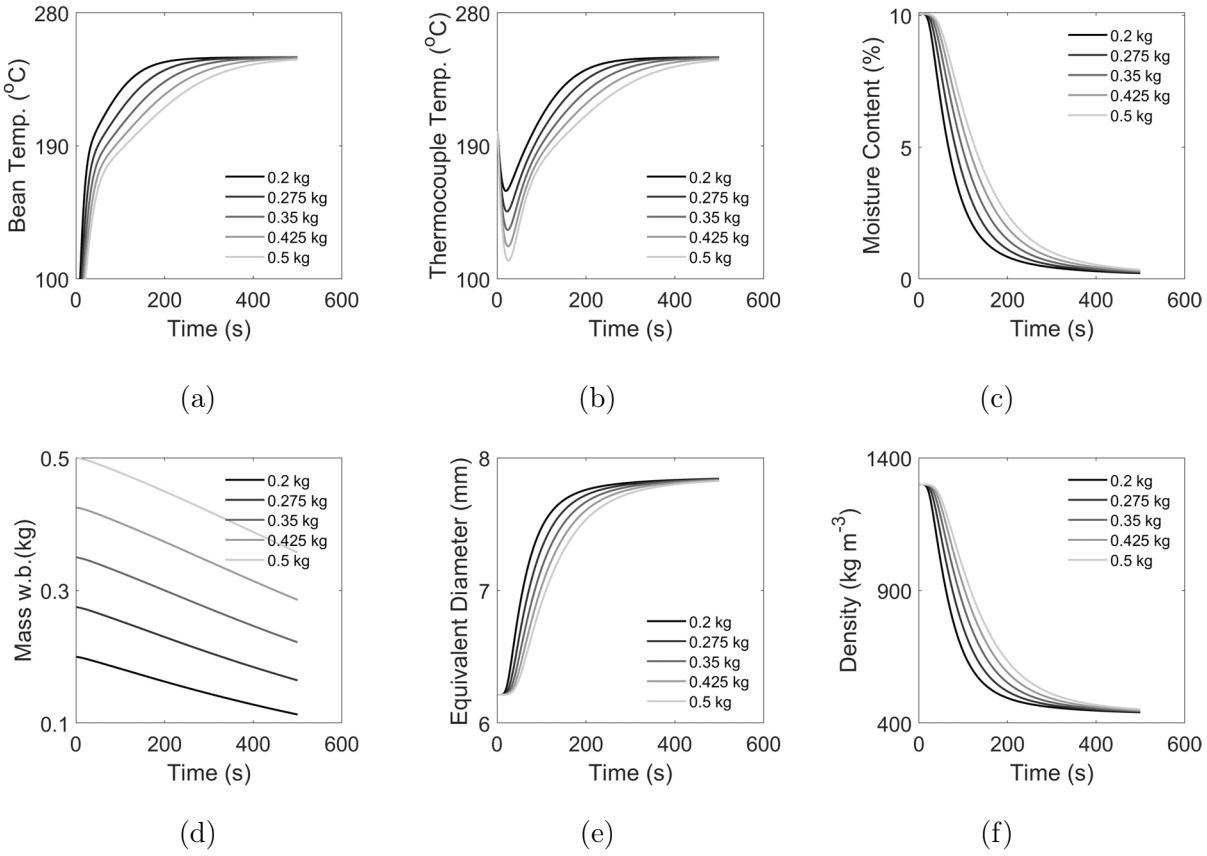

Figure 6.8: The effect of batch size (mass basis) in the range of 200-500 g on predicted (a) bean temperature, (b) thermocouple temperature, (c) moisture, (d) batch size (mass), (e) bean size (equivalent diameter) and (f) density.

6.2.3 Parameter estimation

Based on the analysis above, the air-to-metal heat transfer rate was assumed negligible (i.e., $Q_{am} = 0$ W) for the following simulations. In this way, the thermocouple response coefficient, K (s^{-1}), and the heat transfer effectiveness factor, η_A, were estimated in the bounds of

$0.01 \leq K \leq 1.00\ s^{-1}$ and $0.01 \leq \eta_A \leq 1.00$, respectively. Using the least squares fitting procedure outlined in Sections 6.1.4, η_A and K were estimated such that the RMSE between the predicted (thermocouple) and experimental time-temperature profiles was minimised up to first crack.

Estimated parameters (thermocouple response coefficient, K (s^{-1}) and heat transfer effectiveness factor, η_A), as well as the Root Mean Square Error (RMSE) between the predicted and experimental time-temperature profiles corresponding to the two case studies - i.e., (i) variation of constant inlet air temperature and (ii) variation of batch size and airflow - are displayed in Tables 6.3 & 6.4, respectively.

Variation of constant inlet air temperature

Prediction of the time-temperature profiles corresponding to different constant inlet air temperatures on coffee's roasting transformation (at moderate batch size (0.35 kg) and airflow (48 Hz fan frequency)) was achieved with good accuracy. The estimated parameters and corresponding RMSE of the predicted time-temperature profiles are outlined in Table 6.3. Figure 6.9 presents a comparison of the estimated and predicted (from Eqs. 7.17-7.14) parameter values for both the thermocouple response coefficient (Figure 6.9(a)) and heat transfer effectiveness factor (Figure 6.9(b)).

Both the thermocouple response coefficient, K (s^{-1}) and heat transfer effectiveness factor, η_A, were found to be a function of the input variable, i.e., the constant inlet air temperature, T_{ai} (°C) (R^2=0.876; RMSE=0.001 s^{-1} & R^2=0.929; RMSE=0.01, respectively):

$$K = 9.86 \times 10^{-13} T_{ai}^{4.22} + 0.0253 \tag{6.16}$$

$$\eta_A = -1.94 \times 10^{-3} T_{ai} + 0.930 \tag{6.17}$$

Figure 6.9(a) shows that the thermocouple response coefficient increased as the constant inlet air temperature increased. A similar effect was observed during the analysis of the model's sensitivity, in that the applied constant inlet air temperature affected the time and temperature of the roasting profile's global minimum (i.e., the 'turning point'). In Figure 6.9(b), the heat transfer effectiveness is shown to decrease as the applied constant inlet air

temperature increases. Whilst the heat transfer effectiveness factor is not affected by airflow, a lower heat transfer effectiveness factor corresponds to a greater heat transfer coefficient, α (W m^{-2} K^{-1}), as the Nusselt number approximation (Eq. 6.11) overestimates the convective heat transfer coefficient, h_{ab} (W m^{-2} K^{-1}). Note that as $\eta_A \to 0$, $\alpha \to h_{ab}$. Values of η_A are in the range determined by (Schwartzberg, 2002) for spouted bed roasters of different scales.

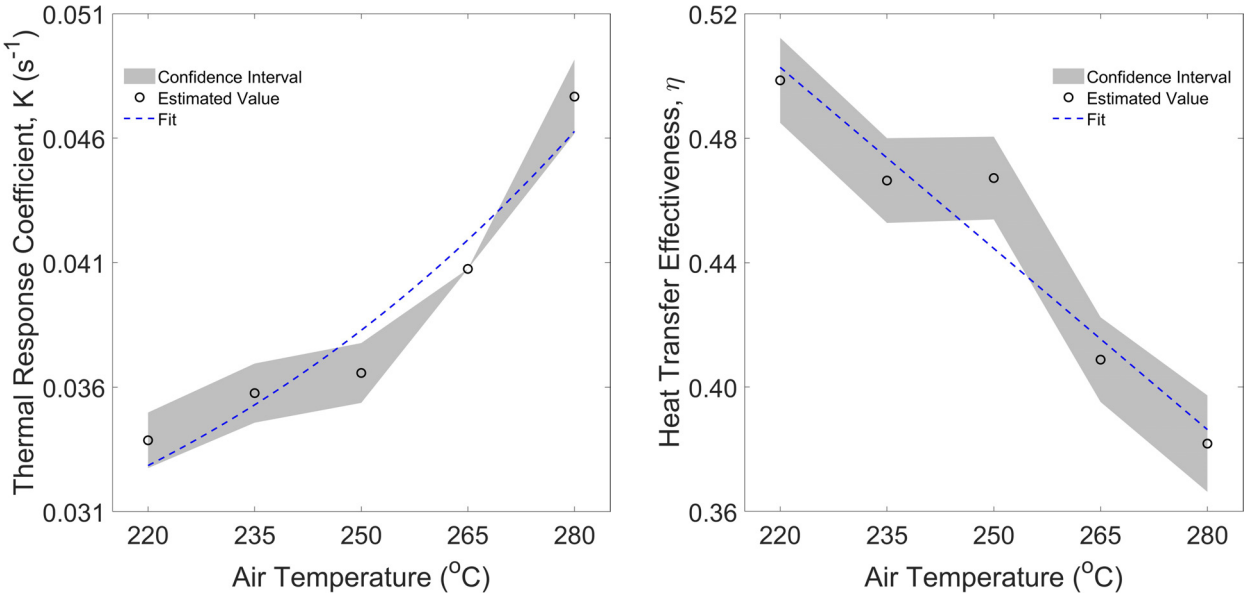

(a) Thermocouple Response Coefficient

(b) Heat Transfer Effectiveness

Figure 6.9: Estimated (a) thermocouple response coefficient and (b) heat transfer effectiveness factor as a function of constant inlet air temperature.

Table 6.3: Estimated parameters from the batch-scale, zero-dimensional simulation of time-temperature roasting profiles for the study of different constant inlet air temperatures.

Inlet Air Temp. (°C)	**Batch Size (kg)**	**Fan Freq. (Hz)**	**Thermal Response Coefficient (s^{-1})**	**Effectiveness Factor**	**RMSE (°C)**
220	0.35	48	0.034±0.001	0.50±0.01	4.4
235	0.35	48	0.036±0.001	0.47±0.01	4.7
250	0.35	48	0.037±0.001	0.47±0.01	4.9
265	0.35	48	0.041±0.000	0.41±0.01	4.3
280	0.35	48	0.048±0.001	0.38±0.02	5.1

Variation of batch size & airflow

The goodness-of-fit of the predicted time-temperature profiles corresponding to different batch sizes and airflows was reasonable for most process conditions (as indicated in Table 6.4), although the time-temperature profiles corresponding to roasts of low batch size and/or low airflow combinations were not so well predicted, likely due to the bean bed dynamics that influence the bias of the thermocouple measurement toward the temperature of either the air or beans. This measurement bias therefore results in a confounding problem for the simulations, as they attempt to capture the thermophysical interactions of both the air and the beans with the thermocouple. This in turn reveals the limits of the simulations, being robust for different batch sizes operated at moderate to high airflow, but not fully capturing the phenomena for low batch size and low airflow conditions.

Both estimated parameters were found to be a function of the input variables. The thermocouple response coefficient, K (s^{-1}), can be defined based on the air mass flow rate, G_a (kg s^{-1}), and batch size, m_{bs} (kg), (R^2=0.873; RMSE=0.006 s^{-1}):

$$K = -8.13 \times 10^{-3} + 1.05 G_a + 7.66 \times 10^{-2} m_{bs} \tag{6.18}$$

The heat transfer effectiveness factor, η_A, can be described based on the batch size (R^2=0.944; RMSE=0.06):

$$\eta_A = 1.82 m_{bs} - 0.105 \tag{6.19}$$

The inclusion of the Biot number in Eq. 6.10 reduces the heat transfer coefficient to account for the thermal inertia of the bean bed. The Nusselt number approximation (Eq. 6.11) therefore overestimates the heat transfer coefficient. It is interesting that the heat transfer effectiveness was not significantly affected by airflow. This suggests that estimation of the heat transfer coefficient sufficiently accounts for variation of airflow due to its relation with Nusselt, Reynolds and Prandtl numbers (i.e., Eq. 6.11). Yet, this also suggests that the heat transfer effectiveness factor, in conjunction with the Biot number, is sufficient to account for variation in bean bed dynamics observed in Chapter 4. Figure 6.10 presents a comparison of the estimated and predicted (from Eqs. 7.18-7.15) parameter values for both the thermocouple response coefficient (Figure 6.10(a)) and heat transfer effectiveness factor (Figure

6.10(b)).

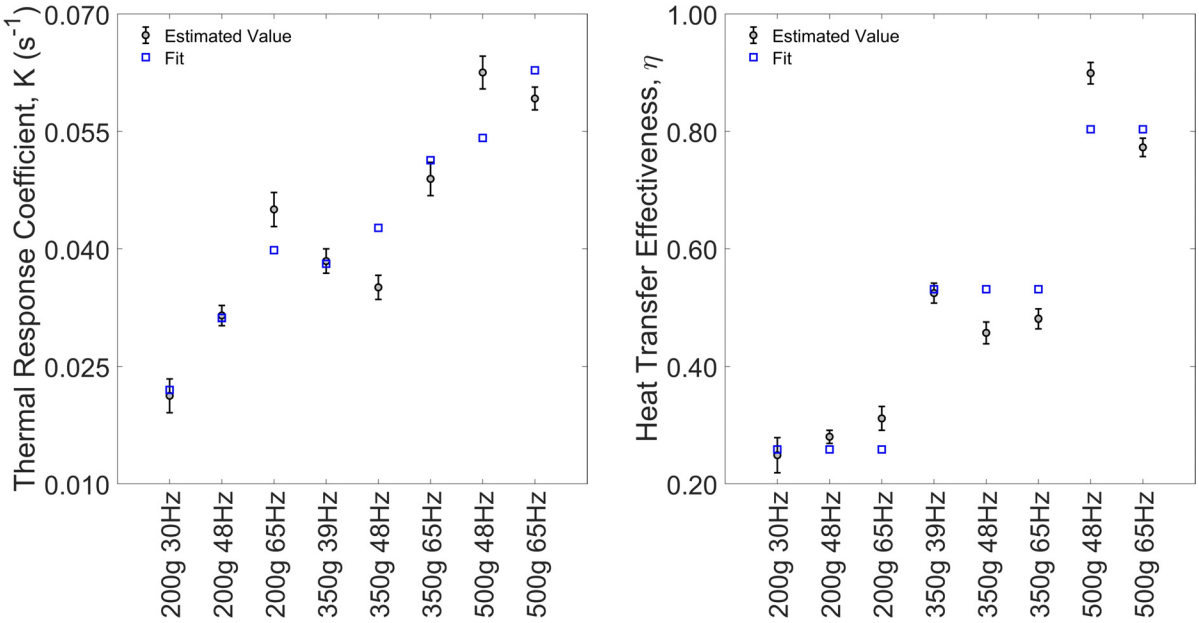

(a) Thermocouple Response Coefficient (b) Heat Transfer Effectiveness

Figure 6.10: Estimated (a) thermocouple response coefficient and (b) heat transfer effectiveness factor as a function of batch size and airflow.

Table 6.4: Estimated parameters from the batch-scale, zero-dimensional simulation of time-temperature roasting profiles for the study of different batch size and airflow combinations.

Inlet Air Temp. (°C)	**Batch Size (kg)**	**Fan Freq. (Hz)**	**Thermal Response Coefficient (s^{-1})**	**Effectiveness Factor**	**RMSE (°C)**
250	0.20	30	0.021±0.002	0.25±0.03	8.4
250	0.20	48	0.031±0.001	0.28±0.01	4.3
250	0.20	65	0.045±0.002	0.31±0.02	4.2
250	0.35	39	0.038±0.002	0.52±0.02	6.5
250	0.35	48	0.035±0.002	0.46±0.02	5.7
250	0.35	65	0.049±0.002	0.48±0.02	4.8
250	0.50	48	0.063±0.002	0.90±0.02	4.1
250	0.50	65	0.059±0.001	0.77±0.02	3.3

Effect of thermocouple diameter

For this study, the same roasting conditions were used for each roast, whilst the thermocouple used to measure the 'product' time-temperature profile varied in diameter. Therefore, there are no expected differences in air-to-bean heat transfer rates, thus similar heat transfer effectiveness factors are expected. During calibration, the thermocouple response coefficient and heat transfer effectiveness factor were first estimated within the previously stated bounds ($0.01 \leq K \leq 1.00\ s^{-1}$ and $0.01 \leq \eta_A \leq 1.00$). From this first estimation, the standard deviation of the heat transfer effectiveness factor was low (0.02 s^{-1}), so the mean value (0.43 s^{-1}) was specified for a second pass parameter estimation, wherein only the thermocouple response coefficient was estimated within the same bounds as before.The estimated thermocouple response coefficient and RMSE corresponding to the four temperature responses are provided in Table 6.5.

Table 6.5: Estimated thermocouple response coefficient obtained via non-linear least squares fitting, that minimises the RMSE between simulated and experimental roasting profiles measured using thermocouples of 0.50, 0.75, 1.00 and 1.50 mm diameters.

Thermocouple Diameter (mm)	**Thermocouple Response Coefficient (s^{-1})**	**RMSE (°C)**
0.50	0.059±0.003	8.0
0.75	0.049±0.002	5.7
1.00	0.0300±0.001	6.0
1.50	0.0271±0.001	3.9

Prior to the onset of endo-/exo-thermic reactions shortly after first crack, the predicted time-temperature profiles agree with the experimental data (3.9°C $\leq$ RMSE $\leq$ 8.0°C), although the greatest error between the predicted and experimental profiles is seen around the turning-point ($0 \leq t \leq 60$ s), particularly for thin thermocouples. This is likely due to noise incurred by bean-thermocouple collisions.

Figure 6.11 depicts the relationship between the estimated thermocouple response coefficient, K (s^{-1}) and thermocouple diameter (d_T); these parameters can be described using a single-term power law model (R^2=0.917; RMSE=0.004 s^{-1}), which can be implemented as a subroutine into the time-temperature profile simulation with no significant impact on the predicted profile's RMSE.

$$K = 0.0353 d_T^{-0.774} \tag{6.20}$$

If we recall the definition of the thermocouple time constant, τ from Chapter 2, we can redefine the thermocouple response coefficient, such that it's inversely related to τ, i.e., $K = f(\tau^{-1})$. Correlation of the thermocouple response coefficients (i) determined using the experimental model-system (K_e) and (ii) predicted via first principles (K_{fp}) with thermocouple diameter can be redefined as a function of thermocouple diameter such that:

$$K_e = 0.198 d_T^{-0.807} \tag{6.21}$$

$$K_{fp} = 0.54 d_T^{-1.47} \tag{6.22}$$

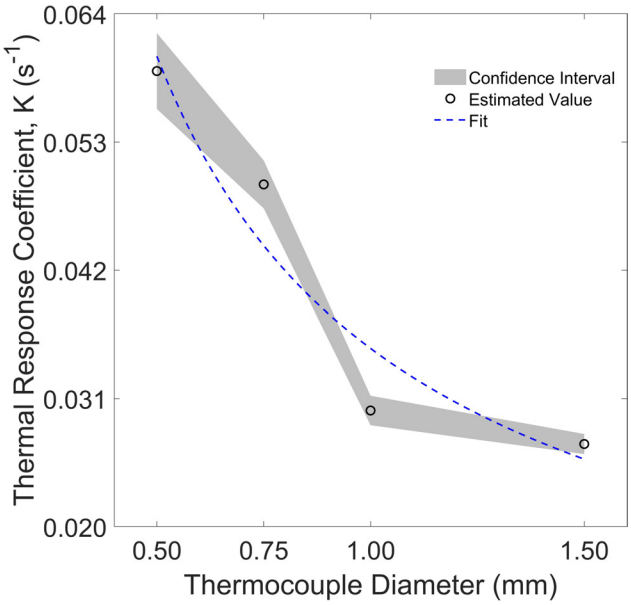

Figure 6.11: Correlation of thermocouple response coefficient obtained via non-linear least squares fitting with thermocouple diameter.

Interestingly, extrapolation of Eq. 6.20 enables users to predict the time-temperature profiles measured by larger diameter thermocouples ($d_T \geq 1.50$ mm). To demonstrate, the time-temperature profile simulation was implemented with a subroutine (resolved from 6.20) for large diameter thermocouples ($1.5 \leq d_T \leq 9.0$ mm) – the predicted time-temperature profiles are presented in Figure 6.12 alongside predictions corresponding to thin thermocouples ($0.5 \leq d_T \leq 1.5$ mm) for reference.

Eq. 6.20 can be used as a subroutine within the time-temperature profile simulations without further experimentation, although thermocouple response times from the first principles and model-system approach do not translate directly to those in the roasting chamber. This reveals the complexity of translating thermocouple measurements across roaster design and scale, although assuming that the observed differences between Eqs. 6.20 & 6.22 can be generalised, the following linear correlation could be used to translate thermocouple response times from first principle predictions to those observed in real roasting systems (R^2=0.988):

$$K' = 0.0282K_{fp} - 0.0191 \tag{6.23}$$

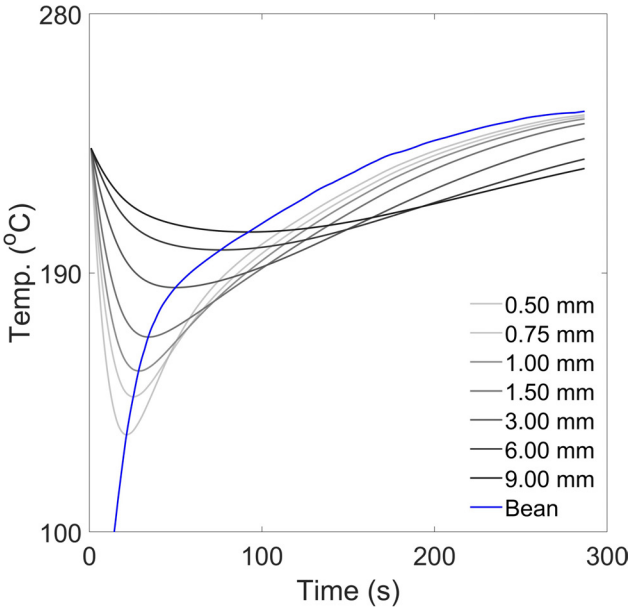

Figure 6.12: Predicted time-temperature roasting profiles measured using thermocouples of diameters in the range of $0.5 \leq d_T \leq 9.0$ mm) corresponding to the same roasting conditions.

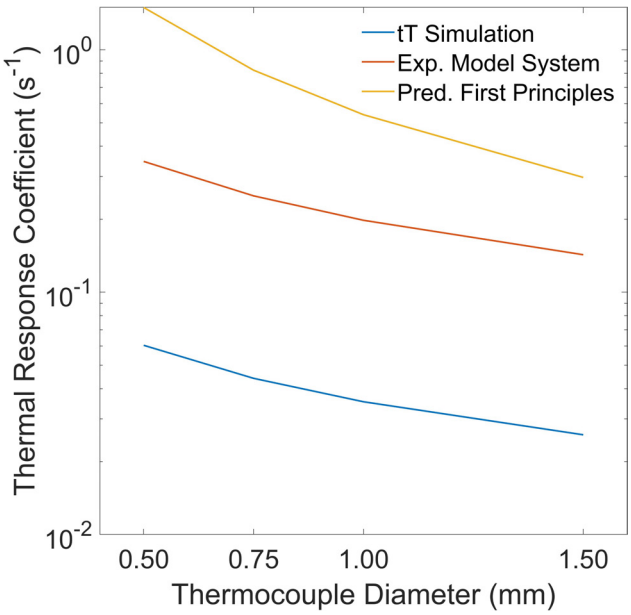

Figure 6.13: Comparison of thermocouple response coefficient obtained via (i) non-linear least squares fitting, (ii) first principles prediction and (iii) experimental, model system with thermocouple diameter.

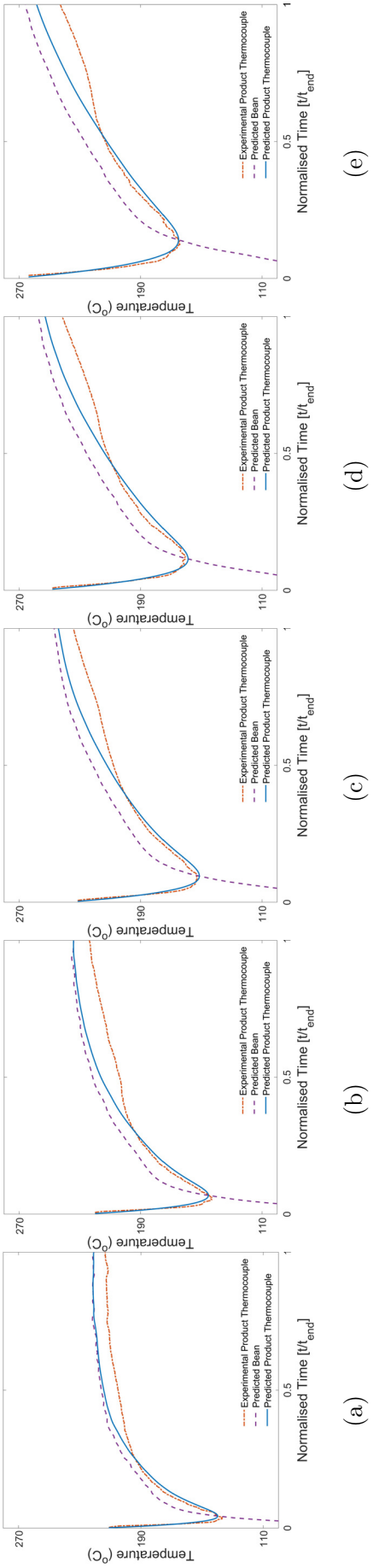

Figure 6.14: Predicted and experimental time-temperature roasting profiles corresponding to (a) 350g 220°C 48Hz, (b) 350g 235°C 48Hz, (c) 350g 250°C 48Hz, (d) 350g 265°C 48Hz and (e) 350g 280°C 48Hz.

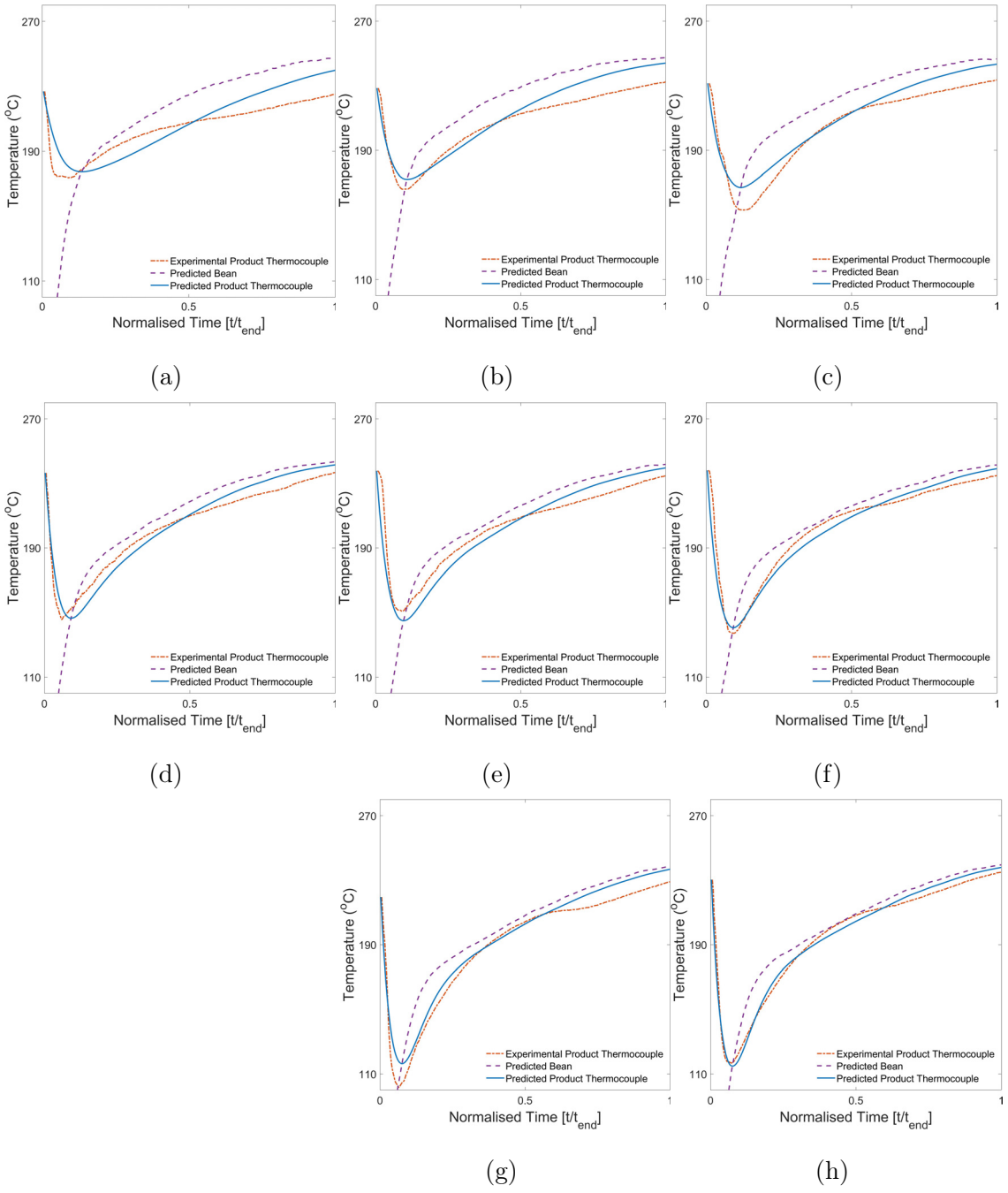

Figure 6.15: Predicted and experimental time-temperature roasting profiles corresponding to (a) 200g 250°C 30Hz, (b) 200g 250°C 48Hz, (c) 200g 250°C 65Hz, (d) 350g 250°C 39Hz, (e) 350g 250°C 48Hz, (f) 350g 250°C 65Hz, (g) 500g 250°C 48Hz and (h) 500g 250°C 65Hz.

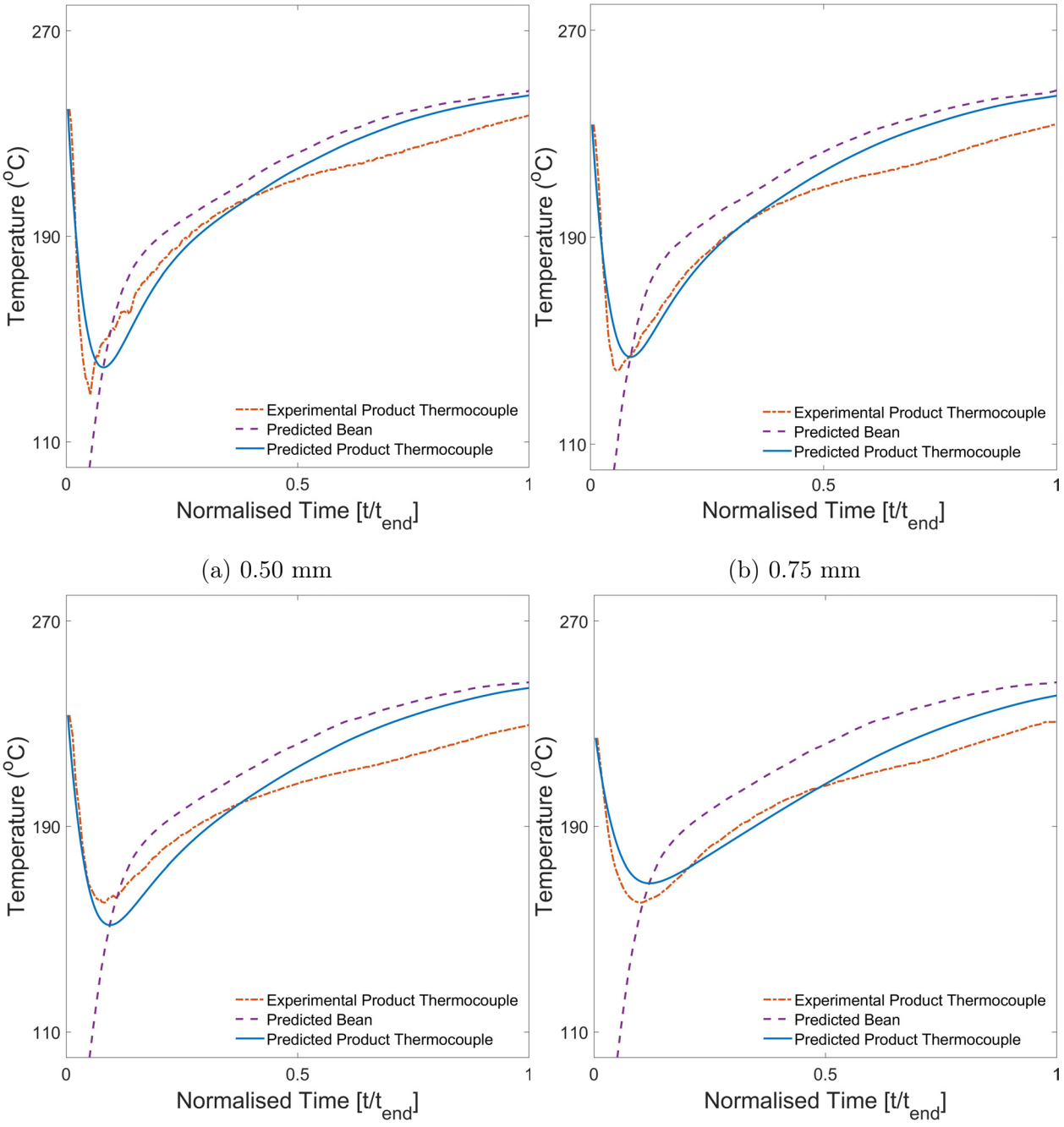

(a) 0.50 mm

(b) 0.75 mm

(c) 1.00 mm

(d) 1.50 mm

Figure 6.16: Predicted and experimental time-temperature profiles corresponding to a constant inlet air temperature roast at 250°C measured using thermocouples with diameters of (a) 0.50 mm, (b) 0.75 mm, (c) 1.00 mm and (d) 1.50 mm.

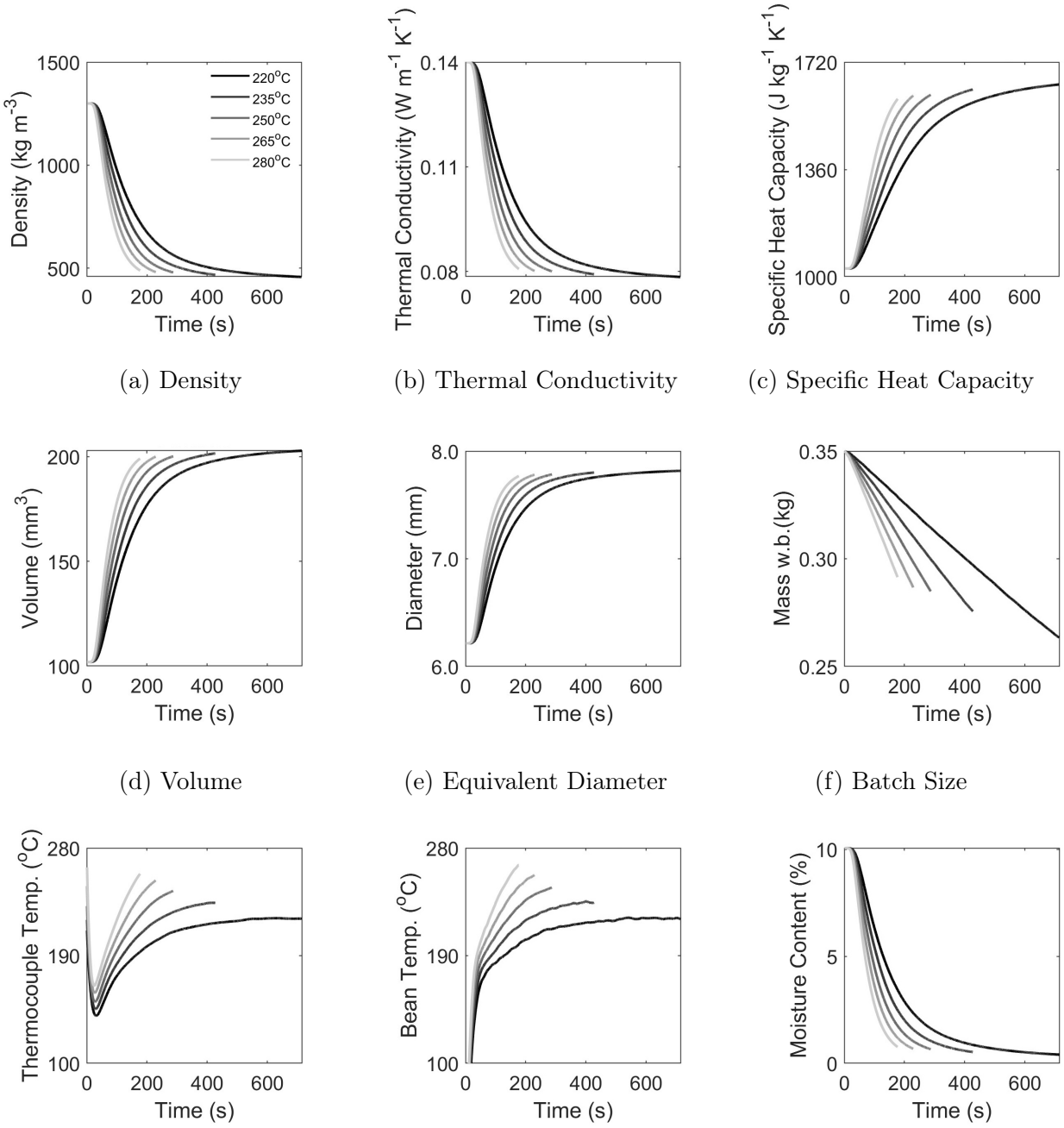

(a) Density (b) Thermal Conductivity (c) Specific Heat Capacity

(d) Volume (e) Equivalent Diameter (f) Batch Size

(g) Thermocouple Temp. (h) Bean Temp. (i) Moisture

Figure 6.17: Predicted time-temperature profiles and corresponding physicochemical development of coffee during simulated roasting at different constant inlet air temperatures. Subplots demonstrate the effect of process conditions on (a) density, (b) thermal conductivity, (c) specific heat capacity, (d) volume, (e) equivalent diameter, (f) batch size (mass basis), (g) thermocouple temperature, (h) bean temperature and (i) moisture. Data legend is displayed only in (a) for visual clarity.

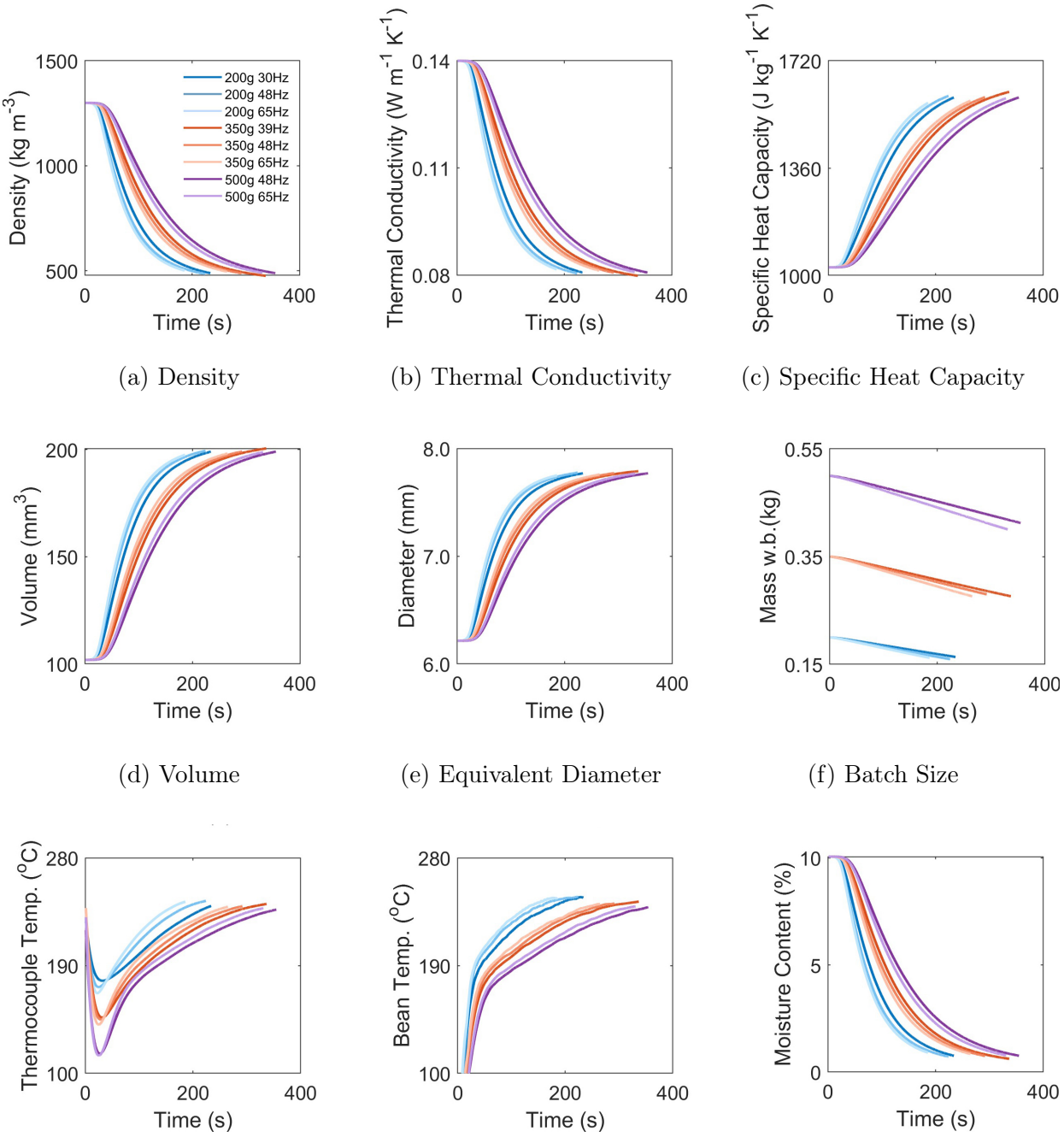

(a) Density (b) Thermal Conductivity (c) Specific Heat Capacity

(d) Volume (e) Equivalent Diameter (f) Batch Size

(g) Thermocouple Temp. (h) Bean Temp. (i) Moisture

Figure 6.18: Predicted time-temperature profiles and corresponding physicochemical development of coffee during simulated roasting with different batch size and airflow combinations. Subplots demonstrate the effect of process conditions on (a) density, (b) thermal conductivity, (c) specific heat capacity, (d) volume, (e) equivalent diameter, (f) batch size (mass basis), (g) thermocouple temperature, (h) bean temperature and (i) moisture. Data legend is displayed only in (a) for visual clarity.

6.2.4 Time-temperature roasting profiles

A comparison of experimental and predicted time-temperature profiles corresponding to the three case studies are presented. These simulations utilise empirical measurements for the initial conditions of bean temperature, thermocouple temperature, batch size (mass basis) and moisture content. Simulation test cases intended to replicate the studies that established the variation of constant inlet air temperature and variation of airflow and batch size. For both studies, the coffee bean's thermal properties, i.e., the density, thermal conductivity and specific heat capacity, are calculated via correlations in Chapter 3.3-3.4 The mass loss rate coefficient was calculated specifically for each study. Moisture loss kinetics are suitable for both studies and were therefore implemented in that way. The thermocouple response coefficient and effectiveness factor were also calculated specifically for each study, such that Eqs. 7.18 & 7.15 were used for a constant inlet air temperature of 250°C with different batch sizes and/or airflows, whereas Eqs. 7.17 & 7.14 were implemented for different inlet air temperatures at constant batch size and airflow. All other methodologies are consistent across both case studies.

Comparisons of predicted and experimental time-temperature profiles are presented in Figures 6.14, 6.15 & 6.16 for data corresponding to case study I (variation of constant inlet air temperature), II (variation of batch size and airflow) and IV (effect of thermocouple diameter), respectively.

Predicted thermocouple time-temperature profiles agree well at early times, accurately capturing the response of the thermocouple and the 'turning point'. Considering the highest constant inlet air temperature condition (Figure 6.14(e)), the predicted profile begins to diverge from the experimental profile at approximately $t = 0.5t_{end}$, wherein the predicted profile significantly overestimates the temperature. As the constant inlet air temperature decreases, the time at which divergence occurs decreases, such that for the lowest constant inlet air temperature condition (Figure 6.14(a)), divergence occurs at approximately $t = 0.25t_{end}$. The temperature difference observed in the later stages of roasting has previously been attributed to exothermic reactions (Schwartzberg, 2002), yet these data suggest

that the washed-processed coffee used in these studies behaves differently. Particularly at high constant inlet air temperatures, there is an apparent plateau attributed to a decrease in the heating rate or possibly the effect of endothermic cooling.

Whilst off-line (analytical) measurements of coffee's thermal degradation indicate that moisture is generated in the late stages of roasting due to Maillard-type reactions, as well as pyrolysis (Schwartzberg, 2002; Geiger, 2004), by monitoring the levels of water and carbon dioxide in the exhaust of a roaster, Geiger (2004) observed that even with the combined on- and off-line measurements, there is not sufficient evidence to indicate that this alone is responsible for the reduced heating rate. The change in temperature response in the late stages of roasting could therefore be attributed to the cell wall's return to the glassy state (Geiger, 2004), melting of galacto-mannans (Redgwell et al., 2002; Geiger, 2004), or the generation of carbon dioxide (Geiger, 2004) and carbon monoxide. It is expected that differences in coffee's cellular composition established during plant growth and cherry ripening, as well as the extent of cellular degradation due to different post-harvest processing methods, will determine both the cellular and chemical degradation during the softening and hardening phenomena that occur during roasting.

Similar effects were observed for time-temperature profiles corresponding to the variation of batch size and airflow that are outlined in Figure 6.15, although it is clear that airflow has a significant effect on the thermocouple response at early times. It is of course critical to recall the batch size used in this study, as well as the thermocouple position in the roasting chamber. As both batch size and airflow produce different particle dynamics (as established in Chapter 4), the bean-thermocouple and air-thermocouple interactions are expected to be dependent on the BBMF and the packing of beans around the thermocouple. Although the predicted time-temperature profiles are generally, reasonably accurate, those for smaller batch sizes (0.2 kg) struggle to accurately capture the response of the thermocouple, whilst the fit for larger batch sizes ($>$0.2 kg) is significantly better at early times. When considering the poor fitting at early times with the lack of fit beyond first crack, it is clear that the simulations struggle with low batch sizes. This is most probably due to the small scale of

the roaster and in particular, the loose packing of beans around the thermocouple and the bias toward measurement of air temperature. For larger spouted bed and rotating drum roasters with greater batch sizes, the effect of this measurement bias is expected to be lower and so scale-up of the simulations to larger roasters is anticipated to yield good results.

6.2.5 Physicochemical transformation

Predictions of coffee's corresponding physicochemical development were computed during simulation of the time-temperature profiles via correlations established in Chapter 4 and kinetic models in Chapter 5. Figures 6.17-6.18 present coffee's physicochemical development during simulated roasting for different process conditions. Figure 6.17 depicts simulations corresponding to different constant inlet air temperatures (200, 235, 250, 265, 280°C) using a moderate batch size (0.35 kg) and moderate airflow (48 Hz fan frequency). Figure 6.18 exhibits simulations corresponding to different batch sizes (0.20-0.50 kg) and airflows (30-65 Hz fan frequency) using a moderate constant inlet air temperature (250°C). In both figures, the effect of process conditions on density, thermal conductivity, specific heat capacity, volume, equivalent diameter, batch size (mass basis), moisture, thermocouple temperature and bean temperature are illustrated.

In Section 6.2.2, the effect of input variables on moisture, batch size, bean size (equivalent diameter) and density were discussed. These observations also apply to Figures 6.17-6.18. Changes in volume, specific heat capacity, thermal conductivity and volume are estimated based on moisture kinetics, therefore, a higher rate of moisture loss corresponds to a more rapid (i) decrease in density and thermal conductivity and (ii) increase in volume and specific heat capacity.

Both Figures 6.17 & 6.18 demonstrate that all input variables (constant inlet air temperature, batch size and airflow) have a significant effect on the simulated responses and their evolution rates. So if these responses were evaluated at a specified time, for example at $t = 100$ s, the physicochemical properties wouldn't depend on the process conditions. Yet, if the same responses were evaluated at times that correspond to equivalent whole bean coffee colours that reflect realistic commercial products, the simulated (and experimental) findings indicate

that some of these responses (moisture, volume and density) might be insensitive to process conditions.

6.2.6 Modelling coffee's exothermic reactions

For simplification, exothermic reactions that initiate around first crack were assumed to have no impact on coffee's time-temperature response. Differences between simulated and experimental time-temperatures profiles after first crack (Figures 6.14-6.16) are clear. Figure 6.19 depicts the residuals (i.e., the difference in temperature (simulated minus experimental) corresponding to each of the simulated case studies. Temperature data before first crack is considered within the confidence interval of the simulated profile and thus discounted from analysis.

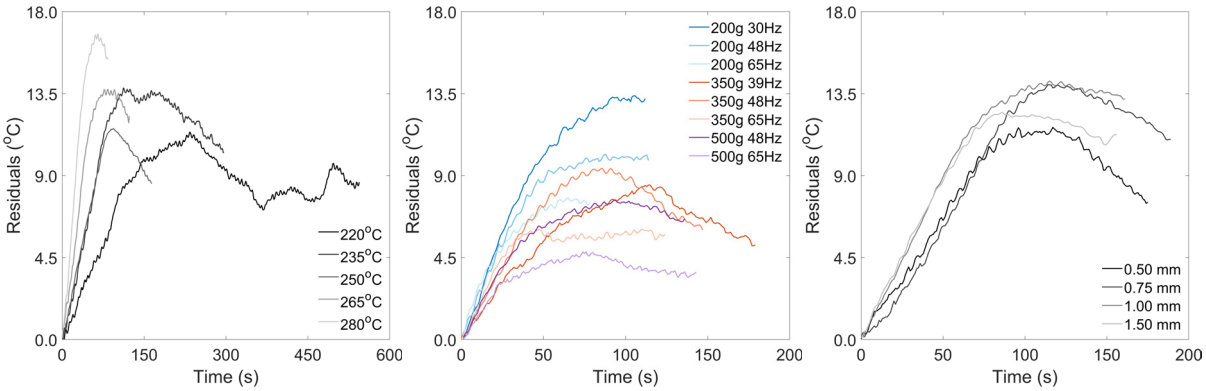

(a) case study I: Constant Inlet Temp. (b) case study II: Batch Size & Airflow (c) case study IV: Thermocouple Diameter

Figure 6.19: Residuals of the simulated time-temperature profiles corresponding to data from (a) case study I: variation of constant inlet air temperature (Figure 6.14), (b) case study II: variation of batch size and airflow (Figure 6.15) and (c) case study III: effect of thermocouple diameter (Figure 6.16) that show the influence of endo- and/or exo-thermic reactions on the simulation's accuracy.

The residuals in Figure 6.19 suggest that exothermic reactions in the later stages of roasting do not fully explain the findings of this study. It is proposed that around first crack there is an endothermic event that might result from complex cellular degradation, which occurs prior to the onset of exothermic reactions. Whilst there is anecdotal (not peer-reviewed) evidence that the endothermic cooling is attributed to the release of water vapour or CO_2,

observations of Geiger 2004 indicate that this is unlikely.

To estimate the radiant power associated with exothermic reactions, q_{exo} (W), the coffee's emissivity, ε, surface area, A_b (m^2) and temperature, T_b (K) must be analysed. The coffee batch's total surface area is approximated by the product of the mean individual bean surface area and number of beans in the batch (estimated via the batch mass and packing density), and the total surface area of coffee is assumed equal for all process conditions (neglecting process dependent differences in the rates of mass loss and volumetric expansion). Coffee's emissivity was taken from literature (Ngoensod, Nunak, and T.Suesut, 2017) - $\varepsilon = 0.765$, the Stefan Boltzmann constant, $\sigma = 5.67{\times}10^{-8}$ W m^{-2} K^{-4} (Bergman et al., 2011) and the surrounding temperature, T_s (K) is assumed to be the constant inlet air temperature:

$$q_{exo} = A_b \sigma \varepsilon (T_b^4 - T_s^4) \tag{6.24}$$

For the Kenyan Arabica green coffee used in the case studies here, the mean individual bean surface area, $A_{s,b}$ is 128.73 mm^2; the packing density, 7966 kg^{-1}, which equates to 2788 beans in a 350 g batch, so total batch surface area, A_b is 0.359 m^2. If the actual bean temperature T_b (K) is considered in the range 25-265°C, q_{exo} against time will be a scaled plot of T_b against time (in the range of $0.5 \leq q_{exo} \leq 6.5$ kW). In this way, radiant heat transfer associated with these beans in this temperature range is not sufficient to explain the observed temperature disturbances.

Estimation of heat fluxes are critical for integration with the prescribed thermal balance and the formulated models estimate the thermal load that corresponds to the endo- and/or exo-thermic reactions that disturb the time-temperature profile after first crack. However, in their current state of development, the simulations in this Chapter already facilitate process development, demonstrating both the timing and the magnitude of the step change required to control the coffee's development during the late stages of roasting.

6.3 Best practices for roasters

6.3.1 Limitations & robustness

Whilst the data driven approach to this study provides novelty and enables well-calibrated simulations that accurately capture the real-system behaviour of coffee during roasting, it is an approach that limits the applicability of the simulations when it comes to more diverse process conditions, different roaster designs and scales, as well as different foodstuffs.

Kinetic models of mass loss were developed for each case study due to the sequential, compartmentalised approach to roasting exploration. This resulted in the need to implement "IF" functions that select the relevant subroutines used to determine the mass loss rate coefficient. As this action restricts the current simulation to specify either a different constant inlet air temperature, or a different batch size and airflow combination, a larger study that follows a design of experiments approach and encompasses all input variables within a reasonable range would enable a global mass rate coefficient subroutine to be established and subsequently implemented in the simulation to query a broader range of roasting scenarios.

The correlations used in this study to include coffee's volumetric expansion is relevant only for roasting and cannot account for (i) different initial bean sizes, (ii) swelling due to rehydration, or (iii) shrinkage due to low temperature ($<$100°C) drying. Development and implementation of a kinetic model to describe coffee's density and volumetric expansion would enable a greater range of scenarios to be queried, although inclusion of these models as ODEs can affect numerical stability during parameter estimation protocols. It was for this reason that the kinetic models in Section 5.4-5.5 were not implemented here.

After first crack, predicted time-temperature profiles overestimated the batch-mean temperature. This significant deviation indicates that the thermodynamics of first crack do not correspond to sensible heating only and might be attributed to cellular degradation or latent heat.

The thermocouple response times determined via both first principles and model systems

in Chapter 2 were compared with values estimated from the time-temperature profile simulations to assess the predictive capabilities of the correlations. Whilst the general trend of thermocouple response coefficient versus thermocouple diameter are similar from each of the three approaches, the absolute values vary due to (i) various assumptions during the first principles approach, (ii) temperature and airflow conditions in the experimental model-system approach and (iii) bean-thermocouple interactions and installed location within the roasting chamber.

6.3.2 Tools for process and product development

Once parameters relating to characteristics of the roasting system (thermocouple response coefficient) and applied process conditions (heat transfer effectiveness factor and heat loss across the roaster) are estimated for a range of process conditions they can be fixed for the roaster, reducing further need for process characterisation. The simulation, shown to be robust to different constant inlet air temperatures, batch sizes and airflows, thus enables the batch temperature, volume-averaged bean temperature, bean moisture content, batch mass, bean diameter, bean density and thermal properties to be predicted for known raw material properties and applied process conditions.

Characterisation of the thermocouple response coefficient both *in-silico* and *in-situ* equip developers with a tool to translate process measurements of bean-bed temperatures to those of the beans themselves. In this way, these time-temperature profile simulations could permit direct translation of process conditions across roasting systems via the predicted bean temperature, as opposed to the current convention of the bean-bed thermocouple temperature.

For application, developers can use prescribed raw material properties and process parameters to explore the impact of batch size, constant inlet air temperature and airflow on the coffee's time-temperature response. Furthermore, prescribed process parameters can be used in conjunction with user provided coffee properties (different moisture contents, bean sizes and thermal properties) to explore their impact on final product properties.

6.4 Conclusions & outlook

Using a data driven approach, a zero-dimensional, batch-scale simulation of coffee roasting time-temperature profiles was developed. Empirical characterisation of coffee's thermal and physicochemical evolution from green to part-roasted and roasted enabled calibration of the simulation to confidently predict coffee behaviour of coffee during roasting under a variety of process conditions.

Through measurements of airflow and temperature, the roaster's process parameters were characterised and used for model calibration to improve the accuracy and usefulness of the simulations. Correlations of coffee's physicochemical properties, used to determine the volumetric expansion, changes in density, specific heat capacity and thermal conductivity, as well as kinetic models to describe changes in mass and moisture, were employed to inform coffee's physicochemical development during roasting. Dimensionless Reynolds, Prandtl and Nusselt numbers were used to approximate the heat transfer coefficient and used in conjunction with the batch's surface area to estimate the heat flux.

Two estimated parameters were introduced to capture the characteristics of the roasting system that are not easily measured, the (i) thermocouple response coefficient and (ii) heat transfer effectiveness factor. Using a non-linear least squares fitting procedure (implemented as a trust-region-reflective algorithm), system-specific parameters were estimated and correlated with relevant input variables. These correlations were implemented as subroutines to include process-dependent parameters.

These simulations of heat and mass transfer during roasting provided accurate predictions of time-temperature profiles prior to first crack. The simulations were robust to variation of roasting process parameters including constant inlet air temperature, batch size and airflow, although the physics of real-system behaviour beyond first crack were not well captured. As many commercial control strategies decrease the thermal load as roasting progresses, comprehension of the observed deviations are necessary to improve the functionality of the simulations.

That said, this chapter demonstrated a robust tool for developers whose input variables are simple and rapid to measure and whose output provides predictions of coffee's time-temperature roasting profile and resulting physicochemical development. This work digitises process and product development procedures and therefore allows developers to virtually determine requirements for green coffee properties, process conditions or roasted coffee properties depending on their approach.

Chapter Seven

Bean-scale simulations of heat and mass transfer of coffee roasting in spouted bed roasters

Coffee's in-bean colour distribution indicates its thermal history and can inform expected in-cup flavour. To identify the development of coffee's in-bean, spatial variation of temperature during roasting, a three-dimensional simulation was developed. The approach was similar to the zero-dimensional, batch-scale simulation in Chapter 6, in that measured process parameters and product properties (from Chapters 2, 3 and 4), as well as calibrated models (from Chapters 5 and 6) were used to reduce the number of free parameters. Here, heat transfer to a single coffee bean was determined via energy balance wherein dynamic, convective boundary conditions were evaluated using particle motion data established in Chapter 4. Development of the simulation considered the accuracy of particle geometry and accounted for changes in coffee's thermophysical properties (mass, moisture, density, thermal conductivity and specific heat capacity) that occur during roasting. These calibrated, conjugate heat transfer simulations provide predictions of both the volume-averaged bean bed temperature (when coupled with the zero-dimensional simulation), and the spatial temperature distribution within coffee beans during roasting. Knowledge of the bean's temperature distribution can then be used to inform expected colour (and other chemical concentrations) in roasted coffee products.

7.1 Methodology

These methodologies outline the data-driven approach used to develop and calibrate a bean-scale heat transfer simulation of coffee during roasting in a spouted bed roaster.

The experimental approach consisted of (i) characterisation of the flow properties of the roaster, the corresponding thermophysical properties of the roasting air and specification of time-temperature roasting profiles (i.e., the roasting conditions) (extracted from Chapters 2-3), (ii) characterisation of the coffee on its transformation from green to roasted using various measurement techniques (detailed in Chapter 3) and (iii) analysis of particle motion data (established in Chapter 4) to determine the coffee's particle trajectories through the roaster.

Using these data, the modelling approach is outlined such that: (i) an energy balance over the roaster is formulated to describe the air-to-bean heat transfer during roasting, (ii) the regional variation of the heat transfer coefficient is determined as a function of the bean's position in the roaster and the relative effects on the flow properties, according to the dimensionless Reynolds number (as presented in Chapter 4), (iii) the kinetic behaviour of coffee's physicochemical transformation is implemented based on data established in Chapter 5 and (iv) the bean geometry is evaluated to optimise accuracy and computational time.

7.1.1 Experimental approach: Process characterisation

Roasting process specification

Pilot-scale roasting trials were performed using a spouted bed roaster (RFB-S, Neuhaus Neotec) to generate comprehensive data later used to calibrate the batch-scale heat and mass transfer simulations. Two case studies relating to relevant process parameters were considered: (i) case study I - variation of constant inlet air temperature for a specified batch size and constant airflow (Chapter 3.3) and (ii) case study II - variation of batch size and airflow at a specified constant inlet air temperature (Chapter 3.4).

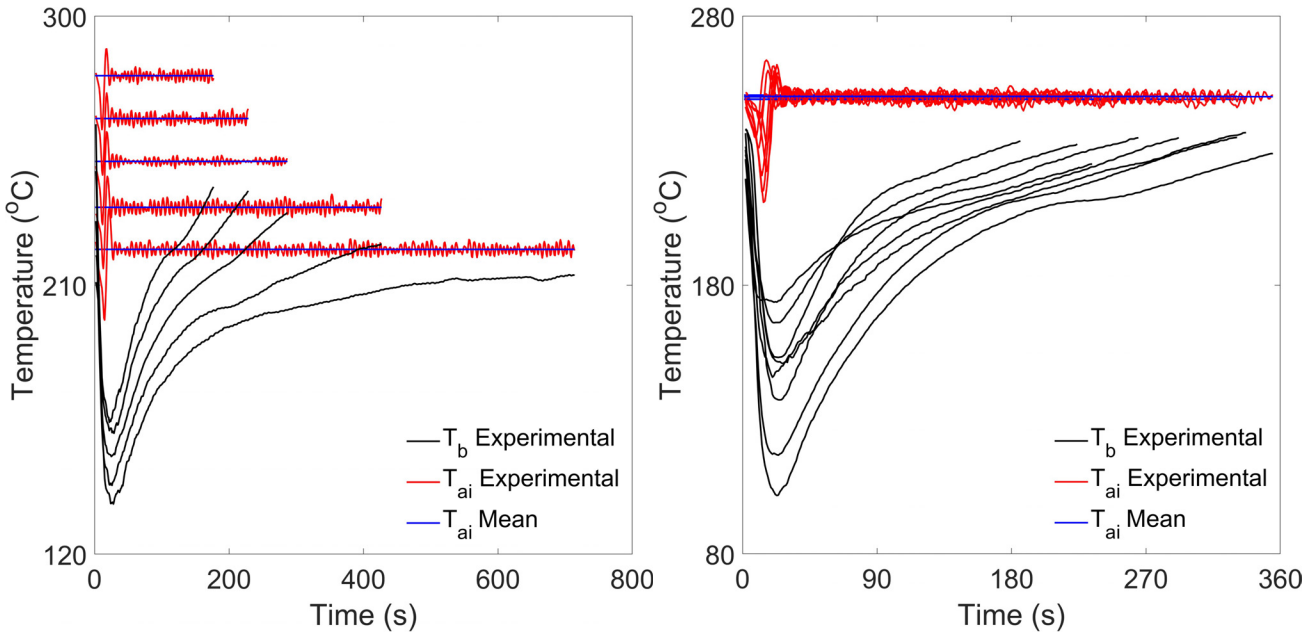

(a) Case Study I (b) Case Study II

Figure 7.1: Observed fluctuations of inlet air temperature shown relative to the product time-temperature profiles obtained from constant inlet air temperature roasts of Kenyan Arabica coffee in a spouted bed roaster with variation of (a) constant inlet air temperatures of 220, 235, 250, 265 and 280°C and (b) batch sizes (200, 350 and 500 g) and airflows (30, 39, 48 and 65 Hz fan frequencies). Red lines correspond to the recorded inlet air temperatures, blue lines with the implemented (mean) inlet air temperatures and black lines the recorded bean temperatures.

Implementation of inlet air temperature

The measured inlet air temperature profile for each roasting condition demonstrated precise control of the roaster. As beans were loaded into the roaster, airflow and heating are temporarily stopped as a safety precaution. This produced large fluctuations in the air temperature response at early times, so the first 30 s of data were discounted in calculation of the mean inlet air temperature. To ensure accuracy of the simulations whilst maintaining realistic process conditions, the mean of the measured inlet air temperature profile for times greater than 30 s was used to represent the temperature of the drying air for the model's boundary conditions. Calculated mean inlet air temperature values were in good agreement with set points (±2°C from set point) and were assumed to be robust for other constant

inlet air temperature conditions. Figure 7.1 presents time-temperature profiles corresponding to roasts with a constant inlet air temperature, clearly indicating the fluctuation in inlet air temperature at early times. In Figure 7.1, the red lines indicate the recorded inlet air temperature, whilst the blue lines indicate the mean air inlet temperature implemented in the modelling work.

Heat loss

Air-to-metal heat transfer was estimated through consideration of heat loss in the roaster. As described in Chapter 2, pre-heating the roaster until steady-state (i.e., thermal equilibrium) ensures consistent process conditions are established prior to roasting. Readers are reminded of Figures 2.5(a) and 2.6(a) in Chapter 2, which show a typical pre-heating time-temperature profile corresponding to a constant inlet air temperature and the impact of inlet air temperature airflow on steady-state temperatures in a spouted bed roaster, respectively. These figures demonstrate the heat loss across the system.

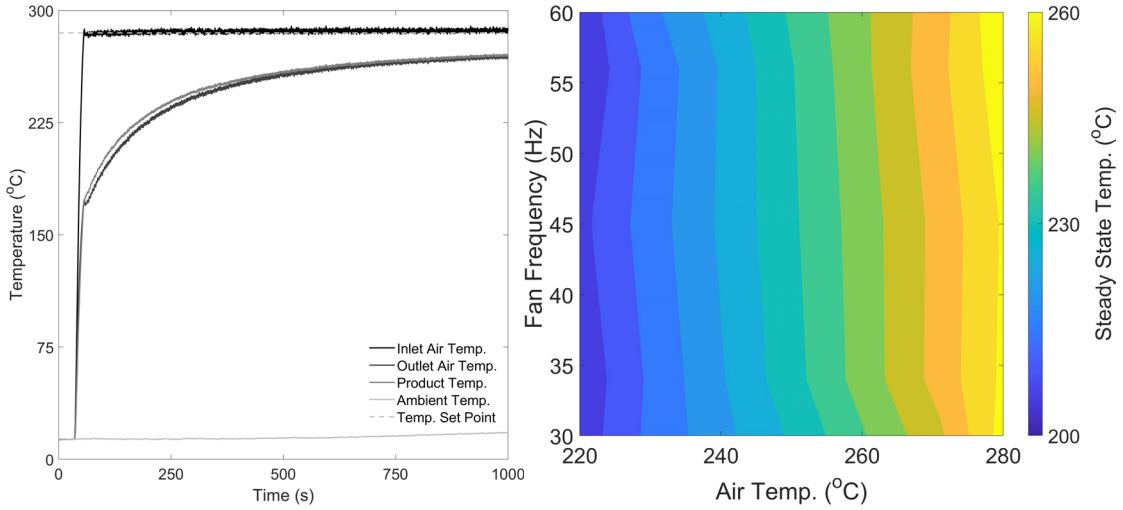

(a) (b)

Figure 7.2: The temperature differential of the spouted bed roaster during pre-heating as illustrated by (a) the measured time-temperature profile from ambient temperature to thermal equilibrium, and (b) a contour plot of product thermocouple temperatures at thermal equilibrium as function of inlet air temperature and airflow setpoints.

Here, heat loss is accounted for in the bean-scale model using Eq. 2.1 as in Chapter 2, wherein heat loss is the temperature difference between the inlet air ($T_{a,i}$) and product

thermocouples at steady-state ($T_{s,s}$). Inlet air temperature data were used to approximate the applied thermal load, assuming no temperature differential before and after the air is distributed by the orifice plate.

Airflow calibration & the effect of the air distributor

Many roasters use fan frequency for airflow set-points, yet conversion of these settings to velocity and mass flow rate is required for implementation in heat and mass transfer models. For the airflow calibration, both the air velocity, u_a (m s^{-1}) and mass flow rate, G_a (kg s^{-1}), through the roaster were determined as a function of airflow setting, f (Hz), using a hot-wire anemometer (405i, Testo) as described in Chapter 2.

For the pilot-scale spouted bed roaster, fan frequencies of 30-65 Hz correspond to air velocities of 4.2-10.0 m s^{-1} and inlet air mass flow rates of 0.0141-0.0311 kg s^{-1} at the inlet of the roaster. The effect of the roaster's air distributor (Figure 7.3) on air velocity in the roasting chamber (i.e., the superficial air velocity) was considered to increase model accuracy (Che et al., 2023).

The air velocity at the roaster's spout was estimated via the distributor's open area across the largest 5 rows of the plate design, according to the continuity equation (Bergman et al., 2011). Small orifice diameters ($d < 2.5$ mm (rows 6-13)) are expected to have little impact on the spout's air velocity due to the greater mass of beans above those orifices. For an open area of 1.36 cm^3 (sum of area in rows 1-5), assuming no change in density, the superficial air velocity through the orifice and into the roasting chamber for fan frequencies of 30, 39, 48 and 65 Hz are 8.79, 11.87, 14.95 and 20.77 m s^{-1}, respectively, at ambient temperature (ca. 20°C).

Thermophysical properties of air

The thermophysical properties of air are dependent on air temperature and influence airflow through the roaster. Utility functions generated via regression of thermophysical data from Engineering-ToolBox were imported from Chapter 2 to describe the air's thermal conductivity, k_a (W m^{-1} K^{-1}), specific heat capacity, $C_{p,a}$ (J kg^{-1} K^{-1}), viscosity, μ_a (Pa s) and

density, ρ_a (kg m^{-3}).

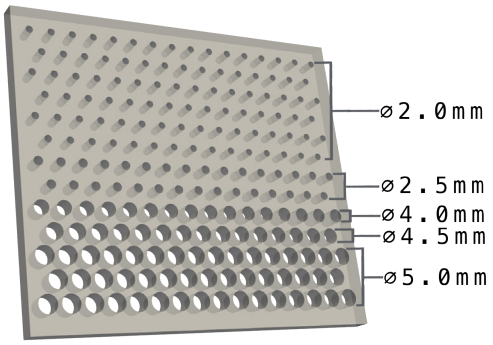

Figure 7.3: Geometry of the air distributor of the spouted bed roaster used to determine the air velocity at the roaster's spout.

7.1.2 Experimental approach: Product characterisation

For both case studies, green and roasted coffee analyses included mass, intrinsic and packing density, moisture content, colour (whole bean), principal dimensions, volume and surface area. For roast & ground coffee analyses, coffees were ground using a flat burr grinder (EG1, Weber Workshops) and analyses included colour, thermal properties (thermal conductivity, specific heat capacity & thermal diffusivity) and median particle size (via laser diffraction). Grinding was performed to achieve a target ground coffee median particle size, $x_{50} \approx 500$ μm, to reduce sample-to-sample variation. Further details on product characterisation are presented in Chapter 3.

7.1.3 Experimental approach: Particle motion data

Extraction of particle residence times & velocities

From the particle motion studies in Chapter 4.2, both the Lagrangian (individual particle trajectories) and Eulerian (time-averaged flow fields) data were used to inform the dynamic boundary conditions for the bean-scale thermal model. From the Eulerian occupancy profiles, the bean bed was delineated using an Otsu method threshold, so the size and shape of the bean bed and in-flight/freeboard regions were enumerated for beans of different roast degrees subject to different process conditions (variation of batch size and airflow). The Lagrangian trajectories were segregated using the known locations of each region, i.e., the bean-bed and the in-flight regions. The residence time and velocity of particles in each region was

thus established for all coffee samples and process conditions. An example of the delineated Lagrangian trajectories is presented in Figure 7.4; each colour indicates a different individual trajectory.

Regional variation of particle motion

In Figure 7.5, data corresponding to the delineated trajectories in Figure 7.4 is presented as histograms to illustrate the regional differences in residence times (Figure 7.5(a)) and velocities (Figure 7.5(b)).

Figures 7.6-7.8 illustrate how residence times and velocities in the bean bed and freeboard are influenced by roast degree, batch size and airflow, respectively. These data illustrate the significant effect of process conditions and product properties on particle motion. Process conditions determine: (i) the fraction of beans in the freeboard and the bean bed, (ii) the velocity of beans in each region and (iii) the residence time in each region. The implications for heat transfer (discussed in Chapter 4.4) are such that if the heat transfer coefficient in each region is distinct, the overall heating rate can be controlled by modulating process conditions that determine the residence time and velocity in each region. As the coffee's physicochemical properties develop during roasting, it is also evident that the heating rate will vary as roast degree increases (and density decreases) as the bean's motion is greatly influenced by its density.

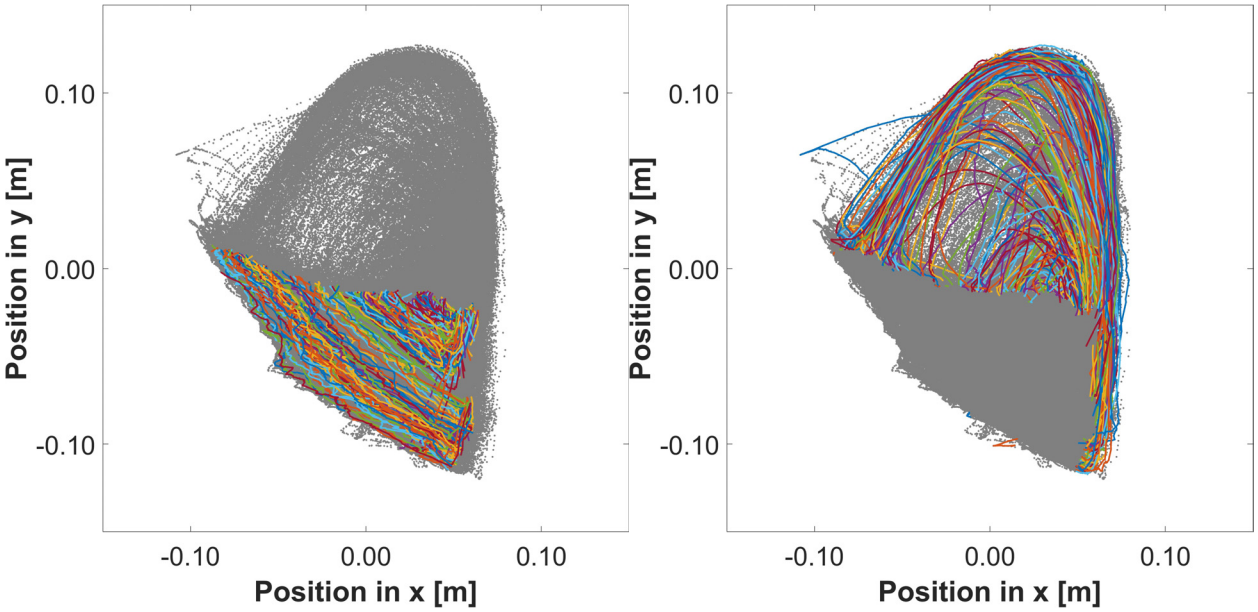

(a) Bean-Bed Trajectories (b) In-Flight/Freeboard Trajectories

Figure 7.4: Delineated Lagrangian particle trajectories in the (a) bean-bed and (b) in-flight/freeboard regions corresponding to 350 g of roasted coffee (278 s roasting time) with a fan frequency of 48 Hz.

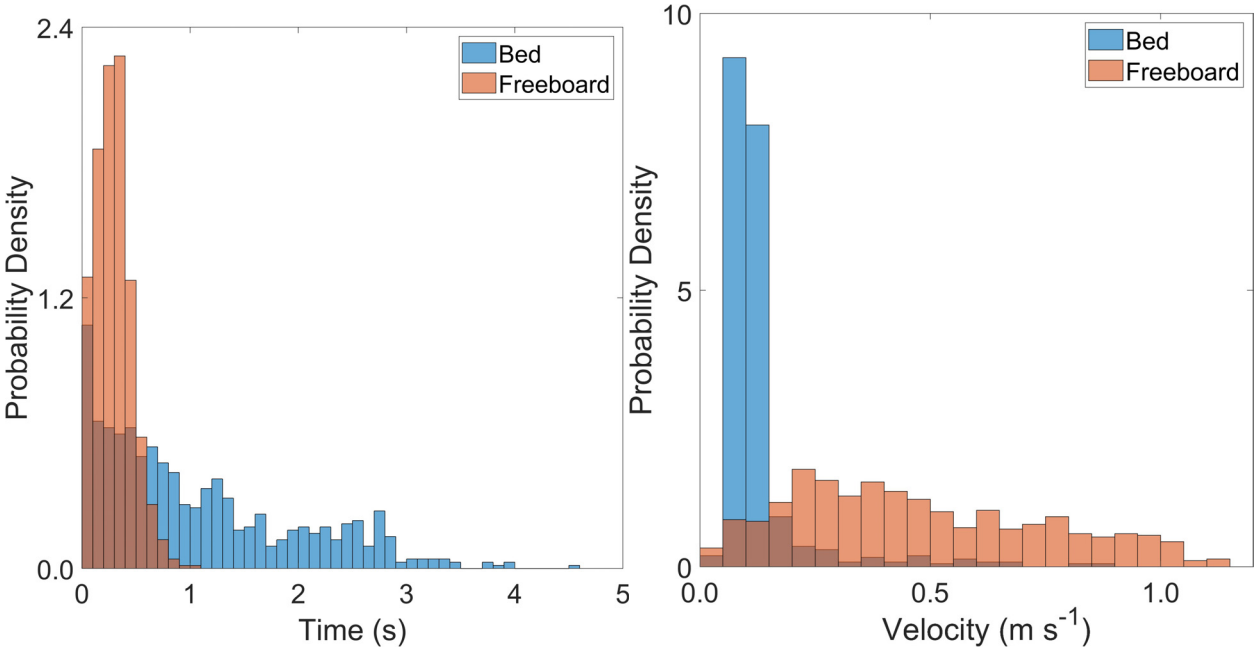

(a) Residence Time (b) Bean Velocity

Figure 7.5: Distribution of (a) residence time and (b) bean velocity in the bean-bed and in-flight/freeboard regions - data corresponds to 350 g of roasted coffee with a fan frequency of 48 Hz in a spouted bed roaster.

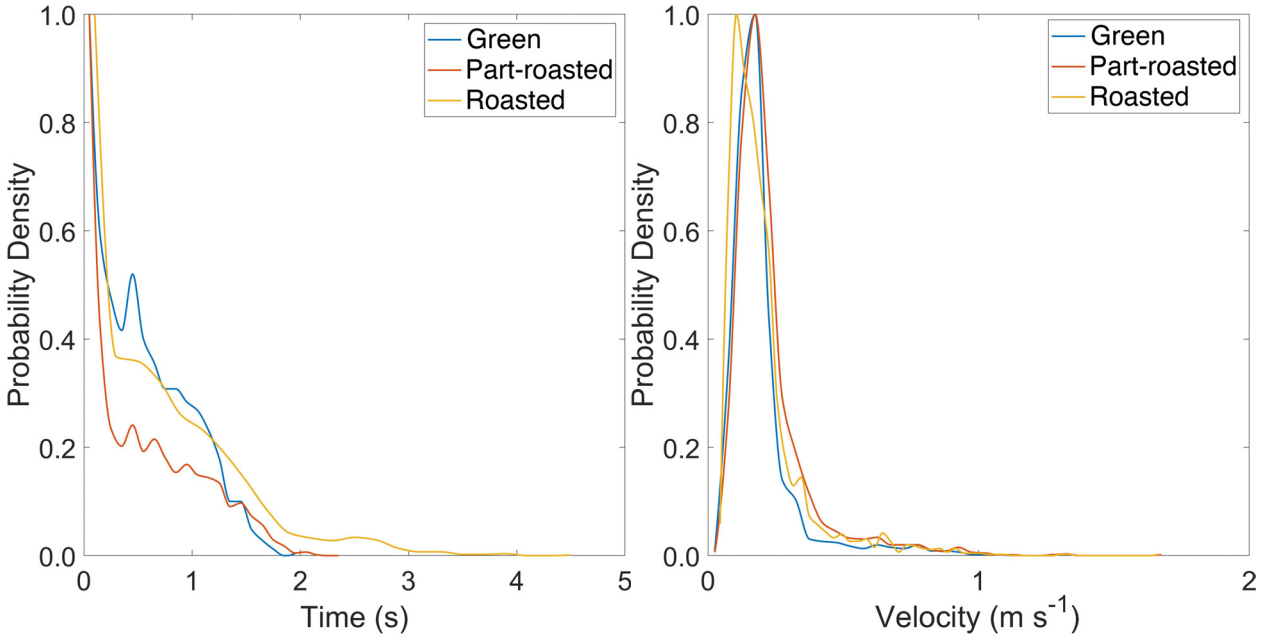

(a) Residence Time Bean Bed

(b) Velocity Bean Bed

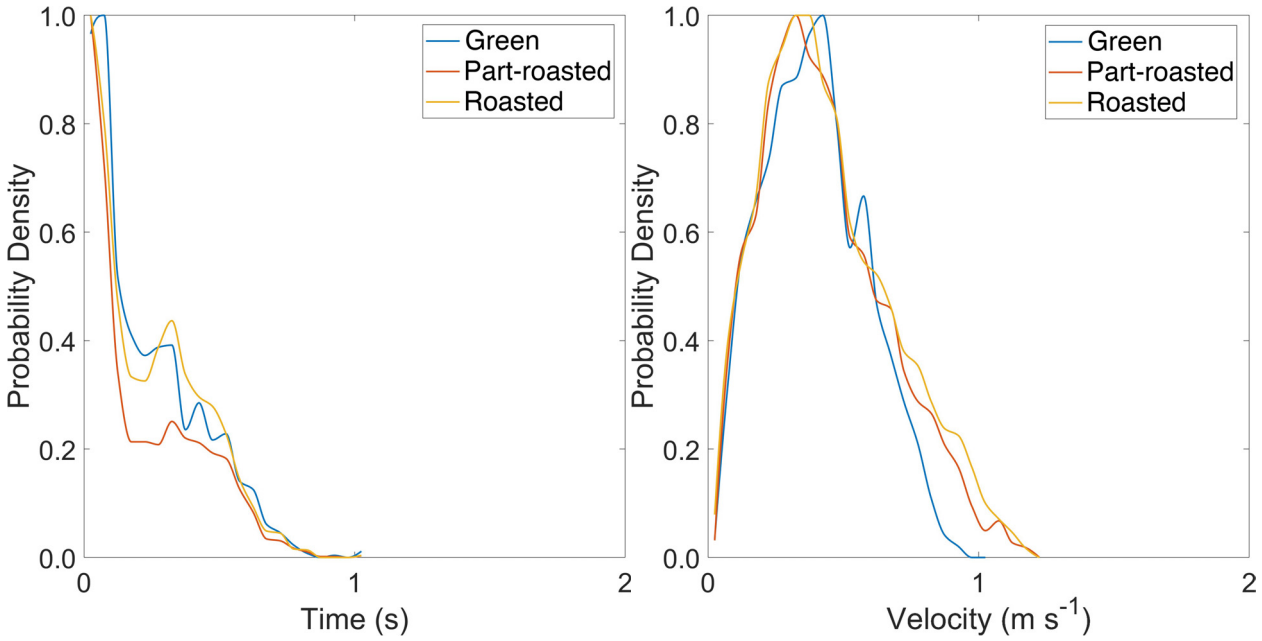

(c) Residence Time Freeboard

(d) Velocity Freeboard

Figure 7.6: Impact of roasting degree on the distribution of (a)&(c) residence time and (b)&(d) velocity of delineated Lagrangian particle trajectories in (a)-(b) the bean-bed and (c)-(d) the in-flight/freeboard regions extracted from real particle motion data corresponds to 350 g of green, part-roasted and roasted coffee with a fan frequency of 48 Hz.

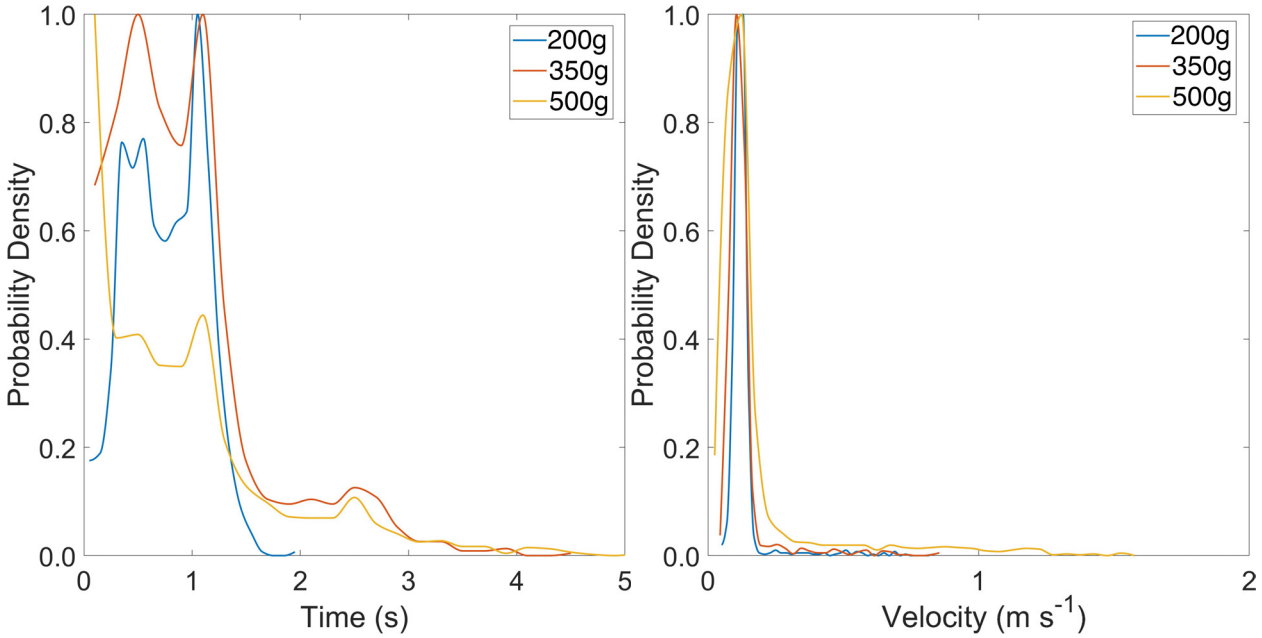

(a) Residence Time Bean Bed

(b) Velocity Bean Bed

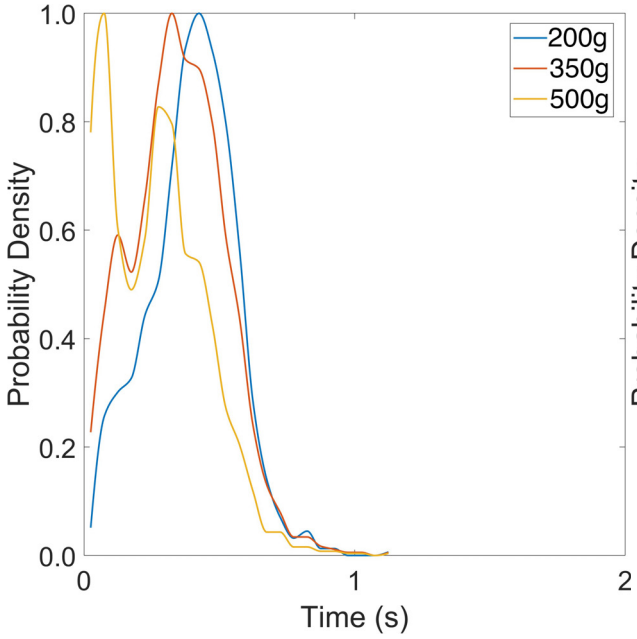

(c) Residence Time Freeboard

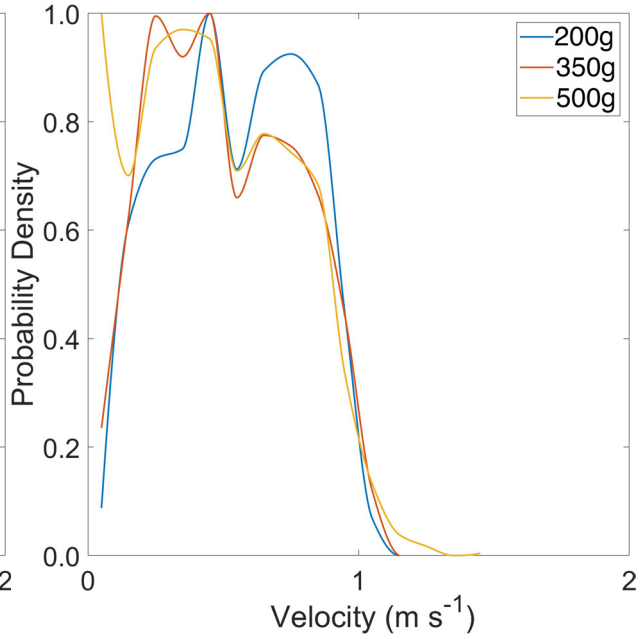

(d) Velocity Freeboard

Figure 7.7: Impact of batch size on the distribution of (a)&(c) residence time and (b)&(d) velocity of delineated Lagrangian particle trajectories in (a)-(b) the bean-bed and (c)-(d) the in-flight/freeboard regions extracted from real particle motion data corresponds to 200, 350 and 500 g of roasted coffee with a fan frequency of 48 Hz.

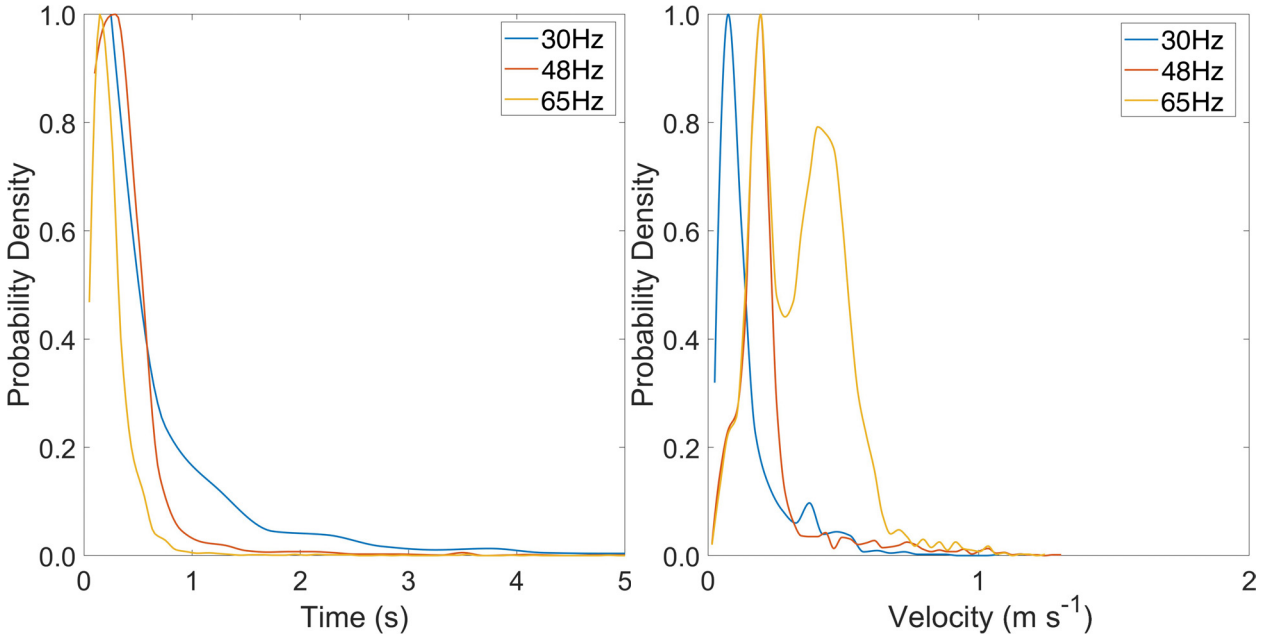

(a) Residence Time Bean Bed

(b) Velocity Bean Bed

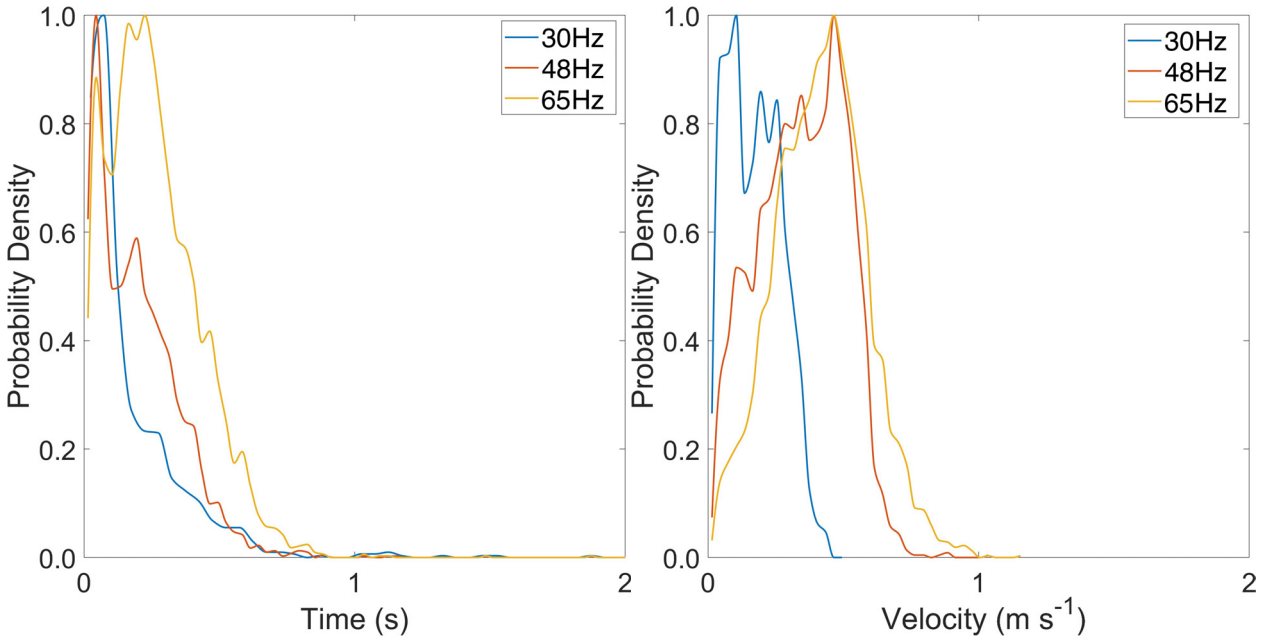

(c) Residence Time Freeboard

(d) Velocity Freeboard

Figure 7.8: Impact of airflow on the distribution of (a)&(c) residence time and (b)&(d) velocity of delineated Lagrangian particle trajectories in (a)-(b) the bean-bed and (c)-(d) the in-flight/freeboard regions extracted from real particle motion data corresponds to 200 g of green coffee with fan frequencies of 30, 48 and 65 Hz.

Implementation of particle motion data

For implementation within the bean-scale model, a random segment of time-stamped Cartesian data and velocity (t,x,y,z,v) (as in Figure 7.4) – where the time span of data is equivalent to the experimental roasting time – is extracted from the real particle motion data corresponding to the green coffee. Particle velocities correspond to the mean velocity in each regionally-segmented trajectory and determine the convective boundary conditions, while residence times (being the difference between the end time and start time of each regionally-segmented trajectory) defined the time-step of the heat transfer simulation. Figure 7.9 provides a sample of extracted particle motion data to demonstrate the numerical array implemented within the time-temperature profile simulations, wherein the region ID (1 refers to the bean bed; 2 refers to the freeboard), velocity and residence time is evaluated for each delineated Lagrangian trajectory.

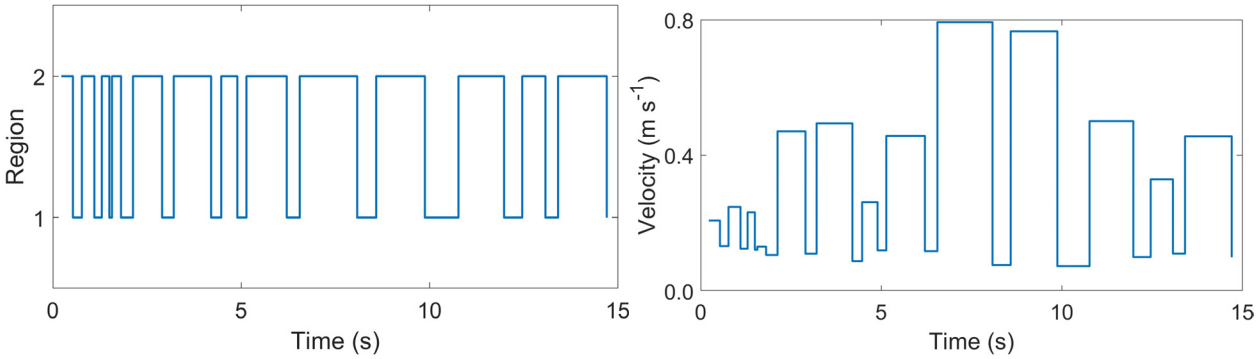

(a) Region ID

(b) Mean Bean Speeds

Figure 7.9: Extracted particle motion data to demonstrate the implemented numerical array, wherein each delineated Lagrangian trajectory was evaluated such that the (a) region ID (1 refers to the bean bed; 2 refers to the freeboard) and (b) mean bean speeds were determined for piece-wise continuous residence times - data corresponds to 350 g of roasted coffee with a fan frequency of 48 Hz.

7.1.4 Modelling approach: Bean-scale simulation

This subsection outlines the mathematical basis of the simulations, wherein an energy balance is first introduced to describe the temperature response of the coffee during roasting, with subsequent estimation of the regional heat transfer coefficients that determine the dynamic boundary conditions. The simulation's initial conditions and conversion of spatial bean temperatures to the expected thermocouple temperature are also detailed.

Energy balance at the bean-scale

The generalised thermal balance used to describe the unsteady state temperature of a coffee bean during roasting is:

$$q_b = q_{cd} + q_{e,c} + q_r \tag{7.1}$$

where (i) the transient energy flux into unit volume of the bean at some position, q_b (W m^{-3}),

$$q_b = \rho_b C_{p,b} \frac{\partial T_b}{\partial t} \tag{7.2}$$

(ii) the conductive heat flux into unit volume of the bean, q_{cd} (W m^{-3}):

$$q_{cd} = \nabla.(-k_b \nabla T_b) \tag{7.3}$$

(iii) moisture content is spatially uniform within the bean and water vaporisation is assumed to occur only within the bean, such that the endothermic heat flux (associated with water vaporisation) into unit volume of the bean, q_e (W m^{-3}):

$$q_e = \rho_{db} \Delta H_v \left(-\frac{\partial X_b}{\partial t} \right) \tag{7.4}$$

and (iv) the exothermic heat flux (due to pyrolysis reactions) out of unit volume of the bean, q_r (W m^{-3}):

$$q_r = \Delta H_r \left(\frac{\partial \rho_{db}}{\partial t} \right) \tag{7.5}$$

Thus, the generalised thermal balance describing heat transfer within the bean is

$$\rho_b C_{p,b} \frac{\partial T_b}{\partial t} + \nabla.(-k_b \nabla T_b) = \rho_{db} \Delta H_v \left(-\frac{\partial X_b}{\partial t} \right) + \Delta H_r \left(\frac{\partial \rho_{db}}{\partial t} \right) \tag{7.6}$$

The gradient of the function T_b, with geometry specified as Cartesian coordinates (i.e., (x, y, z)) is

$$\nabla T_b \equiv \left(\frac{\partial T_b}{\partial x}, \frac{\partial T_b}{\partial y}, \frac{\partial T_b}{\partial z} \right) \tag{7.7}$$

Thus, the Laplacian of the function T_b is

$$\nabla.(-k_b \nabla T_b) \equiv \frac{\partial}{\partial x}\left(-k_b \frac{\partial T_b}{\partial x}\right) + \frac{\partial}{\partial y}\left(-k_b \frac{\partial T_b}{\partial y}\right) + \frac{\partial}{\partial z}\left(-k_b \frac{\partial T_b}{\partial z}\right) \tag{7.8}$$

The convective heat flux, j_{cv} (W m^{-2}), from the drying air to the bean surface (i.e., the bean-air interface):

$$j_{cv} = h_{ab}(T_{a,i} - T_{bs}) \tag{7.9}$$

With no heat generation (i.e., $q_r = 0$) and a fraction of endothermic cooling occurring at the bean surface (i.e., $0 < q_{e,s} \leq q_e$), the thermal balance at the bean-air interface is:

$$q_{cd} = j_{cv} + q_e \tag{7.10}$$

Imposed boundary conditions are thus:

$$\hat{\text{n}}.(-k_b \nabla T_b) = \hat{\text{n}}.h_{ab}(T_{a,i} - T_{bs}) \tag{7.11}$$

Initial conditions

Initial conditions for the simulation consisted of the bean temperature, T_b (K), thermocouple temperature, T_T (K), moisture content, X_b (kg kg^{-1}) and batch size m_{bs} (kg).

Initial product (thermocouple) temperature, $T_{T,0}$, was the measured value at product loading during roasting trials, whilst the initial bean temperature, $T_{b,0}$, was assumed equal to the ambient temperature (c. 20 °C). For the first time-step, initial bean temperature was uniform (i.e., all elements were assigned a single value of 20 °C), whilst for subsequent time-steps, initial bean temperatures were the nodal solutions of the previous time-step. Initial conditions for batch size and moisture content were specified as the measured green coffee properties (as in Table 7.1).

Dynamic boundary conditions informed by particle motion

The convective heat transfer coefficient was estimated as a function of the dimensionless Nusselt, Reynolds and Prandtl numbers (i.e., using the Ranz-Marshall equation) as described in Chapter 6. For the bean-scale model, the convective thermal load (i.e., the boundary conditions) – governed by the region-differentiated convective heat transfer coefficient - varied based on the particle's location in the roaster and residence times in each region. Using particle motion data, the velocity, u (m s^{-1}) used to define the Reynolds number was adjusted

Table 7.1: Initial condition values used in simulation of time-temp profiles.

Property	**Units**	**Value**
Moisture, X_b	%	10.06
Dimension a	mm	6.18
Dimension b	mm	3.84
Dimension c	mm	8.54
Equivalent Diameter, d_b	mm	5.87
Packing Density	kg^{-1}	10224
Bean Temperature, T_b	°C	20

to account for regional variation of airflow. In the bean bed, airflow was assumed to be negligible, such that the air velocity over the bean was assumed equal to be velocity of the bean itself (i.e., $u \rightarrow u_b$). The Reynolds number in the bean-bed, Re_{BB} is then:

$$Re_{BB} = \frac{d_b \rho_a u_b}{\mu_a} \tag{7.12}$$

In the freeboard, the air velocity over the bean was the relative velocity between the air and the bean (i.e., $u \rightarrow (u_a - u_b)$). The Reynolds number in the freeboard, Re_{FB} is therefore:

$$Re_{FB} = \frac{d_b \rho_a (u_a - u_b)}{\mu_a} \tag{7.13}$$

In this way, as the bean traverses the roasting chamber, it is propelled rapidly from the spout where it is subject to convective heat transfer rates governed by Eq. 7.13, before returning to the bean-bed where it travels slowly and is subject to heat transfer rates determined via Eq. 7.12.

The boundary conditions are implemented at the normal of all faces of the geometry, thus assuming that the entirety of the bean's surface area is available for heat transfer. The heat transfer effectiveness factor was introduced to account for inhibited convective heat transfer rates incurred by the close packing of beans in the bed, which limits the availability of the coffee's surface area.

In Chapter 6, the heat transfer effectiveness factor, η_A, was introduced to account for dy-

namic changes in the bean-bed during roasting. η_A estimated for the batch-scale simulations correlated with process conditions, such that for (i) case study I, $\eta_{A,I}$ correlated with the constant inlet air temperature, T_{ai} (°C) (R^2=0.929; RMSE=0.01), and (ii) case study II, $\eta_{A,II}$ correlated with batch size, m_{bs} (kg), (R^2=0.944; RMSE=0.06):

$$\eta_{A,I} = -1.94 \times 10^{-3} T_{ai} + 0.930 \tag{7.14}$$

$$\eta_{A,II} = 1.82 m_{bs} - 0.105 \tag{7.15}$$

Eqs. 7.14-7.15 were implemented within the bean-scale simulation to adjust the effective heat transfer area available. Implementation in this way enables the convective heat transfer coefficient to be calculated as a function of the bean velocities derived from the PEPT data, whilst the bean-bed dynamics and incurred flow reduction within the bean-bed and reduction of available surface area of the beans to be captured:

$$\alpha_{ab} = \eta_A h_{ab} \tag{7.16}$$

Thermocouple response

The thermal response coefficient, K (s^{-1}), discussed in Chapters 2, 3 and 6, corrects for the response time of the thermocouple in the roasting chamber. From Chapter 6, the thermal response coefficient correlated with process conditions, such that for (i) case study I, K_I correlated with the constant inlet air temperature, T_{ai} (°C) (R^2=0.876; RMSE=0.001 s^{-1}), and (ii) case study II, K_{II} correlated with the air mass flow rate, G_a (kg s^{-1}) and batch size, m_{bs} (kg), (R^2=0.873; RMSE=0.006 s^{-1}):

$$K_I = 9.86 \times 10^{-13} T_{ai}^{4.22} + 0.0253 \tag{7.17}$$

$$K_{II} = -8.13 \times 10^{-3} + 1.05 G_a + 7.66 \times 10^{-2} m_{bs} \tag{7.18}$$

In this way, the volume-averaged bean temperature from the bean-scale simulations can be converted to the product thermocouple temperature via implementation of Eqs. 7.17-7.18 within a solver for the thermocouple response's corresponding ODE.

7.1.5 Modelling approach: Coffee's physicochemical development

During roasting, coffee's thermophysical properties evolve due to heat and mass transfer phenomena; dehydration drives porous development, with coffee density decreasing due to both volumetric expansion and loss of organic matter. Thermophysical properties are therefore inherently related to density and moisture content (Singh et al., 1997; Burmester and Rudolf Eggers, 2010; Fabbri, Cevoli, Alessandrini, et al., 2011; Cardoso et al., 2018). In this subsection, correlations and models of coffee's physicochemical transformation are developed.

Transient physicochemical properties

The rate of change of both mass and moisture were shown in Chapter 3 to depend on airflow and batch size. For a given batch size, an increasing airflow increased the rate of change of mass and moisture due to greater heat transfer rates, whilst increasing batch size at a specified fan frequency decreased the rate of change of mass and moisture due to the increased batch mass and reduced heat transfer rates. Although rates of mass and moisture loss are dependent on process conditions, when roasting to similar whole bean surface colours, the final mass and moisture are invariant.

In Chapter 3.4, the relationship between coffee's effective thermal properties (density, specific heat capacity and thermal conductivity) and moisture were evaluated. These correlations were implemented here to consider coffee's transient properties and account for their variation during roasting. Due to the implementation method and resulting constraints of the software used to develop these simulations (2022b, MATLAB, Mathworks), a dynamic volume expansion (i.e., moving boundary) was not viable. In this way, the bean's expansion was assumed negligible, with the effects of bean expansion represented by the change in density, thermal conductivity and specific heat capacity, which were implemented for nodal solutions (i.e., for times greater than zero - $t > 0s$).

Kinetic models of mass & moisture Loss

Using the chemical reaction analogy (detailed in Chapter 5), whereby n^{th} order reaction kinetics are combined with Arrhenius-type rate constants, coffee's mass and moisture were

likened to chemical concentrations and modelled using n^{th} order reaction kinetics. These kinetic models were implemented within the heat transfer simulation to instruct the endo- and exo-thermic effects and changes in physicochemical properties during roasting.

7.1.6 Modelling approach: Validation with analytical solution for transient conduction in a sphere

In this subsection, the numerical scheme was analysed to ensure convergence with an analytical solution. To validate the numerical scheme, a simulation was developed to describe transient thermal conduction in spherical geometry with a fixed boundary (i.e., surface) temperature. The resolved temperature distributions for different spatial and temporal discretisation schemes were therefore checked for convergence with the analytical solution.

Implementation

A fixed surface temperature was instantaneously applied to a sphere's surface, with no convective heat transfer (i.e., $h_{ab}(T_{ai} - T_b) = 0$); endothermic cooling due to moisture vaporisation and exothermic heat generation were assumed negligible (i.e., $\rho_{db}\Delta H_v \left(-\frac{\partial X_b}{\partial t}\right) = 0$; $\Delta H_r \left(\frac{\partial \rho_{db}}{\partial t}\right) = 0$). The analytical solution for transient conduction in a sphere of radius, r_b, with a fixed, instantaneously applied boundary temperature was implemented in MATLAB (v2021b, Mathworks). Process parameters and product properties used in the simulation are detailed in Table 7.2. The thermophysical properties were considered constant through the particle and with time; process parameters were held constant with time.

Spatial discretisation

A spatial scaling factor (ε_s), was introduced such that the number of elements (N_e) is conserved for spherical beans with different radii. In this way, for 2 spheres, where $N_e = f(h, r_b)$, $N_{e,1} = N_{e,2}$, therefore $r_{b,1}/h_1 = r_{b,2}/h_2$ and the mesh's maximum element size, h (mm) can be defined as a function of the coffee bean's radius:

$$h = \frac{r_b}{\varepsilon_s} \tag{7.19}$$

To demonstrate the effect of the spatial scaling factor on the number of mesh elements, meshes were generated for a sphere with radius, $r = 2.88mm$ for ε_s in the range of $4 \leq \varepsilon_s \leq$

16. Figure 7.10 shows the meshed geometries corresponding to different scaling factors; the number of elements corresponding to spatial scaling factors of 4, 8 and 16 are 1626, 12772 & 98507.

Table 7.2: Parameter values used for simulations of transient conduction in a sphere to check for convergence with the analytical solution.

Parameter	**Description**	**Value**	**Units**
r_b	Particle radius	0.029	m
ρ_b	Particle density	1310.8	kg m^{-3}
$C_{p,b}$	Particle specific heat capacity	1040	J kg^{-} K^{-1}
k_b	Particle thermal conductivity	0.10	W m^{-1} K^{-1}
T_{bs}	Particle surface temperature	523.15	K
$T_{b,0}$	Particle initial temperature	298.15	K
t_0	Simulation start time	0	s
t_∞	Simulation end time	500	s

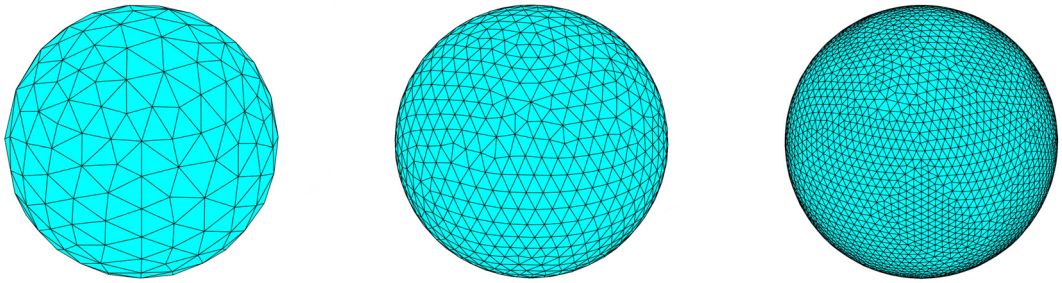

(a) $h = R/4$ (b) $h = R/8$ (c) $h = R/16$

Figure 7.10: Impact of mesh element size (ε) on generated mesh for a sphere with radius, $r = r_b$, where (a) $\varepsilon_s = 4$, (b) $\varepsilon_s = 8$ and (c) $\varepsilon_s = 16$.

Temporal discretisation

When coupled with the mesh element size, the thermal diffusivity (i.e., the rate of conductive heat transfer) indicates the system's timescale (Çengel, Boles, and Kanoğlu, 2002). The coffee's thermal diffusivity, κ_b (m^2 s^{-1}), is a function of its density, ρ_b (kg m^{-3}), specific heat capacity, $C_{p,b}$ (J kg^{-1} K^{-1}), and thermal conductivity, k_b (W m^{-1} K^{-1}):

$$\kappa_b = \frac{k_b}{\rho_b C_{p,b}} \tag{7.20}$$

For temporal discretization of explicit solvers, the time-step (Δt) is a function of the thermal diffusivity relative to the mesh element size (Çengel, Boles, and Kanoğlu, 2002):

$$\Delta t \leq \frac{h^2}{6\max(\kappa_b)} \tag{7.21}$$

For implicit solvers, as employed here by the MATLAB PDE toolbox, large time-steps can be used with little impact on the accuracy of the solution. To be robust to systems with different thermal diffusion rates and spatial discretisation, the time-step here is scaled relative to the thermal diffusivity and mesh element size with a temporal scaling factor, ε_t, using a similar approach to Eq. 7.21:

$$\Delta t \leq \varepsilon_t \left(\frac{h^2}{6\max(\kappa_b)} \right) \tag{7.22}$$

Error analysis & computational cost analysis

The optimal temporal and spatial discretisation depends on the desired accuracy and computational capabilities. Here, the impact of discretisation parameters on the simulation's error and computational requirements is evaluated. Figure 7.11 illustrates the impact of the discretisation parameters on the simulated time-temperature profile, as compared with the analytical solution, whilst Figure 7.12 shows the corresponding error, ϵ, of the time-temperature profiles in Figure 7.11.

Error analysis

For each of the meshed geometries in Figure 7.10, the temporal scaling factor was varied in the range of $4 \leq \varepsilon_t \leq 16$ to assess its impact on the solution. For parameter determination, the time-step (via Eq. 7.22) was rounded to the nearest 0.25 s to simplify calculation of error between the simulated and analytical solutions. Error, ϵ (°C) is expressed as the mean Root Mean Square Error (RMSE) calculated for radial temperature profiles at the end of each time step:

$$\epsilon = \frac{\sum_{t=1}^{n} RMSE_t}{n} \tag{7.23}$$

For fixed boundary temperature problems with significant temperature differences (here, $(T_{t=\infty} - T_{t=0}) \approx 200°C$), transient conduction is rapid, so these conditions are expected to

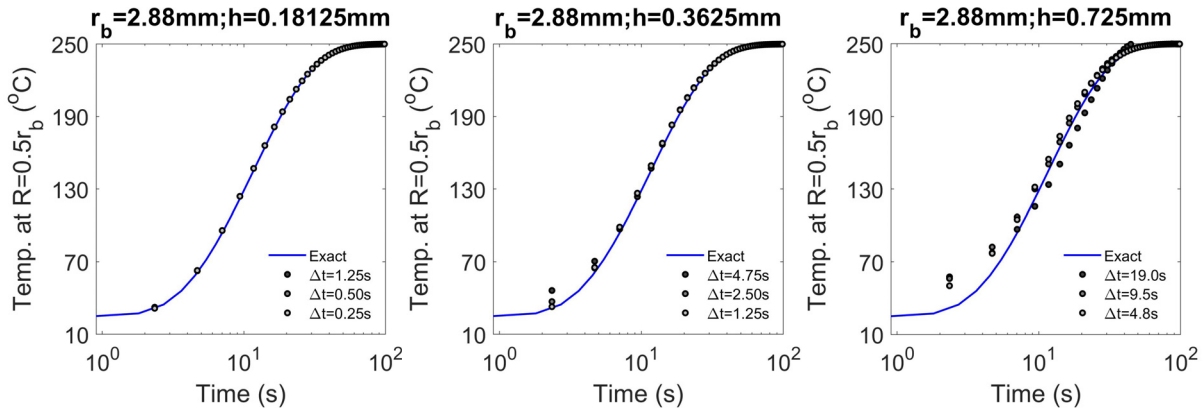

(a) $h = 0.18125$ mm (b) $h = 0.3625$ mm (c) $h = 0.725$ mm

Figure 7.11: Comparison of simulated particle temperature at $R = 0.5r_b$ with analytical solution: illustrating the impact of discretisation parameters on the solution's error for a sphere with radius, $r_b = 2.88mm$, with mesh element sizes of (a) 0.18125 mm (b) 0.3625 mm and (c) 0.725 mm.

incur greater error near the surface than in problems with convective boundary conditions where heat flux at the surface is lower. Figures 7.11-7.12 show that for all meshes at long times, error tends to zero (i.e., simulated solution converges with the analytical solution).

Figures 7.11-7.12 also show little influence of time-step on error for all mesh sizes, and at all times. Figure 7.12(b) shows that for a fine mesh (where h=0.18125 mm), large time-steps ($\Delta t > 1$ s) have no apparent impact on the solution's error but incur loss of temporal resolution for early times and computational times for a simulation of 120 s of heating are excessive (>60 s). Computation times correspond to a Dell XPS 15 9570 with an Intel Core i9-8950HK CPU @ 2.90 Hz, 32GB DDR 4 RAM and an NVIDIA GeForce GTX 1050 Ti GPU.

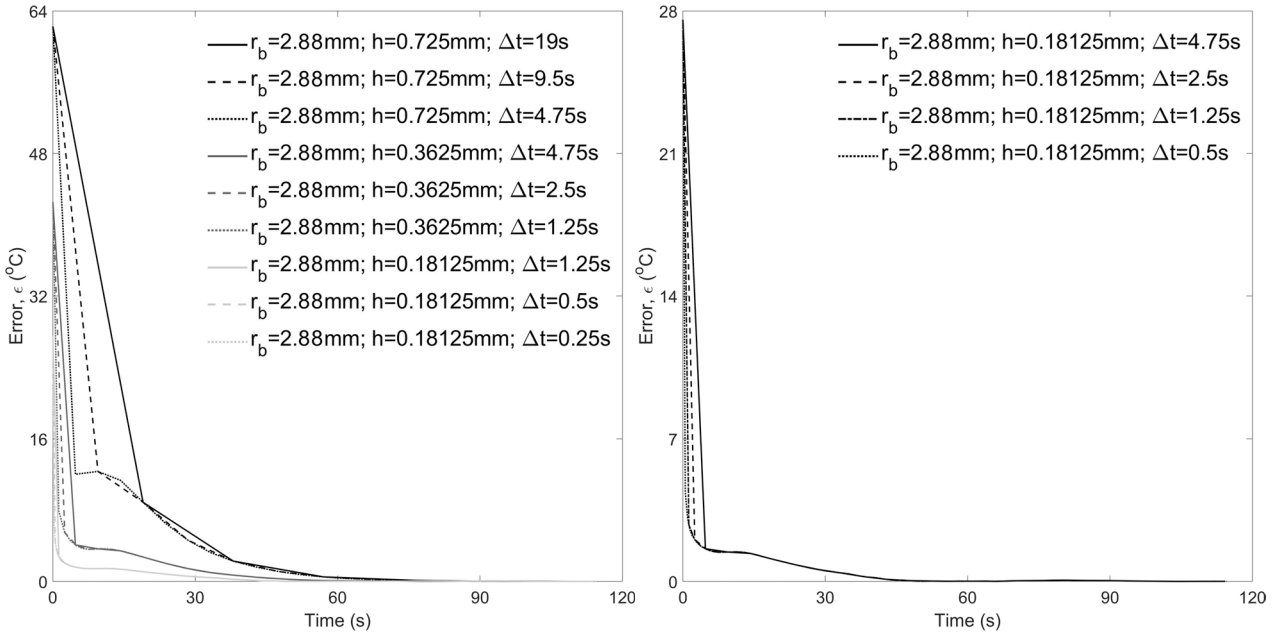

(a) $0.18125 \leq h \leq 0.72500$ mm; $0.25 \leq \Delta t \leq 19.00$ (b) h=0.18125 mm; $0.5 \leq \Delta t \leq 4.75$

Figure 7.12: Comparison of simulated particle temperature at $R = 0.5r_b$ with analytical solution: illustrating the impact of discretisation parameters on the solution's error for a sphere with radius, $r_b = 2.88mm$, mesh element sizes of (a) $0.18125 \leq h \leq 0.72500$ mm and (b) h=0.18125 mm.

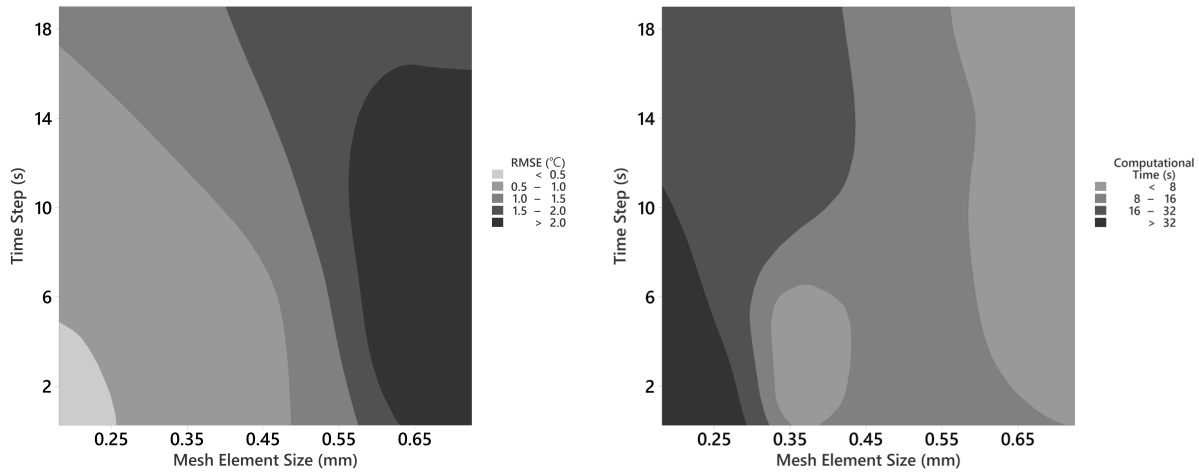

(a) RMSE (b) Computation Time

Figure 7.13: Contour plots illustrating the impact of discretisation parameters on (a) simulation error (ϵ) and (b) computation time.

Computational Cost Analysis

Figure 7.13 informs the selection of appropriate discretisation parameters – presenting their impact on ϵ and computational time. Figure 7.13 shows that: (i) large element sizes and long time steps incur significant error but requires little computational resources, and (ii) small element sizes and short time steps require significant computational resources but yields low error. Discretisation parameters should be selected to minimise ϵ without incurring excessive computation times. These parameters will be re-evaluated to ensure that the fully-developed model is optimised for accuracy and computational requirement.

7.1.7 Modelling approach: Particle geometry & spatial discretisation

Particle geometry

Coffee geometry can be approximated by three geometries: (i) spherical, (ii) ellipsoidal and (iii) hemi-ellipsoidal - modelled geometry is dependent on application. For most coffees, where $\psi_b \leq 0.8$, hemi-ellipsoidal geometry is recommended; for high sphericity (peaberry) coffees, where $0.8 \leq \psi_b \leq 0.9$, ellipsoidal geometry is more appropriate; for very high sphericity coffees where $\psi_b \geq 0.9$, spherical geometry is appropriate. For approximate geometry implemented here, spherical and hemi-ellipsoidal geometry will be reproduced from the measured principal dimensions, a, b, c (mm) of coffee beans. These two cases were chosen to reflect simple geometries that will allow for rapid computation during simulations. For comparison, accurate bean geometry was also captured and analysed.

Using the measured principal dimensions, hemi-ellipsoidal geometry was constructed in Blender (v3.3, Blender). Spherical geometry was constructed using MATLAB's 'multisphere' function to reproduce a sphere with an equivalent volume.

Accurate three-dimensional geometry of particles can be generated using optical methods. Here, a single coffee bean was selected from each sample set of coffees used in particle motion studies (i.e., green, part-roasted and roasted coffees), where principal dimensions of the selected beans were within one standard deviation of the batch's mean (determined

using digital calipers). Coffee bean geometry was captured using a three-dimensional optical scanner (EinScan-SE). Coffee beans were sprayed with a non-reflective coating to improve capture quality – the coating layer did not significantly impact bean size or shape. Capture settings consisted of a non-texture (i.e., no colour) scan, with 'low-detail' interpolation used for surface post-processing. The generated geometry (.STL) file was imported into MATLAB for re-meshing and implementation.

Exemplar 3D replications of the three different geometries (spherical, hemi-ellipsoidal and 3D scanned) with equivalent volume diameters are presented in Figure 7.14.

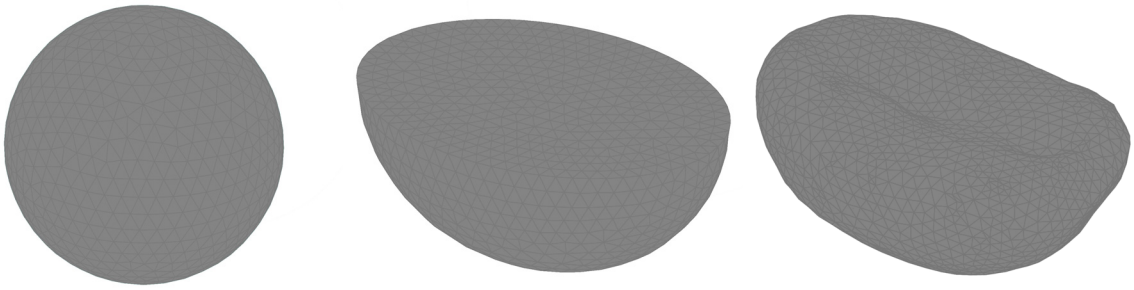

(a) Sphere (b) Hemi-ellipsoid (c) 3D-scanned bean

Figure 7.14: Comparison of geometries with equivalent diameters: (a) sphere, (b) hemi-ellipsoid and (c) 3D scanned bean.

Discretisation

For each of the geometries in Figure 7.14, the spatial scaling factor was varied to assess its impact on the number of elements and time for mesh generation - both of which influence the solver's accuracy and computational costs. For comparison, the generated meshes for equivalent volume diameter spheres with different spatial discretisation factors, varied in the range of $4 \leq \varepsilon_t \leq 16$, are presented in Figure 7.15.

Comparison of geometry & discretisation

Mesh generation times depend on the element size and geometric complexity. A comparison of mesh generation times and number of elements for spherical, hemi-ellipsoidal and 3D scanned, equivalent volume diameter geometries using different element sizes are displayed in Table 7.3 - as visualised in Figure 7.15.

These data demonstrate that the differences between mesh generation for spherical and hemi-ellipsoidal geometries are small, whilst computational requirements for mesh generation of the 3D-scanned bean are considerably greater. For a sphere, or a hemi-ellipsoid, with a radius, $R = r_b$, reasonable parameters to ensure that $\epsilon < 2°C$ and computational requirements are minimised are: (i) a spatial scaling factor, $\varepsilon_s = 8$, so mesh element size, $h = r_b/8$, yielding a mesh with 12772, or 14283, elements and (ii) a temporal scaling factor, $\varepsilon_t = 8$, so time-step, $\Delta t = (8h^2)/(6\max(\kappa_b))$.

Table 7.3: The impact of geometry and spatial discretisation parameters on number of elements and computation times for mesh generation.

Geometry Type	**Discretisation Factor**	**Element Length (h)**	**Number of Elements**	**Mesh Generation Time (s)**
Sphere	R/4	0.00072	1626	0.39±0.01
Sphere	R/8	0.00036	12772	0.62±0.04
Sphere	R/16	0.00018	98507	2.57±0.06
Hemi-Ellipsoid	R/4	0.00072	1795	0.11±0.00
Hemi-Ellipsoid	R/8	0.00036	14283	0.37±0.01
Hemi-Ellipsoid	R/16	0.00018	112607	2.67±0.05
3D Scan	R/4	0.00072	5333	11.66±0.24
3D Scan	R/8	0.00036	28216	13.69±0.20
3D Scan	R/16	0.00018	156823	15.17±0.19

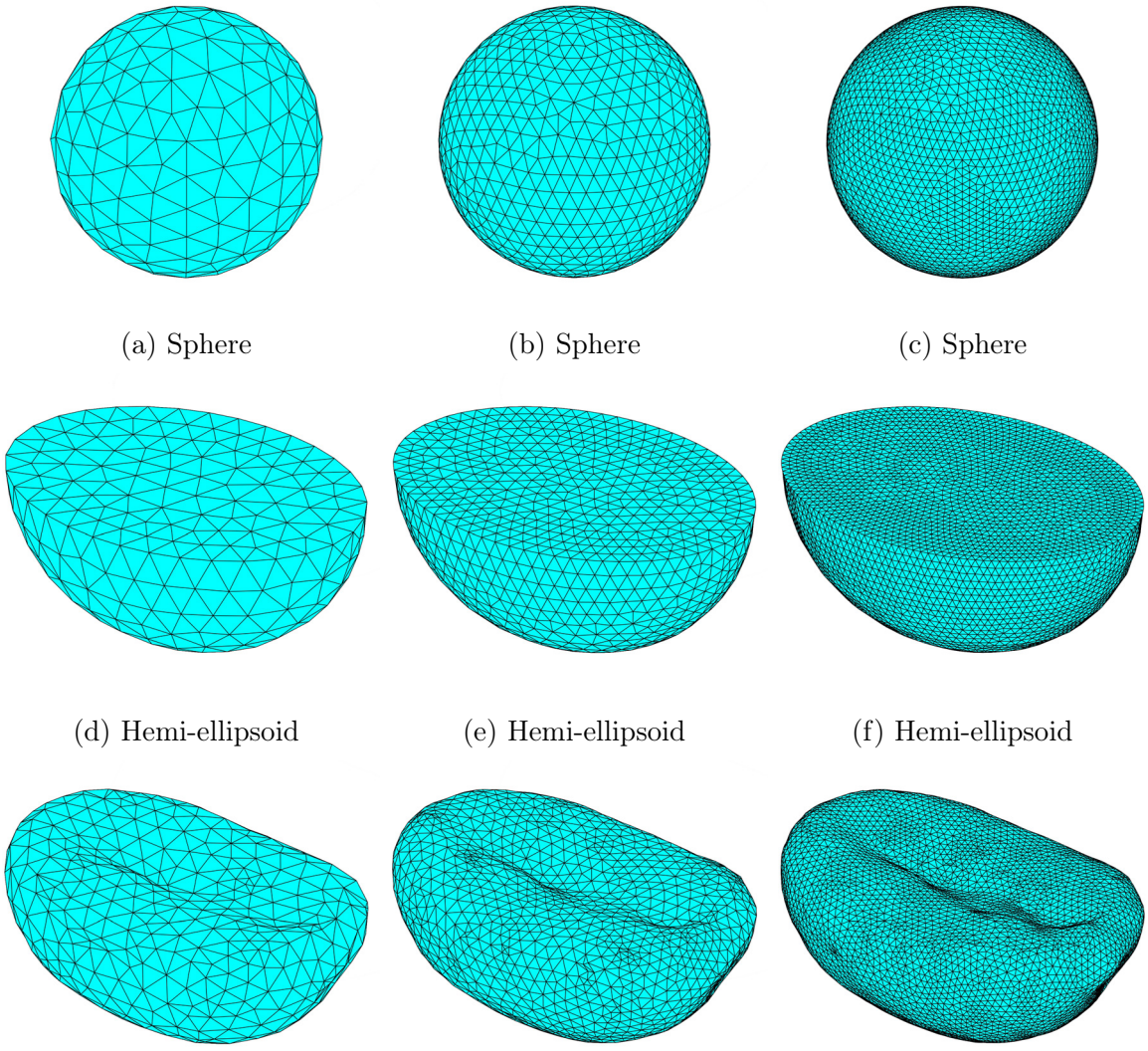

(a) Sphere (b) Sphere (c) Sphere

(d) Hemi-ellipsoid (e) Hemi-ellipsoid (f) Hemi-ellipsoid

(g) 3D-scanned bean (h) 3D-scanned bean (i) 3D-scanned bean

Figure 7.15: Meshed geometries corresponding to (a)-(c) spheres, (d)-(f) hemi-ellispoids and (g)-(i) 3D scanned beans using a spatial discretisation factor of (a),(d),(g) R/4, (b),(e),(f) R/8 and (c),(f),(i) R/16.

7.1.8 Modelling approach: Endothermic & exothermic effects

Endothermic and exothermic reactions influence coffee's temperature response during roasting. According to Eq. 7.4, endothermic effects from the latent heat of vaporisation of moisture within the bean are integrated within the thermal model. In this way, the endothermic cooling was implemented as described in Chapter 6, as a function of the enthalpy of vaporisation of water, where the water temperature was assumed equal to the mean bean temperature.

As in Chapter 6, air-to-metal heat transfer (heat loss to the metal parts of the roaster) and exothermic reactions were assumed negligible - so $q_{am} = 0$ and $q_r = 0$. Combining these endothermic and exothermic effects with the heat loss across the roaster, the net heat generation, $q_n = q_{am} + q_r + q_e$. The net heat generation is implemented equally at all nodes within the bean.

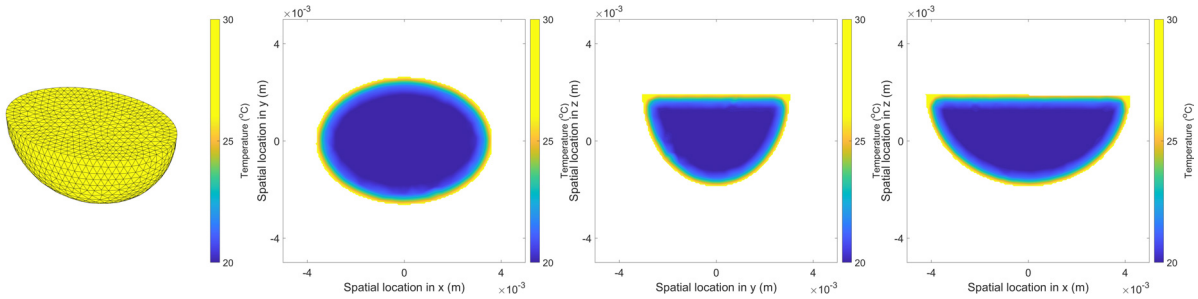

(a) 3D surface (b) x, y at $z = 0$ (c) y, z at $x = 0$ (d) x, z at $y = 0$

Figure 7.16: Visualisation of the thermal model's nodal solution (a) evaluated at the three-dimensional surface and interpolated in the planes (a) x, y at $z = 0$, (a) y, z at $x = 0$ and (a) x, z at $y = 0$.

7.1.9 Modelling approach: Evaluation of nodal solution

The model's solution at the end of each time-step (according to the regional residence times extracted from the PEPT data) consists of a nodal temperature solution, the temperature gradient values (in x, y, z co-ordinates) and their corresponding mesh data (nodal locations). These data can be plotted as-is to visualise the 3D surface heating rate (Figure 7.16(a)) and are then interpolated at specified query points to enable spatial temperatures to be resolved at different planes within the bean - i.e., to generate temperature fields (visualised in Figure

7.16(b-d)). For visualisation of the two-dimensional data in all geometries, nodal solutions are evaluated (interpolated) in a given plane, for example in the plane x, y at $z = 0$ (at the midpoint of the bean). Each of these data can be used to compare roasting conditions and bean geometries.

7.1.10 Modelling approach: Validation of the time-temperature profile

To validate the spatial temperature solution, the volume-averaged bean temperature (i.e., the mean bean temperature across the entire three-dimensional volume) was converted to the expected product thermocouple temperature measurement using the approach described in Chapter 6 (i.e., via Eq. 6.15, which accounts for the thermocouple's temperature response). The predicted thermocouple temperature was resolved by implementation of an ODE solver based on the thermal response coefficient and the volume-averaged bean temperature from the bean-scale simulation.

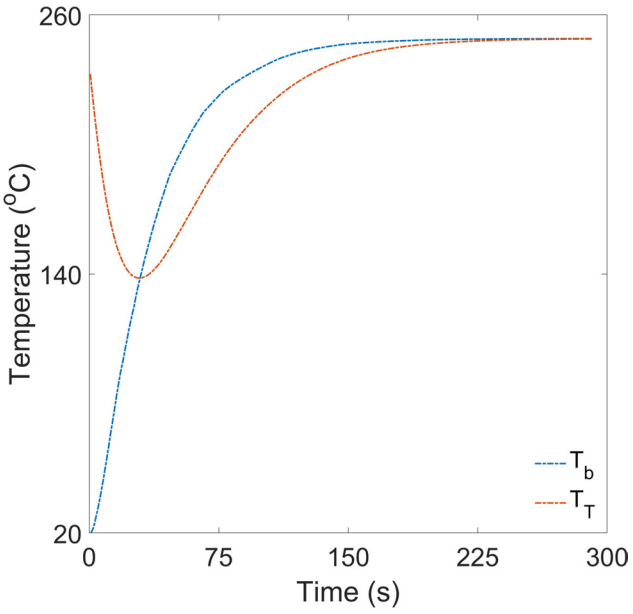

Figure 7.17: Visualisation of the volume-averaged bean temperature resolved from the three-dimensional thermal model, overlaid with the predicted thermocouple measurement.

The volume-averaged bean temperature (T_b) and predicted thermocouple temperature (T_T) responses can then be compared be overlaid (as demonstrated in Figure 7.17) and later, thermocouple time-temperature profiles resolved from the bean-scale simulation can be compared

with those obtained experimentally. This conversion process is critical, as thermocouple measurements are current process consistency and product quality indicators but do not directly relate to bean temperatures.

7.1.11 Modelling approach: Implementation

Based on the described experimental and modelling approaches, the simulation's architecture comprised:

- extraction of the relevant experimental time-temperature profile (air temperature, bean temperature and time) from Chapter 3
- specification of the airflow properties (mass flow rate (Eq. 2.6), temperature, thermophysical properties (Eqs. 2.9-2.11)) from Chapter 2
- assignment of the bean's initial conditions (temperature, size, moisture, mass, density, specific heat capacity, thermal conductivity) from Chapter 3
- construction of the geometry, relevant scaling, and subsequent mesh generation
- importation of the corresponding particle motion data (velocity, time and region ID) from Chapter 4
- prediction of mass and moisture loss (kinetic models in Eqs. 5.3-5.7; Ordinary Differential Equations (ODEs)) from Chapter 5
- calculation of the bean's transient properties (density, thermal conductivity & specific heat capacity via Eqs. 3.29, 3.33 & 3.34) as in Chapter 3
- specification of dynamic, convective boundary conditions (regional heat transfer coefficient, heat transfer effectiveness factor, air temperature) as in Eqs. 7.12, 7.13, 7.14 & 7.15
- calculation of endothermic and specification of exothermic (negligible here) reactions as in Eq. 7.4 & 7.5

- evaluation of the bean's temperature distribution (nodal solution)
- estimation of the thermocouple response coefficient via Eq. 7.17 & 7.18 as in Chapters 2 & 6
- conversion of the mean bean temperature to the batch-mean thermocouple temperature via Eq. 6.15 as in Chapter 6
- post-processing of the resolved spatial temperatures for comparison across roasting conditions
- visualisation of temperature fields (2D & 3D), batch-mean temperature and physicochemical properties

The simulation architecture was implemented in MATLAB (v2022a, Mathworks), calling the integrated PDE Toolbox and coupled ODE solver. All computational work was performed using the BlueBEAR HPC service of the University of Birmingham.

7.2 Results

This section begins with a sensitivity analysis of the bean-scale simulation and subsequent prediction of the in-bean temperature distributions, batch-scale time-temperature profiles and physicochemical transformation that correspond to case study I (with different constant inlet air temperatures (200, 235, 250, 265, 280°C) using a moderate batch size (0.35 kg) and moderate airflow (48 Hz fan frequency)) and case study II (with different batch sizes (0.20-0.50 kg) and airflows (30-65 Hz fan frequency) using a moderate constant inlet air temperature (250°C)).

7.2.1 Sensitivity analysis: Geometry

This subsection aims to identify the sensitivity of the simulation (and the predicted time-temperature response) to particle geometry - spherical, hemi-ellipsoidal and 3D-scanned bean geometries were considered. From these analyses, the most appropriate geometry will be selected for the calibrated simulations, with relevant criteria being computation time (for

both mesh generation and the solver) and accuracy (assuming that the 3D-bean geometry is the most accurate representation).

Figure 7.18 compares predicted time-temperature (thermocouple and mean-bean) profiles for different particle geometries (sphere, hemi-ellipsoid and 3D-scanned bean). Figure 7.19 is complementary to Figure 7.18 and illustrates the impact of particle geometry on the resolved in-bean temperature fields - data presented as contour plots correspond to roasting conditions of 350g 250°C & 48 Hz for spherical, hemi-ellipsoidal and 3D-scanned bean geometries. Figures 9.1-9.4 in the Appendix - Section 9.4 show the impact geometry on resolved time-temperature profiles under different process conditions in each plane.

Figure 7.18 demonstrates that a clear distinction between the temperature response of the spherical geometry and both the hemi-ellipsoidal and 3D-scanned geometries, such that the temperature response of the spherical geometry is lower than that of both the hemi-ellipsoidal and 3D-scanned bean geometries - also seen by previous modellers (Fabbri, Cevoli, Romani, et al., 2011). The difference between the hemi-ellipsoidal geometry (with the greatest temperature response) decreases as the heat transfer coefficient increases (data shown in the Appendix - Section 9.4).

Figure 7.19 clarifies the distinction between the spherical geometry and both the hemi-ellipsoidal and 3D-scanned geometries. In spherical geometry (Figure 7.19(a),(d)&(g), thermal symmetry is evident, whilst end-localised heating is observed for both the hemi-ellipsoidal (Figure 7.19(b),(e)&(h)) and 3D-scanned (Figure 7.19(c),(f)&(i)) geometries due to the larger aspect ratio - this was also seen in previous simulations (Hobbie and Eggers, 2001; Fabbri, Cevoli, Alessandrini, et al., 2011).

The solution time for the different geometries (data presented in Table 9.11 in the Appendix - Section 9.4) show that for simulated roasting conditions with different simulated roasting times, solver times for the 3D-scanned bean geometry were up to 10 times greater than the spherical and hemi-ellipsoidal geometries. Despite the spherical geometry being generated within the MATLAB environment, and the hemi-ellipsoidal and 3D-scanned bean geometries

being rendered in Blender and later imported into MATLAB for regeneration of the mesh, the hemi-ellipsoidal typically had the fastest solver times (and mesh generation times - as in Table 7.3). Based on these data, with the shortest mesh generation times, solver runtimes and accuracy (relative to the 3D-scanned bean geometry), hemi-ellipsoidal geometry will be used for further sensitivity analysis and in the calibrated simulations.

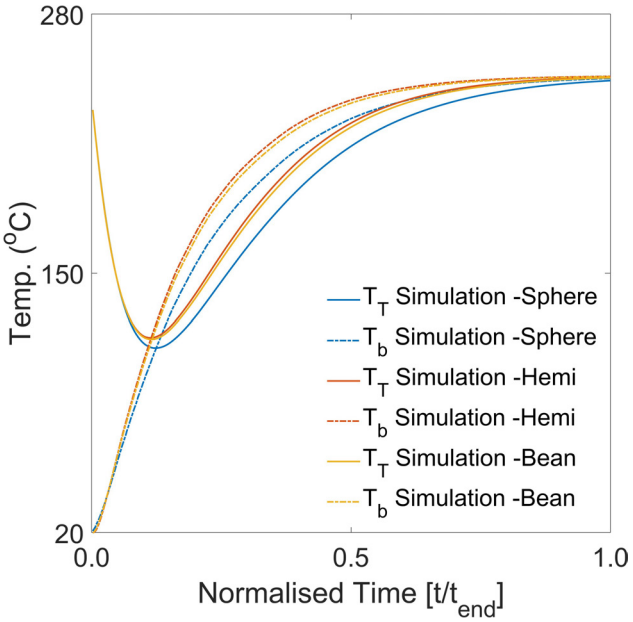

(a) 350g 250°C 48Hz

Figure 7.18: Comparison of the predicted bean and thermocouple time-temperature profiles that illustrate the impact of coffee bean geometry (sphere, hemi-ellipsoid and 3D-scanned bean) on the resolved roasting profiles - data corresponds to roasting conditions of 350g 250°C & 48 Hz.

7.2.2 Sensitivity analysis: Coffee properties & process parameters

This subsection aims to identify the sensitivity of the simulation (and the predicted time-temperature response) to variation of airflow, batch size and inlet air temperature. From these analyses, a feasible range of parameter values can be used to define the constraints of the parameters during estimation. Figure 7.20 compares predicted time-temperature profiles that illustrate the model's sensitivity to coffee's initial product properties and heat transfer effectiveness - data correspond to hemi-ellipsoidal particle geometry, with parameter values (Y) varied in the range of $0.5 \leq Y \leq 2.0$.

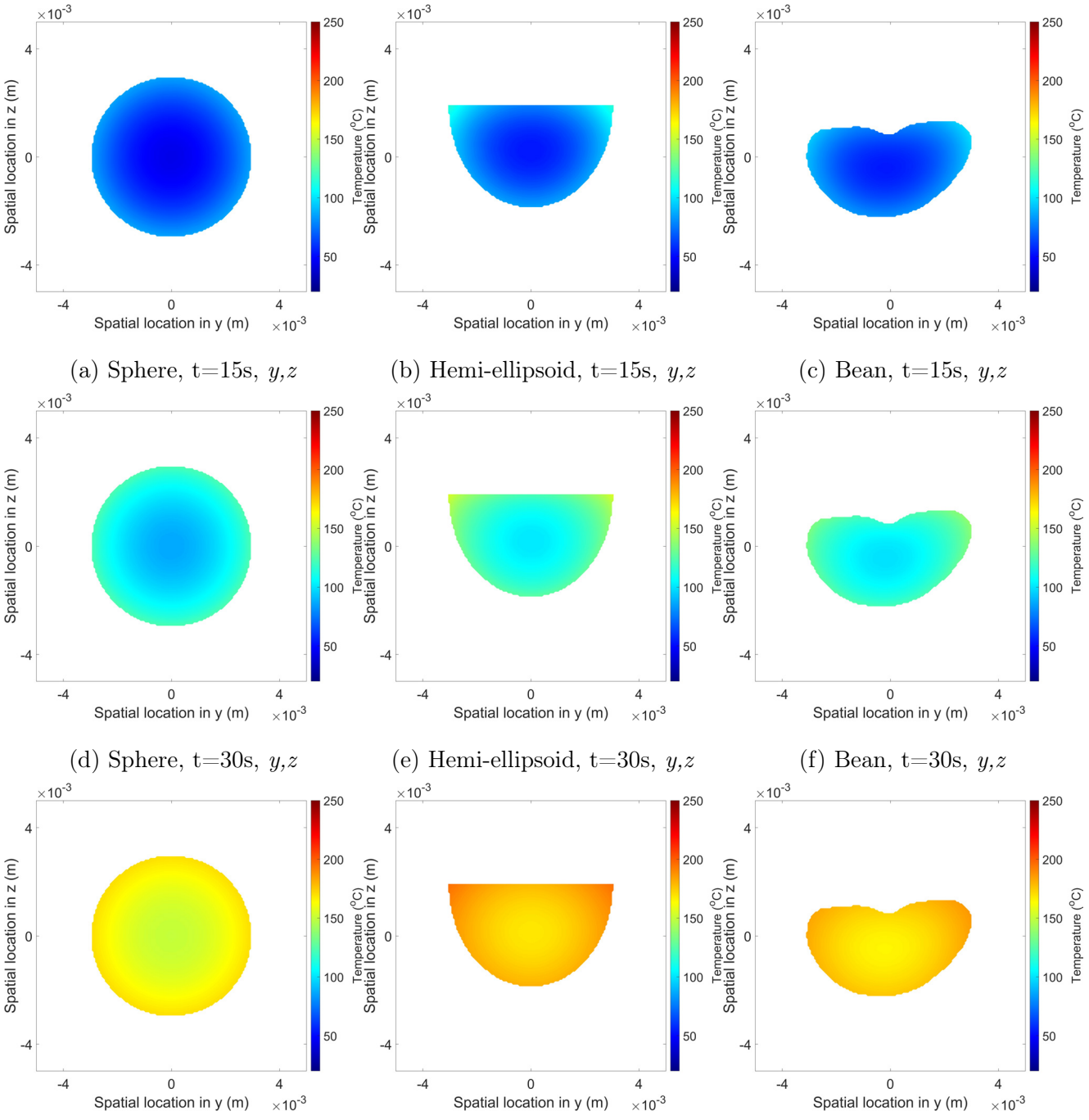

(a) Sphere, t=15s, y,z (b) Hemi-ellipsoid, t=15s, y,z (c) Bean, t=15s, y,z

(d) Sphere, t=30s, y,z (e) Hemi-ellipsoid, t=30s, y,z (f) Bean, t=30s, y,z

(g) Sphere, t=60s, y,z (h) Hemi-ellipsoid, t=60s, y,z (i) Bean, t=60s, y,z

Figure 7.19: Comparison of the predicted in-bean temperature distributions in the plane y,z for (a),(d),(g) spherical, (b),(e),(h) hemi-ellipsoidal and (c),(f),(i) 3D-scanned geometries at simulated roasting times of (a)-(c) 15 s, (d)-(f) 30 s and (g)-(i) 60 s - data corresponds to roasting conditions of 350g 250°C & 48 Hz.

This analysis demonstrated that the heat transfer rate decreases as (i) density increases, (ii) specific heat capacity increases, (iii) thermal conductivity decreases, (iv) diameter (& volume) decreases and (v) effectiveness factor decreases - as shown in Figure 7.20(a), (b), (c), (d) and (f), respectively. The model is therefore sensitive to each of these parameters but the effect of the bean's specific heat capacity (Figure 7.20(b)), bean diameter (Figure 7.20(d)) and the heat transfer effectiveness factor (Figure 7.20(f)) clearly illustrate that determination of these parameters are critical for model accuracy. Inaccuracies in initial and transient product properties (i.e., the subroutines based on physichochemical correlations) are therefore most likely to propagate error through to the resolved time-temperature profiles.

Variation of the latent heat of vapourisation (ΔH_v) in the range of $0.5 \leq \Delta H_v \leq 2.0$ had almost no effect on the temperature response - as shown in Figure 7.20(f); the range was expanded to $0.1 \leq \Delta H_v \leq 10.0$ and still the effect on the resolved time-temperature profiles was inappreciable. The model is therefore not sensitive to estimation of ΔH_v, suggesting that the effect of endothermic cooling on the temperature response is not relevant for heat transfer in roasting.

Figure 7.21 outlines the predicted changes in the regional heat transfer coefficients during roasting. The heat transfer coefficient (Eq. 7.16) is adjusted for the freeboard and bean bed via modified Reynolds numbers (Eqs. 7.12 & 7.13, respectively) and depends on the bean's thermal conductivity (which increases during roasting), therefore the heat transfer coefficient (with a constant thermal load) decreases during roasting. In the bean bed, the modified Reynolds number is based on the bean's velocity only (whereas in the freeboard it is the velocity of the air relative to the bean), and small fluctuations are seen. Figure 7.21 also shows that the heat transfer coefficient is greater in the freeboard than in the bean bed, yet is more sensitive to the bean's thermal properties. Table 7.4 outlines the median bean velocity in both the freeboard and bean bed, alongside the median regional heat transfer coefficient.

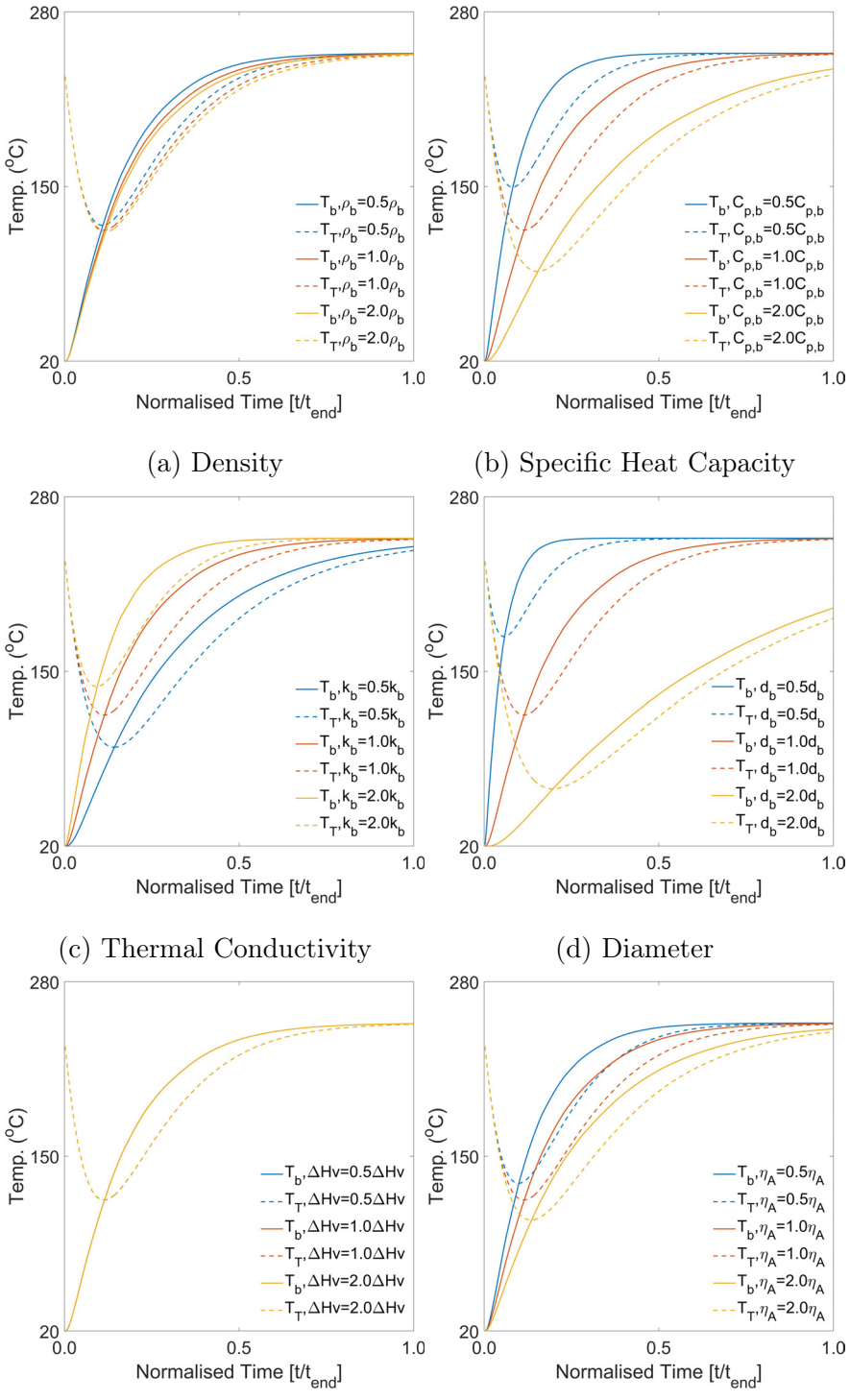

(a) Density (b) Specific Heat Capacity

(c) Thermal Conductivity (d) Diameter

(e) Heat of Vapourisation (f) Effectiveness Factor

Figure 7.20: Comparison of the predicted bean and thermocouple time-temperature profiles that illustrate the impact of coffee bean (a) density, (b) specific heat capacity, (c) thermal conductivity, (d) diameter (& volume), (e) moisture's heat of vapourisation and (f) the heat transfer effectiveness factor on the resolved roasting profiles - data corresponds to roasting conditions of 350g 250°C & 48 Hz.

For case study I, as the inlet air temperature increases, the regional heat transfer coefficients (in both the freeboard and bean bed) increase. For case study II, bean velocity in the freeboard increases with airflow, whilst bean velocity in the bed decreases as batch size increases. Therefore, the heat transfer coefficient in the freeboard increases with airflow, whereas the bean bed heat transfer coefficient decreases with batch size.

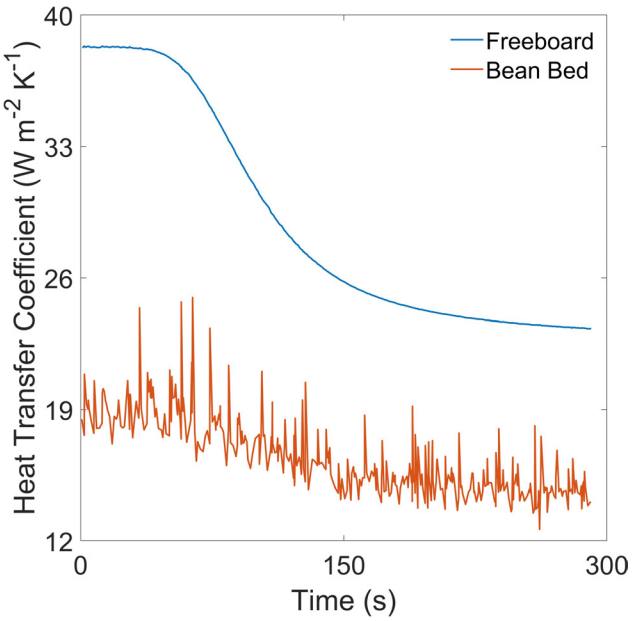

Figure 7.21: Changes in the regional heat transfer coefficients (in the freeboard and in the bean bed) during roasting - data corresponds to roasting conditions of 350g 250°C & 48 Hz.

7.2.3 Thermocouple time-temperature profiles

In this subsection, the bean-scale simulations are calibrated with experimental process and product data. Comparisons of predicted and experimental time-temperature profiles corresponding to case studies I and II are presented in Figures 7.22 & 7.23, respectively, whilst the parity plot in Figure 7.24 compares predicted and experimental temperature data for all simulated roasting conditions.

Figures 7.22 & 7.23 show that both the predicted bean and thermocouple temperatures tend to the inlet air temperature for all simulated conditions. In the experimental profiles in Figure 7.1, there is an apparent heat loss that is not captured by the current simulation. This can be explained by the position of the "product" thermocouple, as when idling between roasts the product temperature is lower than the inlet air temperature. In this way, it is not

Table 7.4: PEPT-determined bean velocities (u_b), estimated regional heat transfer coefficient (Hab) and the predicted time-temperature profile's RMSE corresponding to different batch sizes, airflows and inlet air temperatures.

Batch Size (g)	**Fan Freq. (Hz)**	**Inlet Air Temp. (°C)**	**Roast Time (s)**	**u_b [Freeboard] (m s^{-1})**	**H_{ab} [Freeboard] (W m^{-2} K^{-1})**	**u_b [Bean Bed] (m s^{-1})**	**H_{ab} [Bean Bed] (W m^{-2} K^{-1})**	**RMSE (°C)**
200	30	250	233	0.18	46.5	0.11	20.6	18
200	48	250	223	0.42	47.4	0.21	22.5	18
200	65	250	185	0.45	50.2	0.45	26.1	14
350	39	250	336	0.28	25.3	0.13	15.4	21
350	48	250	291	0.40	25.4	0.18	15.9	23
350	65	250	264	0.55	26.8	0.18	15.9	19
500	48	250	354	0.30	17.6	0.11	11.7	21
500	65	250	330	0.38	18.5	0.12	12.0	20
350	48	220	713	0.40	25.2	0.18	15.4	15
350	48	235	426	0.40	27.2	0.18	16.4	20
350	48	250	286	0.40	29.4	0.18	17.4	22
350	48	265	228	0.40	31.9	0.18	18.2	25
350	48	280	176	0.40	35.8	0.18	19.1	26

expected that the batch temperature measured by the product thermocouple will converge with the inlet air temperature unless exothermic reactions become dominant (relevant mostly for high temperature roasts). To account for this effect, either the steady-state temperature (as a function of inlet air temperature and air flow - as in Eq. 2.1 in Chapter 2) could be implemented in the boundary conditions, or the thermal response coefficient could be re-calibrated to convert from the mean single-bean temperature to the thermocouple (i.e., batch-mean) temperature.

Data in Figure 7.24, which details the simulation's RMSE, are normally distributed. Relative to the experimental time-temperature profiles, Figures 7.22 & 7.23 show that the predicted thermocouple profile's turning-point occurs at a greater time and lower temperature - in the range of $24 \leq t \leq 37$ s & $92 \leq T_T \leq 156\ ^oC$, respectively. Beyond the turning-point, the predicted bean's temperature exceeds the thermocouple temperature until both inevitably converge with the inlet air temperature. The thermocouple temperature in the range of $0 \leq T_T \leq 210\ ^oC$ is underestimated. Beyond this temperature, the predicted thermocouple temperature is overestimated, as the bean's predicted temperature tends toward the inlet air temperature.

7.2.4 In-bean temperature distributions

The effect of roasting conditions on predicted in-bean temperature distributions are presented in Figures 7.26-7.27. Figure 7.26 corresponds to case study I and show the effect of constant inlet air temperature on the time-temperature evolution of the bean for roasting conditions of 220°C, 250°C and 280°C, respectively - with corresponding time-temperature profiles in Figure 7.22). Figure 7.27 corresponds to case study II and show the effect of different batch sizes on the time-temperature evolution of the bean for roasting conditions of 200g, 350g and 500g, respectively - with corresponding time-temperature profiles in Figure 7.23. Each figure depicts the temporal evolution of the bean's temperature field for specified roasting conditions.

Figure 7.26 shows that as the constant inlet air temperature increases, the heat transfer rate increases, resulting in a more rapid temperature response, with the core temperature

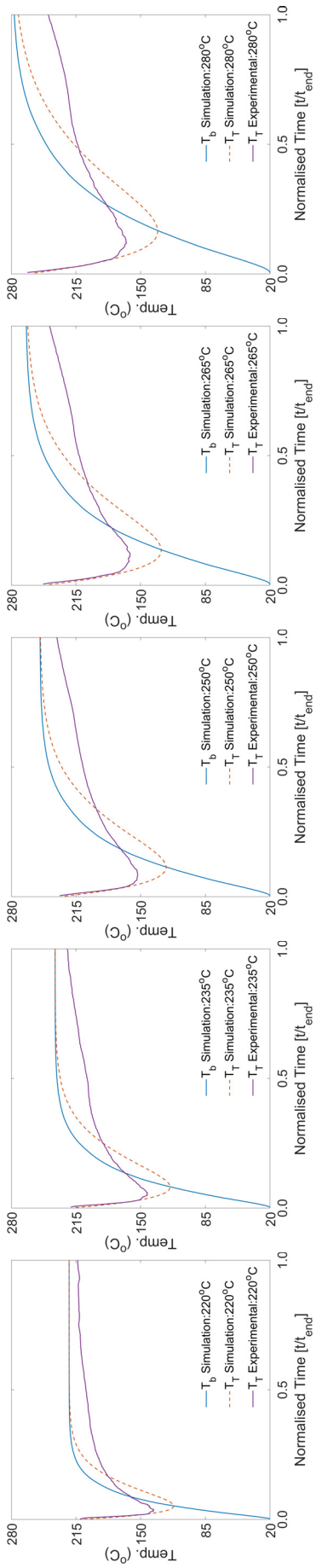

(a) 220°C (b) 235°C (c) 250°C (d) 265°C (e) 280°C

Figure 7.22: Predicted and experimental time-temperature roasting profiles corresponding to (a) 350g 220°C 48Hz, (b) 350g 235°C 48Hz, (c) 350g 250°C 48Hz, (d) 350g 265°C 48Hz and (e) 350g 280°C 48Hz.

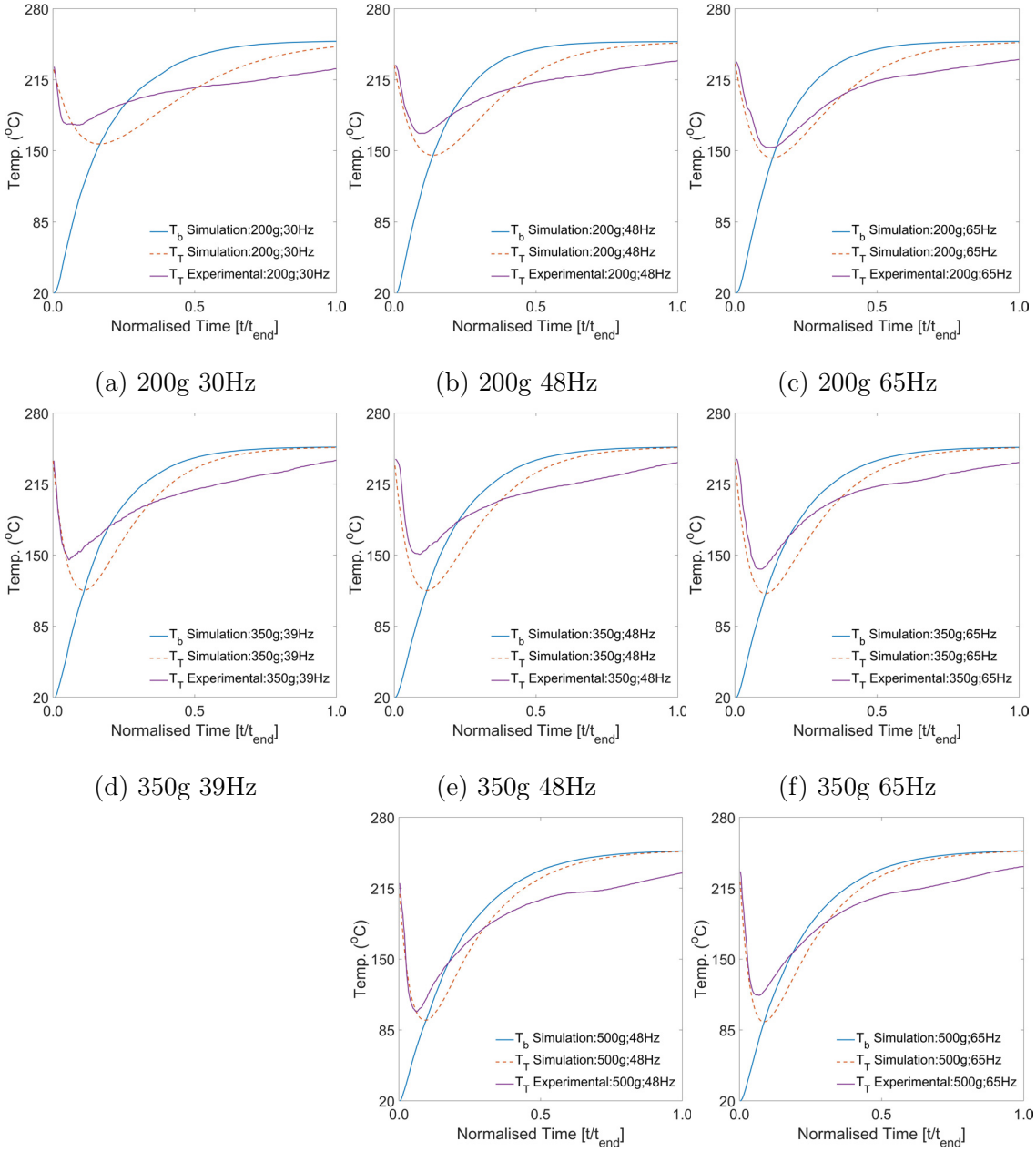

(a) 200g 30Hz (b) 200g 48Hz (c) 200g 65Hz

(d) 350g 39Hz (e) 350g 48Hz (f) 350g 65Hz

(g) 500g 48Hz (h) 500g 65Hz

Figure 7.23: Predicted and experimental time-temperature roasting profiles corresponding to (a) 200g 250°C 30Hz, (b) 200g 250°C 48Hz, (c) 200g 250°C 65Hz, (d) 350g 250°C 39Hz, (e) 350g 250°C 48Hz, (f) 350g 250°C 65Hz, (g) 500g 250°C 48Hz and (h) 500g 250°C 65Hz.

rising more rapidly. Figure 7.27 demonstrates that as batch size increases - and the bean's residence time in the bed increases whilst the bean's recirculation rate decreases - the heat transfer rate to the core decreases.

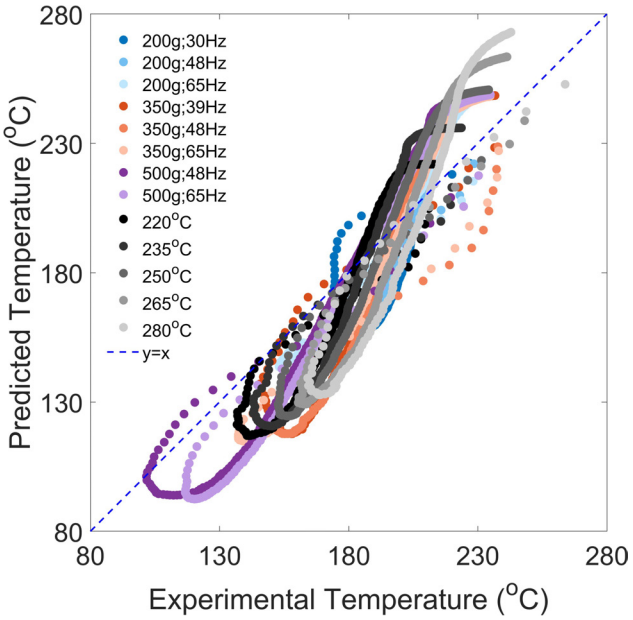

Figure 7.24: Parity plot of predicted and experimental thermocouple temperatures resolved from time-temperature profile simulations - corresponding data plotted in Figures 7.22 - 7.23.

As the displayed time-temperature profiles in Figures 7.22-7.23 depict the mean bean temperature, it's worth considering the temperature differential within the bean and how it evolves during roasting. Although this can be qualitatively observed from Figures 7.26-7.27, Figure 7.25 illustrates the temporal evolution of the in-bean temperature differential (defined here as the difference between the maximum and minimum nodal temperature), wherein the temperature differentials are overlaid to compare roasting conditions.

The profiles in Figure 7.25 reveal that the temperature differential decays over time. Figure 7.25(a) shows that for higher airflows (with higher heat transfer coefficients) the temperature differential is initially ($0 \leq t \leq 50$ s) larger than the responses for lower airflows but, later in the roast ($t \geq 50$ s), higher airflow roasts will have a lower temperature differential. From the profiles in Figure 7.25(b), after approximately 120 s, the temperature differentials for different constant inlet air temperature profiles converge - although this is likely due to the

overestimation of the bean's temperature at long times. In both case studies, the simulations indicate that the temperature differential in the bean is less than 10°C for the majority of the roast, with much of the disparity occurring at early times.

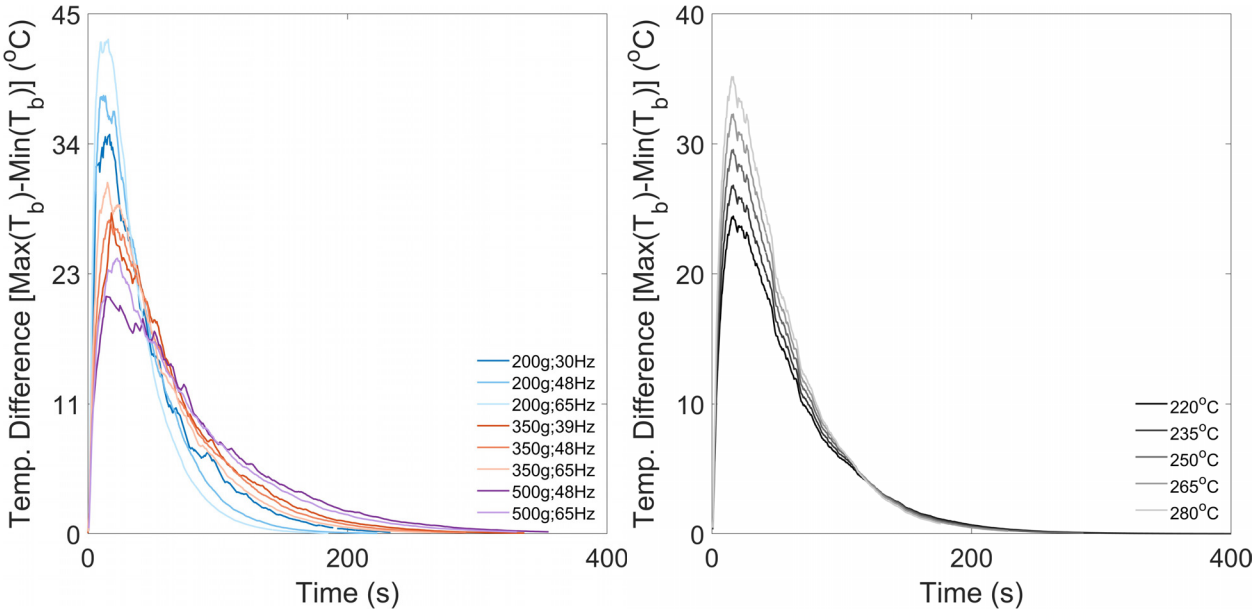

(a) Variation of batch size and airflow (b) Variation of constant inlet air temperature

Figure 7.25: Temporal evolution of the in-bean temperature differential extracted from temperature field data (as in Figures 7.26-7.27 for roasting with different (a) batch sizes and airflows and (b) constant inlet air temperatures.

7.2.5 Coffee's physicochemical transformation

Predictions of coffee's corresponding physicochemical development were computed during simulation of the time-temperature profiles, alongside correlations of (i) density and moisture, (ii) thermal conductivity and density and (iii) specific heat capacity and density. Figures 7.28-7.29 present coffee's physicochemical development during simulated roasting for different process conditions. Figure 7.28 depicts simulations corresponding to case study I, Figure 7.29 case study II. In both figures, the effect of process conditions on the evolution of density, thermal conductivity, specific heat capacity, batch size (mass basis), moisture, thermocouple temperature and bean temperature are illustrated. Figure 7.28 demonstrates that the magnitude of the rate of change of mass, moisture, density, thermal conductivity and specific heat capacity increases with the constant inlet air temperature (i.e., the applied thermal load). This is also observed in Figure 7.29, as a function of decreasing batch size

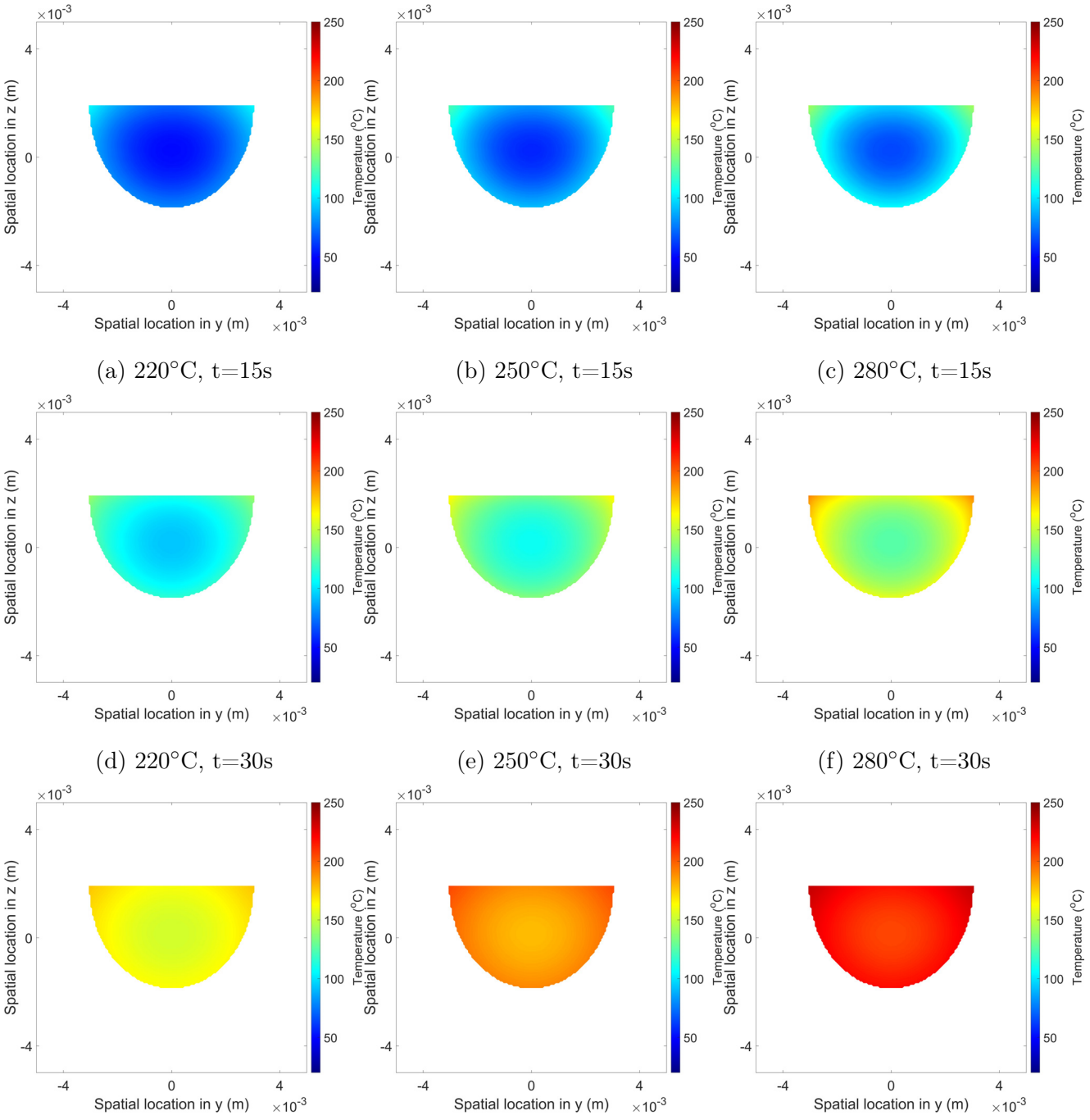

(a) 220°C, t=15s (b) 250°C, t=15s (c) 280°C, t=15s

(d) 220°C, t=30s (e) 250°C, t=30s (f) 280°C, t=30s

(g) 220°C, t=60s (h) 250°C, t=60s (i) 280°C, t=60s

Figure 7.26: Predicted in-bean temperature distributions in the plane *y,z* for roasting conditions of (a),(d),(g) 350g, 220°C & 48 Hz, (b),(e),(h) 350g, 250°C & 48 Hz and (c),(f),(i) 350g, 280°C & 48 Hz at simulated roasting times of (a)-(c) 15 s, (d)-(f) 30 s and (g)-(i) 60 s for hemi-ellipsoidal geometry showing the effect of inlet air temperature on the evolution of in-bean temperature distribution.

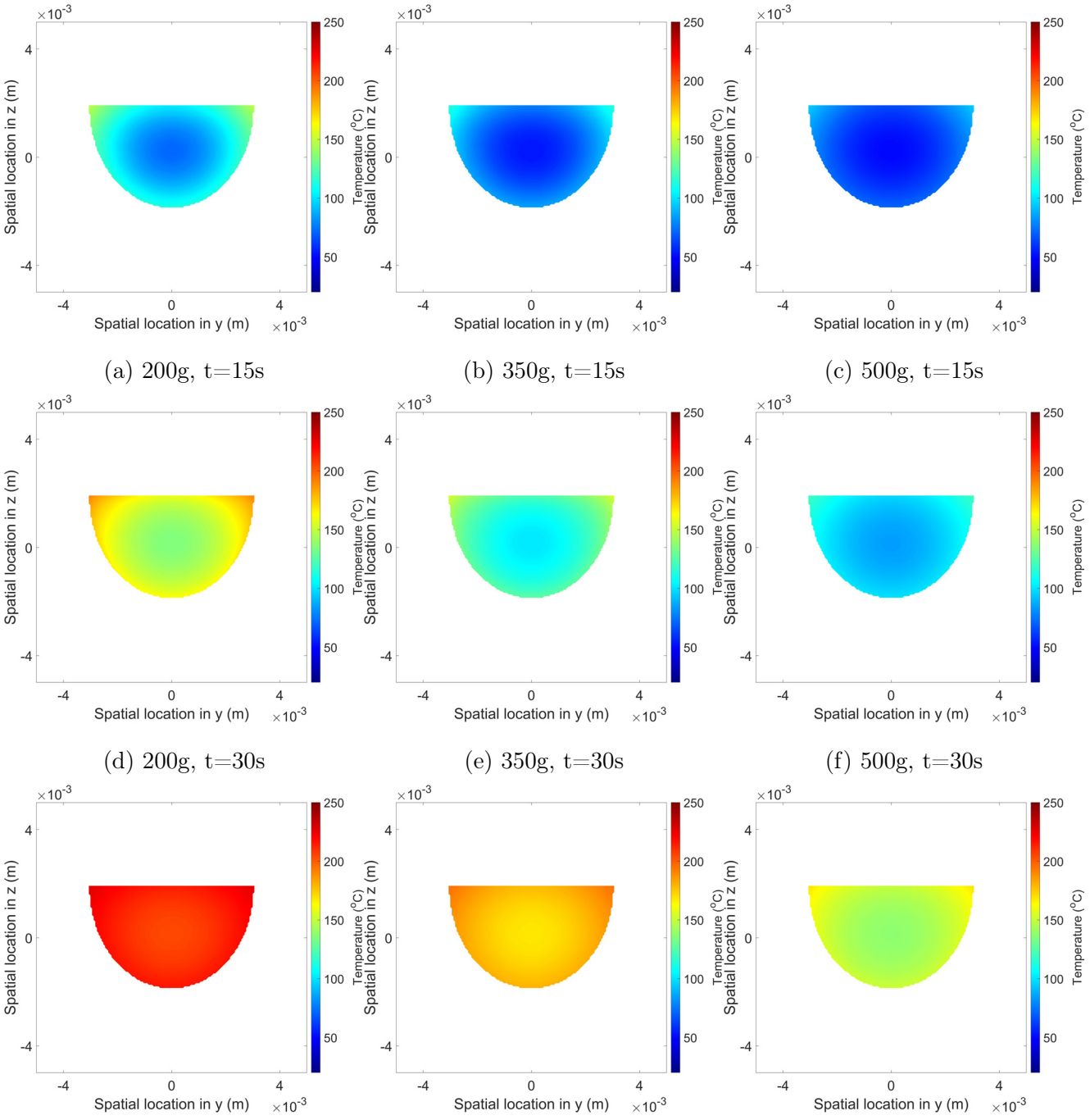

(a) 200g, t=15s (b) 350g, t=15s (c) 500g, t=15s

(d) 200g, t=30s (e) 350g, t=30s (f) 500g, t=30s

(g) 200g, t=60s (h) 350g, t=60s (i) 500g, t=60s

Figure 7.27: Predicted in-bean temperature distributions in the plane *y,z* for roasting conditions of (a),(d),(g) 200g, 250°C & 48 Hz, (b),(e),(h) 350g, 250°C & 48 Hz and (c),(f),(i) 500g, 250°C & 48 Hz at simulated roasting times of (a)-(c) 15 s, (d)-(f) 30 s and (g)-(i) 60 s for hemi-ellipsoidal geometry showing the effect of batch size on the evolution of in-bean temperature distribution.

and increasing airflow.

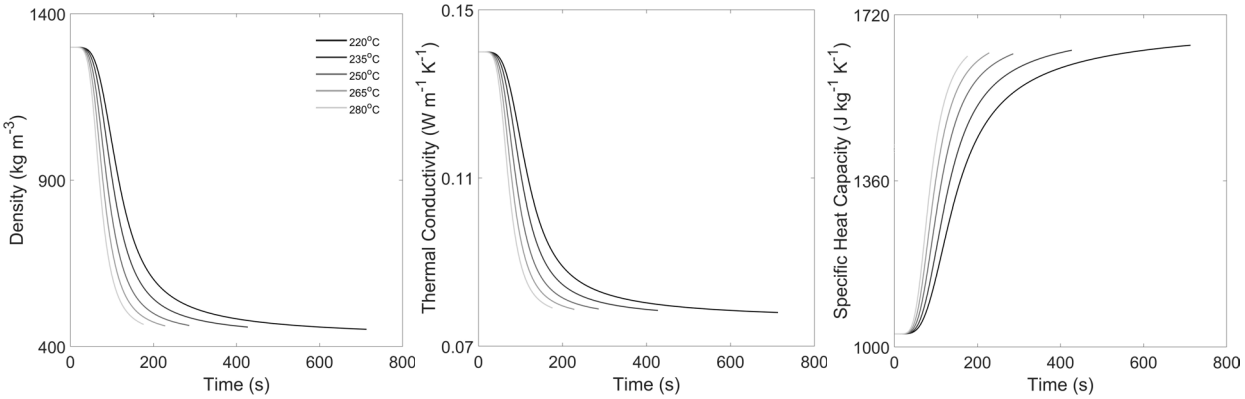

(a) Density (b) Thermal Conductivity (c) Specific Heat Capacity

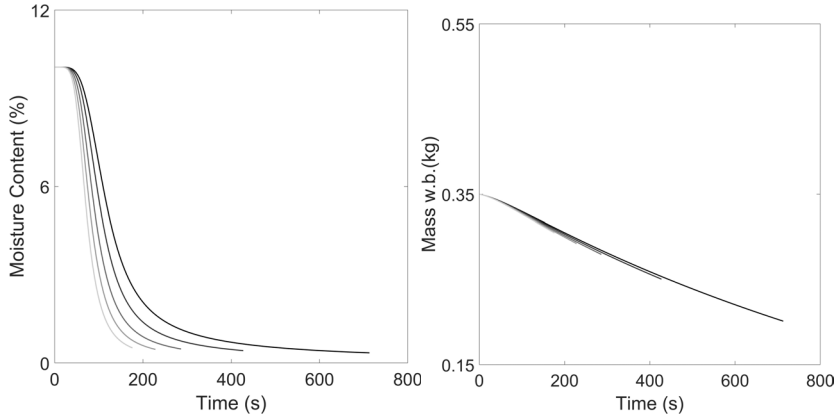

(d) Moisture (e) Batch Size

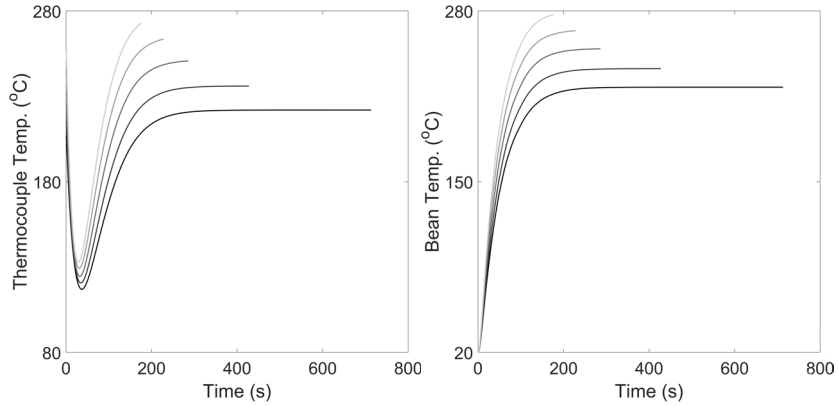

(f) Thermocouple Temp. (g) Bean Temp.

Figure 7.28: Predicted time-temperature profiles and corresponding physicochemical development of coffee during simulated roasting at different constant inlet air temperatures. Subplots demonstrate the effect of process conditions on (a) density, (b) thermal conductivity, (c) specific heat capacity, (d) batch size (mass basis), (e) moisture, (f) thermocouple temperature and (g) bean temperature. Data legend is displayed only in (a) for visual clarity.

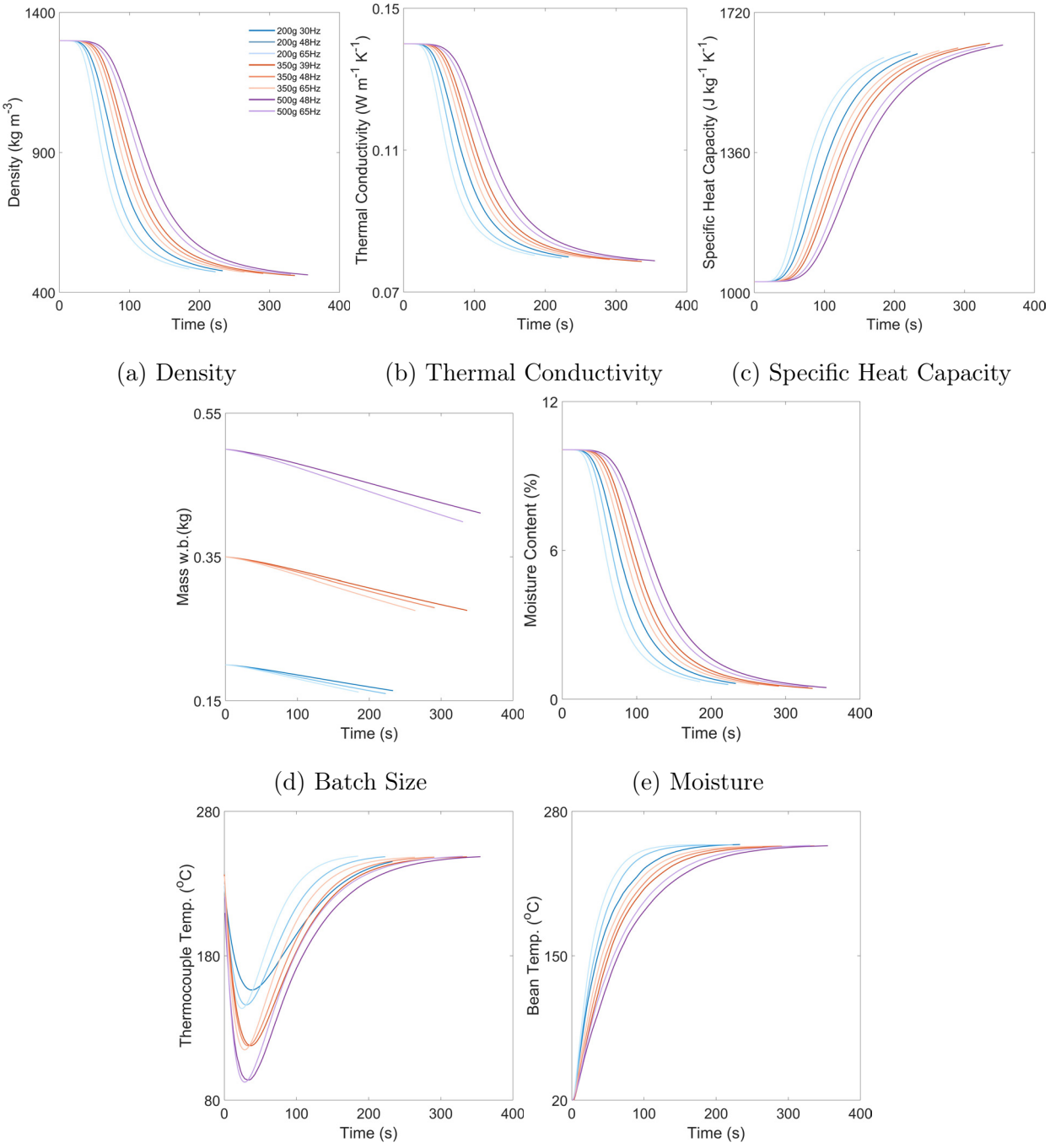

(a) Density (b) Thermal Conductivity (c) Specific Heat Capacity

(d) Batch Size (e) Moisture

(f) Thermocouple Temp. (g) Bean Temp.

Figure 7.29: Predicted time-temperature profiles and corresponding physicochemical development of coffee during simulated roasting at different with different batch size and airflow combinations. Subplots demonstrate the effect of process conditions on (a) density, (b) thermal conductivity, (c) specific heat capacity, (d) batch size (mass basis), (e) moisture, (f) thermocouple temperature and (g) bean temperature. Data legend is displayed only in (a) for visual clarity.

7.2.6 Comparison with batch-scale simulations

This subsection compares the time-temperature profiles and corresponding physicochemical development resolved from the bean-scale simulation with both the batch-scale simulations from Chapter 6, as well as the experimental, calibration data from Chapter 3.

Figure 7.30 displays time-temperature profiles resolved from the batch-scale and bean-scale simulations, outlining the effect of batch size (in Figure 7.30(a)-(c)) and constant inlet air temperature (in Figure 7.30(d)-(f)). For all simulated conditions, the rate of change of the 3D-resolved bean temperature was lower than that via the batch-scale simulations at early times. Shortly after the turning-point, the rate of change of the bean temperature resolved from the batch-scale simulation decreases and tends toward a lower temperature than observed for the 3D simulation, therefore the bean temperature resolved from the bean-scale simulation is higher in the later stages of simulated roasting. The thermocouple temperatures resolved from both simulations follow a similar trend. For case study I, the difference between the temperatures (both thermocouple and bean temperatures) from the simulations increases with batch size, although for case study II, the difference decreases as the constant inlet air temperature decreases.

Figure 7.32 compares the time-temperature profiles and corresponding physicochemical development resolved from the 3D bean-scale simulations, batch-scale simulations and experimental roasting data - data corresponds to a moderate batch size (350 g), moderate constant inlet air temperature (250°C) and moderate airflow (48 Hz).

The predicted physicochemical development is governed by the bean's time-temperature profile, so the disparities between the bean temperatures resolved from the batch-scale and bean-scale simulations propagate through to the physicochemical development. In this way, the rate of change of physicochemical properties resolved from the batch-scale simulation are initially greater than those from the bean-scale simulations, although the rate of change decreases during roasting. Overall, the difference between the final properties predicted via the batch-scale and bean-scale simulation are small.

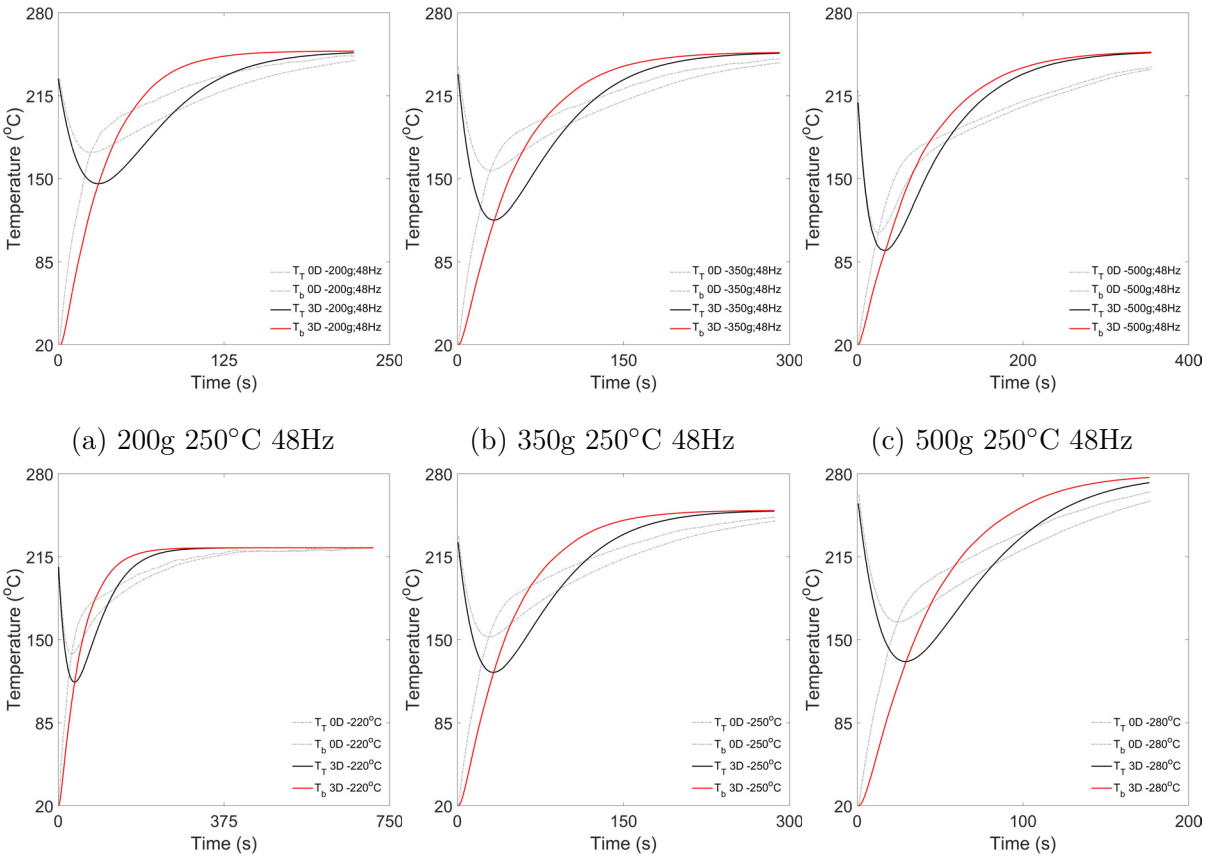

(a) 200g 250°C 48Hz (b) 350g 250°C 48Hz (c) 500g 250°C 48Hz

(d) 350g 220°C 48Hz (e) 350g 250°C 48Hz (f) 350g 280°C 48Hz

Figure 7.30: Comparison of predicted bean and thermocouple time-temperature profiles from both batch-scale (0D) and bean-scale (3D) simulations that illustrate the impact of process conditions on the resolved roasting profiles for roasting with different (a)-(c) batch sizes and (d)-(f) constant inlet air temperatures - data corresponds to roasting conditions of (a) 200g 250°C & 48 Hz, (b) 350g 250°C & 48 Hz, (c) 500g 250°C & 48 Hz, (d) 350g 220°C & 48 Hz, (e) 350g 250°C & 48 Hz and (f) 350g 280°C & 48 Hz.

Figures 7.22 & 7.23 show that the predicted thermocouple temperature profile's turning-point occurs at a greater time and lower temperature than the experimental profile - indicating that the thermal response coefficient determined for the batch-scale simulations is not directly translatable to the single-bean simulation - this is seen again here in Figure 7.32(f). Figure 7.31 details the effect of the thermal response coefficient on the predicted thermocouple temperature and reveals that its variation greatly affects the conversion from bean temperature to thermocouple temperature and can increase model accuracy, although re-calibration of the thermal response coefficient was not predictable across different process conditions, and

is therefore not sufficient to explain the disparities.

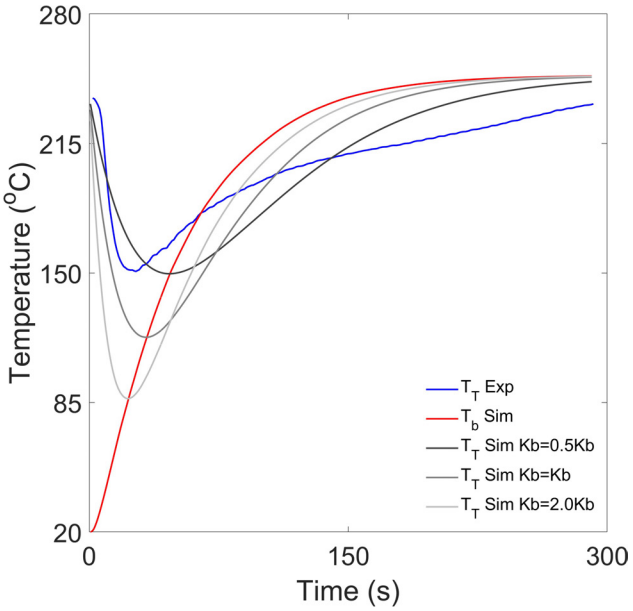

Figure 7.31: Comparison of the predicted bean and thermocouple time-temperature profiles from the bean-scale (3D) simulations that illustrate the impact of the thermal response coefficient on resolved roasting profiles - data corresponds to roasting conditions of 350g 250°C & 48 Hz.

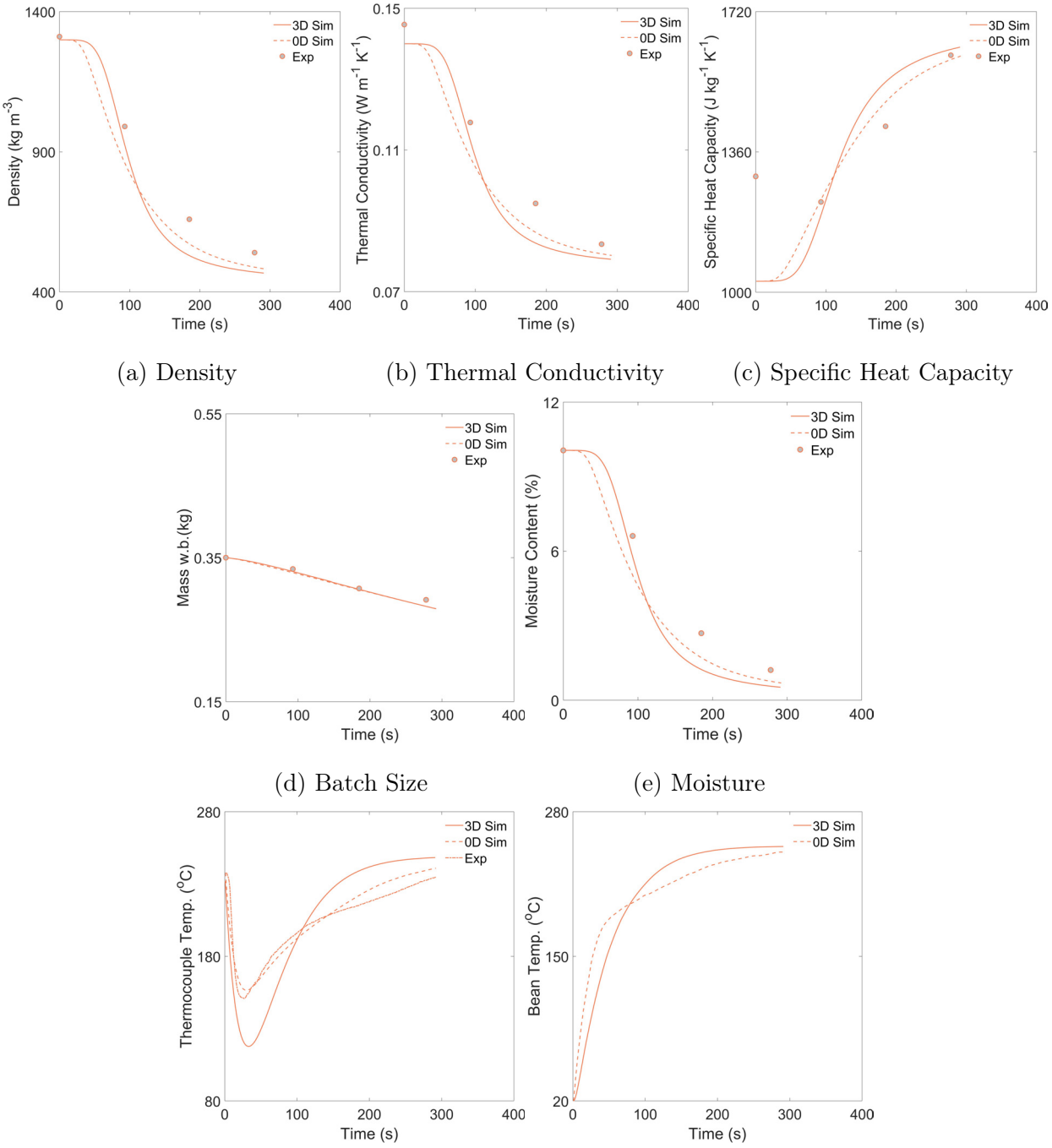

(a) Density (b) Thermal Conductivity (c) Specific Heat Capacity

(d) Batch Size (e) Moisture

(f) Thermocouple Temp. (g) Bean Temp.

Figure 7.32: Comparison of responses of predicted time-temperature profiles and corresponding physicochemical development of coffee during roasting, resolved via the batch-scale (0D) and bean-scale (3D) models. Data corresponds to roasts of 350g with a fan frequency of 48Hz and a constant inlet air temperature of 250°C. Subplots demonstrate the accuracy of simulations for (a) density, (b) thermal conductivity, (c) specific heat capacity, (d) batch size (mass basis), (e) moisture and (f) thermocouple temperature - subplot (g) compares the simulated bean temperatures only (i.e., without experimental validation).

7.3 Best practices for roasters

7.3.1 Limitations & robustness

Whilst the data-driven calibration approach ensured that the relevant physics were captured and implemented within the model, the specificity of the simulation requires more process and product specific measurements to be performed to achieve the accuracy obtained here.

Coffee properties

As mentioned in Chapters 5 & 6, the calibrated models of mass and moisture capture the kinetic behaviour well within the bounds of the experimental conditions. The rate coefficients were robust to different process conditions in the spouted bed roaster, although distinct green coffees and diverse process conditions will yield different mass and moisture kinetics. Extrapolation of these kinetic models will be robust to different roaster designs provided the overall heat transfer coefficient and roasting time are both comparable.

Coffee's thermal properties (density, specific heat capacity and thermal conductivity) were implemented as empirical correlations that are based on the coffee's moisture loss. Similar correlations have been observed (Singh et al., 1997; Burmester and Rudolf Eggers, 2010; Fabbri, Cevoli, Alessandrini, et al., 2011; Cardoso et al., 2018), although validation of these correlations using a larger number of coffees and process conditions would test the correlation's robustness.

Particle geometry affected both the accuracy and runtime of the simulation. Despite the geometrical accuracy of the 3D-scanned bean, the predicted time-temperature profile corresponding to the hemi-ellipsoidal geometry was not dissimilar. Assuming the aspect ratio of the coffee studied here can be generalised, developers need only to measure the equivalent diameter of their coffee for accurate application of the simulation. Similarly, particle size had a significant effect on the predicted time-temperature profiles and although coffee's volume expands by a factor of 2 during roasting, the implementation of a moving boundary problem was inhibited by the software (MATLAB's PDE toolbox).

Process conditions

The novel implementation of dynamic boundary conditions informed by particle motion data enabled regional heat transfer coefficients to be derived. This approach provides insight not yet explored in literature but requires developers to have an appreciation for the particle dynamics in their roaster. For developers who wish to implement these models, assumption of the residence times in each region, alongside estimation of the relative difference of particle and air velocity in each region would be sufficient to emulate the particle motion data.

Particle motion data corresponding to a rotating drum roaster was presented in Chapter 4. The calibration approach detailed here could also be developed for a rotating drum roaster using the PEPT-data. Modification of the energy balance to include heat transfer from the drum's surface would be sufficient to adapt the thermal model (Palma et al., 2021).

7.3.2 Commercial implementation

Although these bean-scale simulations provide insight that cannot be obtained from the batch-scale simulations, the current computational requirements mean that these simulations are not yet appropriate for integration within commercial control systems. The batch-scale simulations in Chapter 6 however, are sufficient for such application. That said, these bean-scale simulations are valuable for process and product developers.

These calibrated simulations of the coffee bean's temperature field can be used to infer the in-bean distribution of moisture, colour and other chemical compounds. Whilst not explicitly studied in this Chapter, the difference between the whole bean and ground coffee colour could be estimated if kinetic models of colour were developed. This would be of interest for developers, as large colour differences can be indicative of in-cup complexity - although very large differences could result in high acidity and harsh roasted notes that clash (Giacalone et al., 2019). To develop coffee in a more uniform way, the calibrated simulation suggests that residence time in the bean is critical for the in-bean development of temperature (and therefore colour). In this way, based on particle motion data and Figure 7.25, more uniform colour development could be achieved when roasting with greater batch sizes and lower

airflow with moderate constant inlet air temperature, conditions which maximise bean bed residence time. When considering the sensorial aspect of this, it likely that these conditions significantly degrade the bean's potential acidity Münchow et al., 2020.

The question of bean size and its effect on roasting is of commercial relevance not just for roasting different varieties, but also when roasting blends. Data in Figure 7.20(d) outlines the effect of particle diameter on the temperature response during roasting - it is worth noting that this assumed an equivalent intrinsic density. In practice, smaller beans often have greater density. Anecdotally, the heating rate of beans with a greater density is lower, yet Figure 7.20(a) suggests that density has only a small effect on the temperature profile. Instead, Figure 7.20(b)-(c) indicate that the heating rate is more sensitive to the specific heat capacity and thermal conductivity. As these thermal properties correlate with density, it could be that variation in the density measurement is a proxy for the variation in specific heat capacity and thermal conductivity. That said, the thermal properties and bean size are in opposition regarding heat transfer, typically with a net lower heating rate for smaller, more dense beans.

Regarding blending, these data indicate that coffees should be blended according to their specific heat capacity and thermal conductivity and suggests that differences between Arabica and Robusta varieties are attributable to their thermal properties (and chemical composition). As thermal property measurements are not readily accessible to most product and process developers (due to cost of the measurement device), density measurements could be used as a proxy. Other coffee properties such as cherry ripeness, size distribution and post-harvest processing (particularly demucilagination and drying) are all factors that also influence the coffee's heating rate but are more difficult to quanitify.

7.4 Conclusions & outlook

In a data driven approach, empirically derived data were used to calibrate a 3D heat transfer model of a coffee bean's temperature response during roasting. The model was developed based on an energy balance over the roaster, wherein heat transfer rates to the bean were governed by convection and the internal development of the bean by conduction.

Using real particle motion data established in Chapter 4, the bean's position in the roaster varied over time, traversing between the dilute freeboard and dense bean bed. Therein, regional heat transfer coefficients were derived using dimensionless Reynolds numbers calculated from real bean and air velocities extracted from PEPT data, such that when beans in the freeboard are subject to greater heat transfer rates than in the bean bed. In this way, dynamic, convective boundary conditions were derived, with the residence time in each region implemented as the simulation's time-step.

Further empirical data relating to the coffee's initial properties were used to calibrate the conductive term of the thermal balance, including the mass, moisture, size, density, specific heat capacity and thermal conductivity. Kinetic models of mass and moisture developed in Chapter 5 were used as the drivers for coffee's physicochemical transformation, with empirical correlations from Chapter 3 used to estimate the transient behaviour of the thermal properties.

Process characteristics established in Chapters 2 were used to calibrate the process conditions of the model, whereby the airflow calibration, effect of the air distributor, thermophysical properties of the drying air were implemented. Similarly, estimated process characteristics, such as the thermal response coefficient and heat transfer effectiveness factor from Chapter 6 were also implemented to translate from the predicted bean temperature to the temperature measured by the product thermocouple.

Approximate particle geometry and its spatial discretisation were shown to influence the solver's run time and mean squared error. Hemi-ellipsoidal geometry gave results very sim-

ilar to the 3D-scanned geometry, but run time similar to the spherical geometry, so is recommended.

The calibrated 3D simulations demonstrated the temporal evolution of the temperature field within the bean during roasting. Subsequent calculation of the mean bean temperature, estimation of the corresponding physicochemical transformation and translation of temperature to determine the thermocouple's temperature response enabled comparison with batch-scale simulations and experimental data (i.e., the calibration data).

Whilst disparities between the bean temperatures resolved from batch-scale and bean-scale simulations are relatively small, the simulations show relatively high error when considering the predicted thermocouple temperature. This is explained by the implementation of the thermal response coefficient and heat transfer effectiveness factor from the batch-scale simulations. To reduce the error, these translation factors need to be re-calibrated to facilitate conversion from a single-bean to the batch-mean response. That said, the predicted physicochemical transformation of coffee during roasting was well captured within the boundaries of the calibrated model.

These rigorously calibrated simulations demonstrate the thermal and physicochemical transformation of coffee during roasting under different process conditions. The predicted in-bean temperature distributions could be used in conjunction with established kinetic models to infer moisture, colour and other chemical distributions within the bean. Overall, this Chapter establishes a digital model that can be used by product and process developers to help navigate flavour and aroma development during coffee roasting.

7.5 Appendix: Sensitivity analysis - Geometry

Figure 9.1 compares predicted time-temperature (thermocouple and mean-bean) profiles for different roasting conditions and particle geometry (sphere, hemi-ellipsoid and 3D-scanned bean). Figure 9.1(a)-(c) shows the effect of particle geometry and different fan frequencies (i.e., airflow rates), Figure 9.1(d)-(f) the effect of particle geometry and different batch sizes and Figure 9.1(g)-(i) the effect of particle geometry and constant inlet air temperature. Figures 9.2, 9.3 & 9.4 are complementary to Figure 9.1 and illustrate the impact of particle geometry on the resolved in-bean temperature fields - data presented as contour plots correspond to roasting conditions of 350g 250°C & 48 Hz for spherical, hemi-ellipsoidal and 3D-scanned bean geometries, respectively.

7.6 Appendix: In-bean temperature distributions

The effect of roasting conditions on predicted in-bean temperature distributions are presented in Figures 9.5-9.10. Figures 9.5-9.7 correspond to case study I and show the effect of constant inlet air temperature on the time-temperature evolution of the bean for roasting conditions of 220°C, 250°C and 280°C, respectively - with corresponding time-temperature profiles in Figure 7.22. Figures 9.8-9.10 correspond to case study II and show the effect of different batch sizes on the time-temperature evolution of the bean for roasting conditions of 200g, 350g and 500g, respectively - with corresponding time-temperature profiles in Figure 7.23. Each figure depicts the temporal evolution of the bean's temperature field for specified roasting conditions.

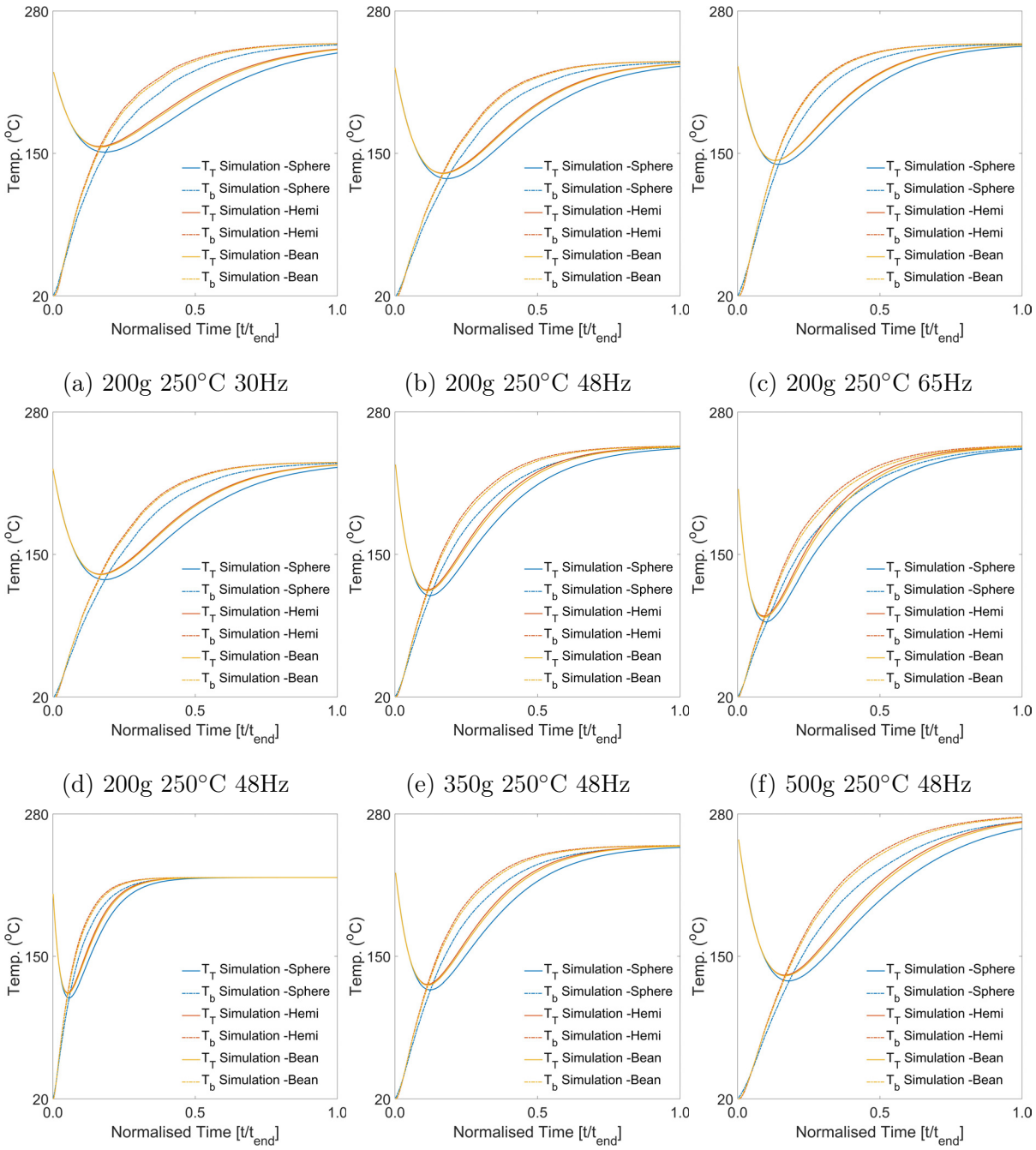

(a) 200g 250°C 30Hz (b) 200g 250°C 48Hz (c) 200g 250°C 65Hz

(d) 200g 250°C 48Hz (e) 350g 250°C 48Hz (f) 500g 250°C 48Hz

(g) 350g 220°C 48Hz (h) 350g 250°C 48Hz (i) 350g 280°C 48Hz

Figure 7.33: Comparison of the predicted bean and thermocouple time-temperature profiles that illustrate the impact of coffee bean geometry (sphere, hemi-ellipsoid and 3D-scanned bean) on the resolved roasting profiles for roasting with different (a)-(c) airflows, (d)-(f) batch sizes and (g)-(i) constant inlet air temperatures - data corresponds to roasting conditions of (a) 200g 250°C & 30 Hz, (b) 200g 250°C & 48 Hz, (c) 200g 250°C & 65 Hz, (d) 200g 250°C & 48 Hz, (e) 350g 250°C & 48 Hz, (f) 500g 250°C & 48 Hz, (g) 350g 220°C & 48 Hz, (h) 350g 250°C & 48 Hz and (i) 350g 280°C & 48 Hz.

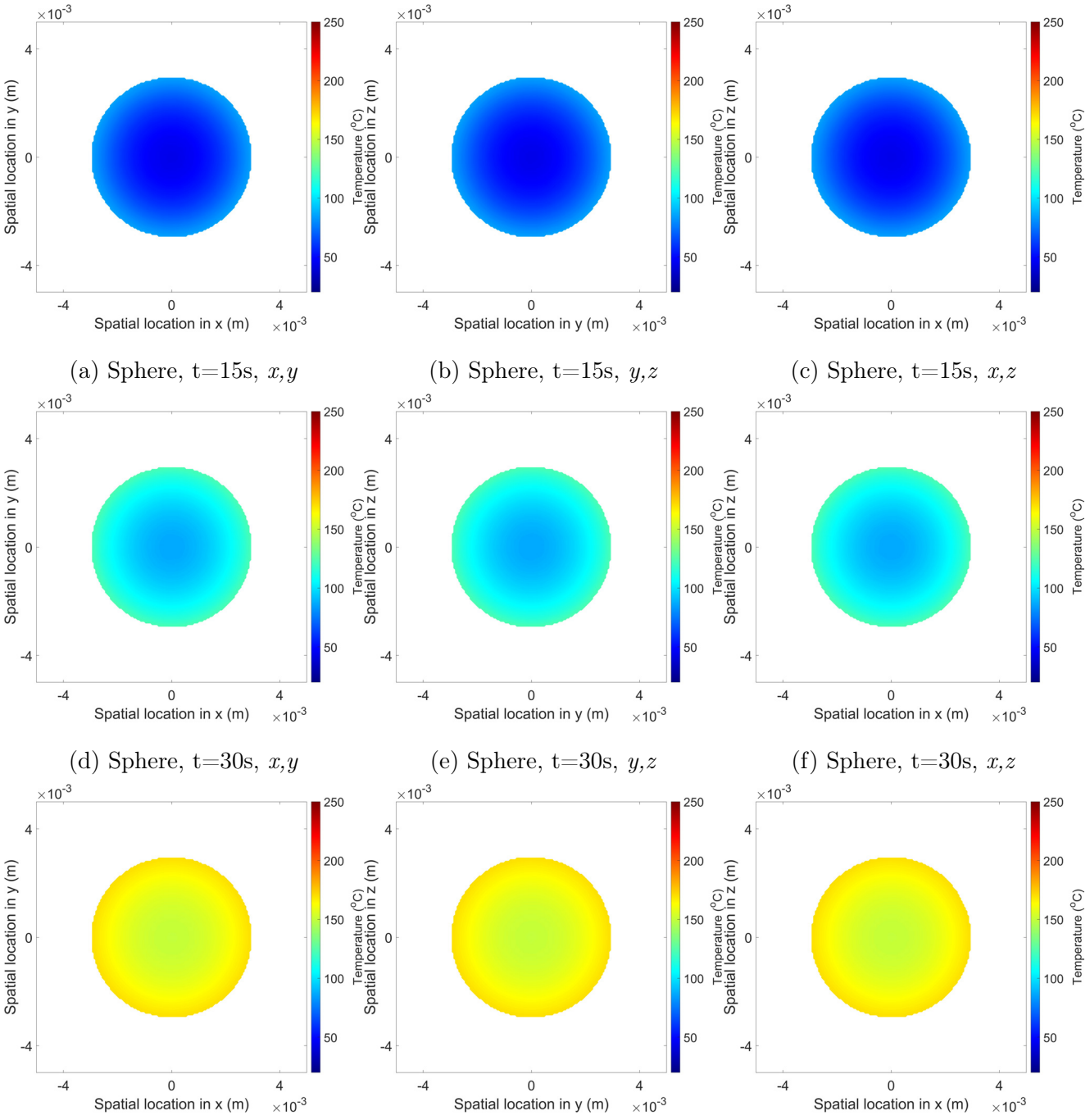

(a) Sphere, t=15s, x,y (b) Sphere, t=15s, y,z (c) Sphere, t=15s, x,z

(d) Sphere, t=30s, x,y (e) Sphere, t=30s, y,z (f) Sphere, t=30s, x,z

(g) Sphere, t=60s, x,y (h) Sphere, t=60s, y,z (i) Sphere, t=60s, x,z

Figure 7.34: Comparison of the predicted in-bean temperature distributions in the plane (a),(d),(g) x,y, (b),(e),(h) y,z and (c),(f),(i) x,z at simulated roasting times of (a)-(c) 15 s, (d)-(f) 30 s and (g)-(i) 60 s for spherical geometry - data corresponds to roasting conditions of 350g 250°C & 48 Hz.

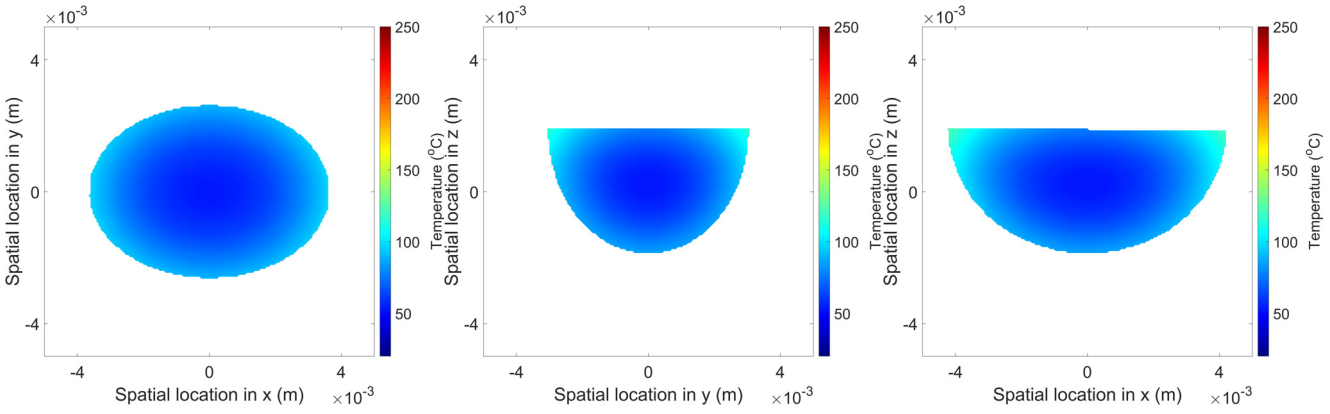

(a) Hemi-ellipsoid, t=15s, x,y (b) Hemi-ellipsoid, t=15s, y,z (c) Hemi-ellipsoid, t=15s, x,z

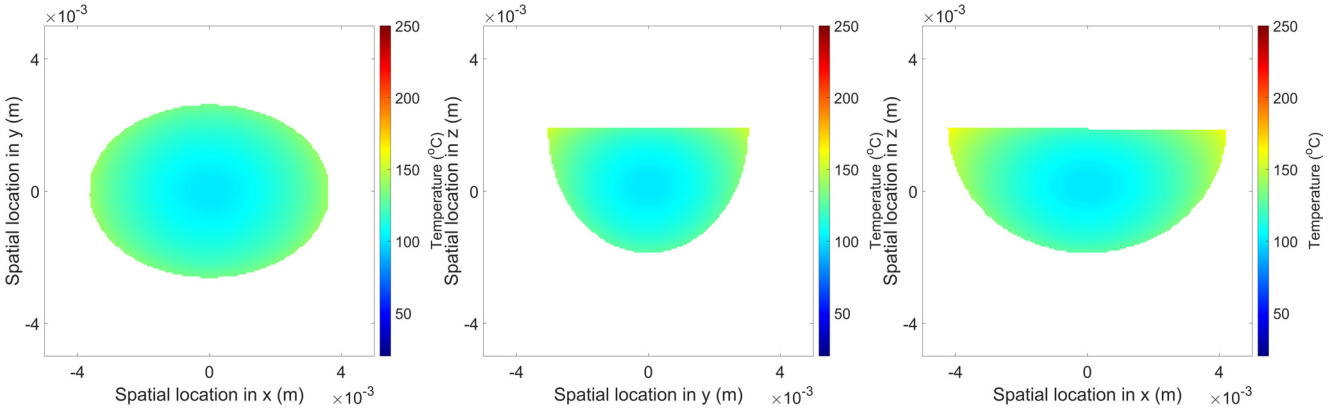

(d) Hemi-ellipsoid, t=30s, x,y (e) Hemi-ellipsoid, t=30s, y,z (f) Hemi-ellipsoid, t=30s, x,z

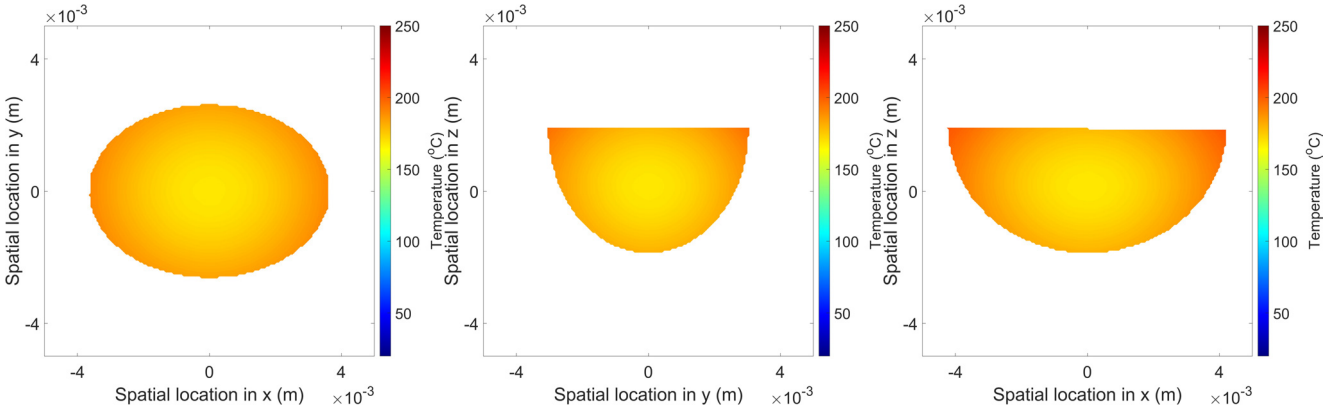

(g) Hemi-ellipsoid, t=60s, x,y (h) Hemi-ellipsoid, t=60s, y,z (i) Hemi-ellipsoid, t=60s, x,z

Figure 7.35: Comparison of the predicted in-bean temperature distributions in the plane (a),(d),(g) x,y, (b),(e),(h) y,z and (c),(f),(i) x,z at simulated roasting times of (a)-(c) 15 s, (d)-(f) 30 s and (g)-(i) 60 s for hemi-ellipsoidal geometry - data corresponds to roasting conditions of 350g 250°C & 48 Hz.

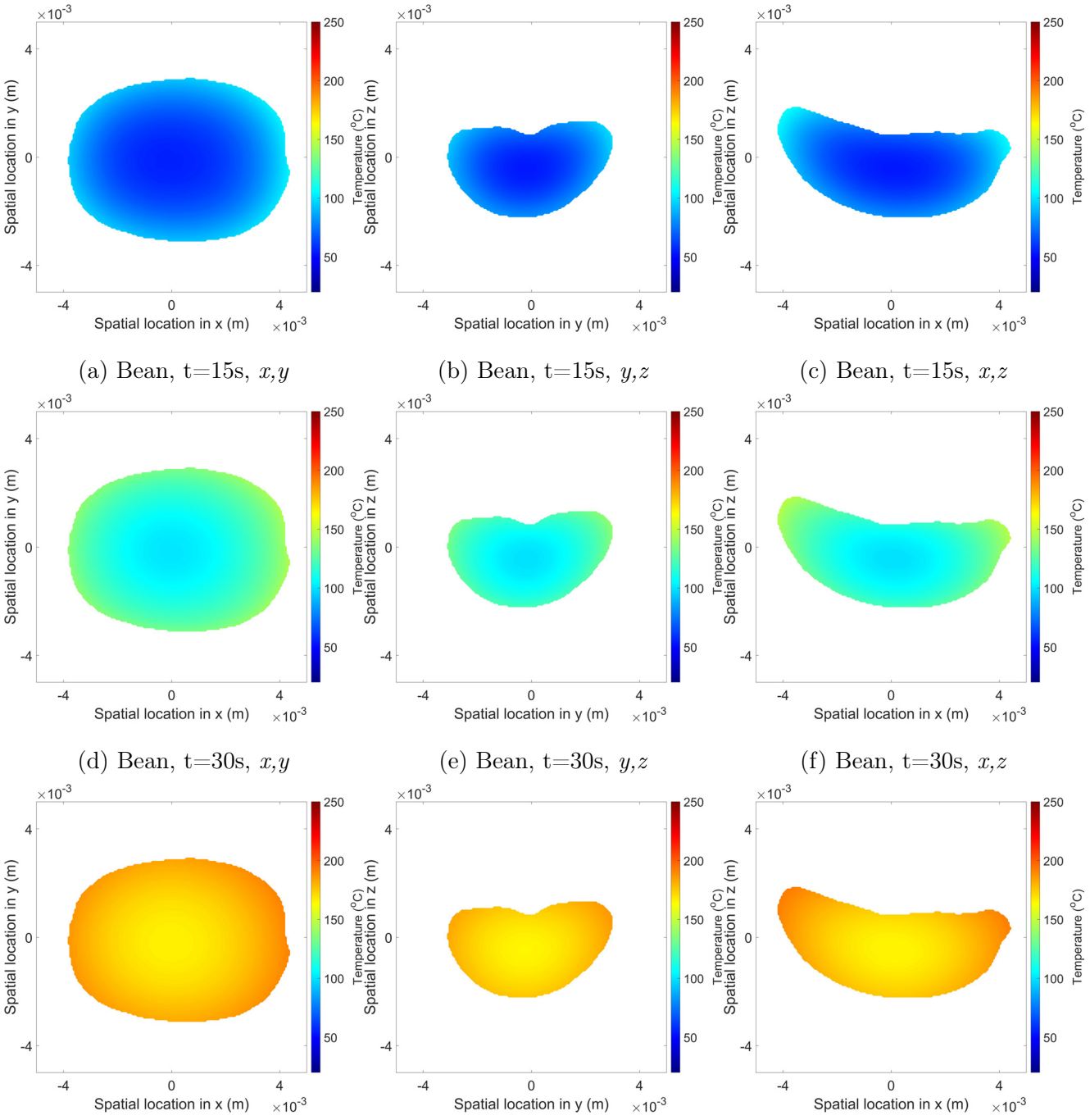

(a) Bean, t=15s, x,y (b) Bean, t=15s, y,z (c) Bean, t=15s, x,z

(d) Bean, t=30s, x,y (e) Bean, t=30s, y,z (f) Bean, t=30s, x,z

(g) Bean, t=60s, x,y (h) Bean, t=60s, y,z (i) Bean, t=60s, x,z

Figure 7.36: Comparison of the predicted in-bean temperature distributions in the plane (a),(d),(g) x,y, (b),(e),(h) y,z and (c),(f),(i) x,z at simulated roasting times of (a)-(c) 15 s, (d)-(f) 30 s and (g)-(i) 60 s for 3D scanned bean geometry - data corresponds to roasting conditions of 350g 250°C & 48 Hz.

Table 7.5: Solver times corresponding to different particle geometries and process conditions.

Batch	**Fan Freq.**	**Inlet Air**	**Roasting**	**Solver Run Time (s)**			**Specific Solver Run Time (s s^{-1})**		
Size (g)	**(Hz)**	**Temp. (°C)**	**Time (s)**	**Sphere**	**Hemi-Ellipsoid**	**Bean**	**Sphere**	**Hemi-Ellipsoid**	**Bean**
200	30	250	233	1153	1044	9179	4.9	4.5	39.4
200	48	250	223	1546	1292	15010	6.9	5.8	67.3
200	65	250	185	1459	1310	11021	7.9	7.1	59.6
350	39	250	336	1423	1249	13318	4.2	3.7	39.6
350	48	250	291	1476	1305	13746	5.1	4.5	47.2
350	65	250	264	1154	1065	11135	4.4	4.0	42.2
500	48	250	354	1032	943	9630	2.9	2.7	27.2
500	65	250	330	723	859	9157	2.2	2.6	27.7
350	48	220	713	3370	3058	27098	4.7	4.3	38.0
350	48	235	426	2035	1833	15806	4.8	4.3	37.1
350	48	250	286	1263	1263	10999	4.4	4.4	38.5
350	48	265	228	1077	966	8432	4.7	4.2	37.0
350	48	280	176	803	740	6374	4.6	4.2	36.2

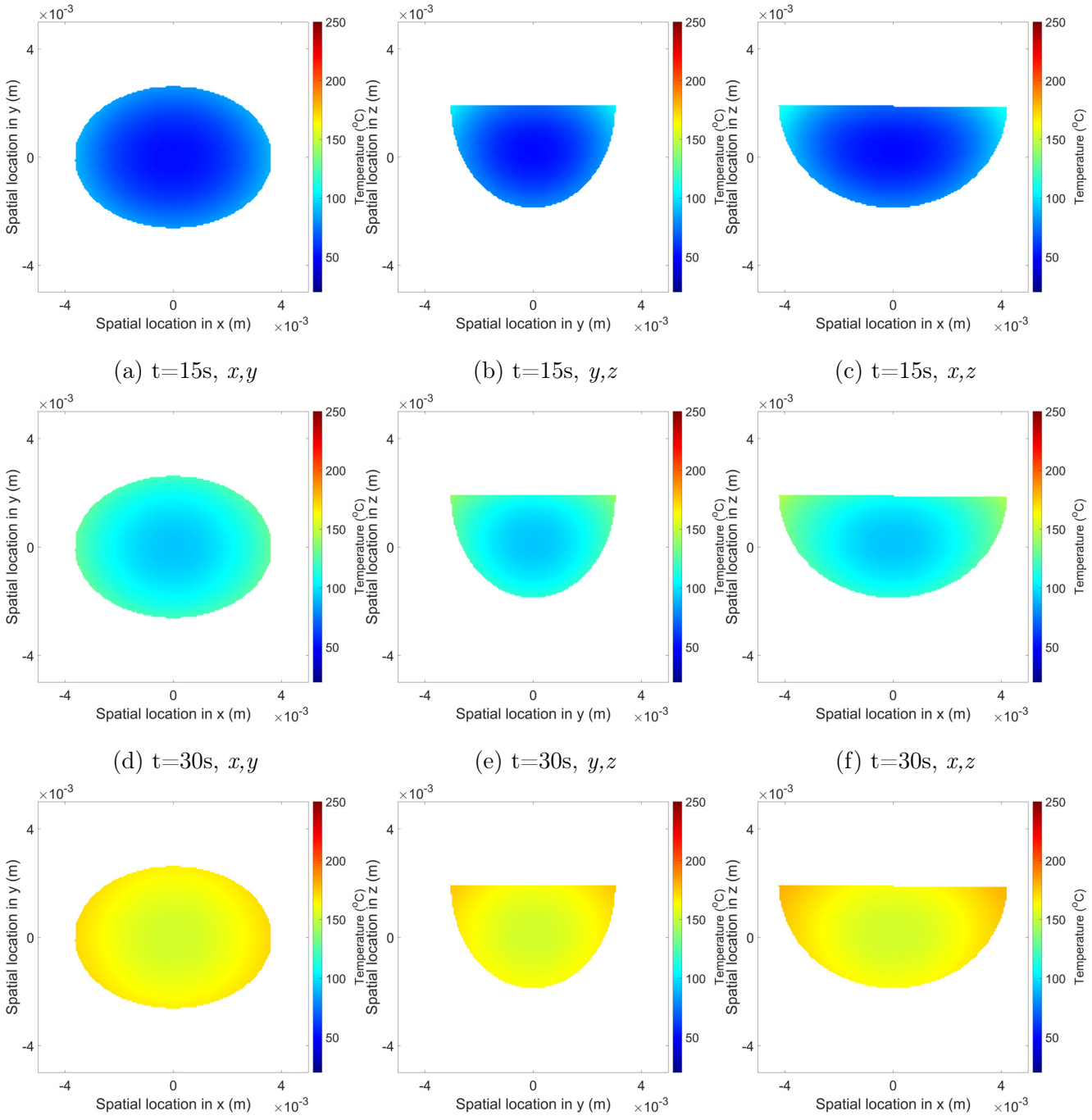

(a) t=15s, x,y (b) t=15s, y,z (c) t=15s, x,z

(d) t=30s, x,y (e) t=30s, y,z (f) t=30s, x,z

(g) t=60s, x,y (h) t=60s, y,z (i) t=60s, x,z

Figure 7.37: Predicted in-bean temperature distributions in the plane (a),(d),(g) x,y, (b),(e),(h) y,z and (c),(f),(i) x,z at simulated roasting times of (a)-(c) 15 s, (d)-(f) 30 s and (g)-(i) 60 s for hemi-ellipsoidal geometry - data corresponds to roasting conditions of 350g, 220°C & 48 Hz.

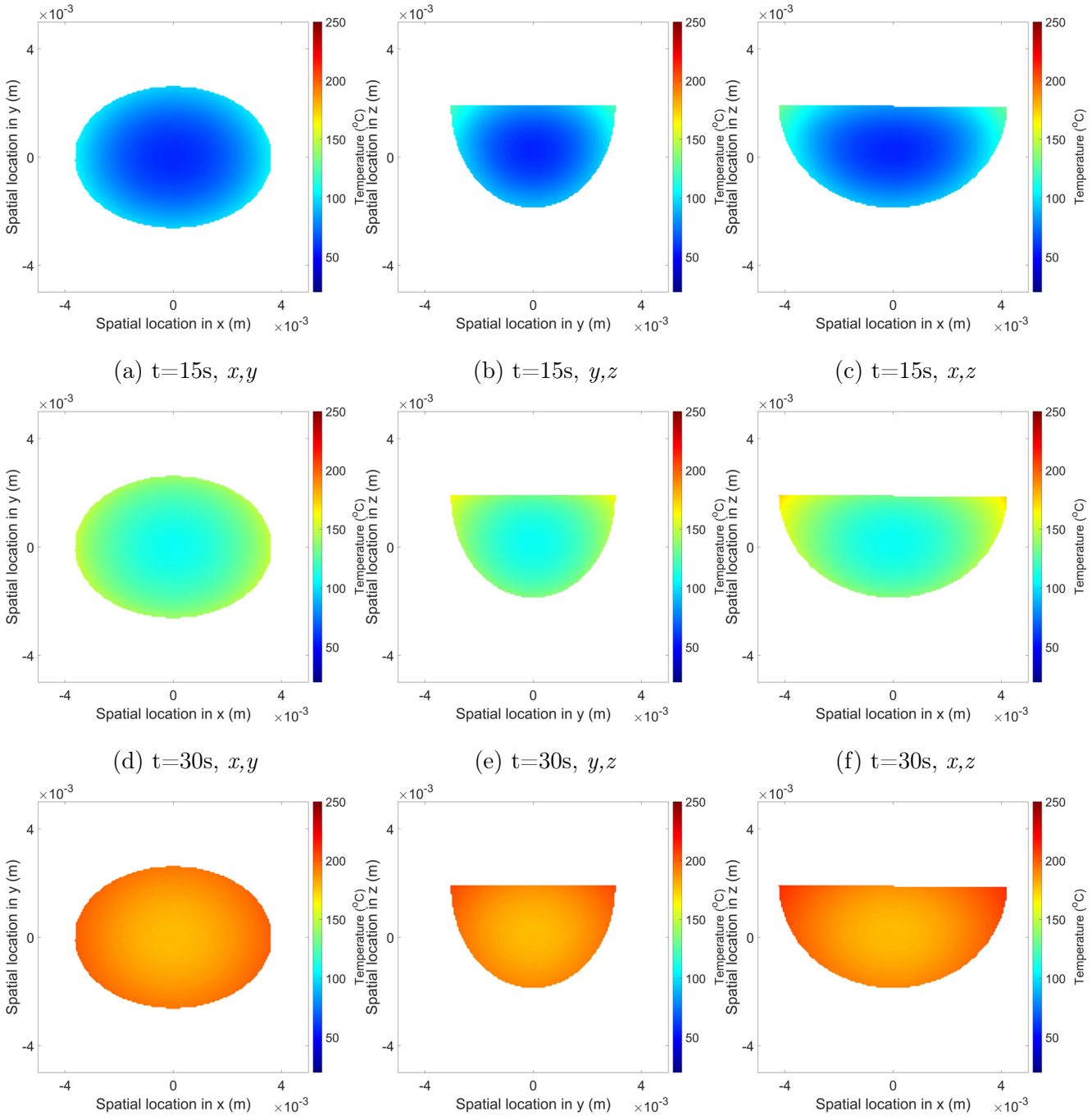

(a) t=15s, x,y (b) t=15s, y,z (c) t=15s, x,z

(d) t=30s, x,y (e) t=30s, y,z (f) t=30s, x,z

(g) t=60s, x,y (h) t=60s, y,z (i) t=60s, x,z

Figure 7.38: Predicted in-bean temperature distributions in the plane (a),(d),(g) x,y, (b),(e),(h) y,z and (c),(f),(i) x,z at simulated roasting times of (a)-(c) 15 s, (d)-(f) 30 s and (g)-(i) 60 s for hemi-ellipsoidal geometry - data corresponds to roasting conditions of 350g, 250°C & 48 Hz.

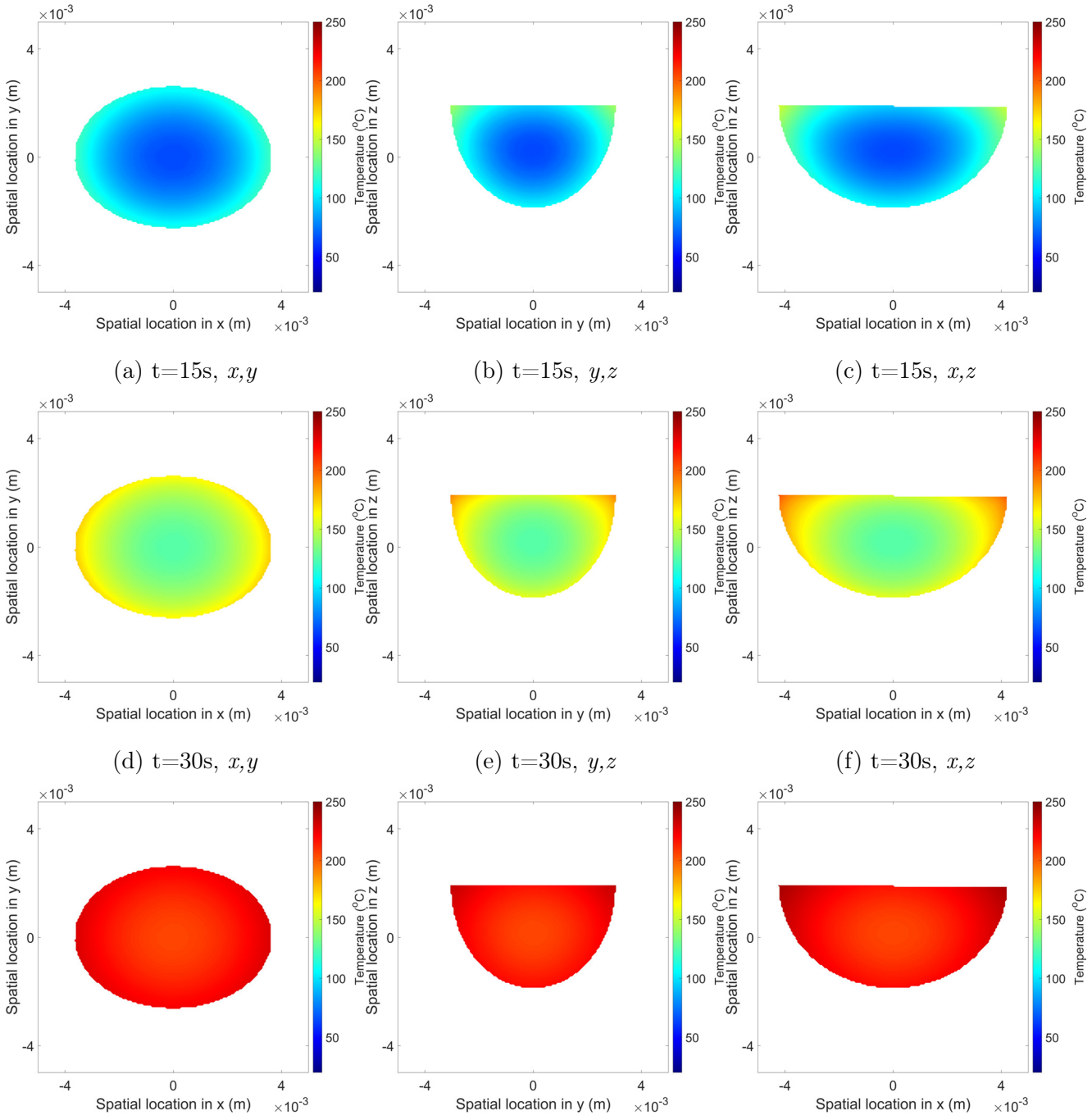

(a) t=15s, x,y (b) t=15s, y,z (c) t=15s, x,z

(d) t=30s, x,y (e) t=30s, y,z (f) t=30s, x,z

(g) t=60s, x,y (h) t=60s, y,z (i) t=60s, x,z

Figure 7.39: Predicted in-bean temperature distributions in the plane (a),(d),(g) x,y, (b),(e),(h) y,z and (c),(f),(i) x,z at simulated roasting times of (a)-(c) 15 s, (d)-(f) 30 s and (g)-(i) 60 s for hemi-ellipsoidal geometry - data corresponds to roasting conditions of 350g, 280°C & 48 Hz.

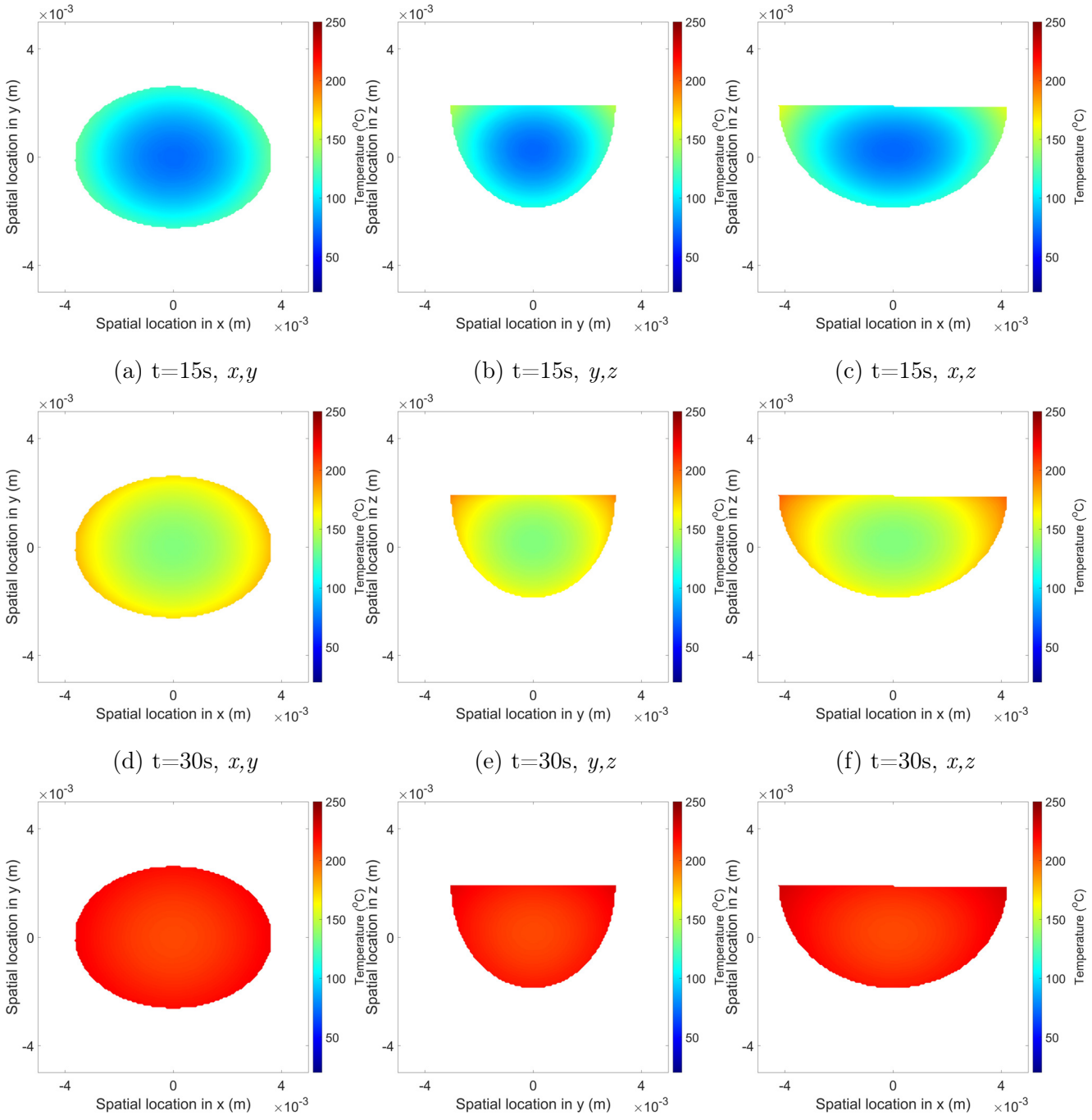

(a) t=15s, x,y (b) t=15s, y,z (c) t=15s, x,z

(d) t=30s, x,y (e) t=30s, y,z (f) t=30s, x,z

(g) t=60s, x,y (h) t=60s, y,z (i) t=60s, x,z

Figure 7.40: Predicted in-bean temperature distributions in the plane (a),(d),(g) x,y, (b),(e),(h) y,z and (c),(f),(i) x,z at simulated roasting times of (a)-(c) 15 s, (d)-(f) 30 s and (g)-(i) 60 s for hemi-ellipsoidal geometry - data corresponds to roasting conditions of 200g, 250°C & 48 Hz.

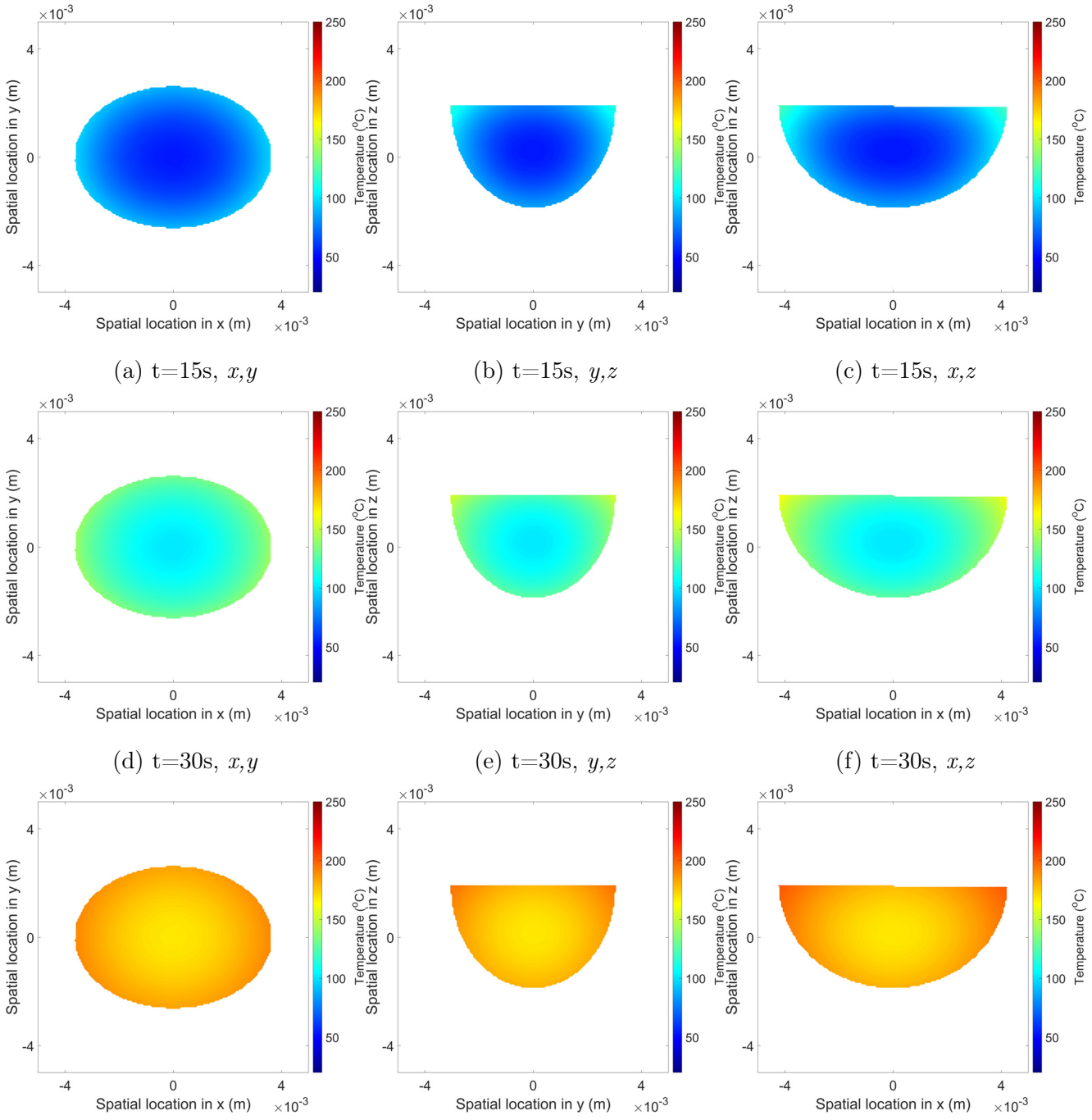

(a) t=15s, x,y (b) t=15s, y,z (c) t=15s, x,z

(d) t=30s, x,y (e) t=30s, y,z (f) t=30s, x,z

(g) t=60s, x,y (h) t=60s, y,z (i) t=60s, x,z

Figure 7.41: Predicted in-bean temperature distributions in the plane (a),(d),(g) x,y, (b),(e),(h) y,z and (c),(f),(i) x,z at simulated roasting times of (a)-(c) 15 s, (d)-(f) 30 s and (g)-(i) 60 s for hemi-ellipsoidal geometry - data corresponds to roasting conditions of 350g, 250°C & 48 Hz.

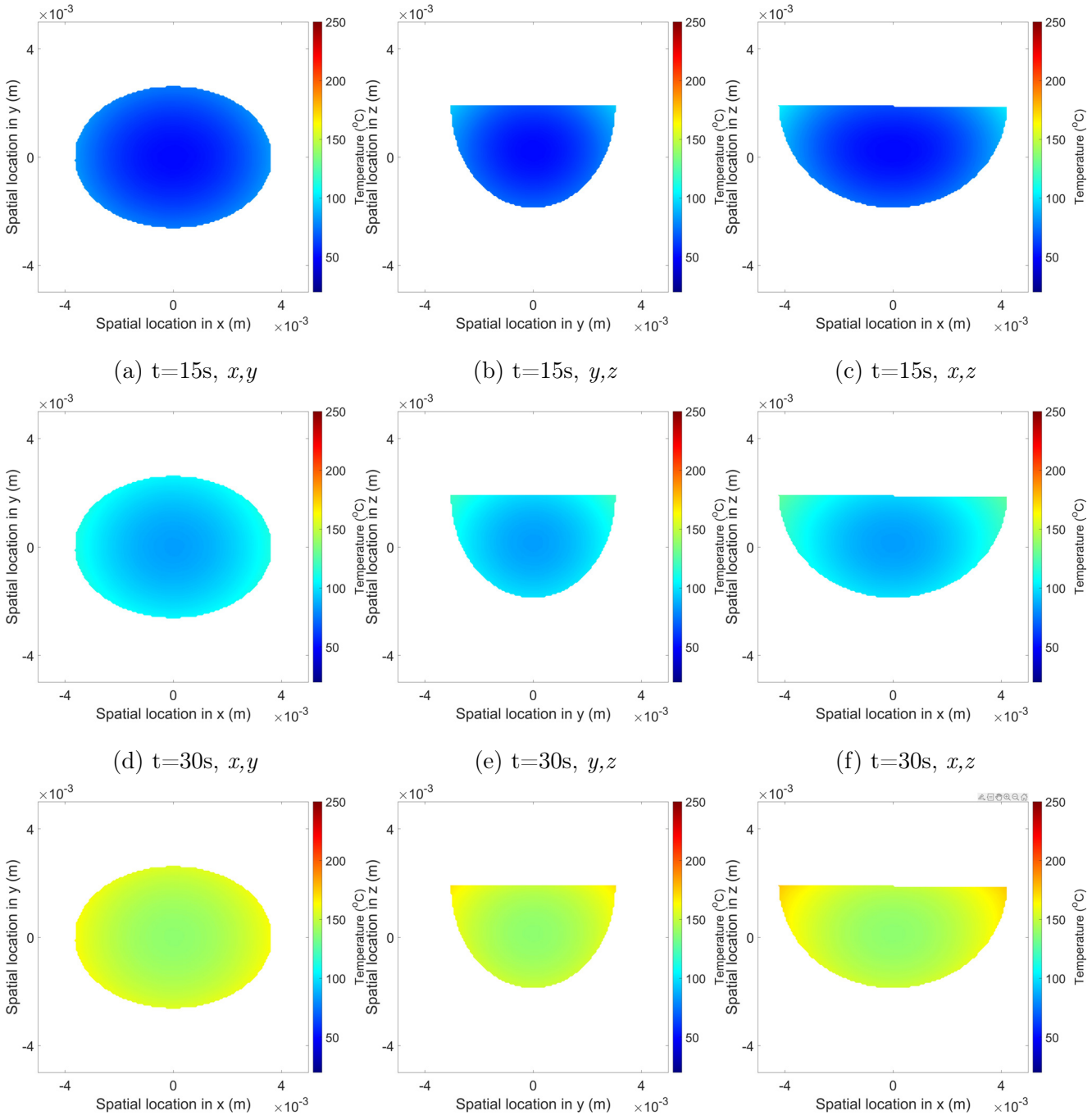

(a) t=15s, x,y (b) t=15s, y,z (c) t=15s, x,z

(d) t=30s, x,y (e) t=30s, y,z (f) t=30s, x,z

(g) t=60s, x,y (h) t=60s, y,z (i) t=60s, x,z

Figure 7.42: Predicted in-bean temperature distributions in the plane (a),(d),(g) x,y, (b),(e),(h) y,z and (c),(f),(i) x,z at simulated roasting times of (a)-(c) 15 s, (d)-(f) 30 s and (g)-(i) 60 s for hemi-ellipsoidal geometry - data corresponds to roasting conditions of 500g, 250°C & 48 Hz.

Chapter Eight

Conclusions, outlook & future work

This thesis provides an engineer's perspective on coffee roasting, wherein each Chapter sequentially considers the framework to develop digital models of a coffee roaster. Through virtualisation of the process and rigorous calibration using an experimentally derived data-driven approach, the transient behaviour of coffee during roasting was mapped using various techniques new to the coffee industry. Each Chapter contributes to the fundamental understanding of the engineering and science behind coffee roasting and provides readers with comprehensive, novel data that can be used to make informed decisions and to calibrate or validate their simulations.

8.1 Conclusions

8.1.1 Characterisation of a coffee roaster

For cross-comparison of roasters, process parameters and their effect on process conditions must be defined. As the use of arbitrary values and thermal application strategies are typical across the industry, this chapter detailed methods that convert arbitrary setpoints to SI units, such that process conditions can be compared across roaster design and scale and parameter values could be used for model calibration. The chapter also established feasible operating conditions (i.e., the appropriate bounds of relevant process parameters) that were used as scoping experiments to inform the subsequent roasting studies. The impact of thermocouple diameter on temperature measurement was probed using first-principle and experimental

approaches that later inform the accuracy of thermocouple measurements in roasting and implications during simulation of time-temperature profiles.

8.1.2 Coffee's physicochemical transformation during roasting

Kinetic studies of coffee's physicochemical transformation are comprehensively outlined in this Chapter, wherein the impact of diverse process conditions on coffee's transformation are established using a variety of novel measurement techniques. These data were core to the calibration of the digital model. The two case studies in this Chapter outlined the effect of (i) different constant inlet air temperatures and (ii) different batch size and airflow combinations on the rate of coffee's physicochemical development. Variation of constant inlet air temperature had a dominant effect on coffee's transformation rate, whereas batch size and airflow largely influenced energy consumption, batch homogeneity and temperature measurement. The novel use of MicroCT to characterise coffee's porous development during roasting revealed that the evolution of porosity corresponds with moisture loss and likely corresponds to glass transition phenomena. The effect of thermocouple diameter on temperature measurement identified in Chapter 2 was confirmed, with distinct temperature profiles generated for the same process conditions.

8.1.3 Coffee bean particle motion in pilot-scale roasters measured using Positron Emission Particle Tracking (PEPT)

The particle motion of coffee beans in two different roaster designs was studied using Positron Emission Particle Tracking (PEPT), wherein the real particle trajectories of coffees traversing a spouted bed and a rotating drum roaster were mapped. The studies revealed that coffee's particle motion depends on both the process conditions (different batch sizes and airflows) and product properties (density/volume/roast degree). The Lagrangian trajectories were converted to time-averaged Eulerian flow fields and revealed distinct, regional behaviours apparent in both roaster designs that correspond to a dense bean bed and dilute in-flight region. These regional differences in particle motion imply regional variation of heat transfer, so these data were used to instruct dynamic convective boundary conditions in the later described heat transfer simulations.

8.1.4 Modelling coffee's physicochemical transformation during roasting

The experimental studies of coffee's kinetic roasting behaviour were mapped out in Chapter 3. In this Chapter, these data were modelled using chemical reaction analogies to simplify the complex physics and chemistry driving coffee's transformation during roasting. Kinetic models of mass and moisture were robust to different process conditions and were later used as subroutines in the heat transfer simulations. Although robust models of density, volume and porosity were developed, they were not able to fully capture the real-system behaviour after first crack, implicit of a significant physical change that cannot be easily reduced to an Arrhenius-type rate equation.

8.1.5 Batch-scale simulations of heat and mass transfer during roasting

Heat transfer at the batch-scale was modelled based on an energy balance over the roaster. The zero-dimensional model was calibrated with process data from Chapter 2, product data from Chapter 3 and models developed in Chapter 5. The time-temperature profiles (and consequential physicochemical transformation) corresponding to the three case studies (I: effect of constant inlet air temperature, II: effect of batch size and airflow, II: effect of thermocouple diameter) were predicted with reasonable accuracy. The simulations capture the real-system behaviour prior to first crack, although beyond first crack, the effect of endothermic and exothermic reactions become important and the simulations deviate from reality. As was shown in Chapter 5, there is an apparent physical change that cannot easily be resolved.

8.1.6 Bean-scale simulations of heat and mass transfer during roasting

Heat transfer at the bean-scale was modelled using an energy balance over a bean. The three-dimensional, thermal model was the culmination of the thesis. Whilst the three-dimensional model was also calibrated with process data from Chapter 2, product data from Chapter 3

and models developed in Chapter 5, the bean-scale model was further calibrated using real particle motion data described in Chapter 4 and the estimated parameters from Chapter 6. The effect of different process conditions on the development of a coffee bean's internal temperature distribution was evaluated and illustrated that greater heat transfer rates correspond to a more rapid development of a uniform in-bean temperature field. Comparison of the bean-scale and batch-scale simulations exhibited reasonable agreement for both the predicted time-temperature profiles and the corresponding physicochemical transformation.

8.2 Outlook

With the appropriate instrumentation, process parameters can be monitored and used to guide product developers as they navigate the thermal-physicochemical pathways of roasting. Without relevant process feedback, developers might continue to arbitrarily change setpoints. It's therefore critical that developers equip themselves with the right tools to inform their approach. As roasteries expand and acquire roasters of different designs and scales, developers must construct a framework for translation of products to different roasters. In this way, exploring the viable operating range of each roaster and cross-comparison of certain products is a fruitful activity. In relation to modelling, data from the appropriate instrumentation can be used not only for calibration of simulations but also as input variables for their implementation in real-time control systems.

Roasting is a multi-variate problem, with each process parameter having some effect on the physicochemical transformation of coffee. It's clear that some variables have a greater impact than others. It's invaluable to learn first-hand how the relevant process parameters influence the roasting process, as each machine will react differently, depending on their mechanics and control system. Once the viable operating conditions are established, developers should minimise user inputs (i.e., maximise autonomy) to reduce process variance and hence improve product consistency. Developers should also establish a framework for exploring the flavour potential of each of their coffee offerings. In this way, exploration of different time-temperature profiles within the viable operating range ensures that the full flavour potential of a coffee is discovered whilst minimising coffee to be reworked (blended) or wasted. If developers wish to generate time-series data to calibrate physicochemical simulations, sample frequency should be focused on the stages of roasting most relevant to the studied property, although data here suggests more than 5 data points in time are required to fully capture the physical and chemical phenomena that span a roast.

This thesis demonstrated the complexity and rigour necessary to develop and calibrate the heat transfer simulations and the inter-related network of correlations and kinetic models but digital models of coffee roasters are powerful tools once calibrated. Predicted time-

temperature profiles and corresponding physicochemical development show that process parameters and product properties were determined with sufficient accuracy. Comparison of the temperature profiles resulting from the multi-scale heat transfer simulations illustrated that whilst the mean bean temperature differed between the bean-scale and batch-scale approaches, both could be used to evaluate the zero-dimensional solution. It was only with the bean-scale simulation that the spatial (i.e., three-dimensional) temperature distribution within the bean could be resolved.

Once the simulation's architecture is formulated, data structures are established and the relevant programs are developed and linked to parameter estimation protocols, validation of the models with different process conditions, different green beans and different roasters requires minimal effort. To maximise the usability of these simulations for the every-day user, human-machine graphical interfaces will be critical. Nevertheless, the simulations formulated here can be readily used by developers to accurately inform the relative effects of green coffee variability and variation of process conditions.

8.3 Future work

Time is both relative and finite. Five years of learning, development and technical investigations was sufficient to establish a new framework for coffee roasting knowledge, yet there are infinitely more studies that could be valuable to the industry. The following studies would validate and further strengthen the simulations developed here.

8.3.1 Diverse green coffees

The effect of coffee species, cultivar and post-harvest processing on coffee's roasting performance is anecdotally known. Although they were not evaluated here, determination of the intrinsic properties of more diverse green coffees via the described characterisation techniques could facilitate analysis of the simulation's sensitivity and robustness to different initial conditions. Roasting of these diverse green coffees to generate time-series data can further validate the simulations and the data can be compared with the differences observed during roasting under diverse process conditions.

8.3.2 Diverse roasting profiles

The data generated in this thesis followed a simplified roasting approach, whereby a constant inlet air temperature was used to maintain a constant thermal input to the roaster. To test the effect of different time-temperature profiles, a multi-step inlet air temperature approach should be tested to assess the current simulation's ability to predict more diverse time-temperature profiles and their corresponding physicochemical development. This study would demonstrate the simulation's applicability to commercial roasting approaches.

8.3.3 Translation across scale & roaster design

Regarding commercial implementation, the heat transfer simulations were developed for a pilot-scale spouted bed roaster. The effect of scalability and translation to different roasting designs (i.e., rotating drum or tangential roasters) should be considered. The particle motion data established for the rotating drum could be used as a starting point to translate the simulations from the spouted bed to the rotating drum roasters. As the heat transfer rates

in most commercial roasters are expected to scale sensibly according to the energy balance, the heat transfer mechanism (i.e., conductive or convective) might be difficult to quantify without assumption or measurement of the roasting chamber's temperature. These models could then be utilised to drive new product innovation and control roasters at the factory scale.

8.3.4 Complementary chemical & sensorial analyses

To improve the relevance of these simulations, determining the effect of process conditions on chemical and sensorial properties would reinforce the digital models and enable process indicators to inform the in-cup chemistry and sensory attributes. In this way, the influence of endothermic and exothermic reactions on the coffee's temperature response at first crack could be established.

8.3.5 Simulations of particle motion

A further step towards real-system accurate digital models is to use the real particle motion data to calibrate CFD-DEM simulations of particle motion that can be coupled with heat transfer equations to predict the spatial distribution of the bean bed at both the batch- and bean-scale. These PEPT-validated simulations could also be used to (i) assess *what if?* scenarios that prevent trial and error approaches, (ii) compare and make first-principle predictions of performance of roasters via both the particle dynamics and heat transfer mechanics and (iii) suggest process parameters leading to step-changes in performance according to the physical development of coffee during roasting.

References

Abdul Ghani, Nur Hamizah, Gokhan Bingol, Bing Li, Wei Yu, and Brent Young (2019). "Development of a novel 2D single coffee bean model and comparison with a 3D model under varying heating profiles". In: *Journal of Food Process Engineering* 42.4, e13063. DOI: 10.1111/JFPE.13063.

Adnan, Adnan, Dieter von Hörsten, Elke Pawelzik, Mörlein, and Daniel (2017). "Rapid Prediction of Moisture Content in Intact Green Coffee Beans Using Near Infrared Spectroscopy". In: *Foods (Basel, Switzerland)* 6.5, p. 38. DOI: 10.3390/foods6050038.

Aillio (2023). *Personal communication.*

Alessandrini, Laura, Santina Romani, Giangaetano Pinnavaia, and Marco Dalla Rosa (2008). "Near infrared spectroscopy: An analytical tool to predict coffee roasting degree". In: *Analytica Chimica Acta* 625.1, pp. 95–102. DOI: 10.1016/j.aca.2008.07.013.

Alonso-Salces, Rosa M, Francesca Serra, Fabiano Reniero, and Károly Héberger (2009). "Botanical and Geographical Characterization of Green Coffee (Coffea arabica and Coffea canephora): Chemometric Evaluation of Phenolic and Methylxanthine Contents". In: *Journal of agricultural and food chemistry* 57.10, pp. 4224–4235. DOI: 10.1021/jf8037117.

Alonso-Torres, Beatriz, José Alfredo Hernández-Pérez, Fernando Sierra-Espinoza, Stefan Schenker, and Chahan Yeretzian (2013). "Modeling and Validation of Heat and Mass Transfer in Individual Coffee Beans during the Coffee Roasting Process Using Computational Fluid Dynamics (CFD)". In: *Chimia* 67.4, pp. 291–294. DOI: 10.2533/chimia.2013.291.

Arntz, Marleen, Wouter den Otter, Wim Briels, Paul Bussmann, Hendrik Beeftink, and Remko Boom (2008). "Granular mixing and segregation in a horizontal rotating drum: A simulation study on the impact of rotational speed and fill level". In: *AIChE Journal* 54.12, pp. 3133–3146. DOI: 10.1002/AIC.11622.

Azmir, Jannatul, Qinfu Hou, and Aibing Yu (2018). "Discrete particle simulation of food grain drying in a fluidised bed". In: *Powder Technology* 323, pp. 238–249. DOI: https://doi.org/10.1016/j.powtec.2017.10.019.

Baggenstoss, Juerg (2008). "Coffee roasting and quenching technology - formation and stability of aroma compounds". en. PhD thesis. DOI: 10.3929/ethz-a-005666902.

Baggenstoss, Juerg, Luigi Poisson, Ruth Kaegi, Rainer Perren, and Felix Escher (2008a). "Coffee Roasting and Aroma Formation: Application of Different TimeTemperature Conditions". In: *Journal of agricultural and food chemistry* 56.14, pp. 5836–5846. DOI: 10.1021/jf800327j.

— (2008b). "Roasting and aroma formation: Effect of initial moisture content and steam treatment". In: *Journal of Agricultural and Food Chemistry* 56.14, pp. 5847–5851. DOI: 10.1021/JF8003288.

Beaulieu, Christine, David Vidal, Carine Niyonkuru, Anthony Wachs, Jamal Chaouki, and François Bertrand (2022). "Effect of particle angularity on flow regime transitions and segregation of bidisperse blends in a rotating drum". In: *Computational Particle Mechanics* 9.3, pp. 443–463. DOI: 10.1007/S40571-021-00421-1/FIGURES/18.

Berbert, Pedro, Daniel Queiroz, Jaurez Silva, and José Filho (1995). "Simulation of Coffee Drying in a Fixed Bed with Periodic Airflow Reversal". In: *Journal of Agricultural Engineering Research* 60.3, pp. 167–173. DOI: https://doi.org/10.1006/jaer.1995.1010.

Bergman, T L, D P DeWitt, F Incropera, and A S Lavine (2011). *Fundamentals of Heat and Mass Transfer*. Vol. 997.

Bicho, Natalina Conceicao, Antonio Eduardo Leitao, Jose Cochicho Ramalho, and Fernando Cebola Lidon (2014). "Application of colour parameters for assessing the quality of Arabica and Robusta green coffee". In: *Emirates Journal of Food and Agriculture* 26.1, p. 9. DOI: 10.9755/ejfa.v26i1.17190.

Blumm, J., A. Lindemann, B. Niedrig, and R. Campbell (2007). "Measurement of selected thermophysical properties of the NPL certified reference material stainless steel 310". In: *International Journal of Thermophysics* 28.2, pp. 674–682. DOI: 10.1007/S10765-007-0177-Z.

Bopape, Ntsitlola, Abraham van der Merwe, Johandri Vosloo, and R G Ross (2016). "Validation and Improvement of Heat and Mass Transfer Model in Prediciting the Coffee Roasting Profile". In: *International Conference on Advances in Science, Engineering, Technology and Natural Resources*. Parys, South Africa, pp. 225–232. DOI: http://doi.org/10.15242/IAE.IAE1116440.

Borém, Flávio Meira and Ednilton Tavares de Andrade (2019). "Processing and Drying of Coffee". In: *Drying and Roasting of Cocoa and Coffee*. Ed. by Ching Lik Hii and Flávio Meira Borém. 1st Edition. Boca Raton: CRC Press. Chap. 8, pp. 235–268. DOI: https://doi.org/10.1201/9781315113104.

Bottazzi, Davide, S Farina, Massimo Milani, and Luca Montorsi (2012). "A numerical approach for the analysis of the coffee roasting process". In: *Journal of Food Engineering* 112.3, pp. 243–252. DOI: 10.1016/j.jfoodeng.2012.04.009.

Brown, Steven and Brian Lattimer (2013). "Transient gas-to-particle heat transfer measurements in a spouted bed". In: *Experimental Thermal and Fluid Science* 44, pp. 883–892. DOI: https://doi.org/10.1016/j.expthermflusci.2012.10.004.

Bruchmüller, Jörn, Sai Gu, Kai Luo, and Berend Van Wachem (2010). "Discrete Element Method for Multiscale Modelling". In: *Journal of Multiscale Modelling* 02.01n02, pp. 147–162. DOI: 10.1142/S1756973710000254.

Burmester, Katrin and Rudolf Eggers (2010). "Heat and mass transfer during the coffee drying process". In: *Journal of Food Engineering* 99.4, pp. 430–436. DOI: 10.1016/j.jfoodeng.2009.12.021.

Bustos-Vanegas, Jaime, Paulo Correa, Marcio Martins, Fernanda Baptestini, Renata Campos, Gabriel Horta de Oliveira, and Eduardo Nunes (2018). "Developing predictive models for determining physical properties of coffee beans during the roasting process". In: *Industrial Crops and Products* 112, pp. 839–845.

Cao, Xiaotong, Hanjing Wu, Claudia Viejo, Frank Dunshea, and Hafiz Suleria (2023). "Effects of postharvest processing on aroma formation in roasted coffee – a review". In: *International Journal of Food Science and Technology* 58.3, pp. 1007–1027. DOI: 10.1111/IJFS.16261.

Caporaso, Nicola, Martin Whitworth, Stephen Grebby, and Ian Fisk (2018). "Non-destructive analysis of sucrose, caffeine and trigonelline on single green coffee beans by hyperspectral imaging". In: *Food Research International* 106, pp. 193–203. DOI: 10.1016/j.foodres.2017.12.031.

Carbon, M, H Kutsch, and G Hawkins (1950). "The Response of Thermocouples to Rapid Gas-Temperature Changes". In: *Journal of Fluids Engineering* 72.5, pp. 655–657. DOI: 10.1115/1.4016788.

Cardoso, Danilo Barbosa, Ednilton Tavares de Andrade, Renso Alfredo Aragón Calderón, Mariane Helena Sanches Rabelo, Camila de Almeida Dias, and Isabela Ávila Lemos (2018). "Determination of thermal properties of coffee beans at different degrees of roasting". In: *Coffee Science; Vol 13, No 4 (2018)*.

Carroll, R and R Shepard (1977). "Measurement of the transient response of thermocouples and resistance thermometers using an in situ method". In: DOI: 10.2172/7221079.

Casal, Susana, Rui Alves, Eulália Mendes, Beatriz Oliveira, and Margarida Ferreira (2003). "Discrimination between Arabica and Robusta Coffee Species on the Basis of Their Amino Acid Enantiomers". In: *Journal of agricultural and food chemistry* 51.22, pp. 6495–6501. DOI: 10.1021/jf034354w.

Çengel, Yunus A., Michael A. Boles, and Mehmet Kanoğlu (2002). "Thermodynamics : an engineering approach". In: p. 948.

Che, Hanqiao, Mark Al-Shemmeri, Peter J. Fryer, Estefania Lopez-Quiroga, Tzany Kokalova Wheldon, and Kit Windows-Yule (2023). "PEPT validated CFD-DEM model of aspherical particle motion in a spouted bed". In: *Chemical Engineering Journal* 453, p. 139689. DOI: 10.1016/J.CEJ.2022.139689.

Cheng, Guojian, Jieqing Gan, Delong Xu, and Aibing Yu (2020). "Evaluation of effective thermal conductivity in random packed bed: Heat transfer through fluid voids and effect

of packing structure". In: *Powder Technology* 361, pp. 326–336. DOI: https://doi.org/10.1016/j.powtec.2019.07.106.

Chiang, Chao Ching, Dai Yuan Wu, and Dun Yen Kang (2017). "Detailed Simulation of Fluid Dynamics and Heat Transfer in Coffee Bean Roaster". In: *Journal of Food Process Engineering* 40.2, e12398. DOI: 10.1111/JFPE.12398.

Chindapan, Nathamol, Supatcha Soydok, and Sakamon Devahastin (2019). "Roasting Kinetics and Chemical Composition Changes of Robusta Coffee Beans During Hot Air and Superheated Steam Roasting". In: *Journal of Food Science* 84.2, pp. 292–302. DOI: 10.1111/1750-3841.14422.

Chu, Bingquan, Keqiang Yu, Yanru Zhao, and Yong He (2018). "Development of Noninvasive Classification Methods for Different Roasting Degrees of Coffee Beans Using Hyperspectral Imaging". In: *Sensors (Basel, Switzerland)* 18.4, p. 1259. DOI: 10.3390/s18041259.

Clarke, R J and O G Vitzthum (2001). "Coffee: recent developments". English. In.

Corradini, Maria G. and Micha Peleg (2006a). "Linear and non-linear kinetics in the synthesis and degradation of acrylamide in foods and model systems". In: *Critical Reviews in Food Science and Nutrition* 46.6, pp. 489–517. DOI: 10.1080/10408390600758280.

— (2006b). "Prediction of vitamins loss during non-isothermal heat processes and storage with non-linear kinetic models". In: *Trends in Food Science & Technology* 17.1, pp. 24–34. DOI: 10.1016/J.TIFS.2005.09.004.

Cortés-Macías, Erika Tatiana, Cristina Fuentes López, Piergiorgio Gentile, Joel Girón-Hernández, and Ana Fuentes López (2022). "Impact of post-harvest treatments on physicochemical and sensory characteristics of coffee beans in Huila, Colombia". In: *Postharvest Biology and Technology* 187, p. 111852. DOI: 10.1016/j.postharvbio.2022.111852.

Cristo, Helder P, Márcio A Martins, Leandro S Oliveira, and Adriana S Franca (2006). "Transverse flow of coffee beans in rotating roasters". In: *Journal of Food Engineering* 75.1, pp. 142–148. DOI: 10.1016/j.jfoodeng.2005.04.010.

De Vleeschouwer, Kristel, Iesel Van der Plancken, Ann Van Loey, and Marc E Hendrickx (2010). "The Effect of High PressureHigh Temperature Processing Conditions on Acrylamide Formation and Other Maillard Reaction Compounds". In: *Journal of agricultural and food chemistry* 58.22, pp. 11740–11748. DOI: 10.1021/jf102697b.

Díaz-Heras, M., J. F. Belmonte, and J. A. Almendros-Ibáñez (2020). "Effective thermal conductivities in packed beds: Review of correlations and its influence on system performance". In: *Applied Thermal Engineering* 171, p. 115048. DOI: 10.1016/J.APPLTHERMALENG.2020.115048.

Ding, Y. L., R. Forster, J. P.K. Seville, and D. J. Parker (2002). "Segregation of granular flow in the transverse plane of a rolling mode rotating drum". In: *International Journal of Multiphase Flow* 28.4, pp. 635–663. DOI: 10.1016/S0301-9322(01)00081-7.

Dong, Wenjiang, Lehe Tan, Jianping Zhao, Rongsuo Hu, and Minquan Lu (2015). "Characterization of Fatty Acid, Amino Acid and Volatile Compound Compositions and Bioactive Components of Seven Coffee (Coffea robusta) Cultivars Grown in Hainan Province, China". In: *Molecules* 20.9, pp. 16687–16708. DOI: 10.3390/molecules200916687.

Dutra, E R, L S Oliveira, A S Franca, V P Ferraz, and R J C F Afonso (2001). "A preliminary study on the feasibility of using the composition of coffee roasting exhaust gas for the determination of the degree of roast". In: *Journal of Food Engineering* 47.3, pp. 241–246. DOI: 10.1016/S0260-8774(00)00116-3.

Eggers, R (2001). "Heat and mass transfer during roasting - new process developments". In: *19th International Scientific Colloquium on Coffee*. Association for science and information on coffee.

Eggers, R and A Pietsch (2008). "Technology I: Roasting". English. In: pp. 90–107.

Eggers, R, M Von Blittersdorf, C Fischer, and H Cammenga (2004). "Temperature Field during Roasting and Cooling of Coffee Beans". In: Conference Proceedings. ASIC.

Engineering-ToolBox (2020). *Resources, Tools and Basic Information for Engineering and Design of Technical Applications*.

Esteban-Díez, I, J M González-Sáiz, and C Pizarro (2004). "Prediction of Roasting Colour and other Quality Parameters of Roasted Coffee Samples by near Infrared Spectroscopy. A Feasibility Study". In: *Journal of Near Infrared Spectroscopy* 12.5, pp. 287–297. DOI: 10.1255/jnirs.437.

Fabbri, Angelo, Chiara Cevoli, Laura Alessandrini, and Santina Romani (2011). "Numerical modeling of heat and mass transfer during coffee roasting process". In: *Journal of Food Engineering* 105.2, pp. 264–269. DOI: 10.1016/j.jfoodeng.2011.02.030.

Fabbri, Angelo, Chiara Cevoli, Santina Romani, and Marco Dalla Rosa (2011). "Numerical model of heat and mass transfer during roasting coffee using 3D digitised geometry". In: *Procedia Food Science* 1, pp. 742–746. DOI: 10.1016/j.profoo.2011.09.112.

Fadai, Nabil T, John Melrose, Colin P Please, Alexandra Schulman, and Robert A Van Gorder (2017). "A heat and mass transfer study of coffee bean roasting". In: *International Journal of Heat and Mass Transfer* 104, pp. 787–799. DOI: 10.1016/j.ijheatmasstransfer.2016.08.083.

Farah, Adriana (2019). *Coffee*. Book, Whole. London: Royal society of chemistry.

Fernandes, Fernando (2019). "CHAPTER 8 Roasting". In: *Coffee: Production, Quality and Chemistry*. The Royal Society of Chemistry, pp. 230–257. DOI: 10.1039/9781782622437-00230.

Fiore, A G, C Severini, R Romaniello, and G Peri (2006). "Study of Physical Properties of Coffee Beans during Roasting. Application of Hyperspectral Image Analysis". In: Conference Proceedings. Unpublished. DOI: 10.13140/2.1.1070.4005.

Fischer, Monica, Silvia Reimann, Véronique Trovato, and Robert J Redgwell (2001). "Polysaccharides of green Arabica and Robusta coffee beans". In: *Carbohydrate Research* 330.1, pp. 93–101. DOI: 10.1016/S0008-6215(00)00272-X.

Franca, Adriana S, Leandro S Oliveira, Rafael C S Oliveira, Pamela C Mancha Agresti, and Rodinei Augusti (2009). "A preliminary evaluation of the effect of processing temperature on coffee roasting degree assessment". In: *Journal of Food Engineering* 92.3, pp. 345–352. DOI: 10.1016/j.jfoodeng.2008.12.012.

Frisullo, P, M Barnabà, L Navarini, and M A Del Nobile (2012). "Coffea arabica beans microstructural changes induced by roasting: An X-ray microtomographic investigation". In: *Journal of Food Engineering* 108.1, pp. 232–237. DOI: 10.1016/j.jfoodeng.2011.07.036.

Froessling, Nils (1968). *The Evaporation of Falling Drops*. Vol. 52, p. 37.

Garcia, Cinthia Da Conceição et al. (2018). "Relative importance and interaction of roasting variables in coffee roasting process". In: *Coffee Science* 13.3, p. 379. DOI: 10.25186/cs.v13i3.1483.

Garrett, Rafael, Boniek G Vaz, Ana Maria C Hovell, Marcos N Eberlin, and Claudia M Rezende (2012). "Arabica and Robusta Coffees: Identification of Major Polar Com-

pounds and Quantification of Blends by Direct-Infusion Electrospray Ionization–Mass Spectrometry". In: *Journal of agricultural and food chemistry* 60.17, pp. 4253–4258. DOI: 10.1021/jf300388m.

Geiger, Raphael (2004). "Development of coffee bean structure during roasting – Investigations on resistance and driving forces". en. PhD thesis. DOI: 10.3929/ethz-a-004717409.

Geiger, Raphael, Rainer Perren, Roland Kuenzli, and Felix Escher (2005). "Carbon Dioxide Evolution and Moisture Evaporation During Roasting of Coffee Beans". In: *Journal of Food Science* 70.2, E130. DOI: 10.1111/j.1365-2621.2005.tb07084.x.

Geiger, Raphael, Rainer Perren, Stefan Schenker, and Felix Escher (2001). "Mechanism of Volume Expansion in Coffee Beans During Roasting". In: Conference Proceedings. ASIC.

Giacalone, Davide, Tina Kreuzfeldt Degn, Ni Yang, Chujiao Liu, Ian Fisk, and Morten Münchow (2019). "Common roasting defects in coffee: Aroma composition, sensory characterization and consumer perception". In: *Food Quality and Preference* 71, pp. 463–474. DOI: 10.1016/J.FOODQUAL.2018.03.009.

Gilchrist, Alan L (2007). "Lightness and brightness". In: *Current Biology* 17.8, R267–R269. DOI: 10.1016/j.cub.2007.01.040.

González, S., C. R.K. Windows-Yule, S. Luding, D. J. Parker, and A. R. Thornton (2015). "Forced axial segregation in axially inhomogeneous rotating systems". In: *Physical Review E - Statistical, Nonlinear, and Soft Matter Physics* 92.2, p. 022202. DOI: 10.1103/PHYSREVE.92.022202/FIGURES/7/MEDIUM.

Govender, Indresan (2016). "Granular flows in rotating drums: A rheological perspective". In: *Minerals Engineering* 92, pp. 168–175. DOI: 10.1016/J.MINENG.2016.03.021.

Green Coffee Collective (2023). *Green Coffee Collective*.

Haile, Mesfin, Won Hee Kang, Mesfin Haile, and Won Hee Kang (2019). "The Harvest and Post-Harvest Management Practices' Impact on Coffee Quality". In: *Coffee - Production and Research*. DOI: 10.5772/INTECHOPEN.89224.

Hammerschmidt, Ulf and Muhammad Abid (2016). "Thermophysical properties of a single coffee bean, a single peanut and an IC-Package". In: *International Journal of Thermal Sciences* 100, pp. 20–28. DOI: 10.1016/j.ijthermalsci.2015.09.009.

Henein, H., J. K. Brimacombe, and A. P. Watkinson (1983). "Experimental study of transverse bed motion in rotary kilns". In: *Metallurgical Transactions B* 14.2, pp. 191–205. DOI: 10.1007/BF02661016/METRICS.

Herald, Matthew, Tzany Wheldon, and Christopher Windows-Yule (2021). "Monte Carlo model validation of a detector system used for Positron Emission Particle Tracking". In: *Nuclear Instruments and Methods in Physics Research, Section A: Accelerators, Spectrometers, Detectors and Associated Equipment* 993. DOI: 10.1016/J.NIMA.2021.165073.

Hernández, J A, B Heyd, C Irles, B Valdovinos, and G Trystram (2007). "Analysis of the heat and mass transfer during coffee batch roasting". In: *Journal of Food Engineering* 78.4, pp. 1141–1148. DOI: 10.1016/j.jfoodeng.2005.12.041.

Hernández, J A, B Heyd, and G Trystram (2008). "Prediction of brightness and surface area kinetics during coffee roasting". In: *Journal of Food Engineering* 89, pp. 156–163. DOI: doi:10.1016/j.jfoodeng.2008.04.026.

Hernández Pérez, José Alfredo (2002). "Modelling and determining coffee roasting quality on line". PhD thesis.

Hernández-Díaz, W N, I I Ruiz-López, M A Salgado-Cervantes, G C Rodríguez-Jimenes, and M A García-Alvarado (2008). "Modeling heat and mass transfer during drying of green coffee beans using prolate spheroidal geometry". In: *Journal of Food Engineering* 86.1, pp. 1–9. DOI: 10.1016/j.jfoodeng.2007.08.025.

Herrera, Juan Carlos and Charles Lambot (2017). "Chapter 1 - The Coffee Tree—Genetic Diversity and Origin". In: *The Craft and Science of Coffee*. Ed. by Britta Folmer. Academic Press, pp. 1–16. DOI: https://doi.org/10.1016/B978-0-12-803520-7.00001-3.

Heyd, B, B Broyart, J A Hernandez, B Valdovinos-Tijerino, and G Trystram (2007). "Physical Model of Heat and Mass Transfer in a Spouted Bed Coffee Roaster". In: *Drying Technology* 25.7-8, pp. 1243–1248. DOI: 10.1080/07373930701438683.

Hobbie, M and R Eggers (2001). "The Influence of Endothermic and Exothermic Energies on the Temperature Field of Coffee Beans during the Roasting process". In: *19th International Scientific Colloquium on Coffee*. Trieste, Italy.

Hoos, Rob (2015). *Modulating the Flavour Profile of Coffee*. Book, Whole.

Huamaní-Meléndez, Víctor J and Roger Darros-Barbosa (2018). "Diffusion of water and caffeine in coffee beans using the hemispherical geometry approach". In: *Journal of Food Process Engineering* 41.6, n/a. DOI: 10.1111/jfpe.12809.

ICO (2023). *Coffee production by exporting countries*.

Ingram, A., J. P.K. Seville, D. J. Parker, X. Fan, and R. G. Forster (2005). "Axial and radial dispersion in rolling mode rotating drums". In: *Powder Technology* 158.1-3, pp. 76–91. DOI: 10.1016/J.POWTEC.2005.04.030.

Jones, C R, A Corona, C Amador, and P J Fryer (2021). "Drying Technology Dynamics of fabric and dryer sheet motion in domestic clothes dryers Dynamics of fabric and dryer sheet motion in domestic clothes dryers". In: DOI: 10.1080/07373937.2021.1918706.

Juarez, Gabriel, Pengfei Chen, and Richard M. Lueptow (2011). "Transition to centrifuging granular flow in rotating tumblers: a modified Froude number". In: *New Journal of Physics* 13.5, p. 053055. DOI: 10.1088/1367-2630/13/5/053055.

Kar, Kenneth, Stephen Roberts, Richard Stone, Martin Oldfield, and Boyd French (2004). "Instantaneous Exhaust Temperature Measurements Using Thermocouple Compensation Techniques". In: *SAE Technical Papers*. DOI: 10.4271/2004-01-1418.

Kikic, I and M Basile (2009). *A Lumped Specific Heat Capacity Approach for Predicting the Non-stationary Thermal Profile of Coffee During Roasting*. Tech. rep. Report, p. 167.

Kim, Su-Yeon, Jung- A Ko, Bo-Sik Kang, and Hyun-Jin Park (2018). "Prediction of key aroma development in coffees roasted to different degrees by colorimetric sensor array". In: *Food Chemistry* 240, pp. 808–816. DOI: 10.1016/j.foodchem.2017.07.139.

Kwak, Han Sub, Seokgeun Ji, and Yoonhwa Jeong (2017). "The effect of air flow in coffee roasting for antioxidant activity and total polyphenol content". In: *Food Control* 71, pp. 210–216. DOI: 10.1016/J.FOODCONT.2016.06.047.

Ky, C L, J Louarn, S Dussert, B Guyot, S Hamon, and M Noirot (2001). "Caffeine, trigonelline, chlorogenic acids and sucrose diversity in wild Coffea arabica L. and C. canephora P. accessions". In: *Food Chemistry* 75.2, pp. 223–230. DOI: 10.1016/S0308-8146(01)00204-7.

Lechler, Tobias, Jonathan Fuchs, Martin Sjarov, Matthias Brossog, Andreas Selmaier, Florian Faltus, Toni Donhauser, and Jörg Franke (2020). "Introduction of a comprehensive Structure Model for the Digital Twin in Manufacturing". In: *IEEE International*

Conference on Emerging Technologies and Factory Automation, ETFA 2020-September, pp. 1773–1780. DOI: 10.1109/ETFA46521.2020.9212030.

Lee, Liang Wei, Mun Wai Cheong, Philip Curran, Bin Yu, and Shao Quan Liu (2015). "Coffee fermentation and flavor – An intricate and delicate relationship". In: *Food Chemistry* 185, pp. 182–191. DOI: 10.1016/J.FOODCHEM.2015.03.124.

Levenspiel, Octave (1999). "Chemical reaction engineering". In: *Industrial & Engineering Chemistry Research* 38.11, pp. 4140–4143. DOI: 10.1021/IE990488G.

Lim, S. Y., J. F. Davidson, R. N. Forster, D. J. Parker, D. M. Scott, and J. P.K. Seville (2003). "Avalanching of granular material in a horizontal slowly rotating cylinder: PEPT studies". In: *Powder Technology* 138.1, pp. 25–30. DOI: 10.1016/J.POWTEC.2003.08.038.

Louzada Pereira, Lucas and Taís Rizzo Moreira (2021). "Quality Determinants In Coffee Production". In.

Ma, Huaqing, Lianyong Zhou, Zihan Liu, Mengyao Chen, Xiuhao Xia, and Yongzhi Zhao (2022). "A review of recent development for the CFD-DEM investigations of non-spherical particles". In: *Powder Technology* 412, p. 117972. DOI: 10.1016/J.POWTEC.2022.117972.

Machado, M.V.C., I.A. Resende, R.M. Lima, R.J. Brandão, M.R. Pivello, S.M. Nascimento, C.R. Duarte, and Marcos A.S. Barrozo (2018). "The role of boundary conditions on the dynamics of green coffee beans in a rotated dryer". In: *21st International Drying Symposium*, pp. 11–14. DOI: 10.4995/ids2018.2018.7455.

Majdak, Marek and Magdalena Jaremkiewicz (2016). "The analysis of thermocouple time constants as a function of fluid velocity". In: *Measurement Automation Monitoring* 62.9.

Mellmann, J. (2001). "The transverse motion of solids in rotating cylinders—forms of motion and transition behavior". In: *Powder Technology* 118.3, pp. 251–270. DOI: 10.1016/S0032-5910(00)00402-2.

Melo Pereira, G V de, D P de Carvalho Neto, A I Magalhaes Junior, Z S Vasquez, A B P Medeiros, L P S Vandenberghe, and C R Soccol (2019). "Exploring the impacts of postharvest processing on the aroma formation of coffee beans - A review". In: *Food Chem* 272, pp. 441–452. DOI: 10.1016/j.foodchem.2018.08.061.

Mendes, Luciane C, Hilary C de Menezes, M Aparecida, and A P da Silva (2001). "Optimization of the roasting of robusta coffee (C. canephora conillon) using acceptability

tests and RSM". In: *Food Quality and Preference* 12.2, pp. 153–162. DOI: 10.1016/S0950-3293(00)00042-2.

Morrison, A. J., I. Govender, A. N. Mainza, and D. J. Parker (2016). "The shape and behaviour of a granular bed in a rotating drum using Eulerian flow fields obtained from PEPT". In: *Chemical Engineering Science* 152, pp. 186–198. DOI: 10.1016/J.CES.2016.06.022.

Münchow, Morten, Jesper Alstrup, Ida Steen, and Davide Giacalone (2020). "Roasting Conditions and Coffee Flavor: A Multi-Study Empirical Investigation". In: *Beverages 2020, Vol. 6, Page 29* 6.2, p. 29. DOI: 10.3390/BEVERAGES6020029.

Nagaraju, V D, C T Murthy, K Ramalakshmi, and P N Srinivasa Rao (1997). "Studies on roasting of coffee beans in a spouted bed". In: *Journal of Food Engineering* 31.2, pp. 263–270. DOI: 10.1016/S0260-8774(96)00026-X.

Ngoensod, A., N. Nunak, and I. T.Suesut (2017). "Detection of Foreign Bodies in Roasted Coffee by using Active Thermography". In.

Nicuşan, A and C Windows-Yule (2020). "Positron emission particle tracking using machine learning". In: *Review of Scientific Instruments* 91.1. DOI: 10.1063/1.5129251/1020252.

Olam Speciality (2023). *Coffee Processing Methods*.

Oliveira, Gabriel Henrique Horta de, Paulo Cesar Corrêa, Ana Paula Lelis Rodrigues de Oliveira, Fernanda Machado Baptestini, and Guillermo Asdrúbal Vargas-Elías (2017). "Roasting, Grinding, and Storage Impact on Thermodynamic Properties and Adsorption Isotherms of Arabica Coffee". In: *Journal of Food Processing and Preservation* 41.2, n/a. DOI: 10.1111/jfpp.12779.

Oliveira, Luís, Damien Hudebine, D Guillaume, and Jan Verstraete (2016). "A Review of Kinetic Modeling Methodologies for Complex Processes". In: *Oil & Gas Science and Technology* 71, p. 45. DOI: 10.2516/ogst/2016011.

Oliveira, Pedro Damasceno de, Marco Antônio Martin Biaggioni, Flávio Meira Borém, Eder Pedroza Isquierdo, and Mariana de Oliveira Vaz Damasceno (2018). "Quality of natural and pulped coffee as a function of temperatures changes during mechanical drying". In: *Coffee Science - ISSN 1984-3909* 13.4, pp. 415–425.

Oliveros, Nadia O, J A Hernández, F Z Sierra-Espinosa, R Guardián-Tapia, and R Pliego-Solórzano (2017). "Experimental study of dynamic porosity and its effects on simulation of the coffee beans roasting". In: *Journal of Food Engineering* 199, pp. 100–112. DOI: 10.1016/j.jfoodeng.2016.12.012.

Otsu, Nobuyuki (1979). "Threshold selection method from gray-level histograms." In: *IEEE Trans Syst Man Cybern* SMC-9.1, pp. 62–66. DOI: 10.1109/TSMC.1979.4310076.

Palma, Federico Di, Francesca Iacono, Chiara Toffanin, Andrea Ziccardi, and Lalo Magni (2021). "Scalable model for industrial coffee roasting chamber". In: *Procedia Computer Science* 180, pp. 122–131. DOI: 10.1016/J.PROCS.2021.01.362.

Papaioannou, Nick, Felix Leach, and Martin Davy (2018). "Effect of Thermocouple Size on the Measurement of Exhaust Gas Temperature in Internal Combustion Engines". In: *SAE Technical Papers* 2018-September. DOI: 10.4271/2018-01-1765.

Parker, D J (2017). "Positron emission particle tracking and its application to granular media". In: *Review of Scientific Instruments* 88.5. DOI: 10.1063/1.4983046.

Parker, D J, C J Broadbent, P Fowles, M R Hawkesworth, and P McNeil (1993). "Positron emission particle tracking-a technique for studying flow within engineering equipment". In: *Nuclear Instruments and Methods in Physics Research Section A: Accelerators, Spectrometers, Detectors and Associated Equipment* 326.3, pp. 592–607.

Parker, D. J., R. N. Forster, P. Fowles, P. S. Takhar, D. J. Parker, R. N. Forster, P. Fowles, and P. S. Takhar (2002). "Positron emission particle tracking using the new Birmingham positron camera". In: *NIMPA* 477.1-3, pp. 540–545. DOI: 10.1016/S0168-9002(01)01919-2.

Pathmathas, Thirunavukkarasu (2015). "Granular flow modelling of rotating drum flows using positron emission particle tracking". In.

Peleg, Micha, Mark D. Normand, and Maria G. Corradini (2012). "The Arrhenius equation revisited." In: *Critical reviews in food science and nutrition* 52.9, pp. 830–851. DOI: 10.1080/10408398.2012.667460.

Pereira, Lucas Louzada, Dério Brioschi Júnior, Luiz Henrique Bozzi Pimenta de Sousa, Willian dos Santos Gomes, Wilton Soares Cardoso, Rogério Carvalho Guarçoni, and Carla Schwengber ten Caten (2021). "Relationship Between Coffee Processing and Fer-

mentation". In: *Food Engineering Series*, pp. 255–301. DOI: 10.1007/978-3-030-54437-9{_}6.

Perrone, Daniel, Raul Donangelo, Carmen M Donangelo, and Adriana Farah (2010). "Modeling Weight Loss and Chlorogenic Acids Content in Coffee during Roasting". In: *Journal of agricultural and food chemistry* 58.23, pp. 12238–12243. DOI: 10.1021/jf102110u.

Pittia, Paola, Marco Dalla Rosa, and Carlo Lerici (2001). "Textural Changes of Coffee Beans as Affected by Roasting Conditions". In: *LWT Food Science and Technology* 34.3, pp. 168–175. DOI: 10.1006/fstl.2000.0749.

Pittia, Paola, Maria Cristina Nicoli, and Giampiero Sacchetti (2007). "Effect of Moisture and Water Activity on Textural Properties of Raw and Roasting Coffee Beans". In: *Journal of Texture Studies* 38.1, pp. 116–134. DOI: 10.1111/j.1745-4603.2007.00089.x.

Pittia, Paola, Giampiero Sacchetti, Lucia Mancini, Marco Voltolini, Nicola Sodini, Giuliana Tromba, and Franco Zanini (2011). "Evaluation of Microstructural Properties of Coffee Beans by Synchrotron X-Ray Microtomography: A Methodological Approach". In: *Journal of Food Science* 76.2, E231. DOI: 10.1111/j.1750-3841.2010.02009.x.

Pizarro, Consuelo, Isabel Esteban-Díez, José-María González-Sáiz, and Michele Forina (2007). "Use of Near-Infrared Spectroscopy and Feature Selection Techniques for Predicting the Caffeine Content and Roasting Color in Roasted Coffees". In: *Journal of agricultural and food chemistry* 55.18, pp. 7477–7488. DOI: 10.1021/jf071139x.

Poisson, Luigi, Imre Blank, Andreas Dunkel, and Thomas Hofmann (2017). "Chapter 12 - The Chemistry of Roasting—Decoding Flavor Formation". In: *The Craft and Science of Coffee*. Ed. by Britta Folmer. Academic Press, pp. 273–309. DOI: https://doi.org/10.1016/B978-0-12-803520-7.00012-8.

Poisson, Luigi, Frank Schmalzried, Tomas Davidek, Imre Blank, and Josef Kerler (2009). "Study on the role of precursors in coffee flavor formation using in-bean experiments". In: *Journal of Agricultural and Food Chemistry* 57.21, pp. 9923–9931. DOI: 10.1021/JF901683V.

Pramudita, D, T Araki, Y Sagara, and A H Tambunan (2017). "Roasting and Colouring Curves for Coffee Beans with Broad Time-Temperature Variations". In: *Food and Bioprocess Technology* 10.8, pp. 1509–1520. DOI: 10.1007/s11947-017-1912-5.

Probat (2019a). *Jupiter Tangential Roaster*.

— (2019b). *Neptune Drum Roaster*.

— (2019c). *Saturn Centrifugal Roaster*.

Putra, Satya Andika, Umi Hanifah, and Mirwan Ardiansyah Karim (2019). "Theoretical study of fluidization and heat transfer on fluidized bed coffee roaster". In: *AIP Conference Proceedings* 2097.1, p. 30112. DOI: 10.1063/1.5098287.

Ram, A. S., M. S. Sreenivasan, and P. K. Ramaiah (1990). "A study of peaberry development: its implications in coffee breeding." In: *Journal of Coffee Research* 20.1, pp. 69–76.

Ramírez-Martínez, A., M. A. Salgado-Cervantes, G. C. Rodríguez-Jimenes, M. A. García-Alvarado, F. Cherblanc, and J. C. Bénet (2013). "Water transport in parchment and endosperm of coffee bean". In: *Journal of Food Engineering* 114.3, pp. 375–383. DOI: 10.1016/J.JFOODENG.2012.08.028.

Rao, M, S Rizvi, and A Datta (1994). *Engineering Properties of Food, Second Edition*. Taylor & Francis.

Rao, Scott (2014). *The Coffee Roaster's Companion*. Book, Whole.

— (2020). *Coffee Roasting Best Practices*.

Redgwell, Robert J, Véronique Trovato, Delphine Curti, and Monica Fischer (2002). "Effect of roasting on degradation and structural features of polysaccharides in Arabica coffee beans". In: *Carbohydrate Research* 337.5, pp. 421–431. DOI: 10.1016/S0008-6215(02)00010-1.

Resende, Isabela A, Marcela V C Machado, Claudio R Duarte, and Marcos A S Barrozo (2017). "An experimental analysis of coffee beans dynamics in a rotary drum". In: *The Canadian Journal of Chemical Engineering* 95.12, pp. 2239–2248. DOI: 10.1002/cjce.22961.

Ribeiro, Fabiana Carmanini, Flávio Meira Borém, Gerson Silva Giomo, Renato Ribeiro De Lima, Marcelo Ribeiro Malta, and Luisa Pereira Figueiredo (2011). "Storage of green coffee in hermetic packaging injected with CO2". In: *Journal of Stored Products Research* 47.4, pp. 341–348. DOI: 10.1016/J.JSPR.2011.05.007.

Rodrigues, Carla, Filipe Correia, Tiago Mendes, Jesus Medina, and Cláudia Figueira (2019). "CHAPTER 9 Post-roasting Processing: Grinding, Packaging and Storage". In: *Coffee:*

Production, Quality and Chemistry. The Royal Society of Chemistry, pp. 258–271. DOI: 10.1039/9781782622437-00258.

Romani, Santina, Chiara Cevoli, Angelo Fabbri, Laura Alessandrini, and Marco Dalla Rosa (2012). "Evaluation of Coffee Roasting Degree by Using Electronic Nose and Artificial Neural Network for Off-line Quality Control". In: *Journal of Food Science* 77.9, p. C965. DOI: 10.1111/j.1750-3841.2012.02851.x.

Rotta, Neil M, Stephen Curry, Juliet Han, Rommel Reconco, Edward Spang, William Ristenpart, and Irwin R Donis-González (2021). "A comprehensive analysis of operations and mass flows in postharvest processing of washed coffee". In: *Conservation & Recycling* 170, p. 105554. DOI: 10.1016/j.resconrec.2021.105554.

Rusinek, Robert et al. (2022). "How to Identify Roast Defects in Coffee Beans Based on the Volatile Compound Profile". In: *Molecules* 27.23, p. 8530. DOI: 10.3390/MOLECULES27238530/S1.

Santos, João Rodrigo, Miguel Lopo, António O S S Rangel, and João Almeida Lopes (2016). "Exploiting near infrared spectroscopy as an analytical tool for on-line monitoring of acidity during coffee roasting". In: *Food Control* 60, pp. 408–415. DOI: 10.1016/j.foodcont.2015.08.007.

Santos, João Rodrigo, Olga Viegas, Ricardo N M J Páscoa, Isabel M P L V O Ferreira, António O S S Rangel, and João Almeida Lopes (2016). "In-line monitoring of the coffee roasting process with near infrared spectroscopy: Measurement of sucrose and colour". In: *Food Chemistry* 208, pp. 103–110. DOI: 10.1016/j.foodchem.2016.03.114.

Schenker, Stefan (2000). "Investigations on the hot air roasting of coffee beans". PhD thesis. DOI: 10.3929/ethz-a-003889071.

Schenker, Stefan, Stephan Handschin, Beat Frey, Rainer Perren, and Felix Escher (2000). "Pore Structure of Coffee Beans Affected by Roasting Conditions". In: *Journal of Food Science* 65.3, pp. 452–457. DOI: 10.1111/j.1365-2621.2000.tb16026.x.

Schenker, Stefan, C Heinemann, M Huber, R Pompizzi, Rainer Perren, and Felix Escher (2002). "Impact of Roasting Conditions on the Formation of Aroma Compounds in Coffee Beans". In: *Journal of Food Science* 67.1, pp. 60–66. DOI: 10.1111/j.1365-2621.2002.tb11359.x.

Schenker, Stefan and Trish Rothgeb (2017). "The Roast - Creating the Beans' Signature". In: *The Craft & Science of Coffee*. Ed. by Britta Folmer. Academic Press, pp. 245–271. DOI: 10.1016/B978-0-12-803520-7.00011-6.

Schwartzberg, Henry (2002). "Modeling Bean Heating during Batch Roasting of Coffee Beans". In: DOI: 10.1201/9781420010169.ch52.

— (2006a). *Improving Industrial Measurement of the Temperature of Roasting Coffee Beans*.

— (2006b). *Modeling Exothermic Heat Generation during the Roasting of Coffee*.

— (2013). "Batch Coffee Roasting; Roasting Energy Use; Reducing That Use". In: Book, Whole, pp. 173–195.

Silva Araújo, Cintia da, Wallaf Costa Vimercati, Leandro Levate Macedo, Adésio Ferreira, Luiz Carlos Prezotti, Luciano José Quintão Teixeira, and Sérgio Henriques Saraiva (2020). "Predicting the Electric Conductivity and Potassium Leaching of Coffee by NIR Spectroscopy Technique". In: *Food Analytical Methods* 13.12, pp. 2312–2320. DOI: 10.1007/S12161-020-01843-Y/FIGURES/4.

Singh, Prem C, Rakesh K Singh, S Bhamidipati, Shyam N Singh, and Pete Barone (1997). "Thermophysical properties of fresh and roasted coffee powders". In: *Journal of Food Process Engineering* 20.1, pp. 31–50. DOI: 10.1111/j.1745-4530.1997.tb00409.x.

Sjarov, Martin, Tobias Lechler, Jonathan Fuchs, Matthias Brossog, Andreas Selmaier, Florian Faltus, Toni Donhauser, and Jörg Franke (2020). "The Digital Twin Concept in Industry - A Review and Systematization". In: *IEEE International Conference on Emerging Technologies and Factory Automation, ETFA* 2020-September, pp. 1789–1796. DOI: 10.1109/ETFA46521.2020.9212089.

Small, L E and R S Horrell (1993). "High Yield Coffee". In: 15th International Scientific Colloquium on Coffee.

Smrke, Samo, Marco Wellinger, Tomonori Suzuki, Franz Balsiger, Sebastian E W Opitz, and Chahan Yeretzian (2018). "Time-Resolved Gravimetric Method To Assess Degassing of Roasted Coffee". In: *Journal of agricultural and food chemistry* 66.21, pp. 5293–5300. DOI: 10.1021/acs.jafc.7b03310.

Solis, Lucia (2023). *Luxia Coffee*.

Telis-Romero, J., A. L. Gabas, M. A. Polizelli, and V. R.N. Telis (2009). "Temperature and water content influence on thermophysical properties of coffee extract". In: *International Journal of Food Properties* 3.3, pp. 375–384. DOI: 10.1080/10942910009524642.

Tsiafitsa, Anthi, Vasiliki Oikonomopoulou, Marina Stramarkou, Magdalini Krokida, and Nymphodora Papassiopi (2022). "Effect of heat treatment on physicochemical and sensory properties of selected coffee varieties". In: *European Food Research and Technology* 248.8, pp. 2009–2020. DOI: 10.1007/S00217-022-04025-8/FIGURES/6.

Tugnolo, Alessio, Roberto Beghi, Valentina Giovenzana, and Riccardo Guidetti (2019). "Characterization of green, roasted beans, and ground coffee using near infrared spectroscopy: A comparison of two devices". In: *Journal of Near Infrared Spectroscopy* 27.1, pp. 93–104. DOI: 10.1177/0967033519825665.

Uren, Kenneth R., Johandri Vosloo, Abraham F. van der Merwe, and George van Schoor (2023). "Heat and mass transfer modeling of an artisan coffee roasting process: A comparative study". In: *Drying Technology*, pp. 1–17. DOI: 10.1080/07373937.2023.2175851.

Van Boekel, M. A.J.S. (1996). "Statistical aspects of kinetic modeling for food science problems". In: *Journal of Food Science* 61.3, pp. 477–486. DOI: 10.1111/J.1365-2621.1996.TB13138.X.

Vargas-Elias, Guillermo, Paulo Correa, Natalia de Souza, and Evandro Melo (2016). "Kinetics of Mass Loss of Arabica Coffee During Roasting Process". In: *Engenharia Agrícola* 36.2, pp. 300–308. DOI: 10.1590/1809-4430-Eng.Agric.v36n2p300-308/2016.

Vosloo, J (2017). *Heat and mass transfer model for a coffee roasting process*.

Wang, Niya (2012). "Physicochemical Changes of Coffee Beans During Roasting". PhD thesis.

Wang, Niya and Loong-Tak Lim (2012). "Fourier Transform Infrared and Physicochemical Analyses of Roasted Coffee". In: *Journal of agricultural and food chemistry* 60.21, pp. 5446–5453. DOI: 10.1021/jf300348e.

Wang, Xiuju and Loong-Tak Lim (2014a). "A Kinetics and Modeling Study of Coffee Roasting Under Isothermal Conditions". In: *Food and Bioprocess Technology* 7.3, pp. 621–632. DOI: 10.1007/s11947-013-1159-8.

— (2014b). "Effect of roasting conditions on carbon dioxide degassing behavior in coffee". In: *Food Research International* 61, pp. 144–151. DOI: 10.1016/j.foodres.2014.01.027.

Wang, Xiuju and Loong-Tak Lim (2017). "Investigation of CO2 precursors in roasted coffee". In: *Food Chemistry* 219, pp. 185–192. DOI: 10.1016/j.foodchem.2016.09.095.

Whitaker, Stephen (1972). "Forced convection heat transfer correlations for flow in pipes, past flat plates, single cylinders, single spheres, and for flow in packed beds and tube bundles". In: *AIChE Journal* 18.2, pp. 361–371. DOI: 10.1002/AIC.690180219.

Wildman, R. D., J. M. Huntley, J. P. Hansen, D. J. Parker, and D. A. Allen (2000). "Single-particle motion in three-dimensional vibrofluidized granular beds". In: *Physical Review E* 62.3, p. 3826. DOI: 10.1103/PhysRevE.62.3826.

Wilson, Preston S (2014). "Coffee roasting acoustics". In: *The Journal of the Acoustical Society of America* 135.6, EL269. DOI: 10.1121/1.4874355.

Windows-Yule, C, J Seville, A Ingram, and D Parker (2020). "Positron Emission Particle Tracking of Granular Flows". In: *Annual review of chemical and biomolecular engineering*.

Windows-Yule, C. R.K., B. J. Scheper, A. J.Van Der Horn, N. Hainsworth, J. Saunders, D. J. Parker, and A. R. Thornton (2016). "Understanding and exploiting competing segregation mechanisms in horizontally rotated granular media". In: *New Journal of Physics* 18.2, p. 023013. DOI: 10.1088/1367-2630/18/2/023013.

Windows-Yule, C. R.K., A. J. Van Der Horn, D. R. Tunuguntla, D. J. Parker, and A. R. Thornton (2017). "Inducing axial banding in bidisperse-by-density granular systems using noncylindrical tumbler geometries". In: *Physical Review Applied* 8.2, p. 024010. DOI: 10.1103/PHYSREVAPPLIED.8.024010/FIGURES/7/MEDIUM.

Windows-Yule, Kit, Leonard Nicuşan, Matthew T Herald, Samuel Manger, and David Parker (2022). "Positron Emission Particle Tracking". In: *Positron Emission Particle Tracking*. DOI: 10.1088/978-0-7503-3071-8.

Yergenson, Nathan (2019). "Coffee Roasting Process Monitoring with In Situ NIR Spectroscopy". PhD thesis. University of Idaho.

Yilmaz, Nadir (2011). "Detailed multiphysics modeling and validation of thermocouple readings in fires". In: *http://dx.doi.org/10.1177/0734904111405303* 29.5, pp. 443–464. DOI: 10.1177/0734904111405303.

Zhu, Mengting, You Long, Yingjie Ma, Yousheng Huang, Yin Wan, Qiang Yu, Jianhua Xie, and Yi Chen (2022). "Investigation of thermal contaminants in coffee beans induced

by roasting: A kinetic modeling approach". In: *Food Chemistry* 378, p. 132063. DOI: 10.1016/J.FOODCHEM.2022.132063.

Chapter Nine

Appendices

9.1 Appendix: Determination of the viable operating range

For each roaster, the feasible operating range with regards to particle motion were determined qualitatively. Under ambient temperature conditions (such that coffee properties can be assumed constant with time), coffees of different density (green, part-roasted and roasted), selected to emulate physical changes during roasting, were loaded into the roaster, and batch size (mass basis), (m_{bs}), drum rotation speed (where appropriate), S_r (rpm, or arbitrary setpoint), and airflow (Hz, %, or arbitrary setpoint) were varied according to manufacturer recommendations (see Table 2.1). Different density coffees were obtained by roasting 8 kg of natural-processed Brazilian Arabica coffee in a drum roaster (TT8-10, Petroncini) to different roast degrees using a constant inlet air temperature (525°C) for 0, 5 and 10 mins to obtain green, part-roasted and roasted coffee samples whose bulk densities, ρ_{bulk} (kg m^{-3}), were 666, 456 and 319 kg m^{-3}, respectively.

For spouted (and fluid) bed roasters (RFB-S, RFB-Jr and Ikawa), airflow was increased from the minimum setpoint until particles spouted and motion in the bean-bed was established. Airflow required for minimum spouting was thus dependent on batch size, with larger batches requiring higher airflow for spouting. The maximum airflow setting was specified to ensure no beans were propelled beyond the roasting chamber (i.e., into the outlet, or chaff bin). Based on preliminary experiments, the recommended operating range for spouted (and fluid) bed roasters (RFB-S, RFB-Jr and Ikawa) are detailed in Table 9.1. For RFB-S and RFB-Jr

roasters, the maximum airflow set point (allowed by the control system) was appropriate for all tested batch sizes and coffee densities. For the Ikawa, the maximum airflow set point was dependent on coffee density only (i.e., batch size had no statistical impact).

Table 9.1: Utility functions that predict the recommended range of airflow setting (f) for RFB-S, RFB-Jr and Ikawa roasters according to coffee's batch size (m_{bs}) and bulk density (kg m^{-3}) (i.e., fill volume).

Roaster	**Set Point Type**	**Utility Function**	**R^2**
Neotec RFB-S	Minimum (Hz)	$f = 4.41 \times 10^{-3}\rho_{bulk} + 0.0389 m_{bs} + 23.72$	0.930
	Recommended (Hz)	$f = 2.20 \times 10^{-3}\rho_{bulk} + 0.0194 m_{bs} + 44.36$	0.930
	Maximum (Hz)	$f = 65$	
Neotec RFB-Jr	Minimum (Hz)	$f = -0.0199\rho_{bulk} + 4.71 m_{bs} + 30.67$	0.797
	Recommended (Hz)	$f = 9.95 \times 10^{-3}\rho_{bulk} + 2.35 m_{bs} + 40.33$	0.797
	Maximum (Hz)	$f = 50$	
Ikawa Pro V3	Minimum (%)	$f = 0.0284\rho_{bulk} + 0.50 m_{bs} + 37.20$	0.921
	Recommended (%)	$f = 0.0416\rho_{bulk} + 0.25 m_{bs} + 51.26$	0.892
	Maximum (%)	$f = 0.0548\rho_{bulk} + 65.33$	0.822

Table 9.2: Utility functions that predict recommended range of rotational speeds, (S_r) for the Petroncini drum roaster - units *au* refer to arbitrary units.

Roaster	**Set Point TYpe**	**Utility Function**	**R^2**
Bullet R1 V2	Minimum (au)	$S_r = 1$	
	Recommended (au)	$S_r = 5$	
	Maximum (au)	$S_r = 9$	
Petroncini TT8-10	Minimum (rpm)	$S_r = -0.0416\rho_{bulk} + 2.67 m_{bs} + 53.32$	0.888
	Recommended (rpm)	$S_r = -0.0350\rho_{bulk} + 2.33 m_{bs} + 63.48$	0.951
	Maximum (rpm)	$S_r = -0.0284\rho_{bulk} + 2.00 m_{bs} + 73.64$	0.993

For rotating drum roasters (Bullet and Petroncini), the drum's rotation speed was increased from the minimum setpoint until bean-bed motion was established and the flow regime resembled cascading motion. The minimum drum rotation speed was that at the transition

from rolling to cascading motion (Henein, Brimacombe, and Watkinson, 1983). For all roasters, these tests were repeated for batch sizes in the range given in Table 2.1 and for coffees of different densities (green, part-roasted and roasted). Recommended operating ranges for Petroncini and Bullet roasters are detailed in Table 9.2 – the R-squared of the function is also displayed to indicate goodness of fit. For the Bullet roaster, all applicable rotation speeds were appropriate for roasting and thus utility functions are invariant.

9.2 Appendix: Experimental data

Table 9.3: Experimental Data - Case Study I (Table 1 of 3)

Air Temp. (°C)	Initial Mass (g)	Final Mass (g)	Dimension (mm) a (mm)	b (mm)	c (mm)	Surface Area (mm^2)	Volume (mm^3)	Density ($kg\ m^{-3}$)
220	349.98	328.50	6.75±0.08	4.17±0.06	8.88±0.17	147.29±2.90	130.93±3.58	1058.13±29.23
220	350.01	303.85	7.57±0.09	4.95±0.10	9.84±0.16	188.62±4.13	193.58±6.88	669.93±17.65
220	350.03	295.23	7.31±0.12	4.88±0.09	9.74±0.17	181.61±4.44	182.72±6.41	653.35±8.77
220	349.97	290.44	7.60±0.07	4.83±0.08	10.27±0.15	193.70±3.95	198.47±6.15	607.57±12.64
235	350.05	336.07	6.33±0.08	4.07±0.11	8.14±0.15	129.89±3.29	110.34±4.34	1110.98±29.12
235	349.95	314.50	7.17±0.09	4.64±0.10	8.98±0.18	163.61±4.01	157.07±5.76	739.46±18.96
235	350.02	298.80	7.38±0.12	4.81±0.10	9.54±0.22	178.60±5.12	178.44±7.40	626.25±14.86
235	350.02	292.48	7.55±0.11	4.91±0.09	9.92±0.20	189.11±5.29	193.93±7.92	575.92±10.28
250	350.00	339.45	6.60±0.08	4.18±0.11	8.64±0.13	142.22±2.92	125.09±4.04	1082.75±29.23
250	350.01	321.83	7.08±0.10	4.42±0.09	9.07±0.16	159.92±4.81	150.55±7.14	844.23±22.57
250	350.00	302.26	7.49±0.08	5.01±0.08	10.17±0.13	193.39±3.19	200.21±5.18	626.59±11.33
250	350.02	292.19	7.63±0.07	4.90±0.08	10.42±0.10	197.65±2.92	204.26±4.90	589.18±8.27
265	349.99	341.40	6.24±0.09	4.28±0.10	8.36±0.17	134.69±3.27	117.08±4.13	1136.31±20.65
265	349.99	327.15	7.09±0.09	4.39±0.09	9.07±0.18	159.10±3.59	148.07±5.00	803.79±23.15
265	350.00	305.06	7.50±0.09	4.69±0.09	9.98±0.21	185.06±4.90	184.92±6.93	615.65±14.85
265	349.96	291.75	7.49±0.10	5.01±0.15	9.69±0.18	186.47±4.95	191.42±7.63	550.58±8.06
280	350.01	342.46	6.37±0.09	3.95±0.10	8.50±0.11	133.22±3.11	112.58±4.25	1189.61±24.56
280	349.98	330.09	6.90±0.12	4.38±0.11	9.10±0.16	156.86±4.69	145.64±6.66	942.99±29.04
280	349.98	310.28	7.58±0.13	4.83±0.09	10.07±0.18	190.37±4.79	193.91±6.90	610.84±14.91
280	350.02	294.85	7.65±0.10	5.00±0.11	10.04±0.14	194.23±4.21	201.88±6.78	574.41±10.57
Green	350.00	350.00	6.18±0.07	3.84±0.08	8.54±0.12	128.73±2.15	105.84±2.78	1310.8±11.75

Table 9.4: Experimental Data - Case Study I (Table 2 of 3)

Air Temp. (°C)	Time (s)	Moisture (kg kg^{-1})	Dry Mass (g)	Colour Whole	Colour Ground	Median Particle Size (µm)	Porosity (%)
220	175	0.0577±0.0003	309.54±0.12	46.94±0.68			48.79±4.68
220	350	0.0213±0.0002	297.37±0.09	61.36±0.29	55.57±0.04	461.70±2.86	56.11±1.52
220	525	0.0113±0.0001	291.90±0.06	66.02±0.63	64.27±0.05	454.65±2.42	57.03±0.91
220	700	0.0101±0.0002	287.50±0.07	69.06±0.38	68.51±0.20	462.06±3.06	57.14±1.25
235	104	0.0701±0.0002	312.50±0.09	36.89±0.75	21.13±0.09	476.57±1.83	45.4±2.94
235	208	0.0399±0.0005	301.94±0.23	53.19±0.21	40.25±0.43	463.44±4.73	56.07±1.52
235	312	0.0143±0.0001	294.53±0.03	62.75±0.37	56.74±0.26	433.12±0.88	56.73±1.77
235	415	0.0106±0.0004	289.39±0.16	69.22±0.32	62.65±0.07	428.87±0.05	58.32±2.03
250	69	0.0777±0.0001	313.09±0.04	36.00±0.29			49.13±2.48
250	138	0.0526±0.0001	304.89±0.04	50.13±0.72	36.08±0.27	473.06±2.51	51.55±7.95
250	209	0.0212±0.0003	295.85±0.11	62.83±0.19	56.12±0.13	444.81±1.05	57.25±1.88
250	278	0.0135±0.0003	288.23±0.13	70.36±0.41	68.37±0.14	471.44±1.23	58.41±1.79
265	054	0.0806±0.0001	313.88±0.07	33.44±0.45			44.13±4.37
265	108	0.0595±0.0003	307.69±0.13	45.52±0.32	31.22±0.20	470.27±0.58	48.5±5.66
265	164	0.0259±0.0002	297.15±0.09	58.96±0.10	49.04±0.52	441.46±0.04	57.1±2.83
265	218	0.0112±0.0000	288.49±0.02	70.19±0.25	65.05±0.14	459.51±1.58	59.06±0.53
280	42	0.0826±0.0002	314.17±0.10	37.92±0.51			44.73±1.58
280	84	0.0632±0.0007	309.24±0.34	46.03±0.36			56.96±2.82
280	126	0.0340±0.0003	298.90±0.14	56.97±0.07	45.79±0.14	451.65±1.77	61.98±1.03
280	168	0.0163±0.0001	290.03±0.04	70.44±0.11	66.18±0.30	453.86±1.31	65.35±0.61
Green	0	0.1006±0.0003	314.80±0.14	42.22±0.39			40.89±0.82

Table 9.5: Experimental Data - Case Study I (Table 3 of 3)

Air Temp. (°C)	Time (s)	Thermal Diffusivity ($mm^2\ s^{-1}$)	Volumetric Heat Capacity ($J\ m^{-3}$)	Thermal Conductivity ($W\ m^{-1}\ K^{-1}$)	Specific Heat Capacity ($J\ kg^{-1}\ K^{-1}$)
235	104	0.094±0.000	1.21±0.01	0.114±0.000	1088.3±4.7
235	208	0.100±0.001	1.05±0.03	0.104±0.004	1417.4±39.9
235	312	0.102±0.001	0.95±0.02	0.096±0.001	1509.6±29.4
235	415	0.103±0.001	0.92±0.01	0.095±0.000	1598.3±26.7
250	69	0.097±0.001	1.22±0.01	0.118±0.002	1126.9±12.7
250	138	0.101±0.001	0.94±0.01	0.095±0.000	1113.7±14.8
250	209	0.103±0.001	0.91±0.00	0.093±0.001	1451.9±4.3
250	278	0.096±0.000	0.87±0.02	0.083±0.002	1474.9±28.7
265	054	0.091±0.002	1.20±0.06	0.109±0.003	1060.0±50.3
265	108	0.097±0.001	1.12±0.03	0.109±0.001	1391.9±36.6
265	164	0.104±0.000	0.94±0.01	0.098±0.001	1532.9±12.1
265	218	0.105±0.000	0.88±0.01	0.092±0.001	1596.6±22.0

Table 9.6: Experimental Data - Case Study II (Table 1 of 2)

Batch Size (kg)	Fan Freq. (Hz)	Roast Time (s)	Mass Loss (%)	Bulk Density (kg m^{-3})	Water Activity	Moisture Content (%)	Porosity (%)	Dimension a (mm)	b (mm)	c (mm)	d (mm)
200	30	0	0	730.0±4.1	0.529±0.002	10.06±0.06	40.9±0.8	6.2±0.3	3.8±0.4	8.5±0.6	5.9±0.7
200	30	75	3.920588	541.0±10.1	0.464±0.004	6.88±0.01	44.3±1.7	6.7±0.7	4.2±0.5	8.4±0.9	6.1±1.0
200	30	150	11.05611	355.8±7.0	0.257±0.013	3.38±0.01	55.0±0.5	7.3±0.4	4.7±0.5	9.2±0.8	6.8±0.8
200	30	225	15.86238	319.6±0.7	0.130±0.015	1.37±0.00	57.9±0.2	7.6±0.7	5.0±0.6	9.9±1.0	7.2±1.1
200	48	0	0	730.0±4.1	0.529±0.002	10.06±0.06	40.9±0.8	6.2±0.3	3.8±0.4	8.5±0.6	5.9±0.7
200	48	72	0.669967	506.1±0.2	0.461±0.001	6.37±0.04	46.3±0.4	6.7±0.7	4.3±0.4	8.7±1.0	6.3±0.9
200	48	143	13.08631	334.5±2.6	0.169±0.020	2.36±0.02	57.1±1.2	7.3±0.5	5.1±0.6	9.6±0.9	7.1±1.0
200	48	215	16.63167	313.0±2.2	0.106±0.017	1.23±0.01	59.8±1.8	7.7±0.4	5.1±0.6	10.1±0.9	7.3±1.0
200	65	0	0	730.0±4.1	0.529±0.002	10.06±0.06	40.9±0.8	6.2±0.3	3.8±0.4	8.5±0.6	5.9±0.7
200	65	58	4.570457	510.4±10.1	0.485±0.001	6.75±0.08	48.8±1.7	6.7±0.5	4.5±0.5	8.8±0.8	6.4±0.9
200	65	117	11.91262	341.5±3.9	0.241±0.021	2.90±0.06	59.6±1.5	7.5±0.5	5.0±0.7	9.5±1.0	7.1±1.1
200	65	175	15.71107	321.8±3.7	0.145±0.023	1.37±0.02	59.0±0.8	7.5±0.5	4.8±0.6	9.9±1.0	7.1±1.1
350	39	0	0	730.0±4.1	0.529±0.002	10.06±0.06	40.9±0.8	6.2±0.3	3.8±0.4	8.5±0.6	5.9±0.7
350	39	109	4.91213	542.1±16.2	0.448±0.004	6.44±0.03	41.6±3.1	6.6±0.5	4.5±0.5	8.9±1.0	6.4±0.9
350	39	218	13.00323	353.5±0.7	0.179±0.004	2.27±0.05	56.9±1.3	7.4±0.4	4.9±0.7	9.4±0.8	7.0±1.1
350	39	328	17.27468	317.0±0.5	0.105±0.016	1.05±0.01	60.8±1.2	7.6±0.4	4.9±0.6	10.0±0.8	7.2±0.9
350	48	0	0	730.0±4.1	0.529±0.002	10.06±0.06	40.9±0.8	6.2±0.3	3.8±0.4	8.5±0.6	5.9±0.7
350	48	93	4.503243	551.0±7.2	0.464±0.002	6.61±0.19	46.2±2.7	6.7±0.5	4.3±0.6	8.9±0.9	6.3±1.0
350	48	185	12.13533	359.7±3.0	0.223±0.000	2.70±0.01	55.8±2.5	7.4±0.5	4.7±0.5	9.2±1.0	6.8±1.0
350	48	278	16.62094	321.5±3.1	0.093±0.011	1.22±0.01	59.6±1.5	7.5±0.5	5.0±0.6	10.2±0.8	7.3±1.0
350	65	0	0	730.0±4.1	0.529±0.002	10.06±0.06	40.9±0.8	6.2±0.3	3.8±0.4	8.5±0.6	5.9±0.7
350	65	85	5.044849	529.4±3.8	0.436±0.010	6.50±0.04	48.4±2.8	6.8±0.8	4.4±0.5	8.6±1.0	6.3±1.1
350	65	170	12.95032	350.0±0.1	0.171±0.008	2.33±0.09	57.2±0.8	7.6±0.6	5.0±0.6	9.9±0.9	7.2±1.0
350	65	255	17.01611	319.7±1.2	0.096±0.018	1.20±0.02	59.7±0.6	7.4±0.4	5.1±0.6	9.8±0.9	7.2±1.0
500	48	0	0	730.0±4.1	0.529±0.002	10.06±0.06	40.9±0.8	6.2±0.3	3.8±0.4	8.5±0.6	5.9±0.7
500	48	115	4.383649	569.8±6.5	0.465±0.003	6.49±0.06	46.6±3.1	6.8±0.6	4.1±0.4	8.6±0.8	6.2±0.9
500	48	230	12.10248	374.9±6.6	0.194±0.004	2.72±0.03	56.5±1.8	7.2±0.4	4.7±0.5	9.2±0.9	6.8±0.9
500	48	345	15.846	322.1±0.8	0.078±0.015	1.11±0.01	62.4±0.7	7.5±0.6	4.9±0.5	9.9±0.9	7.1±1.0
500	65	0	0	730.0±4.1	0.529±0.002	10.06±0.06	40.9±0.8	6.2±0.3	3.8±0.4	8.5±0.6	5.9±0.7
500	65	107	4.847709	553.6±3.4	0.463±0.000	6.39±0.06	56.6±4.1	6.7±0.5	4.3±0.5	8.6±0.8	6.2±0.9
500	65	213	12.80902	361.4±0.9	0.170±0.005	2.36±0.06	54.6±1.9	7.4±0.3	4.9±0.5	9.4±0.9	7.0±0.9
500	65	320	17.30331	318.7±3.1	0.071±0.004	1.13±0.04	57.9±0.4	7.6±0.4	5.0±0.5	10.1±0.9	7.3±0.9

Table 9.7: Experimental Data - Case Study II (Table 2 of 2)

Batch Size (kg)	**Fan Freq. (Hz)**	**Roast Time (s)**	Surface Area (mm^2)	Volume (mm^3)	Intrinsic Density ($kg\ m^{-3}$)	Colour Whole Bean	Colour Ground	Thermal Diffusivity ($mm^2\ s^{-1}$)	Heat Capacity ($kJ\ m^{-3}$)	Thermal Conductivity ($W\ m^{-1}\ K^{-1}$)	Specific Heat Capacity ($kJ\ kg^{-1}$)
200	30	0	161.6±15.2	105.8±13.9	1310.8±58.7	38.9±3.1	26.04±2.69	0.086±0.001	1698±20	0.145±0.003	1297.3±17.0
200	30	75	173.4±28.0	123.1±29.2	1047.1±114.5	33.9±3.1	19.25±2.65	0.097±0.000	1206±5	0.117±0.001	1153.9±8.4
200	30	150	213.5±27.5	168.9±30.9	670.4±66.1	54.8±3.8	42.62±2.30	0.100±0.001	952±27	0.095±0.003	1423.2±37.6
200	30	225	239.3±38.7	199.1±50.0	529.7±60.1	69.2±4.0	63.60±2.82	0.101±0.001	849±3	0.085±0.000	1596.6±8.6
200	48	0	161.6±15.2	105.8±13.9	1310.8±58.7	38.9±3.1	26.04±2.69	0.086±0.001	1698±20	0.145±0.003	1297.3±17.0
200	48	72	181.8±28.3	131.5±29.8	916.6±153.1	37.8±4.0	23.78±2.64	0.099±0.000	1156±17	0.115±0.002	1262.8±18.7
200	48	143	230.6±32.0	187.4±36.2	613.2±41.0	60.7±3.6	51.76±2.42	0.100±0.001	889±2	0.089±0.001	1449.0±3.2
200	48	215	248.0±28.5	207.1±33.1	542.4±54.0	70.3±3.7	66.22±2.98	0.101±0.000	850±5	0.086±0.000	1565.4±9.0
200	65	0	161.6±15.2	105.8±13.9	1310.8±58.7	38.9±3.1	26.04±2.69	0.086±0.001	1698±20	0.145±0.003	1297.3±17.0
200	65	58	188.8±27.7	138.2±29.8	956.4±148.2	37.0±4.0	21.65±2.81	0.097±0.003	1160±8	0.113±0.004	1216.9±10.3
200	65	117	228.7±32.8	187.1±38.1	612.7±69.6	57.0±3.7	45.43±2.31	0.102±0.001	912±7	0.092±0.000	1485.1±11.5
200	65	175	234.9±38.0	191.5±44.3	555.9±43.4	69.3±3.9	64.38±2.89	0.099±0.001	825±3	0.084±0.004	1530.6±51.4
350	39	0	161.6±15.2	105.8±13.9	1310.8±58.7	38.9±3.1	26.04±2.69	0.086±0.001	1698±20	0.145±0.003	1297.3±17.0
350	39	109	190.4±28.9	138.8±28.9	964.4±163.6	38.4±3.3	21.93±2.67	0.100±0.001	1171±5	0.117±0.001	1208.5±4.6
350	39	218	222.7±28.6	179.2±32.4	611.3±59.4	60.5±3.8	50.64±2.38	0.100±0.000	896±6	0.090±0.000	1465.7±6.9
350	39	328	238.3±22.3	194.1±26.1	537.8±44.8	70.4±3.9	67.08±3.00	0.099±0.001	856±2	0.084±0.001	1594.2±3.2
350	48	0	161.6±15.2	105.8±13.9	1310.8±58.7	38.9±3.1	26.04±2.69	0.086±0.001	1698±20	0.145±0.003	1297.3±17.0
350	48	93	185.3±29.5	133.4±31.3	990.4±136.1	37.3±3.6	20.15±2.74	0.097±0.001	1217±13	0.118±0.002	1232.0±13.9
350	48	185	212.5±32.5	168.0±35.1	659.6±62.4	56.5±3.7	46.47±2.44	0.101±0.001	942±11	0.095±0.000	1425.5±18.9
350	48	278	244.5±31.5	201.6±39.4	540.6±44.9	69.4±3.9	65.65±2.96	0.096±0.000	869±18	0.083±0.002	1608.1±31.3
350	65	0	161.6±15.2	105.8±13.9	1310.8±58.7	38.9±3.1	26.04±2.69	0.086±0.001	1698±20	0.145±0.003	1297.3±17.0
350	65	85	184.1±32.9	135.6±35.6	935.4±132.6	39.9±3.5	22.98±2.85	0.101±0.001	1176±10	0.118±0.001	1256.8±17.1
350	65	170	239.0±29.2	196.2±35.9	606.1±48.5	58.4±3.8	48.16±2.41	0.101±0.001	898±12	0.090±0.000	1483.3±16.2
350	65	255	236.6±27.7	193.6±32.3	554.5±52.4	69.5±4.0	66.16±2.94	0.098±0.001	865±23	0.085±0.001	1558.0±44.6
500	48	0	161.6±15.2	105.8±13.9	1310.8±58.7	38.9±3.1	26.04±2.69	0.086±0.001	1698±20	0.145±0.003	1297.3±17.0
500	48	115	179.0±26.6	128.5±28.1	1021.2±160.9	37.9±3.5	19.60±2.64	0.100±0.001	1170±4	0.116±0.001	1145.1±3.7
500	48	230	208.9±30.9	163.4±35.0	693.2±61.7	56.1±3.4	47.54±2.29	0.099±0.001	942±15	0.093±0.001	1356.9±27.6
500	48	345	234.9±32.6	191.8±39.9	547.1±48.1	69.3±3.7	66.94±2.99	0.098±0.002	854±46	0.083±0.002	1561.6±77.7
500	65	0	161.6±15.2	105.8±13.9	1310.8±58.7	38.9±3.1	26.04±2.69	0.086±0.001	1698±20	0.145±0.003	1297.3±17.0
500	65	107	178.4±23.4	127.6±24.3	986.8±186.4	39.3±3.1	22.39±2.96	0.100±0.001	1189±19	0.119±0.001	1208.5±22.3
500	65	213	221.5±25.3	177.3±26.9	641.0±64.1	57.8±3.4	49.62±2.35	0.101±0.000	898±4	0.090±0.000	1396.4±4.4
500	65	320	244.1±31.3	202.1±36.0	536.6±41.5	69.8±3.6	66.64±2.97	0.097±0.000	840±7	0.082±0.001	1572.4±14.9

9.3 Appendix: Experimental data

Table 9.8: Estimated parameters corresponding to kinetic models of coffee's physicochemical transformation during roasting.

Coffee	Inlet Air	Batch	Fan Freq.	Time	Mass Loss		Moisture Loss	
Type	Temp. (oC)	Size (g)	(Hz)	(s)	$k_{m_{bs}}$	$E_{a_{m_{bs}}}$	k_{X_b}	$E_{a_{X_b}}$
Kenyan Arabica	220	350	48	700	3.29×10^{-4}	0	4.13×10^{6}	7908
Kenyan Arabica	235	350	48	415	4.86×10^{-3}	2	4.13×10^{6}	7908
Kenyan Arabica	250	350	48	278	4.97×10^{-3}	902	4.13×10^{6}	7908
Kenyan Arabica	265	350	48	218	3.33×10^{-2}	1704	4.13×10^{6}	7908
Kenyan Arabica	280	350	48	168	7.40×10^{-2}	2015	4.13×10^{6}	7908
Kenyan Arabica	250	200	30	225	3.35×10^{-3}	657	4.13×10^{6}	7908
Kenyan Arabica	250	200	48	215	3.97×10^{-3}	657	4.13×10^{6}	7908
Kenyan Arabica	250	200	65	175	4.56×10^{-3}	657	4.13×10^{6}	7908
Kenyan Arabica	250	350	39	328	2.69×10^{-3}	657	4.13×10^{6}	7908
Kenyan Arabica	250	350	48	278	2.97×10^{-3}	657	4.13×10^{6}	7908
Kenyan Arabica	250	350	65	255	3.40×10^{-3}	657	4.13×10^{6}	7908
Kenyan Arabica	250	500	48	345	2.38×10^{-3}	657	4.13×10^{6}	7908
Kenyan Arabica	250	500	65	320	2.74×10^{-3}	657	4.13×10^{6}	7908

Table 9.9: Estimated parameters corresponding to kinetic models of coffee's physicochemical transformation during roasting.

Coffee	Inlet Air	Batch	Fan Freq.	Time	Volumetric Expansion				Density Evolution	
Type	Temp. (oC)	Size (g)	(Hz)	(s)	k_{V_b}	$E_{a_{V_b}}$	k'_{X_b}	$E'_{a_{X_b}}$	k_{ρ_b}	$E_{a_{\rho_b}}$
Kenyan Arabica	220	350	48	700	7.79	1500	0.04	3000	0.001	2901
Kenyan Arabica	235	350	48	415	7.85	1500	0.04	3000	0.001	2689
Kenyan Arabica	250	350	48	278	12.67	1500	0.04	3000	0.001	2563
Kenyan Arabica	265	350	48	218	13.22	1500	0.04	3000	0.001	2431
Kenyan Arabica	280	350	48	168	16.69	1500	0.04	3000	0.001	2409
Kenyan Arabica	250	200	30	225	12.79	1500	0.04	3000	0.001	2437
Kenyan Arabica	250	200	48	215	16.83	1500	0.04	3000	0.001	2305
Kenyan Arabica	250	200	65	175	20.96	1500	0.04	3000	0.001	2222
Kenyan Arabica	250	350	39	328	11.90	1500	0.04	3000	0.001	2488
Kenyan Arabica	250	350	48	278	11.89	1500	0.04	3000	0.001	2489
Kenyan Arabica	250	350	65	255	15.74	1500	0.04	3000	0.001	2377
Kenyan Arabica	250	500	48	345	9.35	1500	0.04	3000	0.001	2588
Kenyan Arabica	250	500	65	320	11.22	1500	0.04	3000	0.001	2508

Table 9.10: Estimated parameters corresponding to kinetic models of coffee's physicochemical transformation during roasting.

Coffee	Inlet Air	Batch	Fan Freq.	Time	Porosity Development			
Type	Temp. (oC)	Size (g)	(Hz)	(s)	k_{γ_b}	$E_{a_{\gamma_b}}$	k'_{X_b}	$E'_{a_{X_b}}$
Kenyan Arabica	220	350	48	700	0.63	1000	0.025	1000
Kenyan Arabica	235	350	48	415	0.72	1000	0.025	1000
Kenyan Arabica	250	350	48	278	0.89	1000	0.025	1000
Kenyan Arabica	265	350	48	218	0.93	1000	0.025	1000
Kenyan Arabica	280	350	48	168	1.64	1000	0.025	1000
Kenyan Arabica	250	200	30	225	0.92	1000	0.025	1000
Kenyan Arabica	250	200	48	215	1.15	1000	0.025	1000
Kenyan Arabica	250	200	65	175	1.56	1000	0.025	1000
Kenyan Arabica	250	350	39	328	0.76	1000	0.025	1000
Kenyan Arabica	250	350	48	278	0.89	1000	0.025	1000
Kenyan Arabica	250	350	65	255	1.06	1000	0.025	1000
Kenyan Arabica	250	500	48	345	0.83	1000	0.025	1000
Kenyan Arabica	250	500	65	320	0.94	1000	0.025	1000

9.4 Appendix: Sensitivity analysis - Geometry

Figure 9.1 compares predicted time-temperature (thermocouple and mean-bean) profiles for different roasting conditions and particle geometry (sphere, hemi-ellipsoid and 3D-scanned bean). Figure 9.1(a)-(c) shows the effect of particle geometry and different fan frequencies (i.e., airflow rates), Figure 9.1(d)-(f) the effect of particle geometry and different batch sizes and Figure 9.1(g)-(i) the effect of particle geometry and constant inlet air temperature. Figures 9.2, 9.3 & 9.4 are complementary to Figure 9.1 and illustrate the impact of particle geometry on the resolved in-bean temperature fields - data presented as contour plots correspond to roasting conditions of 350g 250°C & 48 Hz for spherical, hemi-ellipsoidal and 3D-scanned bean geometries, respectively.

9.5 Appendix: In-bean temperature distributions

The effect of roasting conditions on predicted in-bean temperature distributions are presented in Figures 9.5-9.10. Figures 9.5-9.7 correspond to case study I and show the effect of constant inlet air temperature on the time-temperature evolution of the bean for roasting conditions of 220°C, 250°C and 280°C, respectively - with corresponding time-temperature profiles in Figure 7.22. Figures 9.8-9.10 correspond to case study II and show the effect of different batch sizes on the time-temperature evolution of the bean for roasting conditions of 200g, 350g and 500g, respectively - with corresponding time-temperature profiles in Figure 7.23. Each figure depicts the temporal evolution of the bean's temperature field for specified roasting conditions.

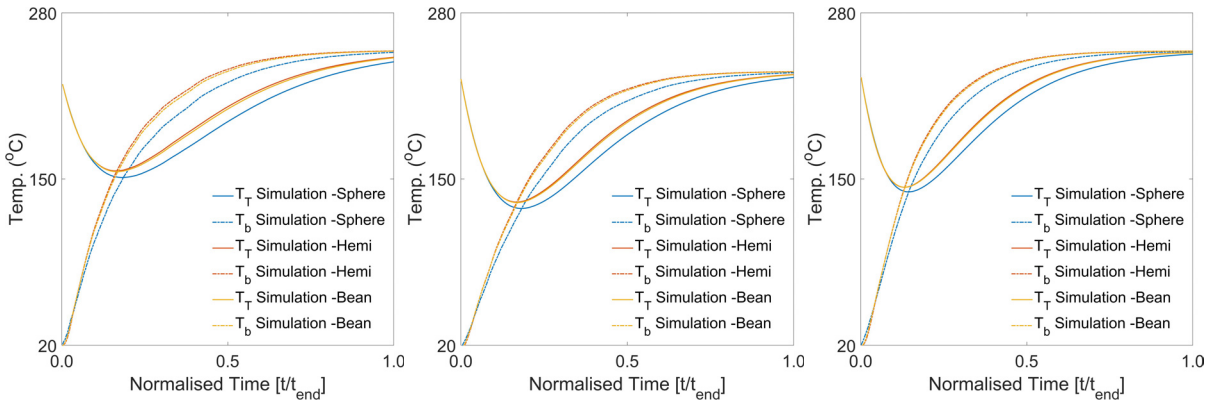

(a) 200g 250°C 30Hz (b) 200g 250°C 48Hz (c) 200g 250°C 65Hz

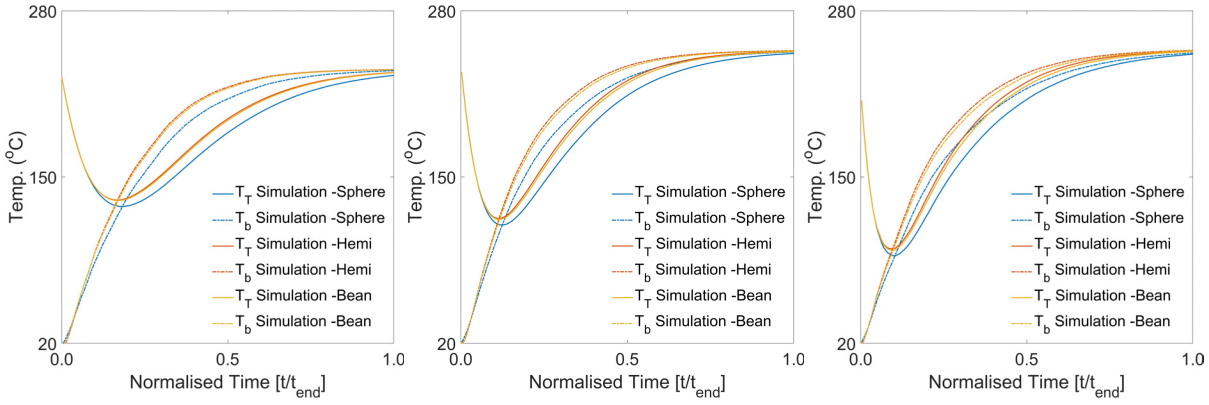

(d) 200g 250°C 48Hz (e) 350g 250°C 48Hz (f) 500g 250°C 48Hz

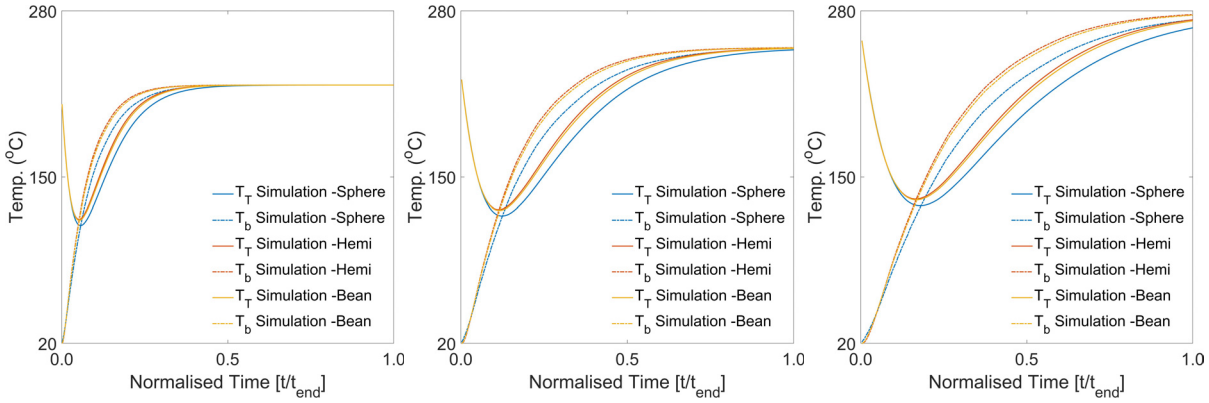

(g) 350g 220°C 48Hz (h) 350g 250°C 48Hz (i) 350g 280°C 48Hz

Figure 9.1: Comparison of the predicted bean and thermocouple time-temperature profiles that illustrate the impact of coffee bean geometry (sphere, hemi-ellipsoid and 3D-scanned bean) on the resolved roasting profiles for roasting with different (a)-(c) airflows, (d)-(f) batch sizes and (g)-(i) constant inlet air temperatures - data corresponds to roasting conditions of (a) 200g 250°C & 30 Hz, (b) 200g 250°C & 48 Hz, (c) 200g 250°C & 65 Hz, (d) 200g 250°C & 48 Hz, (e) 350g 250°C & 48 Hz, (f) 500g 250°C & 48 Hz, (g) 350g 220°C & 48 Hz, (h) 350g 250°C & 48 Hz and (i) 350g 280°C & 48 Hz.

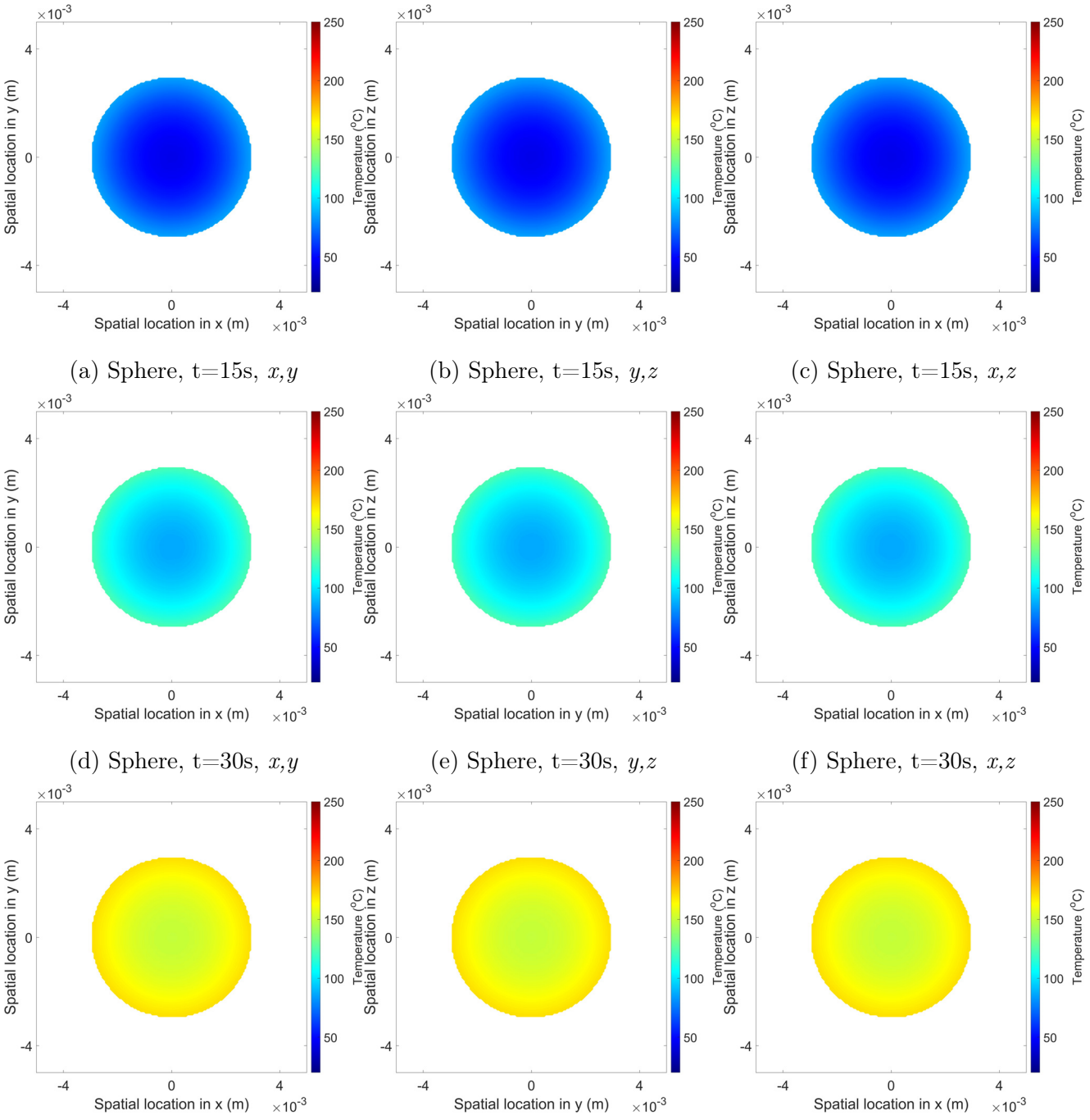

(a) Sphere, t=15s, x,y (b) Sphere, t=15s, y,z (c) Sphere, t=15s, x,z

(d) Sphere, t=30s, x,y (e) Sphere, t=30s, y,z (f) Sphere, t=30s, x,z

(g) Sphere, t=60s, x,y (h) Sphere, t=60s, y,z (i) Sphere, t=60s, x,z

Figure 9.2: Comparison of the predicted in-bean temperature distributions in the plane (a),(d),(g) x,y, (b),(e),(h) y,z and (c),(f),(i) x,z at simulated roasting times of (a)-(c) 15 s, (d)-(f) 30 s and (g)-(i) 60 s for spherical geometry - data corresponds to roasting conditions of 350g 250°C & 48 Hz.

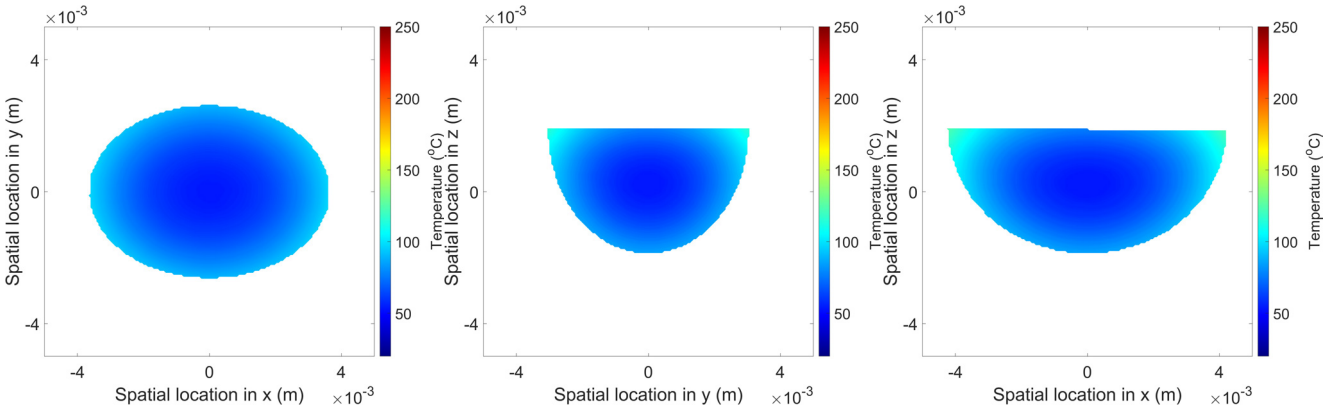

(a) Hemi-ellipsoid, t=15s, x,y (b) Hemi-ellipsoid, t=15s, y,z (c) Hemi-ellipsoid, t=15s, x,z

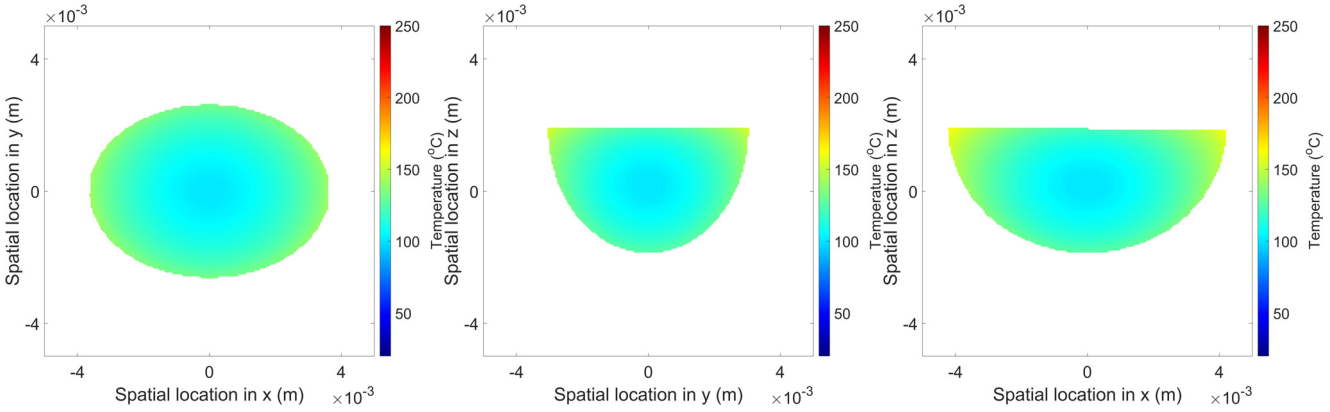

(d) Hemi-ellipsoid, t=30s, x,y (e) Hemi-ellipsoid, t=30s, y,z (f) Hemi-ellipsoid, t=30s, x,z

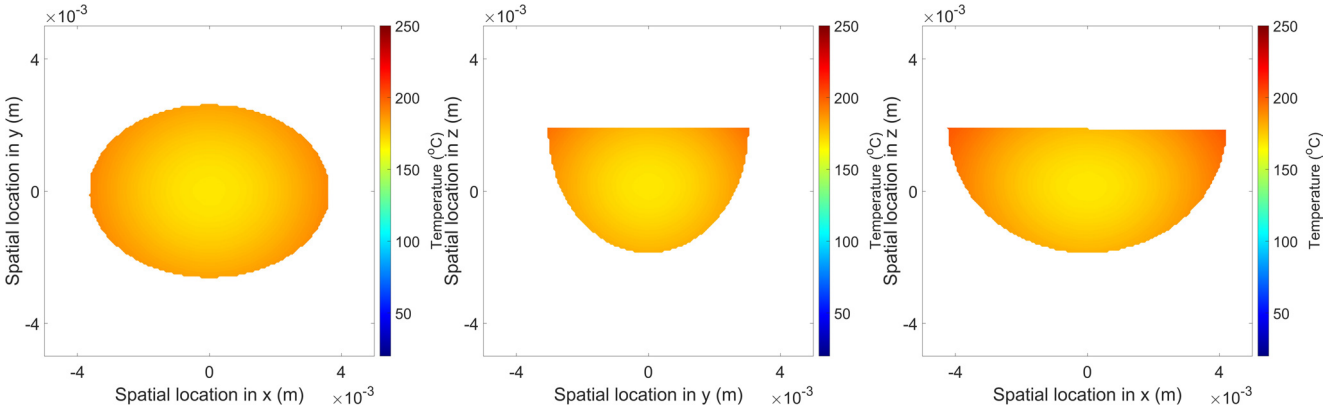

(g) Hemi-ellipsoid, t=60s, x,y (h) Hemi-ellipsoid, t=60s, y,z (i) Hemi-ellipsoid, t=60s, x,z

Figure 9.3: Comparison of the predicted in-bean temperature distributions in the plane (a),(d),(g) x,y, (b),(e),(h) y,z and (c),(f),(i) x,z at simulated roasting times of (a)-(c) 15 s, (d)-(f) 30 s and (g)-(i) 60 s for hemi-ellipsoidal geometry - data corresponds to roasting conditions of 350g 250°C & 48 Hz.

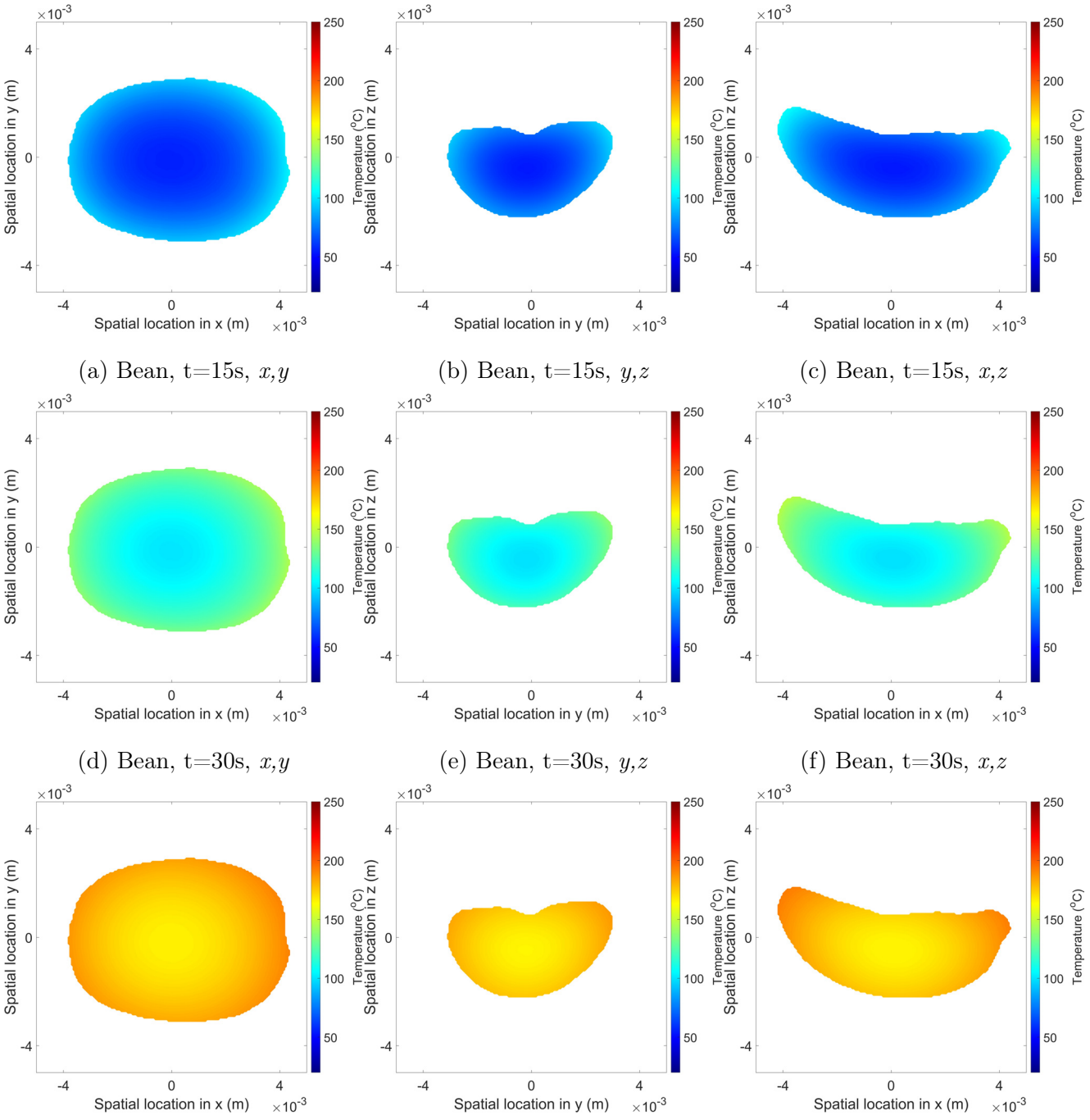

(a) Bean, t=15s, x,y (b) Bean, t=15s, y,z (c) Bean, t=15s, x,z

(d) Bean, t=30s, x,y (e) Bean, t=30s, y,z (f) Bean, t=30s, x,z

(g) Bean, t=60s, x,y (h) Bean, t=60s, y,z (i) Bean, t=60s, x,z

Figure 9.4: Comparison of the predicted in-bean temperature distributions in the plane (a),(d),(g) x,y, (b),(e),(h) y,z and (c),(f),(i) x,z at simulated roasting times of (a)-(c) 15 s, (d)-(f) 30 s and (g)-(i) 60 s for 3D scanned bean geometry - data corresponds to roasting conditions of 350g 250°C & 48 Hz.

Table 9.11: Solver times corresponding to different particle geometries and process conditions.

Batch	Fan Freq.	Inlet Air	Roasting	Solver Run Time (s)			Specific Solver Run Time (s s^{-1})		
Size (g)	**(Hz)**	**Temp. (°C)**	**Time (s)**	**Sphere**	**Hemi-Ellipsoid**	**Bean**	**Sphere**	**Hemi-Ellipsoid**	**Bean**
200	30	250	233	1153	1044	9179	4.9	4.5	39.4
200	48	250	223	1546	1292	15010	6.9	5.8	67.3
200	65	250	185	1459	1310	11021	7.9	7.1	59.6
350	39	250	336	1423	1249	13318	4.2	3.7	39.6
350	48	250	291	1476	1305	13746	5.1	4.5	47.2
350	65	250	264	1154	1065	11135	4.4	4.0	42.2
500	48	250	354	1032	943	9630	2.9	2.7	27.2
500	65	250	330	723	859	9157	2.2	2.6	27.7
350	48	220	713	3370	3058	27098	4.7	4.3	38.0
350	48	235	426	2035	1833	15806	4.8	4.3	37.1
350	48	250	286	1263	1263	10999	4.4	4.4	38.5
350	48	265	228	1077	966	8432	4.7	4.2	37.0
350	48	280	176	803	740	6374	4.6	4.2	36.2

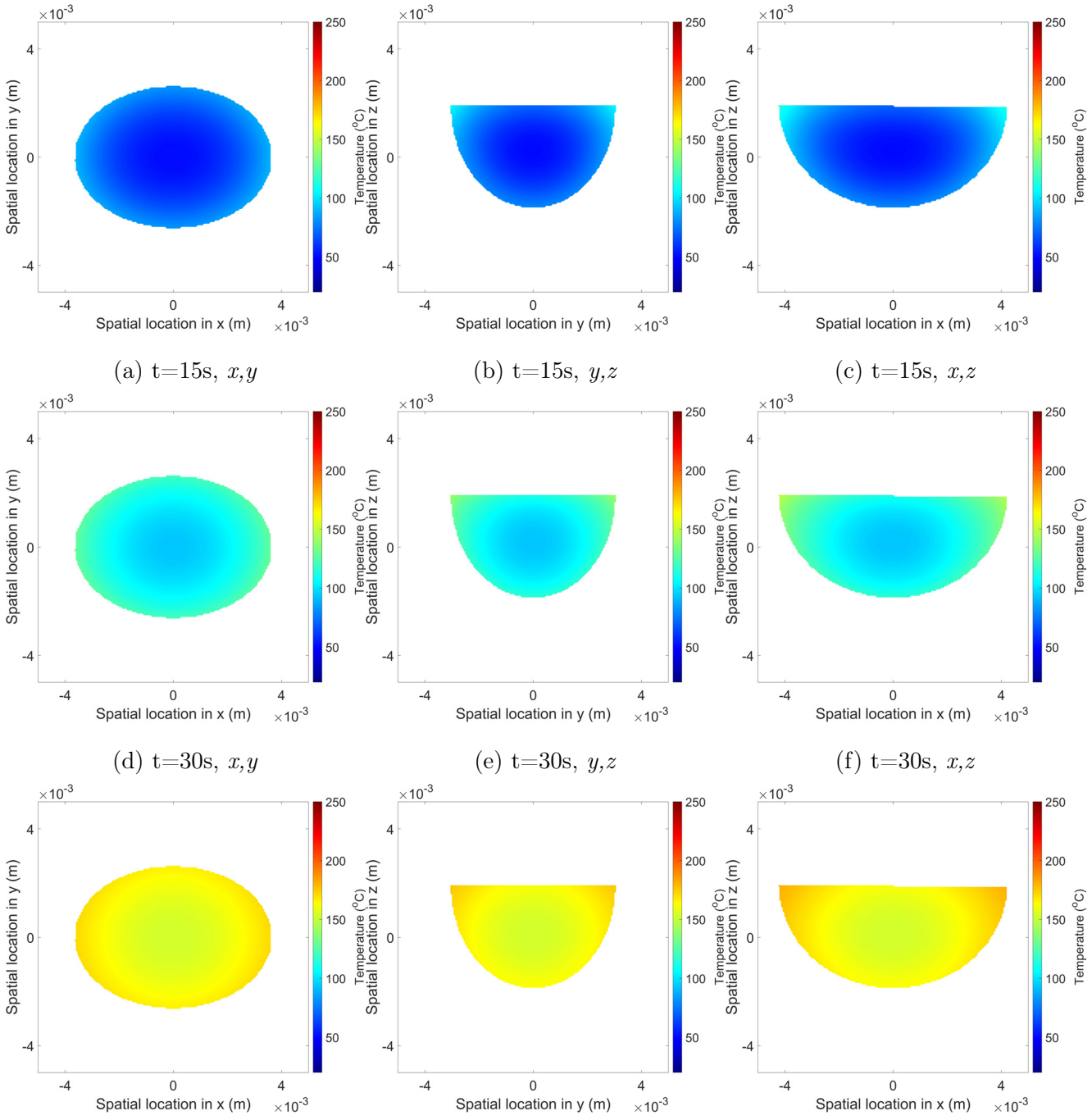

(a) t=15s, x,y (b) t=15s, y,z (c) t=15s, x,z

(d) t=30s, x,y (e) t=30s, y,z (f) t=30s, x,z

(g) t=60s, x,y (h) t=60s, y,z (i) t=60s, x,z

Figure 9.5: Predicted in-bean temperature distributions in the plane (a),(d),(g) x,y, (b),(e),(h) y,z and (c),(f),(i) x,z at simulated roasting times of (a)-(c) 15 s, (d)-(f) 30 s and (g)-(i) 60 s for hemi-ellipsoidal geometry - data corresponds to roasting conditions of 350g, 220°C & 48 Hz.

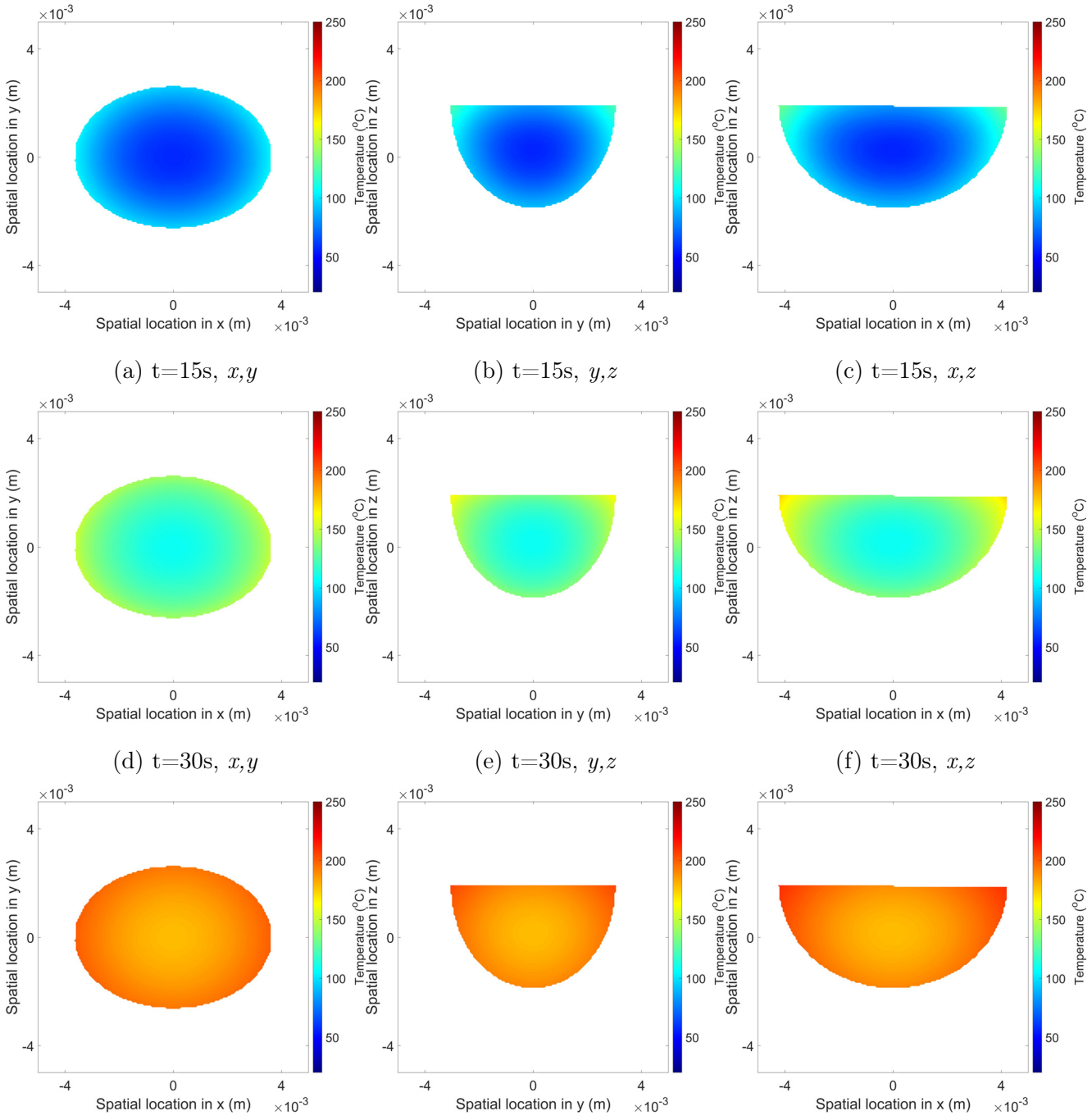

(a) t=15s, x,y (b) t=15s, y,z (c) t=15s, x,z

(d) t=30s, x,y (e) t=30s, y,z (f) t=30s, x,z

(g) t=60s, x,y (h) t=60s, y,z (i) t=60s, x,z

Figure 9.6: Predicted in-bean temperature distributions in the plane (a),(d),(g) x,y, (b),(e),(h) y,z and (c),(f),(i) x,z at simulated roasting times of (a)-(c) 15 s, (d)-(f) 30 s and (g)-(i) 60 s for hemi-ellipsoidal geometry - data corresponds to roasting conditions of 350g, 250°C & 48 Hz.

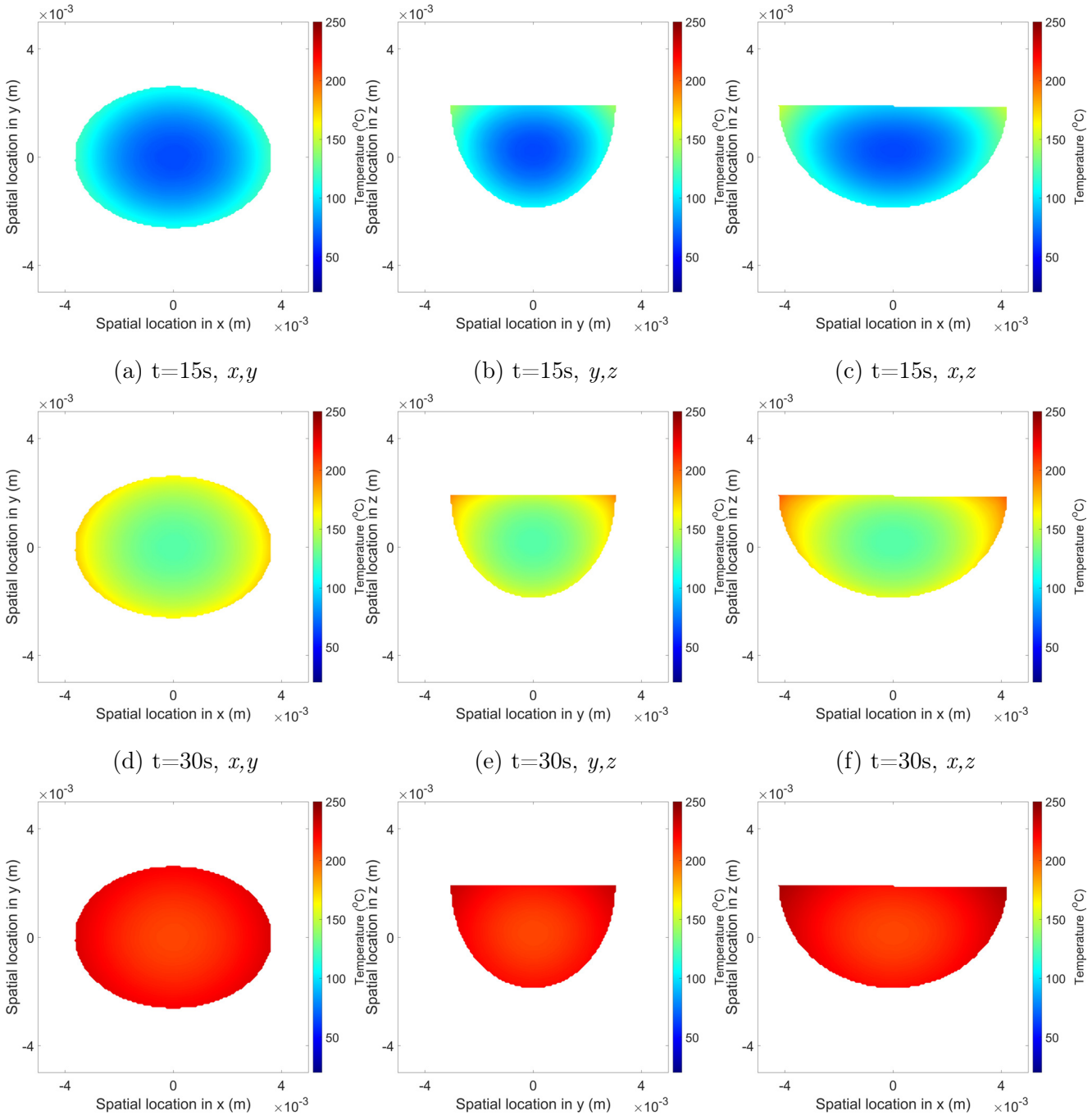

(a) t=15s, x,y (b) t=15s, y,z (c) t=15s, x,z

(d) t=30s, x,y (e) t=30s, y,z (f) t=30s, x,z

(g) t=60s, x,y (h) t=60s, y,z (i) t=60s, x,z

Figure 9.7: Predicted in-bean temperature distributions in the plane (a),(d),(g) x,y, (b),(e),(h) y,z and (c),(f),(i) x,z at simulated roasting times of (a)-(c) 15 s, (d)-(f) 30 s and (g)-(i) 60 s for hemi-ellipsoidal geometry - data corresponds to roasting conditions of 350g, 280°C & 48 Hz.

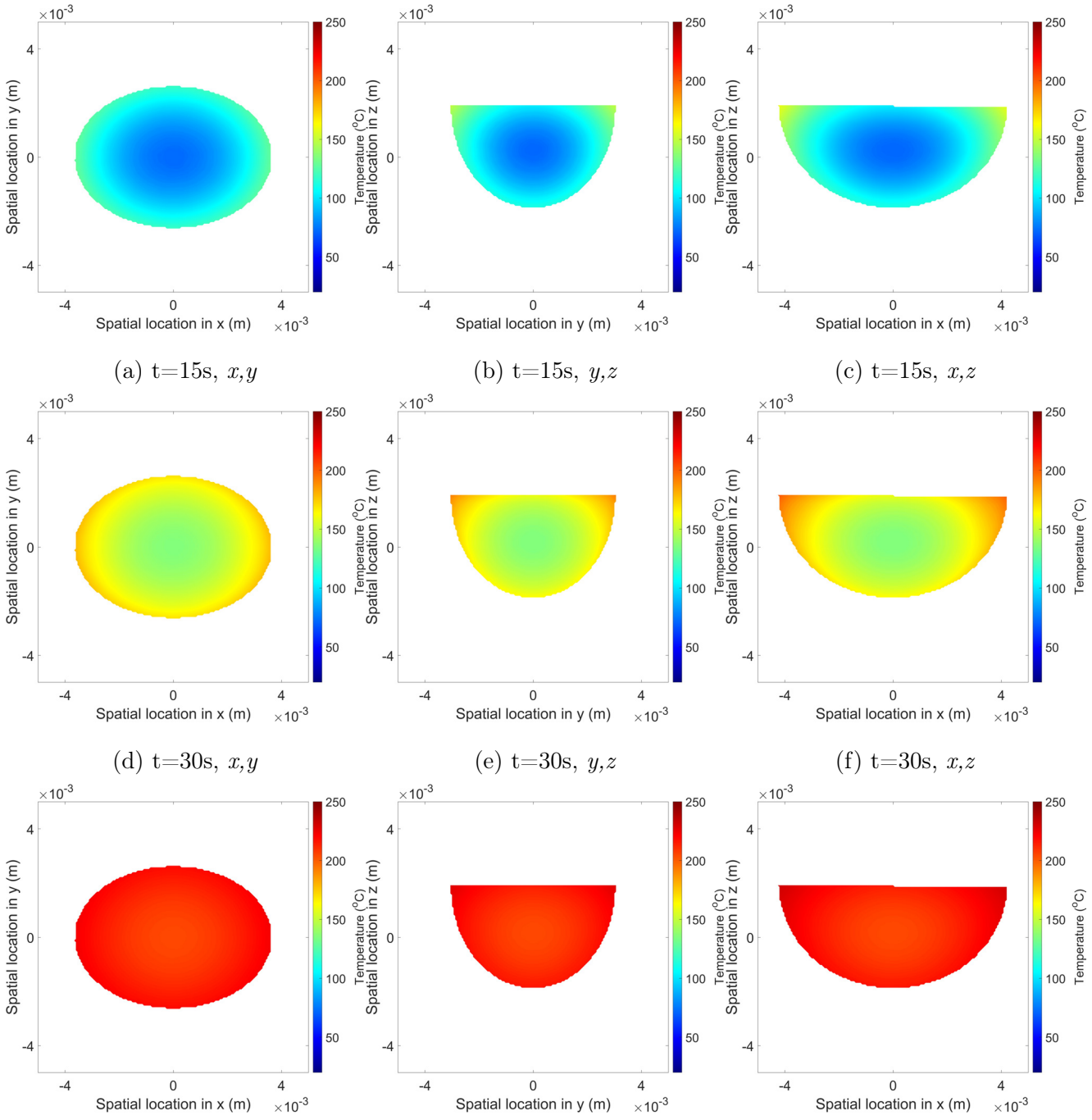

(a) t=15s, x,y (b) t=15s, y,z (c) t=15s, x,z

(d) t=30s, x,y (e) t=30s, y,z (f) t=30s, x,z

(g) t=60s, x,y (h) t=60s, y,z (i) t=60s, x,z

Figure 9.8: Predicted in-bean temperature distributions in the plane (a),(d),(g) x,y, (b),(e),(h) y,z and (c),(f),(i) x,z at simulated roasting times of (a)-(c) 15 s, (d)-(f) 30 s and (g)-(i) 60 s for hemi-ellipsoidal geometry - data corresponds to roasting conditions of 200g, 250°C & 48 Hz.

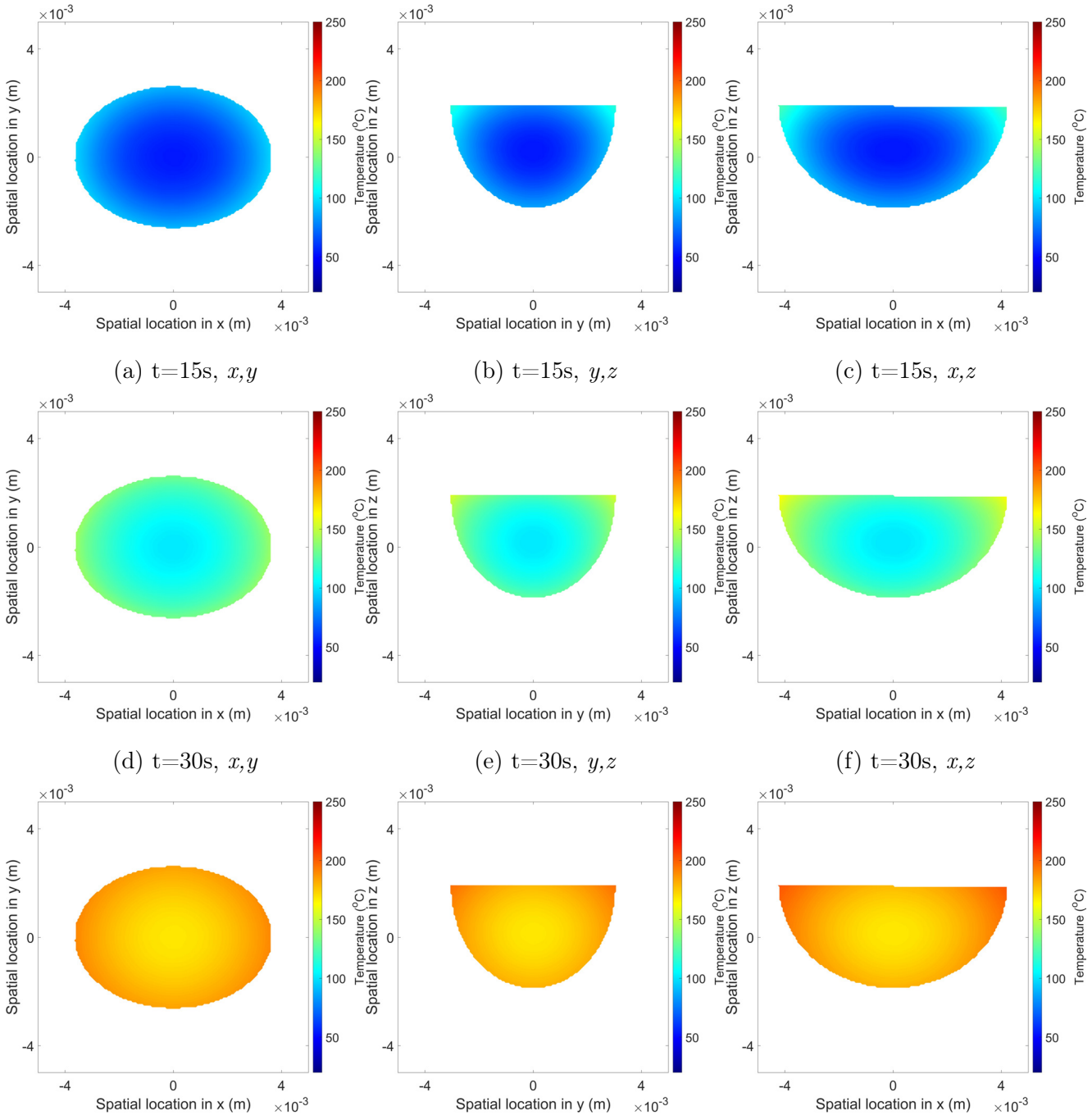

(a) t=15s, x,y (b) t=15s, y,z (c) t=15s, x,z

(d) t=30s, x,y (e) t=30s, y,z (f) t=30s, x,z

(g) t=60s, x,y (h) t=60s, y,z (i) t=60s, x,z

Figure 9.9: Predicted in-bean temperature distributions in the plane (a),(d),(g) x,y, (b),(e),(h) y,z and (c),(f),(i) x,z at simulated roasting times of (a)-(c) 15 s, (d)-(f) 30 s and (g)-(i) 60 s for hemi-ellipsoidal geometry - data corresponds to roasting conditions of 350g, 250°C & 48 Hz.

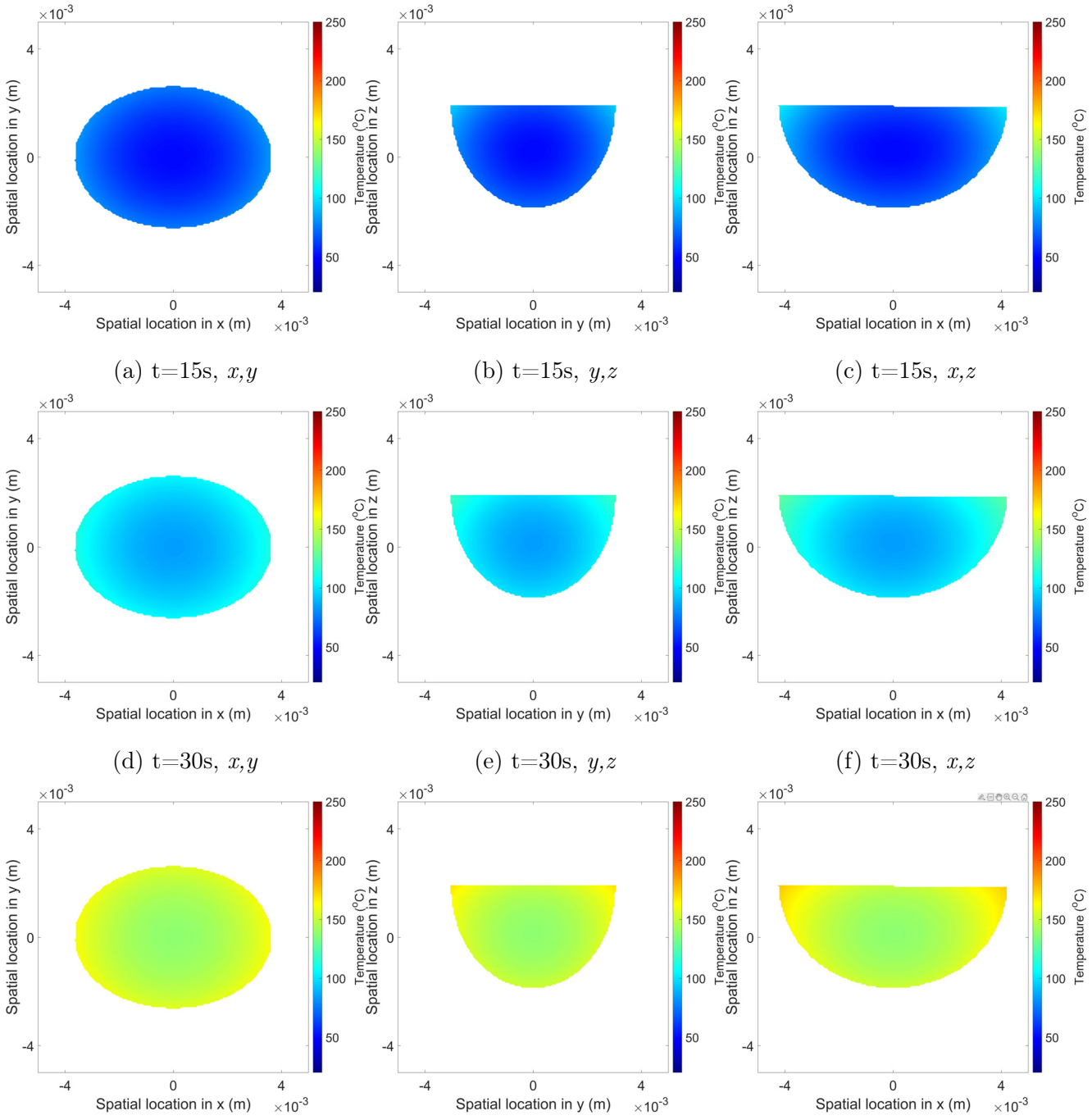

(a) t=15s, x,y (b) t=15s, y,z (c) t=15s, x,z

(d) t=30s, x,y (e) t=30s, y,z (f) t=30s, x,z

(g) t=60s, x,y (h) t=60s, y,z (i) t=60s, x,z

Figure 9.10: Predicted in-bean temperature distributions in the plane (a),(d),(g) x,y, (b),(e),(h) y,z and (c),(f),(i) x,z at simulated roasting times of (a)-(c) 15 s, (d)-(f) 30 s and (g)-(i) 60 s for hemi-ellipsoidal geometry - data corresponds to roasting conditions of 500g, 250°C & 48 Hz.